9902040045 - Part 8

YUCCA MOUNTAIN SITE DESCRIPTION

BOOK 3 SECTIONS 6,7

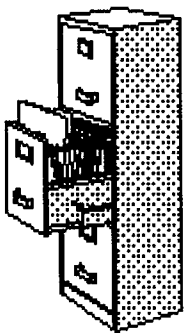

RECIEVED WITH LETTER DATED 9/30/98
FILE CODE 102.8 ACCESSION # 9902040045

WBS: 1.2.3.9
QA: L

Civilian Radioactive Waste Management System
Management & Operating Contractor

BOOK 3 - SECTIONS 6, 7

YUCCA MOUNTAIN SITE DESCRIPTION

B00000000-01717-5700-00019 REV 00

September 1998

Prepared for:

U.S. Department of Energy
Yucca Mountain Site Characterization Office
P.O. Box 30307
North Las Vegas, Nevada 89036-0307

Prepared by:

TRW Environmental Safety Systems Inc.
1261 Town Center Drive
Las Vegas, Nevada 89134-6352

Under Contract Number
DE-AC08-91RW00134

Disclaimer

CONTENTS

CONTENTS (Continued)

CONTENTS (Continued)

CONTENTS (Continued)

CONTENTS (Continued)

CONTENTS (Continued)

CONTENTS (Continued)

CONTENTS (Continued)

CONTENTS (Continued)

INTENTIONALLY LEFT BLANK

PREFACE

The *Yucca Mountain Site Description* (Site Description) presents our current understanding of the natural system at Yucca Mountain. The natural system is being characterized because of its key role in establishing the ability of the proposed repository at Yucca Mountain to demonstrate a safety case for the preclosure and postclosure periods. The natural system forms the environment for which engineered barriers must be designed. Working in concert, the natural and engineered systems must provide reasonable assurance that the health and safety of the public will be protected.

The safety strategy for the proposed repository relies on a number of key attributes of the natural and engineered systems at Yucca Mountain. These attributes are:

- The combined systems will limit water contacting the waste packages.
- The lifetime of the waste packages will be long.
- The rate of release of radionuclides from the waste form will be slow.
- The concentration of radionuclides will be reduced as they are transported through the engineered and natural barriers.

Site characterization activities have, in large part, addressed the scientific underpinnings of these attributes. They have focused on producing an adequate understanding of the natural system such that the performance of the proposed repository can be assessed. In addition, they also provide the framework for design of the proposed repository and the information needed to address requirements described in Part 60 of Title 10 of the Code of Federal Regulations.

The description of the site and surrounding region represents a snapshot in time. Results of characterization activities completed by the end of September 1997 are included. In some exceptional cases, additional work carried out during the early part of fiscal year 1998 is also discussed (e.g., results of a seismic hazard assessment). Because it represents a snapshot in time, and because it summarizes work carried out at different times, there are some inconsistencies within the document. As work to characterize the site reaches its completion and more complete integration of results is accomplished these inconsistencies will be resolved, and the technical information will be better integrated both between and within chapters.

The Site Description summarizes and synthesizes both work carried out in accordance with the *Quality Assurance Requirements and Description* (DOE/RW-0333P) and also work performed outside that quality assurance program. Because the Site Description is a summary and synthesis document, no data were generated in preparing it. In general, information on the quality status of data discussed in the Site Description is, therefore, found in the reports forming the basis for the summarized material and cited in the text. In some cases, however, information on the quality status of data is specifically addressed in the Site Description. For Section 3, the Q status of some references is indicated by a [Q] or [NON-Q] notation in the reference list. For references without a notation, the source document should be consulted. In Section 5.3, the Q status of many data sets is addressed in the subsections in which the data are discussed. Q status of data in Sections 6.1 and

6.4 is described at the end of Section 6.4. For data in Section 6.3, the Q status of data is listed in the introduction to the section. For all other sections, readers interested in the Q status of data should consult the source references cited in the text.

For some of the data discussed in the Site Description, a Data Tracking Number (DTN) is provided. These numbers indicate that the data are available in the Technical Data Management System. In other cases, the location of data is addressed in the cited references. Although for future revisions a data verification process will be implemented to ensure data are available in the Technical Data Management System and that the DTNs cited are correct, this version has not benefited from such a quality check. At the present time, therefore, cited data should be considered "to be verified (TBV)."

The Site Description will evolve over the next several years to support the Site Recommendation and, if the recommendation is favorable and approved, a license application. New results will be incorporated and integration of the various sections will be enhanced. Thus, while the findings presented in this document represent our understanding today, ongoing and future work may modify some of the conclusions.

The Site Description begins with a brief discussion of the geography and demography of the site. It then describes relevant facilities that are located at the site or in its vicinity. This is followed by a presentation of the current state of knowledge for the site's geology, climatology and meteorology, hydrology, and geochemistry. Finally, the effects of repository construction, including especially heat, are addressed as they affect the geomechanical, geohydrological, and geochemical aspects of the natural environment in the near-field and altered zone.

ACRONYMS

ADEM	Automated Digital Electron Microscope
AZ	Altered Zone
BLM	Bureau of Land Management
BREN	Bare Reactor Experiment Nevada
CHn	Calico Hills nonwelded
CNWRA	Center for Nuclear Waste Regulatory Analyses
CRWMS	Civilian Radioactive Wast Management System
DOE	U.S. Department of Energy
DOPA	Dihydroxyphenylalanine
DTN	Data Tracking Number
ESF	Exploratory Studies Facility
IARC	International Agency for Research on Cancer
INAA	Instrumental Neutron-activation Analysis
IRSR	Issue Resolution Status Report
LA	License Application
MAP	Mean Average Precipitation
MAT	Mean Average Temperature
M&O	Management and Operating Contractor
MSL	Mean Sea Level
NAFA	Nordic Aquatic Fulvic Acid
NFE	Near-Field Environment
NRC	U.S. Nuclear Regulatory Commission
OIS	Oxygen Isotope Stage
PET	Pentaerythritol
PTn	Paintbrush Tuff Nonwelded
R/EFPD	Radiological/Environmental Field Programs Department
RMR	Rock Mass Rating
RQD	Rock Quality Designation
SMOW	Standard Mean Ocean Water
SNL	Sandia National Laboratories
SZ	Saturated Zone

ACRONYMS (Continued)

TCw	Tiva Canyon Welded
TDIF	Technical Data Information Form
TSPA	Total System Performance Assessment
TSw	Topopah Spring welded
USAF	U.S. Air Force
USGS	U.S. Geological Survey
UZ	Unsaturated Zone
VA	Viability Assessment
YMP	Yucca Mountain Site Characterization Project

SYMBOLS/UNITS

Ag	silver
Al	aluminum
Am	americium
Ar	argon
As	arsenic
Au	gold
Ar	argon
B	boron
b.y.	billions of years
Ba	barium
Be	beryllium
C	carbon
°C	degree celsius
Ca	calcium
Ce	cerium
Cl	chlorine
Co	colbalt
Cr	chromium
Cs	cesium
DC	direct current
Eu	europium
F	fluorine
Fe	iron
Ga	giga-annum
Gd	gadolinium
H	hydrogen
Hf	hafnium
K	potassium
k.y.	thousands of years
ka	kilo-annum
La	lanthanum
Li	lithium
Lu	lutetium
m.y.	millions of years
Ma	mega-annum
md	millidarcy
Mg	magnesium
mL/g	milliliters per gram
Mn	manganese
MPa	megapascals
N	nitrogen
Na	sodium
Nb	niobium
Np	neptunium

SYMBOLS/UNITS (Continued)

O	oxygen
P	phosphorus
Pb	lead
pCi	picocurie
pmc	percent modern carbon
ppm	parts per million
ppmv	parts per million by volume
Pr	praseodymium
Pu	Plutonium
Rb	rubidium
S	sulfur
Sc	scandium
Si	silicon
Sm	samarium
Sr	strontium
Ta	tantalum
Tb	terbium
Tc	technetium
Th	thorium
Ti	titanium
U	Uranium
Y	yttrium
Yb	ytterbium
Zr	zirconiom
‰	parts per mil

6. GEOCHEMISTRY

6.1 GEOCHEMISTRY OF THE SITE AND THE SURROUNDING REGION

Introduction–Petrology and geochemistry provide the fundamental descriptors of any suite of rocks. Comprehensive studies of petrology, mineralogy, and geochemistry were early recognized as important components of site studies (10 CFR 960, *General Guidelines for the Recommendation of Sites for Nuclear Waste Repositories*, Appendix IV). Petrologic studies at Yucca Mountain provide detailed information on rock properties that reveal origins and alteration processes that have operated at the site. This information is important in interpreting the site stratigraphy and structure. The mineralogy of samples from the site is critical information, because minerals are the fundamental units with which the rocks respond to fluids and to thermal stress. Studies of the minerals that comprise the rocks also provide information that is needed to interpret the previous cooling history and the past history of water-rock interaction at the site. The history of mineralogical alteration provides insights into the long-term and large-scale changes that can occur at the site under thermal loading, on scales that can never be matched in the laboratory. This information is vital to validation of complex models of long-term site behavior. Geochemical data collected at the site provide a baseline for comparison with introduced waste elements and chemical species. Geochemical analysis provides evidence of where and how element migration has occurred in the past, both in the unsaturated zone and in the saturated zone. The geochemical studies reveal anomalies that, when interpreted in light of the associated mineralogy, reveal how waste elements may move and where they may be accumulated or dispersed.

Quality Assurance Controls–Yucca Mountain Site Characterization Project (YMP) work summarized in this section comes under the control of the *Quality Assurance Requirements and Description* (DOE 1997). Some of the information presented and discussed, however, was developed outside of the YMP and has been included here through examination of the hydrogeological literature. Thus, the quality assurance status of the data in this section is determined by the activities and reports from which the description was synthesized. To determine the Q status of a particular data set, interested readers should consult the source document cited in the text. As an aid in determining the Q status of data in this section, consult the material on data traceability at the end of Section 6.4.

Analytical Methods–Methods modified or adapted specifically for Yucca Mountain Site Characterization Project (YMP) studies are described below in detail. Methods that are common or routine analyses are described briefly.

Petrographic Analysis–Standard petrographic analysis was performed using polished thin sections. For modal petrography, standard point counts were obtained using both transmitted and reflected light. Between 500 and 5,000 counts were made per sample to determine the abundance of phenocrysts, lithic fragments, and voids in thin sections. For evaluation of textural variability in the devitrified matrix of the Topopah Spring Tuff, the textural categories of granophyric, amygdaloidal, microlitic/spherulitic, and cryptocrystalline were used in point counting. For these studies of textural variability, 5,000 to 6,000 points were generally counted per thin section. In some petrographic studies, optical observations on polished thin sections were supplemented by imaging with either a Tracor-Northern Automated Digital Electron

Microscope or an International Scientific Instruments DS-130 electron microscope in backscattered-electron mode.

Microautoradiography–Splits of samples used for microautoradiography were analyzed by quantitative X-ray diffraction to determine mineral abundance. These splits were obtained from sample portions used for thin-section preparation or from nearby rock portions. A Siemens D-500 diffractometer was used, employing Cu-Kα radiation and a Kevex Psi Si(Li) solid-state detector. A split of each sample was mixed with a 1.0-μm corundum internal standard in a sample: corundum ratio of 8:2 by weight. The quantitative mineralogy was determined by matrix-flushing methods. Accuracies of quantitative X-ray diffraction measurements have been evaluated against a series of standard "test rocks," summarized in Chipera and Bish (1995). In addition to quantitative X-ray diffraction analysis, a hand-separated split of the highly actinide-retentive phase mixture in sample #1895 (zeolitic tuff) was analyzed by semiquantitative X-ray diffraction to verify that this mineral mixture consisted of smectite plus the Mn-oxide mineral rancieite.

The waters used for the sorption experiments were waters from Well J-13 (filtered through a 0.05 μm filter) and a sodium-bicarbonate buffer (simulating the water chemistry of the water from Well UE-25 p#1). The synthetic UE-25 p#1 water was prepared by dissolving 0.39 g of Na_2CO_3 and 8.90 g of $NaHCO_3$ in 10 L of deionized water. The reason for having to use synthetic UE-25 p#1 for the sorption experiments was the unavailability of water from Well UE-25p #1.

The Am, Pu, and U solutions used for the batch-sorption experiments were prepared by taking an aliquot of a well-characterized $^{241}Am(III)$, $^{233}U(VI)$, or $^{239}Pu(V)$ acidic stock and diluting it in the groundwater being studied. Plutonium(V) in the concentrated acidic stock disproportionates into Pu(IV) and Pu(VI); consequently, dilution of the Pu(V) acidic stock was performed immediately after preparation of the stock Pu(V) solution. Nitsche, Gatti et al. (1993) and Nitsche, Roberts et al. (1994) reported the solubility and speciation of Am and Pu in J-13 and UE-25 p#1 well waters at room temperature at pH values of 7 and 8.5. These data are summarized in Tables 6.1-1 and 6.1-2.

The ^{233}U solution used for the autoradiography experiments was prepared by adding an aliquot of a well-characterized U(VI) acidic stock to each groundwater to obtain a U concentration of 10^{-5} M in J-13 water and 10^{-5} M in UE-25 p#1 water. The ^{239}Pu solution used for the autoradiography experiments was prepared by adding an aliquot of a well-characterized Pu(V) acidic stock to each groundwater to obtain a Pu concentration of 2.9×10^{-7} m in J-13 water and 10^{-6} M in UE-25 p#1 water. The ^{241}Am solution used for the autoradiography experiments was prepared by adding an aliquot of a well-characterized Am(III) stock to each groundwater to obtain an Am concentration of 2.4×10^{-9} m in J-13 water and 2.4×10^{-9} M in UE-25 p#1 water.

Using silicone rubber or similar pliable adhesive, a glass rod was attached to the back side of a thin section (the back side of the thin section does not have the actual rock sample attached to it and is etched with the sample I.D.). The rod attached to the thin section was then affixed to a rubber stopper held within a beaker. After the adhesive dried, the stopper, with glass rod and attached thin section, was removed from the beaker. In a clean beaker, 25 mL of the chosen tracer solution was added and the rubber stopper with glass rod and attached thin section

inserted. The thin section was lowered so that only the surface of the thin section was in contact with the tracer solution. The thin sections remained in contact with the tracer solutions for at least 8 hours. Upon removal from the tracer solution, each thin section was placed in a beaker of deionized water for one minute.

The radioactivity in each thin section was measured with a methane flow proportional counter. Each thin section was then immersed in a solution containing 4 g of parlodion in 200 mL of methyl alcohol and 200 mL of ethyl ether, which gives the thin section protection from further contact with water. After the parlodion solution dried, each thin section was counted. A thin layer of gelatin prepared with 2 g of gelatin and 0.25 g of $KCr(SO_4)_2 \cdot 12\ H_2O$ in 400 mL of deionized water was applied to each section and dried. A thin coating of Kodak radiography emulsion was then mounted on the thin sections in a darkroom equipped with red safelights. The emulsion was coated on the thin sections by contacting each section with the surface of the emulsion. Each thin section was then placed in a light-tight box and exposed until about 10^6 α disintegrations of the sorbed radionuclide per cm^2 of emulsion were obtained; exposure time was based on the α activity measured with the methane flow proportional counter. After exposure, the emulsion still in contact with each sample was developed and fixed using Kodak D-19 developer and Kodak fixer. The emulsion dried to a nearly transparent coating.

In parallel with analysis of the emulsion-coated thin sections, petrographic analysis was used to characterize minor and trace minerals in standard thin sections ("library" thin sections). Analysis of developed actinide decay tracks in emulsion-coated microautoradiography sections was done at magnifications up to 500x. Track abundances were estimated optically and comparative track abundances were compiled. Phase identification was aided by references to "library" thin sections that were not exposed to radionuclides or coated by emulsion.

Measurements of Ag in emulsion were obtained with a Cameca SX-50 electron microprobe (15 keV accelerating potential, 15 na beam current, and 10-μm spot size). Emission of the Ag L-line was peaked on a pentaerythritol crystal using pure Ag metal. A representative coating of the radiographic emulsion on a glass slide, exposed to full sunlight for saturation, developed, and fixed, was also examined to evaluate the Ag signal of a saturated emulsion. Backgrounds for both the Ag metal and the saturated emulsion were obtained at $\pm 0.01200\ \sin\Theta$. In analysis of actual samples, line scans were collected across selected locations on the developed emulsion surfaces of actinide-exposed thin sections. The dwell time per spot in each line scan was 15 s, with a ~12-μm spacing between spots along the line of scan. The resolution of individual particle tracks in optical analysis is only possible at track concentrations less than ~5 percent of saturation. In contrast, electron microprobe analysis provides nearly linear Ag abundance data at up to ~60 percent of emulsion saturation and can provide quantitative results at higher saturations with a quadratic fit (Benjamin, T.M. et al. 1977).

"Raw counts" for Ag can be misleading; there is a certain level of background Ag in any developed emulsion, varying with handling and development and fixation parameters, and often triggered by scratching or bruising of the emulsion during processing. Flawed areas in the emulsions must be avoided in electron microprobe analysis or expunged from the line scans collected. Background correction can be obtained by analyzing epoxy, quartz, feldspar, or another essentially track-free substrate; generally, such a track-free spot is measured along any

traverse with a reasonable number of sampling points. These track-free spot data provide a "local background" for correcting raw counts. However, background traces can also be collected over the margins of the thin sections, where only epoxy occurs and radionuclide fixation is rare.

Chemical Analysis–X-ray fluorescence analyses for major elements were performed both at Los Alamos National Laboratory and at J. Husler's laboratory at the University of New Mexico. As part of these analyses, volatile-component loss-on-ignition was also determined. Ion chromatography analyses (Cl, N, S, P_2O_5, and C_2O_4) were obtained at Los Alamos National Laboratory using a Dionex 4500i ion chromatograph with a conductivity detector.

Trace-element analyses and analyses of Ca, Fe, Na, and/or K were obtained by instrumental neutron-activation analysis. These data were collected in the trace-element geochemistry laboratory at Washington University, St. Louis, Missouri, using methods described in Korotev (1991).

Spot quantitative chemical analyses were obtained from thin sections using Cameca CAMEBAX and SX-50 electron microprobes, both operated at 15 kV and 15 na sample current; qualitative chemical data were collected by energy-dispersive scanning electron microscopy at a variety of accelerating potentials.

General Quantitative Mineralogic Analysis–Mineral identification and quantification for fine-grained tuffs is best accomplished by X-ray diffraction. The earliest project X-ray diffraction data were obtained on samples ground under acetone to pass through a 325-mesh (45-μm) sieve. Later X-ray data (samples analyzed since 1985 including reanalyzed early drillholes USW J-13, USW G-1, and UE-25 a#1) were obtained on samples for which a portion was mixed with a 1.0-μm corundum (Al_2O_3) internal standard in the ratio 80 percent sample to 20 percent internal standard and ground under acetone in an automatic Brinkmann Retsch mill (fitted with an agate mortar and pestle) for a time greater than 10 min. This produced a sample with an average particle size of less than 5 μm and ensured thorough mixing of sample and internal standard. The fine particle size is necessary to ensure adequate particle statistics and to reduce primary extinction and other sample-related effects (Bish and Reynolds 1989; Klug and Alexander 1974). The adequacy of grinding times and techniques has been confirmed using a Horiba CAPA-500 automatic particle-size-distribution analyzer calibrated with Duke Scientific glass microspheres. The powders resulting from the above preparation treatment were mounted in a 22 x 44-mm cavity in a glass slide; this sample area is sufficient for the sample to contain the X-ray beam at angles as low as 8.0° 2θ. Powder samples from USW G-4 were mounted in a sample spinner on the diffractometer; all other samples were examined stationary.

All of our analyses, apart from data collected manually, used integrated intensities rather than peak heights. Analysis of manually collected data (USW G-2, UE-25b #1H) employed peak heights. The use of integrated intensities compensates for several sample-related problems, including variations in order-disorder and crystallite size. Early integrated intensities were obtained using the Siemens first-derivative peak-search routine (IDENT) that yields precise intensities for resolved peaks. However, this routine divided the intensity of overlapping peaks at the midpoint between the two, which is only an approximation for most peaks. Closely overlapping or very broad peaks were measured by planimetry, and completely overlapping peaks were not decomposed. More recent analyses employed manual planimetry, which we

found to be superior to the profile-refinement results to decompose diffraction peaks. Currently, we make use of the graphical peak integration program GRAPHINT (Los Alamos National Laboratory, YMP Release Label GRAPHINT-01-00-00) to determine integrated intensities for most diffraction peaks, although reasonable results are also obtained from the current peak-identification program included in the Siemens DIFFRAC5000 software package (Los Alamos National Laboratory YMP Release Label DIFFRAC5000-01-00-00).

Quantitative determination of mineral abundances using X-ray diffraction is a technique that is used widely in a variety of disciplines including the geological and material sciences. One of the most popular and straightforward methods for quantitative X-ray diffraction analyses is the reference-intensity or Chung method (Chung 1974a, 1974b). Although quantitative X-ray diffraction methods exist that can potentially provide more accurate and precise results (for example, the Rietveld analysis (Hill and Howard 1987; Bish and Howard 1988) and full pattern fitting routines (Smith, Johnson et al. 1987)), the Chung method is widely used because it provides reliable results with minimal effort for all sample types. Whenever sufficient sample was available, our recent analyses employed the internal standard or "matrix-flushing" method of Chung (1974a) with 1.0-μm corundum as the internal standard. However, all of our older analyses and several more recent analyses of samples for which amounts were insufficient for the internal standard method employed the external-standard or adiabatic method of Chung (1974b). Both methods require that reference-intensity ratios be determined before quantitative analysis. The reference-intensity ratio is defined as the intensity of the peak of interest for a given phase divided by the intensity of a peak from a standard (usually the 113 reflection of corundum) in a 50:50 mixture (weight ratio) of phase-to-standard (for example, Hubbard et al. 1976). The 1:1 ratio of standard to sample was chosen for convenience. In practice any ratio can be used for standardization because the relative amounts of standard and sample are incorporated into the reduction of standard runs. We have experimentally determined reference-intensity ratios for most phases found in Yucca Mountain Tuffs. In the absence of sufficient pure material, reference-intensity ratios for some phases were calculated using the program POWD10 (Smith, Nichols et al. 1982). The reference-intensity ratio values used have changed over time as more phases were added to the quantitative analyses, as better standards have been obtained, and as new methods have been developed. Modifications of the X-ray diffraction instrument or of the sample preparation and mounting method ideally require remeasurement of reference-intensity ratios for all phases. Standard materials used for YMP studies were obtained from various mineral supply houses or museums, from individuals, or were collected by the authors. Several of the zeolite standards required some processing to remove impurities, which was accomplished by disaggregating the sample and sedimenting in deionized water as outlined by Chipera, Guthrie et al. (1993). Reference-intensity ratio standard mixtures were prepared by mixing 1.0-μm metallurgical grade α-alumina powder (corundum) to each mineral standard, usually in a 50:50 ratio by weight. Several minerals that exhibit significant preferred orientation effects (for example, mica, chlorite, feldspars), however, were prepared in a mixture of 20:80 with the resultant reference-intensity ratio values normalized to represent 50:50 mixtures. The increased corundum matrix helps to support the individual mineral particles, thereby producing a more randomly oriented sample mount.

Several factors were considered in choosing the peaks for quantitative X-ray diffraction by the reference-intensity ratio method, including peak intensity (greater intensity provides greater sensitivity), orientation of crystallographic planes, whether the peaks exhibit overlap with peaks

from other phases with which they are likely to coexist. To determine reference-intensity ratio values for each mineral phase, six replicate X-ray diffraction scans were conducted on each reference-intensity ratio standard. Before each replicate analysis, the standard was removed from the sample mount, remixed with the standard remaining in the sample bottle, and the sample mount was remade. Mean, standard deviation, and percent relative error (σ/mean * 100 percent) were then calculated for each reference-intensity ratio standard. For phases with chemical or preferred-orientation variability (such as feldspar and clinoptilolite), numerous reference-intensity ratio standards were prepared with six replicate runs conducted on each as outlined above. Mean, standard deviation, and percent relative error were then calculated using all data from all reference-intensity ratio standards.

Often, it is more desirable to use the sum of reflections from a localized region in the diffraction pattern than to use individual reflections for a phase. In many cases, it is virtually impossible to decompose overlapping reflections accurately. Calculated patterns from clinoptilolite show, however, that there are actually seven separate $K\alpha_1$-$K\alpha_2$ pairs in the region of the diffraction pattern where it is desirable to sum the clinoptilolite reflections. Using calculated peak positions and intensities as input parameters, this region for clinoptilolites was decomposed using profile fitting. However, any attempt to decompose this region in geological samples that contain clinoptilolite with several other mineral phases, even with a sophisticated peak-decomposition program and a priori information, would result in additional uncertainty. Alternately, the whole region can be used as a single input intensity. The use of sum peaks, by their very nature, helps to normalize effects of both preferred orientation and chemical variation and should be exploited rather then avoided. For most phases, it is advisable to use as many reflections or sum peaks as practical. If two or more reflections or sum peaks are used for an analysis, the results can be averaged to produce a more accurate phase-abundance value. Likewise, if significant differences are noted between values obtained from different reflections or sum for a phase during an analysis, they can signal potential problems with the analysis.

Measurement and use of reference-intensity ratios present few problems for materials whose intensities do not vary with composition. However, problems often arise with materials that show a wide range in chemistry and/or exhibit strong preferred orientation. For example, the reference-intensity ratio value for smectite was obtained from material separated from several samples including USW G-1 1415 (4,31.3 m); this value was the default reference-intensity ratio used for most analyses. There were instances, however, for which a more appropriate standard was used that better matched the characteristics of the smectite in the samples. For example, samples below 1036 m (3,400 feet) in USW G-1 showed evidence for some chloritic interlayers, and the reference-intensity ratio for these samples was obtained from the smectite from USW G-1 3490 (1,063.8 m). Smectite analyses for UE-25 p#1 used reference-intensity ratios measured on smectites separated from samples at different depths within the UE-25 p#1 drillhole.

Early quantitative X-ray diffraction analyses used a calculated reference-intensity ratio for tridymite. Later analyses used an reference-intensity ratio measured on a tridymite-rich sample from Yucca Flat, Nevada Test Site, Nevada. The reference-intensity ratio for this tridymite was determined such that it yielded a matrix-flushing-analysis total of 100 percent for this sample when the other crystalline phases present in the sample were included in the analysis. The

reference-intensity ratio for this tridymite standard was thus of lower precision than reference-intensity ratios for other samples that can be obtained in pure form. Current quantitative X-ray diffraction analyses use reference-intensity ratio values measured on two tridymite standards (USW G-1 619 at Yucca Mountain and sample OU-1106 Strat 2-18 from the Pajarito Plateau, Los Alamos, New Mexico). These tridymite standards were separated from the bulk rock using sodium polytungstate heavy liquid (Torresan 1987), resulting in a standard with only trace feldspar impurities. Current reference-intensity ratio values when compared with the previous reference-intensity ratio values obtained from the Nevada Test Site tridymite show that the reference-intensity ratio value for the 20.6° peak changed only slightly (old = 1.18, current = 1.16), although a significant difference in reference-intensity ratio value was obtained for the 21.9° peak (old = 1.10, current = 2.05). Past analyses, however, are still acceptable since the 20.6° peak is always used when conducting an analysis for tridymite whereas the 21.9° peak was seldom input (used only when cristobalite was not present as a major phase). Early quantitative X-ray diffraction analyses included opal-CT with cristobalite, but recent analyses distinguish between the two.

Stellerite was recently found in significant quantities in drill core UE-25 UZ#16 (Chipera, Vaniman et al. 1995). Consequently, our analysis methods were modified to include stellerite, requiring that appropriate reference-intensity ratio values be determined. Concentrated stellerite was obtained from sample UE-25 UZ#16 1029 using sodium polytungstate heavy liquid to produce approximately 300 mg of purified stellerite. Because only a small amount of stellerite was obtained (which still contained ~20 percent impurities of cristobalite and feldspar, with which stellerite has significant peak overlaps), an indirect method for obtaining reference-intensity ratio values was used. The stellerite sample was examined by X-ray diffraction, and the data were analyzed using Rietveld analysis (Post and Bish 1989) to refine the crystal structure of the stellerite that occurs in UE-25 UZ#16. The stellerite structure of Galli and Alberti (1975) was used as the starting model for the Rietveld analysis. The refined structure was then input into POWD10 (Smith, Nichols et al. 1982) to calculate reference-intensity ratio values that were incorporated into QUANT.

The earliest quantitative X-ray diffraction analyses employed a reference-intensity ratio for clinoptilolite measured for a clinoptilolite from the 506 m (1,660 feet) depth in drillhole UE-4P at the Nevada Test Site. More precise reference-intensity ratio values for a reflection or sum peak can be obtained by plotting the reference-intensity ratio for a given peak(s) versus the ratio of intensities measured for this peak(s) to a second peak or reflection. This technique minimizes the effects of both preferred orientation and chemical variability by producing curves of reference-intensity ratio values. From these curves, improved reference-intensity ratio values can be obtained during analysis of unknowns and can thus provide more precise and accurate determination of mineral abundance. Thus, recent reference-intensity ratios for clinoptilolite were measured for five different samples to assess the effects of composition and preferred orientation on reference-intensity ratio . Measured reference-intensity ratio values for the 020 reflection show significant sample-to-sample variability (mean = 0.909, $\sigma = 0.202$, $n = 36$). The reference-intensity ratio for the sum of the reflections in the 22.1 to 23.0° 2θ region, however, is considerably more precise (mean = 1.004, $\sigma = 0.064$) due to the normalizing effect of multiple reflections. The reference-intensity ratio value used for the 020 reflection can be significantly improved if it is obtained by plotting RIR_{020} against the intensity ratio (020/22.1 to 23.0°). A strong linear relationship ($r = 0.97$) exists both between the various samples (probably

representing chemical variability) and within each sample (probably representing orientation effects). Thus, our current analyses use the ratio of the 9.8° peak to the sum of the 22.4 to 22.7° 2θ peaks to determine, during the quantitative analysis, the reference-intensity ratio of the 9.8° 2θ 020 reflection and use a fixed reference-intensity ratio for the 22.4 to 22.7° 2θ cluster. When the intensity between 22.4 and 22.7° 2θ was not measurable, we used a value of 0.97 for the 9.8° 2θ 020 reference-intensity ratio .

A word of caution about these reference-intensity ratio calculation methods, however, is warranted. The reference-intensity ratio value for a peak or reflection, if obtained by taking the ratio of it against the intensity of a second peak or reflection, is directly correlated to the intensity of the second peak or reflection. For example, the reference-intensity ratio value for the clinoptilolite 020 reflection is obtained from the [020/(22.1 to 23.0°)] intensity ratio. Considering the equation for the clinoptilolite 020 reference-intensity ratio (RIR_{020} = -0.139 + 1.164∗[$INT_{020}/INT_{22.1-23.0}$]), it is readily apparent that a 20 percent error in the intensity of the (22.1 to 23.0°) intensity region will produce a 20 percent error in the reference-intensity ratio value obtained for the 020 reflection and thus a 20 percent error in the clinoptilolite abundance as determined from the 020 reflection. A 20 percent error in the intensity of the 020 reflection will also produce a 20 percent error in the calculated RIR_{020}, but the error in the 020 intensity determination and the RIR_{020} offset each other, resulting in only a minor error in clinoptilolite abundance as determined using the 020 reflection. Consequently, it is very important to measure accurately the intensities for the peaks or intensity regions used to calculate variable reference-intensity ratios.

Feldspar, one of the more abundant minerals in tuffaceous rocks, has significant chemical and structural variability, which also makes it one of the most difficult minerals to quantify accurately and precisely by X-ray diffraction. In addition, geologic samples seldom contain only a single feldspar but often contain two to four feldspar species, especially when additional factors such as exsolution are considered. Early quantitative X-ray diffraction analyses employed reference-intensity ratios for alkali feldspar obtained from natural albite and sanidine for peaks in the range 13.4 to 14.0° 2θ and at about 23.6° 2θ. These peaks are relatively free from interference from other phases. Current analyses, however, make use of a method for the determination of feldspar abundance similar to that used for clinoptilolite determination. This method uses the feldspar intensity region from 27.0 to 28.75° 2θ and calculates more accurate reference-intensity ratio values for the 13.4° sum peak and the 23.6° peak from predetermined calibration curves that ratio these peaks to the 27.0 to 28.75° intensity region as outlined in Chipera and Bish (1995). Improved reference-intensity ratio values for the feldspar 13.4° sum peak were obtained by plotting $RIR_{13.4}$ versus the intensity ratio [13.4°/(27.0 to 28.75°)] for the 12 feldspar standards. Using only the intensities for the 13.4° peak and the 27.0 to 28.75° region for the feldspar in an unknown sample pattern, the improved reference-intensity ratio for the 13.4° sum peak can be used to calculate feldspar abundance more accurately. Likewise, a more accurate reference-intensity ratio for the 23.6° reflection can be obtained by plotting the $RIR_{23.6}$ versus the [23.6°/(27.0 to 28.75°)] intensity ratio for the 12 feldspar standards. Obtaining feldspar reference-intensity ratio values using this method has the added advantage that it normalizes for differing reference-intensity ratio values if there is more than one feldspar species in a sample, which is usually the case in geologic materials. The reference-intensity ratio values obtained for feldspar reveal very large variability in measured reference-intensity ratio values for

a single reflection (or sum peak), and average reference-intensity ratio values for the group do not precisely represent individual reference-intensity ratio values. For example, for 12 feldspar standards, the feldspar 13.4° sum peak has a mean reference-intensity ratio of 0.13 with a σ of 0.07 and the 23.6° reflection has a mean reference-intensity ratio of 0.26 with a σ of 0.14. The 27.0 to 28.75° intensity region, however, was more precise with a mean reference-intensity ratio of 2.07 and a σ of 0.29. Although reference-intensity ratio values for individual feldspar species are precise ($n = 6$), they are very imprecise among the different feldspar species, resulting in a large standard deviation for the mean ($n = 72$) reference-intensity ratio values.

For more quantitative determinations or for coding into a computer program, a curve can be fit to the data to obtain equations from which the reference-intensity ratio values can be readily calculated. It is important to note that although reference-intensity ratio values and determinative equations are provided in this report, reference-intensity ratio values are dependent also on the instrument geometry and physical dimensions of the sample holder. Hence, reference-intensity ratio values should be measured for each instrument/sample configuration. To appreciate the significance of this, one need only examine the reference-intensity ratio data compiled by B.L. Davis and Smith (1988) and B.L. Davis et al. (1989). The measured reference-intensity ratio values reported for individual phases vary significantly. For example, the reported reference-intensity ratio values for the 101 reflection of quartz, a phase that does not suffer from preferred orientation or chemical variability, varies from 2.7 to 5.1.

Special Quantitative Mineralogic Analysis: Erionite–During the examination of rocks for the presence of erionite, samples were analyzed on an automated Siemens D500 X-ray powder diffractometer using Cu Kα radiation, 1.0° receiving and divergence slits, a 0.05° scatter slit, incident- and diffracted-beam Soller slits, and a Kevex solid-state Si(Li) detector. Older analyses used the same instrument with a scintillation detector, pulse-height analysis, and a graphite monochromator. The use of both incident- and diffracted-beam Soller slits was crucial in reducing the low-angle broadening of reflections due to axial divergence of the X-ray beam. Their use improved both the detection of weak erionite reflections at low 2θ angles and the discrimination between the erionite 100 and the clinoptilolite 110 reflection. NIST SRM640b silicon was used to calibrate the instrument. All sample mounts were sufficiently long to accept the X-ray beam fully at the lowest angle of interest, ~6° 2θ. X-ray diffraction traces were collected twice on each sample. Samples were first examined from 2 to 36° 2θ, with a step size of 0.02° and count times of at least 2 s per step, to characterize the total mineralogy. They were then run from at least 6° to 9° 2θ, with a step size of 0.02° and count times of between 120 and 999 s per step, to improve the peak-to-background ratio in the region of the major erionite X-ray reflection (100) at about 7.67° 2θ. The long-term stability of the X-ray generator was evaluated by making 50 repetitive measurements over the region of the quartz 100 reflection for a three-day period. The mean maximum intensity for this reflection was 4,062 $\pm$ 16.3 (1 σ) counts. There was no detectable long-term drift in intensities.

The erionite 100 reflection at approximately 7.67° 2θ is commonly used to indicate the presence of erionite because this is its most intense reflection. Identification of trace amounts of erionite in clinoptilolite-bearing samples, however, is complicated by the presence of the relatively weak clinoptilolite 110 reflection at approximately 7.48° 2θ (note the calculated clinoptilolite pattern in von Ballmoos (1984)). The presence of the 110 clinoptilolite peak can result in the misidentification of erionite in clinoptilolite-bearing samples, an easy mistake because none of

the observed X-ray diffraction patterns for clinoptilolite from the International Centre for Diffraction Data (Joint Committee on Powder Diffraction Standards 1986) indicate the existence of this reflection. Great care must therefore be used when postulating the presence of erionite in clinoptilolite-bearing samples.

Peak positions and integrated intensities were measured using the Siemens DIFFRAC 5000 first-derivative peak-search routine, although recent analyses used the Los Alamos National Laboratory code GRAPHINT to measure integrated peak intensities. Quantifications of the trace abundances of erionite in the Yucca Mountain rocks were conducted by comparing the integrated intensity obtained for the erionite peak with the intensity obtained for a known abundance of erionite in an erionite-clinoptilolite standard mixture (for example, 2.5 wt% erionite and 97.5 wt% clinoptilolite). The assumption was made that the erionite-bearing samples have mass absorption coefficients similar to those of the erionite-clinoptilolite standards and that the absolute diffracted intensities for erionite in the samples are also similar to those of erionite in the standards. Quantification of the abundant erionite and other mineral phases in USW UZ-14 samples was conducted using the reference intensity ratio method (Chung 1974a, 1974b) as described in Bish and Chipera (1988, 1989) and Chipera and Bish (1995).

Bish and Chipera (1987, 1991) showed that erionite coexisting with clinoptilolite can be detected in amounts below 0.05 wt% using X-ray diffraction. They prepared numerous mixtures of erionite in clinoptilolite ranging from 0.05 to 20.0 wt% erionite. Mixtures containing less than 0.05 wt% (500 ppm) erionite were not prepared due to the uncertainties involved in weighing and homogenizing very small amounts of erionite with large amounts of clinoptilolite. They found that erionite in relatively pure clinoptilolite can be readily detected down to 0.25 wt% using average run conditions, and amounts down to 0.05 wt% can be detected using long count-time runs. Because of diffraction from smectite, the detection limits of erionite in clinoptilolite are significantly worse when smectite is present, but glycolation of the sample allows increased resolution of the clinoptilolite/erionite reflections by shifting the smectite peaks to lower 2θ values. In samples that do not contain clinoptilolite or smectite, the limit of detection for erionite is below 0.05 percent, down to as low as 185 ppm for some samples.

Lower-limit-of-detection calculations were conducted on samples from USW SD-7 and UE-25 ONC#1. Generally, a peak is considered observed if it is at least three times the standard deviation (σ_b) of the background intensity at a given 2θ position, where the standard deviation of background intensity is the square root of the background counts accumulated in t seconds (C_b). The lower limit of detection in intensity is then $3\sigma_b$ or $3\sqrt{C_b}$. For the analyses used in this summary, a minimum detectable integrated intensity for erionite was calculated by assuming a triangular peak profile with a full-width at half-maximum of ~0.14° 2θ (typical measured full-width at half-maximum for erionite). The minimum detectable integrated intensity is equal to the minimum detectable peak intensity times the full-width at half-maximum, or $3\sigma_b(0.14)$. The minimum detectable integrated intensity is then compared with the intensity obtained for a known abundance of erionite in an erionite-clinoptilolite standard mixture (for example, 2.5 wt% erionite in 97.5 wt% clinoptilolite) to determine the lower limit of detection of erionite in that sample. The limit of detection for a given sample is a function of the count time per 2θ-step and of the background counts, which vary significantly primarily due to the presence or absence of smectite. Typical limits of detection vary from 180 to 350 ppm for samples analyzed at 999 s/step, and from 300 to 500 ppm for samples analyzed at 360 s/step.

Mineralogic Analysis of Sorption Samples–Samples for sorption studies were either small aliquots of the powdered material actually used in sorption experiments or small chunks of the parent material. For each chunk sample, the sample was crushed and powdered in a shatterbox. For all rock samples, an aliquot of the powder was mixed with 1.0-μm corundum (Al_2O_3) internal standard in the ratio 80 percent sample to 20 percent corundum. Each sample was then ground under acetone in an automatic Brinkmann Micro-Rapid mill (fitted with an agate mortar and pestle) for a time greater than 10 minutes. This produced a sample with an average particle size of less than 5 μm and ensured thorough mixing of sample and internal standard. The fine particle size is necessary to ensure adequate particle statistics and to reduce primary extinction and other sample-related effects (Klug and Alexander 1974; Bish and Reynolds 1989). To confirm the adequacy of our grinding times and techniques, the particle size distributions of several samples were measured using a Horiba CAPA-500 automatic particle size distribution analyzer. For most of the "pure" mineral samples, the sample was not mixed with an internal standard on the assumption that they were ~100 percent pure phase. They were, however, ground for the same amount of time in the Brinkmann Micro-Rapid mill to produce the required fine particle size.

Samples used in sorption experiments were prepared by crushing pieces of whole rock into a powder and then obtaining the desired size fractions (typically 75 to 500 μm) by dry-sieving through ASTM sieves. To determine the effects of water chemistry on the samples, several different aliquots of each sample were prepared for further study. One was the material pretreated with J-13 water, a second was the material pretreated with a synthetic Ca-Mg rich water, which is designed to represent a water composition comparable to a Paleozoic source as found deeper in Yucca Mountain, and a third was the original dry-sieved sample. It was found that the pretreatment did not significantly alter the mineralogy of the samples (Chipera and Bish 1995). Consequently, in later analyses, only one of the processed samples (usually the J-13 washed samples) was analyzed by quantitative X-ray diffraction for mineralogy.

The J-13 and synthetic Ca-Mg pretreated samples were washed in the pretreatment water in a manner such that some of the <38 μm size fraction material was removed. It is worth noting that this removal of fine-grained material may have some effect on the sorption results. Daniels et al. (1982) found that the fine material had an effect on sorption results for some radionuclides, possibly due to the high cation-exchange capacity of fine-grained smectite. Also, the fine-grained material has a significantly larger surface area, which may also affect sorption results (Rogers and Chipera 1994).

All diffraction patterns were obtained on automated Siemens D-500 diffractometers using Cu-Kα radiation. Data were collected in the step-scan mode with a step size of 0.02° 2θ and count times of at least 2.0 s per step, typically from 2.0 to 50.0° 2θ. Mineral identification was accomplished by comparing observed patterns with patterns of pure standards, published patterns from the Joint Committee on Powder Diffraction Standards (1986), or calculated mineral patterns obtained from the program POWD10 (Smith, Nichols et al. 1982).

All quantitative analyses employed either the internal standard or "matrix-flushing" method of Chung (1974a), using synthetic 1.0-μm corundum as the internal standard, or the external standard or "adiabatic" method of Chung (1974b), which assumes that the phases analyzed sum to 100 percent. It is important to note that the methods of data collection and analysis used for

these samples are not conducive to identifying phases present below ~0.5 wt%, and potentially important trace phases may be present in the samples. Analysis for such trace phases requires either special data collection techniques (for example, Bish and Chipera (1991) for determinations of erionite abundance) or concentration by magnetic or heavy-liquid methods. Quantitative analyses were conducted using the computer program, QUANT, written at Los Alamos. Details of the quantitative methods used are outlined in Bish and Chipera (1988, 1989) and Chipera and Bish (1989, 1995).

Several samples had elevated sorption for neptunium. The prominent mineralogy of these samples was opal, calcite, and a clay (believed to be sepiolite). To confirm the identification of the clay as sepiolite and not smectite, a small amount of sample was suspended in deionized water and allowed to settle for 1 hr to leave the finer material (for example, clay) in suspension. A small aliquot of the suspension was then pipetted onto an off-axis cut quartz plate and allowed to dry undisturbed to make an oriented 001 sample mount. The mount was then ethylene-glycol solvated overnight at 40°C and examined by X-ray diffraction to determine if the structure had expanded (smectite will expand; sepiolite will not).

Geopetal Petrofabric Measurement–A petrofabric technique for dating zeolitization by tectonic criteria was developed specifically for this project. The petrofabric technique is based on the examination of geopetal structures in zeolitized tuffs. A geopetal structure is any rock feature whose form is influenced by gravity. The geopetal structures in tuffs at Yucca Mountain are pores <2 mm across, such as bubbles in glass shards and cavities left by dissolved shards, that have been partly to completely filled with opal, zeolite, clay, or fine-grained detritus. The geopetal fillings of interest for this study are those in which the filling material was extremely fine grained and likely to have been deposited by settling from aqueous suspension. The upper surfaces of the deposits are highly planar, and internal layering—either mineral layering or opal color banding—may be present. Layering phenomena in aqueous colloidal suspensions have been investigated experimentally by Merchant and Rosauer (1969), and Fitch (1979) provided a description of the processes involved. Under a wide variety of conditions, the fine suspended particles segregate into horizontal planar layers during settling. Layering in the natural colloidal material in Yucca Mountain altered tuffs is more highly developed and better preserved than in the experimental material because the natural suspensions were chemically more heterogeneous and reactive than the experimental suspensions, which consisted solely of clay particles. A population of geopetal fillings in any particular sample is easily distinguished from "angle of repose" deposits or cross-bedded deposits by the very narrow range of angular orientations (commonly <25°) in the layers of the geopetal fillings.

A basic assumption of this technique is that the surfaces of geopetal fillings in zeolitized tuffs were horizontal at the time of deposition. If the geopetal fillings at a particular location in a tuff were deposited over a period during which the enclosing rock was being subjected to tectonic tilting, then the upper surfaces of the fillings in a sample of that rock may have differing orientations and the angular difference indicates the minimum amount of tilting that occurred during deposition. Filling orientations do not record the total amount of tilting unless the fillings were deposited both before and after the period(s) of tilting. The same logic applies to the orientations of internal layering.

The geopetal fillings must postdate zeolitization if the rationale for placing a minimum age on zeolitization is to be valid. Most of the cavities with geopetal fillings are secondary pores created by the dissolution of glass shards. Petrographic and scanning-electron-microscopic studies of partially and completely zeolitized tuffs (e.g., Levy 1984c; Vaniman, Bish, Broxton et al. 1984) indicate that large glass shards are the last primary material to be affected by alteration. The shard cavities are commonly lined with zeolite crystals that are in turn covered by geopetal fillings, if present. These textural relations indicate that many geopetal fillings do in fact postdate zeolitization in the rocks where they were deposited.

Approximately 150 standard petrographic thin sections prepared from unoriented core samples of zeolitic tuff were examined for the presence of geopetal fillings. The screening set, representing drillholes J-13, UE-25 a#1, G-1, G-2, G-3/GU-3, G-4, H-3, H-4, H-5, and VH-1, included clinoptilolite-bearing units from the basal Topopah Spring Tuff downward to the Bullfrog Tuff. Thin sections that contained abundant geopetal fillings were selected for further study and geopetal orientation measurement.

The geopetal orientation measured in thin section is the orientation of the line of intersection between the planar geopetal surface and the plane of the thin section. Figure 6.1-52 illustrates the geometric principles for the measurement of geopetal orientations. Planes A and B represent the orientations of two geopetal filling surfaces in a zeolitized tuff. Planes C, D, and E (all depicted as vertical) represent three possible thin-section orientations. The true angle between planes A and B (20°) can be measured only in a third plane (for example, plane C, representing a thin section) that is perpendicular to both planes A and B (and to their line of intersection). As shown in Figure 6.1-52, the true angle between planes A and B is the angle between the lines of intersection of planes A and B with plane C (Miller, H. 1941). Plane D is not perpendicular to the line of intersection of planes A and B. Therefore, the angle between the lines of intersection of planes A and B with plane D (16°) is less than the true angle between planes A and B. Plane E is parallel to the line of intersection between planes A and B. The angle between planes A and B, as seen in a thin section represented by plane E, would appear to be 0°.

As described above, the angular difference between two geopetal orientation measurements is an apparent angle less than or equal to the true angle between the planar geopetal surfaces. The detection of tectonic rotation from geopetal-orientation measurements is based on simple documentation of angular differences within sets of measurements, but estimates of tectonic rotation from orientation measurements are less than or equal to the true amount of rotation. In the special case that geopetal surfaces with different orientations happen to have a common line of intersection with the plane of the thin section (e.g., plane E in Figure 6.1-52), orientation measurements would show no angular differences. A collection of measurements suggesting no angular spread is checked by measuring a new thin section of the same sample, cut at a high angle to the original section, to distinguish between genuine and apparent evidence for no rotation within the time span of geopetal filling deposition. Note that all thin sections are assumed to be approximately vertical by cutting parallel to the drill-core axis.

Measurements were made on the mechanical stage of a petrographic microscope. The geopetal orientation is the microscope stage vernier reading as the thin section is rotated to bring the trace of a geopetal surface parallel to the east-west crosshair. Because there is no internal reference orientation in the thin section, the numerical values of orientation measurements have no

absolute significance. Orientation measurements from a given sample have meaning only with respect to each other, as elements of a measurement distribution showing the angular spread among measurements. Measurement distribution patterns can be compared among samples, but absolute numerical values cannot be so compared. Duplicate readings for each geopetal surface are measured to the nearest 0.5°, then averaged. Readings that differ by more than 1° are rejected.

The distribution pattern of geopetal orientation measurements in samples in which rotation has accompanied or followed alteration is a function of the timing and rate of tilting, the hydrologic conditions, the availability of colloidal material, and the changing porosity and permeability of the altered rock. The observed tendency of orientation data to cluster could be an effect of one or more of these conditions. If either tilting or geopetal deposition occurred as discrete episodes rather than as a continuous process, the geopetal orientation data would tend to cluster. Clustering of data would also occur if continuing rock alteration progressively changed the pattern of pore availability or accessibility, such that only certain pores existed or were open to the introduction of colloidal suspension or its precursor solution at any particular time. The latter explanation receives some support from the observation that individual rock pores rarely contain multiple geopetal fillings with different orientations.

Analytical Methods for K/Ar Studies–Zeolitized tuff samples were crushed and pulverized, after which the zeolites and clays were separated by sedimentation and centrifugation in deionized water. Additional purification of zeolite separates from some samples was carried out using a mixture of S-tetrabromoethane heavy liquid and acetone with a density range of 2.1 to 2.45 g/cm^3 to separate clinoptilolite from other, generally denser primary and secondary minerals by centrifugation. Although clinoptilolite has a measured density of 2.1 to 2.2 g/cm^3 (Roberts et al. 1989) and is much less dense than other common minerals in the tuff matrix, the heavy-liquid separations were not completely effective. All geochronology aliquots were further cleaned by dialysis in deionized water for about a week.

Size fractions obtained by sedimentation and centrifugation were analyzed by X-ray diffraction. Random and oriented mounts were prepared and analyzed by an automated Siemens D-500 diffractometer using CuKα radiation, 0.02° 2θ steps, and counting times of 1 second per step from 2° to 36° 2θ for all mounts. X-ray diffraction patterns for pure mineral standards were used to identify the minerals in the separates. X-ray diffraction patterns of mixtures of pure clinoptilolite, K-feldspar, and illite/smectites with ≤20 percent illite layers were used to estimate the amounts of contaminant K-feldspar and illite/smectites in the geochronology aliquots (Figure 6.1-58). The purified samples were estimated to contain ≥75 percent clinoptilolite.

Geochronology aliquots of ~130 to ~200 mg of clinoptilolite, mordenite, or illite/smectites separates, with grain sizes of 0.1 to 0.35, 1 to 3, or 3 to 20 μm, were prepared for Ar extraction. The K/Ar system was prebaked at 180°C while the samples were cooled by continuously running water. Ar measurements were made using an MS10 mass spectrometer equipped with an online multiloaded extraction system and a bulb-pipetted ^{38}Ar tracer calibrated with the LP-6 biotite interlaboratory standard containing 19.3 × 10^{10} mole/g of radiogenic Ar (Odin et al. 1982). The K contents were determined in duplicate by flame photometry using a lithium internal standard.

K/Ar apparent ages were calculated using ^{40}K abundance and decay constants proposed by Steiger and Jager (1977).

The total percentage uncertainties in the calculated K/Ar dates represent the combination of errors from the determination of radiogenic Ar contents of samples (Cox and Dalrymple 1967), K_2O analysis, and sample inhomogeneity. Replicate analyses of standards analyzed with the unknown samples for K (LP-6 and USGS standards BCR-1 and G-2) and Ar (LP-6) vary by less than 3 percent from the published values. The precision of multiple analysis of some of the unknown samples, especially clinoptilolites that yielded younger apparent ages, is not as good as the results from the standards. The variations of the apparent ages are sometimes greater than can be explained by analytical error alone.

Other Analyses–Plant root samples were ashed to obtain mineral matter by heating for 502 hours under O_2 flow in an LFE Corporation LTA-504 low-temperature asher to determine proportions of ashable organic material. In addition, nine soil samples (four samples of argillic (Bt) soil horizons and five samples of calcrete) were heated for 266 hours in the same instrument under the same conditions. For the soil samples, both weight loss from LTA ashing and weight regained on cooling in atmosphere were measured to determine both the amount of ashable organic matter and the weight changes attributable to dehydration or rehydration of inorganic constituents (clay and opal).

Bulk density determinations were made on rectangular blocks cut from calcretes and from spring deposits. Densities were determined by dividing the measured volumes of right-rectangular blocks into the block weights.

6.1.1 Petrology and Geochemistry of the Yucca Mountain Site and Environs

Introduction–The petrologic and geochemical character of the geologic units most relevant to the site are described in this section. Very little is presented here about the Paleozoic rocks beneath Yucca Mountain for which few samples have been obtained in deep drilling, but considerable detail is given on the Cenozoic Rocks and on the Tertiary and Quaternary surface deposits. The stratigraphy and structural setting of the Yucca Mountain site area are given in Subsections 3.5 and 3.6, respectively.

6.1.1.1 Paleozoic Rocks

The Paleozoic rocks beneath Yucca Mountain are dominated by carbonate series, principally by dolomitic rocks. Detailed descriptions of the Paleozoic stratigraphy can be found in Subsection 3.2.2.1.2. Samples of Paleozoic rocks from beneath Yucca Mountain are rare and whether the few samples available are representative is unknown. A brief discussion of the Roberts Mountain Dolomite from drill core UE-25 p#1, with mineralogic and chemical data, can be found in Vaniman, Furlano et al. (1995). Data from the UE-25 p#1 sample are cited below where appropriate to the discussion of site geochemistry (also see Figure 6.1-26). The role of Paleozoic rocks in potential repository performance will be minimal. The most likely potential impact would be in interaction with clasts of Paleozoic rocks in alluvium should transport effects extend to the south into the thick alluvial sequences of southern Jackass Flat and the Amargosa Valley.

6.1.1.2 Cenozoic Rocks

The major rock types at Yucca Mountain are silicic volcanic tuffs. Emplaced across the landscape as airfalls or ashflows, these rocks were initially vitric (glassy tuffs with mineral phenocrysts), but ashflows that were thick enough to retain their heat were largely devitrified (that is, the glass crystallized, principally to silica minerals and feldspar). The thickest ashflows exsolved a vapor phase during devitrification that deposited minerals from vapor along fractures and within gas pockets (lithophysal cavities).

Subsection 3.5 of this report describes the site stratigraphy and the use of petrographic features (for example, phenocryst types and abundances) and geochemical criteria in defining stratigraphic units among the Cenozoic volcanic rocks. The data presented here include greater mineralogic and chemical detail for the volcanic units that are most important for understanding flow, transport, and thermal stability of the site. The reader is referred to Subsection 3.5 for a broader discussion of site volcanic stratigraphy. In the text that follows, the major tuff units at Yucca Mountain are described from youngest to oldest, in stratigraphic order going down-section. This approach is used to present the site in the same orientation, as downward flow would encounter these units.

Compositionally, the most important chemical constituents of both vitric and the devitrified tuffs are SiO_2 and Al_2O_3. Figure 6.1-1 compares the abundances of these constituents in unaltered representatives of the major rocks forming Yucca Mountain, normalized to water-free compositions. These rocks include high-silica rhyolites (> 75 percent SiO_2) and rhyolites (72 to 75 percent SiO_2), with some distinctive quartz-latitic rocks (< 70 percent SiO_2). This figure will be used in the discussion below to describe the geochemical stratigraphy of Yucca Mountain, because alumina and silica are the major framework constituents that defined the mineralogy formed in devitrification, in vapor-phase alteration, and in the later zeolitization of extensive portions of those rocks that remained vitric after emplacement and initial cooling.

6.1.1.2.1 Timber Mountain Group (Tm)

The only significant occurrence of Timber Mountain Group volcanic rocks at Yucca Mountain is of valley-fill and low, ridge-capping lenses of the Rainier Mesa Tuff. The younger of the principal volcanic cycles of the Timber Mountain Group, the Ammonia Tanks Tuff, is virtually absent at Yucca Mountain (see Subsection 3.5.3.9). These two tuffs are products of the explosive eruptions at 11.4 and 11.6 Ma (Sawyer et al. 1994) that produced the largest and best preserved caldera of the region, the Timber Mountain Caldera.

Rainier Mesa Tuff (Tmr)–Little of the Rainier Mesa Tuff remains at Yucca Mountain. The patches preserved in lowlands along the flanks of Yucca Mountain suggest that all of the area may have been blanketed with at least the airfall portions of this tuff if not by the ashflows, but any remnants of this unconsolidated material have since eroded from the crests and slopes of higher terrain. The areal distribution and tectonic significance of the Rainier Mesa Tuff are discussed in Subsection 3.6.2.3 and are mapped in detail in Day et al. 1998b. With this limited distribution, the Rainier Mesa Tuff would be expected to be of little consequence at Yucca Mountain were it not for the fact that the Rainier occurrences at Yucca Mountain are vitric. As

such, they are likely sources for silica and trace minerals released by chemical weathering over the ~11 Ma history of Yucca Mountain.

Figure 6.1-2 shows that the Rainier Mesa Tuff includes both high-silica rhyolite and quartz latite subunits. The minor quartz-latitic subunit overlies and is gradational into the more voluminous high-silica rhyolite (Broxton, Warren, Byers et al. 1989). Chondrite-normalized lanthanide patterns for these two subunits show light-lanthanide enrichment and minimal or no Eu anomaly in the quartz latites; this type of pattern is characteristic and is seen repeatedly in quartz-latitic compositions at Yucca Mountain. This quartz-latite lanthanide pattern contrasts with those of the rhyolites, which have much less light-lanthanide enrichment and a variable but generally strong negative Eu anomaly that reflects plagioclase removal from source magmas (Figure 6.1-2). This compositional variation, representing the progressive disgorgement of a stratified magma chamber, is common to the major tuffs of the Paintbrush Group (Tiva Canyon and Topopah Spring) as well (Broxton, Byers et al. 1985).

6.1.1.2.2 Paintbrush Group (Tp)

The Paintbrush Group at Yucca Mountain is dominated by the Tiva Canyon and Topopah Spring Tuffs. These tuffs provide, respectively, most of the surface exposures of Yucca Mountain and the potential host rock for a waste repository. Between these two tuffs, the Yucca Mountain Tuff and the Pah Canyon Tuff are volumetrically minor but of potential hydrologic importance because of their contrasting high matrix porosity compared to the Tiva Canyon and Topopah Spring Tuffs, which, except for their nonwelded tops and bases, are densely welded and of low matrix porosity. The welded tuffs also have higher fracture abundances and connectivities, providing stratified contrasts in unsaturated hydrologic properties in the Paintbrush Group rocks above the potential repository.

Tiva Canyon Tuff (Tpc)–The Tiva Canyon Tuff is compositionally zoned from a minor quartz-latitic, vitric to devitrified upper portion to a predominantly high-silica rhyolitic, devitrified lower sequence. This compositional zonation is similar to that of the Rainier Mesa and Topopah Spring Tuffs. The high-silica rhyolites of the Paintbrush Group have an exceptionally small compositional range (Figure 6.1-1). The quartz-latitic upper part of the Tiva Canyon Tuff forms ~1/5 of the surface exposures at Yucca Mountain in the region above the potential repository; the other exposures are in the high-silica rhyolite or in the alluvial fill of canyons, fill that is derived mostly from Tiva Canyon Tuff detritus. Most vertical recharge pathways for groundwater that passes through the potential repository block thus encounter the Tiva Canyon Tuff; moreover, because the modification of low-pH rainwater and the definition of the unsaturated-zone groundwater composition is largely determined in the soil zone or in the uppermost alluvium and bedrock, the minerals of the Tiva Canyon Tuff play a large part in determining unsaturated-zone groundwater composition.

Across parts of Yucca Mountain, the quartz-latitic upper part of the Tiva Canyon Tuff is vitric or partially vitric; these glasses may be particularly reactive in interactions with recharge waters or with waters that are diverted and flow laterally along slopes and ravines. Phenocryst abundances in the quartz-latitic parts of the Tiva Canyon are high (to > 20 percent) and consist predominantly of feldspar (Figure 6.1-4). The chondrite-normalized lanthanide pattern of the quartz latite (Figure 6.1-3) is similar to that of the quartz-latite subunit of the Rainier Mesa Tuff

(Figure 6.1-2), but the Tiva Canyon quartz latite is volumetrically much more important at Yucca Mountain. However, as will be seen below, the Pah Canyon and Topopah Spring quartz-latitic compositions are the only tuffs of this composition that span the entire area of the potential repository above the host rock (the rhyolitic Topopah Spring Tuff).

The lowest part of the Tiva Canyon Tuff consists of densely-welded to nonwelded high-silica rhyolitic glass. This interval provides another horizon of potential water accumulation in the unsaturated zone, with associated dissolution. Note, however, that water composition resulting from dissolution of rhyolitic glass will be compositionally distinct from waters that interact with the upper quartz-latitic glass in the same tuff.

Yucca Mountain Tuff (Tpy)–The Yucca Mountain Tuff is chemically very similar to the high-silica rhyolites of the Tiva Canyon and Topopah Spring units (Figure 6.1-1). The chondrite-normalized lanthanide patterns for this tuff are typical of high-silica rhyolites (Figure 6.1-5). At Yucca Mountain, the Yucca Mountain Tuff is largely vitric, nonwelded, and porous but may be locally devitrified to silica minerals and feldspar. Although this unit is rhyolitic, it contains both plagioclase and sanidine phenocrysts (Figure 6.1-6), whereas the only feldspar phenocrysts in the rhyolitic Tiva Canyon Tuff are of sanidine (Figure 6.1-4). This two-feldspar phenocryst composition is characteristic also in the rhyolitic portions of the Topopah Spring Tuff (see below).

Pah Canyon Tuff (Tpp)–The Pah Canyon Tuff is a chemical anomaly within the Paintbrush Group. It is somewhat poorer in silica content than the high-silica rhyolites (Figure 6.1-1), and even more different from the other rhyolites in its trace-element chemistry, having rare-earth-element composition more akin to quartz latites than to rhyolites (Figure 6.1-7). The Pah Canyon Tuff is, like the Yucca Mountain Tuff, nonwelded, porous, and largely vitric (but locally devitrified). The high saturation of porous nonwelded units, such as the Yucca Mountain and Pah Canyon units, begins to be more effective in producing alteration where an underlying barrier to transmission becomes effective; thus, because of the relatively impermeable upper vitrophyre of the underlying Topopah Spring Tuff, the alteration of the Pah Canyon Tuff (principally to smectite) is often more extensive than that of the overlying Yucca Mountain Tuff. Therefore, despite its minor volume, the Pah Canyon Tuff has a significant impact on the reactions between unsaturated-zone waters and the host tuffs.

Phenocryst abundances in the Pah Canyon Tuff (Figure 6.1-8) are ~5 to 14 percent, with a mode of ~7 percent that is intermediate between that of high-silica rhyolites (generally <5 percent) and the quartz latites (5 to 18 percent, with a mode in the Topopah Spring Tuff of ~14 percent). The Pah Canyon Tuff is a two-feldspar tuff that has markedly Na-rich plagioclase (commonest plagioclase composition is Na-rich oligoclase, contrasted with a commonest composition in the oligoclase-andesine range for most other Paintbrush Tuffs).

Topopah Spring Tuff (Tpt)–At Yucca Mountain, the single most important unit for possible repository development is the Topopah Spring Tuff. At present the lower half of the Topopah Spring Tuff is targeted as the potential repository horizon. Although the most critical property for repository development is the presence of a thick, competent, and mineable rock mass, the matching of these requirements with the available Topopah Spring rock mass at Yucca Mountain places the potential repository within one of the most chemically homogenous rock types of the

region. However, the combined expression of this chemistry in variable devitrification, vapor-phase, and low-temperature alteration minerals provides variability in rock texture and mineralogy that is not seen in chemistry.

Figure 6.1-1 indicates the limited extent of major-element variability in all of the high-silica rhyolites of the Paintbrush group—including that of the Topopah Spring Tuff; this figure also shows the distinctly more aluminous quartz latite of the upper Topopah Spring Tuff. The same homogeneity within the high-silica rhyolite extends to trace elements. There is greater variability in the upper quartz latite, which includes a nonwelded glass, a vitrophyre, and the upper 15 percent of the thick Topopah devitrified sequence.

Figure 6.1-9 shows that the characteristic differences between quartz-latitic and rhyolitic lanthanide-element compositions occur in the Topopah Spring Tuff. The Topopah Spring quartz latite, although above the potential repository horizon, is a particularly important geochemical subunit because it includes a relatively impermeable upper vitrophyre (Tptrv1). Impedance of downward flow and reaction of water with quartz-latitic glass provides an important geochemical marker in unsaturated-zone waters (Vaniman and Chipera 1996).

Geochemical and Textural Stratigraphy Within the Topopah Spring Tuff–Geochemical variability of the Topopah Spring Tuff is dominated by the two prominent geochemical end members that were derived from chemical zonation within the parental magma chamber. This magma chamber was stratified in composition, with an extensive mass of high-silica rhyolite overlying a more mafic zone. Disgorgement of the magma chamber apparently occurred in several pulses, sequentially voiding the higher portions of the chamber and ultimately tapping into the more mafic subzone to provide the quartz-latitic portion of the later and final eruptions, with episodic injection of more mafic magma as the system evolved (Broxton, Warren, Byers et al. 1989). The result of this eruption sequence is the chemically stratified mass of pyroclastic rocks that remains today, with an average thickness of ~360 m, the upper ~15 percent of which is predominantly quartz-latitic and the lower ~85 percent is high-silica rhyolite (Figure 6.1-10). These percentages are approximate because the lower two-thirds of the quartz-latitic zone grades into the high-silica rhyolite, representing a complex intermixture of the high-silica and lower-silica magma types.

Following eruption and emplacement of the Topopah Spring Tuff, the uppermost (quartz latitic) and lowermost (high-silica rhyolite) portions of this compound volcanic series were rapidly cooled below glass quenching and rheomorphic temperatures to preserve thin, nonwelded vitric margins. Glassy portions at top and bottom that retained enough heat to flow but not to crystallize were densely welded to form vitrophyres (the quartz-latitic upper vitrophyre and the high-silica rhyolite lower vitrophyre). The vast majority (~90 percent) of the erupted material, between these two vitrophyres, retained enough heat to promote crystallization of all glass. This is the devitrified core of the Topopah Spring Tuff. Water vapor released from crystallizing glasses in this devitrified core formed a supercritical fluid from which vapor-phase minerals crystallized along early-formed fractures and within pockets formed by gas expansion (lithophysal cavities). The vapor-phase minerals are dominantly feldspars and silica minerals (especially tridymite), but include a wide variety of other minerals (including amphibole, pseudobrookite, rare Mn-garnet, and rare andalusite). Crystallization of some of these minerals may have continued as the possibly supercritical fluid cooled to water vapor and ultimately

condensed as liquid water. Many fractures are filled with vapor-phase minerals; larger fractures may have surfaces that have cracked to form anastomosing channels with vapor-phase minerals. Much of the tridymite along fractures is now pseudomorphed by quartz that may have formed during this transition. Minerals have continued to form within fractures long after the end of the volcanic cooling cycle; minerals that may still be forming in fractures and cavities of the potential host rock include zeolites, clays, opal, and calcite.

Textural Basis for Subdividing the Topopah Spring Tuff–For over 30 years, coarse-scale textural stratigraphy has been used to subdivide the Topopah Spring Tuff. The stratigraphy and petrology of the Topopah Spring Member were first formally treated by Lipman et al. (1966), who described the welding, crystallization, and primary compositional zonation from measured and sampled outcrops in the vicinity of Yucca Mountain. These authors recognized the distinctive upper lithophysal zone, which they called the "main lithophysal zone," as well as the obvious lower and upper vitrophyres. The microcrystalline (devitrified) tuff, including the "candidate host rock" (Myers et al. 1983) between the lower vitrophyre and the upper lithophysal zone, was recognized as having "several thin vapor-phase and lithophysal zones . . . within it" (Lipman et al. 1966, p. F5), but the lower lithophysal zone was not recognized as such by Lipman et al., owing to limited exposures. Their paper also deals with the primary compositional zonation as it relates to the chemistry of the magma chamber in the source vent area, later considered to be the Claim Canyon caldera north of Yucca Mountain (Byers, Carr, Christiansen et al. 1976).

In this section, a matrix textural stratigraphy is described for the Topopah Spring Tuff based on the 3-D integrated site model, as described in Subsection 3.9 of this report. A short description of the Topopah Spring Tuff subunits is given in Subsection 3.6.3.7.1; a more detailed description of texture, mineralogy, and chemistry is provided here. Relations between the matrix textural stratigraphy and current symbology used for the Topopah Spring Tuff are, from top to bottom:

a) Vitric nonwelded (Tptrv3) and vitric moderately-welded (Tptrv2) quartz latite	2 to 3 m; locally devitrified; zeolitic in core G-2
b) Upper, quartz-latite vitrophyre (Tptrv1)	~1 m; densely welded and impermeable
c) Nonlithophysal transitional zone (Tptrn,rl)	36 to 48 m; grades downward into rhyolite
d) Upper lithophysal rhyolite (Tptpul)	54 to 85 m; large spherical lithophysae
e) Middle nonlithophysal rhyolite (Tptpmn)	27 to 54 m, except 9 m in core G-2
f) Lower lithophysal rhyolite (Tptpll)	43 to 117 m; large flattened lithophysae
g) Lower nonlithophysal rhyolite (Tptpln)	44 to 60 m, except 9 m in core G-2
h) Lower, rhyolite vitrophyre (Tptpv3)	9 to 25 m; densely welded and impermeable
i) Moderately-welded (Tptpv2) and nonwelded (Tptpv1) basal rhyolite	7 to 42 m, except 4 m in core G-2, lower 0 to 9 m zeolitic except in G-3

Matrix studies relevant to the potential repository horizon focus on horizons d) to g), which represent the rhyolitic devitrified portion of the Topopah Spring Tuff.

Relation of Textures to Emplacement History–In the Topopah Spring matrix, the textural variation with depth is genetically related to cooling and chilling of two major rhyolitic eruptive pulses and an upper gradational zone caused by mixing of a third quartz latitic magma; all erupted about 13 ma ago (Sawyer et al. 1994). The basal vitrophyre and its overlying thick lower nonlithophysal zone represent the chilled lower part of the welded ashflow tuff that was very hot at the time of emplacement (~700°C; Lipman 1971). The middle nonlithophysal zone is a partially chilled zone that never chilled to a vitrophyre (glass), probably because of a low-temperature gradient. This zone's contact with the underlying lower lithophysal zone is gradational, suggesting only a brief hiatus. The upper surface of the lower lithophysal zone was probably still liquid but bubbling with exsolved gases when the second major rhyolitic ashflow erupted. During the cooling and degassing of the second rhyolitic eruptive pulse, the upper lithophysal zone formed above the middle nonlithophysal zone. The upper quartz latitic cryptocrystalline lenticular groundmasses that increase upward are former clots of quartz latitic magma. They accumulated when the lower part of a zoned magma chamber, underlying the Claim Canyon caldera to the north, was drawn down by the eruption (Lipman et al. 1966; Byers, Carr, Christiansen et al. 1976). This quartz latitic magma, however, has a higher melting point (900°C; Lipman 1971) than the eruptive temperature of the rhyolitic magma (~700°C). Therefore, the quartz latitic magma had a greater tendency to chill to a cryptocrystalline groundmass, whereas the rhyolitic magma with its volatiles crystallized to spherulites and granophyre.

The textures in the upper one-fifth of the Topopah Spring illustrate interactions of welding crystallization and compositional zones. The compositional effect is generally one of increasing quartz latitic cryptocrystalline matrix and phenocrysts; the increasing crystal assemblage is quartz latitic and includes clinopyroxene. Specimens of this interval contain voids and abundant vesicles indicative of vapor phase action, where parts of the quartz latitic matrix have crystallized to tiny spherulites 100 to 200 μm in diameter. The maximum phenocryst content increases upward to ~15 percent; this increase is related to original crystal content of the quartz latitic magma and the degree of welding. Microscopically, the upper vitrophyre is mostly cryptocrystalline quartz latite, chilled near the upper surface of the ashflow; only a small amount of colorless rhyolitic glass remains.

The variation of phenocryst proportions with depth is related inversely to the original proportions with depth in the magma chamber before eruption (Lipman et al. 1966). That the phenocrysts precipitated at depth and not at the surface is demonstrated by occurrence of essentially the same phenocryst assemblage in the basal vitrophyre, which is supercooled magmatic glass, as in the overlying microcrystalline groundmasses including spherulites and granophyre. The phenocryst crystals did not grow after eruption of the Topopah Spring at the surface as did those of the granophyre; rather, they grew at depth before eruption from the magma chamber. The succession of phenocryst assemblages upward from the basal vitrophyre was originally the succession of phenocrysts downward from the top of the magma chamber before eruption.

Small (<1 mm) quartz phenocrysts are characteristic of the first eruptive pulse, represented from the basal vitrophyre to the top of the lower lithophysal zone, and were present in the upper part of the magma chamber before eruption. Inasmuch as the phenocrysts constitute only about 1 percent of the rhyolitic section, the quartz is exceedingly sparse, even though a few small phenocrysts are seen in every thin subsection that sampled the first eruptive pulse. Had there

been no further magma erupted, the Topopah Spring would be characterized as a high-silica quartz-bearing rhyolite, like the underlying tuffs of the Calico Hills Formation. The rhyolites of the Calico Hills formation form an arc of exposures around the Claim Canyon caldera segment from whence the Topopah Spring Member came (Byers, Carr, Orkild et al. 1976). The Calico Hills lavas are petrologically similar to the overlying basal tuff of the Topopah Spring, and the feldspars of these units show a continuum in composition upward through them (Warren, Byers, Caporuscio 1984). In fact, some studies indicate that the Crater Flat Group, Calico Hills Formation, and Paintbrush and Timber Mountain Groups are all successive eruptive products from the same magmatic system (Scott, R.B., Byers et al. 1984; Warren and Byers 1985; Broxton, Byers et al. 1985). However, the volume of ashflow tufts of the Crater Flat Group and Calico Hills Formation is relatively minor compared with that of the Topopah Spring Tuff. In other words, by tapping deep into the magma chamber, the eruptive products of the Topopah Spring not only siphoned off the quartz-bearing rhyolitic top but also tapped quartz-free crystal-rich quartz-latitic magma at significantly greater depth.

Nomenclature of Matrix Textural Features in the Topopah Spring Tuff–The matrix of the Topopah Spring Tuff is defined herein as the major bulk of the unit, exclusive of open fractures, of fracture fillings larger than about 200 μm (0.2 mm), and of lithophysal cavities and xenoliths larger than about 5 mm. This is a practical definition based on statistical considerations related to the small area (20 x 30 mm) of thin sections used for examining the matrix. These thin sections may cut sparse veinlets less than 200-μm wide, and in the upper lithophysal zone, it is difficult, if not impossible, to avoid intersecting small lithophysal cavities with diameters of 5 mm or less. The microveinlets observed in slides, however, are almost always filled with silica minerals and alkali feldspar, and they commonly connect with those in the lithophysal cavity linings and in the flattened granophyric cores of former pumice (Carlos 1985). Granophyric pumice is a significant matrix constituent because of the larger size of its crystals (up to 0.5 mm) and because the crystals commonly line cavities in the interiors of pumice. In several drillholes, microscopic heulandite and rare mordenite (Bish, Caporuscio et al. 1981; Caporuscio et al. 1982; Spengler, Byers et al. 1981) also occur in the centers of microveinlets and in granophyric pumice within a few tens of feet above the lower vitrophyre.

An example of textural mapping within the Topopah Spring Tuff is illustrated in Figure 6.1-11, in which the data from drill core USW G-4 are used as representative of the more complete multiborehole information to be found in Byers (1985) and in Byers and Moore (1987). The elongate bar graphs in the central parts of Figure 6.1-11 compare coarse to fine textures between the different stratigraphic levels, starting with coarsest (crystals and lithic fragments) at the left and ranging to finest (cryptocrystalline, glass, and voids) at the right. Phenocrysts and lithic fragments are generally the coarsest, ranging from 0.1 mm to about 2.0 mm for phenocrysts and as much as 5 mm for lithics. The granophyric intergrowths (alkali feldspar and silica minerals) and silica-filled microvesicles (cristobalite and/or tridymite) both range from approximately 0.05 mm to approximately 0.5 mm and are most abundant in the lithophysal zones. Feldspar-silica intergrowths with individual crystals smaller than about 0.05 mm produce a microlitic or spherulitic aggregate in which it is difficult or impossible to identify individual minerals; however, spherulitic crystals are elongate, radiate from a common center, and rarely attain several millimeters in length. Nearly all spherulite crystals in the Topopah Spring matrix are less than 0.5 mm in length and 0.05 mm in width. Any smaller grain-size aggregates (individual crystals less than about 0.005 mm) are called cryptocrystalline, because the

individual crystals cannot be distinguished even at 200x; X-ray diffraction studies indicate that in addition to alkali feldspars and silica minerals, the cryptocrystalline aggregates may include smectite and other hydrous secondary minerals above the basal vitrophyre (Levy 1984b, 1984c, 1985). In thin section, the cryptocrystalline aggregates are semitranslucent to nearly opaque and may grade into a glassy groundmass or into the vitrophyre.

Correlations of Matrix-Textural Stratigraphy Across Yucca Mountain–Figure 6.1-11 summarizes the matrix-textural stratigraphy of the Topopah Spring Tuff in drillhole USW G-4. Figure 6.1-12 is a fence diagram that relates the matrix stratigraphy between all drillholes for which matrix textures have been quantified. The text that follows provides details of the four principal subunits in the devitrified Topopah Spring Tuff (Tptpul, Tptpmn, Tptpll, and Tptpln) and a statistical analysis of the significance of these stratigraphic distinctions within the potential host rock. First, however, it is important to single out specific differences in the drillhole to the north, USW G-2, that make it distinct from the holes around the current exploration block. The differences in G-2 may become important if the repository boundaries are extended to the north from the present exploration block.

Distinctive Properties of the Devitrified Topopah Spring Tuff in USW G-2–Drillhole USW G-2, about 3 km north of the present exploration block, differs significantly in the nature of its Topopah Spring Tuff textural stratigraphy from the drillholes farther south. For example, a unique xenolithic zone first described by Lipman et al. (1966) is present between the upper lithophysal and the overlying transitional rhyolite-to-quartz latite zone (Tptrn to Tptrl). The xenolithic zone, containing lava fragments, probably records a major collapse in the Claim Canyon Caldera to the north, during the eruption of the Topopah Spring Tuff (Lipman et al. 1966). Other features of the Topopah Spring Tuff in drillhole USW G-2 are also significantly different from the same unit in drillholes to the south. In USW G-2, each nonlithophysal zone is only about 9 m thick. This thickness is approximately one-third that of the thinnest nonlithophysal zones in the other cored holes. A thin section from the middle nonlithophysal zone in USW G-2 is nearly all spherulitic and microlitic, whereas this zone in the other holes generally has a substantial cryptocrystalline content in addition to the spherulitic texture. Thus, it appears that the Tpt penetrated in USW G-2 is essentially one thick lithophysal zone from the top of the upper lithophysal zone to the base of the lower lithophysal zone.

Petrographic Comparison of Devitrified Rhyolite Zones Between Cored Holes–Figure 6.1-12 shows the overall relation of the Topopah Spring Tuff devitrified rhyolite zones to stratigraphically adjacent units and to the static water level. Only that portion of the cored holes above the static water level (Robison 1984) is shown, and faults, such as the Ghost Dance Fault (Scott, R.B. and Bonk 1984), are not shown. The thicknesses of the four devitrified rhyolitic zones vary in the cored holes based on U.S. Geological Survey (USGS) contacts (Maldonado and Koether 1983; Spengler, Muller et al. 1979; Spengler, Byers et al. 1981; Spengler and Chornack 1984; Scott, R.B. and Castellanos 1984). The thinning of the two nonlithophysal zones northward toward USW G-2 is especially evident.

The distinguishing microscopic features among the four zones, independent of variation among holes, are as follows. The lower nonlithophysal (Tptpln) zone generally has a greater percentage of quartz phenocrysts, lithic fragments, and cryptocrystalline texture and is the most densely welded in contrast to the overlying zones. The lower lithophysal zone (Tptpll) is generally

distinguished by little or no cryptocrystalline texture but has cristobalite rather than tridymite. The middle nonlithophysal zone (Tptpmn) has a moderate amount of cryptocrystalline texture but is distinguished generally from the Tptpln by fewer quartz phenocrysts and lithics and by moderate welding. The upper lithophysal zone (Tptpul) is readily identifiable in hand specimen or drill core and microscopically contains abundant tridymite in the microvesicles and granophyric pumices.

Within individual zones, variability from the base to the top ranges from barely perceptible to distinct. The lower nonlithophysal and middle nonlithophysal zones have fairly obvious decreasing cryptocrystallinity from base to top. The lower lithophysal zone has increasing crystallinity that progressively obliterates primary shard textures from base to top, whereas granophyre tends to increase. The upper lithophysal zone shows increasing quartz-latitic lenticles only in the uppermost part. Finally, as in the extreme case of hole USW G-2, the four cored holes within and near the Yucca Mountain Exploration Block, especially UE-25 a#1 just outside the block, show slight variation laterally within zones among the holes. Within the lower nonlithophysal zone, USW GU-3 contains slightly less quartz phenocrysts and cryptocrystalline texture than do the other holes. Within the lower lithophysal zone, UE-25 a#1 contains a minor amount of cryptocrystalline texture compared with the near absence of this texture in the other three holes. Within the middle nonlithophysal zone, the cryptocrystalline texture is less abundant in both UE-25 a#1 and USW G-1 than in the other two cored holes, and quartz phenocrysts are more abundant in USW G-1. Finally, within the upper lithophysal zone no quartz latite lenticles were observed in the upper part of the zone in USW GU-3, probably owing to lack of samples. These variations are illustrated in the report by Byers and Moore (1987).

Statistical Analysis of Host-Rock Groundmass Data–The statistical analysis of Topopah Spring Tuff textural data provides important information on how well we understand the major source of variability in the potential host rock, a variability that is directly observable in matrix texture. Details of statistical analysis are summarized in Byers and Moore (1987). A brief synopsis is given here.

The eight matrix texture types quantified by point counting of the Topopah Spring Tuff are phenocrysts, lithic fragments, granophyre, amygdules, microlites/spherulites, cryptocrystalline groundmass, glass, and voids. Phenocrysts are further subdivided into quartz, sanidine, plagioclase, mafic minerals, and accessory minerals. No glass is present in the devitrified rhyolite, so only the seven remaining textures need be considered. For reasons discussed above, samples from USW G-2 are excluded from statistical analysis.

Two levels of comparison can be made concerning the petrographic composition of the four devitrified rhyolite zones. The first comparison is based on variability within a fixed zone, such as vertical trends or gradational differences near contacts between the zones. However, the statistical analyses undertaken by Byers and Moore (1987) are concerned with the second level of comparison, involving differences in petrographic composition between the four zones. In this context, interest was in the broader generalization to the average observation obtained from a particular zone and whether or not a given sample may be assigned to the broader zone classifications of upper lithophysal, middle nonlithophysal, lower lithophysal, or lower nonlithophysal, based on the textural type percent data collected.

The results of discriminant analysis (Byers and Moore 1987) give some idea of the accuracy that may be expected from attempting to classify a thin section slide sample into the appropriate zone. This analysis confirms that texture is the most variable parameter within the devitrified rhyolitic Topopah Spring Tuff. Significant variation between holes also is indicated, so further analyses may be required to assess the extent to which lateral variation affects ability to discriminate between stratigraphic zones. An additional but less robust parameter of increase in quartz phenocryst abundance with depth suggests that mineralogy may be a useful but less definitive discriminant of stratigraphy within the devitrified rhyolitic Topopah Spring Tuff. Finally, chemistry appears to be almost invariant in the rhyolitic Topopah Spring Tuff, with the exception of minor superposed alteration where zeolitization occurs or where the rock is exposed to near-surface weathering (see discussion below).

Chemical Stratigraphy in the Rhyolitic Topopah Spring Tuff: Little Variability–The textural variability and the lesser variability in mineralogy discussed above are both linked to cooling history. Because of the complex superposition of multiple cooling zones over the relatively simple quartz-latite to high-silica rhyolite zonation in the Topopah Spring Tuff, the chemical stratigraphy of the Topopah Spring Tuff is much simpler than the mineral and textural stratigraphy. This situation is particularly true in the lower 85 percent of the Topopah Spring Tuff, below the gradational quartz-latite to high-silica rhyolite transition. Indeed, all of the rhyolitic compositions within the Paintbrush Group (with the exception of the low-silica Pah Canyon rhyolite) form an exceptionally tight compositional group, in contrast to the other rhyolitic tuffs at Yucca Mountain (Figure 6.1-1). Here we examine the nature and causes of deviations from homogeneous chemistry in the high-silica rhyolite of the Topopah Spring Tuff.

Chemical Effects of Local Zeolitization Within the Potential Host Rock–Table 6.1-3 provides X-ray fluorescence data for major-element compositions of the high-silica rhyolite from core samples in UE-25 UZ#16. This core was particularly important in that this was the first drill sampling in which zeolitic alteration of the matrix of the Topopah Spring high-silica rhyolite was observed. This alteration takes the form of trace to 14 percent development of stellerite in the matrix of the high-silica rhyolite. The chemical consequences of this alteration can be seen in the two subparts of Table 6.1-3; the altered portions, containing stellerite, have modestly higher CaO but show little other difference compared with the unaltered high-silica rhyolite. This rise in CaO is strongly correlated with stellerite content (Figure 6.1-13). The unaltered samples in the upper part of Table 6.1-3 provide a good estimate of "typical" composition of the Topopah Spring Tuff high-silica rhyolite as encountered at depth in the vicinity of the exploration block at Yucca Mountain.

Chemical Effects Associated With Soil Carbonate Invasion Into Near-Surface Samples of the Topopah Spring Tuff–Other than stellerite alteration, the only significant concern in considering deviations from typical at-depth composition are encountered in the collection of samples from outcrop. Table 6.1-4 summarizes the variability within 105 outcrop samples of high-silica rhyolite collected at the western margin of the exploration block in Solitario Canyon. Significant alteration occurs in the outcrop material, evident from the higher maximum content of CaO, MgO, and possibly Fe_2O_3 (contrasted with the unaltered Topopah Spring Tuff composition reported in Table 6.1-4). The principal deviation is in CaO content, but all three of these deviations can be attributed to the incursion of surface-derived carbonate into fractures and matrix. The rise in CaO can be related petrographically to the invasion of microcrystalline

calcite, similar to that found in surface calcretes, both along fractures and into pores of the tuff matrix. The rise in MgO is related to the minor amounts of sepiolite that occur as part of this calcrete invasion. The Fe_2O_3 increase is also characteristic of the calcretes, which have an eolian constituent that has high Fe and a characteristic Fe/Sc ratio (Vaniman, Chipera et al. 1995). The calcrete contamination is often visible as small root and fungal fossil forms and can occur to depths at least as great as 15 m.

6.1.1.2.3 Calico Hills Formation (Tac) and Underlying Bedded Tuffs (Tacbt)

The Calico Hills Formation is one of the most complex units at Yucca Mountain. Not only is it compositionally variable (Figure 6.1-1), but it also consists of a complex series of composite primary and reworked eruptive units that grade laterally from completely zeolitized to unaltered, vitric rock from east to west across the potential repository area at Yucca Mountain. The ash falls and ashflows that comprise the Calico Hills Formation beneath the exploration block give way to the north and east to lava flows. Fine-scale variations in matrix properties occur within centimeters and lateral continuity in properties is poor (Broxton, Chipera et al. 1993). The available lanthanide data follow the generally rhyolitic pattern of little light-lanthanide enrichment and a prominent negative Eu anomaly (Figure 6.1-14). Phenocryst abundances vary from <3 to 25 percent; the lower percentages occur in the upper three-fourths of the unit and the higher phenocryst percentages occur in the lower part of the unit (Figure 6.1-15 and Broxton, Chipera et al. 1993). In more recent stratigraphic treatments (Moyer and Geslin 1995), the crystal-rich lower one-fourth is separated as unassigned bedded tuffs (Tacbt) beneath the Calico Hills Formation, distinct from the overlying Calico Hills Formation (Tac). Phenocrysts of both are predominantly quartz, feldspar, and biotite, with trace magnetite and accessory clinopyroxene, ilmenite, allanite, and zircon.

The Calico Hills Formation and the underlying bedded tuffs comprise one of the most significant barriers to waste migration at Yucca Mountain. Despite the great heterogeneity of the Calico Hills, it has a consistently high matrix porosity (average 28 to 35 percent) and poor fracture development that point to an important role for matrix flow and interaction. Other properties, particularly permeability, are extremely variable and strongly dependent on mineralogy; permeability drops by about two orders of magnitude and sorption by cation exchange rises by up to five orders of magnitude in the transition from vitric to zeolitic character within the Calico Hills.

6.1.1.2.4 Crater Flat Group (Tc)

The tuffs of the Crater Flat Group are all rhyolitic, with a compositional range that falls between the high-silica rhyolites of the majority of the Paintbrush Group and the distinctive lower-silica rhyolites of the Pah Canyon Tuff (Figure 6.1-1). Despite this spread of rhyolitic compositions, the tuffs within the Crater Flat Group may be related by a progressive deepening of negative Eu anomaly and decrease in La/Sm from the oldest (Tram Tuff) to youngest (Prow Pass Tuff) eruptive cycle (Figure 6.1-16). This observation is, however, currently based on only three analyses (Broxton, Warren et al. 1989). This possible trend in lanthanide-element composition could indicate progressive feldspar removal from the magma source over time. However, simple fractionation models fail to adequately account for the variation between tuffs in the Crater Flat Group (Broxton, Warren et al. 1989). In addition to the lanthanide element variations, the

abundances of Na, Rb, Cs, Ta, and U all increase from oldest to youngest whereas Ti, Fe, Co, Sr, Ba, Zr, and Hf decrease (Broxton, Warren et al. 1989). These variations are important in considering the "background" tuff compositions against which chemical compositions have changed as a result of matrix alteration and fracture transport at Yucca Mountain (see point c in Figure 3.6.1-39).

Prow Pass Tuff (Tcp)–The Prow Pass Tuff, with the deepest negative Eu anomaly and least light-lanthanide enrichment of the Crater Flat Group, is distinguished from the other tuffs of the group by presence of more orthopyroxene (altered orthopyroxene) than biotite as phenocrysts and by characteristic inclusions of oxidized, fine-grained lithic inclusions of a red "mudstone." Both the orthopyroxenes and the mudstone lithic inclusions need to be considered in evaluating the interactions of this unit with radionuclides (see Subsection 6.1.8.6). Other phenocrysts of the Prow Pass Tuff include quartz, biotite, plagioclase, and sanidine (Figure 6.1-17). With the exception of variations in pyroxene content, this phenocryst assemblage is found throughout the Crater Flat Tuff (Warren, Byers et al. 1984). Although the central part of the Prow Pass Tuff is devitrified, it is poorly welded and more porous than the extensive devitrified portions of the overlying Paintbrush Group Tuffs (the Tiva Canyon and Topopah Spring Tuffs). The vitric base of the Prow Pass Tuff is preserved where it is high above the water table but is altered to the zeolites clinoptilolite and/or mordenite where close to or beneath the water table. Analcime occurs in the lower part of the Prow Pass Tuff to the north, in USW G-2, but is not found in any part of the Prow Pass Tuff to the south.

Bullfrog Tuff (Tcb)–The Bullfrog Tuff has a modest negative Eu anomaly and intermediate light-lanthanide enrichment within the Crater Flat Group (Figure 6.1-16). The Bullfrog Tuff lacks the orthopyroxene phenocrysts of the overlying Prow Pass Tuff but has trace amounts of clinopyroxene. The central part of the Bullfrog Tuff is more densely welded than the central Prow Pass Tuff, being poorly to moderately welded, but is nevertheless not as densely welded as the tuffs of the Paintbrush Group (the Tiva Canyon and Topopah Spring Tuffs). Across the exploration block, both the nonwelded top and the nonwelded bottom of the Bullfrog Tuff are altered to clinoptilolite ± mordenite; to the north, in USW G-2, the Bullfrog Tuff is entirely within the analcime zone and the zeolitized base of the Bullfrog Tuff differs from sections to the south by absence of clinoptilolite; instead, the zeolitized base of the Bullfrog Tuff in USW G-2 contains mordenite + analcime.

Tram Tuff (Tct)–The Tram Tuff is thicker and more densely welded than the other tuffs of the Crater Flat Group. This tuff has the greatest light-lanthanide enrichment of the Crater Flat Group and has essentially no Eu anomaly, suggesting little or no feldspar fractionation from portions of the magma series that gave rise to this tuff (Figure 6.1-16). At the southern end of Yucca Mountain and probably beneath most of the exploration block, both the upper and lower parts of the Tram Tuff are altered to clinoptilolite ± mordenite. In the vicinity of USW G-1, however, analcime appears in the lower part of the Tram Tuff, and in USW G-2, analcime is the dominant zeolite in both upper and lower parts of the Tram Tuff. Authigenic albite also begins to appear in the base of the Tram Tuff in USW G-2.

Older Tuffs and Lavas (Lavas and Flow Breccias (Tll); Lithic Ridge Tuff (Tr); Older Tuff Units A, B, and C (Tta, Ttb, and Ttc))–The initial compositions of the older tuffs and lavas, beneath the Crater Flat Group, are poorly known, because of the extensive alteration that has

modified these units. Moreover, few of the drillholes at Yucca Mountain penetrate to the depths at which these units are found, providing only a meager amount of data on their nature.

Lanthanide-element data for the least altered of the older tuffs and for dacite lava are relatively similar, with little or no Eu anomaly (Figure 6.1-18). Other, more siliceous lavas (for example, rhyolite and rhyodacite in USW G-2) may have had different initial lanthanide compositions but are heavily altered to albite + calcite and are likely to carry the chemical signature of this alteration.

Because of the lack of data and the likelihood that transport of radionuclides can not extend to these depths, the most significant aspects of these units relate to alteration history and to the definition of deep groundwater compositions, rather than to radionuclide transport. In USW G-2, these volcanic units are all altered to albite + calcite; closer to the exploration block, near USW G-1 and UE-25b #1H, alteration is to calcite + analcime occurs throughout much of the Tram Tuff down to the Lithic Ridge Tuff, with alteration to calcite + albite beginning at about the depth where dacitic lavas and/or the Lithic Ridge Tuff occur.

6.1.1.3 Tertiary and Quaternary Surface Deposits

The surficial geology of the Yucca Mountain area is considered in the context of physiography and erosion rates in Subsection 3.3.9 of this report. Included in that section is a treatment of "History of the Issue of the Existence of a Potentially Adverse Condition" within Subsection 3.3.5.3.4. The text below provides mineralogic and petrologic information about a representative sampling of the calcretes, B soil horizons, and spring deposits discussed in Subsection 3.3.5. Some relevant information on plant roots and their impact on surficial-deposit development at Yucca Mountain is included. The Project has devoted significant effort to the distinction between pedogenic and spring deposits. Because of the importance of this topic to the Project, the characteristics of such deposits near the site are described in some detail.

6.1.1.3.1 Petrography of Calcretes, B Soil Horizons, Plant Roots, and Spring Deposits

Petrography of Calcretes, Soils, and Plant Roots–The petrographic data collected on calcretes from Exile Hill include thin-section and backscattered-electron-scanning-electron microscopy analysis of grain size, texture, density, and fossil structures. These data are summarized in Vaniman, Chipera et al. (1995). Petrographic analysis permits mapping of five general types of laminae within the siliceous calcretes. The listing below is arranged in order from laminae with most detritus to laminae with essentially no detritus. An example of a calcrete deposit containing all of these lamina types is shown in Figure 6.1-19.

- *Porous and Friable Ooidal Laminae.* These laminae contain abundant ooids and pellets. The term ooid is used here to refer to single detrital grains or fragments of recycled calcrete enveloped by concentric layers of calcite and opal, often with some sepiolite (note that in these calcretes the structure of authigenic mineral rims around ooid cores is always concentric, never radial). The term pellet is used to describe composite grains of either single or multiple detrital or calcrete fragments encased in fine-grained calcite and opal without internal structure. Pellets are generally larger than ooids (pellets: 70 μm to 1 mm, av. 520 ± 610 μm; ooids: 50 μm to 1 mm, av. 200 ±

160 μm). The abundance of inherited rock and mineral fragments in both ooids and pellets gives these laminae a large component of detritus (for typical examples, 3 to 31 percent, av. 14 percent detritus).

Within this classification is a relatively rare set of laminae in the vein calcretes that stand out in exposures because they are dark in color. These laminae are largely vertical and, although discontinuous, seldom have low-angle crosscutting orientations. The dark color of these laminae is due in part to their relatively abundant basaltic ash. However, the bulk of the detritus in these laminae is derived from tuffaceous rocks. Modal analysis of one such lamina shows 48 percent tuffaceous detritus, 4 percent basaltic ash, and 48 percent authigenic calcite plus silica (volume percentages). This analysis is in good agreement with the results of quantitative X-ray diffraction of this lamina indicating 54 percent detritus (w%). Although detritus-rich, the ooid forms in these ash-bearing laminae have thin and poorly developed rinds of authigenic minerals, indicating either young or arrested authigenic mineralization.

- *Root-Rich, Friable Laminae.* These laminae are weak, porous, and contain abundant root fossils. The root fossils in these laminae are generally ~1 mm in diameter or less; coarser root features are not preserved. The characteristic root fossil in these laminae is an opalized root sheath, preserving the cell structure of the root wall (*rhizoderm*). The interior cells (the *cortical parenchyma*) are not fossilized, leaving a void that is typically lined by *calcified filaments* (hollow tubules about 5 μm in diameter and tens of μm long, made up of small, equant, subhedral to euhedral calcite crystals <1-μm in size). Within this lining of calcified filaments, the void left by the cortical parenchyma contains extremely delicate splays of needle-fiber calcites. Descriptive references for the terms listed in italics can be found in Jaillard et al. (1991) (root structure) and in Klappa (1979); Phillips and Self (1987); Wright (1986, 1989); and Vaniman, Chipera et al. (1994) (calcified filaments and needle-fiber calcites). Calcified filaments are common in pedogenic calcretes, where they may be formed by a number of microorganisms or by calcite precipitation around root hairs (Klappa 1979). The small diameters and hyphae-like morphology of the calcified filaments, and the demonstration of calcite precipitation by soil fungi in culture experiments (Monger et al. 1991), support a fungal origin for these features. Needle-fiber calcite has been described from a number of pedogenic environments and attributed to calcification of fungal hyphae within decaying roots (Phillips and Self 1987; Wright 1986, 1989). Also found within some of the root casts are extremely delicate acicular microcrystals, tapering from ~0.5 μm at their bases to narrow points (Vaniman, Chipera et al. 1994). This fossil form can develop within fungal hyphae and consists of either calcite or Ca-oxalate crystals (Klappa 1979; Simkiss and Wilbur 1989). The root-rich, friable calcrete laminae have variable amounts of rock and mineral fragments, giving them a range of detrital-mineral contents (detritus: 0 to 13 percent, av. 5 percent).

- *Dense and Resistant Laminae.* These laminae often show evidence of shearing within the vein calcretes. They consist of densely intergrown, fine-grained (<5 μm) calcite plus opal; they constitute the hardest component in the calcretes, appearing dense in hand sample with vitreous luster and brown to white color. Evidence of shearing is best seen in thin section as a sigmoidal fabric within some of the dense laminae.

Interestingly, these dense laminae also commonly contain root fossils, like the root-rich, friable laminae that are much softer (see above). However, the root fossils within the dense laminae include the delicately opalized roots described above with calcified filaments and needle-fiber calcites in dense laminae that are unsheared, and root fossils in which the cells of the cortical parenchyma are sometimes outlined by opal (and/or sepiolite) and often filled by calcite crystals. Other root fossil forms include relicts of calcareous fossilization in which the root fossil and its surroundings have been opalized. As in the root-rich, friable laminae described above, root fossils larger than ~1 mm are not preserved. The dense and resistant laminae generally have few detrital rock or mineral grains (detritus: 0 to 9 percent, av. 2 percent).

- *Rare Sepiolite-Plus-Calcite Laminae.* Although rare, these laminae can be found. Sepiolite, a chain-structure clay mineral [$Mg_4(Si_2O_5)_3(OH)_2 \cdot 6H_2O$], is common in all of the laminae described above but only in abundances less than ~5 percent. There are a few small, discontinuous laminae with higher sepiolite concentrations and one sample block from the south wall of Trench 14 in which a late-formed lamina of intergrown calcite-plus-sepiolite drapes earlier laminae in a small-scale unconformity.

- *Laminae of Pure Opal.* These opaline laminae are discontinuous and thin, and they occur within fractures, particularly in the vein calcretes. They provide the only authigenic minerals that can readily be separated from other authigenic minerals in the calcretes; the other common authigenic minerals (calcite and sepiolite) are too fine-grained and too intimately intergrown to be separated. In all other laminae, the opal is also too intimately intergrown with fine-grained calcite to be separated. In contrast, the pure opaline laminae may be a few millimeters wide and several centimeters long. Most of these laminae occur in open fractures and have a botryoidal surface morphology indicating precipitation against one wall of the fracture and outward growth into the fracture void. Both opal-A and opal-CT can occur as pure laminae; these laminae contain no detectable detritus.

In addition to the petrographic analysis of calcrete laminae, thin-section and/or scanning electron microscope studies were made of the overlying B-soil horizons and of plant roots from some of the species currently growing at Exile Hill (creosote bush: *Larrea divaricata*; Mormon tea or Nevada joint fur: *Ephedra nevadensis*; and desert thorn or twin fruit: *Menodora spinescens*) and some that have been inferred to have grown in the vicinity under past pluvial climates (piñon: Pinus monophylla; juniper: Juniperus osteosperma). Further discussion of these and other plants, with their relevance to the calcretes at Exile Hill, can be found in Quade and Cerling (1990).

In the B-horizon soils, weathered detrital grains are abundant and include both vitric and devitrified tuff fragments as well as mineral fragments of quartz, tridymite, cristobalite, alkali feldspars, biotite, pyroxenes, amphiboles, Fe, Ti-oxide minerals, sphene, and zircon. Smectite with weathered mica remnants is common; opal is seldom visible but can be seen associated with calcite in deposits that coat the undersides of pebbles. Rare occurrences of gypsum and halite are associated with decayed roots. In the lower (2Btj) horizon at Trench 14, above the calcrete, opalized root fossils occur with a form similar to those that occur in the underlying root-rich, friable laminae of the calcretes (see above).

The petrographic observations on roots from living plants are limited; most of the plant solids are amorphous, and although whewellite [$CaC_2O_4 \cdot 2H_2O$] occurs as a mineral in all of the roots studied, it is seldom visible as discrete crystals. The sole exception is in the roots of the creosote bush, where whewellite can be seen as equant crystals (Figure 6.1-20).

Petrography of Spring Deposits–Spring deposits of the Amargosa Valley and Death Valley, as well as calcified plant material from a seep at Crater Flat, were studied for comparison with the calcite-silica deposits at Exile Hill. The vein deposits and tufa mounds associated with spring activity are laminated, but the laminae are markedly different from those observed in the calcretes. Laminated vein deposits at spring localities typically include mm-scale or finer bands that represent growth bands within splays of calcite crystals that radiate from the fracture walls toward the vein center (Figure 6.1-21). Alternations in texture, crystal size, and morphology typically parallel the fracture walls. Massed growths of fibrous calcites are common, although in some veins individual crystal sizes range up to 1 cm or more. The laminae in tufa mounds are developed without the fine growth banding seen in the veins but contain instead a variety of fine-grained calcite textures. Most spring deposits contain fossil remnants of a wide range of organisms, ranging from bacteria and algae to encrusted remains of vascular plants (Pentecost 1992). Common in the surface deposits of springs in the vicinity of Yucca Mountain are bacterial clumps and ostracode shells (Figure 6.1-22). Chafetz and Folk (1984) identified bacterial clumps—brownish spots included within single crystals or aggregates of sparry calcite, 10 to 60 mm in diameter—as the elementary building blocks of travertines. Such features are typical of spring mounds in the vicinity of Yucca Mountain but not of the calcretes at Exile Hill.

The fossilized remains of vascular plants in spring deposits of the vicinity are particularly important because they contrast markedly with those found in the calcretes at Exile Hill (Figure 6.1-23). Root fossils are typical of the calcretes at Exile Hill, with common preservation of calcified filaments and needle-fiber calcites. In contrast, plant remains associated with spring discharge in the region are dominated by calcite casts that have formed around the stems of plants, preserving none of the cell structure and lacking the delicate filaments and needle-fibers that are characteristic of the calcretes. Indicative of standing water between and within the fossilized plant remains are meniscal septae formed by small calcite crystals that formed by precipitation at the water-air interface. The root fossil from the seep at site 199 has complete calcite replacement of the root form with poor preservation of cellular structure but with abundant bacterial clumps. Features like this are not found in any of the calcretes at Exile Hill.

6.1.1.3.2 Chemistry of Calcretes, B Soil Horizons, Plant Roots, and Spring Deposits

A detailed discussion of the chemical data for calcretes, soils, roots, spring deposits, and seeps can be found in Vaniman, Chipera et al. (1995). The calcretes that form surface slopes and those within faults (vein calcretes) were analyzed. Included in that report are separate discussions of lanthanide elements, zirconium, uranium, and iron-scandium, calcium-strontium, and gold-arsenic systematics. In this section we focus on those aspects of the chemical data that fit the broader needs of this report.

Calcium-Strontium Systematics–Strontium contents of calcites in the calcretes could not be measured directly because pure calcite separates could not be obtained for instrumental neutron activation analysis. Actual Sr contents of calcretes, spring deposits, ashed plant roots, soil

materials, and Roberts Mountain Formation dolomite are plotted against CaO in Figure 6.1-24. The Sr contents of the pedogenic calcites can be estimated at ~800 to 2100 µg/g based on comparisons of Sr with Ca data and with quantitative X-ray diffraction data for calcite abundances in the calcrete samples. All other constituents within the calcretes have relatively low Ca contents, with the exception of the ashed-root samples. The ashed-root samples, with the exception of piñon, have a narrow range of Ca compositions. There is exceptionally high Sr in two of the common plants presently found at Exile Hill (boxthorn and creosote bush). The plants that are now absent at Exile Hill but were more common in the past (piñon and juniper) have lower Sr contents in their root ashes and Ca-Sr ratios more similar to the calcretes. The Ca-Sr ratios for most soil and spring calcites are fairly similar.

Uranium–Uranium is associated with opal in the calcretes and in the B-horizon soil samples (Figure 6.1-25). A pure opal-A lamina from vein calcrete in Trench 14 contains 23 µg/g U, and a pure opal-CT lamina from the slope calcrete contains 18 µg/g U. These contents of U in opal compare with the lower portions of the ~0 to 270 µg/g U range for opals in unsaturated fractures at Yucca Mountain (Paces, Marshall et al. 1997). Aside from the separates of pure opaline laminae, the laminae with highest opal or U contents in the calcretes are typically those that are dense and sheared.

Gold-Arsenic Systematics–The Au and As data discussed here were collected by instrumental neutron activation analysis. Weiss et al. (1991) report Au contents determined by graphite furnace-atomic absorption spectrometry and As contents determined by inductively-coupled plasma emission spectrometry for large (2 to 10 kg) samples. Their detection limits for Au (0.20 ng/g) are lower than those obtained by instrumental neutron activation analysis (generally >0.8 ng/g); the detection limits for As by instrumental neutron activation analysis, however, are generally comparable (~0.2 µg/g). They are capable, therefore, of reporting measurable Au contents for volcanic rocks with <1 ng/g Au that are below detection limits in our data set. In our data set, only one tuff sample, of opalized Tiva Canyon Tuff from Trench 14, has measurable Au (12.6 ng/g). However, Au was measurable by instrumental neutron activation analysis in most of the calcrete samples and can be compared directly with the data of Weiss et al. (1991). They report a range of 0.5 to 7.3 ng/g Au and 4 to 12 µg/g As from Trench 14. Our As and Au values for calcrete samples cover essentially the same range, although the opaline laminae contain essentially no As, and our Au values for most calcrete samples are somewhat higher (2 to 12 ng/g). In Au content, two particular laminae from the vein calcretes are outliers: a sepiolite-plus-calcite lamina (15 ng/g Au) and a clay-, zeolite-rich lamina (29 ng/g Au). The absence of such high Au values from the analyses by Weiss et al. (1991) may be due to the fact that they analyzed large, bulk samples rather than individual calcrete laminae. Even the high-Au calcrete laminae, however, are overshadowed by the high Au contents of most of the root ash materials with the exception of the juniper sample and the outer part of the creosote-bush root (Figure 6.1-26). The ashed material of plants is typically enriched in Au relative to the soils in which the plant grows, with higher Au contents in the ultrastructure than in the roots (Boyle 1979). In this regard, most of the plants that now exist at Trench 14, and one (piñon) that once existed there, appear to concentrate Au in their root-ash components by moderate amounts (average of ~8x).

Arsenic is sometimes useful as a "pathfinder" element in Au exploration. Figure 6.1-26 shows considerable As variation and an apparent lack of strong correlation with Au. The ashed-root

materials that are strongly Au-enriched have little As. Any correlation of Au with As is weak in the calcretes and nonexistent in the root-ash materials.

6.1.1.3.3 Interpretations of Petrographic and Chemical Data for Surficial Deposits

There is a considerable body of evidence that the calcite in many desert soils is derived from Ca dissolved in rainwater, or carried as eolian dust, and from atmospheric or root-respired CO_2 (Machette 1985; Quade et al. 1989; Reheis et al. 1992). Considerations of this evidence and the data from calcretes at Yucca Mountain indicate that these calcretes have sources and accumulation rates comparable to other calcretes in the Southwestern United States. Details of this determination are found in Vaniman, Chipera et al. (1995) and are summarized in Subsection 3.5.3.4.2.3 of this report. Other aspects of chemical, textural, and mineralogic comparisons with spring deposits and seeps are given below.

The intimate intergrowth of calcite and opal in the calcretes of Yucca Mountain is atypical of spring deposits. Cool and warm springs, from deep or perched sources, have higher water flow and can maintain stable pH regimes that precipitate either calcite or silica but rarely both (White, D.E. et al. 1956; Chafetz and Folk 1984; Viles and Goudie 1990). In contrast, evaporative processes within arid soils formed of siliceous detritus can cause a rise in pH from only slightly alkaline to > 9 (Chadwick et al. 1989; Boettinger and Southard 1990), passing from regimes of calcite dissolution and silica precipitation into those of calcite precipitation and silica dissolution (Watts 1980). Numerous wetting and drying cycles can thus lead to repeated pH-driven dissolution-precipitation cycles that can account for the complex calcite and opal intergrowths seen in the calcretes of Trench 14. The closest analogous spring deposits are surface discharges that may deposit both calcite and silica, as at GMC and IMV spring localities. In these deposits, however, the opal and calcite are largely segregated or easily separable and not as intimately intergrown as in the calcretes of Yucca Mountain. Spring deposits have a greater bulk density than the calcretes at Yucca Mountain (Vaniman, Chipera et al. 1995). This fact is particularly true for the vein deposits at known spring localities. However, the more porous tufa mounds, as at Nevares, can develop low-density deposits with densities low enough to approach those of the most dense of the vein deposits at Yucca Mountain. Other physical and chemical features provide more definitive distinctions between the calcite-silica deposits of spring or soil-process origins.

Many of the same authigenic minerals (calcite, opal, and sepiolite) that occur in the calcretes can also be found in known spring or seep deposits. However, there are certain key differences in the deposits that form in these two different environments. Veins of pure calcite are common at spring localities but do not occur in the calcretes. Individual calcite crystals of > 1 cm are common in travertine veins at springs but are not found in any of the calcretes, including the vein calcretes. Where comparable fine-grained calcite does occur in travertine mounds at springs, it is still very common to obtain deposits of relatively pure calcite with characteristic bacterial clumps and ostracode fossils. Fossil casts from the stems of phreatophyte plants, connected by meniscal septae (Figure 6.1-23a), provide readily visible field evidence of spring activity. None of these features are found in the calcretes at Yucca Mountain.

Springs and evaporative seeps retain biogenic evidence of their past higher water content, including ostracode fossils, casts of phreatophyte plants, and algal or diatomaceous deposits of

opal-A. Pedogenic calcretes have a different set of fossils. Calcified filaments are typically pedogenic. Superficially similar calcareous filaments occur as algal products in active springs, but these delicate filaments are not preserved in accumulated inactive spring deposits whereas bacterial "shrub" structures commonly are (Chafetz and Folk 1984; Viles and Goudie 1990). In contrast, the calcified filaments in the Yucca Mountain calcretes are found in the oldest as well as the youngest laminae. Moreover, algal filaments in springs are not restricted to associations with fossil roots, as are the calcified filaments of the Yucca Mountain calcretes. Needle-fiber calcites are unlikely to form and less likely to be preserved in areas of spring discharge.

These delicate fossils within root casts provide two important constraints on the origins of the siliceous calcretes. First, the fragile fossil forms are preserved even within the earliest-formed calcrete laminae (Figure 6.1-19); such preservation would be unlikely if the calcretes were emplaced by successive forceful fluid injections with catastrophic brecciation. Indeed, the pervasive distribution of root fossils suggests that root penetration plays a distinctly noncatastrophic but nevertheless forceful role (Klappa 1980) in the brecciation of these calcretes. The dense, sheared laminae are pervaded by root-fossil remnants and may represent collapsed zones where coarser roots were once concentrated. Second, similar needle-fiber calcites and calcified filaments within fossil roots are characteristic of pedogenic calcretes (Klappa 1979; Phillips and Self 1987; Wright 1986, 1989). In evaporative seeps and in calcareous tufa mounds around springs, the fossilization of vascular plants typically leaves casts of the plant form without preserving such fine features of root decay. The high water flux in seeps and springs flushes out the products of decay, leaving only the plant casts behind. Calcified filaments, needle-fiber calcites, and other delicate fungal fossils within root forms thus provide an important guide to pedogenic calcretes, particularly where they occur beneath a genetically related B-horizon. Intermittently saturated desert soils without pedogenic horizonation might retain delicate fungal fossils (Mack and James 1992), but the retention of such features is unlikely in zones of forceful spring discharge.

6.1.2 Origins of Primary and Secondary Chemical Variability

The existing chemical variability of the pyroclastic units at Yucca Mountain is the combined effect of magmatic processes, differential pyroclastic transport, syngenetic alteration, regional hydrothermal alteration, diagenesis, and chemical exchange with groundwater. This section provides an overview of the processes responsible for chemical variability. Specific aspects of chemical variability pertinent to reconstruction of the site geochemical history and to predictions of radionuclide interactions are described in detail in appropriate sections of this report.

6.1.2.1 Primary Chemical Variability

Primary chemical variability in the ashflows at Yucca Mountain is traceable to variability in the compositions and relative proportions of pyroclasts within the tuffs. Variations in the composition and content of pyroclasts, in turn, reflect the combined influences of pre-eruptive magmatic processes and post-eruptive pyroclast transport.

6.1.2.1.1 Chemical Zonation in the Paintbrush Group and Other Units

Lipman (1966, 1971) and Lipman et al. (1966) documented a systematic variation in composition with stratigraphic height in the Topopah Spring Tuff. The zonation from phenocryst-poor high-silica rhyolite upward into phenocryst-rich quartz latite was interpreted to reflect compositional zonation of magma in the source chamber prior to eruption. A more detailed study of major-, minor-, and trace-element chemical zonation in the ashflow was undertaken by Schuraytz et al. (1989), who analyzed whole-rock samples as well as glassy pumice lumps separated from the tuff. The pumices were thought to be the best representatives of original magma compositions. Both the crystalline and glassy portions of the pumices from the upper part of the ashflow display two populations that are chemically distinct with respect to major, minor, and trace constituents. Relatively few intermediate values were observed. The following interpretations of chemical zonation are abstracted from these studies.

Schuraytz et al. (1989) concluded that the Topopah Spring Tuff provides a record of progressive evacuation of a single magma chamber that was compositionally zoned downward from phenocryst-poor high-silica rhyolite to phenocryst-rich quartz latite. There was a distinct liquid-liquid interface separating the two contrasting magmas and a large thermal gradient between the layers. The compositional stratification originated by injection of quartz latitic magma below the rhyolitic layer shortly before eruption. Progressive withdrawal of magma during eruption led to upward distortion of the magmatic interface and simultaneous eruption of magma with increasing differences in composition and temperature. The persistence of high-silica rhyolitic pumices throughout the ashflow indicates that none of the pyroclastic rocks represent pure end-member quartz latitic magma and suggests that the eruption was insufficient to exhaust the upper rhyolitic magma layer.

The compositional zonation of major, minor and trace elements with stratigraphic height in the Topopah Spring Tuff may be accompanied by isotopic zonation of related origin. A systematic upward increase in whole-rock $^{87}Sr/^{86}Sr$ within the upper part of the ashflow, persisting into the overlying nonwelded tuffs, has been documented (B. Marshall 1997, written communication cited in Bodvarsson et al. 1997). The existence of zones with distinctive primary chemical and isotopic compositions provides the means to test hypotheses about geochemical transport and rock-water interaction. Such studies are contained in Subsection 6.1.5.2.

Yucca Mountain pyroclastic units other than the Topopah Spring Tuff also exhibit compositional zonation, which has not been studied in as great detail. The Tiva Canyon Tuff is zoned upward from high-silica rhyolite to rhyolite to quartz latite (Byers, Carr, Orkild et al. 1976). The Rainier Mesa Tuff, with minor exposures in the Yucca Mountain area, shows similar zonation (Byers, Carr, Orkild et al. 1976).

6.1.2.1.2 Phenocryst Content in the Calico Hills Formation and Crater Flat Group

Phenocrysts are crystalline components of pyroclastic rocks inherited from the parent magmas. The chemical composition of the phenocryst fraction of a tuff may be substantially different from the composition of the original glassy fraction. The contribution of phenocryst chemistry to whole-rock chemical composition and geochemical behavior is a function of phenocryst content. The phenocryst content is a potential concern for investigations of element mobility during

alteration based on comparisons of unaltered and altered whole-rock chemistry. During the diagenetic alteration of volcanic glass to a zeolite-clay-silica assemblage at Yucca Mountain, the feldspar and crystalline silica phenocrysts were essentially inert and, therefore, represented a geochemical reservoir that didn't participate in the alteration. The effect of an inert geochemical reservoir on mass-transport calculations is to dampen the perceived evidence of element mobility for those constituents, notably Al and Si that are abundant in the phenocrysts. If paired samples of vitric and altered tuff have unequal phenocryst contents, then additional uncertainty is introduced into the mass-transport calculation.

The measured phenocryst content of Yucca Mountain Tuffs varies from less than 1 vol. percent to as much as ~25 volume percent (Byers, Carr, Orkild et al. 1976; Broxton, Chipera et al. 1993; see Subsection 6.1.1.2 for details of phenocryst compositions at Yucca Mountain). Among the major stratigraphic units in the vicinity of Yucca Mountain, the bedded tuff at the base of the Calico Hills Formation (Tacbt) consistently has the highest phenocryst content. Phenocryst-related heterogeneity in the Calico Hills Formation is described in Subsection 6.1.1.2.3. The upper part of the Bullfrog Tuff also has phenocryst content as high as ~25 volume percent (Byers, Carr, Orkild et al. 1976). Crystalline lithic inclusions, like phenocrysts, also modify the bulk chemistry of a tuff in proportion to their abundance.

6.1.2.2 Chemical Variability Associated with Devitrification and Syngenetic Alteration

The term devitrification, as applied to the pyroclastic deposits at Yucca Mountain, denotes high-temperature crystallization of volcanic glass to a largely anhydrous mineral assemblage. Little is known about bulk chemical changes associated with devitrification, although short-range chemical transport (up to mm-scale) must occur during the crystallization of homogeneous glass to an aggregate of discrete mineral phases.

Comparisons of the compositions of brown cryptocrystalline devitrified groundmass and vitrophyre glass in the Topopah Spring Tuff indicate general similarities (Byers 1985). Devitrified groundmass from the lower Topopah Spring devitrified-vitric transition zone, with its higher K content, diverges in composition from vitrophyre glass and groundmass away from the transition zone. The additional K was probably derived from dissolution of vitrophyre glass within the transition zone, a local process that was absent from most of the rock undergoing devitrification. Zeolite-rich portions of the altered transition zone are enriched in Ca (Broxton, Bish et al. 1987; Broxton, Warren, Hagan et al. 1986).

As described above, most syngenetic alteration is located in and near devitrified-vitric transition zones, and the alteration itself represents a transition from devitrification to glass dissolution and secondary-mineral precipitation of mostly zeolites, clay, and silica phases. The principle locations of syngenetic alteration in the Paintbrush Group are described in Subsection 6.1.4.1.2. The volume of rock affected by syngenetic alteration is highly variably throughout Yucca Mountain, but in general, the cumulative thickness of affected rock is of the order of tens of meters or less.

6.1.2.3 Chemical Variability Associated with Diagenetic Alteration

Diagenetic alteration of glassy nonwelded silicic tuffs at Yucca Mountain involved dissolution of glass pyroclasts and precipitation of mostly clinoptilolite, silica, and smectite. Chemical changes and introduction of chemical variability associated with this alteration are functions of the compositions of the secondary minerals and of variability in their relative proportions caused by transport of dissolved or colloidal components into and out of the altered rock (see Subsection 6.1.4.2.2).

6.1.3 Mineralogy of the Yucca Mountain Site and Environs

6.1.3.1 Matrix and Phenocryst Mineralogy of the Tertiary Volcanic Rocks at the Site

Unit-by-unit descriptions of the geochemistry of Tertiary volcanic strata are given in Subsection 6.1.1.2. Some details of phenocryst mineralogy are provided in that section, but a brief synopsis is included here as a prologue to the discussion of basic differences between rhyolitic and quartz-latitic components of the Yucca Mountain stratigraphy. Figure 6.1-27 provides an encapsulated view of summary phenocryst compositions for the volcanic units at Yucca Mountain. There is a broad overlap in compositions for all units, but some trends with stratigraphic significance can be discerned. In general, the Or (potassium) content of sanidine phenocrysts increases with depth among the rocks at Yucca Mountain. Also, the most common of the Fe-Mg-silicate phenocrysts, biotite, provides a measure of Fe/Mg ratios among units; the biotites that occur from the rhyolite of the Topopah Spring Tuff down through the bottom of the Crater Flat Group are more Fe-rich than those that occur above and below. In that phenocryst compositions reflect host magma chemistry, these variations represent a subtle overprint on the generally bivariate compositions (rhyolite versus quartz latite) that characterize the major geochemical subdivisions at Yucca Mountain.

6.1.3.1.1 Rhyolitic Volcanic Units

Outcrops of the vitric, high-silica rhyolite portion of the Rainier Mesa are the only common remnants of this unit at Yucca Mountain. These rocks consist mostly of glass, with ~13 percent phenocrysts of feldspar, quartz, and less common biotite with traces of hornblende, clinopyroxene, and orthopyroxene and accessory magnetite, ilmenite, monazite, zircon, apatite, allanite, and perrierite. The high-phenocryst content in this unit, the only common representative of the Timber Mountain Group at the site, is marked different from the poor (<5 percent) to very poor (<1 percent) phenocryst abundances in the Paintbrush Group rhyolitic units that constitute the bulk of the unsaturated zone at Yucca Mountain. Higher Phenocryst abundances (~10 to 20 percent) are seen again down-section in quartz-latitic portions of the Tiva Canyon Tuff and the Topopah Spring Tuff, and in bedded tuff below the Calico Hills Formation and in the Crater Flat Group rhyolites, the latter forming the principal units that comprise saturated zone transport pathways (Figure 6.1-27).

Unsaturated-Zone Rhyolites–In the gradational zone into high silica rhyolite of the Tiva Canyon Tuff and in most of the high-silica rhyolite, the rock is devitrified and the major devitrification products, feldspar and silica minerals, account for more than 95 percent of the rock mass (Figure 6.1-27). Sanidine phenocrysts account for most of the rest of the rock. Other

phases include trace abundances of biotite, hornblende, and clinopyroxene and accessory magnetite, ilmenite, sphene, perrierite, apatite, and zircon.

In contrast with the other high-silica rhyolites at Yucca Mountain, the Yucca Mountain Tuff is markedly aphyric, with <0.1 percent phenocrysts (Figure 6.1-27). The high matrix porosity of this unit, and its largely vitric nature, provide the potential for significant increase in water/rock ratios and for transition from fracture to porous flow in a rock type that is more reactive than the overlying devitrified high-silica rhyolite of the Tiva Canyon Tuff.

Within the potential host rock, the devitrified rhyolitic portion of the Topopah Spring Tuff, phenocrysts are minor constituents (<5 percent) of the rock, with the remaining >95 percent consisting of fine-grained devitrification minerals. These devitrification products are principally feldspars plus a variable combination of the silica polymorphs tridymite, cristobalite, and quartz. Quartz phenocryst abundance is a useful stratigraphic marker within the devitrified rhyolitic Topopah Spring Tuff, but quartz phenocrysts are nevertheless much less abundant (<0.5 percent) than groundmass quartz (~20 percent) throughout this interval. The silica polymorph distributions are particularly important because of their thermal stability, dissolution properties, and properties as inhalation hazards. Moreover, although the feldspar abundances in the devitrified rhyolitic Topopah Spring Tuff are essentially constant at ~55 percent, the proportions of silica polymorphs vary with depth and between lithophysal and nonlithophysal zones. These variations are discussed below.

Variability of Silica Polymorph Abundances in the Rhyolitic Topopah Spring Tuff– Variation in the abundances of silica polymorphs has significance in thermal stability calculations, silica dissolution and precipitation calculations, and estimation of silica inhalation hazards for repository construction workers. Figure 6.1-28 is a plot of normalized tridymite:cristobalite:quartz abundances in the devitrified rhyolitic Topopah Spring Tuff. These data are obtained from bulk-rock X-ray diffraction analyses and thus include both phenocrysts and groundmass, although the groundmass far outweighs the phenocryst contributions in the makeup of the rhyolitic Topopah. The data plotted are from the particularly closely sampled core UE-25 UZ#16. Similar general trends of silica polymorph distributions can be found in other drill cores, but the close sample spacing in UZ-16 provides a particularly good illustration of this variation in silica polymorph distributions (at present there are insufficient data to make comparisons to other drill cores). The upper devitrified zone, where the rock composition is quartz-latitic, has essentially no quartz as either phenocrysts or groundmass. This is a property common to this zone in virtually all cores from the exploration block. There is a fairly uniform increase in the tridymite/cristobalite ratio with depth within the quartz latite, although this at present does not seem to be a uniform property in all of the cores yet analyzed (confidence in this conclusion is limited by lack of data). Quartz begins to appear as the rhyolitic interval is encountered in the upper lithophysal zone, although abundances are small and the dominant silica polymorphs are still cristobalite and tridymite. There is a relatively constant decrease in tridymite abundance with depth in the upper lithophysal zone (again, this is well documented in UZ-16 but difficult to extrapolate to the entire exploration block because of lack of data). From the base of the upper lithophysal zone to the basal vitrophyre, the predominant silica polymorphs in the Topopah Spring Tuff are quartz and cristobalite, with a quartz/cristobalite ratio that has no apparent correlation with depth. However, there are some subtle patterns to silica polymorph distributions that are important in this zone, where a repository may be developed:

First, the tridymite abundances in the lower lithophysal zone extend to higher values than either of the adjacent nonlithophysal zones. Tridymite occurrences at this depth, where the rhyolitic bulk composition is constant, are a marker of vapor-phase crystallization.

Second, there is a small but consistent increase in tridymite with the higher cristobalite contents within both of the nonlithophysal zones. This correlation reflects the dispersion of many smaller, and probably unmappable, vapor-phase pockets within the otherwise nonlithophysal zones.

These variations in silica polymorph composition, using UE-25 UZ#16 as an example, illustrate that the predominant silica polymorphs within the target host rock are quartz and cristobalite. The data suggest that within this interval, the relative proportions of quartz versus (tridymite + cristobalite) may be developed into a guide to small-scale variations in lithophysal versus nonlithophysal character. Further analysis of this possibility is necessary, however, for it is evident from fracture mineralogy studies (Subsection 6.1.3.2) that earlier generations of tridymite growth may be pseudomorphed by later quartz development; such temporal variation could make simple models of silica polymorph origins problematic. For construction effects, it is important to note that the cristobalite/quartz ratios are highly variable. Mapping of lateral variability in this ratio may be useful in defining portions of the host rock where hazards of cristobalite inhalation may be mitigated and in avoiding the more thermally sensitive cristobalite concentrations.

A plot of normalized tridymite:cristobalite:quartz abundances in the devitrified rhyolitic Topopah Spring Tuff from drillhole UE-25 UZ#16.

The textural and chemical aspects of the potential host rock are important considerations in extrapolating physical and engineering properties from one part of the rhyolitic Topopah Spring Tuff to another. How homogeneous is the potential host rock, and do the large differences in texture, superposed on chemical homogeneity, as described below, provide a basis for interpreting the results yet to be obtained from excavation experience at the site? Of greater importance is the variability in mineralogy. The silica polymorphs, quartz, tridymite, and cristobalite are all found in the rhyolitic Topopah Spring Tuff, but their occurrence and abundance are quite variable. Important considerations in silica-polymorph distributions are:

- All silica polymorphs are of concern in regulatory guidelines that limit silica dust inhalation, but cristobalite has a threshold limit value approximately half that for either quartz or tridymite. Because of this higher regulatory sensitivity, cristobalite dust concentrations have already caused concern in the operations of the tunnel-boring machine at Yucca Mountain.

- The silica polymorphs have differing solubilities in water, with cristobalite > tridymite > quartz. The different solubilities of the silica polymorphs will be a factor in silica dissolution and transport, depending on which zones of the host rock serve as horizons of condensation and collection of water heated by the thermal load of a repository.

- Cristobalite undergoes a phase transformation from the α to the β form at about 250°C, a temperature likely to be reached within a relatively hot repository. This transition is accompanied by a volume increase of a few percent. Strains imposed by this phase transformation should be considered in repository design.

Other minerals, less common than the silica polymorphs, are of concern in the potential host rock. Although generally devoid of zeolites, except for minor occurrences along some fractures, the devitrified rhyolitic Topopah Spring Tuff was found to contain up to 14 percent of the zeolite mineral stellerite in drillhole USW UZ-16 (Chipera, Vaniman, Carlos et al. 1995). This unexpected occurrence of a low-temperature hydrous mineral intergrown with groundmass devitrification indicates that surprises, with implications for thermal response, may still be found in the potential host rock. Future drill core samples will be examined to determine the lateral limits of stellerite occurrence within the potential host rock.

A final aspect of host-rock mineralogy that needs to be mentioned is the occurrence of the fibrous zeolite erionite, which is a known carcinogen. Erionite has been found, usually in trace abundances, in the lower part of the Topopah Spring Tuff, usually associated with the basal vitrophyre. Concerted effort has been devoted to examining the distribution of erionite at Yucca Mountain and the results of these studies are described in detail in Subsection 6.4 of this report. Because erionite has not been found above the altered zone at the top of the basal vitrophyre, in the potential host rock, the occurrences of erionite are not discussed in greater detail in this section.

Calico Hills Formation Rhyolites: Unsaturated-Zone/Saturated-Zone Boundary–Ashflows of the Calico Hills Formation (Tac) have phenocryst abundances that are generally <3 percent; the underlying bedded tuff (Tacbt), however, can have phenocryst abundances of up to 25 percent (Figure 6.1-27; Broxton, Chipera et al. 1993). Phenocrysts of both are predominantly quartz, feldspar, and biotite, with trace magnetite and accessory clinopyroxene, ilmenite, allanite, and zircon. Figure 6.1-1 shows that the ashflows of the Calico Hills Formation have exceptionally large variability in composition, with normalized anhydrous SiO_2 values ranging between 76 percent and 80 percent. These values are based only on unaltered, vitric samples. With alteration, the silica content is diminished (see Subsection 6.1.2).

The matrix of the tuffs of the Calico Hills Formation varies from vitric, porous, and nonwelded with moderate matrix transmissivity ($\sim 10^{-8}$ m/s; Loeven 1993) to zeolitized, porous, and nonwelded with low matrix transmissivity ($\sim 10^{-10}$ m/s; Loeven 1993). The typical alteration phases are clinoptilolite plus minor smectite; mordenite becomes as abundant or more abundant than clinoptilolite toward the north at Yucca Mountain. Chabazite occurs in addition to clinoptilolite toward the south.

Crater Flat Group Rhyolites: Critical Pathways in the Saturated Zone–The common phenocryst assemblage of the Crater Flat Group is feldspar, quartz, biotite, and magnetite, with trace hornblende and accessory ilmenite, allanite, apatite, and zircon. Pyroxene occurs in the upper two tuffs (Prow Pass and Bullfrog) and, despite its minor abundance, may play an important role in radionuclide retardation in the Prow Pass Tuff (based on evidence of strong Pu retention by altered orthopyroxenes; see Subsection 6.1.8.6). Figure 6.1-27 summarizes the general similarity in quartz-sanidine-plagioclase-biotite phenocryst populations throughout the

Crater Flat Group; within this general similarity is a general increase in Or content of sanidine and in An content of plagioclase with depth, from the Prow Pass to the Tram Tuffs. All three of the Crater Flat Tuffs have devitrified central portions, with abundant feldspar and quartz, and at least initially had vitric margins, much of which has been altered to zeolites in the early alteration history of Yucca Mountain.

Throughout the exploration block and to the north, the alteration of original glass in the nonwelded margins and interlayered bedded units of the Crater Flat Group to zeolites is pervasive, with the exception of the upper nonwelded margin of the Prow Pass Tuff beneath parts of the crest of Yucca Mountain. The zeolitization is dominated by clinoptilolite in the south and by clinoptilolite + mordenite to the north. The nonsorptive zeolite analcime partially displaces these sorptive zeolites up into to lower parts of the Prow Pass Tuff in the northern part of Yucca Mountain, but within and to the south of Drill Hole Wash, analcime does not occur in any significance above the lower alteration zone in the Tram Tuff.

6.1.3.1.2 Quartz-Latitic and Related Volcanic Units

The principal quartz-latitic units of interest at Yucca Mountain are within the upper zones of the Tiva Canyon and Topopah Spring Tuffs (Figure 6.1-1). The Rainier Mesa Tuff also contains an upper quartz-latitic portion, but this is of very minor significance at Yucca Mountain. Included as a unit of considerable significance, however, is the low-silica rhyolite of the Pah Canyon Tuff (Figure 6.1-1) because it has chemical affinities to the quartz latites (Figure 6.1-7).

The quartz-latitic portion of the Tiva Canyon Tuff forms about 1/4 to1/3 of the surface outcrop in the vicinity of the exploration block at Yucca Mountain, and up to ~1/2 of the surface outcrop in the north (see Figure 3.6-4 in Subsection 3.6). Most of the remaining outcrops are of the rhyolitic Tiva Canyon Tuff. The quartz-latitic portion is also referred to as the "crystal-rich member" because of the high phenocryst abundance in the quartz latite (to >20 percent) compared to the rhyolite (<5 percent). The phenocrysts consist predominantly of plagioclase and sanidine, with traces of clinopyroxene and biotite and accessory amphibole, quartz, magnetite, ilmenite, sphene, perrierite, apatite, and zircon.

The phenocrysts in the next lowest-quartz latitic horizon, the Pah Canyon Tuff, are principally plagioclase and sanidine plus lesser biotite, with compositions as shown in Figure 6.1-27. Trace phenocrysts include quartz, clinopyroxene, and magnetite, with accessory ilmenite, sphene, perrierite, apatite, and zircon. Phenocrysts in this low-silica rhyolite are intermediate in abundance (~5 to 12 percent) between the high-silica rhyolites and the quartz latites of the Paintbrush Group. The Pah Canyon Tuff is nonwelded and, where relatively unaltered, is porous. Alteration, however, is common and the most abundant alteration product is smectite, which reduces both the porosity and permeability of the unit. Alteration to zeolites (clinoptilolite or heulandite) is observed in some locales, as is the occurrence of associated calcite.

The transition from quartz latite to rhyolite in the Topopah Spring Tuff is marked by progressively decreasing abundances of phenocrysts (from ~17 to 2 percent) and, in particular, by the appearance of quartz phenocrysts and the loss of clinopyroxene phenocrysts. Figure 6.1-27 illustrates the sharp difference in quartz-plagioclase-sanidine phenocryst populations between the quartz-latitic and rhyolitic portions of the Topopah Spring Tuff, despite the

generally similar compositions of individual phenocrysts within both subunits. Other phenocrysts are common throughout the Topopah Spring Tuff, principally feldspar and biotite with trace quartz, and trace to accessory magnetite, ilmenite, allanite, perrierite, apatite, and zircon.

6.1.3.1.3 Other Volcanic Units

The older volcanic units at Yucca Mountain include the Lithic Ridge Tuff and unnamed older tuffs designated A, B, and C, plus occurrences of dacitic lavas. These deeper units are far below the water table (~1.5 to 2.5 km) and are therefore unlikely to be of significance in considering transport from the potential repository. In general, these tuffs and, to the north, associated lavas, are thoroughly altered to analcime and, with increasing depth (grade), to albite, with associated smectite/illite, calcite, and lesser pyrite, barite, and other phases.

The major phenocryst compositions for the Lithic Ridge Tuff and for units A, B, and C of the older tuffs are summarized in Figure 6.1-27. Where feldspars are preserved, the plagioclase compositions generally become more calcic with depth. However, it is not uncommon to find feldspar phenocrysts pseudo-morphed by calcite. All of these older tuffs also include biotite, hornblende, magnetite, ilmenite, sphene, allanite, apatite, and zircon as trace phenocrysts.

6.1.3.2 Fracture and Fault Mineralogy of the Tertiary Volcanic Rocks at the Site

Fractures provide important pathways for fluid movement through rocks that are otherwise impermeable. This is particularly the case in densely welded, devitrified tuffs; indeed, the densely welded Topopah Spring Tuff is the principal aquifer at Jackass Flats, immediately to the east of Yucca Mountain, providing 28,000 to 100,000 gpd per foot from the producing wells, almost entirely from fracture storage and transmission (Winograd and Thordarson 1975). Flow along fractures in the unsaturated zone may be more inhibited, but occurrences of young calcite deposits along fractures in the unsaturated zone strongly indicate that such flow does occur (Whelan, Vaniman et al. 1994). Because minerals along fractures may differ significantly from minerals in the rock matrix, and because many fracture minerals may have important sorptive properties, it is important to consider the contributions that fracture mineralogy can make to site performance at Yucca Mountain.

6.1.3.2.1 Unsaturated-Zone Fracture Mineralogy

Fracture mineralogy provides a record of fluid transport and water-rock interaction, especially in the densely welded, devitrified tuffs where fracture flow is a dominant process. The minerals in fractures of the unsaturated zone originated under a variety of conditions. Syngenetic minerals are the products of high-temperature vapor-phase alteration and low- to moderate-temperature alteration in cooling pyroclastic deposits. In the deeper unsaturated zone, some fracture-filling minerals were deposited during a period when the static water level stood at a higher elevation than at present. The minerals associated with this transient period of saturation include products of diagenetic alteration of glassy tuffs and deposits that incorporated solutes transported from the deep Paleozoic carbonate aquifer. The dominant minerals deposited during about the last twelve million years are widespread occurrences of calcite and opal that have grown very slowly by incremental deposition from percolating meteoric water.

Applications of Unsaturated-Zone Fracture Mineralogy to Repository Performance–The data of fracture mineralogy address a number of issues relevant to flow and transport in the unsaturated zone. Among these are issues of fluid percolation, solute transport and deposition, radionuclide sorption by fracture coatings, and modification of fracture permeability by natural and repository-induced dissolution, precipitation, and transformation of fracture minerals.

Studies of several isotopic systems have established that percolating water moves by fracture flow even in the unsaturated zone at Yucca Mountain (Paces, Neymark et al. 1996; Paces, Marshall et al. 1997; Fabryka-Martin, Flint et al. 1997). In particular, the existence of fast-flow paths through nonwelded tuffs of the Paintbrush Group requires fractured rocks associated with faults (Fabryka-Martin, Flint et al. 1997). Information on the distribution and abundances of calcite and opal in fractures and voids has been used along with the geochronologic studies of the same minerals to estimate long-term-averaged percolation flux rates in the Exploratory Studies Facility (Paces, Neymark et al. 1996; Marshall 1997).

Well-documented mineral identifications provide the basic information for investigating relationships between fracture mineralogy and other properties of interest for repository performance. Because some minerals are more abundant in fracture coatings than in the adjacent rock matrix and because there is incomplete fluid communication between fractures and matrix over time scales less than about 10,000 years in the unsaturated zone (Fabryka-Martin, Flint et al. 1997), the fractures can represent a distinctive geochemical environment.

Data Sources and Analytical Methods for Unsaturated-Zone Mineralogy–Data on fracture mineralogy in the unsaturated zone come primarily from studies of drill core and Exploratory Studies Facility samples with additional information from surface samples. Records of fracture fillings from the detailed line surveys in the Exploratory Studies Facility up to Station 40 (4 km from North Portal) also provide information on the distributions of some fracture-filling minerals (data packages GS950508314224.002, GS950808314224. 004, GS951108314224.005, GS960408314224.002, GS960608314224.006, GS960608314224.007, GS960708314224.008, GS960808314224.011). The abundances of calcite and opal fracture and void fillings in the Exploratory Studies Facility were surveyed by the U.S. Geological Survey (Paces, Neymark et al. 1996; Paces, Marshall et al. 1997).

Most drill-core samples were studied by stereomicroscopy, X-ray diffraction, and scanning-electron microscopy with energy-dispersive X-ray analytical capability. Quantitative chemical analysis of representative fracture-filling minerals was performed by electron microprobe. Mineral identifications from the detailed line surveys in the Exploratory Studies Facility are based on in situ examination of fractures. Most of the Exploratory Studies Facility samples characterized for fracture mineralogy were collected in connection with ^{36}Cl investigations of infiltration; these samples were examined by stereomicroscopy and ultraviolet lamp, and the mineralogy of a subset was determined by X-ray diffraction and scanning-electron microscopy.

6.1.3.2.1.1 Distribution of Fracture Minerals in the Unsaturated Zone

This subsection provides an overview of the three principal environments—syngenetic, diagenetic, and percolation—that have resulted in deposition of fracture fillings. Following the overview, mineral occurrences in fractures are described for individual minerals or groups of

minerals related by chemistry or structure. For the cases in which sufficient information exists, the occurrences are subdivided by origin into syngenetic, diagenetic, and percolation categories.

Syngenetic Mineralogy of Fractures–Syngenetic processes that generate fracture fillings include all cooling-related processes from high-temperature vapor-phase alteration and transport to near-ambient-temperature aqueous rock alteration and mineral deposition. The mineralogic record of syngenetic alteration associated with the cooling of the pyroclastic deposits is generally well preserved in the unsaturated zone, whereas the syngenetic fracture mineralogy of the saturated zone has been substantially modified by subsequent alteration processes. The significance of syngenetic mineralogy for repository performance includes natural analog data for repository effects on rock alteration and fracture permeability in the near-field environment. In addition, the relatively large number of syngenetic minerals and the well established paragenetic relationships allow researchers to reconstruct the evolution of multifracture pathways and fault zones.

Environments of distinctive syngenetic alteration existed at the boundaries between the central devitrified portions of ashflows and the overlying or underlying vitric margins. These transition zones typically contain a great variety of secondary minerals, especially silica minerals and zeolites, in both the matrix and fractures. There is some evidence that this alteration occurs late in the cooling history of the ashflow at temperatures only slightly above ambient values (see Subsection 6.1.4.1.2.2.1). In well characterized examples, the constituents of the fracture deposits are traceable to nearby alteration in the rock matrix. These hydrothermal alteration environments are described in detail in Subsection 6.1.4.1.2.

Diagenetic Mineralogy of Fractures–Nonwelded tuffs of the lower Topopah Spring Tuff, the Calico Hills Formation, and the Crater Flat Group have been subjected to diagenetic zeolitization at ambient temperatures in some parts of Yucca Mountain, perhaps under saturated conditions below a former static water level higher than the present one. Alteration of volcanic glass provided local sources of solutes for mineral deposition in fractures. Some diagenetic alteration may have occurred higher in the stratigraphic section within zones of perched water in the unsaturated zone. These zones have not been characterized in detail, but the available data suggest they are mineralogically similar to the more extensive altered zones lower in the stratigraphic section.

Percolation-Related Mineralogy of Fractures–The rocks of the unsaturated zone have received infiltration during the last 12 million years since they were deposited. The infiltrating water contained solutes derived from the ground surface and, to a variable but lesser extent, from the rocks through which the fluids pass (Paces, Neymark et al. 1996; Paces, Marshall et al. 1997). The solutes have been deposited as fracture and void coatings, and their presence attests to the long-term persistence of fracture flow in the unsaturated zone.

Silica Minerals in the Unsaturated Zone

Syngenetic Occurrences–Within unsaturated-zone fractures, the silica polymorphs quartz, cristobalite, and tridymite are common in fractures in devitrified tuff intervals, and their distribution corresponds to the occurrences of these polymorphs in the adjacent rock matrix. Lithophysal cavities and many fractures in and near lithophysal intervals contain tridymite and/or

quartz crystals. These cavities and fractures are often rimmed with lighter-colored zones of vapor-phase alteration. In some places, the tridymite morphology of fracture coatings has been retained (Figure 6.1-29) although the tridymite is partially or wholly replaced by quartz or cristobalite.

The silica mineralogy of devitrified-vitric transition zones includes quartz (including chalcedony), amorphous opal-A, opal-CT (with short-range cristobalite and tridymite ordering), and rare moganite, a monoclinic crystalline silica. Euhedral quartz crystals up to 1 cm long may be present. Opal-A is transparent and colorless with morphologies reminiscent of water or wax drips. Locally, the opal-A deposits are covered by an outer gray to white botryoidal shell of opal-CT, with or without moganite. In at least some altered intervals, most notably the devitrified-vitric transition zones of the lower Tiva Canyon and Topopah Spring Tuffs, the silica is derived from alteration of pumice clasts that escaped devitrification when the rest of the rock matrix devitrified. Dissolution of volcanic glass and crystallization of smectite and zeolites slightly lower in the transition zone also released silica as transportable solutes and colloids. The mass-transport aspects of this alteration with respect to silica are described in Subsection 6.1.4.1.2.2.2.

Diagenetic Occurrences–Silica is a co-product of the diagenetic alteration of silicic volcanic glass to zeolites and smectite. Cristobalite commonly occurs as small acicular crystals, especially in zeolitic intervals just above the saturated zone. In the lower parts of the Topopah Spring Tuff, some opal has recrystallized to cristobalite.

Percolation-Related Occurrences–Opal-A is a common deposition product of percolating groundwater in fractures and voids of the unsaturated zone at least as deep as the Tptpmn, based on observations in the Exploratory Studies Facility (Paces, Neymark et al. 1996; Paces, Marshall et al. 1997; Fabryka-Martin, Flint et al. 1997). Opal-A of percolation origin has not been observed in the nonwelded Paintbrush Tuffs between the Tiva Canyon and Topopah Spring Tuffs. Elsewhere, it is commonly intergrown with calcite, which is much more abundant. Zones in the Topopah Spring Tuff with larger amounts of percolation deposits (dominantly calcite) also contain the largest amounts of opal; some zones contain calcite-dominant fracture and void coatings with no opal apparent on a macroscopic scale (Paces, Neymark et al. 1996). The morphology of opal-A coatings on calcite includes sheets and spherules or "bubbles," as described by Paces, Neymark et al. (1996) and Paces, Marshall et al. (1997). The drip-like texture of syngenetic opal-A is absent.

Zeolites in the Unsaturated Zone

Syngenetic Occurrences–Zeolites are common products of the syngenetic alteration that occurred at the boundaries between the central devitrified portions of ashflows and the overlying or underlying vitric margins. This association was first recognized in the devitrified-vitric transition between Tptpln devitrified tuff and Tptpv3 basal vitrophyre in the lower Topopah Spring Tuff (Levy 1984a; see also Subsection 6.1.4.1.2.2). Although the most abundant fracture coatings in the vitrophyre are smectite, opal-CT, and manganese-oxide dendrites, fractures may also contain heulandite or mordenite as well as other zeolites that are uncommon at Yucca Mountain. Phillipsite coexists with smectite in isolated occurrences in fractures within the basal vitrophyre from drillholes USW GU-3 and UE-25 a#1. Erionite generally occurs in fractures and

rock matrix in very limited intervals within the vitrophyre and the altered tuff in the overlying transition zone in several drillholes where it comprises <1 wt% of the matrix but may be as much as 45 wt% of the fracture coating within single fractures (Bish and Chipera 1989, 1991). Erionite has also been identified in significant abundances in a 3-m thick zone in the vitric tuff matrix immediately below the basal vitrophyre in drillhole USW UZ-14 (up to 35 wt%; Guthrie, Bish et al. 1995). In most samples, fine-grained erionite fibers (<30 μm long) closely resemble mordenite and cannot be distinguished in hand samples or in scanning electron microscopy images. Immediately above South Ramp vitrophyre in USW GU-3, small acicular crystals visible at 25X magnification are probably erionite. The occurrences of both erionite and phillipsite are limited to an interval of a few meters in or near the devitrified-vitric transition zone in all of the pre-1984 cores in which they have been identified. A sample from USW GU-3 at 1,189 foot depth (upper part of the transition zone) contains a phase tentatively identified as kenyaite, a layered hydrous sodium silicate.

Chabazite has been identified by X-ray diffraction in fracture coatings within the basal vitrophyre of the Topopah Spring Tuff in water in Well J-13 in Jackass Flat (Carlos 1989) and in drillhole USW VH-1, about 8 km southwest of Yucca Mountain in Crater Flat. The vitrophyre in both of these holes is below the present static water level, but was probably in the unsaturated zone when syngenetic alteration occurred. Chabazite also occurs with smectite and heulandite-clinoptilolite in the devitrified-vitric transition zone of drillhole USW SD-7 at the south end of the exploration block (Chipera, Vaniman, Bish et al. 1997).

Fracture fillings associated with syngenetic alteration at the devitrified-vitric boundary in the lower Tiva Canyon Tuff (Tpcplnc/Tpcpv boundary) have not been recognized in drill core but are known from outcrop in Harper Valley (southeast Yucca Mountain) and exposures in the Exploratory Studies Facility South Ramp (see Subsection 6.1.4.1.2). Very minor heulandite-clinoptilolite is the only zeolite species identified at Harper Valley, where it has been identified visually as scattered crystals overlying fracture coatings of opal-CT and quartz/chalcedony in the densely welded, devitrified Tpcplnc. It is also present as a breccia cement where Tpcplnc fragments have been displaced downward along open joints into the vitric Tpcpv. The Exploratory Studies Facility exposure at Station 75 + 20 is a breccia zone developed along a high-angle cooling joint that crosses the Tpcplnc/Tpcpv2 boundary. Within the Tpcplnc, heulandite-clinoptilolite is a minor constituent. Fractures in the underlying moderately to densely welded partly devitrified Tpcpv2 are coated with white <1 mm spherules and round aggregates. The spherules have cores of kenyaite, with minor heulandite-clinoptilolite and chabazite, coated with moganite and quartz/chalcedony. Unidentified zeolites are also present as coatings of clear prismatic crystals on fracture surfaces. Erionite has not been positively identified as a fracture coating in this exposure, but it is present in quantities less than 1 wt% in the altered Tpcpv2 matrix adjacent to and within the breccia zone.

Additional zeolite occurrences of probable syngenetic origin have been recognized but not studied in detail. Highly fractured and brecciated Tiva Canyon Tuff in the Exploratory Studies Facility North Ramp starter tunnel is loosely cemented by fibrous white material, up to 1 cm thick, consisting of 57 wt% mordenite and 2 wt% heulandite-clinoptilolite, plus major feldspar and minor quartz, smectite, and cristobalite (Levy, Norman et al. 1996).

In the densely welded, devitrified portions of the Paintbrush Group within the upper unsaturated zone, the zeolite minerals mordenite, heulandite, and stellerite are widespread in fractures. Heulandite and stellerite occur as 10 to 50 μm long prismatic crystals on fractures throughout the devitrified intervals of the Topopah Spring Tuff in at least one drill core (USW G-1). Although peak overlaps with heulandite, mordenite, cristobalite, and feldspar make X-ray diffraction identification of minor amounts (<10 percent) of stellerite difficult, heulandite and stellerite can be distinguished in scanning electron microscopy images by the pinacoidal terminations of stellerite and the pyramidal terminations of heulandite (Figure 6.1-30) and by energy-dispersive X-ray analyses because Ca is the major exchangeable cation in stellerite, whereas heulandite contains Mg and minor amounts of Na and K in addition to Ca. Stellerite is particularly common in both fractures and matrix of the Topopah Spring Tuff in drillholes UE-25 UZ#16 and USW UZ#14 (Chipera, Vaniman, Bish et al. 1997). The occurrences of stellerite in the matrix of the devitrified tuff suggests that the zeolite fracture fillings are derived from local alteration of the rock matrix. The alteration has not been studied sufficiently to establish whether it is of syngenetic origin, but the occurrences most closely resemble known syngenetic alteration.

Diagenetic Occurrences–Clinoptilolite and mordenite both occur in fractures within the zeolitized Calico Hills Formation and in the upper Crater Flat Group, wherever zeolites are common in the adjacent tuff matrix. These occurrences are located in the lower unsaturated zone and into the upper saturated zone. Unlike the matrix alteration, which is commonly dominated by clinoptilolite, mordenite rather than clinoptilolite is the principal fracture-lining zeolite. Mordenite forms mats and crusts of fibers on fracture surfaces, with individual mordenite crystals in the Calico Hills Formation usually from 2 to 15 μm long, locally as much as 30 μm long. Opal-CT commonly occurs interstitial to the mordenite crystals, but it also can occur as spheres as much as 10 μm in diameter underlying mordenite. Mordenite forms thin, discontinuous coatings or thick mats of fibers 10 to 30 μm (rarely as much as 100 μm) long in the Crater Flat Group (Figure 6.1-31). It also occurs in Ca-rich compositions as an apparent reaction product of calcite alteration in the upper saturated zone.

Clinoptilolite coexists with mordenite in this zone, which extends to the base of the Crater Flat Group in the south (in drillhole USW G-3) but includes only the upper tuffs of the Carter Flat Group in the more northern hole. Prismatic or tabular crystals of clinoptilolite as long as 200 μm occur locally in fractures in the Calico Hills Formation and in the Prow Pass and Bullfrog Tuffs of the Crater Flat Group over most of Yucca Mountain, but they also occur in the Tram Tuff of the Crater Flat Group in the southernmost drillhole, USW G-3. In some fractures, small crystals of clinoptilolite (5 to 10 μm diameter) are covered by or intergrown with mordenite. Analyses of some of the larger clinoptilolite crystals from this zone, spanning the water table, are plotted in Figure 6.1-32. Although the exchangeable-cation composition varies greatly among samples, insufficient chemical data exist on fracture-lining clinoptilolites at Yucca Mountain to determine whether the compositions follow the same trends with increasing depth as do matrix clinoptilolites (Broxton, Bish, Warren 1987). However, the fracture-lining clinoptilolites are similar in composition to those in the matrix in all samples. Within this zone that spans the water table, the cation compositions of matrix clinoptilolites range from K-dominant to Na-dominant on the western side of Yucca Mountain and to Ca-dominant on the eastern side.

Clays in the Unsaturated Zone–Smectite is nearly ubiquitous in fractures throughout the volcanic sequence at Yucca Mountain. The genesis of many occurrences is not readily apparent, particularly in cases in which the clay is not abundant. Available data have been categorized by origin as much as possible to convey a sense of large-scale patterns of clay distribution and abundance in fractures.

Syngenetic Occurrences–The syngenetic origin of some smectites in fractures is established by textural relations and mineralogic associations. Within the lower Topopah Spring devitrified-vitric transition zone, smectite and small amounts of extremely fine-grained heulandite-clinoptilolite commonly crystallized at glass-dissolution sites, including fracture surfaces, as spherical aggregates, 2 to 50 μm across (Levy 1992).

Smectite occurs, particularly in the lower Topopah Spring Tuff, as individual plates as much as 10 μm in diameter or as clusters of plates similar to the spherical aggregates noted above. It may occur alone, beneath zeolites, or as overgrowths on zeolites. Kaolinite is much less common but has been identified by X-ray diffraction from fractures in drill cores USW G-1 and G-2, where it occurs with smectite.

Percolation-Related Occurrences–The chain-structure clay minerals palygorskite and sepiolite occur sporadically in fractures in the Paintbrush Group, either in varying combinations with smectite or singularly. Occurrences of chain-structure clays do not extend below the middle of the Topopah Spring Tuff; the sepiolite may have surface origins that provide a marker of downward transport (Vaniman, Chipera et al. 1995). Trace amounts of kaolinite have been found within fracture calcites. In drill core USW GU-3, smectite, sepiolite, and palygorskite form white and yellow crusts on fractures in the Tiva Canyon and upper Topopah Spring Tuffs, commonly over manganese-oxide minerals. It is not known whether the clays are intergrown or form separate crusts on the fracture surfaces. There is no apparent sequence of clay deposition with depth, except that palygorskite and sepiolite do not occur below about 260 m depth.

Manganese Oxides and Minor Hematite in the Unsaturated Zone–Manganese-oxide minerals occur in fractures in the moderately to densely welded vitric and devitrified tuffs throughout the pyroclastic sequence at Yucca Mountain and are less common in zeolitic zones. These Mn oxides form spots and patches (0.5 to 2 mm across) and dendrites (1 mm to 2 cm across), some of which are organized into Liesegang band patterns extending tens of centimeters or more along fracture surfaces. Manganese-oxide deposits are present in densely welded, devitrified intervals of the Tiva Canyon and Topopah Spring Tuffs, as well as in the partially welded Yucca Mountain Tuff. They are not common in lithophysal intervals, but there are notable occurrences of black mineral aggregates with the prismatic habit and Ba + Mn signature of hollandite within large altered pumice clasts near the top of the Tiva Canyon Tuff (Tpcrn3) in the Exploratory Studies Facility North Ramp (Levy, Norman et al. 1996). The latter example is clearly of syngenetic origin, but the genesis of most deposits is uncertain.

The layer-structure manganese oxides lithiophorite (Li-, Al-bearing hydrous Mn oxide) and rancieite (Ca-bearing hydrous Mn oxide) are the principal Mn-oxide minerals coating fractures of the unsaturated zone. Although spots and crusts may be either rancieite or lithiophorite, dendrites are predominantly rancieite. The dendrites commonly display μm-scale compositional banding corresponding to variations in Al, Ce, and Pb content (Figure 6.1-33). Pyrolusite is a

rarer Mn-oxide phase in the unsaturated zone but, like rancieite, may be a sink for Ce in groundwaters. Pyrolusite has been texturally associated with calcite precipitation. The importance of Mn oxides in nuclear-waste interaction is discussed in Subsection 6.1.5.

In many cases within the Paintbrush Group, Mn-oxide deposits on fracture surfaces are directly traceable to altered mafic minerals or Fe-Ti oxide grains in the rock matrix adjacent to the fracture, indicating local derivation and short-range transport of Mn during water-rock interaction (Fabryka-Martin, Flint et al. 1997). The existence of m-scale dense Mn-oxide coatings and Liesegang banding on fractures in the Exploratory Studies Facility suggests that somewhat longer-range transport of Mn must have occurred as well. Liesegang banding is a product of diffusive transport in the presence of strong concentration gradients or post-nucleation particle growth (Venzl and Ross 1982; Henisch 1986). Within the unsaturated zone at Yucca Mountain, these conditions were most likely to exist within thin fluid films between smooth, extensive fracture surfaces. Carlos, Chipera, Bish et al. (1993) observed that Mn-oxide coatings in core samples are especially abundant on smooth-surfaced cooling joints, which are most common in the middle nonlithophysal zone of the Topopah Spring Tuff. In contrast, the coatings are not common in lithophysal intervals. This observation is supported by data from Exploratory Studies Facility samples documenting a transition from uncommon to nearly ubiquitous Mn-oxide minerals that corresponds very approximately to the boundary between the upper lithophysal and middle nonlithophysal zones. This boundary also marks a downsection change from less frequent and shorter fractures to more frequent and longer ones (Fabryka-Martin, Flint et al. 1997). The two lithostratigraphic intervals differ only slightly in mean matrix porosity, 0.113 cm^3/cm^3 for the Tptpul versus 0.086 cm^3/cm^3 for the Tptpmn in drillhole USW SD-7 (Rautman and Engstrom 1996a), but the rougher and more irregular fracture surfaces of the Tptpul (Buesch, Spengler et al. 1996) may have inhibited the formation of continuous fluid films that facilitate Mn transport. Examination of an altered-pumice cavity from the Tpcrn3 in the Exploratory Studies Facility North Ramp suggested additional processes that could contribute to the paucity of Mn-oxide fracture coatings in the Tptpul. The secondary-mineral assemblage in the cavity, representing vapor-phase and post-vapor-phase deposition, includes hollandite, a manganese mineral, and manganiferous Fe-oxides. The manganese in these minerals was probably derived from vapor- or steam-phase alteration of primary mafic oxides. The new manganese-bearing minerals deposited in rock cavities are apparently less susceptible to alteration than are the primary oxides and therefore are not ready sources of Mn for fracture coatings.

Specular hematite occurs in and near lithophysal cavities and as a component of mineral coatings in vapor-phase partings. It is especially prominent in the upper Tptpmn of the northern Exploratory Studies Facility. Earthy hematite is a common alteration product in both matrix and fractures of the Tpbt2 bedded tuff between the Pah Canyon and Topopah Spring Tuffs in the Exploratory Studies Facility North Ramp (Levy, Norman et al. 1996). These occurrences are all of syngenetic origin. Hematite is a probable constituent of the red-brown siliceous fracture fillings in Tpki nonwelded tuffs above the Tiva Canyon Tuff, also in the Exploratory Studies Facility North Ramp, and is a likely minor component of many fracture coatings in the Paintbrush Group.

Calcite in the Unsaturated Zone–Calcite commonly occurs in fractures as well as in lithophysal cavities. It is most abundant in, but not limited to, the densely welded and devitrified

portions of the Tiva Canyon and Topopah Spring Tuffs in the unsaturated zone. Recent aggressive efforts to date calcites and associated opals from the Exploratory Studies Facility (especially recent U-Pb dating efforts) and to investigate their stable-isotope compositions (Paces, Neymark et al. 1996; Paces, Marshall et al. 1997) have established that some calcites probably are of syngenetic age and origin. Most calcites were deposited incrementally during all or part of the past 8 to 10 m.y. A detailed discussion of calcite compositions as a guide to groundwater transport processes is presented in Subsection 6.1.5.

Fluorite in the Unsaturated Zone

Syngenetic Occurrences–Superficial examination of fracture surfaces in the Exploratory Studies Facility indicates that pink to purple, fine-grained fluorite is a widespread and locally prominent fracture coating in the densely welded, devitrified portions of the Topopah Spring Tuff (Levy, LANL Notebooks, 1996a, LA-EES-1-NBK-96-001, p. 46, and 1996b, LA-EES-1-NBK-96-002, p.8). There is no obvious pattern to the lateral variability in abundance. Colorless fluorite occurs as a fracture filling and matrix constituent with secondary quartz, cristobalite, and opal-CT in silicified Tpbt2 tuff in the Exploratory Studies Facility North Ramp (Levy, Norman et al. 1996). This alteration is described in detail in Subsection 6.1.4.1.3.1.2. The formation of the fluorite was related to syngenetic alteration associated with late-stage cooling of the underlying Topopah Spring Tuff.

Fluorite has been observed in lithophysal cavities in several drill cores, particularly UE-25 a#1 and USW GU-3. It has been most commonly observed in samples from the densely welded, devitrified portions of the Tiva Canyon and Topopah Spring Tuffs.

6.1.3.2.2 Saturated-Zone Fracture Mineralogy

Quartz and Opal-CT in Saturated-Zone Fractures–The silica polymorphs tridymite and, to a large extent, cristobalite are essentially absent in fractures of the saturated zone. These polymorphs are the more soluble of the anhydrous-silica polymorphs and are commonly supplanted by opal-CT, which occurs with mordenite and clinoptilolite in the Calico Hills Formation and Crater Flat Group, whether in the saturated or unsaturated zones. Quartz is common in fractures in the devitrified intervals of the saturated zone, usually as euhedral crystals. Lithophysal-type fracture coatings occur in the Bullfrog and Tram Tuffs of the Crater Flat Group; although the tridymite morphology has been preserved, the silica mineral is now quartz. Quartz-lined fractures often contain manganese-oxide minerals and may also contain calcite or mordenite.

Zeolites in Saturated-Zone Fractures (Equivalence with Wall Rock)–The upper saturated zone typically contains mordenite and lesser clinoptilolite as fracture-lining zeolites in which the adjacent tuff matrix is also altered to clinoptilolite ± mordenite (see discussion of unsaturated zone zeolites, above). Mordenite is generally the only zeolite found in fractures in the devitrified Crater Flat Group, and its distribution and abundance vary across the mountain. The greatest abundance of fracture-associated mordenite is in the southernmost drillholes (USW GU-3 and USW G-3). This result contrasts with the absence of mordenite in zeolitized intervals within the Crater Flat Group of this drill core. Chabazite from one sample (UE-25 b#1 2165) in the Crater Flat Group at Yucca Mountain coexists with clinoptilolite and alkali feldspar. Euhedral crystals

of analcime occur in fractures only at the northern end of Yucca Mountain, where analcime also occurs in the altered tuff matrix. Clinoptilolite-heulandite can also occur in fractures at these depths and may coexist in the matrix with analcime (Bish and Chipera 1989). The fracture analcime has a Si rich, Na end-member composition, similar to the analyses of matrix analcime.

Common Occurrence of Hematite and Mn-Oxides in Saturated-Zone Fractures– Manganese-oxide minerals and iron oxides, with quartz and calcite, are the most abundant fracture coatings below the water table in the devitrified Crater Flat Group over most of Yucca Mountain. In these devitrified intervals below the static water level, hematite is the dominant iron-oxide mineral. It occurs as rusty-red powder, as staining in fine-grained quartz coatings, and as intergrowths with manganese oxides. In the northernmost hole (USW G-2), goethite occurs with hematite in several fractures.

Cryptomelane-hollandite is the most common manganese-oxide mineral throughout the Crater Flat Group below the static water level. It may occur with lithiophorite, todorokite, pyrolusite, aurorite, or in one sample, rancieite. Hollandite surrounds large lithiophorite crystals in the Prow Pass Tuff and sometimes appears less corroded than the lithiophorite (Figure 6.1-34), suggesting that the lithiophorite was partially dissolved by later fluids, which then deposited hollandite. Hollandite also surrounds or partially replaces pyrolusite in the Crater Flat Group. There appears to be a chemical continuum between cryptomelane (K rich) and hollandite (Ba rich). In analyses of these minerals, all Mn is assumed to be Mn^{4+}, although Mn^{3+} is known to substitute for Mn^{4+} in the octahedral sites (Post et al. 1982). Most samples contain a fairly restricted range of compositions within each sample, although there is considerable chemical variation between samples. The ternary plots in Figure 6.1-35 illustrate the most significant variations in tunnel cation chemistry (that is, variability in those cations that occur in the largest structural opening of the Mn minerals). Carlos, Chipera et al. (1993) contains a more detailed discussion of the manganese-oxide mineral chemistry.

Clays in Saturated-Zone Fractures–Smectite occurs with mordenite in some fractures in the devitrified intervals in the Crater Flat Group below the water table. Several occurrences of illite have been identified in the deeper tuffs of the saturated zone; green clay (illite) associated with calcite and hematite are the most abundant fracture-filling minerals in the deepest portions of the Tram Tuff, where clinoptilolite gives way to analcime in the tuff matrix. Illite/smectites with high illite content are likely to be less sorptive than the expandable smectites; for most of the exploration block, however, large illite contents are only found at great depth. Large illite content is generally associated with the zones of albite alteration.

Calcite in Saturated-Zone Fractures–Calcite is unevenly distributed but is locally abundant as a fracture filling in the Crater Flat Group. As mentioned above, it is the most common fracture filling in extensively analcime- or albite-altered tuffs of the deep saturated zone, but it also occurs over restricted depth intervals in the devitrified tuffs of the shallower saturated zone, usually with manganese-oxide minerals arrayed along transmissive fractures. In most of these shallower saturated zone occurrences, the calcite is pitted or corroded and shows evidence of alteration to Ca-mordenite. Although some wastes could be removed from solution by calcite precipitation, the pervasive etching of calcite surfaces in the shallow saturated zone indicates that present aqueous geochemistry in this zone does not favor calcite precipitation. At higher temperatures and altered water compositions, however, calcite might again precipitate.

6.1.3.2.3 Fault Mineralogy

Fault mineralogy can be a critical component in evaluating flow and transport. Faults can operate as highly transmissive features, particularly if the faults contain no mineralization or if mineralization along the fault is limited to minerals with very low surface area (for example, sparry calcite). Alternatively, minerals with very high effective surface area such as clays and zeolites can turn a fault into a barrier against flow. These distinctions are important, because calcite, smectite, and zeolite have all been observed as fault-filling minerals at Yucca Mountain. Although a simplified consideration suggests that any fault is a discontinuity likely to divert flow, regardless of whether the fault opening is the pathway or the fault barrier is deflecting flow, the very different flow rates and different interactions of minerals such as clays or calcite with radionuclides makes the distinction of mineralogy important.

Fault Mineralogy and Transmissivity–In the course of ^{36}Cl investigations of flow and transport in the Exploratory Studies Facility, all major faults were sampled for isotopic characterization (Fabryka-Martin, Flint et al. 1997). Bomb-pulse levels of ^{36}Cl, indicating that a component of percolating water traveled from the surface to the Exploratory Studies Facility level in less than 50 years, were associated with the traces of the Bow Ridge, Drill Hole Wash, Sundance, and Ghost Dance (southern exposure only) faults. The secondary mineralogy of all fault samples, as well as of fractures, breccia zones, and other features was determined by stereomicroscopic study, examination under short-wave ultraviolet radiation, and X-ray diffraction and scanning electron microscopy of selected samples.

In the unsaturated zone as deep as the Tptpmn, common secondary minerals most likely to affect fault transmissivity include calcite, opal, and clays. The ^{36}Cl data set was used as a basis to compare the mineralogy of fast-path faults, fractures, and breccia zones and non-fast-path transmissive features. The results suggest that the amount of secondary-mineralogy deposition in faults was insufficient to affect the transmissivity of the faults, at least in the portions of the fault flow paths within densely welded tuff. Secondary minerals are not especially abundant within the faults, nor are they more abundant in the faults than in cooling joints or thin, minor-offset breccias with or without fast-path isotopic signatures.

There are several possible reasons why the transmissivity of faults in welded tuffs is relatively unaffected by secondary-mineral deposition. The most important reason probably is that faults at Yucca Mountain do not exist as simple, single-trace features, either at the surface or in the subsurface (Potter et al. 1995). The existence of multiple fault branches and meters-wide breccia zones means that numerous individual alternative flow paths are associated with a fault. The rate of calcite and opal deposition during the past eight to ten million years has been too low to plug all of the flow paths within fault zones. Even where secondary mineral deposition may be sufficient to seal a fault, periodic tectonic reactivation can dilate the fault and allow renewed fluid transmission. Fault reactivation is likely along zones of existing weakness, as present in most instances of secondary mineralization along faults.

An additional reason for the insignificant effect of secondary minerals on fault transmissivity is pertinent to the observation that calcite and opal abundances are lower in faults than in subsidiary features. Conceptual models of calcite deposition in the subsurface stress the slow kinetics of the precipitation process (Paces, Marshall et al. 1997). Most or all faults that cut the

Paintbrush nonwelded hydrogeologic unit probably are fast paths, even if present net infiltration along their surface traces is too low to support fast-path flow during the last 50 years. Fluid flow along the faults in the subsurface may be fast enough to discourage mineral precipitation.

The effectiveness of secondary minerals in modifying the flow characteristics of faults within nonwelded tuffs is less well addressed by the ^{36}Cl data set because fewer exposures of nonwelded tuffs exist in the Exploratory Studies Facility and the ^{36}Cl sample density is lower in these exposures than in the welded tuffs. The conceptual model of fast-path features requires the presence of faults that cut the nonwelded tuffs between the devitrified portions of the Tiva Canyon and Topopah Spring Tuffs (equivalent to the PTn hydrogeologic unit). None of the ^{36}Cl samples analyzed to date from Exploratory Studies Facility exposures of this interval represent faults with fast-path isotopic signatures, so a basis does not exist for comparing the mineralogy and flow behavior of faults in these nonwelded tuffs.

Textural Studies of Breccia/Wall Rock Paired Sample–The introduction of bomb-pulse ^{36}Cl into infiltrating water provides a fortuitous tracer whose $^{36}Cl/Cl \times 10^{-15}$ isotopic value is significantly higher than the pre-1950s values of natural infiltration and percolating groundwater. Detection of bomb-pulse ^{36}Cl in the subsurface is the primary documentation for the existence of a fast-fluid pathway, a transmissive feature that has received at least a small component of water that traveled from the surface in the last 50 years or less. Most such pathways in the Exploratory Studies Facility are fractures, shears, breccia zones, or faults with direct or indirect connections to major throughgoing faults. Because active fast pathways have received percolation from the surface within the past 50 years, and because the isotopic composition of the percolation they receive has changed significantly over this short period due to input of bomb-pulse ^{36}Cl, isotopic disequilibrium within the fluid pathway is readily detectable. In areas of the Exploratory Studies Facility where groundwater travel times are on the order of tens of thousands of years, the changes of isotopic composition in the infiltrating water moving through these rocks probably occurred so gradually over this period that isotopic disequilibrium between breccia and wall rock, for example, would not be detectable by a comparison of their ^{36}Cl values. Cosmogenic production rates of ^{36}Cl have varied by a factor less than 0.5 during the past 10,000 years (Plummer et al. 1997).

Sample Preparation–The kilogram-size samples required for isotopic analysis preclude our investigating the fine-scale spatial distribution of bomb-pulse ^{36}Cl within samples. Researchers have made preliminary attempts to detect variations in isotopic ratios for pairs of texturally distinct materials collected at a single site. The goal is to detect differences between breccia and adjacent wall rock as possible indicators of local factors that affect water flow. Six breccia samples from stations 13+00 to 36+00, which had been collected into single sample bags, were manually sifted in the laboratory into separates with particle sizes either larger or smaller than ~0.5 cm. One sample from station 56+93 was separated into fractions with particle sizes larger or smaller than 2 mm. The finer fractions were processed for analysis without further size reduction. For the coarser fractions, the larger rock fragments were individually crushed with a steel plate and hammer to a maximum size of ~2 cm, then processed for analysis. Eleven additional sample pairs from approximately station 34+00 to 77+00 represent a variety of texturally distinct materials, such as breccia and the adjacent rock or cooling joint surface or separate generations of fault fillings, collected into separate bags. The texturally distinct

materials of each pair were processed and analyzed separately. Details of the analytical procedures are given in Fabryka-Martin, Flint et al. (1997).

Several factors may potentially complicate the comparison of isotopic results for paired samples. Even weakly cemented fine breccia fragments can end up in the coarse breccia fraction during the size separation process, obscuring any existing isotopic differences between size separates. Differences between paired samples in the amount of size reduction (that is, fragment breakage) required to prepare a sample for leaching may lead to a systematic difference in the proportion of rock chloride to infiltration-derived chloride in the leachate. Fine grained samples would require little or no size reduction, minimizing the creation of newly exposed rock surface, whereas coarser material would require the most reduction and consequently would have more new rock surface and associated rock chloride exposed for leaching. The sulfate content of sample leachates—expressed as the ratio SO_4/Cl—may serve as a guide to differences in the amount of rock chloride released into the leachates. Researchers are currently exploring the value of sulfate as an indicator of rock chloride contamination.

Our attempts to investigate differences in the bomb-pulse ^{36}Cl content of fracture zones or breccias and adjacent wall rock are in the developmental stage, in terms of both sample preparation and data interpretation. The choice of 0.5 cm as the criterion for separating breccia samples into coarse and fine fractions does not result in the production of separates with true genetic significance because it does not consistently separate "wall rock" from "fault gouge," or "broken but intact rock" from "mineralogically altered gouge," or "bedrock fragments" from "cement." Despite this cautionary note, the paired analyses of coarse and fine fractions or of broken wall rock and adjacent breccia from stations 13+67 to 35+93 show a consistent pattern of higher $^{36}Cl/Cl$ values in the coarse fractions (Figure 6.1-36). All of the coarse-fraction values and about half the fine-fraction values in this interval have $^{36}Cl/Cl$ ratios above 1250×10^{-15}, which is the threshold value indicating the unambiguous presence of bomb-pulse ^{36}Cl. Samples from station 36+55 and beyond have lower values and generally smaller differences between the ratios measured for the different size separates.

Bomb-pulse values have not been detected in the southern part of the Exploratory Studies Facility beyond station 45 except for one sample with a value slightly below the bomb-pulse threshold value of 1250×10^{-15}. The main reason for this difference is the prevalence of lower net-infiltration values in the south (Flint and Flint 1994; Flint et al. 1996; Hevesi, Flint et al. 1994, 1996). The effect of such a distribution on this study is to restrict our ability to detect changing patterns of ^{36}Cl abundance in wall-rock/breccia pairs along the full extent of the Exploratory Studies Facility. The preliminary results presented here are based on a pair from the northern Exploratory Studies Facility in the vicinity of the Sundance fault.

Results of Paired-Sample Analysis–Petrologic and mineralogic examination of the analyzed separates are in progress, but a few generalized observations may be relevant to the isotopic results. The baseline interpretation supported by the results from stations 13+67 to 35+93 is that the fluids occupying accessible pore spaces of the fast-fluid pathways were not in equilibrium with respect to the ^{36}Cl isotopic signal. Because these samples all represent active fast pathways that have apparently received infiltration from the surface within the past 50 years, and because the isotopic composition of the infiltration they receive has changed significantly over this short period due to input of bomb-pulse ^{36}Cl, isotopic disequilibrium within the fluid pathway is

readily detectable. In areas of the Exploratory Studies Facility that have received no detectable bomb-pulse ^{36}Cl input and where groundwater travel times may have been significantly longer, as indicated by lower $^{36}Cl/Cl$ ratios, the changes of isotopic composition in the infiltrating water moving through these rocks probably occurred so gradually over this period that a lack of isotopic equilibrium between matrix and fracture pore water would not be detectable by a comparison of their ^{36}Cl signals.

The wall rock and breccia subsamples E154-3 and E154-1, with $^{36}Cl/Cl$ values of 3,767 x 10^{-15} and 803 x 10^{-15}, respectively (Fabryka-Martin, Flint et al. 1997), differ substantially with regard to rock fragment sizes. Pervasive multidirectional fracturing of the bedrock has broken it into intact rock domains of ~10 cm dimensions. The breccia deposit, bounded by two cooling joint faces oriented 031/86W, consists of ~1-cm to <0.1-mm fragments and contains additional translocated silt- and clay-size material (<~0.1 mm) near the outer edges of the deposit. With a relatively fine-grain size and a porous clastic texture, the breccia should have hydrologic properties approaching those of a nonwelded tuff in which slower matrix flow predominates over fracture flow. Fluids entering the breccia deposit may travel through tortuous intergranular pathways.

The nature of the interfaces between the rock fracture surfaces and the breccia deposit provides indications of the long-term importance of these features as fluid pathways. The 1-mm-thick clay coating on the outer surfaces of the breccia deposit is several times thicker than the similar coatings on breccia clasts and wall-rock blocks. The clay coatings did not originate *in situ*, but rather had to be transported to their present locations by water. The greater thickness of the clay coating on the breccia deposit could reflect a larger aperture between the wall rock and the breccia deposit than between either wall-rock blocks or breccia clasts, allowing the interface to accommodate a thicker clay coat. In addition, the interface may have received more fluid input than the breccia deposit or the unmodified fractures within the bedrock. Clearly, these two potential factors are not mutually independent because a fluid pathway with larger aperture and greater continuity would likely receive more influx.

The existence of finer-grained translocated material in the outermost few mm of the breccia deposit indicates that the fracture or fractures hosting the deposit experienced mm-scale dilation after the main portion of the deposit was formed. Through the processes of compaction and clay deposition, the breccia gradually developed sufficient cohesion to prevent the component clasts from totally collapsing into newly opened space as the fracture dilated. Later dilation provided space for transport and deposition of the 1-mm clay coating on the outer surfaces of the breccia deposit.

In summary, it appears that repeated dilation occurred as this fracture-breccia system accommodated tectonic extension. By means of this process, a fracture pathway could be maintained along the interface between the bedrock and the breccia that allows at least some percolating water to bypass the breccia. The possible role of the clay coatings in restricting access of fracture fluids to either the breccia or the wall rock is uncertain, and no special attempt was made to separate the coatings from either subsample.

Discussion and Conclusions About Paired-Sample Studies–The Sundance fault and associated subsidiary flow paths constitute the best and perhaps only example of distinctive mineralogy associated with a fault zone but not the discrete fault trace itself. The two mineralogic characteristics are the presence of calcite and thick clay/mordenite fracture coatings. Both of these attest to the particularly high fracture connectivity in the station 34+28 to 35+93 interval north of the Sundance fault. The thicknesses and textures of the clay coatings suggest that the apertures of cooling joints were increased by minor tectonic movement shortly after the Topopah Spring Tuff was deposited. The widespread occurrence of calcite precipitates in this interval also indicates excellent inter-fracture and fracture-fault connectivity. These findings support the conclusions from the structural analysis of the Sundance fault zone in Fabryka-Martin, Flint et al. (1997): the vicinity of the Sundance fault is distinguished, not only by the presence of an additional local fracture set, but by the mineralogic evidence for multiple episodes of fracture dilation and extension.

The small-scale fluid-flow characteristics of fracture-breccia systems in densely welded tuff may reflect an influence of the local tectonic stress system responsible for the formation of these transmissive features. In tectonic domains in which extension predominated and shearing was minor, the cooling-joint boundary between wall rock and breccia remained planar and was maintained as an open fracture during multiple episodes of dilation. Deposition of translocated clay in the breccia pore spaces and along the cooling-joint-surface/breccia boundary helped to isolate the breccia deposit from the periodically re-opened bounding fracture because the clay coatings tended to adhere to the breccia. As a result, downward-percolating water tends to stay in the bounding fracture and bypass the breccia matrix. This process is detectable where bomb-pulse ^{36}Cl is present as higher values of $^{36}Cl/Cl$ in the wall rock containing the bounding fracture surface than in the breccia. The mineralogy and textures of secondary-mineral deposits in breccia zones are highly useful for interpreting the tectonic processes that affect the transmissivity of the breccias.

Busted Butte: A Zeolitized Fault in Vitric Unsaturated Zone Tuff–Broxton, Chipera et al. (1993) sampled and analyzed the vitric basal Topopah Spring Tuff (Tptpv1) adjacent to and within the Busted Butte fault. The alteration of the vitric tuff along the fault is extreme with samples varying from 95 percent glass with no clay or zeolite within a few feet of the fault to 98 percent clinoptilolite and no glass within the fault. The fault separates vitric basal Topopah Spring Tuff from highly fractured, devitrified Topopah Spring Tuff. This locale provides evidence of mineralization along a fault in the unsaturated zone that juxtaposes vitric nonwelded tuff against welded devitrified tuff. The result here is the most thorough zeolitization (98 percent) of vitric tuff yet observed in any sample from Yucca Mountain, with the zeolitization strictly confined to the fault zone. This fault mineralization apparently resulted through delivery of water through the fractured, devitrified tuff to the nonwelded vitric tuff. The very restricted penetration of zeolitization into the vitric tuff provides a useful illustration of limited unsaturated zone transport through this rock type.

The composition of the zeolites in the mineralized fault is typical of many unsaturated zone clinoptilolites, with Ca + Mg enrichment and Na + K loss relative to the unaltered glass (Broxton, Chipera et al. 1993). The most significant effects in trace-element alteration are a > 2 x increase in Sr content and a decrease in uranium content of comparable amount in the zeolitized tuff. Figure 6.1-37 illustrates the relatively small decrease (~10 percent) in lanthanide-

element concentration that occurs in the zeolitized fault, with the exception of the development of a modest positive Ce anomaly. Limited data suggest that other zeolites such as erionite may concentrate Ce relative to the other lanthanides, although the principal phases implicated in Ce fractionation at Yucca Mountain are the Mn oxides (Vaniman and Chipera 1996). Although the timing of zeolitization along the Busted Butte fault is not certain, the similarity to other early-formed clinoptilolites indicates early alteration with rapidly diminished permeability in the vitric tuffs along the fault as zeolitization progressed. Further studies of this and similar mineralized faults may help to clarify the geologic record of sorptive-mineral interactions with metals in solution at Yucca Mountain.

C-Wells Tracer Complex: Fault and Fracture Mineralization in the Saturated Zone–The C-Wells tracer complex (UE-25 c#1, #2, and #3) provides the opportunity to compare fault-zone mineralogy along faults in the Tram Tuff with fracture-zone mineralogy in the Bullfrog Tuff. Both the faults and the fracture zone host productive aquifers. Preliminary data only permit the recognition of fault and fracture mineralization that apparently represents a combination of clay and oxide-mineral development in both aquifers. Most of the flow production is from the Bullfrog fracture zone (Geldon 1993). Samples from both aquifers are now being studied to determine the nature of the fracture and fault mineralogy and the chemical composition of the fracture minerals as a guide to past water-rock interactions.

6.1.3.3 Mineralogy of Soils, Eolian Deposits, and Relevant Playa, Seep, and Spring Deposits

Mineralogy of Calcretes, Soils, Seeps, and Springs–Calcretes at the surface of Yucca Mountain represent the most extensive near-surface authigenic mineralization. The only pure mineral separates obtained from the calcretes have been of opal, from the opaline laminae as mapped in Figure 6.1-19. Large opaline root fossils have also been collected from sand ramps east of Exile Hill (Vaniman, Bish, Chipera 1988). In all other calcrete laminae, calcite and opal, or calcite and sepiolite, are closely intergrown. Calcite crystals are small; most (> 95 percent) are <5 μm. Attempts to obtain pure calcite separates by crushing and density separation have failed because of intimate intergrowth with other minerals. Sepiolite is locally abundant (~40 percent) in only a few laminae (Figure 6.1-19); the overall abundance of sepiolite and amorphous Fe, Mn, Ti-oxides is <1 percent. Smectites and weathered micas are abundant in the overlying B horizons, but these phyllosilicates are of mostly eolian origin. Rare evaporite minerals (gypsum and halite) have been found in association with decayed roots in a B soil horizon.

Calcite Compositional Ranges–Calcite is the most abundant authigenic mineral in the calcretes. Calcite contents of the calcretes, determined by quantitative X-ray diffraction, range from 26 to 70 percent for individual laminae (with the exception of ash-bearing laminae, containing only 17 percent calcite, and pure opaline laminae containing no calcite). Averages representing multiple laminae ("bulk" or "channel" samples) contain 47 to 59 percent calcite. There are no pure-calcite laminae and, as noted above, the fine grain size and intimate intergrowth of calcite with other minerals made separation and concentration of calcite impractical. Contrasted with its abundance in the calcretes, calcite is only a rare constituent of the overlying B horizons. Calcite can be seen in hand sample and in thin section in Btk horizons as fine-grained coatings on the undersides of pebbles, where the calcite is commonly associated with opal.

Although chemical compositions of pure calcite in the calcretes could not be determined on mineral separates, some of the calcites in thin section are large enough (>10 μm) to permit electron-microprobe analysis. Calcite analyses from the calcrete are listed in Table 6.1-5, along with calcite and dolomite analyses from the seep at Site 199 and calcite analyses from several springs. The seep locality in particular is exceptionally Mg rich, with an association of high-Mg calcite and dolomite. In general, spring deposits have higher-Mg calcite than the calcretes (Vaniman, Chipera, Bish 1995). Electron microprobe analyses of 20 calcrete calcites from Trench 14 indicate a lack of any calcites with MgO > 1 percent. This result contrasts with the calcites from seeps and springs that may have calcites with such low MgO contents but generally include calcites with higher MgO (Table 6.1-5). The generally higher MgO content of most of the spring calcites sampled is in accord with the minor occurrence of dolomite along with calcite in several of the samples from Travertine Point veins and from an active spring mound at Nevares.

Calcite is the only significant reservoir for Ca and for Sr in the calcretes; even though calcite could not be separated for analysis, the chemical and quantitative X-ray diffraction data for the calcretes can be used to plot Sr against either percent CaO (with 56 percent CaO representing ideal calcite) or against the X-ray diffraction-determined percent calcite to estimate the range of Sr contents in calcites of the calcretes. The results show a range of Sr contents in calcite of the calcretes from ~800 to 2100 μg/g. Comparable Sr contents are found in calcites of the site 199 seep and in the spring deposits. The coarsest calcite observed in the calcretes, anhedral crystals of up to ~60 μm intergrown in open voids, have no detectable Sr in electron microprobe analysis (Table 6.1-5), although the calculation discussed above indicates that the more typical, fine-grained calcites of the calcrete should have SrO contents ranging from ~0.09 to 0.25 percent. Some electron microprobe analyses of relatively coarse calcite from calcretes do report detectable SrO at the lower end of this range (Vaniman, Bish, Chipera 1988), but the highest SrO contents apparently occur in the more abundant, fine-grained calcites that are too small (<5 μm) for electron microprobe analysis. It is worth noting that the highest SrO contents observed in any sample are in ostracode fossils from the spring mound at Nevares (sample 760,t1a; Table 6.1-5).

Opal Compositions–The calcretes at Yucca Mountain are siliceous, containing variable amounts of opaline silica. The forms of opal in these deposits include both opal-A (amorphous silica) and opal-CT (largely amorphous but with both cristobalite-like and tridymite-like stacking). Opal contents of individual calcrete laminae range from 0 to 57 percent (with the exception of ~100 percent pure opaline laminae). Averages representing multiple laminae ("bulk" or "channel" samples) contain 31 to 42 percent opal. As in the calcretes, both opal-A and opal-CT are found in spring deposits. However, the opal-A that occurs in springs is generally in algal mats near active discharge zones. Small veins of opal-CT occur in older, inactive portions of some springs, sometimes as massive white nodules of vitreous luster, often several centimeters in diameter. A notable distinction from the calcrete silica deposits is the occurrence of authigenic masses or bands of authigenic quartz, which has not been found in any calcrete deposits.

Sepiolite–Sepiolite is ubiquitous in the calcretes but reaches significant abundances (up to 39 percent) only in rare laminae, where sepiolite is intergrown with calcite in pods several millimeters in length. Elsewhere in the calcretes, sepiolite can occur within ooid rims, as a component of fossilized roots, as small fibrous deposits, or as clasts reworked into later-formed

calcretes. The abundances of sepiolite in individual laminae containing these other occurrences do not exceed 5 percent. Sepiolite has not been found in the B-horizon soil samples. Vaniman, Chipera, Bish (1995) find that there is a range of sepiolite compositions in the calcretes. The ideal sepiolite formula is $Mg_4(Si_2O_5)_3 \cdot (OH)_2 \cdot 6(H_2O)$, or $4MgO + 6SiO_2 + 7H_2O$. The data from calcretes show some substitution of Al for Si, plus substitution of Al, Fe, Ca, Na, and/or K for Mg.

Amorphous Fe, Mn, Ti-oxides–Voids in the calcretes and B-horizon soils of at Yucca Mountain may contain fillings or linings of amorphous Fe, Mn, Ti-oxides. These deposits are a minor constituent of the vein calcretes (generally <1 percent), but because of their often high Fe contents, they can be a significant reservoir for Fe and associated elements (especially Sc). The possibility of some crystallinity within these features cannot be ruled out, but the compositions of these metal-rich deposits are highly variable, suggesting largely amorphous composition or a fine-grained mixture of poorly crystalline phases (Vaniman, Chipera, Bish 1995). Electron-microprobe data analyses suggest some intergrowth of calcite and opal with these oxide deposits, as well as intermixtures of lesser amounts of Mg and Al, particularly within the more Mn-rich deposits. In some instances, these deposits appear to fill root-fossil voids; in other instances, they line cavities or fractures of inorganic origin in the calcretes. Electron-microprobe analyses separate these opaque deposits into three types: Fe-rich deposits with minor amounts of Mg; Ti-rich deposits with minor amounts of Al; and complex Mn-rich deposits with appreciable amounts of Si, Al, and Mg. Energy-dispersive spectra of some Fe-rich amorphous deposits indicate minor amounts of S, Cu, Zn, and perhaps Ni. These are many of the same elements that are highly elevated in the root-ash samples (Subsection 6.1.1.3).

Smectite and Illite–Smectites are more of widely varying abundance (~1 to 34 percent) in the calcretes of Yucca Mountain. X-ray diffraction analyses of the separated smectites indicate poor crystallinity. What appears as a well-crystallized illitic component in the 1-to-3-μm fraction is generally much degraded in the <0.35-μm fraction (Vaniman, Chipera, Bish 1995). This poorer crystallinity with finer grain size, plus the exceptionally Fe-rich composition of the finest (<0.35 μm) clay fraction (> 5 percent FeO), indicate that the "illitic" component is in fact largely due to degradation of detrital biotite. Much of the clay may be eolian. Long-range eolian transport is especially effective at size ranges of ~2 to 40 μm (Junge 1979).

The clay minerals in the spring deposits often include a well-crystallized illite component, unlike the B-horizon soils and calcretes at Exile Hill where the clays consist of smectite, sepiolite, and an "illitic" component that appears to be predominantly a degradation product of detrital biotite.

Other Minerals in Yucca Mountain Soils–The only other authigenic minerals yet found associated with B-horizon soils or calcretes at Yucca Mountain are whewellite, gypsum, and halite. Gypsum and halite are rare; they are found in trace amounts in the B-horizon soils in association with decaying roots or with deposits in open soil voids. Gypsum occurs within some voids as small, curved crystals resembling the gypsum "cave flower" forms found in some underground deposits. Whewellite appears to be strictly restricted to occurrences within living roots. Despite this restriction, whewellite may be a significant contributor of Ca to the near-surface calcite deposits by virtue of many repetitions of root growth and death cycles in the upper 15 m of soil and rock into which roots penetrate (Vaniman and Whelan 1994).

Other Minerals in Spring Deposits–The active deposits at Grapevine Spring include surface efflorescence features that are white, fragile, and have a slightly bitter taste. X-ray diffraction analysis of this efflorescence reveals major amounts of the minerals halite, trona ($Na_3H(CO_3)_2 \cdot 2H_2O$), and thenardite ($Na_2SO_4$) with minor amounts of aphthitalite ($K_3Na(SO_4)_2$) and possible burkeite ($Na_6CO_3(SO_4)_2$). Halite, trona, and burkeite have also been reported from efflorescence deposits in Oasis Valley (Vaniman, Bish, Chipera 1988). With the exception of halite, none of these minerals have yet been identified at Yucca Mountain, and certainly no significant deposits comparable to those at Grapevine Spring have been found.

The Paleozoic dolomite of the Roberts Mountain Formation was collected from drill core UE-25 p#1. This sample consists almost entirely of dolomite, with minor calcite and quartz. Deep carbonates with abundant dolomite could be contributors of Mg to the relatively Mg-rich carbonates found in spring deposits of the region.

6.1.3.4 A Three-Dimensional Mineralogic Model of the Site

For subsurface mineralogic studies at Yucca Mountain, there is a need to link the quantitative mineralogic analyses, obtained by X-ray diffraction, with the site geologic model. The result of this linkage is a 3-D mineralogic model of the Yucca Mountain site.

The mineralogical data for the 3-D Mineralogic Model were obtained from quantitative X-ray powder diffraction analyses of core and cuttings from drillholes at Yucca Mountain. X-ray diffraction offers the most direct and accurate analytical method for determining mineral abundance because the data are fundamentally linked to crystal structure. Other methods based on down-hole logs or chemical or spectral properties from which mineral identities are inferred are subject to much greater uncertainty. Significant effort has gone into the development of quantitative X-ray diffraction for application to core and cuttings analysis at Yucca Mountain (Bish and Chipera 1988; Chipera and Bish 1995). This analytical capability has resulted in the development of a database of mineral abundances as a function of map position and depth at Yucca Mountain that is one of the most accurate mineral frameworks for a large area anywhere in the world. This framework provides a powerful tool for 3-D visualization of mineral abundances at Yucca Mountain. Furthermore, this model of mineral distributions can serve as the basis for performing reactive-transport calculations and mineral-reaction modeling.

The stratigraphic framework for the 3-D Mineralogic Model was derived from the Updated Integrated Site 3-D Framework Model (ISM 2.0, Zelinski and Clayton [CRWMS M&O 1996], Appendix Rev. 3.1). The units used in the 3-D Mineralogic Model are shown in Table 6.1-6 in relation to the Integrated Site Model. The stratigraphy as defined by Buesch, Spengler et al. (1996) and the strata used by Zelinski and Clayton (CRWMS M&O 1996) are also included for comparison. The mineralogic units follow the framework grid of Zelinski and Clayton (CRWMS M&O 1996) in which many of the units correspond to the Integrated Site Model units on a one-to-one basis (for example, unit 25 is equivalent to Tpp).

In some instances, depositional stratigraphic boundaries correlate well with major mineralogic transitions. However, in other places, mineralogic transitions occur within geologic/lithologic units, and/or the contacts between geologic/lithologic units do not correlate with any significant mineralogic changes. Each of the mineralogic units has been subdivided into a minimum of 10

equal subunits to account for mineralogic transitions within units. These subdivisions result in 333 distinct mineralogic layers that allow for a reasonably accurate characterization of mineralogic variations across Yucca Mountain. The observation (see below) that boundaries between stratigraphic units do not always coincide with changes in mineral abundances emphasizes the importance of incorporating material properties (mineralogy, permeability, etc.) rather than relying solely on depositional stratigraphic units for average material properties in modeling site behavior.

The need for a complete and accurate 3-D Mineralogic Model of Yucca Mountain is driven by several concerns having a direct effect on radionuclide transport. For example, despite the project's long-standing concept of the role of stacked zeolite horizons as barriers to radionuclide migration between the potential repository horizon and the water table (for example, Vaniman, Bish, Broxton et al. 1984), there is a common and continuing misconception that there are "holes" at Yucca Mountain where no zeolitic barriers occur between the potential repository and the water table. This misconception is unsupported by available data. Misconceptions such as this demonstrate the critical need for a quantitative 3-D model of mineral distributions for accurate visualization and use of site properties in calculations.

The 3-D Mineralogic Model is still being developed but has been applied or will be applied to several aspects of site characterization and assessment:

- *Mineralogy and Fluid Flow*–Mineralogy is strongly correlated with the hydrologic properties and behavior of rock units. For example, vitric nonwelded tuffs and zeolitized tuffs with very similar porosities can have very different hydraulic conductivities reflecting the impact of zeolitization (Loeven 1993). Smectite intervals, even in thin occurrences, can give aquitard characteristics to porous intervals that would otherwise be highly transmissive when saturated. As discussed below, the use of a combination of mineralogic and hydrologic data (the latter derived from geophysical measurements) would provide a powerful means of providing potentially accurate physical descriptions of fluid and reactive-transport pathways that are specific to the Yucca Mountain site.

- *Mineralogy and Radionuclide Transport*–Zeolitic horizons have long been an important factor in models of radionuclide transport at Yucca Mountain. A preliminary 3-D transport model has already been developed using a 3-D distribution of zeolite horizons that was not based on the Integrated Site Model (Robinson, B.A. et al. 1995). In this earlier study, constant-abundance zeolite horizons were defined based on arbitrary cutoff values of zeolite percentage. The present Mineralogic Model incorporates zeolite and other mineral percentages as the basic distributed property, allowing mineral volumes to be defined explicitly in an accurate, spatial manner as needed for specific performance studies. The present effort provides a much more robust and more widely accessible model of zeolite distributions with ties to the Integrated Site Model. Moreover, the potentially large impact of minor minerals, particularly smectite, is presented in a manner that can be considered in transport modeling.

- *Mineral Distributions and Thermal Stability of Rocks*–Hydrous minerals and volcanic glass are particularly susceptible to reactions caused by repository-induced heating.

These reactions can release or absorb water, can result in changes in porosity, permeability, retardation characteristics, and can moderate heat flux within the rock mass. Other minerals, particularly silica polymorphs, may be structurally affected or may control the aqueous silica concentrations of fluids migrating under thermal loads, resulting in silica dissolution or precipitation and rock-property modification at distal locations. All of these effects should be considered in three dimensions to adequately address the impact of various repository loading strategies. The 3-D Mineralogic Model will also permit modeling of reactions involving the breakdown of glass to zeolites and smectite, the reaction of zeolites to analcime, and the transformation and redistribution of silica polymorphs. Such work has already been initiated in an effort to explicitly couple the Conceptual Model of Mineral Evolution to the 3-D Mineralogic Model (Carey, Robinson et al. 1995).

- *Mineral Distributions and Health Hazards*–Distributions of crystalline silica polymorphs have had an important impact on the requirement for respirator protection for those working in the Exploratory Studies Facility. The Topopah Spring Tuff has highly variable ratios of the crystalline silica polymorphs and an accurate knowledge of the distributions of these minerals in three dimensions may help in planning for mitigation of dust inhalation hazards. The 3-D model also allows the prediction of the location of possible occurrences of the hazardous zeolite, erionite (Bish, Carey et al. 1997). Such predictions can be used as a basis for performing work carefully in suspect zones without having to subject all work to stringent safety requirements.

- *Prediction of Mineral Distributions and Repository Performance*–Repository performance guidelines will include thermal limits for particular reactive mineral-bearing zones (for example, zeolites). Previous guidelines have used somewhat arbitrary horizons for particular thermal goals due to a lack of 3-D mineralogic data. The new model will allow thermal model studies to indicate much more precisely the maximum possible thermal loads consistent with maintaining relatively low temperatures for zeolite-rich zones. When models coupling the 3-D mineralogic model to mineral-reaction and heat-flow calculations are developed, thermal limits can be explicitly modeled with fewer assumptions.

6.1.3.4.1 Software Used to Conduct Modeling

To formulate the 3-D Mineralogic Model, the commercially available computer code STRATAMODEL (available from Landmark Graphics Corporation, Houston, Texas) was used (Landmark Graphics Corporation 1995). STRATAMODEL is a computer program generally used to create 3-D models of geological formations using stratigraphy and associated lithologic properties (attributes such as rock porosity, permeability, mineralogy, etc.). The program conducts weighted interpolations of stratigraphically controlled properties between known data locations (that is, drillholes) to produce a volumetric distribution of the rock properties associated with each stratigraphic horizon.

The current version of the 3-D Mineralogic Model uses a deterministic method for distributing mineral abundances that is standard with the STRATAMODEL program. Probabilistic distributions of minerals will be developed in the future using the software package RC2. This

geostatistical program calculates experimental variograms from mineralogic data and allows determination of characteristic curves giving mineral-abundance variance as a function of distance from experimental data.

Six classes of minerals have been incorporated in the 3-D Mineralogic Model, Rev. 1. Only the most abundant of the potentially sorptive or reactive phases were included, based on their significance in modeling waste migration or thermal loading. Minerals such as quartz and feldspar were not included because they are almost ubiquitous at Yucca Mountain and are comparatively inert. Cristobalite/quartz/tridymite ratios will be considered in later versions of the model to address thermal-loading concerns and concerns about the principal inhalation hazards when mining in the Topopah Spring Tuff. The minerals, mineral groups, or glasses presently used in the 3-D model are as follows:

- Smectite + Illite
- Sorptive Zeolites (the sum of clinoptilolite, heulandite, mordenite, chabazite, erionite, and stellerite)
- Tridymite
- Cristobalite + Opal-CT
- Volcanic Glass
- Nonsorptive zeolite (analcime)

Improvements to the Three-Dimensional Mineralogic Model–The 3-D model will be significantly improved by using geophysical well-log data. Rautman and Engstrom (1996a, 1996b) and Engstrom and Rautman (1996) have demonstrated a correlation between hydrologic properties and hydrous minerals in neutron log data. These data can be relatively easily incorporated into the 3-D model as soft constraints on zeolite and smectite/illite distributions. In particular, well-log data can compensate somewhat for sparse sampling of analyzed drillholes and can provide data for drillholes for which the project has no mineralogic data. Conversely, the mineralogic data can help to define more sharply the transitions in hydrologic properties and their correlation with stratigraphic units. The integration of mineralogic and geophysical data would improve both the mineralogic and hydrologic models and could be accomplished relatively easily.

The current 3-D Mineralogic Model represents faults as zones of steeply dipping but continuous stratigraphic units. As a consequence, mineralogic predictions in the vicinity of the major fault zones (Solitario Canyon and Ghost Dance) are not particularly accurate. Data to be obtained in future drilling and from the construction of tunnel-boring machine excavated drift to the west, across the Solitario Canyon fault, will aid significantly in addressing these uncertainties.

There are regions in the model that show unexpected mineralogic variations, primarily in the form of unusual results for particular drillholes. Future modeling efforts will focus on developing a means of minimizing the discrepancies (for example, by using cuttings-data only as

soft constraints) and by developing the mineralogic analysis to identify questionable data. This capability will be important in the future, because planned future drillholes (for example, SD-6 and WT-24) will not be continuously cored.

6.1.3.4.2 Abundance of Zeolites at Yucca Mountain

The distribution of zeolites (the sum of clinoptilolite + mordenite + erionite + stellerite + chabazite) at Yucca Mountain is shown in north-south and west-east cross-sections in Figure 6.1-38 extracted from the 3-D Mineralogic Model for Yucca Mountain. The location of drillholes with respect to the cross sections is also shown.

The extensive layers of zeolites are quite evident. The total volume of zeolites within the region depicted is about 9 percent of the total volume and about 14 percent of the region occurring above the water table (~730 m elevation).

The abundance of zeolite varies across the repository block. In the northern section, near drillhole USW G-2, the Calico Hills Formation contains the highest percentage of sorptive zeolites, and the thickness of zeolite above the water table is greatest. To the south, stacked strata with large volumes of sorptive zeolites occur in the Calico Hills Formation and in the nonwelded and bedded units interposed between tuffs of the Crater Flat Group. Although the abundance of zeolite minerals in the Calico Hills Formation decreases to the west and south, the abundance of zeolites in the Crater Flat Group persists beneath the nonzeolitized parts of the Calico Hills Formation. Detailed cross sections demonstrate the continuity of zeolite throughout the exploratory block (Carey, Chipera, Vaniman et al. 1997). Zeolite-rich horizons exist between the water table and the potential repository in all locations. All of the available drillhole data do not support the existence of a "zeolite hole" in the exploratory block. In addition to the models of zeolite distribution built drillhole data, here is consistent evidence of zeolitization extending at least 100 m above the present water table (see Subsection 6.1.5.1.1). As long as nonwelded tuffs occur within this interval, zeolite barriers exist.

Clinoptilolite and mordenite are the most abundant zeolites at Yucca Mountain. Major, laterally extensive intervals of clinoptilolite occur in all drillholes, from ~100 to 150 m above the water table to ~500 m below. Heulandite is fairly common at Yucca Mountain but is lumped with clinoptilolite in X-ray diffraction analyses because the two minerals are isostructural. Mordenite often occurs along with clinoptilolite but is less abundant in drillholes farther to the south and is virtually absent in bulk-rock samples from drillhole USW GU-3/G-3. The zeolite analcime occurs as a prograde alteration product at greater depths, but these depths are so great that little interaction with waste is likely. The locations of zeolitic intervals are strongly controlled by tuff stratigraphy. In general, zeolites formed from the glasses of nonwelded and bedded intervals that occur between devitrified tuffs. These zeolitic intervals and their significant effects on Np transport have been modeled recently by B.A. Robinson et al. (1995, 1997).

Until 1995, chabazite was known only as a rare zeolite at Yucca Mountain. However, samples from the Calico Hills Formation in USW SD-7 contain significant amounts (up to 9 percent) of chabazite in an ~14-m zeolitized interval consisting principally of clinoptilolite + chabazite, occurring above a clinoptilolite + mordenite zone (Chipera, Vaniman, Bish 1996). This

relatively new occurrence indicates that the sorptive zeolite assemblages may be more complex at the southern end of the exploration block than previously thought.

In addition to clinoptilolite, mordenite, analcime, and minor chabazite, restricted occurrences of a few other zeolites have been found at Yucca Mountain. Stellerite is common in fractures of the Topopah Spring Tuff and is particularly common in both fractures and matrix of the Topopah Spring Tuff in drillhole UE-25 UZ#16. The new data in this model extend stellerite distributions to the lower devitrified portion of the Topopah Spring Tuff in drillhole UZ-14, spanning an interval where perched water was observed during drilling. Phillipsite is a rare zeolite at Yucca Mountain and has been found only in a zone of alteration above the water table at the top of the basal vitrophyre of the Topopah Spring Tuff (Carlos, Bish et al. 1991; Carlos, Chipera, Bish et al. 1995; Carlos, Chipera, Bish 1995). Laumontite occurs in very small amounts (<4 percent) in deep, altered tuffs of drillhole UE-25 p#1 and perhaps in USW G-1 (Bish and Chipera 1989) Phillipsite and laumontite are so rare that they are not important factors in developing zeolite volume estimates for this model.

Erionite is another rare zeolite at Yucca Mountain that was at first observed only in fractures at the top of the Topopah Spring Tuff basal vitrophyre. However, it has since been found in significant quantities (up to 34 percent) in a 3 m thick sequence in the bulk rock underlying the Topopah Spring Tuff basal vitrophyre in drill core USW UZ#14 (Guthrie, Bish et al. 1995) and has been found in trace amounts (1 percent) in a breccia zone in the South Ramp of the Exploratory Studies Facility. Although the occurrence of erionite is rather sporadic and, where found, its abundance is typically low, it is a significant health concern due to its known carcinogenicity. The 3-D model has been used to assist predictions of erionite-bearing zones in drillhole SD-6 (Bish, Carey et al. 1997).

6.1.3.4.3 Abundance of Smectite + Illite at Yucca Mountain

Figure 6.1-39 illustrates a north-south cross-section extracted from the 3-D Mineralogic Model representing the amount of smectite + illite at Yucca Mountain. At the scale shown, smectite + illite is seen to be ubiquitous but present in low abundance throughout Yucca Mountain except in some thin horizons and at depth in data obtained from USW G-1. X-ray diffraction analyses show that smectite occurs in virtually all analyzed samples, typically in amounts <2 percent. Volumes of smectite + illite increase at depth, particularly in the northern and central portions of the block where a fossil geothermal system occurs.

Above the water table, there are two mappable zones of up to 75 percent smectite in the Paintbrush Tuff, one within the vitric nonwelded section above the Topopah Spring Tuff and one at the top of the basal vitrophyre of the Topopah Spring Tuff. These smectites typically have nonexpandable illite contents of 10 to 20 percent. These thin units are difficult to resolve at the scale shown in Figure 6.1-39, and future work will generate more detailed graphics for areas of special interest such as these. Well beneath the water table (depths > 1000 m), the ancient (~10.7 Ma) geothermal system generated abundant smectite/illite but with a much higher illite content (~80 to 90 percent; Bish 1989). Illitic clays have a higher layer charge than smectites, reducing their effective cation-exchange capacity. However, the illitic clays occur at such great depths that they are of little importance for transport modeling at Yucca Mountain.

6.1.3.4.4 Volume of Tridymite and Cristobalite/Opal-CT at Yucca Mountain

The common silica polymorphs at Yucca Mountain include quartz, cristobalite, and tridymite. In addition, opal-CT is usually found in association with sorptive zeolites. Tridymite occurs primarily above the potential repository horizon, particularly in those parts of the Topopah Spring and Tiva Canyon Tuffs where vapor-phase crystallization is common. It occurs very rarely below the water table. This distribution, as well as the common occurrence of tridymite in lithophysal cavities, is evidence of the vapor-phase growth of tridymite. Pseudomorphs of quartz after tridymite in deep fractures and cavities are evidence of the instability of tridymite under low-temperature aqueous conditions. Tridymite occurrences have been interpreted as a possible limit on past maximum rises in the water table at Yucca Mountain (Levy 1991). Volumes of exceptionally high tridymite content are restricted to the upper strata within the Tiva Canyon and Topopah Spring Tuffs. These volumes are mostly above the potential repository horizon. The restricted occurrences of tridymite within the Topopah Spring Tuff make tridymite a potential guide to stratigraphic position within this unit.

Cristobalite is typically a devitrification product that is found in virtually every sample above the water table. Opal-CT is a typical byproduct of zeolitization and is found below the water table before disappearing at depths at or below the Tram Tuff. In the 3-D Mineralogic Model, cristobalite and opal-CT are combined, partly because the extra analytical procedures necessary to distinguish them were not commonly applied to the drillhole data, but also because the two minerals yield very similar aqueous silica activities. Cristobalite and opal-CT disappear at depth and are replaced by quartz-bearing assemblages (Figure 6.1-40). Cristobalite and opal-CT represent about 6 percent of the mineral volume at Yucca Mountain.

Other Applications of the Three-Dimensional Mineralogic Model–There are many other mineral distributions that can be treated quantitatively in modeling Yucca Mountain. The examples of zeolite distributions shown in Figures 6.1-84 to 6.1-89 are but one of many mineral distributions that can be modeled. Other figures for clay mineral distributions, distributions of the silica polymorphs, and glass distributions can be found in Carey, Chipera, Vaniman et al. (1997). Indeed, data exist for all mineral constituents that occur in amounts measurable by X-ray diffraction (that is, more than about 1 w%) can be so modeled. Future versions of the model are planned to address the mineralogy of fractures and faults, but the linkages between fracture/fault mineralogy and the lithostratigraphy and structure are not presently known at a level that permits quantitative modeling.

Carey, Chipera, Vaniman et al. (1997) studied cross-sections extracted from the 3-D Mineralogic Model showing the amounts of smectite + illite at Yucca Mountain. Smectite + illite can be shown to be ubiquitous but present in low abundance throughout Yucca Mountain, except in some thin horizons within the unsaturated zone and shallow saturated zone and in greater abundance at depth. The 3-D mineralogic model shows that smectite occurs in virtually all analyzed samples, typically in amounts <2 percent. However, above the water table there are two mappable zones of up to 75 percent smectite in the Paintbrush Tuff, one within the vitric nonwelded section above the Topopah Spring Tuff (the PTn geohydrologic unit) and one at the top of the basal vitrophyre of the Topopah Spring Tuff. These smectites typically have nonexpandable illite contents of 10 to 20 percent. These thin units are prominent in sections generated from the 3-D Mineralogic Model. Well beneath the water table (depths >1,000 m), the

ancient (~10.7 Ma) geothermal system contains abundant smectite/illite but with a much higher illite content (~80 to 90 percent; Bish 1989). Illitic clays have a higher layer charge than smectites, reducing their effective cation-exchange capacity. However, the illitic clays occur at such great depths that they are of little importance for transport modeling at Yucca Mountain. Future work will address the relationships between clays and other alteration minerals in both rock matrix and fractures or faults. These relationships are important in transport modeling, because clays have demonstrated importance in retarding movement of actinide elements (Pu in particular; see Subsection 6.1.8.6).

Carey, Chipera, Vaniman et al. (1997) also address the importance of silica polymorph distributions at Yucca Mountain. The 3-D Mineralogic Model is able to display the quantitative distributions of quartz, cristobalite, tridymite, and opal-CT. Tridymite occurs primarily above the potential repository horizon, particularly in those parts of the Topopah Spring and Tiva Canyon Tuffs where vapor-phase crystallization is common. It occurs very rarely below the water table. This distribution, as well as the common occurrence of tridymite in lithophysal cavities, is evidence of the vapor-phase growth of tridymite. Pseudomorphs of quartz after tridymite in deep fractures and cavities are evidence of the instability of tridymite under low-temperature aqueous conditions. Tridymite occurrences have been interpreted as a possible limit on past maximum rises in the water table at Yucca Mountain (Levy 1991). Volumes of exceptionally high tridymite content are restricted to the upper strata within the Tiva Canyon and Topopah Spring Tuffs. These volumes are mostly above the potential repository horizon. The restricted occurrences of tridymite within the Topopah Spring Tuff make tridymite a potential guide to stratigraphic position within this unit.

Cristobalite is typically a devitrification product that is found in virtually every sample above the water table. Opal-CT is a typical byproduct of zeolitization and is found below the water table before disappearing at depths at or below the Tram Tuff. In the 3-D Mineralogic Model, cristobalite and opal-CT are combined, principally because the two minerals yield very similar aqueous silica activities. The 3-D Mineralogic Model shows that cristobalite and opal-CT disappear at depth and are replaced by quartz-bearing assemblages. In future work, the occurrence of cristobalite and opal-CT will be examined in more detail using correlations with other minerals and petrologic constraints to resolve their petrogenetic relations. Cristobalite and opal-CT represent about 6 percent of the mineral volume at Yucca Mountain.

The distributions of silica polymorphs are important factors in determining the long-term response of Yucca Mountain to thermal loads. Cristobalite and tridymite have the potential to experience significant reactivity in the near-field environment due to thermal expansion and silica dissolution/precipitation reactions. The α to β reaction in cristobalite is of particular concern in thermal-load designs and their effects on porosity, permeability, and mechanical strength.

6.1.3.4.5 Volcanic Glass at Yucca Mountain

Volcanic glass is almost entirely restricted to regions above the water table at Yucca Mountain (Figure 6.1-41). The most significant occurrences of glass occur in the upper and basal vitrophyres of the Topopah Spring Tuff and in the vitric zone of the Tiva Canyon Tuff to the

north. Minor occurrences of glass below the water table in a flow breccia below the Tram Tuff (for example, Spengler, Byers et al. 1981) are not included in the model.

6.1.4 Alteration History of the Yucca Mountain Site

Much of the discussion in this section deals with detailed descriptions of moderate-temperature post-emplacement alteration. The features described can be compared with the surficial calcite, opal, and sepiolite that form in the ambient surface environment (Subsection 6.1.3.3). The features are quite distinct.

The alteration history of Yucca Mountain pertains directly to the nature and rates of geochemical and hydrologic processes active at the site. Regulatory requirements stress the special importance of geochemical and hydrologic processes active during the Quaternary Period (10 CFR 960, pp. 60-7–60-17). A substantial effort has been devoted to identifying geochemical processes that predate the Quaternary Period and establishing that these processes have not recurred during the Quaternary and will not recur in the future.

The mineralogy and geochemistry of Yucca Mountain are important basic attributes of the site as a natural barrier to radionuclide transport. An understanding of the origins of mineralogic alteration is key to predicting the broad patterns of secondary-mineral distribution, especially where drillhole data are sparse. For example, where large between-hole variations in zeolite content exist, the predictive capability of a mineral-distribution model based only on mineral-abundance data and statistical criteria is poor. In such a case, a conceptual model of zeolitization might be used to guide the interpolation of zeolite-abundance values between drillholes.

6.1.4.1 Syngenetic Alteration

Thick pyroclastic deposits like the Topopah Spring and Tiva Canyon Tuffs were erupted and emplaced at temperatures up to around 700 to 900°C (Schuraytz et al. 1989) and probably required about 10^2 to 10^3 years to cool (Riehle 1973). Early in the cooling period, the interiors of such tuffs welded by viscous flow and compaction of the glass particles. The process of welding continued to temperatures as low as 475°C in the basal vitrophyre of the Topopah Spring Tuff (Rosenbaum 1986). After substantial welding had occurred, the tuff in the hottest parts of the interior devitrified, that is, crystallized to an assemblage of feldspars and silica minerals plus a variety of accessory minerals. The faster-cooling upper and lower margins of the deposits did not weld and experienced little or no devitrification. Some of the moderately to densely welded portions toward the outer margins did not devitrify and have survived in a glassy state (vitrophyres). Localized alteration, caused by a combination of water entrained in the ashflow and infiltrating meteoric water that interacted with the rock, occurred during the very late stages of cooling, at near-ambient temperatures (Levy and O'Neil 1989). The tuffs were also subject to fracturing, faulting, and brecciation during cooling (Levy 1993a).

The significance of syngenetic alteration for site characterization lies in two general areas. The original distribution pattern of devitrified and vitric tuffs largely determined the locations of zeolitic and nonzeolitic rocks in those parts of Yucca Mountain where the rocks have been subject to zeolitization. In addition, the field-scale distribution of hydrologic properties reflects the distribution of devitrified and nondevitrified and of zeolitic and nonzeolitic tuffs. The

distribution of devitrified tuffs, based on mineralogy, is described in Subsection 6.1.3. This information places important limitations on genetic interpretations of the main vitric zeolitic transition.

The bulk of alteration history research into syngenetic alteration pertains to late-stage syngenetic alteration and the interaction of still-hot rock with infiltrating meteoric water. Alteration of this type can serve as a natural analog for hydrothermal alteration in a repository environment. This research also addresses the detection of recent surface-discharging hydrothermal activity in the Yucca Mountain area and how it might be distinguished from syngenetic alteration that occurred more than ten million years ago.

6.1.4.1.1 Devitrification and Vapor-Phase Crystallization

Devitrification in the Topopah Spring Tuff–The central portion of the Topopah Spring Tuff is devitrified, whereas the lower and upper parts of the unit are vitric. The distribution of vitric and devitrified rock within the pyroclastic deposit is a function of eruption chronology, emplacement temperatures, unit thicknesses, and volatile contents, all of which directly or indirectly affect the crystallization kinetics of volcanic glass. Distinctive zones of mineralogy and rock devitrification texture exist within the devitrified tuff (Bish and Chipera 1989; Byers and Moore 1987). The major mineralogic components of the devitrified rocks are alkali feldspar and two or more silica phases. From the top of the Topopah Spring Tuff down through the top of the lower lithophysal zone, the typical secondary silica phases in the groundmass are cristobalite and tridymite. The characteristic silica phases in the remainder of the devitrified section, including the candidate host rock, are cristobalite and quartz. The quantitative mineralogy of the entire unit is described in Subsection 6.1.3.

Groundmass devitrification textures in the Topopah Spring Tuff were studied in detail by Byers (1985) and Byers and Moore (1987). The devitrification textures can be classified as either microcrystalline or cryptocrystalline. The finer-grained cryptocrystalline textures are characteristic of nonlithophysal intervals and are especially well developed in the lower part of the lower nonlithophysal zone (Tptpln, the candidate host rock; Buesch, Spengler et al. 1996). Cryptocrystalline textures are generally very finely fibrous with excellent preservation of relict shard forms. Near the bottom of this interval, there are distinctive brown and yellow varieties of cryptocrystalline-textured rock. The brown cryptocrystalline tuff has about the same bulk chemical composition as the original glass (Byers 1985), but the yellow variety has higher normative alkali feldspar contents and the feldspar is richer in potassium. Crystallization of volcanic glass to yellow cryptocrystalline devitrified tuff must have occurred under conditions conducive to mass transport.

Vapor-Phase Minerals in the Tiva Canyon Tuff–A general sense of the devitrification and vapor-phase mineralogy of the Tiva Canyon Tuff can be gained from the whole rock X-ray diffraction data (Bish and Chipera 1989, and Subsection 6.1.3.1). Samples from the Exploratory Studies Facility starter tunnel and North Ramp include a number of minerals not previously identified as vapor-phase components of the Tiva Canyon Tuff.

In the Exploratory Studies Facility, the wealth of fresh lateral exposure—approximately 700 m—in the moderately to densely welded, devitrified Tiva Canyon Tuff has provided an opportunity

to observe and sample zones of concentrated vapor-phase mineral deposition. Vapor-phase alteration products observed in unusual abundance in a large altered but nonwelded pumice clast are typical of syngenetic mineral deposits near the top of the unit. The phases identified by secondary electron imagery and energy-dispersive X-ray spectroscopy include very pale yellow apatite with a distinctive tabular morphology, sub-mm black aggregates of slender prismatic hollandite (a hydrous barium-manganese oxide), orange to golden needles of probable amphibole, flat round grains of Fe-Ti oxide, and prismatic zircons (NR-4-SSL, SPC 508430, station 3+69.93, 2 m above springline, left rib). Most of these phases overlie older coatings of corroded potassium feldspar or spherulitic opal-CT and are themselves partly coated with opal. The flat hexagonal plates of apatite are up to about 300 μm across. Many of the smaller crystals have a skeletal morphology. The zircons are up to about 20 μm long and are well terminated.

The zircon and apatite occurrences are noteworthy because of their potential value for geochronologic and paleothermal studies. For example, the ages of zircons in Tiva Canyon breccias from Trench 14 have been cited as evidence for and against a recent hydrothermal eruption origin of the breccias (Raleigh et al. 1992). The in situ origin of the Exploratory Studies Facility zircons is clear from textural relations and mineral associations so that chronological and geochemical data for these zircons could form a basis for comparison with other populations of more ambiguous or heterogeneous origin. Besides providing additional information about the origins of the breccias, characterization of the zircons would help us distinguish the eolian, alluvial, and local weathering contributions to the surficial deposits that condition the geochemistry of meteoric recharge water at Yucca Mountain.

6.1.4.1.2 Moderate-Temperature Hydrothermal Alteration

Although the alteration examples described in this section represent several different stratigraphic intervals within the Paintbrush Group, they have in common that all are located at or near devitrified-vitric transitions. These transition zones are favored sites for alteration during the late-stage cooling of thick tuff deposits because the reactive glass can be contacted by heated fluids—steam or liquid water—coming from the warmer interior of the deposit.

6.1.4.1.2.1 Alteration in Tiva Canyon Tuff and Underlying Bedded Tuffs

Distinctive alteration related to water-rock interaction during the cooling of the Tiva Canyon Tuff has been observed in outcrops of the informally named Harper Valley of southeast Yucca Mountain, at Southwestern Busted Butte, and in Exploratory Studies Facility South Ramp exposures. The best exposures and maximal development of the alteration are in Harper Valley, where the hydrologic properties of the rock have been substantially modified. Hydrologic properties have been affected within a smaller vertical extent in the Exploratory Studies Facility exposures, but the unusual mineralogy of the alteration has potential implications for the composition and amount of groundwater percolation at these sites.

Harper Valley (Southeastern Yucca Mountain)–Alteration in the interval from the Tpcplnc downward to the bedded tuffs below the Tiva Canyon Tuff was studied in the informally named Harper Valley of Southeastern Yucca Mountain, a heavily faulted area (Lipman and McKay 1965). There are excellent exposures of preserved fluid pathways from the time about 12.7 Ma ago (Sawyer et al. 1994) that the Tiva Canyon Tuff was cooling after deposition. The lower

portion of the devitrified interior of the tuff has prominent vertical semicolumnar cooling cracks. Crack surfaces within about 1 m above the transition to underlying partly vitric tuff have patchy coatings of chalcedony and opal-CT (Table 6.1-7) that are quite prominent even though they cover less than 10 percent of the fracture surfaces. The mostly glassy, moderately welded tuff below (Tpcpv2) is also fractured but has a less columnar appearance. Chalcedony is a minor fracture coating in this interval, whereas opal (probably opal-A) is abundant. Areas of fracture surface up to at least one-half square meter are almost completely covered with silica. The sequence of alteration and silica production and deposition in the moderately welded tuff began as hot fluids penetrated up to 2 mm into the rock matrix adjacent to the fractures, resulting in the formation of cristobalite-feldspar devitrification rims on the glass pyroclasts and preservation of the remaining glass within the 2-mm selvage (Table 6.1-7). In the body of the rock behind the selvages, the glass-particle surfaces are covered with etch pits from substantial but incomplete dissolution. Most of the glass was altered to alkali feldspar, cristobalite, smectite, and possibly opal-A (indistinguishable from glass by X-ray diffraction; Table 6.1-7). Glass alteration also provided the silica for the abundant opal fracture coatings in the moderately welded tuff. Opal deposits in the larger-aperture fractures (up to several-mm apertures) have a distinctive "dripstone" texture with opal "drips" hanging downward into the void space of the fractures.

The silica-bearing solutions from the lower Tiva Canyon Tuff penetrated further downward into underlying bedded, nonwelded, glassy tuffs. Individual beds range in thickness from about 5 cm to several m and in pyroclast size from fine-grained ash layers to pumice lapilli tuffs with clasts up to 1 cm or more. Opal-A cement has preserved the paths of fluid flow in these tuffs (YM-4-SSL-1, Table 6.1-7). Because the cemented tuff is more resistant to weathering than the uncemented rock, many of the former fluid pathways now stand out in relief from the rest of the outcrop. Cemented tuff concretions are tooth-like in shape, massive at the top and tapering straight downward to multiple thinner projections. Despite the nonwelded character of the tuff, fractures played an important role in directing the flow. The concretions are found in a variety of linear alignments consistent with fracture traces, but in many cases, the fractures themselves are only barely visible or not visible at all.

One or more pumice lapilli layers, about 15 cm thick, have been cemented so as to form a pervasive honeycomb network of vertical interconnected walls several cm thick. Wall-to-wall honeycomb dimensions are about 5 to 10 cm. The opal-A cement has the same "dripstone" texture seen in the overlying Tiva Canyon moderately welded tuff. The honeycomb "cells" are sealed by opal at the bases of the pumice layers. Pumice within the cemented walls is glassy and pristine, but the pumice in the uncemented centers of the cells has been altered to a zeolite-smectite assemblage. This pattern of alteration probably indicates perching of water caused by permeability differences at the base of the pumice layer and enhanced by the opal cementation.

The Harper Valley silica deposits should be considered in the context of larger-scale structures. The deposits lie within a northwest-southeast-trending fault zone that was probably active around the time the pyroclastic flows were emplaced. Other exposures of the same stratigraphic sequence reveal that the alteration is not ubiquitous. The only site identified to date with comparable alteration is on the west side of Busted Butte close to a fault zone that is very nearly in alignment with the Harper Valley fault zone. The distribution of this distinctive alteration highlights the possible role of the faults in channeling infiltration water at depth.

Exploratory Studies Facility South Ramp, Stations 75+20 and 75+07–Harper Valley-type alteration in the bedded tuffs below the Tiva Canyon Tuff has not been observed in the Exploratory Studies Facility. Alteration at two South Ramp sites extends from the Tpcplnc downward just to the top of the Tpcpv1. The sites were selected for study to help delimit the northernmost expression of the alteration observed in Harper Valley. Both sites are also examples of fractures or faults that cut across the TCw-PTn hydrogeologic boundary, providing potential pathways for fast percolation. A portion of the original study sample from station 75+20 was found to contain erionite, a carcinogenic zeolite (Table 6.1-8). Additional sampling was undertaken to investigate the distribution of erionite at the site, and the results of special X-ray diffraction studies optimized for erionite detection are reported by Bish, Carey et al. (1997). The general mineralogy of these samples, excluding glass and any other amorphous constituents, is given in Table 6.1-9. Locations for all the station 75+20 samples are shown in Figure 6.1-42.

All samples are from the vicinity of a formerly open, breccia-filled cooling joint in the lowermost Tpcplnc that changes into a breccia-fracture zone below the Tpcplnc-Tpcpv2 boundary (Figure 6.1-42). The Tpcplnc bedrock (SR75+20SSL05A, SR75+20SSL04A) is devitrified tuff with a trace to a few percent of smectite. The breccia fracture filling (SR75+20SSL05B, Table 6.1-9) is also devitrified tuff with a cement that probably consists of opal-CT, smectite, and clinoptilolite, comparable to a fracture-filling breccia of similar appearance within the Tpcpv from Harper Valley (YM-2-SSL, Table 6.1-7).

The Tpcpv2 bedrock adjacent to the breccia-fracture zone is moderately to densely welded and partially devitrified to a feldspar-cristobalite assemblage (SR75+20SSL01, LANL 2756, p1, p2, Table 6.1-8). In its least altered condition, the bedrock is moderately to densely welded, partially vitric tuff consisting mostly of reddish yellow shards (7.5 YR 4/6) in a light brown (5 YR 6/4) matrix. The rock contains 5 to 10 percent well-aligned, elongate pumices (length: width $\geq$ 3:1). The pumices are moderate brown (5 YR 3/4) to grayish black (N2), many with a whitish veneer, and may be partly devitrified.

With increasing alteration of the matrix and shards, the rock colors change toward dark yellowish orange (10 YR 6/6), finally to mottling of pale yellowish orange (10 YR 8/6) and moderate orange pink (5 YR 8/4). The most highly altered rock is recrystallized to an assemblage of feldspar, smectite, and cristobalite, plus the zeolites chabazite, clinoptilolite, and erionite (SR75+20SSL01, p2, Table 6.1-8).

Fracture coatings within the breccia zone, but only below the Tpcplnc-Tpcpv2 boundary, are extremely varied, both mineralogically and texturally. Silica is the most abundant coating. About 80 percent of the rock surfaces are 80 to 100 percent covered by either <0.01-mm-thick, sheet-like coatings of translucent silica with a crackled texture or granular-textured, translucent gray-blue deposits of irregular thickness <1 mm. Other silica deposits include probable opal-A in clear, colorless $\leq$0.5-mm spherules and deposits, usually <1-mm thick, with draping, layered "dripstone" textures (fluoresces weakly green in short-wave ultraviolet light). Individual $\leq$ 1-mm spherules and $\leq$3-mm-thick deposits of blue gray botryoidal opal-CT (fluoresces strongly green in short-wave ultraviolet light) and white quartz/chalcedony (LANL 2756, p4, Table 6.1-8) usually overlie zeolite fracture coatings. Opal-CT is locally coated by powdery to lacy-white fine-grained aggregates, possibly zeolite and silica.

White <1-mm spherules and round aggregates are most common on top of the thin silica coatings. Locally, the aggregates coalesce into semicontinuous powdery-white fracture coatings <1 mm thick. The spherules are mineralogically complex, with cores of kenyaite ($Na_2Si_{22}O_{41}(OH)_8 \cdot 6H_2O$), smectite, and minor clinoptilolite and chabazite. The cores have variably thick coatings of morganite (monoclinic crystalline silica) and quartz/chalcedony (LANL 2756, p3, Table 6.1-8). Zeolites are also present as coatings of clear prismatic crystals on fracture surfaces.

Manganese minerals are nearly ubiquitous, and their abundance on rock surfaces ranges from ≤1 percent to about 30 percent. The deposits are irregular, slightly dendritic patches ≤1 cm across. Some deposits are localized around the edges of lithic inclusions or Fe-Ti oxide phenocrysts. The Mn deposits are black to dark brown and have submetallic luster where they overlie silica coatings (most common) but appear duller where they are beneath or within the silica. Calcite generally overlies the other fracture coatings and is especially common as a coating on opal-CT. The calcite occurs in dense aggregates, ≤1 cm thick, of mostly equant 2- to 3-mm crystals.

The alteration occurrence at Exploratory Studies Facility Station 75+07 is a fault coating and very minor cementation of the uppermost Tpcpv1. The coating is clear opal-A (LANL 2757, p2, Table 6.1-8) in spherules and draped masses. Opal also cements the tuff within a few mm adjacent to the fault. Botryoidal, translucent opal-CT/cristobalite, quartz, and moganite (LANL 2757, p3, Table 6.1-8) form a <1 mm thick coating on the opal-A. The bedrock is an essentially unaltered vitric tuff (LANL 2757, p1, Table 6.1-8).

6.1.4.1.2.2 Alteration at the Top of the Topopah Spring Tuff

The environment of syngenetic alteration at the top of the Topopah Spring Tuff is difficult to reconstruct because of uncertainties about the timing and sources of eruptive events during the transition from Topopah Spring Tuff to later Paintbrush Tuff deposition (Buesch, Spengler et al. 1996). The exact top of the Topopah Spring Tuff, defined by geochemical affinity, is not known for sure. The issue of timing may be more important than that of formal stratigraphic assignment because the addition of new pyroclastic deposits on top of the still-warm Topopah Spring Tuff would mean that attributes such as the position of the land surface and the local thermal environment could have changed during the period of alteration. Alteration-history research to date does not settle these issues, but there are some indications that alteration in the nonwelded tuffs at, and possibly above, the top of the Topopah Spring Tuff was associated with syngenetic processes in the main body of the unit.

Outcrops at Busted Butte and Harper Valley (Southeastern Yucca Mountain)–Three exposures of mostly white rocks have been identified at Busted Butte (two sites on the east and west sides) and near Harper Valley (Figure 6.1-43). Individual outcrops have less than 1 m of residual relief and lateral extent. Although they occur at different elevations, all exposures are stratigraphically located in the uppermost part of the Topopah Spring Tuff or in the immediately overlying informal units of the pre-Pah Canyon Tuffs. At Northern Busted Butte, where there are abundant fragments of the white rock but no outcrops, the upper limit on distribution of the fragments matches the same stratigraphic boundary.

The rocks are moderately welded and nonwelded tuffs highly modified by brecciation and secondary-mineral crystallization. Tight cementation of the altered rocks by secondary minerals increased their resistance to weathering and accounts for the outcrop relief. The existence of preserved pyroclastic textures is a conclusive indication that the outcrops are not constructional features such as hydrothermal spring mounds. The banding evident in outcrop is a product of pyroclastic welding or alignment of pyroclasts, enhanced in some cases by secondary-mineral crystallization along clast margins.

The principal secondary minerals, formed after the rocks were brecciated, are alkali feldspar, tridymite, and cristobalite (BB-8-SSL, BB-14-SSL, Table 6.1-10). This mineral assemblage is identical to the minerals formed by devitrification (including vapor-phase crystallization) of densely welded tuff farther down in the interior of the ashflow (Bish and Chipera 1989). The feldspars crystallized from breccia clasts are coarser around the edges of the fragments and have grown beyond the original clast boundaries to form fringes radiating from the relict clasts. This texture indicates that some brecciation occurred while the tuff was still at least partly glassy or while devitrification was in progress. Other breccia fragments have no coarse devitrified fringes or have incomplete fringes, broken off in places, suggesting that brecciation continued after devitrification. These textures somewhat resemble vapor-phase feldspar textures within pumice lapilli in the nonbrecciated densely welded tuffs, another localized environment in which space existed for feldspars to grow beyond original clast boundaries. Tridymite and cristobalite are finer-grained in the breccias than in the pumice lapilli of the densely welded tuffs, and have a tight, cement-like texture. Other secondary minerals in the altered rocks include variable amounts of chalcedony and opal-CT, plus minor hematite and apatite.

Most of the feldspar compositions (Figure 6.1-44; Table 6.1-11) are similar to data for vapor-phase feldspar from the devitrified Topopah Spring Tuff, but some of the feldspars from the altered rock on eastern Busted Butte are much more potassic. For comparison, Figure 6.1-44 shows composition fields for two other distinctive occurrences of secondary alkali feldspar at Yucca Mountain. Feldspars interpreted as products of groundwater hydrothermal alteration at about 175 to 200°C (although temperatures locally reached as high as 200 to 275°C; Bish 1989), related to Timber Mountain caldera activity (~11 Ma), have nearly end-member sodic or potassic compositions that are characteristic of authigenic feldspars (Barth 1969). Normative alkali feldspar compositions (Table 6.1-12) for the cryptocrystalline devitrified fracture borders in the lower Topopah Spring devitrified-vitric transition zone (see Subsection 6.1.4.1.2.3) cover a compositional range very similar to the feldspars from the altered rock, including compositions more potassic than the vapor-phase feldspars.

In the Yucca Mountain area, the alkali-feldspar–tridymite–cristobalite assemblage has not been identified in any genetic context other than early post-depositional devitrification and vapor-phase crystallization of ashflows. The restricted occurrence of this mineral assemblage, plus the proximity of the altered tuffs to the top of the devitrified zone, suggest that the altered tuffs represent local variations of normal devitrification. This interpretation is compatible with the general similarity of feldspar compositions among altered and devitrified rocks. The key modifying factor may have been early brecciation at the alteration sites, providing pathways for both the upward escape of hot vapor from the interior of the ashflow and downward infiltration of meteoric water or condensed steam. The altered rocks do not include any textural features, like the layered silica void fillings in the lower Topopah Spring Tuff, that are unequivocal

indications of the presence of liquid water during mineral deposition. However, the dense cristobalite-tridymite cementation of some samples may reflect increased mass transport in the presence of more abundant water or water vapor.

Hydrothermal Alteration in the Tpbt2, Exploratory Studies Facility–There is a highly altered interval extending approximately from station 10+28 to 10+38 on the right rib at the Exploratory Studies Facility and about 10+22 to 10+45 on the left rib. The exposed alteration is located within pre-Pah Canyon Tuffs (Tpbt2) no more than a few meters above the top of the Topopah Spring Tuff. There is a dramatic visual impact to the contrast of the intensely colored and highly disrupted tuffs with the less-altered adjacent rocks. The exposure lends itself to questions about timing and recurrence of hydrothermal circulation and the implications for nuclear-waste repository performance. Clearly, the existence of a recently active hydrothermal system close to the potential repository host rock would be a serious issue even though the subject has already received considerable study and evaluation (Raleigh et al. 1992; Subsections 6.1.1.3 and 6.1.3.3). This preliminary examination of altered samples identifies the major secondary minerals and provides a beginning basis for comparison with other examples of hydrothermal alteration around Yucca Mountain.

The host rock for the alteration is a sequence of nonwelded bedded tuffs between the top of the Topopah Spring Tuff and the base of the Pah Canyon Tuff. The stratigraphy has been described by Moyer et al. (1996), but for the purpose of this investigation, the rocks exposed in the Exploratory Studies Facility have been divided into five units informally designated A through E in chronological order (Figure 6.1-45). Mottled moderate orange pink (5 YR 8/4) to moderate reddish brown (10 R 4/6), medium- to coarse-grained pumiceous tuffs (unit A) predominate for at least several meters upward from the invert. There is some internal layering within this unit. Above this is a thinly laminated interval of fine-grained tuff up to about 2 m thick (unit B). This unit is overlain only locally in former topographic depressions by fine-grained tuffaceous material with disseminated coarser clasts (unit D). Wherever present, this layer has a fairly uniform thickness of about 10 cm. In one former ~30 cm depression developed on unit B, the lower 20 cm are filled by very fine-grained brown material (unit C) with a gradational transition upward to the 10 cm layer. Above the 10 cm layer or directly overlying the laminated interval is a sequence of mostly gray, fine-to coarse-grained nonwelded tuffs (unit E). The lowermost 20 cm of this sequence consists of layers that are a few mm to a few cm thick.

Some inferences about the relative timing of alteration can be drawn from examination of depositional and erosional surfaces, evidence of soft and brittle deformation, fracturing, and faulting, and the distribution of secondary minerals. Each of these attributes is described for the relevant units and the implications are summarized at the end of this section. Descriptions are based primarily on the left rib exposure depicted in Figure 6.1-45.

Stratigraphic Contacts in the Exploratory Studies Facility–The contact between units A and B is difficult to identify in many places because it is obscured by secondary alteration. In general, the contact is highly irregular with as much as several meters of relief. At some sites, such as around station 10+26 and 10+38 to 10+40 (Figure 6.1-45), the relief appears to be a result of erosion on the unit-A surface because unit-B material with relatively flat, undisturbed internal layering has filled depressions on the underlying surface. In the station 10+30 to 10+33

interval, at least some of the irregularities in the contact resulted from deformation that has produced an interfingering of the two units.

Unit B locally consists of a lower part that has undergone both soft and brittle deformation mantled by an upper part with undeformed layering, well exposed in the 10+29 to 10+33 interval. Before the onset of faulting, the upper surface of the unit was very smooth. Given the range of unit thickness, from less than 0.1 m to more than 2 m, the smooth morphology probably resulted from surface scour and reworking. Just to the left of fault (b), the upper part of unit B was completely removed by erosion, exposing a resistant block of the altered lower unit-B rock.

Unit C is restricted to a single depression in the unit-B surface around station 10+29 to 10+30. The setting of this deposit raises the possibility that it could have been a mud pot or some other surficial expression of fumarolic activity or simply a small pond. A definitive answer will require further study, but it is noteworthy that the fragments of unit B incorporated in this deposit do not appear any more altered than the unit-B bedrock. The locally deposited unit D and the overlying widespread sequence of unit E have simple flat contacts and little or no internal deformation.

Mineralogy of Hydrothermal Alteration in the Tpbt2, Exploratory Studies Facility– Alteration of the originally vitric tuffs was more intense and widespread in the rock exposed on the left rib than on the right rib, but the general pattern of secondary mineral distribution is about the same in both exposures. Unit A is altered to a smectite-rich assemblage with minor opal-CT and hematite (NR10+30SSL02,p1, NR10+32SSL01,p1 and p2, NR10+34SSL01,p2, Table 6.1-13). Rock on the right rib that was unaffected by the smectitic alteration was altered instead to heulandite-clinoptilolite with lesser amounts of smectite and opal-CT (NR10+34SSL01,p1, Table 6.1-13). Heulandite-clinoptilolite with subequal amounts of Ca and K as the exchangeable cations and smaller amounts of light-colored smectite are common fracture coatings in locations where the smectitic altered tuffs have been brecciated.

A bleached alteration front is visible within unit A on the left rib in the region of station 10+35 to 10+43. The width of the bleached zone is highly irregular and may be as much as 1 m or more. In some places the front moved preferentially through certain layers in the tuff, but elsewhere, the front transgressed layering. Whether the front exists beyond the boundaries of unit A is unclear; the alteration may have extended slightly into unit B, as described below. Determination of the mineralogic character of the bleached zone will require supplemental sampling.

The laminated deposits of unit B have generally not undergone the smectitic and hematitic alteration responsible for the reddish-brown colors of unit A. Reddish coloration is locally developed where the laminae have cracked and separated near the contact with unit A (Figure 6.1-45, near station 10+26) and in other areas where the rock is disturbed. Prominent silicification is the most distinctive alteration in this unit. Replacement of the tuff by opal-CT (NR10+30SSL01, p2, Table 6.1-13) produced a rock with a chalky to porcellaneous luster. Common colors of the altered rock include grayish orange pink (5 YR 7/2) to pale grayish orange pink (5 YR 8/2), pale yellowish brown (10 YR 8/2), and white (N 9). There is some preservation of original tuff components within the silicified rock. Portions of the rock that

escaped silicification were subsequently altered to a smectite-clinoptilolite assemblage (NR10+30SSL01, p1, Table 6.1-13).

There are a few nodules of distinctly different silica. One example is located on the left rib around station 10+33 within broken blocks of lower unit B. The silica is pale grayish blue (5 PB 6/2) microcrystalline quartz cut by fractures lined with drusy quartz crystals (NR10+33SSL01, p1 and p2, Table 6.1-13). Rare scattered fluorite crystals are intergrown with the drusy quartz, and there are a few fluorite-filled fractures in the body of the nodule. The nodule retains little preserved texture of the original tuff. A nodule from the right rib contains translucent brownish silica texturally similar to the nodules in the left rib. The surrounding unsilicified rock has been zeolitized, and some fracture surfaces are coated with zeolite near the outer margins of the nodule.

Alteration of units C and D awaits further sampling and investigation. Unit E has been zeolitized to an assemblage dominated by heulandite-clinoptilolite (NR10+32SSL02, p1 and p2, Table 6.1-13). A few fractures with apertures less than 1 mm are filled with microcrystalline quartz. At the margins of the quartz fillings are botryoidal spheres of opal-CT, some of which are hollow, perhaps from the dissolution of amorphous opal cores. Heulandite-clinoptilolite encrusts the spheres, including the hollows, suggesting that zeolitization may have occurred after the fracture fillings were deposited.

Interrelationship of Faulting, Fracturing, and Alteration–A basic question about faults and fractures in this exposure is whether they served as conduits for the rock-altering and mineral-depositing fluids. There is clear evidence that many small fractures provided local access for alteration and mineral deposition. For example, fractures up to 1 m long in the lower part of unit B contain concentrations of dark red, probably hematitic material. Narrow fractures ≤1 mm, of unknown extent, in unit E contain quartz and opal-CT. However, the existence of a larger-scale fracture-based transport and alteration system is not obvious. The left rib exposure contains four fractures or faults that extend through much of the affected stratigraphic section. A diagonal fracture labeled (a) in Figure 6.1-45 extends from unit A to the base of unit E. Evidence of offset or alteration along this fracture is ambiguous. The fracture is parallel to bedding in the lower part of unit A, but higher up it follows the boundary of a rotated block and a discontinuity in bedding. Unit B is highly disrupted in about a 2 m wide zone roughly centered on the fracture, but few discontinuities unequivocally coincide with the fracture trace. Units C, D, and E are cut by the fracture with no associated distortion or alteration and less than 1 cm of offset.

The variable styles of deformation present along the fracture trace cannot be accounted for by a single episode of fracturing or faulting. The observed deformation could be attributed to one or more early episodes of brecciation, faulting, and alteration affecting units A and B, followed by deposition of units C, D, and E and propagation of a fracture upward into the younger units during a minor late adjustment. Early faulting at this location could help explain the surface depression formed on unit B and filled by units C and D. One problematic observation is the apparent absence of offset at the A-B contact. It is possible that the offset was accommodated by lateral displacement of the brecciated rocks.

The fault labeled (b) has approximately 1 m of displacement indicated by the offset in unit E. This fault probably extends to the ground surface and offsets the Tiva Canyon Tuff because there

are mapped surface faults that are plausible projections (Lipman and McKay 1965; Buesch, Spengler et al. 1996). At the tunnel level there is no indication of multiple faulting episodes, implying that the fault in its present form did not exist at the time of alteration. Evidence of possible offset of alteration features is ambiguous. For example, the bleached alteration front is so poorly defined near the fault that identification of corresponding features is too subjective to be meaningful. However, if the two walls of the fault are conceptually positioned to reunite the Unit E section, the location of the quartz nodules in the lower part of unit B on the left wall could be a possible extension of the alteration front on the right wall. No conclusion should be made at this time, but the likelihood of association merits further study.

A fault on the right rib with about the same orientation and offset as fault (b) may be the same fault or a branch of the fault. Here, a portion of unit A with smectite-hematite alteration is juxtaposed against zeolitized unit A. Detailed examination of the fault region revealed no evidence of smectitic or hematitic alteration along the fault itself, but fault breccia within the smectite-rich altered tuff contains fractures lined with prismatic and platy heulandite-clinoptilolite. The chronological sense of the textural relations is that heavy argillic alteration predated faulting but at least some zeolitization postdated the offset.

Faults (c) and (d) both offset the bleached alteration front in unit A. In the absence of suitable reference markers, it is difficult to determine whether these faults have had incremental movement. The evidence of the offset alteration front suggests that these faults, like fault (b), may not have existed during the period of intense alteration that produced the bleached zones.

Summary and Discussion of Alteration at the Top of the Topopah Spring Tuff–The evidence of stratigraphic, structural, textural, and mineralogical data generally suggest that the intense smectite-zeolite alteration and silicification of vitric rocks, accompanied by brecciation, was a separate alteration event from the later zeolitization of rocks not previously affected by smectite-zeolite alteration. The smectite-zeolite alteration seems to have been more localized than the later zeolitization. There are indications that units A and B were subaerially exposed and may have undergone pedogenic modification, but the localization of the smectite-zeolite alteration argues against an exclusively or even predominantly pedogenic origin. Similarly, the existence of microcrystalline quartz nodules could not be explained as a pedogenic product except by very advanced soil development over hundreds of thousands of years, for which there is no evidence.

As previously noted, there is no strong association of the smectite-zeolite alteration and silicification with fractures or faults. Most of the faults now present at the study site may not have existed at the time of alteration. The single fracture (a) that seems to be associated with a breccia zone and contemporary with brecciation is not clearly associated with the bleached alteration front or any preferential distribution of smectitic alteration. Examination of hydrothermal alteration near the top of the Topopah Spring Tuff at Yucca Mountain and Busted Butte suggests that the alteration is localized at the upper extremities of fracture-breccia zones, but it is common not to see a clearly defined feeder system below the mineral deposits. The exposures at these locations contain no evidence of mineral-bearing fluid input from below except for variants on the normal vapor-phase mineral deposition.

The major secondary minerals identified so far at the Exploratory Studies Facility North Ramp study site—smectite, Ca, K-rich heulandite-clinoptilolite, cristobalite, opal-CT, and microcrystalline quartz—are known as products of moderate-temperature hydrothermal alteration associated with cooling pyroclastic deposits around Yucca Mountain, particularly in the Paintbrush Group (Levy and O'Neil 1989; Levy 1993a; Vaniman, Bish et al. 1984). The dominant secondary mineralogy of the Tpbt2 alteration in the north ramp location differs from the mineralogy of the hydrothermal alteration at the top of the Topopah Spring Tuff at Busted Butte and from vapor-phase mineral assemblages, as well. Smectite-zeolite assemblages are common in the Exploratory Studies Facility, whereas feldspar-cristobalite is the dominant assemblage at Busted Butte and vapor-phase assemblages in the upper Topopah Spring Tuff are commonly tridymite-cristobalite-feldspar (Bish and Chipera 1989; Chipera, Vaniman et al. 1997). The smectite-zeolite alteration probably formed at temperatures below 100°C (Levy and O'Neil 1989; Whelan, Moscati et al. 1996) and therefore would not be a product of fumarolic activity associated with vapor-phase alteration (≥450°C; Sheridan 1970), as proposed by Moyer et al. (1996) based on a model of alteration in the Bishop Tuff (Sheridan 1970). Peterman, Spengler, Singer et al. (1996) also suggested a fumarolic vapor-phase origin, speculating that the mineralogic evidence of vapor-phase crystallization might have been largely destroyed by subsequent low-temperature water-rock interaction. The only documented recrystallization products of vapor-phase tridymite at Yucca Mountain are quartz and cristobalite that retain the original tridymite morphology (Carlos, Chipera, Bish et al. 1995). Some of the Exploratory Studies Facility rocks have plausible mineralogy, but not texture, to be recrystallized vapor-phase deposits. Moreover, smectite and zeolite have not been observed as alteration products of vapor-phase minerals.

Minor high-temperature vapor-phase alteration may have occurred at this site, but most of the secondary minerals were more likely produced by a combination of vapor-phase alteration at temperatures below ~200°C, steam-environment alteration around 100°C, and alteration in the presence of liquid-water at temperatures only slightly above ambient. Experimental studies of glass alteration in condensed steam and water vapor environments below 200°C have identified smectite and zeolites as some of the most abundant alteration products (Wronkiewicz et al. 1993; Bates, Bourcier et al. 1994).

Additional study is needed to evaluate the roles of water vapor, steam, and liquid water in the alteration. It may be possible to identify textural evidence for perching of meteoric water within the tuffs as they underwent alteration. Several types of layered deposits laid down in standing water within cavities or fractures have been identified elsewhere in the Paintbrush Group (Levy and Valentine 1993; Levy, Sweetkind et al. 1997). In particular, examination of unit C would help determine whether there was standing water in the depression where this unit was deposited and what relation the alteration of this unit bears to other alteration at this site.

6.1.4.1.2.3 Alteration in the Lower Topopah Spring Devitrified-Vitric Transition Zone

The lower Topopah Spring devitrified-vitric transition zone lies below the pervasively devitrified densely welded tuff (the candidate host rock). The transition zone is an interval of partly devitrified vitrophyre (densely welded glassy tuff) in which devitrification is sporadic and localized around fractures. The most common alteration features are fractures with devitrified borders of alkali feldspar and cristobalite, up to 0.3 m thick (Figure 6.1-46). Some of the

devitrified borders are downward extensions from the overlying completely devitrified tuff. The outermost margins of devitrified fracture borders contain zeolites, smectite, and minor silica. Quartz, chalcedony (microscopically fibrous quartz), and opal are locally abundant as fracture and void fillings, along with small quantities of iron and manganese minerals.

The consistent association of the alteration with the transition zone ties the timing of hydrothermal activity to the cooling of the pyroclastic unit ~12.8 Ma (Sawyer et al. 1994), when water infiltrated into the still-warm tuff. Alteration was localized in the boundary between devitrified and glassy tuff because it was a region in which chemically reactive volcanic glass still existed at a relatively high temperature. This was the first glassy rock encountered by water heated during downward flow through the warm, devitrified interior of the tuff.

Products of hydrothermal alteration in the lower Topopah Spring devitrified-vitric transition zone have been identified in all drill cores that contain this syngenetic feature. The transition zone is an interval of variable vertical dimension, extending from about 3 to 30 m downward into the vitrophyre, with discontinuous distributions of secondary minerals both vertically and horizontally. Even where the secondary minerals are concentrated, there is substantial variation in the abundances and proportions of alkali feldspar, smectite, heulandite-clinoptilolite, and silica that comprise the characteristic secondary-mineral assemblage. Table 6.1-14 gives an indication of the variability. This altered zone does not possess the attribute of thickness in the sense that intervals of zeolitized nonwelded tuffs elsewhere in the pyroclastic section have reliably measurable thicknesses.

Oxygen Isotope Study of Alteration–If heulandite-clinoptilolite and smectite in the altered vitrophyre are genetically related to local devitrification, they may have formed at higher temperatures than zeolites and clays of diagenetic origin. The purpose of this oxygen isotope study is to estimate the temperatures at which vitrophyre alteration occurred and consider possible sources of water involved in the alteration (Levy and O'Neil 1989).

Quartz and chalcedony associated with heulandite-clinoptilolite and assumed environmental waters were used for oxygen isotope geothermometry because a calibration curve has not been determined for the clinoptilolite-water system and because many zeolites do not effectively retain their original oxygen. Textural relations of zeolite and quartz in altered vitrophyre samples indicate contemporaneous or alternating crystallization of the two minerals. In drill-core samples VH-2 3545-q and VH-2 3565a, the quartz is a fracture filling, along with zeolite. Both of these samples come from below the present-day static water level (Robison 1984). Outcrop sample YF-4-q is a filling in a geode, with zeolites in the rind of the geode. The $\delta^{18}O$ values of quartz separates (in per mil relative to standard mean ocean water) are given in Table 6.1-15. The number of samples analyzed is small but includes all existing samples that contain separable quartz in amounts sufficient for isotopic analysis. The quartz-smectite geothermometer was not used because smectite from this altered zone is too intimately intergrown with zeolite to provide a usable separate.

The isotopic composition of water most suitable to use in the temperature calculations depends on the genetic interpretation. If vitrophyre alteration is occurring at present, then the best choice of isotopic composition would be that of modern local groundwater. Alteration that occurred

soon after pyroclastic deposition could involve meteoric water of Tertiary age (that is, the age of the pyroclastic unit), modified meteoric water, or nonmeteoric water.

To investigate the possibility that hydrous minerals in the core samples of altered vitrophyre are the products of present-day alteration, formation temperatures for the quartz were calculated using a $\delta^{18}O$ value of -13.5‰ based on measurements of groundwater samples from various drillholes in the area (Benson et al. 1983). Temperatures were calculated using temperature-fractionation relations of both Clayton, O'Neil, and Mayeda (1972) and Bottinga and Javoy (1973). Calculated temperatures for the drill-core samples, shown in Table 6.1-15, are much higher than the present measured temperature (48°C) at the 1,086.6 m (3,565 feet) depth in drillhole VH-2 (J.H. Sass, U.S. Geological Survey, personal communication to S.S. Levy, Los Alamos National Laboratory, December 1984). The large difference between calculated and measured temperatures rules out the possibility that alteration products in these samples could be forming at depth under present thermal conditions.

For outcrop sample YF-4-q, a present-day origin of the quartz and associated hydrous minerals would require a surface or near-surface environment of alteration. To test this interpretation, the $\delta^{18}O$ measured for the quartz sample was used to solve the temperature-fractionation relation alternatively for water $\delta^{18}O$ and temperature. The $\delta^{18}O$ value of water calculated by assuming mineral deposition at ~25°C is between -25 and -17‰ depending on which calibration is used. Such $\delta^{18}O$ values are much lower than observed precipitation or groundwater values in the area of interest (Benson et al. 1983; Claassen 1983), and this effectively rules out formation at this low a temperature. Solution of the temperature-fractionation relation for temperature, assuming a water $\delta^{18}O$ of -13.5‰ gives a value of between 40 and 70°C. A surface origin would require some mechanism, such as solar heating of ponded surface water or spring discharge of heated water from depth, to produce the warm water. Neither mechanism explains the general restriction of alteration and quartz deposition to the devitrified-vitric transition zone despite the proximity of other glassy tuff outcrops that should be equally susceptible to alteration.

Alteration textures of the devitrified-vitric transition zone are the same in both outcrop and core, suggesting a common mode of origin for the alteration products from both sample sources. The geothermometry results do not unequivocally support this interpretation in that they indicate somewhat lower temperatures of origin for the outcrop sample than for the core samples. The temperatures for the outcrop sample, although higher than surface temperatures, are comparable to present-day temperatures in the transition zone of drillhole VH-2. Therefore, it is conceivable that vitrophyre at the YF-4 site, before being exposed in outcrop, could have been altered as a result of burial or possible proximity to a heat source. This interpretation offers no explanation for the localization of alteration in the devitrified-vitric transition zone. Present-day surface or near-surface alteration remains an unlikely interpretation for sample YF-4-q, as explained in the preceding paragraph. It would be even more difficult to find a common present-day mode of moderate-temperature origin for altered material now located anywhere from the surface to a depth of ~1,087 m below the surface. Attributing the alteration to perched water (for example, Broxton, Bish, Vaniman 1982) incurs all of the above-mentioned problems.

If alteration took place shortly after pyroclastic deposition, there would be no problem with major differences in depth of burial because the land surface would have been the top of the pyroclastic unit. The $\delta^{18}O$ composition of Tertiary age water in this part of Nevada may have

been essentially the same as that of modern water, based on δD studies by O'Neil and Silberman (1974), or may have had slightly higher values (Lawrence 1970). A Tertiary water isotopic composition with higher $\delta^{18}O$ (calculated from Lawrence 1970) used for temperature calculations would yield quartz formation temperatures ~5°C higher than those calculated with a modern water isotopic composition.

Meteoric waters that had exchanged oxygen isotopes with silicic tuff, magmatic water, or metamorphic water are probably all isotopically heavier than unmodified meteoric water (for example, Craig, H. 1961; Kononov and Polyak 1982). Thus, the temperatures calculated using isotopic compositions of meteoric waters might represent lower limits to the true temperatures during alteration. Drill-core mineralogy in active hydrothermal systems at Yellowstone National Park, Wyoming, provides some evidence that heulandite-clinoptilolite, although not a sensitive temperature indicator, forms below ~180°C (Bargar and Beeson 1981).

Volume Changes Associated With Alteration in the Transition Zone (Tptpln to Tptpv3)– Alkali feldspar is concentrated in the upper part of the transition zone, closest to the completely devitrified rocks. Alteration assemblages from lower in the transition zone, with little or no feldspar, are simpler to model and may be more representative of alteration products to be expected in a waste repository-induced hydrothermal regime (Knauss and Peifer 1986). This investigation is a potential source of natural analog information for predicting repository performance.

Dissolution of vitrophyre glass and precipitation of secondary minerals is represented qualitatively by the reaction,

$$\text{glass} \rightarrow \text{smectite} + \text{heulandite} + \text{cristobalite} \qquad \text{(Eq. 6.1-1)}$$

Smectite and zeolite, alone or in combination, were typically the first-formed alteration products of glass dissolution and were commonly deposited at or near the dissolution sites. Silica was more likely to be transported and deposited elsewhere as fracture or pore fillings of cristobalite, chalcedony, quartz, or opal. Aluminum was the limiting constituent that determined the maximum amount of smectite or zeolite that was produced, so long as no additional Al was introduced in solution or colloidal suspension. Figure 6.1-47 is a graphic representation of reaction (Equation 6.1-1), balanced for all possible combinations of smectite and heulandite-clinoptilolite. Input values for the figure are from Table 6.1-16. The graph balances the reaction with respect to Al and Si, but not Na, Ca, K, or other elements. Also, the very small primary porosity was not factored into the calculations.

The most important result illustrated in Figure 6.1-47 is that any combination of secondary minerals produces an increase of 13 to 24 percent over the volume of the reacted glass. The higher value is for a smectite-rich assemblage in which the smectite accounts for less than the original glass volume and cristobalite is almost half of the original volume. In a zeolite-dominated assemblage, the volume of zeolite produced is approximately equal to the volume of glass consumed, with cristobalite comprising the additional 13 percent.

For vitrophyre with bulk porosity around 1.4 percent (Anderson 1984), alteration products in principle could seal all the porosity in a volume of rock at least ten times larger than the volume

of altered vitrophyre. This effect has not been observed in the naturally altered rock. Bulk porosity in the vitrophyre probably corresponds to the pervasive perlitic fracture system (Blacic et al. 1982), but larger-aperture throughgoing fractures also exist. The wider fractures, along with devitrification cavities, provided pathways for fluid flow and space for secondary-mineral deposition during the period of alteration. The alteration must have caused an overall reduction in porosity, but this does not appear to have resulted in pervasive sealing or plugging of flow paths below the repository horizon because open fractures still exist.

6.1.4.2 Diagenetic Alteration

The most extensive post-cooling mineralogic change affecting the rocks at Yucca Mountain has been the zeolitization of nonwelded glassy tuffs. In the affected rocks, the glassy component was altered to the zeolite clinoptilolite with or without lesser amounts of mordenite, smectite, silica, Fe-Mn oxides and hydroxides, and other minor phases. Rocks in the deeper parts of Yucca Mountain have been subjected to differing and additional alteration (Bish 1989, and Subsection 6.1.4.3).

Most zeolitized tuffs are products of diagenetic alteration in which the original glass dissolved and the zeolites precipitated at ambient temperatures in a water-rich environment. The distribution of diagenetically altered zeolitic rocks is important evidence for paleohydrologic interpretations and for relating the timing of zeolitization to pyroclastic depositional events and tectonism.

6.1.4.2.1 Occurrences of Zeolitic Rocks

The downward transition from vitric to zeolitized tuffs is a gross feature common to all Yucca Mountain drillholes and outcrops. The exact position of the vitric-zeolitic transition at any given location cannot be precisely fixed, but the persistence of this feature across the mountain makes it an attractive candidate for investigation as a paleohydrologic indicator. Of particular importance for nuclear waste repository performance, the transition also marks changes in the hydraulic and sorptive properties of nonwelded tuffs.

Researchers studying zeolitization in the Yucca Mountain region have made a variety of inferences about the hydrologic regimes in which zeolitization occurred. Most studies predating the YMP attribute zeolitization to unsaturated-zone hydrologic processes; either from localized active recharge creating a zone of near-saturation and rock alteration above the static water level (Claassen and White 1979) or from permeability barriers responsible for the formation of local or regional perched-water tables and associated alteration (Gibbons et al. 1960; Hoover 1968). Yucca Mountain researchers recognize a few probable examples of perched-water alteration but tend to favor alteration at or below a static water level (Broxton, Warren, Hagan et al. 1986; Hoover 1968; Levy 1985). The Yucca Mountain glass- and zeolite-distribution data provide no support for the existence or former existence of a regional perched-water table. Known examples of probable perched-water zeolitization are of much smaller vertical and lateral extent than the main mass of zeolitized tuffs. The working hypothesis is that most zeolitization occurred around or below the static water level in place at the time of alteration. As described below, numerous factors make the vitric-zeolitic transition a much less precisely definable position than the position of the static water level at any given time. Therefore, the concept of

vitric tuffs being subject to zeolitization around or below the static water level must cover at least a small range of localized hydrologic conditions.

Even without a consensus on the relationship between the transition zone and the static water level position at the time of alteration, researchers generally agree that zeolitization required the presence of abundant water over a long period of time (Claassen and White 1979; Broxton, Warren, Hagan et al. 1986; Levy 1984c; Gibbons et al. 1960; Hoover 1968). The underlying assumption is that glass in nonwelded tuffs is preserved only where the rocks have not been subjected to prolonged saturation. This assumption is based on the generally accepted model of zeolitization in open systems, where water percolation is implicated in alteration of glass to zeolites. Because water movement is limited in porous nonwelded tuffs at less than complete saturation, zeolitization is also curtailed in this model. Although the model fits with observation at Yucca Mountain, it will be tested with the development of fully coupled chemical, thermal, and hydrologic modeling (FEHM) applied to the 3-D mineralogic model of Yucca Mountain. This concept forms one basis for estimating the highest elevation ever occupied by the static water level.

The present static water level lies within zeolitic or devitrified tuffs more than 100 m below the boundary that separates most vitric tuffs from most zeolitic tuffs. There are uncertainties associated with any attempt to correlate the boundary between vitric and zeolitized tuffs with a past static water level position. An inherent problem in equating the configuration of vitric-zeolitic boundaries with a past static water level is that the position of the mineralogic boundary cannot be defined or measured in so straightforward a manner as the position of a static water level. The free-water surface in a borehole can be directly observed and readily measured to the nearest 0.1 m. In contrast, the vitric-zeolitic boundary is actually a transition zone with vertical extent up to 10 m or more from the first appearance of zeolite to the last disappearance of glass. The boundary can be functionally defined at a certain weight percent content of zeolite, which is reasonable for estimating amounts of zeolite available to interact with radionuclides but has no demonstrated genetic significance.

Another problem of definition stems from the fact that the generalized upper boundary of zeolitic rocks at Yucca Mountain transgresses the more highly inclined stratigraphic boundaries of the pyroclastic units. Because the pyroclastic section originally consisted of alternating intervals of mostly devitrified welded tuffs and vitric nonwelded tuffs, the position of the zeolitic boundary in some places is artificially fixed at an original boundary between devitrified and vitric tuff. The zeolitic boundary in such a place may be either lower or higher than the hydrologic boundary existing at the time of alteration. Drillholes in which the position of the zeolitic boundary was probably constrained by parent lithology include J-13, UE-25 a#1, USW G-2, USW G-3/GU-3, USW H-5, and USW H-6. This factor precludes the indiscriminate construction of a vitric-zeolitic "surface" from drillhole mineralogic data as a tool for modeling the evolution of the vitric-zeolitic transition. In addition, it has been estimated that zeolitization requires periods of the order of 10^4 yr. (Dibble and Tiller 1981), and it is not known how much the static water level might fluctuate during this time and what effects the fluctuation might have on the development of the transition zone.

6.1.4.2.2 Chemical-Textural Studies of the Vitric-Zeolitic Transition

The basic data for most chemical comparisons of vitric and zeolitic tuffs are various combinations of whole-rock chemical analyses, glass and secondary-mineral chemical analyses, whole-rock porosities, and glass and mineral densities. Direct comparison of bulk chemistry for matched pairs of altered rocks and their presumed vitric precursors is the simplest approach to identify chemical changes and transport. This approach was used by Walton (1975). A variation by Yamamoto et al. (1986) compares the bulk chemistry of the zeolitized tuff to analyses of residual glass in partially altered rocks, with both analyses recalculated to a water-free basis. Direct comparisons of bulk analyses as weight percents of constituents are not true indicators of mass changes because they don't account for differences in glass and mineral densities, rock porosities, or water contents. Despite these shortcomings, in some cases, the chemical changes for certain elements are so large that they can be identified in a qualitative manner.

Studies that take density, porosity, and hydration changes into account (for example, Hoover 1968; Moncure et al. 1981) should provide more accurate information about chemical changes during zeolitization. The necessary input data are not always available mainly because unaltered parent materials no longer exist. Researchers attempt to overcome this problem by normalizing chemical analyses to the content of a selected element in the unaltered tuff. The normalizing element must be immobile during alteration. Hay (1963) selected alumina as the basis for normalization, and other investigators have followed his lead (Hoover 1968; Broxton, Bish, Warren 1987). Titanium and silicon (or their oxides) have also been used in this capacity (Yamamoto et al. 1986; de Pablo-Galán 1986).

Hay (1963) chose alumina as a normalizing constituent for its observed equality of content in silicic glass (obsidian) and the heulandite-clinoptilolite that replaced it when compared on a molecular basis for equal volumes. Petrographic textures also seemed to support the constant-alumina convention. In addition, alumina is commonly assumed to be relatively insoluble and therefore immobile (for example, Broxton, Bish, Warren 1987). Both Hay (1963) and Hoover (1968) acknowledge that the assumption of alumina immobility is not absolutely valid but consider it to be generally valid with some local exceptions. Errors caused by the neglect of bulk porosity changes and density differences between reactants and products may partially cancel each other because the decreased porosity of the altered rock is offset by the decreased density of the mineral products.

6.1.4.2.2.1 Chemical-Textural Approach

Many textural features of the Yucca Mountain Tuffs, such as the existence of heulandite-clinoptilolite as pore and fracture fillings, clearly indicate that alumina was mobile during alteration. Because the purpose of the present studies is to identify evidence of geochemical transport during zeolitization, a technique that assumes immobility of a major constituent is inappropriate without strong supporting evidence. However, there is no evidence that equal alumina content between glass and heulandite-clinoptilolite signifies immobility. Therefore, the concept of constant-alumina alteration should not be considered equivalent to an absence of alumina transport. A technique to detect evidence of transport ideally should be sensitive to both addition and removal of a constituent, that is, the total transport. Under the best of circumstances, a constant-alumina comparison cannot detect alumina transport at all and detects

only the net transport of other constituents. Similar objections apply to the use of any other normalizing element or oxide.

Hay (1963) recognized that microscopic textural information can help establish the sequences in which vitric tuff constituents are altered and secondary minerals deposited. The studies reported here use textural observations to reconstruct the major stages of alteration in terms of affected textural constituents. Combined with compositional data for reactants and products, textural studies can place bounds on the amount of element transport during alteration. Estimates of transport can be quantified in some cases and an example is presented here.

Alteration in densely welded vitric tuff (vitrophyre) was treated in Subsection 6.1.4.1.2.3; vitric bedded tuff and vitric nonwelded ashflow tuffs are considered here. Each rock type represents a common Yucca Mountain lithology, but the samples were selected according to suitability criteria for chemical-textural study. Simplicity of texture and mineralogy is desirable because it increases confidence in the identification of the original unaltered rock components and makes calculated chemical changes as unambiguous as possible. Very fine-grained pore fillings, indicating the former existence of colloidal material, are examples of special textural features that can enhance interpretations of transport. The case studies are presented in order of increasing textural complexity.

The interpretation of secondary-mineral fillings in void spaces assumes a general sequence of alteration of the glassy textural components of the ashflow tuff, based on examination of partially zeolitized tuffs. For the purposes of this study, the glassy components of an ashflow tuff can be assigned to one of three textural categories: shards, pumice lapilli, and fine-grained ash matrix. The upper size limit of 0.06 mm defined for "fine ash grains" by Schmid (1981) is acceptable because pyroclasts below this size generally lack vesicles, a significant distinction for the textural studies reported here.

During zeolitization, the fine-grained ash is the first material to be altered although pumices are also altered early. The altered ash matrix provides the structural framework to support and preserve the cavities formed by later dissolution of glass shards. Many glass shards contain vesicles—relic gas cavities—that may be empty of mineral matter or partly to completely filled with ash or secondary minerals. The vesicles represent a component of the primary porosity in the original unaltered tuff. Vesicle forms are preserved only if they are filled or acquire at least a lining of secondary minerals before the host shard dissolves. The vesicle wall must be breached for filling material to enter the cavity. Some vesicles were breached by shard breakage during pyroclastic deposition and compaction, whereas others may have been opened later when shards began to dissolve or when the rock deformed in response to local or regional stress.

One distinctive variety of void-filling clinoptilolite present in the nonwelded tuffs described here is termed massive-texture clinoptilolite. Fillings of this texture occur only in primary void space of vitric or zeolitic tuffs and are distinguished from zeolitized fine-grained ash by an absence of admixed fine-grained primary crystalline material. The fillings are dense masses of clinoptilolite crystals so fine-grained or irregularly shaped as to appear amorphous even at 2500 X magnification. There are web-like networks within the fillings (Figure 6.1-48) that have served as loci for nucleation and growth of clinoptilolite crystals. This growth habit may be a characteristic of some crystallized colloidal aggregates.

Alteration in a Bedded Tuff–Sample G-3 2615 is a bedded tuff from the base of the Bullfrog Tuff of the Crater Flat Group. The tuff originally consisted of hematite-stained sand-size pumice clasts, glass shards, and abundant crystalline clasts. A very small amount of fine-grained ash filled some vesicles in the glassy clasts and formed partial coatings on a few grains. The textural simplicity resulting from the near-absence of fine ash increases the confidence with which the existing textural varieties of zeolite and pore space and the inferred original textural components can be categorized and quantified. This information is required for a quantitative chemical-textural calculation of element transport.

All of the original intergranular pore spaces and some pumice vesicles have been filled with massive-texture clinoptilolite (Figure 6.1-49). The pore-filling zeolite cement was deposited before the glassy clasts began to dissolve and be partly replaced by zeolite because the cement has preserved the relic shapes of the clasts. The cement also provided substrates for zeolite precipitation within the developing cavities. The zeolite replacements of dissolved shards are texturally similar to the zeolite linings and aggregates of prismatic crystals in dissolved shard cavities of ashflow tuffs. Many of the zeolite-lined cavities contain a small amount of unfilled void space. Very small amounts of smectite and secondary silica are also present.

The volumetric proportions of crystalline clasts (phenocrysts and lithic grains), pore-filling zeolite cement (representing original accessible porosity), zeolite replacement of glassy clasts, and secondary porosity within dissolved clast cavities were determined by modal analysis (Table 6.1-17). This information has been used, together with compositional data and density values for zeolite and glass, to calculate the element transport involved in the alteration of this sample. A glass analysis from the Prow Pass Tuff of the Crater Flat Group (Table 6.1-16, analysis 3) was used because no unaltered Bullfrog Tuff glass has survived. The chemical analysis of massive clinoptilolite (Table 6.1-16, analysis 8) was used to represent all the clinoptilolite in the mass calculations because the prismatic clinoptilolite contains Fe-rich impurities (Table 6.1-16, analysis 9). Scanning-electron photomicrographs of the polycrystalline massive clinoptilolite (Figure 6.1-48) suggest a porosity less than 3 percent, which was assumed to be zero for mass calculations. Silica and smectite, present in amounts less than 2 percent (Bish and Chipera 1989), were omitted from the calculations.

The original porosity calculated from modal analysis, ~17 percent, is lower than the 33 to 48 percent range of the laboratory measurements for vitric nonwelded tuffs from higher in the stratigraphic section at Yucca Mountain (Loeven 1993). The low value for this bedded tuff is probably accounted for by strong compaction of the abundant pumice clasts before cementation occurred. For comparison, modal analysis of opal-cemented pumiceous bedded Paintbrush Tuff yielded a calculated original porosity of 48.5 percent (Levy, S.S. 1993b, LANL Notebook, TWS-ESS-1-10-82-19, p. 262). This result indicates that modal analysis can give porosity values comparable to laboratory-measured values.

Calculation of the original glass content in the tuff is based on the sum of the zeolite that replaced glassy clasts and of secondary porosity within dissolved clasts. These are the most ambiguous elements of the modal determination and petrologic interpretation. It is clear that space once occupied by glass is now occupied by a combination of zeolite and void, but it has not been determined whether the zeolite was deposited from locally derived chemical components or from introduced components after some or all of the local dissolved glass

components had been removed. Because of these uncertainties, the calculated element changes associated with alteration of glassy clasts may be considered correct values for net transport but less than or equal to the true total amount of transport.

There is also a potential to overestimate the original glass content because some primary void spaces contained in glass clasts—completely enclosed vesicles within shards and very thin closed bubbles in pumice clasts—might no longer be recognizable in the relic glass clasts of the zeolitized tuff. An overestimate of original glass content would result in too high a calculated value for dissolved glass components removed from the rock. Examination of relic shard textures, however, suggests that most of the shards were small enough and thin enough as not to contain unbreached vesicles. Also, most pumice pores were filled with massive zeolite and would therefore be correctly counted as original porosity.

For Al, the mass transport was calculated as follows from analyses 3 and 8 in Table 6.1-16 and the proportions of inferred original textural constituents in Table 6.1-17:

Al in original glass = (0.00563 mole/cm^3)(0.587 vol. prop.) = 0.003305 mole/cm^3

(Eq. 6.1-2)

Al in portion of original glass replaced by clinoptilolite =(0.00563 mole/cm^3) (0.549 vol. prop.) = 0.003091 mole/cm^3

(Eq. 6.1-3)

Al in massive pore filling = (0.00499 mole/cm^3)(0.172 vol. prop.) = 0.000858 mole/cm^3

(Eq. 6.1-4)

Al in cpt replacement of glass = (0.00499 mole/cm^3)(0.549 vol. prop.) = 0.002740 mole/cm^3

(Eq. 6.1-5)

Al change in alteration of glass = – 0.003305 + (0.00499)(0.549) = – 0.000565 mole/cm^3

(Eq. 6.1-6)

The values obtained from equations (6.1-3), (6.1-4), (6.1-5), and (6.1-6) were divided by the value for equation (6.1-2) and multiplied by 100 to express the amount of Al gained or lost in each process as a percent of the Al originally present in the vitric component of the tuff. Similar calculations were performed for Si, K, Na, and Ca.

The mass calculations show that the Al added to the rock in the introduced zeolite cement represents a 26 percent increase over the Al originally present in the vitric component of the tuff (Table 6.1-18). Dissolution and zeolitization of the glassy clasts decreased the Al content by 17 percent. For the purpose of the mass transport calculations, this step was represented by two processes—the dissolution and replacement of glass by zeolite with a slightly lower Al content and the dissolution of glass and presumed removal of dissolved components, leaving void space. The combination of all the alteration steps resulted in a net Al increase of 9 percent, but the true mobility of Al, represented by both additions and removals, amounts to at least 43 percent of the

glass-held Al originally in the tuff. A small net decrease and a much larger total transport were calculated for Si. The net changes for all the major elements are similar to chemical changes for zeolitized Yucca Mountain Tuffs assumed or calculated by Broxton, Bish, Warren (1987). However, the changes based on comparisons of Al-normalized analyses give no indication of the much greater amount of transport identified by chemical-textural study.

Zeolitization in an Ashflow Tuff–Sample G-4 1392 is a nonwelded ashflow tuff from about 4.5 m above the base of the Topopah Spring Tuff and located within the vitric-zeolitic transition zone (Spengler and Chornack 1984). The original Tuff contained about 40 percent pumice, 30 percent shards, 30 percent fine ash, and less than 5 percent phenocrysts and lithic grains, which were omitted from the mass calculations. The top of the transition zone is no more than about 6 m above the sample level (Bish and Chipera 1989). From at least 3.4 m above to about 17 m below the sample level, the only surviving vitric materials are vitrophyric clasts larger than 0.5 cm

The ash matrix recrystallized to very fine-grained clinoptilolite. Dissolved shard cavities commonly contain geopetal fillings of prismatic clinoptilolite aggregates overlain by opal spherules. About 50 percent of the shard vesicles that contained no ash were filled with massive-texture clinoptilolite. The rest of the vesicles contain very fine-grained layered geopetal fillings of clinoptilolite or opal, aggregates of prismatic clinoptilolite, or thin rinds of prismatic clinoptilolite. The same fillings are present in relic pumice clasts.

Chemical-textural analysis of mass transport is much more difficult for an ashflow tuff that contains large amounts of fine ash because the original proportions of vitric constituents are not easily ascertained. Original porosity cannot be determined by modal analysis, and laboratory measurements of vitric tuffs indicate too much variability to justify selection of a "representative" value. A hypothetical mass balance was calculated for zeolitization of this tuff using the best estimates of the proportions and assumed internal porosities of vitric textural components (Table 6.1-19). An expression for the reaction, using compositions from Table 6.1-16, analyses 2 and 7, and balanced on a volumetric basis for Al and Si,

$$1\ cm^3\ glass \rightarrow 1.15\ cm^3\ clinoptilolite + 0.07\ cm^3\ cristobalite \qquad \text{(Eq. 6.1.7)}$$

results in a reduction to 16 percent porosity with no loss of either Al or Si, or to 21 percent porosity if all the Si in excess of zeolite content is removed. Both of these values are low compared to the 24 to 40 percent published range of porosity values for zeolitized Topopah Spring nonwelded to partly welded tuffs (Loeven 1993) and suggest that models of alteration would be improved by considering Al as a mobile element.

Progression of Zeolitization Through the Tuff–The layered geopetal fillings of clinoptilolite and opal in primary and secondary pores of the altered tuff G-4 1392 (Figure 6.1-50c and d) served as miniature tiltmeters recording progressive tectonic tilting of the rock units during the period of alteration. With knowledge of geopetal orientations relative to vertical, sets of fillings may be assigned to an ordered sequence from earliest to latest (Levy 1984b). The layers in the earliest fillings have the greatest angular divergence from a plane perpendicular to the vertical. Geopetal orientation measurements, in three relative age groups, are plotted on an image of the thin section in Figure 6.1-51. The early- and intermediate-age fillings are distributed more or

less randomly except for an irregular semihorizontal band ~1 cm wide near the center of the thin section. The latest-age fillings are concentrated in this band, where glass shards survived for the longest time. Within the 2-D limits of a thin section, the band is parallel to depositional layering. There is no obvious textural difference between the band and adjacent tuff, although subtle differences corresponding to slight variations in hydraulic conductivity may have existed in the original rock. Alternatively, the areas where alteration began may have reflected random variations in geochemical and hydrologic conditions and the band of late-age alteration marks the location where two such areas coalesced.

6.1.4.2.2.2 Discussion of Element Transport During Alteration

Identification of microscale evidence for substantial element transport during alteration has implications for field-scale transport. A feature common to both of the nonwelded tuffs studied here is the massive-textured clinoptilolite that fills only primary porosity. Clinoptilolite of this texture and depositional restriction is very common in the altered nonwelded rocks of the Paintbrush, Calico Hills, and Crater Flat Tuffs, suggesting that it must have been a characteristic product of glass alteration, which was generated and transported in relatively large quantities. Textural evidence that the massive clinoptilolite fillings existed in colloidal form at the time of crystallization has been presented in this paper. That the massive filling material is externally derived and fills only primary porosity implies that the material could only penetrate nonzeolitized ash or noncemented bedded tuffs. If the same restrictions applied to the source rocks, the material could have migrated only during the early stages of alteration affecting the fine-grained ash matrix. It is possible that the massive clinoptilolite source material began its migration in true solution and gradually aged into a colloidal suspension. Material for the deposits in the Topopah Spring Tuff ashflow (G-4 1392) probably could have traveled downward no more than about 6 m, the distance from the top of the vitric-zeolitic transition zone.

The results of this study suggest that vitric and zeolitic nonwelded tuffs both retard colloids but in different ways. Vitric tuffs provide accessible pore spaces for colloidal suspensions to occupy, where they may settle and crystallize. Zeolitic tuffs may tend to exclude colloids from internal pores. The vitric-zeolitic transition zone at Yucca Mountain may therefore act as a barrier to downward colloid transport in the unsaturated zone.

6.1.4.2.2.3 Conclusions About Element Transport During Zeolitization

Chemical-textural studies of element transport during zeolitization of rocks representing three common Yucca Mountain pyroclastic lithologies reveal mass transport far greater than indicated from conventional comparisons of unaltered-altered rock pairs. For one bedded tuff, the calculated amounts of Al and Si transported into and out of the rock was equal to approximately half the quantities of these elements present in the original glass pyroclasts. Zeolitic and smectitic alteration of vitrophyre must also have involved removal of elements from the immediate vicinity of alteration, otherwise the very low porosity would have been completely sealed. Chemical-textural studies, although proved to be useful, cannot be applied equally well to all altered pyroclastic rocks because some rocks have textures or mineralogy too complex to permit unambiguous reconstruction of original rock properties.

6.1.4.2.3 Geochronology of Diagenesis

The ages of most pyroclastic units in the Yucca Mountain area have been determined by $^{40}Ar/^{39}Ar$ geochronology (Sawyer et al. 1994). The chronology of secondary alteration processes, the most significant perhaps being zeolitization, is important for assessing the suitability of Yucca Mountain as a potential nuclear waste repository. The disposal regulations include requirements to evaluate the rates of geochemical processes operating within the geologic setting during the Quaternary Period to determine the presence or absence of favorable conditions related to geochemical process rates and geochemical conditions [10 CFR 60.122(b)]. By implication, the timing of geochemical processes such as zeolitization must be established. The determination of absolute age of zeolitization by directly dating zeolites would have advantages over relative or indirect dating because it would not be tied to any genetic interpretation. In the absence of absolute-dating techniques generally suitable for zeolites, an effort was made to constrain the timing of glass-to-clinoptilolite alteration at Yucca Mountain by petrofabric studies (Subsection 6.1.4.2.3.1). Based on the published record of limited success in radiometric dating of zeolites, a decision was made subsequently to pursue exploratory K/Ar studies of clinoptilolite and mordenite (Subsection 6.1.4.2.3.2). K/Ar studies of relatively K-rich illite/smectites (I/S) from the deeper portions of Yucca Mountain drillholes (Bish and Aronson 1993) were used to date deep-seated hydrothermal alteration, which may be inferred to place a lower age limit of ~10.7 Ma on the original glass-to-clinoptilolite alteration only in the deeper pyroclastic units.

6.1.4.2.3.1 Petrofabric Studies—Dating Zeolitization With Tectonic and Structural Data

Relative age determinations for zeolitization based on structural data and radiometric dates for igneous units, as described below, can be used to evaluate the acceptability of experimental zeolite-dating results and can be used to estimate the age of original alteration for the case in which the radioisotope systematics may have been reset by later alteration. Successful relative dating requires an understanding of volcanic, tectonic, hydrologic, and geochemical conditions. Thus, it is especially valuable in constructing a comprehensive alteration history because it puts alteration events into the context of interacting processes.

Basis for Relative Dating of Diagenetic Zeolitization–Using tectonic and structural information to date zeolitization requires the identification of well documented and dated tectonic events. In most cases, the ages of tectonic events have been established indirectly by connection to dated pyroclastic units. Zeolitized tuffs must, in turn, contain features that have in some way recorded or been modified by tectonism.

The upper age limits of zeolitization are defined by the ages of the affected pyroclastic units. At least two attempts have been made to set a lower age limit on zeolitization at Yucca Mountain by relating the positions or orientations of certain alteration features to the history of regional tilting. Scott, Spengler et al. (1983) have determined that the major fault blocks of Yucca Mountain are bounded by north-northeast-striking, commonly west-dipping, Basin and Range-style normal faults with displacement up to 100 m or more. Present-day attitudes of the tilted Yucca Mountain fault blocks are probably related to displacement along the bounding normal faults. Field evidence indicates that displacement along these faults and the associated block tilting predated deposition of the 11.6 Ma untilted Rainier Mesa Tuff, which lies unconformably on the

eroded upper surface of the tilted Paintbrush Group both east and west of Yucca Mountain (Scott, Spengler et al. 1983; Sawyer et al. 1994). These field relations imply that regional tilting largely ended at least 11.6 Ma ago, although the Rainier Mesa Tuff and underlying units have been affected by normal faulting (Scott, R.B. and Bonk 1984). In addition, surface studies of faults in the Yucca Mountain area show little or no evidence of major Quaternary displacement (Szabo et al. 1981; Swadley and Hoover 1983; Paces, Mahan et al. 1995). Synvolcanic extension in the area of southern Yucca Mountain was concentrated in the period from about 13 to 11.45 Ma, according to Sawyer et al. (1994). Thus, any rock textural evidence that suggests either contemporaneity of tectonic tilting and zeolitization or completion of zeolitization before cessation of tilting would place a minimum age of ~11.6 to 11.5 Ma on the zeolitization.

One approach to relating the ages of zeolitization and tilting is based on the relative positions and orientations of the Paintbrush and older stratigraphic boundaries, the vitric-zeolitic transition zone, and the static water level (for example, Vaniman, Bish, Broxton et al. 1984; Broxton, Warren, Hagan et al. 1986; Broxton, Bish, Warren 1987). This approach requires several assumptions concerning the vitric-zeolitic transition zone that separates vitric tuffs from underlying zeolitic tuffs. This transition zone is assumed by some of these researchers to be an approximately planar surface whose configuration and position were originally related to the configuration and position of the static water level at the time of alteration. The static water level is assumed to have always been approximately planar and horizontal, though not necessarily at the same elevation or stratigraphic level, and this configuration is assumed to have determined the geometry of the transition zone.

The validity of these assumptions is difficult to assess. Drillhole data show that the vitric-zeolitic transition zone is not planar and does not have a uniform orientation (Bish, Caporuscio et al. 1981; Levy 1984c, 1991; Bish and Chipera 1989). A planar trend surface could be fitted to the transition-zone elevation data, but it is unclear that such a generalized trend would be a meaningful representation.

The assumption of a horizontal static water level presents a similar problem. Data from drillholes UE-25 a#1, H-3, H-4, and G-4 show that the present static water level in the vicinity of these holes is essentially horizontal, but H-5, G-1, and G-2 data show a strongly inclined static water level (Robison 1984). This evidence that the present static water level is not uniformly horizontal beneath Yucca Mountain casts doubts on the assumption that past water tables were horizontal.

Broxton, Warren, Hagan et al. (1986) and Broxton, Bish and Warren (1987) assert that the vitric-zeolitic transition zone is inclined in about the same direction as the pyroclastic units but at a smaller angle of inclination. If one assumes that the transition zone was originally horizontal (that is, parallel to the static water level), then it must have acquired its inclination when the rocks were tilted by tectonic processes more than 11.45 Ma ago. The inclination of the transition zone would imply that zeolitization must have occurred before the cessation of tilting.

The reasoning described above implicitly relies upon several additional assumptions. Foremost, there is an assumption that the zeolitization of tuff right at the vitric-zeolitic transition zone occurred at about the same time everywhere along the transition and was the last zeolitization to take place. This assumption is needed because, strictly speaking, the relative-inclination

rationale constrains the timing of zeolitization only in the vicinity of the transition zone. The 3-D distribution of vitric and zeolitized tuff, including the position and configuration of the vitric-zeolitic transition zone, is a function of pyroclastic deposition and devitrification, changes in the static water level, and tectonic tilting over time. It seems likely that glassy tuffs in the Prow Pass Tuff and overlying units at high elevations around drillholes GU-3, H-3, and H-5 have been preserved because tectonic tilting elevated the tuffs above the highest static water level. Because the transition zone has a lesser inclination than the pyroclastic units, the zone transgresses the time-stratigraphic boundaries between the units. From drillhole GU-3 northeast to G-4, the transition zone passes from an elevation of 923.2 m (3,029 feet) in the Prow Pass Tuff (about 13 Ma) to an elevation of 849.2 m (2,786 feet) in the Topopah Spring Tuff (12.8 Ma); the transition zone is thus at its lowest elevation in the youngest affected unit (Bish and Chipera 1989). Therefore, for the relative inclination rationale to be valid, geometric constraints require this sequence of conditions:

- No zeolitization occurred in the Prow Pass Tuff or younger units around GU-3 during the period in which the Prow Pass, Calico Hills, and Topopah Spring Tuffs were deposited, and by inference, the static water level remained below the level of the Prow Pass Tuff at GU-3.

- The static water level reached its highest position (represented by the present vitric-zeolitic transition zone) and remained in that position long enough for all glassy nonwelded tuff below the static water level to be zeolitized. Little or no tectonic tilting occurred during this period.

- The static water level then fell and tilting resumed, ending before 11.45 Ma.

If, however, zeolitization occurred in multiple episodes interspersed with tectonic tilting and the transition zone is a time-transgressive boundary that becomes younger from GU-3 to G-4, then the timing of zeolitization in the Topopah Spring Tuff is not constrained by the 11.45-Ma age for cessation of major tilting. The relative inclination rationale places too many unrealistic restrictions on hydrologic and tectonic processes.

A petrofabric technique for dating zeolitization by tectonic criteria was developed for this project and does not share the weaknesses of the relative-inclination model. The petrofabric technique also relies on the evidence that tectonic tilting ended about 11.45 Ma. This technique uses microscopic textural evidence of tectonic tilting preserved within the zeolitized rocks in geopetal fillings (Figure 6.1-50). The rationale is that if zeolitized rocks contain textural features indicating tectonic tilting and if these features postdate zeolitization, then the age of zeolitization is greater than 11.45 Ma. Unlike the relative inclination model, the petrofabric technique does not rely upon a general assumption that zeolites in the older or more deeply buried units are either the same age as or older than zeolites in the younger or higher units. In addition, this technique does not require any assumptions about the position or orientation of the vitric-zeolitic transition zone relative to the position of the static water level during zeolitization. The possible time-transgressive nature of the transition zone does not pose a problem, except as noted in the following paragraph.

The main assumption underlying the petrofabric technique is that the zeolitized tuffs containing evidence of tectonic tilting are representative of all zeolitized rocks from the Bullfrog Tuff to the Topopah Spring Tuff as far as timing of zeolitization is concerned. Geopetal fillings are common but not ubiquitous in this interval. In some of the samples examined for this study, geopetal fillings are present but not abundant enough to be measured. The validity of the assumption is enhanced by collecting evidence of tectonic tilting from as many samples and as many stratigraphic levels as possible and, particularly, from the vicinity of the vitric-zeolitic transition zone.

Zeolitized tuff specimens with abundant geopetal fillings were identified from the specimen sets for all old cored drillholes at Yucca Mountain and vicinity and from the sidewall cores and bit-cutting samples described by Levy (1984c). The specimens include, in approximate ascending stratigraphic order, slightly welded Bullfrog ashflow tuff, bedded tuff between the Bullfrog and Prow Pass Tuffs, bedded tuff of the lower Calico Hills Formation, nonwelded Calico Hills ashflow, an unnamed ashflow between the Prow Pass and Topopah Spring Tuffs, and nonwelded basal Topopah Spring ashflow.

Geopetal orientation measurements are plotted in Figures 6.1-53 and 6.1-54. The measured specimens fall into two groups. Measurements for specimens H-5 1917 and G-1 2166 have angular spreads of 3.5° or less. All of the ashflow specimens have angular spreads between 12 and 24°. Clustering of data is characteristic of all the specimens with the larger angular spreads. For several samples, there are single outlier values separated from the main body of measurements by as much as 5°. These values have been included because they met the acceptance criteria and there is no obvious reason, such as a broken or disrupted appearance of the measured fillings, for rejecting them. If outlying values are excluded, the angular measurement spreads fall within the range of measured dip angles in oriented Yucca Mountain core from intervals that contain no geopetal fillings (for example, Spengler and Chornack 1984).

Detailed Study of the Basal Topopah Spring Tuff–The particularly abundant geopetal deposits in specimen G-4 1392 were studied in detail to evaluate some of the assumptions underlying the relative dating rationale for geopetal measurements. The detailed study helped estimate the alteration state of the tuff when the geopetal structures were deposited and ascertain how much zeolitization of primary glass could have occurred after geopetal deposition. This sample is from the basal, nonwelded portion of the Topopah Spring Tuff, the youngest pyroclastic interval that is extensively and consistently zeolitized where the unit is at low elevation. The transition from vitric to zeolitized tuff is located about 3.4 m (11 feet) above the 424.3 m (1,392 feet) depth in drillhole G-4 (Bish and Chipera 1989).

Examination of partially zeolitized tuffs (Levy 1984c) has shown that pumice and fine-grained ash tend to be heavily to completely altered before larger, thicker shards have undergone appreciable alteration. The majority of geopetal deposits in this specimen are within secondary pores created by the complete dissolution of shards; therefore, it is reasonable to assume that the pumice and ash in this specimen, together representing about 75 percent of the rock volume, were already zeolitized when most of the geopetal pore fillings were deposited. Dissolved shard cavities in the sample were examined to estimate what proportion of the shards (originally about 25 vol. percent of the tuff) might have been altered before the deposition of geopetal fillings.

There are two complementary parts to this detailed study. First, an attempt was made to determine whether any of the geopetal fillings could be horizontal (i.e., untilted). This attempt is important because untilted geopetal fillings would not constrain the timing of zeolitization in the parts of the tuff where they are located. Because none of the specimens with abundant geopetal fillings are from oriented cores, it is not possible to make direct determinations of filling orientations. To test indirectly for horizontality, it is necessary to estimate and place bounds on the possible 3-D orientations of geopetal fillings. Measurement of geopetal-filling orientations in thin section provides only 2-D data. By measuring orientations in two mutually perpendicular thin sections of the same specimen, it is possible to obtain two groups of orientation measurements that can be combined to give an indication of 3-D orientations. The geopetal fillings measured in the two thin sections are all separate entities, none of which are sampled by both thin sections. The measurements can be combined only by assuming that the clusters of measurements correspond between thin sections. Because there are no independent criteria for correlating measurement clusters between sections, a trial correlation was made to define planes (representing geopetal surfaces) whose orientations are related to each other by the simplest possible rotational operations (that is, incremental rotations about the same axis). The planes are defined by connecting the middle measurements of postulated corresponding measurement sets.

Two mutually perpendicular thin sections were cut from a portion of G-4 1392 drill core such that the position of the core axis (long axis of the cylindrical core) could be located on each thin section (Figure 6.1-55a). Orientations of geopetal fillings and the orientation of the core axis were measured for each thin section. The results are plotted in Figure 6.1-55b and c. In both thin sections, at least two sets of geopetal orientations were tentatively identified and are labeled sets I and II. The correlation of sets between thin sections is based on assumed correspondence of the largest and next largest sets of measurements from one thin section to the other. This correlation produced planar orientations that are related to each other by simple rotation on a single axis. Approximate reconstructed planar orientations of both sets are shown in Figure 6.1-55a. The angular values depicted in the figure are intended only to help differentiate the measurement sets and have no quantitative significance in the following interpretations.

The rationale for constraining the time of zeolitic alteration with geopetal orientation data has been previously discussed. If any of the geopetal filling surfaces in an altered tuff are horizontal, then those fillings could have been deposited at any time after the last period of tectonism; therefore, the horizontal fillings would place no minimum age constraint on shard dissolution or zeolitization. To identify horizontal geopetal fillings would provide a means of estimating what proportion of filled shard cavities could represent shards that were altered and dissolved after tectonic tilting ceased.

The measured drillhole deviation at the 426.7 m (1,400 feet) depth in drillhole G-4, which indicates the deviation of the core axis from vertical, is 6.0 to 6.5° in the approximate direction S50°W (Eastman Whipstock 1982). Because the drill core is unoriented and the dip directions of the geopetal surfaces cannot be determined, the simplest geometric inference from the drillhole deviation data is that any of the geopetal measurements (Figure 6.1-55b) within 6.5° of the perpendicular to the core axis could be horizontal. The dip directions measured in oriented core from other segments of the Topopah Spring Tuff mostly lie between N53°E and S80°E (Spengler and Chornack 1984). If the dip directions of the geopetal surfaces were within this range, none of the measured geopetal surfaces could be horizontal because rotation of the orientation data to

bring the core axis from the vertical position shown in Figure 6.1-55a to its true southwest-plunging position would increase rather than decrease the dips of the geopetal surfaces. A few of the geopetal surfaces in set II could be horizontal but only if the dip directions of the geopetal surfaces are close to the drillhole deviation direction, opposite to measured dip directions in the Topopah Spring Tuff. This case seems unlikely, but it merits evaluation to help estimate the maximum possible proportion of measured geopetal surfaces that could be horizontal. The number of potentially horizontal surfaces in proportion to all measured geopetal surfaces can be estimated from the data for the G-4 1392A thin section (Figure 6.1-55b) because the plane of the thin section contains the trace of the core axis and is approximately perpendicular to the lines of intersection of the geopetal filling surfaces. Geopetal surface measurements that lie within 6.0 to 6.5° of the perpendicular to the core axis could be horizontal; such measurements represent 27 to 34 percent of all geopetal measurements for this thin section. These values overestimate the possible proportion of horizontal geopetal surfaces because a single rotation could not bring all the measurements to a horizontal position; however, further refinement of the estimate is not practical.

The second part of this study is a survey of dissolved shard cavities in the G-4 1392 thin section to determine what proportion of cavities contain geopetal fillings (including fillings that are not measurable) and zeolites younger than the geopetal fillings. Cavities with no fillings represent alteration whose timing is not constrained by the tectonism-geopetal filling association. Similarly, any zeolites that crystallized within shard cavities after geopetal fillings were deposited would be of younger, but indeterminable, age than the fillings.

The most common type of shard alteration was replacement of the shard boundary by a zeolite rind of variable thickness and dissolution of the remainder of the shard. Geopetal fillings were then deposited in the secondary pores created by shard dissolution. The principal geopetal fillings are clinoptilolite and opal. In nearly all geopetal fillings containing both materials, the clinoptilolite is overlain by opal. It is assumed that the measured geopetal fillings fully represent the time period in which all geopetal fillings were deposited. Textural evidence indicates only slight clinoptilolite deposition or growth within shard cavities after deposition of geopetal fillings, although the fillings themselves experienced some post-depositional recrystallization. In cavities with geopetal fillings, clinoptilolite crystals in the rinds lining the cavities are commonly slightly larger in the void spaces above the fillings than in the portions of the rinds covered by the fillings. Crystals in the rind covered by geopetal fillings were inhibited from further growth by lack of space.

The information recorded for each examined dissolved-shard cavity includes the geopetal filling (if any), other alteration products, and the apparent long dimension of the relict shard. Proportions of shard cavities with geopetal fillings, by size class, are listed in Table 6.1-20. This study has shown that very small dissolved-shard cavities (<0.3 mm) and the thinnest parts of larger shard cavities (indistinguishable from each other in thin section) are unlikely to contain geopetal fillings because the zeolite rind fills most of the pore space. Therefore, data for shard cavities ≥0.3 mm are more reliable indicators of geopetal filling abundance. The emphasis on larger shards is also justified because they would have been the last vitric components to be completely altered.

Results of the survey for shard cavities ≥ 0.3 mm across show that 92 percent of such cavities have geopetal fillings. This number can be combined with values obtained in the first part of this study according to the following relationship:

- Minimum volume percent of vitric material altered before cessation of tectonism (>11.6 Ma ago) =
- Volume percent of pumice and ash in original tuff + [(volume percent shards in original tuff) × (minimum fraction of measured geopetal fillings with nonhorizontal surfaces) × (fraction of shard cavities with geopetal fillings)] =
- 75 percent + [(25 percent) × (0.66 to 1.0) × (0.92)] = 90 to 98 percent

These results suggest conservatively that the tuff were almost completely altered by the time most geopetal fillings were deposited, earlier than 11.6 Ma ago. The value of 90 volume percent is conservative because it is based on an overestimation of the number of geopetal measurements that could possibly be horizontal and therefore overestimates the amount of zeolitization (10 vol. percent) that could have occurred after cessation of tilting. With so little unaltered glass remaining in the rock, little or no zeolitization can have occurred in the studied rock units during the last 11.6 Ma. This result does not imply that clinoptilolite has been unaffected by post-crystallization geochemical processes.

Bedded Tuffs in the Calico Hills Formation and Crater Flat Group–The interpretation of geopetal measurements with large angular spreads is straightforward, but there are several possible reasons why geopetal fillings in a zeolitized tuff would have little or no angular measurement spread. The simplest reason would be that no tilting occurred during geopetal deposition, although the geopetal fillings could all have been uniformly rotated by subsequent tilting. This could mean that alteration occurred during a period of tectonic quiescence before the Rainier Mesa Tuff was deposited or during the long period of relative tectonic quiescence after Rainier Mesa deposition. Alternatively, some condition could have restricted the introduction of pore-filling material to a single episode or to an unusually short period of deposition.

It seems likely that there were periods of tectonic inactivity before as well as after 11.6 Ma ago. An example of the existing record of tectonic tilting, examined in the following section, does not delineate individual periods of tectonism and quiescence. Quiescent periods of considerably less than a million years duration would probably be sufficient for an episode of zeolitization to occur without recording any tectonic tilting (Dibble and Tiller 1981).

Several conditions might have restricted the introduction of pore-filling material to a period of deposition too short to record tectonic tilting. These include conditions that would restrict the period during which pore-filling material was supplied to the altered tuff and conditions that would restrict the time during which rock pores were accessible to deposition of introduced material. Alternatively, if the material transported in a single depositional episode or a few episodes were sufficient to fill up all the available pore space in a short time, there would be no record of tilting. In the section on principles of data interpretation, the possibility was raised that continuing rock alteration might progressively change the patterns of pore connectivity such that

only certain pores would be open to the introduction of filling material at a particular time. To produce the uniform orientations of geopetal fillings observed in the two specimens by this mechanism, all pores would have to have been closed to further deposition soon after the original fillings were deposited.

Specimen H-5 1917 is from the middle of a zeolitized bedded interval about 20 m thick in the Calico Hills Formation (Bentley, Robison, Spengler 1983). The zeolitized interval is distinguished by the presence of vitric tuff both above and below the zeolitized rock. It is possible that alteration was localized by a perched water table within the bedded tuff. Alternatively, the regional static water level could have reached the top of the highly permeable bedded tuff at some time and then retreated downward before less permeable ashflow tuffs immediately below the bedded tuff could be altered. The survival of vitric tuff below the zeolitized interval suggests that these rocks have not been subjected to long-term saturated conditions.

Specimen G-1 2166, from a bedded tuff between the Prow Pass and Bullfrog Tuffs, is about 233.5 m (766 ft) below the vitric-zeolitic transition zone and about 83.2 m (273 feet) below the static water level (Robison 1984). Geopetal fillings in this specimen, like those in H-5 1917, recorded little or no tilting. The location of this specimen is well below the present-day vitric-zeolitic transition zone and static water level, but it could have been at or above the static water level at the time of zeolitization.

Because geopetal fillings in the bedded tuffs did not record tectonic tilting, the timing of zeolitization in these specimens is not constrained by the 11.45 Ma date for cessation of major tilting. The G-1 specimen comes from well below the present vitric-zeolitic transition and is unlikely to have been altered later than specimens from overlying units in a nearby drillhole, both of which have angular measurement spreads of at least 12°. If, however, the G-1 tuff was altered at or above the static water level and not too far below the ground surface, the age of alteration would have to predate the pervasive zeolitization of the overlying Calico Hills Formation and Topopah Spring Tuff and might predate deposition of these units. Similarly, zeolitization of the H-5 1917 tuff may have occurred before the Topopah Spring Tuff was deposited, when the bedded tuff would have been about 50 m below the ground surface.

Although the two specimens with no recorded geopetal evidence of tilting might have been altered near the SWL or in a perched-water zone, zeolitization near the static water level was not invariably associated with deposition of fillings that recorded no tilting. For example, the geopetal orientation data for specimen G-4 1392 show that at least one specimen from near the vitric-zeolitic transition zone, and therefore perhaps altered near the static water level existing at the time of alteration, contains a record of tilting during alteration. The vitric-zeolitic transition in drillhole G-4 is located about 4 m above the specimen position in the lower nonwelded part of the Topopah Spring Tuff (Bish and Chipera 1989). The likelihood for geopetal fillings to record tilting may have been enhanced by the proximity to a high-angle fault zone with silicified breccia observed in the G-4 core about 4.3 m (14 feet) vertically below the G-4 1392 position (Spengler and Chornack 1984). The fault zone has been a transport pathway for dissolved or suspended matter, and tuff within the fault zone may have experienced more tilting than did the large structural blocks. This specimen is also distinguished from many other zeolitized specimens by the abundance of geopetal fillings in primary pore spaces (vesicles) as well as in secondary

pores, a depositional pattern representing a greater-than-usual potential for the geopetal fillings to record tectonic tilting.

Evidence of Tectonic Tilting–The tilting recorded by geopetal filling orientations in the zeolitized tuffs is inferred to have occurred more than 11.45 Ma ago. The identification of multiple tilting events and the inferred timing of the events may place further constraints on the timing of zeolitization or may show that the timing cannot be further constrained by existing tectonic data. Evidence for the duration of tectonism during the periods of interest has been identified from subsurface structure maps.

Drillhole stratigraphic data for the locations shown in Figure 6.1-56 were used to produce structural contour maps of the upper surfaces of the Prow Pass Tuff, the Calico Hills Formation, and the Topopah Spring Tuff in the vicinity of southern and central Yucca Mountain (Figure 6.1-57). The data used to construct the structural contour maps are from Spengler, Muller, Livermore (1979); Spengler, Byers, Warner (1981); Bentley, Robison, Spengler (1983); Maldonado and Koether (1983); Scott, R.B. and Castellanos (1984); Thordarson et al. (1984); Spengler and Chornack (1984); and Whitfield, Thordarson, Eshom (1984). Data from newer drillholes were not incorporated into the figure, but are summarized by Buesch, Dickerson et al. (1994). The configuration of the upper surface of a pyroclastic unit represents the original upper depositional surface as modified by subsequent tectonic and erosional processes. Once a surface has been covered by a younger pyroclastic unit, it is largely protected from modification by erosion. Tectonic processes, however, may effect further modification of a buried surface. Careful comparison among structure maps of the units in a stratigraphic sequence is required to identify the effects of surface-modifying processes.

Subsurface structure maps constructed on the upper surfaces of the three pyroclastic units (Figure 6.1-57) show that all three surfaces dip eastward with decreasing inclination from older to younger units. The processes of tectonic modification included eastward tilting and vertical displacement along predominantly north-south-trending faults. The decrease in surface inclination with decreasing age suggests that tilting occurred between the episodes of pyroclastic deposition. Because pyroclastic deposition was a rapid process compared to tilting, it is equally possible that tectonism was a more or less continuous process punctuated by episodes of deposition.

The two older surfaces include east-west-trending depressions, possibly paleocanyons, in the vicinity of drillholes G-1, G-4, and H-5. A slight depression in the same region on the upper surface of the Topopah Spring and various topographic expressions on the overlying Tiva Canyon Tuffs correspond very generally to several east-west-trending faults mapped by Lipman and McKay (1965) or to the Drill Hole Wash fault zone of Buesch, Dickerson et al. (1994). The orientation and locations of these depressions were probably fault controlled. The persistent reappearance of this topographic feature in the same location after three major episodes of pyroclastic deposition supports the idea of control by recurring tectonism. The greater erodibility of the nonwelded Calico Hills Formation and upper Prow Pass Tuff may account in part for the greater topographic expression of the fault-controlled depression on the lower tuff units. The greater relief difference and development of topographic depression on the Calico Hills surface compared with the upper surface of the overlying Topopah Spring Tuff also supports an interpretation that the top of the Calico Hills Formation, as represented in

Figure 6.1-57, is a good approximation to the original topographic surface upon which the overlying tuff was deposited, not seriously modified by post-Topopah-Spring tectonism.

This comparison of subsurface structure maps for the Prow Pass Tuff, Calico Hills Formation, and Topopah Spring Tuff suggests that tectonic tilting probably occurred during the periods separating each successive pyroclastic deposition, at least in the central portion of Yucca Mountain. The structural data generally support the interpretation that tilting was occurring during most periods of zeolitization but place no tighter constraints on the ages of tilting recorded by geopetal fillings. The tectonic data are also not definitive regarding the question of episodic zeolitization because a history of repeated tectonic tilting is equally compatible with a single period of zeolitization or with multiple episodes of zeolitization affecting progressively younger units.

Summary of Geopetal Study Results–This series of studies has shown that zeolitized tuffs at Yucca Mountain contain geopetal fillings that recorded evidence of tectonic tilting. Textural relations in the Topopah Spring Tuff indicate that geopetal fillings post-date almost all zeolitization and were themselves tilted by subsequent tectonic rotation. Voids in the two specimens with single sets of geopetal orientations were filled in single episodes of deposition or during periods of tectonic quiescence. These specimens may have undergone zeolitic alteration close to the position of the static water level or in perched-water zones, not too far below the ground surface.

The volcano-tectonic interpretations of Sawyer et al. (1994) place a lower age limit of 11.45 Ma on major tectonic tilting and, by inference, on zeolitization. Structural contour maps for the Prow Pass Tuff, Calico Hills Formation, and Topopah Spring Tuff show that tilting probably took place during the periods separating each successive pyroclastic deposition. This evidence that tilting was a continuous or repetitive process means that the age of tilting recorded by geopetal fillings in a particular specimen cannot be more closely constrained than by the age of the pyroclastic unit and the age of the Rainier Mesa Tuff. These constraints apply in the same way to the ages of zeolitization. If the interpretations of the specimens with no recorded tilting are correct, there may be some evidence to suggest that the zeolites are not all the same age and that some zeolitization in units below the Prow Pass Tuff pre-dated either deposition or alteration of the Calico Hills Formation. Whether the zeolites at the vitric-zeolitic transition zone are the same age throughout Yucca Mountain remains an open question that is further addressed by the conceptual model of zeolitization in Subsection 6.1.5.1.

6.1.4.2.3.2 Exploratory K/Ar Dating of Zeolites from Yucca Mountain

For minerals to be dateable by the K/Ar method, they must retain K and radiogenic Ar and must resist incorporation of K or Ar from external sources (Dalrymple and Lanphere 1969; Faure 1986). Independent textural evidence for absence or occurrence of recrystallization is also desirable. Because zeolites have an aluminosilicate framework containing large cavities and channels that allow cations, water molecules, and certain gases to move readily in and out of the crystal structure (for example, Vaughan 1978; Feng and Savin 1993), little research has been conducted on the radiogenic dating of zeolites.

Previous efforts to date zeolites by radiogenic and related techniques were summarized by WoldeGabriel (1995b). Gundogdu et al. (1989) measured K/Ar apparent ages of 1.0 to 14.3 Ma on clinoptilolite from a lacustrine volcaniclastic section of early to middle Miocene age in western Turkey. They concluded that the variation of the clinoptilolite apparent ages is related to the permeability of the host rock from which the clinoptilolite was separated, such that less permeable rocks gave older apparent ages. The loss of radiogenic Ar from clinoptilolite in the more permeable tuffs during chemical exchange and diagenesis resulted in younger apparent ages. Another study of clinoptilolite from tuffs altered in a lacustrine environment in southeastern California found younger apparent K/Ar ages in a folded and faulted portion of the tuff than in the undeformed unit where clinoptilolite apparent ages were close to the eruption age (WoldeGabriel, Broxton, Byers 1996). In the latter study, authigenic illite/smectites and alkali feldspar were also dated. Both studies suggest that clinoptilolite can give a meaningful alteration age but that incompletely understood factors could reset the K/Ar systematics of the zeolite. On the basis of these kinds of data, we decided to proceed with exploratory dating of clinoptilolite from the burial-diagenetic environment of Yucca Mountain.

Clinoptilolite-rich outcrop samples from north and northeast Yucca Mountain and core samples from five drillholes were selected for textural, mineralogical, and geochronological studies. Petrographic observations indicated that most of the zeolites in the altered tuffs are fine grained (~40 μm). All core samples contained ≥ 30 percent clinoptilolite in the original bulk sample (Bish and Chipera 1989). Samples were selected to represent zeolitic tuffs above and below the static water level and to provide spatial coverage of the Yucca Mountain area. Selected samples were analyzed using a scanning electron microscopy to examine paragenetic relations among the secondary minerals.

Results of K/Ar Studies–Table 6.1-21 summarizes the mineralogical and K/Ar results for clinoptilolite, mordenite, and illite/smectite separates. The data are presented in descending stratigraphic order starting with the Topopah Spring Tuff. The nature of the impurities in samples can have a significant effect on the K/Ar apparent ages. Mordenite, opal-CT, cristobalite, quartz, and feldspar are common impurities in the clinoptilolite separates (WoldeGabriel, Broxton, Bish et al. 1992); of these, the K-bearing phases mordenite, feldspar, and illite/smectites can affect the K/Ar apparent ages. Some of the separates from the Tram Tuff contain as much as 10 to 15 wt% finely crystalline quartz and feldspar. The illite/smectites separates contain ≤1 percent clinoptilolite and mordenite. Mordenite separates contain quartz and, possibly, trace amounts of feldspar. Heat treatment and re-analysis of X-ray diffraction aliquots (method of Mumpton 1960) detected no heulandite in the mineral separates.

Topopah Spring Tuff–Five zeolitized tuff samples were analyzed from different levels of the Topopah Spring Tuff from the unsaturated zone of drill cores USW G-2, G-4, and the saturated zone of VH-2. Clinoptilolite and opal-CT are the dominant secondary minerals. The clinoptilolite K/Ar apparent ages are much younger than the eruption age of 12.8 Ma (Sawyer et al. 1994) and increase with depth within the unit. The shallow sample G-2 762, with a K content of 1.99 wt% and ≤1 percent radiogenic Ar, has an apparent age of zero. Two samples from the lower part of the Topopah Spring Tuff belong to the zone of pervasive zeolitic alteration. These samples, from two drillholes ~4 km apart, yielded similar apparent ages of 4.1 and 4.2 Ma. Two samples from below the static water level in drillhole VH-2 have apparent ages of 6.7 and 6.8 Ma.

Calico Hills Formation–Clinoptilolite fractions were separated from several zeolitized surface and subsurface samples of the Calico Hills Formation at Yucca Mountain. Outcrop at and north of the Prow Pass at the northern end of Yucca Mountain contain abundant clinoptilolite and mordenite with trace amounts of opal-CT. Scanning electron microscopy examinations of both surface samples indicate the presence of mordenite compared with corresponding subsurface samples (WoldeGabriel, Broxton, Bish et al. 1992). The mordenite crystallized on clinoptilolite surfaces. The Calico Hills clinoptilolites yielded K/Ar apparent ages younger than the 12.9 Ma age of the tuff (Sawyer et al. 1994). Clinoptilolite samples from outcrops range between 1.5 and 3.5 Ma, whereas those from the drillholes yielded apparent ages of 2 to 4.8 Ma. The apparent ages for drillhole samples increase with depth within the unit.

Prow Pass Tuff–Samples from the Prow Pass Tuff in the unsaturated and saturated zones of drillholes UE-25 p#1 and USW G-1, G-2, GU-3, and G-4 contain abundant altered shards replaced by illite/smectites with ≤10 percent illite layers, clinoptilolite, mordenite, opal-CT, and authigenic alkali feldspar, as indicated by X-ray diffraction and scanning electron microscopy analyses. Based on textural relations in scanning electron microscopy studies, smectite appears to have crystallized first, followed by clinoptilolite, mordenite, and analcime.

The K/Ar apparent ages range from 4.1 to 13 Ma and increase with depth within the Prow Pass Tuff. The oldest clinoptilolite apparent ages are from saturated-zone samples in the lower part of the Prow Pass section and are similar to the <13.25 Ma eruption age of the unit (Sawyer et al. 1994). An apparent age of 13.3 Ma was calculated for a clinoptilolite fraction from sample G-2 3250.0-3250.7. The illite/smectites separate from the same sample yielded a similar apparent age of 12.7 Ma. Comparison of K/Ar results for Prow Pass separates before and after undergoing further purification in heavy liquid highlights the contribution of impurities to the K/Ar apparent ages. An apparent age of 11 Ma was obtained on sample G-2 3191.5-3192, which decreased to 7 Ma after purification in heavy liquid. Sample UE-25 p#1 1740-1750 changed from 8.5 to 6.0 Ma after heavy-liquid purification. There is a possibility, however, that the heavy liquid itself may affect the K/Ar systematics. A separate of high purity (≥ 80 wt. percent clinoptilolite, ≤ 5 wt% mordenite, ≤15 wt% quartz) obtained without heavy-liquid treatment from UE-25 p#1 1790-1800 gave an apparent age of 8.4 Ma, which is closer to the apparent age of the untreated aliquot from ~15 m above.

Bullfrog Tuff–A mordenite sample from the lower part of the Bullfrog Tuff in the saturated zone of drillhole USW G-4 gave an apparent age of 12.3 Ma, similar to values for clinoptilolite and illite/smectites from the saturated zone. Clinoptilolite from the unsaturated zone in drillhole GU-3 yielded an apparent age of 3.9 Ma, close to the clinoptilolite apparent ages for overlying units in the unsaturated zone.

Tram Tuff–The samples from the Tram Tuff in drillholes USW G-1 and G-3 contain clinoptilolite, quartz, and analcime and minor amounts of mordenite, illite/smectites, and microcrystalline feldspar. The amounts of feldspar contaminants in the clinoptilolite separates may be slightly greater in the Tram and underlying tuffs compared with separates obtained from overlying units. Heavy-liquid separation to reduce the quartz and feldspar contents of the dated samples was not significantly effective as noted in the X-ray diffraction patterns of the pre- and post-separation aliquots. Scanning electron microscopy analysis of sample G-3 3854.7-3854.9 indicates that most of the secondary minerals were direct replacements of the original vitric

pyroclasts, except for smectite, which also occurred in the matrix and in altered feldspars and biotites.

Three clinoptilolite separates yielded apparent ages of ~9 to 10 Ma. Two of those had been separated in heavy liquid. The similarity of apparent ages for the treated and untreated separates is compatible with the X-ray diffraction data suggesting the ineffectiveness of heavy-liquid separation for these particular samples.

Older Tuffs (Informal Units B and C)–Two samples from units B (G-1 5458.4-5458.5) and C (G-1 5560) of the unnamed older tuffs contain clinoptilolite, mordenite, quartz, feldspar, and illite/smectites with 15 to 25 percent illite layers. The scanning electron microscopy studies indicate that the feldspar and biotite phenocrysts and the matrix in these samples were replaced by illite/smectites, authigenic K-feldspar, clinoptilolite, and mordenite. K-feldspar crystallized on smectite and clinoptilolite surfaces.

An apparent age of 12 Ma was obtained from both clinoptilolite separates. For comparison, Sawyer et al. (1994) determined an age of 14.0 Ma for the immediately overlying Lithic Ridge Tuff. The clinoptilolite ages are similar to the values from the Tram Tuff. These results represent maximum apparent ages because of the ≤ 20 wt% contamination of feldspar and illite/smectites. In comparison to the clinoptilolite apparent age of 12 Ma for G-1 5458.4-5458.5, an illite/smectites separate from the same sample yielded an apparent age of 8.8 Ma.

Depth-versus-Age Distribution of Apparent Ages–A striking aspect of the K/Ar results is the consistent pattern of increasing apparent age with depth (Figure 6.1-59) seen in samples from drillholes G-1, G-2, GU-3/G-3, and G-4 across the Yucca Mountain block. Apparent ages from surface and near-surface samples range between 2 and 4 Ma, whereas samples from the lower part of the unsaturated zone yielded apparent ages of 4 to 5 Ma. The apparent ages below the static water level increase from 4 to 13 Ma with depth. Possible reasons for the younger apparent ages in this range are investigated in Subsection 6.1.4.2.2.2.3. The oldest apparent ages are similar to the eruption ages of the volcanic units hosting the secondary minerals and may represent the original zeolite and illite/smectites crystallization ages. These results are promising because coexisting minerals separated from clinoptilolite-rich samples yielded apparent ages similar to those obtained for clinoptilolite.

Interpretation and Significance of Clinoptilolite K/Ar Apparent Ages–The zeolite K/Ar results include examples of apparent ages that are difficult to reconcile with each other or with textural evidence of crystallization chronology. Apparent ages of clinoptilolite from the lower Prow Pass Tuff vary from 2.4 Ma for zeolite currently in the unsaturated zone to 13.3 Ma for a sample from 465 m below the present static water level. Clinoptilolites from this stratigraphic interval should all be about the same age according to a conceptual model of episodic but early zeolitization based on petrofabric studies (Levy 1991). The few K/Ar apparent ages obtained from the zeolite mordenite are also at odds with clinoptilolite apparent ages. Textural studies indicate that mordenite formed by diagenetic alteration of clinoptilolite (WoldeGabriel, Broxton, Bish et al. 1992; Sheppard, Gude, Fitzpatric 1988), but the 7 Ma apparent age of mordenite from the shallow saturated zone is significantly older than apparent ages of 4 to 5 Ma for clinoptilolites from 80 m above and 146 m below the dated mordenite (WoldeGabriel, Broxton, Bish et al. 1992). These results are particularly significant because they suggest that the

mechanism responsible for the widespread modification of clinoptilolite apparent ages has operated in addition to any resetting of K/Ar systematics specifically associated with the recrystallization of clinoptilolite to mordenite.

Given that clinoptilolite apparent ages from the deep saturated zone are compatible with other data whereas apparent ages from the unsaturated zone, especially outcrops, seem too young, we have identified and investigated natural processes related to differences in hydrologic environment that could modify the K or Ar contents of the zeolite. Lowering of the K/Ar apparent age could result from K^+ gain by cation exchange, radiogenic Ar loss by diffusion out of the zeolite lattice channels, or a combination of both processes. The effectiveness of these mechanisms could differ in the saturated and unsaturated zones because of differences in pore-water composition, water content of the zeolite lattice channels, or surface hydration of zeolite crystals.

In documenting the patterns of age variation, we have also considered the contribution of K-bearing mineral impurities (WoldeGabriel 1995b). Illite, illite/smectites, and alkali feldspar are mostly ~9 to 14 Ma old and the few mordenite ages are ~7 to 8 Ma. If present as impurities, these minerals would tend to increase the apparent ages of "younger" clinoptilolites. The mineral separates produced for dating are too small for quantitative X-ray diffraction, but diffraction patterns commonly include potassic impurities. Apart from the effects of impurities on individual sample ages, there is an additional question whether systematic variations in impurity content could produce the pattern of increasing clinoptilolite age with depth. The whole-rock contents of mordenite and K-rich illite/smectites generally increase with depth, although exceptions exist. Qualitative comparisons of X-ray diffraction patterns for the suites of mineral separates from any given drillhole (WoldeGabriel 1995b) indicate about equal likelihood of increasing or decreasing potassic impurity content between consecutive samples. There is textural evidence from scanning electron microscopy studies that at least some of the alkali feldspar from the deepest samples is the same age or younger than the clinoptilolite (WoldeGabriel, Broxton, Bish et al. 1992). The feldspar would likely retain radiogenic Ar better than clinoptilolite and, therefore, could be contributing to an older, equivalent, or younger apparent age than would be obtained from the clinoptilolite alone. We conclude that potassic impurities are clearly a concern for individual samples, but no indication exists of systematic contributions to patterns of age distribution.

Investigations of Argon Retention and Loss from Clinoptilolite–The effects of cation exchange and heating under variable hydrologic conditions on the K and radiogenic Ar contents of clinoptilolite were evaluated experimentally to determine whether such processes could be responsible for the younger isotopic ages at Yucca Mountain (WoldeGabriel 1995a). A clinoptilolite-rich rock from the late Miocene Sucker Creek Formation of Sheaville, eastern Oregon, was selected for the experiments. It is interesting to note that the K/Ar apparent ages of the Sucker Creek clinoptilolite is much younger than the suggested late Miocene time of alteration (Sheppard, Gude, Mumpton 1983; Altaner and Grim 1990).

Zeolites were separated from other minerals by sedimentation in deionized water. Some separates were further purified by heavy-liquid separation. The K_2O and radiogenic Ar contents of these samples were measured before and after the ion-exchange and heating experiments. For the ion-exchange experiments, 1 M chloride solutions of Ca^{2+}, K^+, Na^+, and Cs^+ were added to

several splits of clinoptilolite aliquots (5 to 50 μm). Each mixture was placed in an oven at 50°C and periodically shaken. Every 24 hours the exchanged solution was removed by centrifugation and replaced by new chloride solution. The experiments were conducted in three and five steps for total times of 72 and 120 hours, respectively. The 120-hour exchange was intended to maximize the replacement of K^+ by alkali and alkaline-earth cations. The solutions obtained by centrifugation after each step were analyzed for cation content by atomic absorption and gravimetric methods.

Aliquots of about 2 g of clinoptilolite from the same material used in the ion-exchange experiment were heated at 50, 100, 150, and 200°C in air for 16 hours. Additional aliquots were placed in deionized water (2 to 1 water/sample ratio) maintained at 100°C in sealed reaction vessels for periods from one week to about six months. All aliquots were X-rayed using an automated Siemens D-500 diffractometer producing Cu Kα radiation from 2 to 36° 2θ in 0.02° steps and a counting time of 1 s per step.

The K_2O contents of the natural, exchanged, and heated samples were determined using an atomic absorption spectrophotometer on 70 to 100 mg of each sample powder fused with $LiBO_3$ and dissolved in 3 percent HNO_3 solution. Aliquots of about 120 to 250 mg of the sample powders were used for radiogenic Ar measurements using an MS 10 mass spectrometer on line with bulb-pipetted ^{38}Ar. Analyzed values of K_2O and Ar for standards USGS BCR-1 and G-2 and LP-2 were within 2.5 percent of published values (Govindaraju 1989; Odin et al. 1982).

Results–The water-separated and heavy liquid-separated samples contain similar amounts of K_2O but the latter may have lost some of its radiogenic Ar (Table 6.1-22). Additional tests would be required to identify a genuine effect of heavy-liquid separation on the radiogenic Ar content of clinoptilolite. Nevertheless, it seemed prudent to avoid the use of heavy liquids in preparing the starting materials for the cation-exchange and heating experiments.

Most replacement of the natural cations occurred during the first iterations of the cation-exchange experiments and decreased substantially during subsequent steps. The K_2O contents were significantly modified, as expected, whereas less drastic changes were noted in the amounts of radiogenic Ar except for the Cs-exchanged fraction from the 5-day experiment (Table 6.1-22, Figure 6.1-60a). Given the scatter in the data, there is no clear effect of the cation exchange process on radiogenic Ar content. The apparent increase in the radiogenic Ar content of the five-day Cs-exchanged clinoptilolite is not understood and should be verified by further study. We know of no mechanism to account for a genuine increase of radiogenic Ar.

The loss of about half the radiogenic Ar from the five-day Na-exchanged clinoptilolite, although not clearly a significant result, is of interest. The smaller ionic radius of Na, compared to the other exchangeable cations, means that it may less effectively block the movement of water, cations, and gases in and out of the crystal structure.

About 70 percent of the radiogenic Ar was lost from clinoptilolite heated in air at 200°C, with inconclusive results for the samples heated at lower temperatures (Table 6.1-22, Figure 6.1-60b). The quantity of radiogenic Ar remaining in the 200°C air-heated sample is so small that the error of measurement determined according to Cox and Dalrymple (1967) is overestimated. Minor,

possibly insignificant variations from the original radiogenic Ar content were noted in the clinoptilolite fractions heated in water at 100°C for up to 6 months (Table 6.1-22, Figure 6.1-60c).

Implications of Experimental Results for Clinoptilolite Dating–The results of the cation-exchange experiments suggest that the effects of cation exchange on the K/Ar systematics of clinoptilolite would likely be limited to modification of the K_2O contents. Addition of K_2O from pore fluids into the clinoptilolite structure would be consistent with the cation affinity sequence for clinoptilolite reported by Ames (1961). Unsaturated-zone waters above the zeolitized tuffs at Yucca Mountain have slightly higher chemical concentrations and higher Ca+K/Na than saturated-zone waters (Yang 1992). Comparisons of exchangeable cation compositions of clinoptilolite from the saturated and unsaturated zones do not clearly indicate any K_2O enrichment in the unsaturated zone except for a few outcrop samples (Broxton, Warren, Hagan et al. 1986). Therefore, we conclude that post-crystallization K_2O enrichment may have contributed to the young apparent ages of a few surface samples but does not account for the overall pattern of age variation with depth.

Substantial loss of radiogenic Ar was observed in the clinoptilolite fraction heated in air for 16 hours at 200°C. Dehydration caused by dry heating produces increased atomic displacement and disorder in the tetrahedral framework of alkali zeolites (Armbruster 1993), and this may enhance the loss of Ar from the clinoptilolite structure. It is important to note, however, that although the dry-heating experiment was designed to accelerate any loss of Ar that might occur at low-moisture content, it does not represent in situ conditions in the unsaturated zone of Yucca Mountain in terms of either temperature or humidity. Present temperatures in the unsaturated zone are no more than about 35°C (Sass and Lachenbruch 1982), and the survival of the low-temperature minerals clinoptilolite, smectite, and opal-CT suggests that the diagenetic rocks in the unsaturated and shallow saturated zone have not been subjected to high temperatures.

The rate of Ar loss may also be affected by the availability of pore water to wet the surfaces of the clinoptilolite crystals. According to Barrer and Vaughan (1969), Ar diffusion below 110°C can be minimized, at least for short periods of time, by surface rehydration of artificially dehydrated clinoptilolite. The pores of clinoptilolite-rich rocks above the static water level at Yucca Mountain are generally more than 70 percent saturated (Loeven 1993). Varying conditions of liquid undersaturation, existing within a changing recharge environment for millions of years, might contribute to the loss of radiogenic Ar.

Summary of K/Ar Experimental Data–The cation-exchange experiments indicate that the exchangeable cation composition, including the K^+ contents, of clinoptilolite can be significantly modified with little effect on the radiogenic Ar content of the same sample. Ar depletion was apparent in a clinoptilolite fraction heated in air at 200°C. Samples heated in water at 100°C for up to 6 months experienced only minor, inconclusive variations in Ar content. Loss of radiogenic Ar from incompletely hydrated clinoptilolite occurs perhaps because of disorder in the clinoptilolite structure or the effects of decreased surface wetting. Thus, water appears to play an important role in the retention of Ar within the clinoptilolite structure. Other factors such as elevated thermal conditions, addition of K, and late diagenetic reactions appear to be less important in modifying the apparent ages of clinoptilolite.

6.1.4.3 Regional, Deep-Seated Hydrothermal Alteration

The disposal regulations include requirements to evaluate the rates of geochemical and hydrogeologic processes operating within the geologic setting during the Quaternary Period to determine the presence or absence of favorable conditions related to geochemical and hydrologic process rates [10 CFR 60.122(b)]. Alteration processes of the last few million years are best understood in the context of the tectonic, volcanic, hydrologic, and climatic environments that have evolved over a period of ~14 m.y. since the pyroclastic rocks forming the bulk of Yucca Mountain began to be deposited. Alteration assemblages at depth at Yucca Mountain have proved to be valuable natural self-analogs for the behavior of natural geochemical barriers subjected to waste-repository conditions.

Deep-seated alteration associated with hydrothermal activity around the Timber Mountain-Oasis Valley caldera complex, as manifested at Yucca Mountain, was investigated by illite/smectite geothermometry and K/Ar dating (Bish 1989; Bish and Aronson 1993). One focus of these studies was a determination of the extent to which past thermal events have altered the rocks and also the extent to which any future elevation of temperature will affect the rock properties. In addition, evidence of recent alteration would indicate that the site may be subject to continuing hydrothermal activity. Thus, the age and source of the last significant hydrothermal alteration activity at Yucca Mountain is important for evaluating the likelihood of future hydrothermal activity and its effects on the rocks at Yucca Mountain.

Samples from the three deepest cored holes at Yucca Mountain, USW G-1, USW G-2, and USW GU-3/G-3, up to 1,828 m in depth, were selected for illite/smectites geothermometry and K/Ar dating. The rocks are predominantly high-silica rhyolite ashflow tuffs, which vary from poorly consolidated nonwelded units to welded and/or devitrified units (Bish, Ogard et al. 1984). Where they are above the present-day static water level (571.7 m depth in G-1, 524.9 m depth in G-2, and 750.3 m depth in GU-3/G-3), nonwelded units are primarily glassy; below the static water level, they are predominantly zeolitized and contain clinoptilolite, mordenite, and/or analcime. The welded, devitrified units, both above and below the static water level, contain abundant alkali feldspar, quartz, with or without cristobalite and minor tridymite, and densely welded vitrophyric units that remain largely glassy. Illite/smectite is common in small amounts in the rocks irrespective of the degree of welding. The three drillholes studied penetrated ashflow tuffs spanning Iijima's (1978) four alteration zones (glass, clinoptilolite-mordenite, analcime, albite), and there is an apparent northward increase in the degree of alteration at depth (e.g., Bish and Semarge 1982; Smyth 1982). The volcanic rocks at Yucca Mountain range in age from ~12.7 m.y. at the surface to >14 m.y. at depth (Byers, Carr, Orkild 1989). The last significant activity at the Timber Mountain caldera occurred at 11.5 and 11.3 Ma, with intracaldera activity peaking ~10.7 m.y. ago (Jackson 1988). Bish and Aronson (1993) and Jackson (1988) documented the occurrence of hydrothermal activity around the Timber Mountain-Oasis Valley caldera complex between 13 and 10 Ma, mostly between 11.5 and 10.0 Ma.

Our approach used illite/smectites geothermometry and K/Ar dating to obtain a semiquantitative estimate of the past thermal history. The transformation of smectite to illite with increasing temperature in pelitic rocks has been thoroughly studied and well documented (e.g., Burst 1959; Perry and Hower 1970, 1972; Hower et al. 1976; Hoffman and Hower 1979; Hower and

Altaner 1983). When a sufficient supply of K exists, 100 percent expandable smectite reacts through a series of intermediate interstratified illite/smectite clays to a nonexpandable illite containing additional K and Al over that found in the precursor material. The reaction of smectite to illite in nonpelitic rocks such as volcanic tuffs has received considerably less attention, but it appears that the general trends with temperature noted above for pelitic rocks hold for other rocks (e.g., Steiner 1968; Eslinger and Savin 1973; Inoue et al. 1978; Bish and Semarge 1982; Hower and Altaner 1983; Horton 1985; Bish and Aronson 1993). This reaction is influenced by several variables, including time, temperature, mineralogic assemblage, and water composition (e.g., Eberl and Hower 1976; Howard, J.J. 1981; Roberson and Lahann 1981). Because the extent of this reaction is highly temperature dependent (Perry and Hower 1970; Eberl and Hower 1976; Hoffman and Hower 1979; Hower and Altaner 1983; Horton 1985), it is often possible to obtain consistent estimates of the maximum temperatures to which a particular illite/smectite has been subjected, given sufficient K, Al, and reaction time. Thus, in favorable circumstances, the illite/smectites data can be used to construct schematic maximum paleogeothermal gradients, and the areal changes in these gradients may be used to infer source(s) of any existing hydrothermal alteration. Although it is difficult to extrapolate available experimental results to the Yucca Mountain paleohydrologic and paleogeothermal system, the presence of authigenic K-silicates (illite and adularia) in Yucca Mountain rocks (Caporuscio et al. 1982) suggests that sufficient K and Al existed for the smectite-to-illite reaction to proceed.

In addition to using the smectite-to-illite reaction as a geothermometer, K/Ar dating methods were applied to K-rich illite/smectite samples to obtain reproducible estimates of the age of alteration (e.g., Aronson and Hower 1976; Aronson and Lee 1986; Elliott et al. 1991). Thus, it was possible to map the distribution of clay minerals in Yucca Mountain using conventional X-ray diffraction data and to determine the time and temperature of clay mineral formation. Furthermore, by establishing the correlations that exist between the clay mineral transformations and other alteration mineral assemblages, it was possible to establish the extent and timing of alteration in general wherever the clay minerals have been modified. Also, the alteration observed in deeper parts of drillholes might be used as a natural analog to repository-induced alterations (see Subsections 6.1.6 and 6.1.7). Using this natural system to provide information on reaction temperatures and products circumvents some of the problems inherent in laboratory studies, in particular, the requirement that higher than expected temperatures be used to increase reaction rates, with the associated problem of extrapolating high-temperature kinetics to lower temperatures. Assuming the illite/smectite clays record maximum alteration temperatures, inferences can be made concerning the thermal stability of associated minerals, such as the zeolites clinoptilolite and mordenite. The zeolites at Yucca Mountain apparently formed early in the mountain's history based on geopetal structures (Levy 1991) and were presumably subjected to the same temperature and pressure conditions as the smectites.

Finally, the information on the mineral distributions, alteration temperatures, and alteration timing can be compared with data for present-day geothermal systems (e.g., Swanberg and Combs 1986) to draw inferences about paleohydrologic conditions at Yucca Mountain. Such inferences may set limits on the elevation of past water tables and provide information on the hydrothermal circulation system that may have caused the observed alteration.

6.1.4.3.1 Experimental Methods

All samples were obtained as drill core from drillholes USW G-1, G-2, or GU-3/G-3 at Yucca Mountain. Two- to 4-cm slices of core were brushed or washed clean of surface contaminants, broken into pieces smaller than ~0.5 cm, and crushed for 5 minutes in a tungsten-carbide shatterbox. Clay mineral separations were performed by sedimentation in water, after disaggregation using an ultrasonic probe, and the <0.1-μm or <1-μm fraction was usually used to prepare oriented mounts for X-ray diffraction. There were no significant mineralogical differences between these two size fractions. In no cases were heavy liquids or any dispersants used. More than 19, 43, and 30 clay mineral separations were analyzed from USW G-1, G-2, and GU-3/G-3, respectively.

Oriented mounts for X-ray powder diffraction were prepared by sedimentation from an aqueous suspension under gravity onto a glass or cut quartz single-crystal slide; the sample area was large enough so that the X-ray beam was fully contained within the sample at all angles of interest. This preparation method did not produce mounts that were effectively infinitely thick at the maximum angle of interest, and the relative intensities were usually not used. Cavity mounts of the clay separations were prepared from dried fine fractions by front-mounting powders into a shallow cavity in a glass, Al, or stainless steel holder. The bulk-rock mineralogy reported here was described by Bish and Chipera (1989); all data were obtained using cavity-mounted powders that had been ground under acetone to <3 μm using a Brinkmann Micro-Rapid Mill. Quantitative analyses were obtained using a combination of external- and internal-standard methods of Chung (1974a, 1974b), and accuracy and precision of analyses are given in Bish and Chipera (1989).

X-ray diffraction data were obtained using an automated Siemens D-500 diffractometer, counting for 0.6 to 2.0 second every 0.02° 2θ. Cavity mounts were examined under room conditions (relative humidity <30 percent), and oriented mounts were examined under room conditions and after solvating in ethylene glycol vapor for at least 12 hours at ~50°C. X-ray diffraction patterns of ethylene glycol-solvated illite/smectite samples were interpreted using the methods of Reynolds (1980). The approximate percentage of illite (or 10Å) layers was estimated using techniques described by Reynolds (1980) and Srodon (1980), and the estimates were refined by calculating patterns using a FORTRAN version of the program of Reynolds (1980). If other clay minerals were suspected or if the smectite appeared unusual, a variety of other tests were performed, including K saturation, lithium saturation (Greene-Kelly 1955; Bystrom-Brusewitz 1975), water solvation, and heat treatments (see Brindley and Brown 1980). Discrimination between kaolinite and/or chlorite was based on the presence or absence of a reflection near 6° 2θ or on the basis of heating experiments. However, results were usually ambiguous due to the small concentrations (<3 percent).

Fluid inclusions in thin-sections from USW G-2 and GU-3/G-3 were examined using techniques described by Roedder (1984). In general, only calcite contained secondary inclusions that might provide information on secondary alteration conditions, and inclusions large enough for study were very rare. Primary inclusions in phases such as quartz were not usually examined because they yielded the high temperatures typical of the primary constituents of volcanic rocks.

K/Ar dates of illite/smectites were obtained using the methods described by Elliott and Aronson (1987) and Elliott (1988). Amounts of radiogenic Ar in the illite/smectite samples ranged from 25 to 44 percent, and K_2O ranged from 1.78 to 7.56 percent, correlating well with the amount of collapsed layers. All age calculations used the constants of Steiger and Jager (1977). The average internal variation of replicate analyses (±0.25 Ma) was considerably less than the maximum calculated uncertainty of ±0.6 Ma.

6.1.4.3.2 Results

All core samples examined contained dioctahedral illite/smectites as the most abundant clay mineral, and other clay minerals were either uncommon or absent. In general, the illite/smectite clays shallower than 1,448 m in USW G-1 are randomly interstratified ($R = 0$) with <20 percent collapsed layers. Deeper than 1,448 m, $R = 1$ ordered interstratifications occur, with $R > 3$ illite/smectites and chlorite occurring below 1,718 m depth. Trends in illite/smectites mineralogy with depth in drillhole USW G-2 are similar to those observed in USW G-1 but are displaced to shallower depths. Illite/smectite samples from <1,053 m depth in USW G-2 are randomly interstratified ($R = 0$) with <10 percent collapsed layers. There is an abrupt increase in the percentage of collapsed layers below about 1,106 m, with imperfect $R = 1$ ordering appearing at 1,097 m, well-ordered $R = 1$ illite/smectites occurring at 1,128 m, and $R > 3$ illite/smectite clays occurring between 1,158 and 1,524 m depth. Discrete illite predominates below 1,524 m, with lesser amounts of chlorite, randomly interstratified chlorite/smectite, and some 100 percent expandable smectites. Incomplete collapse of heat-treated illite/smectite samples from USW G-1 and G-2 suggests that many of the clays in the deeper portions of these drillholes are partially chloritized. The illite/smectite clays from drillhole USW GU-3/G-3 contrast with those from USW G-1 and G-2 in that they are all randomly interstratified ($R = 0$), with fewer than 25 percent collapsed layers, and they exhibit no evidence of chloritization.

Basal spacings (room temperature, 20 percent relative humidity) and chemical data (Caporuscio et al. 1982; Vaniman, Bish, Broxton et al. 1984) for illite/smectite samples show that they are predominantly Na-Ca saturated, with a tendency to become more K rich with depth. For example, illite/smectites shallower than 975 m in USW G-2 has Ca > Na >> K; illite/smectites abruptly increases in K content below 975 m depth and those below 1,067 m depth are predominantly K saturated.

In addition to the obvious trends in clay mineralogy with depth, significant parallel trends exist in the bulk-rock mineralogy (Bish and Chipera 1989). Most notable are the variations in zeolite mineralogy, with clinoptilolite and mordenite giving way to analcime with depth. In addition, tridymite and volcanic glass occur predominantly in shallower rocks above the static water level, and cristobalite disappears at intermediate depths, probably transforming to quartz. Calcite occurs sporadically in the three drillholes, but it is much more common in the deeper portions of USW G-1 and G-2. Optically identified authigenic albite (Bish, Caporuscio et al. 1981; Caporuscio et al. 1982) occurs only in the deepest portions of USW G-1 and G-2.

Results of analysis of the few fluid inclusions found in secondary minerals in USW G-2 and GU-3/G-3 yield temperatures bracketing those suggested from the illite/smectite systematics. Inclusions in calcite from USW G-2 yielded homogenization temperatures of 94 to 115°C at 1,640 m depth, 147°C at 1,756 m, and 202° to 239°C at 1,774 m depth. Freezing temperatures

for these inclusions ranged from -0.1 to -0.6°C, reflecting low salinities in the inclusions. Homogenization temperatures in calcite from USW GU-3/G-3 were 101° to 227°C at 31 m, 125° to 170°C at 130.8 m, and 97°C at 1,464 m depth.

The K/Ar dates for illite/smectite samples from USW G-1 and G-2 range from 10.0 to 11.5 Ma and average 10.4 Ma (Table 6.1-23). In general, the less illitic illite/smectite clays yielded slightly lower K/Ar dates than the R >3 and illite clays. However, within the estimated error for an individual analysis, all of the K/Ar dates are nearly statistically equivalent.

6.1.4.3.3 Paleogeothermal Conditions

Numerous authors have demonstrated the dependence of illite/smectite structure and composition (i.e., degree of ordering and percentage of collapsed layers) on temperature. For example, Perry and Hower (1970) showed this relationship in comparing data from a number of Gulf Coast wells. Many subsequent studies have confirmed this temperature dependence in a variety of rock types, and Hower and Altaner (1983) illustrated this using data from both pelitic rocks and from several geothermal areas. Consistent trends emerge for a variety of rock types younger than Cretaceous age. The trends in illite/smectite mineralogy with depth in the three Yucca Mountain drillholes may be compared with the compilation by Hower and Altaner (1983) to estimate maximum temperatures to which the Yucca Mountain rocks have been subjected. Briefly, they showed that R = 1 illite/smectites is attained at 90 to 100°C for reaction times >10^7 years and at 130 to 150°C for times <10^6 years. They also concluded that data from geothermal areas are consistent with those from pelitic rocks, showing that R >3 illite/smectites is attained at ~75°C, illite appears at ~260°C, and muscovite occurs at ~310°C. Comparison of these trends with the data in Bish (1989) yields the schematic paleotemperature profiles illustrated in Figure 6.1-61. Present-day measured geothermal gradients (Sass et al. 1983) are shown on this figure for comparison. The schematic profiles for USW G-1 and G-2 in this figure are considerably steeper than present-day gradients, and it is apparent that a significant thermal event has occurred in the northern end of Yucca Mountain but has not significantly affected the southern end. The schematic paleotemperatures in the figure assume reaction times long enough so that kinetic effects are not limiting, and the temperatures in the deeper portions of USW G-1 and G-2, where R>3 illite/smectites and illite occur, were apparently high enough that the smectite-to-illite reaction was not kinetically limited.

The few fluid inclusion data obtained support the illite/smectite temperatures. Lack of evidence to support elevated alteration temperatures in GU-3/G-3 suggests that the higher temperature inclusions at 31 and 130.8 m may have formed during the initial cooling of the tuffs. More likely, the relatively high-homogenization temperatures in the shallow calcites are a result of re-equilibration or variable initial vapor-to-liquid ratios due to deposition in the vadose zone (Goldstein 1986). Fluid inclusions below the static water level in G-2 (524.9 m) and GU-3/G-3 (750.3 m) are not influenced by these effects.

6.1.4.3.4 Alteration Timing

The range in ages described above coincides with the dates published for major Timber Mountain volcanic activity (11.45 and 11.6 Ma; Sawyer et al. 1994), and our average dates for illite/smectites and illite closely match the dates of Timber Mountain intracaldera lava eruption

(10.6 to 10.7 Ma; Byers, Carr, Orkild 1989). The consistency of the illite/smectite ages at different depths in drillholes USW G-1 and G-2, the increasing intensity of alteration observed in rocks going north toward the Timber Mountain complex, and the agreement of the illite/smectite ages with the age of Timber Mountain volcanic activity all argue that hydrothermal effects of the Timber Mountain system are responsible for the mineralogical changes seen at depth in USW G-1 and G-2.

An alternative, which can be discounted, is that the illitization may have taken place earlier when this area was also volcanically active, for example during Paintbrush (~12.7 to 12.8 Ma; Sawyer et al. 1994) or Crater Flat (13.25 Ma) silicic volcanism. If this were the case, the ~11-m.y. ages would then represent resetting of the older illite K/Ar system due to reheating during Timber Mountain volcanism. The blocking temperature above which illite and illite/smectites rapidly lose their accumulated argon is not well established. However, the internal consistency of dates among cogenetic illitic clays of varying size fractions and the consistency of ages for a number of cases from oil well samples in which samples are presently at temperatures as high as 180°C leads us to conclude that a blocking temperature of >180°C is appropriate (Aronson and Hower 1976; Lee et al. 1989; Elliott et al. 1991). The blocking temperature is undoubtedly less than that of muscovite at about 350°C (Robbins 1972), and it may be a function of the crystallite size and perfection of the illite/smectites and, indirectly, a function of the degree of ordering and amount of collapsed layers. Considering the evidence for a moderately high blocking temperature for illite, one would expect to have observed K/Ar dates ranging as high as 12 to 13 Ma if this alternative were true.

The differences between the ages of the less illitic and the highly illitic samples warrant some discussion. It is possible that $R = 0$ and $R = 1$ illite/smectite samples, with an average date of 9.9 Ma, are not as retentive of Ar as is $R > 3$ illite/smectites and illite, with an average date of 11.2 Ma. For example, transmission electron microscopy studies show that, in general, the crystals of more illitic illite/smectites are more regular, well formed, and larger compared with less illitic illite/smectites (Veblen et al. 1990; Ahn and Buseck 1990). Alternatively, it is plausible that the alteration at Yucca Mountain was progressive, and what is seen in shallower cores once characterized the initial stages of alteration at depth, those initial stages now having been mostly obliterated by later higher-temperature alteration. Most of the $R = 0$ and $R = 1$ illite/smectite occurs at shallower depths where hydrothermal activity can be expected to have been retarded (and younger) compared with deeper $R > 3$ illite/smectites. Thus, the $R = 0$ and $R = 1$ dates that are as young as 9 to 10 Ma may be indicative of a 1 m.y. duration of hydrothermal activity beneath Yucca Mountain.

6.1.4.3.5 Paleohydrologic Conditions

Comparison of the Yucca Mountain paleogeothermal gradients (Figure 6.1-61) with those typical of modern-day geothermal systems can potentially provide information on the nature of the hydrologic system existing during hydrothermal alteration. The schematic paleogeothermal gradients for USW G-1 and G-2 in this figure bear a striking resemblance to several published geothermal gradients for geothermal systems. The paleogeothermal gradient for USW G-2, in particular, mirrors the observed temperature-depth gradient in core hole GEO N-1 at Newberry Volcano, Oregon (Swanberg and Combs 1986) in many respects. Swanberg and Combs (1986) concluded that the virtually constant temperature in drillhole GEO N-1 throughout its upper

990 m represents a rain-curtain effect. The abrupt rise in temperature below a certain depth is usually attributed to the existence of a permeability barrier, with shallower more permeable rocks isolated from the deeper rocks. Thus, the relatively constant inferred temperature in USW G-2 to ~1,067 m depth, much deeper than the present static water level (~521.8 m), suggests that a rain-curtain effect existed and/or the rocks near or below 1,067 m were relatively impermeable, thereby isolating the shallower rocks from the deeper hydrothermal system. In support of a rain-curtain effect, limited climatological data suggest that this area was much wetter ~11 m.y. ago, before uplift of the Sierra Nevada (Hay et al. 1986). However, a permeability barrier that could have effectively isolated shallower rocks from the deeper system is not obvious in USW G-2. Although there are several possible fault zones near 1,000 m depth in USW G-2 (Maldonado and Koether 1983), with significantly increased amounts of smectite below this depth, similar features are not present in USW G-1 near the depth of temperature transition. The paleogradients at Yucca Mountain also differ in detail from the gradient observed at Newberry Volcano in that paleotemperatures in USW G-2 do not appear to increase significantly below about 1,220 m depth; that is, the deep system in USW G-2 was approximately isothermal rather than exhibiting the conductive geothermal gradient seen at Newberry Volcano.

The results of Forster and Smith (1990) suggest possible explanations for several of the features seen in Figure 6.1-61 and some of the discrepancies between the Newberry Volcano and Yucca Mountain geothermal gradients. Their numerical models suggest that temperatures could have been progressively set shallower in the system as a function of time, giving the appearance of the existence of an isothermal zone. More importantly, their calculations show, for a hydrothermal system in a region of significant topography (e.g., their Figure 1.15), similar to the Timber Mountain region, that two distinct fluid flow systems can be generated without the presence of a permeability barrier. A deeper recirculating system could become chemically evolved while the shallow hydrologic system (<1 to 2 km depth) could be continuously recharged with fresh meteoric water. Thus, a permeability barrier may not have been required to produce the type of paleogeothermal gradient shown for USW G-2 in Figure 6.1-61. The features observed at Yucca Mountain are most consistent with a hydrothermal outflow plume association in which sufficient convective mixing occurred at depth to generate approximately isothermal conditions.

These analogies with modern-day geothermal systems suggest that the alteration observed at Yucca Mountain was associated, both spatially and temporally, with a hydrothermal outflow zone connected with the Timber Mountain caldera complex. Results of studies of modern geothermal systems such as the Jemez Mountains, New Mexico, system suggest that hydrothermal alteration surrounding a caldera complex occurs in association with late-stage intracaldera volcanic activity rather than the large-scale eruption of rhyolitic tuffs (Heiken and Goff 1983; WoldeGabriel and Goff 1989). The apparent isothermal nature of the deep, high-temperature alteration zone in USW G-1 and G-2 is additional evidence supporting the presence of a hydrothermal outflow plume.

6.1.4.3.6 Summary and Conclusions

These mineralogical data demonstrate that the rocks at depth in the northern end of Yucca Mountain were significantly altered early in their history. The clay mineral reactions are similar to those observed in pelitic rocks, with essentially 100 percent expandable $R = 0$ illite/smectites transforming through ordered intermediates ($R = 1$, $R > 3$) to illite with depth in USW G-2 and to

$R \geq 3$ illite/smectites in USW G-1. The illite/smectite clays in USW G-3 have not significantly transformed with depth. It appears that sufficient K and Al existed in these rocks for the smectite-to-illite transformation to proceed.

Based on estimates from illite/smectite mineralogy and fluid inclusions, the rocks at depth in USW G-2 appear to have been subjected to temperatures of at least 275°C, those in G-1 have reached about 200°C, and the deepest GU-3/G-3 rocks (about 305 m shallower than the bottoms of G-1 and G-2) probably have not exceeded 100°C. The vertical distribution of minerals across Yucca Mountain demonstrates that alteration is most profound to the north in USW G-2. USW G-1 core shows the effects of hydrothermal alteration, but at a greater depth and to a lesser extent than in USW G-2, and there is little evidence for significant elevated-temperature alteration in USW G-3. Data suggest that the shallower Paintbrush Group (erupted ~12.7 to 12.8 Ma) have not been significantly altered in any of the drillholes examined. The distribution of alteration minerals and the K/Ar ages of illite/smectites in USW G-1 and G-2 (~10.4 Ma) are consistent with Timber Mountain moat volcanism as the major source of hydrothermal alteration, rather than caldera-forming main ash-sheet eruptions. The rocks at depth at Yucca Mountain were apparently altered in a hydrothermal outflow plume. The nature of schematic paleogeothermal gradients suggests that a rain-curtain effect existed in USW G-2 to about ~1,067 m, below which there is an abrupt rise in temperature and then the thermal gradients appear essentially isothermal. Alternatively, the gradient could have reflected two distinct fluid flow systems. The widespread distribution of volcanic centers in the area allows for the possibility that some of the alteration may have preceded Timber Mountain volcanism, perhaps during Paintbrush volcanism, culminating with Timber Mountain volcanism, particularly the later stages, at 10 to 11 Ma. It is noteworthy, however, that the mineralogical data suggest that no hydrothermal alteration has occurred since the waning of Timber Mountain volcanism about 10 Ma.

6.1.4.4 Quaternary Surficial Processes

6.1.4.4.1 Transport of Ca and Si from the Surface through the Unsaturated Zone

As noted in Subsection 6.1.1.3, one of the principal chemical processes at the surface of Yucca Mountain is accumulation of pedogenic calcite and opal. The greatest accumulations of calcite and opal occur within the vein calcretes. Using the exceptionally large vein calcrete at Trench 14 as an example, it is possible to examine calcite accumulation in surface materials at the site. This vein calcrete forms a wedge, 2.25 m wide near the surface, that pinches down to a few centimeters width at 4.75 m depth. Six-tenths of the material in this wedge is laminated calcrete; the remainder consists of blocks of altered Tiva wall-rock tuff. The average bulk density of the calcretes is 1.6 g/cm^3. The average calcite weight fraction of the calcretes is 53 percent, leading to an estimated calcite abundance of 1.2×10^6 g per m^2 of overlying surface above this wedge of vein calcrete. Estimates of eolian carbonate accumulation rates for soils on noncalcareous parent materials in the Southwestern United States range from 0.3 to 5 g/m^2/y (Machette 1985; Reheis et al. 1992). At these rates, the amount of calcite within the excavated veins at Trench 14 could accumulate over a time span between 4,000,000 and 240,000 years (1/3 to 1/50 of the age of the wall-rock tuffs).

Carbon and oxygen isotopic data indicate that most of the calcite in Trench 14 was deposited during colder and wetter Pleistocene climates (Quade and Cerling 1990). The time spans

estimated here could allow pedogenic accumulation of ~0.4 to ~7 times the amount of the Trench-14 calcite within the 1.6 m.y. of the Pleistocene Epoch. Separate studies of calcite deposits in fractures of the unsaturated zone tuffs indicate that these calcites are derived from the surface, probably as the surface calcites are dissolved and transported downward (e.g., Whelan, Vaniman et al. 1994; Vaniman and Chipera 1996). Based on the analysis here, it appears that with the more rapid accumulation rates, and considering only the Pleistocene accumulations, ~6 times the amount of Ca bound in surface calcrete may be deposited as calcite at depth. This amount does not include the earlier deposits of isotopically distinct calcite that have been reported by Paces, Marshall et al. (1997).

Because the calcretes of Trench 14 are siliceous, it is possible to compare the rates of silica and calcite accumulation. Within the same calcrete wedge described above, the average opal weight fraction is 36 percent, leading to an estimated opal abundance of 0.8×10^6 g/m^2. The solubility of SiO_2 in arid soils containing abundant siliceous glass may exceed 0.07 g/L (Chadwick et al. 1989). However, waters in local higher-elevation soils at Rainier Mesa, Nevada, have SiO_2 contents of 0.02 to 0.04 g/L (Kerrisk 1987). For the SiO_2 concentration range of 0.07 to 0.02 g/L, 1.1 to 4.0×10^6 cm/cm^2 of rainwater can form enough soil water to deposit the opal within the calcrete wedge. Current rainfall at the elevation of Trench 14 is ~15 cm/year (Spaulding 1983). At this precipitation rate, sufficient rainwater could infiltrate, dissolve local silicates, and evaporate to form the opal in the vein calcrete within 70,000 to 270,000 years. The longer time estimate may be most appropriate, since the wetter and cooler climates that prevailed during calcrete formation (Quade and Cerling 1990) may have resulted in deposition from relatively silica-poor soil waters like those of Rainier Mesa. A 30 to 100 percent increase in rainfall during the Pleistocene (Spaulding et al. 1984) could shorten the longer estimate to as little as 135,000 years. As with the calcite calculations, the 1.6 m.y. duration of Pleistocene time would allow ~6 to ~10 times the amount of opal deposited at the surface to be deposited in fractures of the unsaturated-zone tuff. However, trace-element studies of calcites in the unsaturated zone suggest that glasses at depth have also been dissolved. The silica budget at depth in the unsaturated zone may therefore exceed that of calcite. This contradicts the results of Exploratory Studies Facility studies by Paces, Neymark et al. (1996), which suggest ~6 times as much calcite as opal in unsaturated-zone fracture deposits. Perhaps the most important consideration in assessing this discrepancy is the general undersaturation of Yucca Mountain waters with respect to amorphous silica (Vaniman and Chipera 1996). This result suggests that much of the silica dissolved from the surface will continue to travel to the water table, whereas calcite precipitation may be locally favored in the unsaturated zone.

6.1.4.4.2 Transition Metals and Eolian Contributions

Petrographic, chemical, and X-ray diffraction data indicate an enrichment in the Bt-soil horizons of heavy minerals (principally biotite, amphibole, oxide minerals, and some clinopyroxene; Vaniman, Chipera, Bish 1995). This effect is most notable in the <45 μm and clay fractions; indeed, the clays are notably Fe-rich (5 percent FeO, compared to <1 percent FeO in the bulk tuffs) and may be derived principally from the weathering of mafic minerals. Total concentrations of the heavy minerals are 4 to 6 percent in the <45 μm B-soil horizons, but these minerals are detectable only in trace amounts in the wall-rock tuffs. Disaggregation of the wall-rock tuffs in surface weathering, with subsequent deflation or slopewash, may remove lighter

minerals and leave the heavier minerals behind. However, a contributing factor in this process may be the addition of mafic eolian minerals.

Both the Bt horizons and the calcretes contain small amounts (≤1 percent) of amphibole fragments with characteristic pleochroism (α = light yellow-brown, β = brown, δ = green). These amphiboles occur as small grains, mostly <45 μm in diameter. The FeO contents of these small amphibole grains are mostly higher than the amphibole compositions that occur in the Tiva Canyon Tuff that is a local source of detritus (Warren, Byers, Broxton et al. 1989). Many of these amphibole fragments may be derived from distant sources and brought to Exile Hill by eolian processes.

If detrital grains, particularly those of silt to clay size, are in part brought to the site by eolian processes, then the mineralogic makeup of those sources may provide constraints on the relative proportions of local and distant contributions. Guthrie, Raymond, Chipera et al. (1993) have analyzed eolian dusts from four natural dust traps (under boulders above soil horizons or from fractures within boulders above the soil) near Exile Hill. They used X-ray diffraction methods to determine the quantitative mineralogy of the <425 μm fractions of these eolian samples and of several size fractions from one of them (Table 6.1-24).

In general, the mineral constituents of these eolian deposits are similar to the corresponding <425 μm and <45 μm fractions of the Btk- and 2Btj-soil horizons. Notable differences, however, are the rarity of tridymite and absence of cristobalite, higher feldspar content, and lower clay content (particularly smectite) in the eolian deposits. These differences may reflect the modifications that occur when local detritus is mixed with the eolian materials. Most important to this discussion, however, is the high content of Fe-rich heavy minerals in the eolian samples (amphibole, biotite, chlorite, and hematite total 3 to 7 percent in the <425 μm material and 9 percent in the <45 μm material).

Of the Fe-rich minerals common to the Bt-soil horizons and the calcretes, hematite is the most ubiquitous. Electron microprobe data for Fe-Mn and Fe-Ti contents of fine-grained (<45 μm) hematites from these three rock and soil types are summarized in Figure 6.1-62. The data available show strong similarities between hematites of the Bt-soil horizons and the calcretes but generally lower TiO_2 and higher MnO in the hematites of the local bedrock (Tiva Canyon Tuff). These differences indicate that there is a common source for hematite detritus in both the Bt-soil horizons and the calcretes. Although the data do not prove that the Bt horizon and calcrete hematites are brought in by eolian processes, the foreign compositions of amphiboles and hematites in the Bt horizons and calcretes suggest a large component of eolian input.

The most abundant detrital component of the calcretes, however, is the <425 μm fraction that provides almost all of the detrital nuclei for the very common calcrete ooids (detrital nuclei for the ooids average 163 ± 154 μm; only 5 percent are <45 μm). For this size fraction, in the B-soil horizons, Sc/FeO ratios and other chemical signatures align very well with those of the calcretes and with local tuffs (Vaniman, Chipera, Bish 1995). In this size range, detritus can be moved as drifting sand but is unlikely to be carried as an aerosol suspension from distant sources (Junge 1979). Silt- and clay-sized material in the B-soil horizons, however, may be partly to largely eolian in origin.

6.1.4.5 Quaternary Subsurface Processes

6.1.4.5.1 Evidence of Mineralogic Alteration

The available data contain no clear-cut indications that major mineralogic alteration has occurred during the Quaternary Period, at least in the unsaturated zone. Our inability to obtain reliable ages for zeolites and clays, the major products of diagenetic rock alteration in the unsaturated zone, forces us to rely on indirect observations and reasoning in assessing Quaternary rock alteration. In comparison, the geochronologic record from U-Th, U-Pb, and ^{14}C studies of calcite and opal deposition in fractures and voids is well documented. Yucca Mountain calcites have also been the subject of strontium isotopic studies. These investigations were undertaken to help place bounds on infiltration rates during the last twelve million years by assuming a proportional link between mineral deposition rates and fluid flux (Paces, Marshall et al. 1997). Additional goals include the development and testing of conceptual models of fluid infiltration, diversion, and mixing, and of water-rock interaction. This is an area of active research, in which conceptual models are being rapidly developed and modified. The implications of these studies for mineralogic alteration are summarized here.

Strontium isotopic data for rocks and leached pore salts from the unsaturated zone have been interpreted as indicating enhanced water-rock interaction within the Paintbrush Tuff nonwelded units above the Topopah Spring Tuff, even though the pore-fluid strontium never achieves equilibrium with the rock strontium (Sonnenthal et al. 1997; Marshall 1997). High porosity and permeability and high glass content and reactive surface area are the factors contributing to increased rates of water-rock interaction in the nonwelded tuffs relative to overlying and underlying densely welded tuffs. Part of the isotopic shift occurring within the nonwelded tuffs may be attributable to their somewhat higher strontium content relative to the Tiva Canyon and Topopah Spring Tuffs (Peterman, Spengler, Singer et al. 1993), rather than to enhanced water-rock interaction.

The data necessary for rigorous numerical modeling of strontium geochemistry as an indicator of water-rock interaction and fluid flux do not exist at present. Preliminary modeling efforts are primarily intended to place bounds on the percolation flux, and the rock reaction (dissolution) rate is one of the parameters required for numerical simulations of pore-salt strontium isotopic profiles. The simulations of Sonnenthal et al. (1997) used either the same reaction rates for all units of the Paintbrush Group or rates that are up to two orders of magnitude higher for the nonwelded tuffs than for the welded tuffs. The values themselves have no significance, but a reaction rate of 10^{-9}/year corresponding to about 1 percent alteration in 10 m.y. is thought to be about the right order of magnitude for welded Topopah Spring Tuff. The assignment of a reaction rate two orders of magnitude higher to the nonwelded, vitric tuffs would correspond to more than 10 percent alteration. Based on the natural alteration of the Paintbrush nonwelded tuffs (Levy and Chipera 1997), such reaction rates may be reasonable upper bounds on Quaternary rates of alteration in these tuffs. The rates may be considered conservative because they are expected to have negligible effects on the hydrologic properties of the Paintbrush nonwelded tuffs in a 10,000 year period (Sonnenthal et al. 1997).

6.1.4.5.2 Mineral Deposition in Fractures and Voids

The record of calcite and opal deposition in fractures and voids of the Topopah Spring Tuff is a subject of active research and is becoming increasingly well documented through studies of samples from the Exploratory Studies Facility (e.g., Paces, Neymark et al. 1996; Paces, Marshall et al. 1997). The study results indicate that deposition of calcite and opal have been ongoing processes during at least the last eight to ten million years.

6.1.4.5.3 Cation Exchange in Heulandite-Clinoptilolite

Hay (1963), studying zeolitization in the John Day Formation of Oregon, noted that the proportions of exchangeable cations, principally Na, Ca, and K, may have been modified at any time after the zeolites were formed. This process has been confirmed for the zeolitic rocks of the Topopah Spring lower devitrified-vitric transition zone. Figure 6.1-63 shows the exchangeable-cation compositions for heulandite-clinoptilolite in this zone from outcrop and from the saturated and unsaturated zones in drillholes. The zeolites were formed in the devitrified-vitric transition zone by moderate-temperature hydrothermal alteration during the cooling of the pyroclastic deposit (Levy and O'Neil 1989). The original cation compositions probably were not homogeneous, but the analyses from outcrop samples define a separate population depleted in Na and enriched in Ca + K. Exchangeable cation compositions of zeolites from outcrop have diverged from the compositions of subsurface zeolites, which may have changed as well, but do not seem to represent extremes of composition like the outcrop data.

Existing data are insufficient to determine whether the shifts in exchangeable-cation composition are restricted to zeolites in surface rocks or extend into the shallow subsurface. There is a gap in the heulandite-clinoptilolite compositional data because drillholes at Yucca Mountain are not situated where the Tpt lower vitrophyre occurs at depths less than about 300 m. Because of this limitation, the only documentation of the compositional shift is from surface samples. Studies of erosion and slope stability at Yucca Mountain (DOE 1993) suggest that the present topography is of the order of hundreds of thousands of years old. This should be about the same period of time in which cation exchange between shallow infiltrating water and heulandite-clinoptilolite produced the distinctive exchangeable-cation compositions of the surface zeolite samples.

Exchangeable-cation data for diagenetic clinoptilolites show a similar pattern of K, but probably not Ca, enrichment for outcrop samples (Broxton, Warren, Hagan et al. 1986). The data set contains fewer analyses of outcrop clinoptilolites than the comparable set for transition zone heulandite-clinoptilolite, and may be biased by the locations of the samples close to a possible source of potassic alteration. Within the limits of the data, there is no strong indication that exchangeable-cation compositions of clinoptilolite within Yucca Mountain below the potential repository are changing significantly. In the major zeolite barriers beyond those zones where repository temperatures exceed 100°C, significant change in the future is unlikely. This means that radionuclide sorptive behavior related to the exchangeable-cation composition of clinoptilolite can be confidently modeled from the existing data.

6.1.5 Implications for Paleohydrology, Flow Paths and Rates, and Evidence of Past Radionuclide and Analog Transport

6.1.5.1 Paleohydrology

6.1.5.1.1 Past Positions of the Static Water Level Based on a Conceptual Model of Zeolitization at Yucca Mountain

The zeolitization chronology of the Crater Flat Group, the Calico Hills Formation, and the Topopah Spring Tuff has been partly reconstructed from information about the distribution of zeolitized rocks in these units at Yucca Mountain, the progressive tilting and faulting of the mountain, and microscopic evidence of tilting recorded by textural features called geopetal fillings in zeolitized rocks (Subsection 6.1.4.2.3.1). Two key pieces of evidence suggest that zeolitization in most of the Prow Pass Tuff took place before the Topopah Spring Tuff was deposited. First, the Prow Pass Tuff is the youngest pyroclastic unit that is largely zeolitized in all Yucca Mountain drillholes. The vitric-zeolitic transition lies within the Prow Pass Tuff in the three holes–G-3, H-3, and H-5–where the Prow Pass Tuff is structurally high and also in H-6 on the downdropped western side of the Solitario Canyon fault zone about 2 km southwest of H-5. In H-6, both the stratigraphic top of Prow Pass Tuff and the vitric-zeolitic transition are about 40 m lower than in H-5.

The picture that emerges from this information is of alteration in a flat-lying or slightly-inclined Prow Pass Tuff, producing a vitric-zeolitic transition zone of relatively flat orientation. Subsequent deformation produced the more steeply inclined and faulted feature seen today. In Southern and Western Yucca Mountain, the Prow Pass Tuff is at a higher elevation and the vitric-zeolitic transition within the unit has been preserved, whereas in the eastern part of the mountain, the tuff unit is at a lower elevation and the vitric-zeolitic transition has been overprinted by later zeolitization.

The second key piece of evidence is the chronology of tectonic tilting. Tilting and faulting were at least intermittently active until the Rainier Mesa Tuff was deposited (Levy 1984c; Sawyer et al. 1994; Scott, Spengler et al. 1983). The cumulative offset of the Prow Pass Tuff is greater than in the two overlying younger units because tilting occurred after each of the three units was deposited. By the time the Topopah Spring Tuff was deposited, the Prow Pass Tuff was already tilted close to its present attitude. The Prow Pass unit around G-3 and H-3 probably was structurally high enough to be above the static water level. The maximum duration of zeolitization around G-3 and H-3 would have been the age difference between the Prow Pass and Topopah Spring Tuffs, about 0.3 Ma (Sawyer et al. 1994).

The history of tectonic tilting and the age of the Rainier Mesa Tuff constrain the timing of the later zeolitization in the remaining glassy portion of the Prow Pass Tuff, the Calico Hills Formation, and the lower nonwelded part of the Topopah Spring Tuff in the structurally low central-eastern part of Yucca Mountain. A temporal connection between tilting and zeolitization has been established by microtextural studies of geopetal fillings (Levy 1984b, 1984c; also, see Subsection 6.1.4.2.2.1). These fillings are layered deposits of opal and clinoptilolite in small pores. The deposits were formed by colloidal particles settling out of water, and the layers were horizontal at the time of deposition. Many of the pores in which fillings were deposited are

cavities formed by dissolution of the last remaining glass shards, indicating that the geopetal fillings postdate most of the zeolitic alteration, at least on a local scale.

Tectonic tilting was recorded by the geopetal fillings in the lower Topopah Spring Tuff in drillhole G-4, a few meters below the vitric-zeolitic transition in the structurally low part of the mountain. These are the youngest rocks affected by pervasive zeolitization. The 11.6 Ma age of the untilted Rainier Mesa Tuff overlying the older units places a minimum age on the timing of tectonic tilting (Sawyer et al. 1994; Scott, Spengler et al. 1983) and, by inference, of zeolitization.

The Paintbrush Group and older rocks at drillhole H-6 have been downdropped relative to the H-5 section along the north-south-trending Solitario Canyon fault zone between the two holes. This offset has placed unaltered vitric, nonwelded tuffs in H-6 at a lower elevation than the vitric-zeolitic transition in the central-eastern drillholes. Exact elevation differences between the transitions at the two locations cannot be determined because the transition in H-6 is artificially fixed at the base of a 43 m devitrified zone (Craig, R.W. et al. 1983), but the vitric nonwelded rocks above the devitrified zone in the hole are about 16 m lower than the vitric-zeolitic transition in G-4 (which approximates the lowest true position of the transition in Yucca Mountain proper). The vitric tuff in H-6 remains unaltered because a significant part of the fault offset occurred only after the static water level had dropped well below the zeolitic transition. Thus, the timing of static water level drop can be constrained by the chronology of faulting, which is, in turn, constrained by igneous chronology.

Fault offset of the 12.7 Ma Tiva Canyon Tuff, measured north of H-5, is about 15 m, whereas offset of a 10 Ma unit at the same site is less than 2 m (Carr 1984). In Solitario Canyon west of G-3, the Tiva Canyon Tuff is offset by about 30 m and deposits of the 11.6 Ma Rainier Mesa Tuff are displaced less than 5 m. Therefore, the increment of fault offset that dropped the vitric tuffs in H-6 below the zeolitic transition in G-4 probably occurred no later than 11.6 Ma. The maximum age limit on the timing of offset may be the 12.7 Ma Tiva Canyon age, and the offset cannot be any older than the 12.8 Ma age of the Topopah Spring Tuff. The establishment of the static water level within the lower Topopah Spring Tuff in the central-eastern part of Yucca Mountain, the zeolitization in that unit, and the subsequent lowering of the static water level also took place during this time interval but before the downdropping of the H-6 section.

Major events in the history of the saturated-zone boundary at Yucca Mountain during the last 13 Ma are summarized schematically in Figure 6.1-64. Based on the present distribution of vitric and zeolitized nonwelded tuffs, the vitric-zeolitic transition in the central-eastern part of Yucca Mountain probably marks the highest static water level established at the mountain during the last 12.8 Ma (about 120 m above the present static water level). The static water level remained at its highest position no more than 1.2 Ma. Subsequent water levels may have existed at higher elevations than the present static water level (about 120 m below the zeolitic transition in G-4) but have not been any higher than 16 m below the zeolitic transition and perhaps no higher than 59 m below the transition (adding the 43 m thickness of the devitrified zone in H-6 to the 16-m depth of glassy tuff below the transition). This reconstruction is applicable to central Yucca Mountain but does not extend to the vicinity of drillhole G-2 to the north because available data are insufficient to justify a northward extrapolation.

Tridymite Distribution–Tridymite is a crystalline silica polymorph that is a minor constituent of devitrified tuffs in the Yucca Mountain region. The tridymite distribution at Yucca Mountain is an example of a possible static water level related mineral distribution pattern tentatively identified from drillhole sample sets collected to characterize the site mineralogy. Based on drillhole X-ray diffraction data from Yucca Mountain proper and from several sites east of the mountain, it has been suggested that tridymite is not found below the present static water level (Bish and Chipera 1989; Bish, Ogard et al. 1984). The absence of tridymite below the static water level has been attributed to recrystallization of tridymite to quartz in the presence of water. The published Yucca Mountain data do, however, document an exception in drillhole J-13 (Bish and Chipera 1989). These indications of a possible pattern, even if imperfect, merit a more detailed investigation of tridymite occurrences on a unit-by-unit basis.

The pyroclastic units in which tridymite is found, in order of increasing age and depth, are the Tiva Canyon Tuff, the Topopah Spring Tuff, the Prow Pass Tuff, and the Bullfrog Tuff. Within the Tiva Canyon and Topopah Spring Tuffs, tridymite is mostly in lithophysal zones within densely welded, devitrified tuff. Crystals up to 0.1 mm long occur in small aggregates within the groundmass of the tuffs or as void fillings in gas cavities and fractures. Tridymite in Prow Pass and Bullfrog devitrified tuffs is in small lithophysae and cavities formed by the recrystallization of pumice clasts and may be in the groundmass as well. Individual crystals are less than 0.05 mm long.

Because the Tiva Canyon Tuff is above the static water level at all Yucca Mountain and eastern drill sites and is partly above the static water level in VH-1 west of the mountain, there is no basis for comparison of mineral content in this unit above and below the static water level. Tridymite has been detected by X-ray powder diffraction in seven of eight drillholes from which substantial numbers of Tiva Canyon samples have been analyzed.

Of 13 drillholes for which Topopah Spring whole-sample X-ray diffraction data were examined, 12 contain detectable tridymite. Samples from the exceptional hole, H-6, contain small concentrations of optically identifiable tridymite. Two drillholes east and west of Yucca Mountain contain tridymite below the static water level. Tridymite in J-13 occurs from about 38 m above to about 54 m below the static water level. In VH-1, where the Topopah Spring section is entirely in the saturated zone, tridymite is present as much as 175 m below the static water level (Levy 1991).

Fewer data are available for the Prow Pass and Bullfrog Tuffs. Tridymite has been detected by X-ray diffraction in the Prow Pass Tuff in holes G-3 and H-3 (out of 11 holes with relevant data) and in the Bullfrog Tuff in G-3 (out of five holes with data). The fine-grained character and low abundance of tridymite in these units make it difficult to check optically for tridymite present in amounts below the X-ray diffraction detection limit of ~2 wt% (Bish and Chipera 1989 note that in routine analysis the detection limits for most minerals are less than 1 wt%). G-3 and H-3 are also the only holes in which the Prow Pass sections are entirely above the static water level, and G-3 is the only hole in which any of the Bullfrog Tuff is above the static water level. The 1-km proximity of the two holes and the uncertainty inherent in negative data make it difficult to eliminate original lateral variability in tridymite content or sampling shortcomings as alternative explanations for the restricted occurrence of the mineral. For the purpose of discussion, the distribution data are assumed to be representative and to reflect post-crystallization conditions.

The deepest tridymite occurrences in the Crater Flat Group are approximately 60 m (G-3) and 30 m (H-3) below the vitric-zeolitic transition zone. Hydrologic conditions favorable to zeolitization around Yucca Mountain must have lasted long enough for the vitric nonwelded tuffs above and below the tridymite-bearing rocks to be altered but not long enough for the tridymite to recrystallize. The maximum duration of water-rich conditions associated with this early zeolitization episode was estimated from the conceptual model of zeolitization to be about 0.3 Ma.

The latest episode of zeolitization affecting the low-lying tuffs of central-eastern Yucca Mountain lasted up to about 1.2 Ma from the deposition of the Topopah Spring to the deposition of the Rainier Mesa Tuff. In this location, the maximum cumulative exposure of the Crater Flat Group to water-rich conditions represented by the two periods of zeolitization was about 1.5 Ma. Because most or all of the Crater Flat Group is currently below the static water level in this area (G-1, G-4, H-4, UE-25 a#1, and J-13), the absolute maximum possible exposure could have been as much as ~13 Ma, the age of the unit. The difference between these two time estimates is so large that additional duration-limiting data are needed to make tridymite recrystallization a useful paleohydrologic indicator. Possible sources of additional data might be drillholes in which the Crater Flat Group is situated at elevations intermediate between the high positions of G-3 and H-3 and the central-eastern drillhole locations where the unit is presently below the static water level. The goal would be to obtain samples from several locations where the Crater Flat Tuff was low enough to have experienced both zeolitization episodes but high enough to be above the present static water level. In these locations, the Crater Flat Tuff would have been exposed to water-rich conditions for variable time periods less than 13 Ma. The consistent absence of tridymite from the Crater Flat Tuff in such holes would tend to favor an exposure time closer to the lower estimate. Additional information could be obtained by examination of existing material from H-5. X-ray diffraction data from a few of the newer Q holes could be incorporated into this study.

One potential use of a tridymite paleohydrologic indicator would be to investigate the history of the high-potentiometric gradient across Northern Yucca Mountain that separates a region of relatively high static water level (generally west of the Solitario Canyon fault) from the lower static water level of Central and Southern Yucca Mountain (Waddell et al. 1984). This large-scale feature is thought to indicate the presence of low-permeability rocks in the saturated zone beneath parts of Yucca Mountain but has also been cited as evidence for major in-progress hydrologic changes in response to changing tectonic stresses. With a combination of existing and new data, it may be possible to estimate how long the static water level west of the mountain has maintained its position.

6.1.5.2 Flow Paths and Rates

6.1.5.2.1 Natural Record of Strontium Migration at Yucca Mountain

Strontium distributions in Bulk-Rock Tuff with depth are shown for drillholes UE-25 UZ#16 and USW SD-12 in Figures 6.1-65 and 6.1-66. Evidence of the bulk-rock interaction with groundwater can be seen in these Sr data. The vitric and devitrified tuffs contain very little Sr, but there is a strong correlation between Sr abundance and sorptive phases (especially clinoptilolite/heulandite) in particular portions of the zeolitic horizons. Pronounced

concentrations of Sr occur in UE-25 UZ#16 within an interval of less than 20 m at the top of the major zeolitized horizon beneath the Topopah Spring Tuff (Figure 6.1-65). This result provides direct evidence of the effective extraction of Sr from downward-flowing solutions at Yucca Mountain since the time of zeolite formation. A comparable but more complex picture of the selectivity of zeolites for Sr is seen in USW SD-12 (Figure 6.1-66). Here Sr retention peaks are found in three different zeolitized horizons: peak (a) at the top of the pervasively zeolitized but low-zeolite-abundance zone that extends from the base of the Topopah Spring Tuff through the Calico Hills Formation, peak (b) in the bedded tuffs beneath Calico Hills, and peak (c) at the top of the high-zeolite-abundance zone at the bottom of the Prow Pass Tuff. In occurrences (a) and (c), it is evident that Sr has been removed from the downward-percolating groundwater by the sorptive zeolites. As downward-flowing groundwater encountered these two zeolite-altered horizons, the upper portion of each zeolite sequence stripped Sr from solution, leaving little if any Sr in the groundwater as it proceeded through the remainder of the zeolite sequence. Evidence for effective Sr sorption at point (a), where zeolite abundances are only 2 to 3 percent, emphasizes the very effective interaction of even small amounts of zeolite with groundwater at Yucca Mountain. The Sr peak at (b), within the bedded tuffs beneath the Calico Hills Formation, represents the high original Sr content of the crystal-rich bedded horizons (the bedded tuff contains ~200 to 333 μg/g Sr; the basal "sandstone" interval of the bedded tuff contains up to ~700 μg/g Sr; Moyer and Geslin 1995) and does not reflect Sr transport and accumulation. Both Figures 6.1-66 and 6.1-67 illustrate the high selectivity of zeolites for Sr; the consequence of this selectivity will be a depletion in groundwater Sr contents, an effect that is seen in the record of Sr content in calcites deposited from these groundwaters.

The Sr abundance data in calcites (Figure 6.1-67) add some detail to the distinction of possible sources for this element in calcites at Yucca Mountain. The most Sr-rich sources yet found at Yucca Mountain are the mineral constituents of plant roots, which contain 1,311 to 3,820 μg/g Sr (boxthorn, creosote bush, and Mormon tea; Vaniman and Whelan 1994; Vaniman, Chipera, Bish 1995). These mineral constituents, obtained by low-temperature ashing, are partially amorphous. However, in all of the roots analyzed, the low-temperature ashing products are ~3/4 whewellite ($CaC_2O_4 \cdot H_2O$), which is the only identified authigenic crystalline phase within the roots. When Sr is modeled specifically as a substitute for Ca in whewellite (that is, when Sr is whewellite-normalized), the calculated Sr contents of the whewellite are 1,677 to 5,091 μg/g. Whewellite is not found outside of the roots, but very fine-grained (<5 μm) Sr-rich calcites occur in the surface calcretes at Yucca Mountain with model Sr contents of 800 to 2,100 μg/g (Vaniman, Chipera, Bish 1994). Denniston (1995) analyzed a coarser-grained calcite (~1 mm) from the calcrete by secondary ion mass spectrometry and obtained much lower Sr contents (52 to 89 μg/g). The deepest fracture-filling calcrete analyzed for this report (UZ#16 at 12 m), although fine-grained like the surface calcrete, has a model calcite Sr content of only 170 μg/g. It thus appears that the surface environment and rapid crystallization rates are required to maintain high Sr contents in the unsaturated zone (> 800 μg/g); either slower precipitation at the surface (that is, coarsening grain size) in isolated calcrete voids or crystallization at depths sufficient to preclude evaporative cycling will result in reduced Sr content of unsaturated zone calcites.

The unsaturated zone calcites from the lower lithophysal zone of the Topopah Spring Tuff in G-2 have distinctly lower Sr contents (11 to 94 μg/g) in comparison with the Sr range in calcites from the same horizon in other cores (60 to 338 μg/g). The exceptionally low Sr contents in the G-2

calcites may reflect the removal of Sr from recharge waters by passage through the thick clinoptilolite horizon that occurs above the Topopah Spring Tuff in this core but not in the other cores. Devitrified or vitric tuffs in the local unsaturated zone hydrologic environment that do not contain hydrous or carbonate alteration minerals have Sr contents <175 μg/g; local zeolitic and clay-altered tuffs can contain 400 to > 1,000 μg/g Sr. It is therefore likely that Sr is accumulated from aqueous solution as zeolites and clays form or by cation exchange from subsequent flow. In either case, the recharge waters flowing through the zone of zeolitization above the Topopah Spring Tuff in G-2 may lose much of their Sr, resulting in Sr-depleted calcites at greater depth.

Although the Sr contents of calcites in G-2 are low, even lower Sr concentrations can occur in calcites from the barren interval that extends from the base of the Topopah Spring Tuff to the deep carbonate-altered zone (Figure 6.1-67). Calcites from this interval may have as little Sr as 1 μg/g. Although these calcites occur in both unsaturated and saturated environments, they share a common association with zeolites and smectites. The calcites from the base of the Topopah Spring Tuff occur in the altered smectite- and zeolite-bearing top of the rhyolitic vitrophyre, just beneath this vitrophyre, or actually within the clinoptilolite-bearing sequence at the very bottom of the Topopah Spring Tuff. Deeper calcites from the saturated portion of the barren zone occur in transmissive devitrified tuffs that are sandwiched between thick intervals of clinoptilolite- and mordenite-bearing tuff. In all of these cases, there is abundant local zeolite and/or smectite to accumulate Sr, further depleting it in an environment where slowly precipitating calcite will tend to exclude Sr anyway.

6.1.5.2.2 Lanthanide–Elements and Fracture Minerals at Yucca Mountain

The lanthanide elements (La to Lu, referred to as a group by the symbol "Ln"), are exceptionally useful as geochemical tracers. Figure 6.1-68 summarizes the lanthanide-element distributions in calcites relative to host-rock stratigraphy. These data, normalized to chondrites, generally vary in abundance by a factor of ~10 to 50 within any given stratigraphic unit for which sufficient calcite analyses have been obtained to determine variability. Denniston (1995) was able to find approximately the same or a slightly higher range in lanthanide-element concentration within individual calcite crystals using secondary ion mass spectrometry analysis. In addition to these variations in overall lanthanide-element abundance, there are several features of the chondrite-normalized data that also vary with stratigraphic position. Much of the text that follows deals with anomalies in abundance of Ce in chondrite-normalized plots of lanthanide-element abundances. Anomalous Ce abundances, relative to the other lanthanide elements, are rare in igneous and hydrothermal systems but common in lower-temperature oxygenated or high-pH aqueous and soil systems (see references in Vaniman and Chipera 1996). In the text that follows, chondrite-normalized values of the lanthanide elements (Ln) are represented as "LnN." Chondrite values (μg/g) used for normalization are La(0.33), Ce(0.88), Nd(0.6), Sm(0.181), Eu(0.069), Tb(0.047), Yb(0.2), and Lu (0.034). Because Pr and Gd data are not available for estimating model Ce* and Eu* (zero anomaly) values in the chondrite-normalized system, these model values are approximated as $(LaN^2NdN)^{1/3}$ for Ce* and $(SmN^2TbN)^{1/3}$ for Eu*. However, because of the large distance in atomic number between the lanthanides used for these approximations and because of the somewhat poorer precision in Nd data by instrumental neutron activation analysis, the simple ratio of chondrite-normalized values (N) for LaN/CeN and SmN/EuN are also used. Both approaches were used in evaluating the data and the same conclusions can be reached using either method.

Within the mined workings of the Exploratory Studies Facility beneath Trench 14, calcites from shallow depth (13 to 48 m), represented by clean euhedral crystals rather than calcrete, have moderate light-lanthanide enrichment and no evidence of a Ce anomaly (Figure 6.1-68b). At 48 m, the deepest of these calcites occurs at a depth where calcites with negative Ce anomalies can be found in the same host rock (the Tiva Canyon Tuff) to the southwest at Yucca Mountain (Figure 6.1-68c). The occurrence of exceptionally open fractures at Exile Hill, in the footwall of a major normal fault (the Bow Ridge Fault), may be evidence of a more direct link to the surface than is generally common at Yucca Mountain. Additional data from calcites deeper in the Exploratory Studies Facility are summarized in Figure 6.1-69, representing the Tiva Canyon Tuff (Tpc) and the middle nonlithophysal portion of the Topopah Spring Tuff (Tptpmn).

The majority of the Tiva Canyon Tuff, aside from the Exile Hill samples, is characterized by calcites with prominent negative Ce anomalies (Figures 6.1-68c and 6.1-69). Even a calcrete sample at 12 m depth, with abundant root fossils, has developed a moderate negative Ce anomaly. This result contrasts with calcretes nearer the surface that has no Ce anomaly (Vaniman, Chipera, Bish 1994). In addition to the development of the Ce anomaly, the Eu anomalies in these calcites are deeper than those of Exile Hill (Eu/Eu* <0.1 in most samples versus 0.1 to 0.5). The chondrite-normalized patterns are also generally flatter with little or no light-lanthanide enrichment. This type of pattern is characteristic throughout most of the unsaturated zone, but significant deviations are prominent at just slightly greater depth in the devitrified quartz-latite subunit at the top of the Topopah Spring Tuff.

Within the devitrified quartz latite of the Topopah Spring Tuff, the calcite lanthanide patterns can deviate markedly from those in the rest of the subsurface unsaturated zone. Calcites of this interval from G-4 have little or no Eu anomaly and only a very slight Ce anomaly (Figure 6.1-68d). A calcite from drill core UE-25 A-7 has no Eu anomaly but a very deep negative Ce anomaly. Calcites from G-1 are more similar to calcites above and below, with both Ce and Eu anomalies, but like the other calcites of this quartz-latitic unit, they have a positive light-lanthanide enrichment. More than any other stratigraphic level, the quartz latite of the Topopah Spring Tuff has calcites with highly variable lanthanide compositions.

In contrast, calcites throughout the bulk of the devitrified rhyolitic Topopah Spring Tuff (Figure 6.1-68e through 6.1-68g and 6.1-68i) are characterized by a fairly constant chondrite-normalized lanthanide pattern that is relatively flat, with the sample/chondrites value between 1 and 10 and with prominent negative Ce and Eu anomalies (Ce/Ce* = 0.01 to 0.11; Eu/Eu* = 0.03 to 0.17). The only significant deviation from this range of patterns is in G-2 (Figure 6.1-68h), in which calcites from the lower lithophysal portion of the Topopah Spring Tuff have significantly higher sample/chondrites values (20 to 200) and deeper Ce anomalies (Ce/Ce* = 0.004 to 0.012).

Calcite abundances drop off significantly in the tuffs located approximately 100 to 300 m above the water table to 400 m below; this "barren zone" separates unsaturated-zone and saturated-zone calcites of isotopically distinct origins but contains calcites with lanthanide-element signatures that record transport processes similar to the overlying unsaturated zone (Vaniman and Chipera 1996; Figure 6.1-68). Lanthanide patterns for calcites of the barren zone are shown in Figures 6.1-68j (unsaturated zone barren zone) and 6.1-68k (saturated zone barren zone). Cerium anomalies are deep in these calcite samples (Ce/Ce* as low as 0.001). Most of the

calcites in the barren zone have light-lanthanide enrichment and typically have positive chondrite-normalized slopes that are consistent from La to Lu.

Calcites of the deep saturated zone, which are distinctly Mn rich, are also distinctive in having no significant Ce anomalies and both negative and positive Eu anomalies (Figure 6.1-68l). A similar pattern is found in dolomite of the Roberts Mountain Formation obtained from deep drilling on the eastern edge of Yucca Mountain (Vaniman, Chipera, Bish 1995). More distinctive than the lanthanide patterns, however, is the abundance of Mn (0.25 to 5.8 percent MnO) in these calcites and local intergrowths with dolomite (Vaniman 1994; Denniston 1995).

6.1.5.2.3 Europium and Cerium Anomalies in Calcites and Tuffs as Evidence of Rock Dissolution and Transport

Figure 6.1-70a illustrates the variability in EuN (chondrite-normalized Eu) and SmN (chondrite-normalized Sm) abundances and ratios of calcites from Yucca Mountain compared with the tuffs that occur at the site. The tuff compositions plotted represent the ranges of local rhyolitic and quartz-latitic samples split into both whole-rock and glass-separate analyses. The ratios of EuN/SmN are lower in glasses that are analyzed separately from their feldspar phenocrysts. Most of the calcites at Yucca Mountain fall in a band that passes through the field of rhyolitic compositions; the exceptions are the calcites of the carbonate-altered zone, which scatter over a broader zone with no obvious single source, and four calcite samples from the quartz-latitic subunit of the Topopah Spring Tuff that have little or no Eu anomaly. These latter samples fall near a line of EuN/SmN with the same slope as that of the line passing through the other calcites from above the carbonate-altered zone but having a quartz-latitic rather than a rhyolitic ratio of EuN/SmN. Only drillhole USW G-1 has calcite from the Topopah Spring Tuff quartz latite that fall within the rhyolite rather than quartz latite trend. Note also that some Trench 14 and Exploratory Studies Facility samples can have EuN/SmN ratios that differ from other samples. The unsaturated-zone carbonates at Yucca Mountain proper may thus be geographically distinct from those formed to the east in the vicinity of Trench 14 and the Exploratory Studies Facility portal; however, more data are needed from the Exploratory Studies Facility to test this possibility.

Figure 6.1-70b shows a comparable plot of CeN versus LaN. Here, the calcites from all depths, except those of the Exploratory Studies Facility and Trench 14 and of the carbonate-altered zone, scatter in a broad field beneath the linear trends for rhyolite and quartz-latite tuffs. Clearly, the calcites beneath this line are significantly Ce-depleted compared to the tuffs, the Trench 14 and shallow Exploratory Studies Facility calcites, and the deep hydrothermal calcites of the Yucca Mountain region. For purposes of the discussion that follows, analyses of several Mn-oxide concentrates are also shown in Figure 6.1-70b.

The distribution of lanthanides in Yucca Mountain calcites, demonstrated by EuN/SmN ratios in Figure 6.1-70a, points directly to leaching from local quartz latite or rhyolite sources. The preponderance of calcite with rhyolitic rather than quartz-latitic sources agrees with the much greater abundance of rhyolitic tuffs at the site. Moreover, the calcites with quartz-latitic EuN/SmN (Figure 6.1-70a) and LaN/SmN ratios (Figure 6.1-68d) occur directly beneath the only significant body of quartz-latitic and quartz-latite-like glass (the Topopah Spring Tuff quartz latite and the Pah Canyon low-silica rhyolite) at the site. This location is exactly where these

calcites should occur if downward-flowing waters in the unsaturated zone are perched on top of the Topopah quartz latite vitrophyre, react with the quartz-latitic glass, and then resume downward flow.

In contrast to the calcite EuN/SmN ratios, which deviate little from those of their tuff sources, the Ce anomalies that are defined by CeN/LaN in Figure 6.1-70b vary strongly and, in most calcites, deviate radically from those of the tuff sources. The initial condition for this variability in Ce is the requirement of a high-pH or oxidizing environment, in which Ce^{3+} is oxidized to Ce^{4+}, whereas the other lanthanides remain Ln^{3+}. Among the authigenic minerals known at Yucca Mountain, the likeliest competitors for Ce^{4+} from unsaturated zone and shallow saturated zone waters are the Mn oxides. Although these are trace phases, present in abundances less than calcite (which is itself a minor phase in most of the unsaturated zone), the Mn oxides can incorporate exceptionally large amounts of Ce. Carlos, Chipera, Bish et al. (1993) report electron microprobe data for CeO_2 in several fracture-lining Mn oxides from Yucca Mountain: cryptomelane-hollandite series minerals (0.2 to 0.6 percent CeO_2), pyrolusite (0.2 to 0.9 percent CeO_2), and particularly high values in rancieite (1 to 8 percent CeO_2). Denniston (1995) reported ICP-MS analyses of some Mn-oxide rich separates that had been prepared and characterized by Carlos, Chipera, Bish et al. (1993); CeN/LaN compositions for these Mn-oxides are shown in Figure 6.1-70b. The rancieite-bearing sample in particular has a strong positive Ce anomaly, complementary to those of the Ce-depleted calcites and with concentrations of the other LnN over an order of magnitude higher than those of the calcites, providing a very effective sink for Ce (see Vaniman and Chipera (1996) for a more detailed discussion). Some sink for Ce is necessary because the initial water compositions infiltrating into Yucca Mountain do not have Ce anomalies. The evidence for this is provided by calcites precipitated in calcretes at the surface of Yucca Mountain. Here the waters have not yet penetrated into Mn-oxide bearing fractures and the calcites in the calcretes have no Ce anomalies.

Lanthanide-element data for the calcites of Yucca Mountain indicate at least two distinct depositional environments; an upper oxidizing system in which solutions that precipitate calcite favor Ce^{4+} over Ce^{3+} and a deep carbonate-altered system in which all of the lanthanide elements are Ln^{3+}. The characteristic negative Ce anomalies in calcites of the oxidizing system are present in both unsaturated zone and upper saturated zone rocks. Mn-oxide minerals, particularly rancieite but possibly others, appear to provide the single most important sink for Ce^{4+} at Yucca Mountain. The virtually universal negative Ce anomalies of oxidizing-zone calcites suggest that all flowpaths in the upper 1 km of Yucca Mountain have some effective contact with Mn oxides. This observation is important in considering the potential impact of Mn oxides, and other trace phases, on radionuclide transport at this potential disposal site for high-level radioactive waste. Studies specific to Yucca Mountain point to the potentially significant retardation of radioactive wastes by Mn oxides (Zielinski 1983; Zielinski et al. 1986). However, when such minerals are present in only trace amounts, it is uncertain whether fluids can actually interact effectively with such scarce materials. At Yucca Mountain, the universal record of Ce depletions in calcites of the subsurface oxidizing zone, which includes the proximal portions of all transport pathways for radioactive waste, provides a strong indication that fluids do interact with these minerals, despite their low abundance. The calcite data show that trace minerals, particularly those along fractures, will play an important role in radionuclide interactions should waste be emplaced at

Yucca Mountain. Sorption studies with trace minerals, and particularly with trace minerals distributed along fractures, are discussed in Subsections 6.1.8.2 and 6.3.

6.1.5.2.4 Synopsis: What are the Important Minerals for Retarding Radionuclide Transport?

From the data available, it is possible to draw the conclusion that there are three principal minerals (or mineral groups) that are most important as barriers against possible radionuclide migration at Yucca Mountain. The sorptive zeolites (clinoptilolite, mordenite, chabazite) provide the most massive and mappable barriers at Yucca Mountain. Whether their interactions are strong (as with Sr and Cs) or weak (as with Np), their sheer abundance makes them a formidable obstacle to cationic radionuclide transport. Smectites are not nearly as abundant, but their more ubiquitous occurrence virtually ensures that all transport pathways will eventually encounter some of these clays. Their strong affinity for Pu makes them a valuable barrier. Mn-oxides are less abundant and not as widely distributed as smectites, but their common association with transmissive fractures in the saturated zone and recent evidence of strong Np interactions makes them a key barrier to transport.

In addition to these three mineral groups (zeolites, smectites, and Mn-oxides), there are other potential barrier materials that may or may not be crystalline. This point is mentioned because of the specific and strong interaction of Pu with amorphous Fe alteration of orthopyroxene phenocrysts in the devitrified Prow Pass Tuff. Such features can make horizons that are otherwise unremarkable as barriers, such as the devitrified Prow Pass Tuff with no zeolites and few smectites or Mn-oxides, into effective components of the multiple mineralogic barriers to radionuclide transport at Yucca Mountain.

6.1.5.3 Stability of Sorptive Zeolites Based on Paleogeothermal Studies–Site-Specific Studies

Natural analog studies of paleogeothermal processes in tuffaceous rocks have the advantage of providing information on geochemical processes that have occurred in field-scale systems over time spans of hundreds to millions of years. In this way, natural systems offer an opportunity to circumvent the slow reaction kinetics of mineralogic transformations that hamper conventional laboratory studies of reaction kinetics. Yucca Mountain itself has proved to be a valuable self-analog, with the unique advantages of precisely relevant lithology and mineralogy.

The alteration history from about fourteen to eleven million years ago was a repeating sequence of pyroclastic deposition, localized syngenetic alteration, and zeolitization of glassy nonwelded tuffs below the static water level in existence at the time. Tectonic tilting that occurred during this period affected the distribution of vitric and zeolitic rocks by lifting the rocks of Southwestern and Western Yucca Mountain above the highest position ever reached by the static water level. Regional hydrothermal alteration in the saturated zone was associated with Timber Mountain caldera activity about 11 to 9 million years ago. This alteration included the increasing illitization of mixed-layer illite/smectites and the recrystallization of clinoptilolite to analcime. Geochemical and mineralogic processes in effect since that time include the genesis of new clays in the saturated zone and the modification of the exchangeable cation content of heulandite-clinoptilolites, at least in the shallow unsaturated zone. Meteoric recharge into the

unsaturated zone has deposited calcite and opal in fractures and voids as much as several hundred meters below the surface; the constituents of these deposits are derived from the soil zone where calcite and silica have accumulated through pedogenic processes.

Studies of natural alteration have implications for the response of the geologic system to a potential nuclear waste repository at Yucca Mountain. Products of repository-induced alteration of vitrophyre glass are expected to be smectite, clinoptilolite ± other zeolites, and opal-CT ± other silica minerals. Under ambient conditions, clinoptilolite below the potential repository will not recrystallize to analcime within 10^5 years, and therefore, the sorptive capacity of the zeolites will be available to retard radionuclide migration. Clinoptilolite in rocks heated by the repository to temperatures around 100°C may recrystallize to analcime in the presence of water.

6.1.5.3.1 Applications of Illite/Smectite Studies to Predicting Bulk-Rock Mineral Stability

Long-term mineral stability in the potential repository is important to the performance of a repository but difficult to assess quantitatively. Geologic emplacement of high-level radioactive waste will raise the temperature in the host rocks as a result of the heat produced by the radioactive decay of the waste. Studies on the effects of repository-induced heating include research on the dehydration behavior of clays and zeolites in tuffs (Bish 1984, 1989) and on the hydrothermal stability of tuffs (Blacic et al. 1996; Duffy 1983a, 1983b). In an analysis of the thermal constraints on radioactive waste isolation in zeolitic tuffs, Smyth (1982) concluded that the reaction of clinoptilolite to analcime would begin at about 105°C based on data summarized by Iijima (1975), thereby giving rise to volume reductions and significantly reducing the cation sorptive capacity of the rocks (Vaughan 1978). Smyth advised constraining the maximum temperature in zeolitized tuff to 85°C to prevent reaction. Smyth's paper initiated the long-standing programmatic concern with the effects of repository-induced heating on the zeolitic rocks at Yucca Mountain. The transformation of the abundant clinoptilolite to analcime in rocks underlying the host rock at Yucca Mountain would give rise to large decreases in volume leading to increased rock porosity and probably permeability. The reaction would also yield large amounts of water and greatly reduce the total cation-exchange capacity of the zeolite barrier (Vaniman and Bish 1995). However, the temperature at which the clinoptilolite-to-analcime reaction might occur and the rate of the reaction are difficult to assess experimentally. The reaction is thought to occur in nature at temperatures below 200°C, at which point reaction rates are very slow. Laboratory research on the long-term effects of heating Yucca Mountain Tuffs to relatively low temperatures (<250°C) has been hampered by the slow reaction kinetics, and laboratory experiments either have not reproduced the assemblages observed in Yucca Mountain (Duffy 1983a, 1983b) or only do so at higher temperatures that speed reactions and potentially change reaction mechanisms (Knauss and Beiriger 1984). Furthermore, the reaction is known to be affected greatly by water compositions (for example, Chipera, Bish et al. 1995).

A potentially effective way of circumventing the problems of slow kinetics in laboratory experiments is to use the illite-smectite and associated alteration mineral assemblages observed in drillholes USW G-1 and G-2 as natural analogs to repository-induced thermal alterations. Because the temperatures at which reactions occur are affected by fluid composition (including the activity of water), this approach assumes that future fluid compositions will be approximately the same as those present during the alteration in Yucca Mountain at ~11 Ma. This is probably a

reasonable assumption, as fluid-inclusion waters are dilute. However, although present-day waters are also dilute, waters surrounding the repository environment may vary significantly from the present composition, particularly if they are concentrated by evaporation.

6.1.5.3.2 Zeolite Stability

Potentially valuable data concerning other mineral reactions in tuffs may be obtained by examining the changes in bulk mineralogy with depth and correlating these changes with the illite-smectite reactions and the estimated paleotemperatures. Important variations in mineralogy with depth include the gradation from unaltered volcanic glass to clinoptilolite; mordenite to analcime and finally to authigenic albite. This sequence was first emphasized for these tuffs by Smyth (1982), who related these mineralogic changes to those documented by Iijima (1975, 1980). Smyth correlated the temperatures at which some of these reactions occurred (clinoptilolite-analcime, analcime-albite) to the Na-ion concentration of the waters. In contrast, Kerrisk (1983) conducted reaction-path calculations of mineral formation in tuffs near Yucca Mountain and concluded that aqueous silica activity was the controlling variable in the mineral evolution. He was unable to reproduce the observed mineral assemblages by varying the Na-ion concentration. Duffy (1984) also concluded that the aqueous silica concentration was the variable controlling the stability of clinoptilolite and mordenite in Yucca Mountain. He used thermodynamic calculations to show that clinoptilolite is not stable with respect to albite or analcime at any temperature when the chemical potential of silica is controlled by quartz. Thus, the stability of clinoptilolite appears to depend on whether the silica activity is controlled by cristobalite (or another relatively soluble polymorph) or quartz. The time interval over which clinoptilolite would remain stable would thus be determined by the rate of reaction of cristobalite (or glass, opal-CT) to quartz.

Approximate upper temperature limits at which zeolites have broken down in Yucca Mountain can be obtained from the mineralogic data in Figures 6.1-71 to Figure 6.1-73 and the estimated paleotemperatures in Figure 6.1-61. For example, it is clear from the USW G-1 and G-2 data that clinoptilolite was not part of the stable mineral assemblage at the depth/temperature at which ordered illite-smectite interstratifications occur. This result implies a maximum temperature of stability of 90 to 100°C. Mordenite disappears in USW G-2 below the 1,091 m depth, suggesting an upper stability limit of 100 to 130°C. Finally, analcime is rare below 1,097 m and virtually absent below 1,372 m in USW G-2; its disappearance as a major phase near the first appearance of R >3 illite-smectite implies an upper stability limit for analcime of 175 to 200°C, in agreement with experimental data (Liou 1971). The zeolite mineralogy in USW GU-3/G-3 shows the trends obvious in USW G-1 and G-2, but the illite-smectite mineralogy suggests that temperatures have not been significantly elevated in GU-3/G-3. It is therefore likely that additional factors, probably kinetics and water chemistry (e.g., decreasing Si activity with depth), were controlling factors in zeolite reactions in USW GU-3/G-3 in the absence of significantly elevated temperatures. As discussed below, Si activity probably played a role in mineral reaction in all three holes.

The reaction of clinoptilolite to analcime coincides with the appearance of significant amounts of calcite and minor amounts of chlorite and interstratified chlorite/smectite. The increase in calcite with depth is contrary to what is observed in pelitic rocks (e.g., Hower et al. 1976), reflecting either the differences in mineral assemblages or perhaps an increase in a_{CO_2} with depth (Zen

1961) that may have been contributed by geothermal fluids. It is likely that the breakdown of clinoptilolite provided the source of at least some of the Mg for chlorite formation and the source of some of the Ca for calcite formation, although the formation of one or both of these minerals may have been associated with the hydrothermal fluids circulating at the time of alteration. The clinoptilolite probably also provided the source for at least some of the K in the deeper illite-smectite clays and some or all of the Na for analcime and albite.

Combination of these data with models of the thermal profiles around a repository in tuff as a function of time (Buscheck et al. 1994) and with mineral distribution data from Bish and Chipera (1989), shows that the reaction of clinoptilolite to analcime could potentially occur in the thick, zeolitized CHnz (a functional unit including the nonwelded lower Topopah Spring Tuff, the Calico Hills Formation, and the upper nonwelded Prow Pass Tuff, where some or all components are zeolitic) underlying the candidate repository horizon at high waste loadings. The calculations of Buscheck et al. (1994) predict temperatures in portions of the Calico Hills Formation exceeding 100°C for areal mass loadings of 83.4 and 110.5 metric tons uranium/acre. Predicted temperatures in the Calico Hills Formation do not exceed 100°C for a waste loading of 55.3 metric tons uranium /acre.

Zeolites above the Calico Hills Formation and below the candidate repository horizon (Bish, Ogard et al. 1984) may be significantly heated by the repository thermal pulse, and reactions among the zeolites and smectites may occur in these zones. The calculations of Buscheck and Nitao (1992) show that this interval will approach 90°C after about 1,000 years. If the cristobalite and opal-CT in this interval completely react to form quartz, thereby decreasing the aqueous silica concentration, the clinoptilolite may then transform to analcime. However, there is a large amount of glass/opal-CT in interval I (Bish and Chipera 1989) and this interval is in the unsaturated zone. Ernst and Calvert (1969) estimated that conversion of cristobalite to quartz under saturated conditions would take ~36,000 years at 100°C and 4.3 m.y. at 50°C; all models of repository thermal behavior show that even the repository centerline temperature would be below 60°C by 10,000 years after emplacement. The transformation of volcanic glass and/or opal-CT to quartz is usually observed to proceed via a more ordered intermediate such as cristobalite (for example, Murata and Larson 1975) so that transformation of the existing glass and opal-CT to quartz will likely take longer than the cristobalite-to-quartz reaction. Therefore, it is highly unlikely that the aqueous silica concentration will be controlled by quartz in the required 10,000-year lifetime of a repository (see Subsection 6.1.6.2).

6.1.5.3.3 Chlorite Stability

Chlorite and randomly interstratified chlorite/smectite both occur with illite-smectite and illite in the deeper portions of USW G-1 and G-2. In addition, some of the deeper smectites in these drillholes appear to be partially chloritized. These occurrences are similar to those documented in silicic volcanic rocks at Wairakei, New Zealand (Steiner 1968) and in silicic volcanic rocks in Japan (Inoue et al. 1978; Inoue 1985). Iijima (1978) also documented the occurrence of chlorite in the analcime and authigenic albite zones in altered silicic volcanic rocks. The presence of randomly interstratified chlorite/smectite in the deeper portions of drillhole USW G-2 suggests that this phase is intermediate between shallower smectites and the deeper chlorites, as proposed by Inoue (1985). In contrast to the smectite-to-illite reaction, which requires an adequate supply of K and Al, the reaction of smectite to chlorite requires additional Mg and/or Fe. Steiner (1968)

suggested that the source of Mg and Fe in the silicic volcanics at Wairakei was the glassy groundmass and the alteration of magnetite to pyrite and/or epidote. However, it is likely that the source of Mg and Fe in Yucca Mountain Tuffs was the clinoptilolite and mordenite that reacted to form analcime and albite. Some of the clinoptilolites in Yucca Mountain Tuffs contain significant Mg whereas analcime and authigenic albite contain little or no Mg or Fe (Broxton, Warren, Hagan et al. 1986). Chlorite and/or chlorite/smectite do not coexist with clinoptilolite at Yucca Mountain.

6.1.5.3.4 Stability of Silica Minerals

Several transformations between silica phases in Yucca Mountain are obvious (Figures 6.1-71 to 6.1-73). Among these transformations are the disappearance of glass, opal-CT, tridymite, and cristobalite with depth. The disappearance of volcanic glass and opal with depth in tuffs from other areas is well documented (Iijima 1978), as is the instability of tridymite and cristobalite during alteration of volcanic rocks (Ernst and Calvert 1969; Kano 1983). As noted above, Kerrisk (1983) and Duffy (1984) concluded that decreasing aqueous silica activity, from the shallow rocks containing tridymite, cristobalite, opal, and glass to the deeper rocks containing quartz, appeared to be the most important factor in zeolite evolution in volcanic rocks at the Nevada Test Site. The X-ray diffraction data for USW G-1, G-2, and GU-3/G-3 are consistent with their ideas. It is noteworthy that the disappearance of clinoptilolite and mordenite as major phases coincides closely with the disappearance of cristobalite as a major phase, supporting the conclusions of Kerrisk (1983). The deepest occurrence of cristobalite in USW G-2 core corresponds to an illite-smectite temperature of about 100°C. If temperature is the controlling variable in the transformation of cristobalite to quartz (Ernst and Calvert 1969; Kano and Taguchi 1982), then this reaction may have provided an indirect temperature control on the clinoptilolite-to-analcime reaction. The disappearance of cristobalite as a major phase would have resulted in a lower aqueous silica activity, thus destabilizing clinoptilolite.

6.1.5.3.5 Summary and Conclusions

Estimates of the temperature of formation of illite/smectites yield probable stability limits for several associated minerals at Yucca Mountain. Clinoptilolite apparently became unstable at about 100°C, mordenite was not a major phase above 130°C, and analcime transformed to albite above 175 to 200°C. It appears that cristobalite transformed to quartz at 90 to 100°C in USW G-2 but must have reacted at considerably lower temperatures (and for longer times) in USW GU-3/G-3. The reactions with increasing depth appear coupled, and clinoptilolite and cristobalite disappear approximately simultaneously, supporting the concept that aqueous silica activity is a controlling variable in the clinoptilolite-to-analcime reaction. The reaction of clinoptilolite to analcime also coincides with the appearance of calcite, chlorite, and interstratified chlorite/smectite. Breakdown of clinoptilolite (and mordenite) probably provided the source of some of the Ca for calcite, Mg for chlorite, K for the illite-smectite found deeper in the section, and Na for analcime and albite, although the hydrothermal fluids may have been a source for some of these cations.

Using the rocks in USW G-1, G-2, and GU/G-3 as natural analogs to repository-induced thermal alteration suggests that the bulk of the clinoptilolite- and mordenite-bearing rocks in Yucca Mountain will not react to less sorptive phases such as analcime over the required lifetime of the

potential repository. The zeolites in zeolite interval I, directly underlying the proposed repository horizon, may transform at the predicted repository temperatures. However, the reaction of clinoptilolite to analcime in interval I may require the transformation of all of the abundant opal-CT and glass to quartz, an unlikely scenario considering the unsaturated nature of these rocks and the predicted temperatures of <100°C.

6.1.6 Mineral Stability and the Impact of Thermal Loading

Natural-analog and theoretical studies indicate four potential mineralogical reactions that may be induced or accelerated by a thermal perturbation due to high-level radioactive waste disposal at Yucca Mountain:

- Volcanic Glass ⇨ ± Clinoptilolite ± Smectite ± Opal-CT
- Tridymite, Cristobalite, Opal-CT ⇨ Quartz
- Clinoptilolite, Mordenite ⇨ Analcime + Quartz ± Calcite
- Smectite ⇨ Illite

Ideally, there would be sufficient thermodynamic and kinetic data to calculate the extent of these reactions under various thermal and hydrologic conditions. Unfortunately, at the present time, the thermodynamic and kinetic data are not adequate for the development of a fully quantitative model of mineral evolution. However, an integration of natural-analog, thermodynamic, and kinetic studies permits the development of a practical conceptual model for predictions of repository performance. This subject is also discussed in Subsection 7.5.3.

The following summary of the conceptual model represents a recommended approach to modeling these potential reactions in the repository environment. The data for these results are described more fully in Subsections 6.1.6.1 to 6.1.6.4 as well as by Carey, Bish et al. (1996) and Carey, Chipera, Vaniman et al. (1997).

Volcanic glass is inherently unstable, but persists above the water table at Yucca Mountain. This indicates that volcanic glass reacts relatively rapidly in saturated conditions, although there are no adequate kinetic data to predict these rates quantitatively as a function of temperature and solution composition. Two end-member conditions should be evaluated for their effect on repository performance:

- Volcanic glass does not react during the thermal perturbation created by the repository.
- Volcanic glass reacts to an assemblage of ± clinoptilolite ± smectite ± opal-CT in places that are saturated at elevated temperature.

The first possibility represents a conservative estimate because volcanic glass does not represent a sorptive barrier. The second possibility will help to retard radionuclide migration and will greatly alter hydrologic properties in the affected rocks. In this case, the temperature used to predict the alteration of glass in saturated conditions is estimated at 75°C for vitrophyre glass and 45°C for vitric nonwelded material.

Tridymite also does not persist below the water table. Again, kinetic data are not available for tridymite, but the rate of dissolution may be approximated by that of amorphous silica (to help account for the observation that tridymite is lost more rapidly than cristobalite). Thus, in the conceptual model, tridymite has essentially no reactivity in unsaturated conditions and reacts at a rate given by amorphous silica in saturated conditions.

The natural-analog, thermodynamic, and kinetic studies all identify the paramount significance of cristobalite and opal-CT in the mineral evolution of Yucca Mountain. Reaction of these minerals to quartz can significantly alter the hydrologic properties of Yucca Mountain rocks, particularly through spatial redistribution of silica. In addition, the results described in Subsection 6.1.6.3 indicate that transformations of the silica polymorphs are the rate-limiting step in the reaction of the sorptive zeolites clinoptilolite and mordenite to analcime-bearing assemblages.

Given this significance, it is fortunate that there are more thermodynamic and kinetic data on cristobalite and opal-CT than for any of the other phases of concern. Nonetheless, the kinetic data are not adequate to explain the present-day distribution of cristobalite and opal-CT and, therefore, cannot be used to predict the future evolution with a high degree of certainty (see Subsection 6.1.7).

Cristobalite and opal-CT are unstable with respect to quartz under all likely repository conditions. The rate of reaction to quartz is expected to be essentially zero for unsaturated conditions. For saturated conditions, an upper bound on the rates of reaction can be obtained using precipitation and dissolution rate data of Renders et al. (1995). A lower bound can be obtained by applying the rate data of Ernst and Calvert (1969). An alternative procedure is to use the inferred temperature of reaction of cristobalite and opal-CT to quartz obtained from the self-analog study of Yucca Mountain. In this case, saturated rocks reaching 100°C are assumed to have reacted completely to quartz.

The sorptive zeolites clinoptilolite and mordenite are also expected to have negligible tendency to breakdown under unsaturated conditions. For saturated conditions, natural-analog and thermodynamic studies indicate that these minerals are stable in the presence of cristobalite and opal-CT to temperatures at least as high as 100°C.

In the conceptual model, clinoptilolite and mordenite are stable in the presence of cristobalite and opal-CT. Following the loss of these silica polymorphs, clinoptilolite and mordenite are expected to break down at temperatures in excess of 90°C. The kinetic data are, at present, insufficient to calculate a rate of transformation to analcime. A conservative, bounding assumption is that clinoptilolite and mordenite decompose completely to analcime if cristobalite and opal-CT are lost and if temperatures exceed 90°C. However, the stability of the sorptive zeolites may decrease and the reaction may proceed at lower temperature if pH is substantially lower than under present-day conditions.

The transformation of smectite to illite is progressive, with an increasing proportion of illite as temperature rises and/or the activity of aqueous silica decreases. Two end-member models for the this reaction can be formulated: the transformation to illite occurs only if cristobalite and opal-CT are lost and silica activity is controlled by quartz, and the transformation to illite is

temperature dependent and requires approximately 0.1 m.y. at 75°C (kinetic model of Eberl and Hower 1976). In either case, saturated conditions are required for the transformation to take place.

6.1.6.1 Origins/Processes Controlling Mineral Chemistry, Stability, and Distribution

Diagenetic alteration at Yucca Mountain includes the formation of zeolites, opal-CT, smectite, the smectite to illite transition, and the loss of volcanic glass and metastable silica polymorphs (tridymite, cristobalite, and opal-CT). The following is a brief overview of the primary diagenetic reactions, as these have been covered in more detail in Subsections 6.1.2, 6.1.3.5, and 6.1.5.3.

The primary diagenetic environment may be summarized in terms of four zones of increasing diagenetic intensity described by Broxton, Bish, Warren (1987). Zone I is characterized by vitric tuffs containing unaltered volcanic glass and minor smectite, opal-CT, heulandite, and Ca-rich clinoptilolite. In most places, this zone extends from the surface to the basal Topopah Spring Tuff or upper Calico Hills Formation. Zone II is characterized by the complete replacement of volcanic glass by clinoptilolite ± mordenite and by lesser amounts of opal-CT and smectite. This zone extends down to the appearance of analcime and the loss of all metastable silica polymorphs (tridymite, cristobalite, opal-CT), which defines zone III. The structural depth of zone III is variable and ranges from the Prow Pass Tuff through the Tram Tuff. Zone IV is defined by the replacement of analcime by albite and only occurs in the deepest volcanic units at Yucca Mountain.

The primary formation of zeolites at Yucca Mountain occurred > 11 m.y. and occurred below the water table (Vaniman, Bish, Chipera et al. 1996). The temperature of formation of zeolites was estimated to be in the range of 40 to 100°C (Levy and O'Neil 1989).

Tridymite and volcanic glass do not persist below the water table. Tridymite is presumed to be lost by relatively simple dissolution processes. The loss of volcanic glass is associated with the formation of large quantities of clinoptilolite and mordenite. The formation of zeolites also resulted in the crystallization of opal-CT. The metastable silica polymorphs are absent at depths corresponding approximately to the appearance of analcime and are replaced by quartz through a dissolution/precipitation reaction.

Smectite develops in Zone II through reactions involving the loss of volcanic glass. With depth (and elevated temperatures), smectite is gradually transformed to illite at the lower structural levels of Yucca Mountain (Bish 1989).

6.1.6.2 Silica Polymorph Transformation–Silica Activity

The activity of silica in pore water at Yucca Mountain is one of the most important geochemical parameters affecting repository performance. In dilute solutions, the activity of silica is approximately equal to the concentration of SiO_2 (expressed in mole/kg). This concentration changes as a function of the silica polymorph dominating the solution chemistry. Excellent thermodynamic data, as found in databases such as EQ3/6, allow the calculation of the concentration of SiO_2 as a function of temperature and silica polymorph. At 25°C, the

concentration of SiO_2 increases from 7 ppm for quartz to 14 ppm for cristobalite, to 18 ppm for tridymite, and to 67 ppm for amorphous silica (Robie et al. 1979).

These values have great significance for repository performance in two major areas. First, they affect mineral equilibria through the stabilization or destabilization of mineral species. For example, clinoptilolite, mordenite, and smectite are stabilized by high silica activity, whereas analcime and illite are stabilized by low silica activity. Second, the silica activity reflects the potential for redistribution of silica at Yucca Mountain and its consequent impact on permeability. Elevated silica activity in pore fluids reflects the capacity of the system to deposit silica, whereas depressed values of silica activity reflect the capacity of the system to dissolve metastable silica polymorphs.

The distribution of silica polymorphs at Yucca Mountain changes with depth and with stratigraphic interval (see Subsection 6.1.3.5). Above the static water table, all of the metastable polymorphs (tridymite, cristobalite, and opal-CT) can occur in addition to quartz. Below the water table, tridymite is absent, and cristobalite and opal-CT disappear with depth. Despite the variety of silica polymorph assemblages at Yucca Mountain, all of the water analyses reported by Kerrisk (1987) have silica concentrations near 50 ppm (at temperatures between 25 and 45°C) and, thus, have silica saturations between that of cristobalite and amorphous silica. This observation indicates that as long as metastable silica polymorphs or volcanic glass are present, the silica activity of Yucca Mountain waters lies between that of cristobalite and amorphous silica. Evidently, silica activities will not drop to that of quartz until all of the metastable polymorphs or volcanic glass are consumed.

Changes in silica activity, therefore, are determined by the rate of transformation of the metastable silica phases (tridymite, cristobalite, opal-CT, and volcanic glass) to quartz. As long as any of these silica phases are present, silica activity remains high. These kinetic processes are discussed in greater detail in Subsection 6.1.7, but fundamental data are available from Rimstidt and Barnes (1980) and Renders et al. (1995).

These relations suggest a relatively simple model for the effect of silica activity on zeolite and clay reactions: such reactions are rate limited by the kinetics of the transformation of the metastable silica polymorphs. The relations do not, however, provide much guidance on the process of silica transport and redeposition. Ambient temperature fluids are in equilibrium with the metastable silica polymorphs and ambient-temperature hydrologic flow should therefore not result in additional dissolution. Field observations of fracture surfaces (Paces, Neymark et al. 1996; Paces, Marshall et al. 1997; Fabryka-Martin, Flint et al. 1997; Levy and Chipera 1997) indicate that such fluids can deposit metastable silica polymorphs (chiefly opal-A and opal-CT). These fluids do not appear to deposit quartz. At elevated temperatures, the fluids will become undersaturated with respect to cristobalite and opal-CT, and dissolution of these phases is expected to maintain silica saturation between that of cristobalite and amorphous silica. Fluid flow of such hot fluids into cooler regions should result in the deposition of metastable silica polymorphs, particularly along fluid-flow pathways. These types of deposits have resulted in significant permeability reductions around basaltic sills/dikes intruded into tuffs in the Yucca Mountain region (Matyskiela 1997).

6.1.6.3 Geochemical and Thermal Controls of Zeolite Mineralogy–Theoretical and Natural Analog Studies

The prediction of reactions involving zeolites is difficult because some of the important thermodynamic properties are relatively poorly understood and will occur at low temperatures at which the kinetics of metastable reactions multiply the number of potential reaction paths. As a consequence, the existing thermodynamic and kinetic data do not allow accurate calculations of the stable mineral assemblages at Yucca Mountain as a function of temperature, fluid composition, and time. Fortunately, reaction paths can be constrained by observations made on natural systems.

The two primary sources of natural-analog data for mineral transformations at Yucca Mountain are the Yellowstone caldera and the past alteration of Yucca Mountain itself. In Subsection 7.5.3.5, the Taupo Volcanic Zone and Wairakei geothermal system in New Zealand are discussed as natural analogues. A large variety of other natural systems has been used in a more general sense (e.g., various settings illustrating transformations among silica polymorphs) to help constrain mineral reaction paths. Such natural observations are consistent with a conclusion that many of the minerals present at Yucca Mountain are metastable and, given adequate time or temperature, will transform to more stable assemblages. This condition occurs because many of the minerals formed either by high-temperature devitrification processes or by low-temperature (typically below ~100°C) alteration of volcanic glass.

Field observations suggest that clinoptilolite is metastable because clinoptilolite is only known from rocks younger than ~200 m.y. (for example, Hay 1966). Clinoptilolite is generally also only found in rocks that contain metastable silica minerals (Dibble and Tiller 1981). The lack of occurrence or formation of clinoptilolite in older rocks suggests that clinoptilolite cannot form from the thermodynamically more stable mineral assemblages present in older rocks, even though these assemblages have been subjected to temperatures and pressures consistent with the present-day occurrences of clinoptilolite. Similar considerations probably hold for mordenite.

The important effect of water chemistry on zeolite diagenetic reactions was observed during early studies of saline lakes (Hay 1966; Sheppard and Gude 1968, 1969) in which alkalic, silicic zeolites such as clinoptilolite, erionite, or phillipsite often developed on the margins of the deposits, grading into analcime and then into potassium feldspar at the centers of the lakes (for example, the Big Sandy Formation; Sheppard and Gude 1973). It was inferred that the alkalic, silicic zeolites were the first-formed zeolites, which subsequently transformed into analcime as the aqueous Na^+ concentration increased as water evaporated. Boles (1971) experimentally reproduced this result by reacting various clinoptilolite/heulandites in NaOH and Na_2CO_3 solutions at 100°C to form analcime. He concluded that the reaction to analcime is favored by increased pH and aqueous Na^+ concentration and that the Si/Al ratio of the analcime is largely a function of the Si/Al ratio of the precursor zeolite irrespective of the presence or absence of quartz. Iijima (1975) noted that the clinoptilolite-to-analcime reaction occurred at significantly higher temperatures in marine sedimentary deposits (~84 to 91°C) compared with ambient temperatures in the saline-alkaline lakes. He also suggested that the chemical composition of the pore water (in particular the Na^+ concentration) was the primary factor determining reaction temperatures.

6.1.6.3.1 The Yellowstone Caldera Natural Analog

Meijer (1987) reviewed four potential sites in the continental United States as potential natural analogs to Yucca Mountain: Yellowstone caldera, Newberry crater, Long Valley, and the Jemez volcanic field. He concluded that the Yellowstone caldera most closely duplicates the details of the volcanic rocks at Yucca Mountain and the conditions anticipated in the potential repository. The Yellowstone caldera is an active hydrothermal system in silicic ashflow tuffs, and considerable data on present-day water compositions and temperatures are available. This situation contrasts with most other potential natural analogs, for which temperatures and water compositions must be approximated from geological and geochemical information. The age of the caldera is approximately 0.6 m.y. Zeolites are found in many drillholes at Yellowstone, and clinoptilolite is the most common zeolite, followed by mordenite and analcime. According to Meijer (1987), clinoptilolite commonly occurs as a replacement of glass, as a cement in volcanic sediments, and as a fracture filling. Just as at Yucca Mountain, clinoptilolite usually occurs with the less stable silica minerals but occasionally occurs with quartz.

Although Yucca Mountain waters are not expected to become acid, Meijer (1987) concluded that acid-vapor-dominated systems usually contain opal and cristobalite, with quartz crystallization apparently inhibited. In addition, Yellowstone rocks that coexist with acid waters usually contain clay minerals rather than zeolites. This observation suggests that development of lower pH waters in and around the repository horizon would destabilize zeolites. In the neutral to alkaline waters in Yellowstone rocks, zeolites coexist with clays and K-feldspars; the assemblage K-feldspars + analcime + quartz appears to be stable at higher temperatures. Meijer concluded that this assemblage resulted from the interaction of clinoptilolite- and mordenite-bearing rocks with thermal waters of low aqueous silica activity. At temperatures above 165°C, K-feldspar, mordenite, and quartz often coexist. Clinoptilolite and K-feldspar usually coexist only with cristobalite rather than quartz and always at temperatures <165°C. Thus, in the Yellowstone system, clinoptilolite appears to have an upper temperature stability limit of ~165°C. Meijer also observed that clinoptilolite is restricted to units that either contain glass or were once glassy, suggesting that crystallization kinetics are important in its formation. He concluded that as long as the aqueous silica activity in Yucca Mountain groundwater remains at or above cristobalite saturation with neutral or alkaline pH, neither clinoptilolite nor mordenite will react to form analcime.

6.1.6.3.2 Yucca Mountain as a Self-Analog

Yucca Mountain is perhaps its own best analog for the prediction of mineral evolution, as it is not necessary to extrapolate from differing geochemical or hydrological conditions. Drill-core samples demonstrate down-hole evolution of mineralogy, and a fossil hydrothermal event is preserved to the north towards the Timber Mountain caldera (Broxton, Bish, Warren 1987; Bish 1989; Bish and Aronson 1993). The most significant mineral transformations take place at depths significantly greater than the proposed repository horizon and can therefore be used to predict the effect of elevated temperatures and/or hydrothermal conditions in the potential repository environment.

Studies of illite/smectite relations revealed the presence of a fossil hydrothermal system north of the potential repository block (Bish 1989; Bish and Aronson 1993). Bish used data from

drillholes USW G-2, G-1, and G-3 to define a north to south cross section of Yucca Mountain, clearly documenting a decrease in hydrothermal activity from north to south (Figure 6.1-74). At the southern end, USW G-3 appears to represent an undisturbed section displaying a gradual mineralogical evolution with depth. The observed mineralogy of USW G-3 may be taken to represent the mineralogical evolution of Yucca Mountain from the deposition of the volcanic units to the present day under a geothermal gradient similar to that observed today. The proportion of illitic layers in illite/smectite minerals changes imperceptibly with depth, remaining near ~20 percent, indicating a very shallow geothermal gradient. Under these conditions, tridymite and volcanic glass do not persist below the water table. Cristobalite, opal-CT, and clinoptilolite persist well below the water table with clinoptilolite occurrences as deep as the Lithic Ridge Tuff. Minor amounts of clinoptilolite/heulandite coexist with analcime, and analcime occurs at depth following the disappearance of cristobalite and opal-CT.

At the northern end, the illite/smectite data in USW G-2 document a very steep geothermal gradient occurring in the Bullfrog Tuff in which illitic layers increase from 20 to near 100 percent in illite/smectite over a narrow stratigraphic interval. This transformation coincides with the complete loss of clinoptilolite, mordenite, and cristobalite/opal-CT and the development of analcime + calcite + illite. The illite/smectite data clearly indicate a fossil hydrothermal system with a sharp thermal front and temperatures substantially in excess of the regional gradient. The development of calcite in the rock matrix, probably as a product of the breakdown of clinoptilolite to analcime, represents a particularly striking difference in mineralogy between the hydrothermally altered rocks and those evolving under the regional geothermal gradient.

Drillhole USW G-1 documents intermediate conditions with evidence of an elevated geothermal gradient in illite/smectite crystals evolving from 20 to 60 percent illitic layers with 90 percent illite occurring at the greatest depths. As in USW G-3, clinoptilolite/heulandite coexists with analcime at depth and cristobalite/opal-CT is lost prior to the occurrence of analcime.

The illite/smectite data can be used to infer paleotemperatures of these mineral transformations at Yucca Mountain (Figure 6.1-75; Bish 1989). These data suggest approximate thermal limits of 90 to 100°C for clinoptilolite and cristobalite. Mordenite persists to greater depths, corresponding to limiting temperatures of 100 to 130°C. Analcime reacts at 175 to 200°C to an albite-bearing assemblage. The rocks at the southern end of Yucca Mountain do not appear to have exceeded the present-day geothermal gradient. The conclusions for clinoptilolite support the inferences of Smyth (1982) of a thermal stability near 105°C for clinoptilolite, based on other natural systems and different geochemical arguments.

One of the significant observations that may be derived from Yucca Mountain and many other places is the evolution with depth and temperature of the assemblage clinoptilolite + cristobalite/opal-CT to analcime + quartz. This evolution is evident in much of the drillhole data for Yucca Mountain (Vaniman, Bish, Chipera et al. 1996), although a transitional zone in which clinoptilolite and analcime coexist or analcime and cristobalite occur is often present. These observations support the model of Kerrisk (1983) in which the transformation of clinoptilolite to analcime does not occur until the loss of cristobalite and the lowering of the aqueous silica activity. This approach leads to a conceptual model in which the kinetics of reaction of the metastable silica polymorphs to quartz controls the rate of reaction of clinoptilolite to analcime.

The potential formation of zeolites from volcanic glass at Yucca Mountain is illustrated in the devitrified-vitric transition zone between the candidate host rock for the potential repository and the underlying vitrophyre in the lower part of the Topopah Spring Tuff. This interval is characterized by hydrothermal alteration that is present wherever this syngenetic boundary has been examined, both in outcrop and in drillholes (Levy 1984c; Levy and O'Neil 1989; Peterman, Spengler, Futa et al. 1991). Within this zone, devitrification is incomplete and is localized around fractures. The primary mineralogic constituents of the devitrified rock are alkali feldspar and cristobalite, but the outermost margins of the fracture borders and the adjacent glassy rock also contain hydrous minerals (smectite, heulandite-clinoptilolite, and other minor zeolites) and silica minerals. The hydrous minerals and silica are also present as fracture fillings and replacements of pumice lapilli within the transition zone.

The chief hydrous products of glass alteration are smectite and heulandite-clinoptilolite. Smectite commonly crystallizes as spherical aggregates, 2 to 50 mm across, adhering to each other, with a small amount of intergrown and extremely fine-grained zeolite. A few <1 mm-thick smectite fracture coatings are present in some places.

The timing and development of the thick zeolitized units at Yucca Mountain provide useful constraints on the potential longevity of zeolite-bearing units. Most research indicates that zeolitization required the presence of abundant water over a long period of time (Gibbons et al. 1960; Hoover 1968; Claassen and White 1979; Levy 1984c; Broxton, Warren, Hagan et al. 1986). The underlying observation is that glass in nonwelded tuffs is preserved only where the rocks have not been subjected to prolonged saturation. It has been estimated that zeolitization requires periods of the order of 10^4 years (Dibble and Tiller 1981) and occurred at very close to ambient temperatures.

A minimum age of zeolitization can be established using K/Ar dates obtained from illite/smectite in the hydrothermal altered region of USW G-2 (Bish and Aronson 1993). These place a lower age limit of ~10.7 m.y. on the original glass-to-clinoptilolite alteration only in the deeper pyroclastic units. The age of the pyroclastic units provides a maximum age for zeolitization of ~13 m.y. Thus, sorptive zeolites have existed for at least 12 m.y. at Yucca Mountain.

Two end-member conceptual views of the mineral distribution at Yucca Mountain can be formulated. The static model regards the observed distribution of minerals at Yucca Mountain as essentially unchanged since the early depositional and syngenetic history (> ~10 m.y. of relative stasis). The progressive model regards the observed distribution of minerals as having evolved since the early depositional and syngenetic history by relatively slow dissolution, precipitation, and nucleation processes that have significantly altered the early mineralogy. In the static model, the view is held that, at temperatures of the prevailing geothermal gradient, the rate of reaction of metastable phases is almost insignificant. It is only in the early, syngenetic stages that temperature was sufficiently elevated to permit reasonable reaction rates. In the progressive model, the distribution of silica, to take a specific example, has changed gradually with time with the transformation of metastable polymorphs to quartz. The amount of quartz has increased and that of tridymite, cristobalite, and opal-CT has decreased. The degree of transformation would be directly related to depth (or effective temperature), and with time, the deepest occurrence of a metastable polymorph has gradually decreased. The actual situation is likely to exist somewhere

between these end members, and the reactivity of different minerals may more closely reflect one extreme or the other.

Clinoptilolite and mordenite persist below the water table (Carey, Chipera, Vaniman et al. 1997). As discussed above, a hydrothermal event in the northern region of Yucca Mountain resulted in significantly elevated temperatures. This event changed the distribution of clinoptilolite and mordenite and decreased the maximum depth of these zeolites (e.g., USW G-2). In the southern regions, clinoptilolite and mordenite persist to greater depths (Lithic Ridge Tuff), but in the north, clinoptilolite is absent from strata below the lower Prow Pass Tuff, and mordenite is not found below the lower Bullfrog Tuff. These relations may be taken to suggest that the high temperatures of the hydrothermal event were necessary to result in the loss of clinoptilolite and mordenite, consistent with the static model.

These observations do not clearly indicate whether the static or progressive model is more correct. They do indicate that there is evidence for slow reaction kinetics under ambient conditions at Yucca Mountain that have allowed tridymite, glass, cristobalite, opal-CT, clinoptilolite, and mordenite to survive some 10 m.y.

6.1.6.3.3 Summary of Natural Analog Observations

- The reaction of glass at Yucca Mountain yields primarily an assemblage of smectite + clinoptilolite.
- Clinoptilolite, mordenite, opal-CT, cristobalite, and smectite survive below the water table and are evidently capable of persisting in saturated conditions for times at least on the order of 107 years under the present-day geothermal gradient.
- Hydrothermal systems are capable of destroying clinoptilolite, mordenite, opal-CT, cristobalite, and smectite at temperatures >100°C for time periods no longer than on the order of 106 years, producing an assemblage of analcime, quartz, calcite, and illite.
- Reaction rates in the unsaturated zone (under present-day temperatures and fluid compositions) are probably negligible for time periods <107 years.
- Clinoptilolite reacts at temperatures near 100°C (and as low as 90°C) to form analcime, but it can survive to 165°C at least for some period of time (~105 years) in some hydrothermal environments (Yellowstone caldera).
- Mordenite has greater thermal stability than clinoptilolite and perhaps required temperatures as high as 100 to 130°C before decomposition.
- Accessibility of minerals to fluids (permeability) affects reaction rates.
- Some observations indicate that the mineral distribution has been relatively static during the last 10 m.y., at least for rock units occurring above 400 to 600 m elevation above sea-level.

Thermodynamic data for the zeolites clinoptilolite, mordenite, and analcime are somewhat limited. All of these phases exhibit extensive compositional variability via cation exchange and Al/Si variations in the framework, in addition to hydration/dehydration behavior. The existing data for these phases have been recently reviewed by Carey, Bish, Chipera (1996). Very useful results have been obtained using thermodynamic estimation methods modified for zeolites (Chipera, Bish, Carlos 1995; Chipera and Bish 1997) based on the estimation methods of Berman and Brown (1985), Chermak and Rimstidt (1989), and Holland, T.J.B. (1989).

The bulk-rock zeolite mineralogy at Yucca Mountain consists mainly of clinoptilolite/heulandite, mordenite, and analcime (Bish and Chipera 1989). Significant quantities of stellerite have also been found in the bulk rock in drill core UE-25 UZ#16 (Chipera, Vaniman, Carlos et al. 1995). In addition to the above zeolites, chabazite, erionite, and phillipsite have been identified using X-ray powder diffraction (Carlos, Chipera, Bish et al. 1995). These additional zeolites occur sporadically in fractures, generally above the static water-level, and were identified only in close spatial association with vitric zones. Until recently, erionite was believed to occur only in fractures at the top of the Topopah Spring Tuff lower vitrophyre until it was found in significant quantities (up to 34 percent) in a 3 m thick sequence in the bulk rock below the Topopah Spring Tuff lower vitrophyre in drill core USW UZ#14 (Guthrie, Bish et al. 1995). Laumontite, which occurs at higher temperatures than clinoptilolite, was found at the bottom of drillhole UE-25 p#1 and is suspected at the bottom of USW G-1 (Bish and Chipera 1989).

To investigate the stability relations of these zeolites, thermodynamic models of zeolite equilibria were constructed using estimated thermodynamic values based upon the composition of the specific zeolites of interest and including any variability in exchangeable cation and the Si/Al ratio. The reactions were balanced on Al^{3+}, and the other species (H^+, Na^+, K^+, Ca^{2+}, and SiO_2(aq)) were assigned to the liquid phase. Note that cation concentrations may be buffered by other reactions occurring in the natural system (for example, Ca^{2+} by calcite). For example, modeling of clinoptilolite-analcime equilibria was conducted assuming the following reaction:

$$s\text{Clinoptilolite} + t\text{Na}^+ \Leftrightarrow v\text{Analcime} + w\text{K}^+ + x\text{Ca}^{2+} + y\text{SiO}_2(\text{aq}) + z\text{H}_2\text{O}$$

The equilibrium constant for the clinoptilolite-analcime reaction is approximated as:

$$K = \frac{a_{Ca^{2+}}^{x} a_{K^+}^{w} a_{SiO_2}^{y}}{a_{Na^+}^{t}},$$

where a_x represents the activity of species x. As is obvious from the above equilibrium constant, aqueous cation and silica activity are both important to calculated zeolite equilibria.

Thermodynamic stability calculations were conducted using the Ge0-Calc PTA-SYSTEM software (Brown, T.H. et al. 1989). Thermodynamic data for quartz, cristobalite, and tridymite were obtained from the B88.MIN thermodynamic database (Berman 1988) supplied with the Ge0-Calc software package. Likewise, values for aqueous species (aqueous SiO_2, Ca^{2+}, Na^+, K^+, H^+) were taken from the HKF81.AQU database (Helgeson et al. 1981), also supplied with the Ge0-Calc software. The Ge0-Calc database, however, does not contain thermodynamic data for

amorphous silica. For this study, amorphous silica data were obtained from the SUPCRT92 database (Johnson, J.W., Oelkers et al. 1992). To simplify the calculations, the chemical system was restricted to Na-K-Ca-Al-Si-O-H, defining the major constituents in the reactions of interest.

In the present calculations, pressure was constrained such that all calculations were conducted on the liquid side of the water liquid-vapor curve. Values of pH used for the calculations were constrained to approximately 7.6, a value that is representative of present-day waters at Yucca Mountain (Kerrisk 1987; Perfect et al. 1995) and of J-13 water (Delany 1985). This constraint does not affect the results significantly because H^+ is involved only peripherally in these reactions. For the calculations in this study, only zeolites known to exist at Yucca Mountain were used. Although other mineral phases may be in true equilibrium with respect to zeolites, zeolites often form metastably due to kinetic limitations on the formation of more stable species (Moncure et al. 1981). Consequently, phases that may be more stable under given conditions (for example, feldspars, mica, etc.) were not included in the calculations (see Subsections 6.1.6.3.1 and 6.1.6.3.2).

Figures 6.1-75a through d show the results of modeling in $\log[(a_{K+})^2/a_{Ca2+}]$ versus $\log[(a_{Na+})^2/a_{Ca2+}]$ space at various silica activities and at temperatures of 30 and 100°C. Present-day water chemistry (Kerrisk 1987) has been superimposed on the activity/activity diagrams for reference. The exact stability fields for phases that exhibit significant variations in cation ratios can differ markedly from those used in the calculations. Although attempts were made to use "representative" chemical analyses, chemical compositions have been shown to vary considerably depending on drillhole locations and depth (Broxton, Warren, Hagan et al. 1986). Several calculations were conducted to determine sensitivity of the stability fields to variable-input cation ratios for the phases. These calculations showed that those zeolites that exhibit a large variation in cation composition (for example, clinoptilolite-heulandite, mordenite, and erionite) were most sensitive to changes in input cation ratios. For example, although mordenite retains its central position on the activity-activity diagrams with changes in exchangeable-cation composition, its stability field has a strong negative correlation with that of clinoptilolite. A similar, less-dramatic effect was noted for the stability field of erionite with respect to clinoptilolite and mordenite. Bowers and Burns (1990) also noted that cation composition had an effect on stability and modeled the effects of Ca-Na-K-Mg substitution in clinoptilolite with respect to mordenite and heulandite. They found that increased K or Ca significantly increased the stability field for clinoptilolite.

The effect of silica activity on the zeolite equilibria is clearly illustrated by comparing calculations conducted at amorphous silica saturation (Figure 6.1-75a), cristobalite saturation (Figure 6.1-75b), and quartz saturation (Figure 6.1-75c). The stability fields for the more siliceous zeolites (for example, mordenite and clinoptilolite) are dominant at high silica activity and are greatly reduced at quartz saturation. Less silicic zeolites (phillipsite and laumontite) were found to be stable only under conditions of reduced silica activity (for example, at quartz saturation). Likewise, decreasing silica activity significantly increased the stability of heulandite with respect to clinoptilolite. Although discrete chemical formulae were used in the calculations for clinoptilolite and heulandite, there is a chemical continuum between the two phases and the calculations can be interpreted as two extremes of clinoptilolite/heulandite. Silica activity for the calculations can be constrained by the SiO_2 polymorphs that coexist with the zeolites. For example, opal-CT is generally intergrown with mordenite and clinoptilolite at Yucca Mountain

(Bish and Chipera 1989), whereas stellerite and heulandite are intergrown with tridymite and cristobalite (Chipera, Vaniman, Carlos et al. 1995) and analcime is intergrown with quartz (Bish and Chipera 1989).

Increasing temperature had several effects in the calculations. With increased temperature at a given silica-polymorph saturation, the stability fields for mordenite and clinoptilolite decrease as the surrounding stability fields for heulandite, chabazite, and erionite increase. For an aqueous silica activity in equilibrium with quartz, increasing temperature also increases the stability field for phillipsite and a stability field for laumontite was produced (Figure 6.1-75c).

Chipera, Bish, Carlos (1995) found that the formation of erionite had to be suppressed to produce a stability field for phillipsite. The current study uses a more representative chemical composition for the erionite, and consequently, a stability field for phillipsite was obtained without requiring suppression of erionite. Also in that previous study, stellerite had to be suppressed to obtain a stability field for heulandite. Requiring suppression of stellerite is inconsistent with the common occurrence of both heulandite and stellerite in fractures in devitrified tuffs at Yucca Mountain. Although the stability field for heulandite can be enlarged by varying the exchangeable-cation compositions for heulandite, stellerite, or the other bounding phases, a reasonable stability field for heulandite with respect to stellerite could not be formed within the constraints of the observed chemical formulae for the phases at Yucca Mountain. Yucca Mountain heulandites, however, commonly contain significant Mg and Sr, which were not included in the calculations. Preliminary modeling of heulandite/stellerite stability showed that increasing either the Mg or Sr content in heulandite tended to stabilize it with respect to stellerite (Carlos, Chipera, Snow 1995). Thus, including minor elements in the thermodynamic calculations may stabilize additional zeolites without the need to suppress the formation of particular zeolites.

Varying silica activity in the calculations, although found to have a strong control over whether heulandite/stellerite would form relative to other zeolites (for example, clinoptilolite and mordenite), had little effect on heulandite versus stellerite stability. Stellerite and heulandite often coexist in the same fractures and have similar Si/Al ratios, so it is not surprising that varying silica activity does not affect their relative stability. In the current study, the chemical compositions of several of the zeolites (for example, clinoptilolite) were changed to values that are more representative of an average value at Yucca Mountain. Subsequently, the stability field for stellerite became increasingly large and gave somewhat unrealistic results in comparison with clinoptilolite and the current Yucca Mountain water compositions (Figure 6.1-75d). Apparently, there must be other factors, possibly kinetics, compositional differences, or inaccurate thermodynamic values, which prevent stellerite occurrence more frequently than is reported.

The observed mineral distribution at Yucca Mountain (Bish and Chipera 1989) and the alteration observed in other volcanic ash terranes, such as Yellowstone National Park (Honda and Muffler 1970; Keith et al. 1978), suggest that the most probable breakdown product of clinoptilolite is analcime. In an earlier study, Bowers and Burns (1990) conducted an equilibrium modeling study of the stability of clinoptilolite with respect to the current temperature and water chemistry conditions and with respect to potential changes in water chemistry and increased temperature resulting from emplacement of a potential repository. Bowers and Burns calculated an albite

stability field that separated clinoptilolite and analcime. They did not, however, specifically address the clinoptilolite-to-analcime reaction.

In an attempt to evaluate other factors that may control zeolite diagenesis, several investigators have examined the silica polymorphs coexisting with clinoptilolite and analcime (Honda and Muffler 1970; Keith et al. 1978; Kerrisk 1983; Duffy 1993a). Several of these studies suggested that aqueous silica activity, rather than aqueous Na^+ concentration as suggested by Iijima (1975), is the predominant factor controlling the reaction of clinoptilolite to analcime. Clinoptilolite is often observed to coexist with more soluble silica polymorphs (opal-CT and cristobalite), whereas analcime generally coexists with quartz. This correlation is well documented in the mineralogical data for Yucca Mountain as a function of depth (see above). Equilibrium modeling using EQ3/6 also suggested that high-silica zeolites (clinoptilolite and mordenite) were formed along with smectite during the initial stages of volcanic glass dissolution (Kerrisk 1983). Kerrisk found it necessary to suppress quartz precipitation in his calculations, mimicking the supersaturation of silica, in order to form high-silica zeolites such as clinoptilolite. However, he obtained unrealistic results if cristobalite was also suppressed to allow the silica activity to reach amorphous-silica saturation. If reactions were allowed to continue, silica activity eventually dropped and the reactions progressed to a quartz-analcime-illite assemblage and finally to a quartz-albite-potassium feldspar assemblage with possible calcite.

To further explore clinoptilolite-analcime equilibria, the effect of variable Si/Al ratio in clinoptilolite on equilibria with analcime was modeled using a fixed, representative Yucca Mountain analcime composition but varying the Si/Al ratio in the clinoptilolite (Figure 6.1-76). For this calculation the ratio Na/Ca in clinoptilolite was held at 1 although the total moles of Ca plus Na were varied to charge-balance the variable Si/Al. These calculations demonstrate that equilibria involving siliceous clinoptilolites are sensitive to aqueous silica activity. Equilibria involving aluminous clinoptilolite/heulandite are less sensitive to aqueous silica activity but are more sensitive to the aqueous Na^+/Ca^{2+} ratio. For reference, the Si/Al ratios observed for Yucca Mountain clinoptilolites are shown in the shaded region in Figure 6.1-76. Varying the Si/Al ratio in analcime within values representative of those at Yucca Mountain resulted in insignificant changes to the equilibria in Figure 6.1-76.

The effects of clinoptilolite Na/Ca ratio on equilibria with analcime were modeled in a manner similar to the above calculations except the Na/Ca ratio was allowed to vary and the Si/Al ratio was fixed at 4.45 (a representative value for Yucca Mountain clinoptilolites). Figure 6.1-77 shows that Na-clinoptilolite is more sensitive to the aqueous silica activity and less sensitive to the aqueous Na/Ca ratio than Ca-clinoptilolite, because Na-clinoptilolite can react directly to form Na-analcime. Ca-clinoptilolites are much more sensitive to the aqueous Na/Ca ratio, requiring a substantially increased ratio for analcime formation. Thus, for this particular clinoptilolite Al/Si ratio, increasing the clinoptilolite Ca content expands the clinoptilolite stability field at silica activities $<10^{-3.2}$ and decreases the stability field at silica activities $> 10^{-3.2}$. However, it is important to note that the aqueous Na/Ca ratio must be at least three orders of magnitude greater than is found in water at Yucca Mountain (Kerrisk 1987) to reach the "crossover point" for this clinoptilolite. The exact location of the "crossover point" depends on the chemical compositions of clinoptilolite and analcime used in the calculations. The effects of Na/K composition in clinoptilolite on equilibria with analcime (Figure 6.1-78) were modeled in the same manner as the Na/Ca compositions. Although clinoptilolite-analcime equilibria are

similar to those obtained for the Na/Ca system, present Yucca Mountain water compositions (Kerrisk 1987) plot on the opposite side of the "crossover point". Therefore, increases in aqueous K concentration increase the stability of clinoptilolite with respect to analcime, but increases in clinoptilolite K content decrease clinoptilolite stability.

Using the constraints outlined above, Chipera and Bish (1997) performed calculations using observed chemical formulae for Yucca Mountain clinoptilolites and a representative chemical formula for Yucca Mountain analcime. The 12 clinoptilolites used in the calculations were selected to represent the observed variation in chemical compositions, both in exchangeable-cation ratios and in Si/Al ratios. $Log[(a_{K+})^2/(a_{Ca2+})]$ versus $log[(a_{Na+})^2/(a_{Ca2+})]$ diagrams showing clinoptilolite-analcime equilibria are shown in Figure 6.1-79. The phase boundary for each of the 12 clinoptilolite compositions is portrayed as a line in Figure 6.1-79, where clinoptilolite is stable below that line and analcime is stable above. Figures 6.1-79a and c show equilibria calculated at cristobalite saturation and 100 and 150°C respectively. Assuming J-13 water composition, clinoptilolite is the stable phase with respect to analcime for all 12 clinoptilolite compositions at cristobalite saturation and 100°C. However, when temperature was increased to 150°C, several clinoptilolite/analcime equilibria shifted below the Yucca Mountain water compositions, thereby shifting the stability field for several clinoptilolite compositions to analcime. Likewise, Figures 6.1-79b and d show the results for the 12 clinoptilolites at 100 and 150°C with an aqueous silica activity in equilibrium with quartz. The effect of decreasing the aqueous silica activity was to shift the equilibria further, with several additional clinoptilolite/analcime equilibria shifting below the Yucca Mountain water compositions. At 150°C, with an aqueous silica activity in equilibrium with quartz and assuming J-13 water composition (Figure 6.1-79d), approximately half of the clinoptilolite/analcime equilibria shift to the analcime stability field. Because the chemical composition of Yucca Mountain analcime is fairly constant, the effect of varying the analcime Si/Al ratio within the limits observed at Yucca Mountain was to shift the equilibria only slightly at all silica activities and temperatures. It is important to note that although J-13 water and the pore water chemistry (Yang 1992) are considered representative of water in the Topopah Spring Tuff, other water compositions measured at Yucca Mountain (Kerrisk 1987) result in significantly reduced stability fields for clinoptilolite. Thus, for example, assuming the Na-rich water composition of Kerrisk (1987) at 100 or 150°C in equilibrium with quartz, stability fields for clinoptilolite exist for only a few clinoptilolite compositions (Figures 6.1-80b and d).

The thermodynamic calculations show that silica activity, temperature, and the concentration of K, Na, and Ca in both clinoptilolite and in groundwater are all important in determining clinoptilolite-analcime equilibria. Although the measured cation ratios in clinoptilolite were used in these calculations, clinoptilolite is well recognized for its cation-exchange capacity. For example, based on measured compositions of water migrating through fractures at Rainier Mesa (~50 km north-northeast of Yucca Mountain), White, A.F., Claasen et al. (1980) concluded that water compositions in fractures are dominated mainly by dissolution of vitric tuff but are modified during infiltration through zeolitized tuffs. Thus, the existing clinoptilolite exchangeable-cation composition may well change in response to an increase in temperature and/or a change in water chemistry.

The selectivity of clinoptilolite for various alkali and alkaline-earth cations has been well documented since the early studies by Ames (1964a, 1964b). Cation exchange however is not a

simple process in clinoptilolite and is a function of several factors including the cation species, the selectivity of each exchange site for a particular cation, the temperature at which the exchange occurs, and the ionic strength of the exchange solution. Unfortunately, reliable data at elevated temperatures and in multicomponent systems do not exist. Several generalizations, however, can be drawn from the available literature to predict cation exchange in clinoptilolite under conditions resulting from emplacement of a potential waste repository. At low ionic strengths, clinoptilolite has a greater affinity for divalent versus monovalent cations (Barrer and Klinowski 1974; Bruton et al. 1993; Pabalan 1994; Pabalan and Bertetti 1994). At the ionic strengths present at Yucca Mountain, clinoptilolite has a strong preference for Ca^{2+} over Na^{+}. Bruton et al. (1993) also concluded that the selectivity of clinoptilolite for Ca^{2+} increases with increasing temperature.

Recently, Carey, Chipera, Bish (1997) further explored the implications of cation exchange on the analysis of clinoptilolite-mordenite-analcime equilibria based, in part, on the results of Pabalan (1994). At a given Si/Al ratio, the equilibrium follows the pure Na^{+} end-member breakdown curve at high $\log[(Na^{+})^2/(Ca^{2+})]$ and follows the pure Ca^{2+} end-member curve at low $\log[(Na^{+})^2/(Ca^{2+})]$. The region of transition between the two end-member cases results in only small departures from the end-member curves. Consequently, a useful approximation to these equilibria is given by the two end-member curves. Aluminous clinoptilolite is more stable than siliceous clinoptilolite at lower $\log[(Na^{+})^2/(Ca^{2+})]$ and is little different at higher $\log[(Na^{+})^2/(Ca^{2+})]$. The results for the Na^{+}-K^{+} aqueous fluid are similar, but the deviation from the end-member curves enhances the stability of analcime at higher $\log[(Na^{+})/(K^{+})]$ and has a different sense of curvature.

6.1.6.3.4 Integration of Natural-Analog and Thermodynamic Studies

It is useful to compare the thermodynamic modeling results with the information obtained on zeolite stability at Yucca Mountain. Bish and Aronson (1993) suggested that clinoptilolite reacted to form analcime in drillhole USW G-2, in the northern end of Yucca Mountain, at temperatures of 70 to 100°C. However, these high temperatures were not attained in drillhole USW G-3, much farther to the south, yet clinoptilolite-bearing assemblages nevertheless grade into analcime-bearing assemblages with depth in that drillhole. Data presented in Broxton, Bish, Warren (1987) show a trend in clinoptilolite compositions at Yucca Mountain where, with increasing depth, clinoptilolite compositions change from K rich to Na rich in the western part of Yucca Mountain and to (Ca + Mg) rich in the eastern part of Yucca Mountain. Also, the water in eastern Yucca Mountain is K rich relative to the Na-rich water in western Yucca Mountain. Because drillhole USW G-3 is in the western domain, it appears that the Na-K-Ca cation ratios in both clinoptilolite and groundwater facilitated the reaction of clinoptilolite to analcime in that drillhole at comparatively low temperatures.

Similarly, there is evidence that a reduction in aqueous silica activity affected the clinoptilolite-to-analcime reaction at Yucca Mountain. Using water chemistry from packed-off zones in several drillholes at Yucca Mountain, Duffy (1993a) noted that, although solubility of a given silica polymorph increases with temperature, the deeper, higher-temperature water samples from these drillholes show consistently lower dissolved silica concentrations than do the lower-temperature, shallow samples. Duffy attributed this variation in silica activity to the presence of more soluble silica polymorphs at shallow depths that have been replaced by quartz at greater

depths. A reduction in aqueous silica activity with depth undoubtedly affected clinoptilolite-analcime equilibria in drillhole USW G-3. Clinoptilolite persists to depths greater than the deepest occurrence of opal-CT or cristobalite in many drillholes (USW G-1, USW G-3, USW G-4, UE-25 b1h, UE-25 p#1) and, thus, probably exists at an aqueous silica activity in equilibrium with the abundant quartz at depth in those drillholes. Although an aqueous silica activity equal to or greater than cristobalite saturation stabilizes clinoptilolite, it appears that reduction in the aqueous silica activity to that of quartz saturation, although generally stabilizing analcime, did not automatically result in conversion of all clinoptilolite to analcime at Yucca Mountain. This effect is illustrated well by Figures 6.1-79b and d, which show that several clinoptilolite compositions are stable with respect to analcime at 100 and 150°C in Yucca Mountain waters at an aqueous silica activity in equilibrium with quartz.

The observed distribution of clinoptilolite and analcime in rocks at Yucca Mountain suggests that the reaction does not occur as a sharp, well-defined transition as a function of depth or temperature. Clinoptilolite/heulandite and analcime can and do coexist within single samples, often to depths well beyond the first occurrence of analcime. There are factors other than silica activity that influence clinoptilolite stability. Variable Al/Si ratios and exchangeable cation composition can stretch the stability regime (this variability is not available to analcime – in this regard, it is notable that analcime, which has a much more restricted range of compositions, never occurs with cristobalite/opal-CT). To determine the nature of clinoptilolite/heulandite coexisting with analcime at depth in drillhole UE-25 p#1, Chipera and Bish (1988) concentrated the zeolite fraction from drill cuttings at a depth interval of 1,061/1,064 m (3,480/3,490 feet). The clinoptilolite/heulandite in this interval occurs 536 m (1,760 feet) below the deepest confirmed occurrence of opal-CT or cristobalite, suggesting that the aqueous silica activity is in equilibrium with the abundant quartz. In addition, the temperature appears to have been greater than 100°C as suggested by the presence of an R1 illite/smectite (allevardite; see Perry and Hower 1970) in that interval of the drillhole. Thermal studies confirmed that the zeolite in this sample was heulandite. Other clinoptilolite/heulandite minerals coexisting with analcime at depth in Yucca Mountain are probably also heulandite as suggested by the equilibria calculations conducted in this study. Thus, observations of mineralogical relations at Yucca Mountain broadly agree with the trends predicted by the present thermodynamic calculations.

In summary:

- Clinoptilolite and mordenite are stabilized by elevated silica activity.
- Clinoptilolite of appropriate composition can survive to temperatures of 100°C and probably higher for particular compositions.
- Solution chemistry (Na^+, K^+, Ca^{2+}) affects clinoptilolite-mordenite-analcime equilibria and Na^+-rich solutions stabilize analcime.
- Mineralogical evolution of the silica polymorphs can have a significant affect on clinoptilolite and mordenite stability through changes in silica activity.
- Clinoptilolite and mordenite show little thermodynamic tendency to react under present-day conditions and may be stable in the presence of metastable silica polymorphs.

6.1.6.4 Implications for Thermally Perturbed System

The present-day mineral distribution at Yucca Mountain provides evidence of past alteration that includes the reaction of glass to zeolites and clays at moderate depth, the loss of metastable silica polymorphs at depth, the zeolitization of rock units at moderate depth, the conversion of clinoptilolite and mordenite to analcime at greater depths, and the transformation of smectite (a swelling clay) to illite (a nonswelling clay) at greater depths.

The potential repository would be located in rocks that, for the most part, have not yet experienced this mineral alteration. This indicates that reactions involving glass, the metastable silica polymorphs (cristobalite, tridymite, and opal-CT), and the zeolites (principally clinoptilolite and mordenite) should be the focus of studies of potential mineral reactions in the repository environment. The rock types in which these minerals occur are also important because permeability and porosity are key factors in the accessibility of fluids that may drive reactions. The principal rock types include vitric, welded, nonwelded, and zeolitized units.

A conceptual model outlining the conditions for these reactions was presented in Subsection 6.1.6. However, it should be noted that the focus of the conceptual model is on the bulk mineralogy of Yucca Mountain. Fracture minerals, such as manganese oxides, may play an important role in retardation and may also participate in mineral transformations. However, such transformations of fracture minerals are outside the scope of this model.

The rock immediately underlying the devitrified potential host rock at Yucca Mountain is a vitrophyre composed of ~96 percent glass (Vaniman, Bish et al. 1993). Several factors must be considered in evaluating the effects of heat on this vitrophyre. One factor is the geochemical impact of heating. The vitrophyre contains about 500 to 700 μg chlorine, about 700 μg fluorine, and about 20 to 50 μg sulfur per g (Broxton, Warren, Hagan et al. 1986; Bish, Brown et al. 1987; Vaniman, Bish et al. 1993). These concentrations of potential acid-forming species in the vitrophyre are at least twice as high as in the devitrified or zeolitized tuffs (Broxton, Warren, Hagan et al. 1986). Depending on the water-rock ratio and the dynamics of vapor and saturated systems, zones of altered water composition could form by leaching of halogens from the vitrophyre. The vitrophyre also contains the only appreciable amounts of ferrous iron in the Topopah Spring Member (Caporuscio and Vaniman 1985), but the 0.3 percent FeO detected is too small to cause any significant reduction in the oxidizing state of groundwaters at Yucca Mountain.

Another factor in the heating of the vitrophyre is possible changes in mineralogy with vitrophyre crystallization. Crystallization of the Topopah vitrophyre in saturated conditions can lead to clinoptilolite formation (Knauss and Peifer 1986), a result that could increase sorption of alkaline-earth radionuclides migrating from the waste canisters into the vitrophyre. To design experiments that will provide the required data, it is necessary to consider the expected temperature rise in the vitrophyre and the effects of a_{H_2O}. The conditions of future vitrophyre alteration under repository conditions may be similar to the alteration that occurred soon after tuff emplacement 13 m.y. ago, when silica minerals, feldspars, zeolites, and clays formed along fractures that provided downward pathways through the hot (~40 to 100°C) vitrophyre (Levy and O'Neil 1989).

Other thermal effects, particularly concerning the physical response of the rock mass, are possible. Density or volume or both may decrease if water is extracted from the vitrophyre. The present bulk density of vitrophyre samples ranges from 2.21 to 2.34 g/cm^3 (Nimick and Schwartz 1987), but the effect of temperature on density is not known. The unconfined thermal expansion of vitrophyre samples has been observed to decrease from ~6 x 10^{-6}/°C to 2–5 x 10^{-6}/°C at about 200°C (Nimick and Schwartz 1987). Changes in porosity could also result from water loss. Porosity data for vitrophyre samples range between 1.4 and 7.0 percent (Tien et al. 1985; Lappin et al. 1982; Anderson 1981; Nimick and Schwartz 1987). With such low porosity and an ambient water saturation of 30 to 75 percent (Tien et al. 1985), an increase in water content of only ~2 percent relative to the rock mass could change the hydrologic conditions in the vitrophyre from unsaturated to saturated, with a concomitant loss of matric potential for waste retardation in this unit. This effect may occur in an aureole around the waste canisters.

If the heat load in the repository is ~57 kW/acre, a "dry-out" zone will develop a few tens of meters above and below the repository horizon (Buscheck and Nitao 1992). A much hotter repository with twice this thermal loading would have more extensive dry-out zones (Buscheck and Nitao 1993). At 114 kW/acre, the dry-out zones will expand outward to ~210 m above and ~160 m below the repository in the first 2000 years. These hot, unsaturated zones will slowly migrate back toward the repository over the subsequent 3,000 to 8,000 years, with rewetting to fully ambient conditions at the core of the repository only after 200,000 years (Buscheck and Nitao 1993). Despite the long-term heating effects of the repository, it is likely that the effective a_{H_2O} in the vitrophyre below the repository will remain high. Water vapor is likely to be retained in the dry-out zones because of confinement of the upper condensation zone within the mountain, and vapor communication with the lower condensation zone and ultimately with the static water level. However, this scenario is not a certainty. Net vapor loss could occur if venting takes place above the repository (perhaps along faults), and deposition of silica near the lower condensation zone seals off the repository from vapor communication with the static water level. It is important to remember that the heating time scales being considered are as long as or longer than the longevity of some natural geothermal systems, which may gradually take advantage of singularities such as faults to develop preferred pathways.

Samples of the lower Topopah Spring Tuff vitrophyre were used in short-term and long-term heating experiments (Vaniman, Bish et al. 1993). Thermogravimetric analysis data (short-term heating) collected on vitrophyre samples show that there is a uniform two-part dehydration behavior for all of the vitrophyre samples. The samples analyzed (Vaniman, Bish et al. 1993) represent the northern part of the potential repository block (USW G-1), the eastern part of the block (USW G-4), and the southern part of the block (USW GU-3). The most noticeable variability between these samples is the difference in the amount of lost volatiles, which is greatest in the USW G-1 sample (4.6 ± 0.4 percent) and smaller in the GU-3 sample (2.8 ± 0.04 percent). The USW G-4 sample has an intermediate weight loss (3.5 ± 0.2 percent). These appear to be real variabilities in volatile content of the glasses, because all three are vitrophyre samples with glass abundances of over 90 percent. It is important to note, however, that the second-stage weight loss above 650°C in all 10°C/min thermogravimetric analysis runs is relatively constant at 1 to 1.1 percent for all three samples. This constant second-stage weight loss suggests that the parental obsidian glass of the vitrophyre had a relatively constant water content before it became perlitic. Perlites, with more H_2O, differ from obsidians in that they contain more water than can be dissolved in a magma of their composition at low pressure

(Kennedy 1955). The initial ~1 percent water in the glasses was probably magmatic, whereas the added perlitic water is likely to have been meteoric (Ross and Smith 1955; Friedman and Smith 1958; Nasedkin 1964). The consensus of these researchers, that perlitic water is meteoric, provides independent support for the conclusion by Levy and O'Neil (1989) that vitrophyre alteration in the Topopah Spring Member was accomplished largely by meteoric water.

A two-stage volatile loss is seen in the thermogravimetric analysis data, which suggests that two types of water "sites" occur in these perlitic samples. This two-stage weight loss in thermogravimetric analysis studies is typical of many perlitic glasses (Nasedkin 1964). One possible explanation for this observation is a difference in the glass sites for molecular H_2O and for structural OH. Work on H_2O-OH speciation in rhyolitic glasses, however, suggests that the H_2O/OH ratio is <1 for glasses with less than 5 percent H_2O, and that both H_2O and OH content vary with total water content (Stolper 1982). This observation does not provide a simple explanation for the two-stage weight loss seen in our TGA data, in which a relatively constant ~1 percent weight loss occurs above 650°C regardless of the total volatile content of the vitrophyre glasses. Also, if the two-stage weight loss were due to the difference between H_2O and OH retention, one would expect the more strongly bonded OH to be lost at higher temperatures, and therefore, the major weight loss would be seen in the high-temperature stage of dehydration. This is not the case.

An alternative explanation for the two-stage weight loss is that water in obsidian is not released at temperatures below 600 to 800°C (Hampton and Bailey 1984). This scenario indicates that magmatic water is retained to relatively high temperature. It is possible that the first-stage water loss in perlites below 650° to 700°C represents the loss of most of their acquired post magmatic water, whereas the second-stage water loss at higher temperature is predominantly of magmatic water. The different temperature ranges for the two stages of water loss may be due to the glass transition behavior of rhyolitic compositions on heating. This transition occurs at about two-thirds of the melting temperature, at which point the glass viscosity drops to about 10^{13} p and the glass begins to expand at a more rapid rate (Hampton and Bailey 1984). Some TGA experiments on the G-4 vitrophyre sample were taken to the instrumental limit (1,050°C), at which point the sample melted; experiments at 1,000°C, however, sintered but did not melt the sample. Thus, the melting point is in the range of 1,000 to 1050°C, and the glass transition temperature is probably around 650 to 700°C, which corresponds very closely to the temperature range at which the second-stage dehydration begins in our samples (Vaniman, Bish et al. 1993). The expansion and increasing molecular rearrangements within the glass above this temperature probably account for the second-stage weight loss. This idea neither supports nor detracts from the hypothesis that the second-stage water is largely magmatic but merely provides a mechanism for the second-stage increase in weight loss during thermogravimetric analysis studies.

The two-stage water loss is important in interpreting the long-term isothermal heating experiments. Long-term 400°C oven experiment with the sample from USW G-4 quickly reached a weight loss of 2.57 percent and then stabilized. This plateau represents a somewhat greater loss than the 2.38 percent first-stage weight loss at ~650°C in 10°C/min thermogravimetric analysis studies (Vaniman, Bish et al. 1993). This difference is to be expected because the weight losses in dynamic thermogravimetric analysis runs will always be lower than the equilibrium dehydration loss that would be attained if the sample were allowed to sit at a comparable temperature. This result suggests that in oven experiments as hot as 400°C,

only the first-stage water loss is seen in experiments as long as 3.4 years. On the basis of this experiment, the water loss seen at 400°C appears to coincide with the first-stage water loss observed in thermogravimetric analysis studies; this represents a reasonable "100 percent reaction" limit for long-term dry heating at temperatures of 400°C or less.

A time-temperature-dehydration diagram can be constructed from the long-term heating data (Figure 6.1-80). The contour lines within this figure represent the percentages of water loss from the G-4 1330 perlitic glass, increasing toward the upper right corner with increasing time and temperature. These contours are drawn without curvature; the data available are sufficient to locate the positions of most lines and the slopes of some but are not sufficient to determine any deviations from linearity within the 0.1- to 10,000-hour range of this figure.

Plotted within Figure 6.1-80 are curves for 10°C/min heating from an initial temperature of 20°C, and 2°C/min heating from an initial temperature of 20°C for comparison with 10°C/min and 2°C/min thermogravimetric analysis curves for comparably fine-ground powder. Kinetic effects are important in the evolution and removal of gas during thermogravimetric analysis (Bish and Duffy 1990); extrapolations to such heating curves from the equilibrium water evolution contours of Figure 6.1-80 should therefore show dehydration occurring at lower temperature than in the actual thermogravimetric analysis experiments, which is the case. The kinetically affected 10°C/min TGA pathway has a T_r (temperature of most rapid weight loss) of 318°C, 74°C higher than the equilibrium 10°C/min pathway. With slower heating rates, the differences between actual thermogravimetric analysis water loss curves and those calculated from the equilibrium data become smaller; the shift between actual and equilibrium curves at T_r of a thermogravimetric analysis run at 2°C/min is only 62°C.

No mineralogic alteration or recrystallization of the vitrophyre occurred under dry heating, in accord with the work by Friedman and Long (1984). This result is very different from the observed formation of clinoptilolite from vitrophyre glass in saturated heating experiments (Knauss and Peifer 1986). Dry heating and saturated heating represent end-member alteration conditions. Actual conditions near the potential repository are more likely to involve water vapor. Effects of steam heating remain a topic of study.

The only significant chemical alteration of the vitrophyre under dry heating was a loss of fluorine. After 3.4 years of heating at 100°C, a vitrophyre sample lost 20 percent, and at 400°C, a sample lost 60 percent of the original fluorine. None of the other volatile elements, including chlorine, were lost. Under steam conditions with local condensation of heated water, leaching of both Cl and F may occur.

If 57 kW/acre of radioactive waste are emplaced in the potential repository at Yucca Mountain, the completion of the repository will result in the burial of a heat engine with a slowly decaying power of ~84 MW operating for thousands of years. An even hotter repository design has been suggested (Buscheck and Nitao 1992, 1993). Condensation of water outside the dehydration zone should maintain water-saturated warm air in the rock mass around the canisters as long as the condensation zone is preserved and vapor communication is maintained. Lu et al. (1991) modeled thermally driven vapor movement that will result in a net loss of water vapor from the unsaturated zone. Although they assumed for modeling purposes that the water lost by evaporation is replenished from precipitation or from the water table, they also found that for a

broad range of simulations, the western part of the repository has the most rapid water loss. The western portion of the potential repository is also the portion that will be closest to the vitrophyre. Because of this relationship between repository geometry and the results of Lu et al. (1991), dry heating of some portion of the vitrophyre is not impossible, although it is unlikely. In the absence of definitive modeling to prove otherwise, it is worthwhile to consider the possible consequences of vitrophyre dehydration as a possible end-member response contrasted with saturated heating.

The effective a_{H2O} within the vitrophyre in space and time will determine whether such water exchange takes place. At one extreme, assuming complete loss of 2.5 percent perlitic water from a 15 m-thick portion of the vitrophyre, the water release would be equivalent to an 84 cm column of water. This water could migrate to the condensation zone away from the waste canisters, take part in hydrous alteration of the heated tuff, or be lost from the mountain through vapor transport. On cooling, however, the dehydration zone around the waste canisters will rehydrate, and warm water, probably with elevated ionic strength, will migrate back toward the waste. Under such conditions, it is likely that the ultimate impact on any dehydrated portions of the vitrophyre will be a zeolitic alteration similar to that anticipated for those portions of the vitrophyre that remained saturated while they were heated.

6.1.7 Kinetic Effects in Predictions of Mineral Stability at Yucca Mountain

The factors governing the rates of minerals transformation at Yucca Mountain are complex. There are three classes of kinetic processes that can limit the formation of an equilibrium or more stable mineral assemblage: diffusion, mineral-interface reactions, and nucleation phenomena. In a general sense, it is not possible to predict which of these processes may restrict the rate of transformation for a given reaction. There may be particular geological environments in which the rate of diffusion limits the capacity of a reaction; another in which the same reaction is hindered by surface-complexation of competing species; or the same reaction may be frustrated by a lack of suitable nucleation sites for the development of the product phase. For any given situation, the significance of these processes must be considered with respect to the available experimental and observational data on the character of the rocks in question.

Each of the three kinetic processes can occur by a variety of distinct mechanisms. A diffusion-limited reaction can occur because the rate at which reactant or product species move through the aqueous medium to the site of reactions is slow, as in low-permeability rocks in which the fluid does not communicate readily with the rock volume. This reaction can also be generalized to consider the rate of fluid flux through a rock volume. For example, a fluid may readily equilibrate throughout a limited rock volume (say 1 m^3), but the system is essentially closed because of a restricted fluid flux. In this case, a reaction proceeds rapidly while the system is far from equilibrium but slows as the fluid saturates the rock volume. Diffusion can also limit the rate of solid-state transformations. In this case, reactants and products must diffuse through the mineral structure to the reaction sites. In some minerals, a leached layer may develop, and the rate of reaction then becomes proportional to the rate at which new species move through the leached layer. There are abundant measurements of the diffusion coefficients for aqueous species. There are fewer data for solid-state diffusion, but these can often be estimated. Lastly, this process can also consist of thermal diffusion in that a reaction may be limited by the rate of heat supplied.

Surface-interface reaction kinetics can occur by many distinct mechanisms. Rates of adsorption and desorption of reactant species from surface sites can be an important rate-limiting mechanism. Experimental measurements of dissolution and precipitation reaction rates are commonly measurements of surface-growth processes limited by interface kinetics. Reaction rates can be enhanced or impeded by species extraneous to the reaction itself. Such species can help bind reactants to the surface or they can compete with the reactant for reactive sites, thereby slowing the reaction. Surface processes are limited by the available surface area: large mineral grains have relatively little reactive surface area on a per-unit-mass basis compared with small mineral grains. Porosity plays a role in reaction kinetics because it affects the degree of exposure of mineral surfaces to reactants in the aqueous medium: some regions of a mineral surface may be inaccessible to reactants because they are not exposed to the aqueous medium. In addition, surfaces differ in their degree of reactivity as a function of their defect structure and underlying crystal structure. There are significant data for many of the kinetics of surface reactions, and their magnitude can be reasonably bounded.

Nucleation kinetics are much more poorly understood than either diffusion or surface-interface processes. In general, the rate of nucleation is zero until a certain degree of oversaturation occurs; higher degrees of oversaturation increase the rate of nucleation further. The amount of oversaturation necessary to initiate nucleation is difficult to quantify but depends on surface energy and the nature of the substrates available for nucleation. Homogeneous nucleation within the fluid phase generally requires very high degrees of supersaturation. Nucleation on a substrate having a similar structure (templating) can greatly reduce the amount of supersaturation required to initiate nucleation. Unfortunately, there are very few experimental data that are relevant to nucleation kinetics in the natural environment.

6.1.7.1 Dissolution/Precipitation Processes

The kinetic processes of most likely significance for mineral evolution at Yucca Mountain are surface-interface controlled. For example, Lasaga (1984) has argued that most minerals have sufficiently low solubilities that their dissolution rates are limited by interface processes rather than transport. Fortunately, nucleation kinetics are not likely to be an issue because, for the most significant kinetic processes involving the silica polymorphs, quartz is already present in the rocks.

The dissolution/precipitation kinetics of many minerals has been measured using a given mass of material of known surface area (typically a BET surface area) in a known volume of fluid. The studies are conducted either in a batch mode with continuously changing solution compositions (e.g., Murphy, W.M. et al. 1996) or preferably in flow-through devices at constant solution composition (for example, Nagy et al. 1991). The summary of kinetic data given in Table 6.1-25 has been interpreted using transition state theory (e.g., Nagy et al. 1991) in which the surface-area normalized rate of dissolution or precipitation is expressed as

$$R(\text{moles}/\text{m}^2\text{s}) = -k_{\text{diss}}\left(1-\frac{IAP}{K_{\text{eq}}}\right), \qquad \text{(Eq. 6.1-8)}$$

where the ratio of the ion-activity-product (IAP) to the equilibrium constant (K_{eq}) expresses the degree of saturation and k_{diss} is the rate constant for the dissolution reaction. The parameter k_{diss}

is not an intrinsic rate parameter but may depend on pH and on other surface-adsorbed species (Nagy et al. 1991). The rate equation indicates that the rate of dissolution reaches a constant value ($-k_{diss}$) for significant degrees of undersaturation but that the rate of precipitation increases without bound for increasing supersaturation.

Lasaga, Soler et al. (1994) provided a summary of values of k_{diss} for a number of minerals, many of which are relevant to Yucca Mountain. Table 6.1-25 contains this summary in addition to more recent data obtained for clinoptilolite and analcime by MacInnis et al. (1995) and W.M. Murphy et al. (1996).

The lifetime of 100 μm spherical crystals was calculated assuming that dissolution occurred in continuously undersaturated solution ($R = -k_{diss}$; rates for solutions closer to equilibrium will be slower) with the following equation (Lasaga 1984):

$$\Delta r = -k_{diss} V_{xl} t \,, \qquad \text{(Eq. 6.1-9)}$$

where Δr is the change in radius of the crystal, V_{xl} is molar volume, and t is time. This calculation provides a useful estimate of the time period for significant dissolution to occur at Yucca Mountain. These data suggest that at 25°C metastable minerals at Yucca Mountain that are smaller than 100 μm will probably have dissolved during the 12 Ma history of the mountain.

Higher temperatures would accelerate these rate constants and make the survival of such minerals even less likely. The difference in $\log(k_{diss})$ taking an average activation energy of 15 kcal/mol (Lasaga, Soler et al. 1994) is given by:

$$\Delta \log k_{diss} = 3278\left(\frac{1}{298.15} - \frac{1}{T}\right) , \qquad \text{(Eq. 6.1-10)}$$

where T is absolute temperature. Thus, at 100°C the values of $\log(k_{diss})$ in Table 6.1-25 would increase, on average, by 2.2, decreasing the time to dissolution by a factor of approximately 150. At these rates of dissolution, the calculations indicate that no metastable mineral could survive in moderately undersaturated solutions. These rate constants also suggest that very significant reaction could potentially occur during the period of thermal perturbation at Yucca Mountain (of order 10^4 years).

The dissolution rate obtained for clinoptilolite by MacInnis et al. (1995) using a flow-through apparatus appears to be anomalous with respect to other minerals and is not in agreement with the batch study of W.M. Murphy et al. (1996; Table 6.1-25). Unfortunately, the study of MacInnis et al. is the only source of data for dissolution rates of clinoptilolite at elevated temperatures (50, 80, and 125°C; see Carey and Bish 1996). MacInnis et al. did not observe a constant dissolution rate at significant undersaturation, but they showed data indicating a linear relationship between rate and undersaturation. Consequently, the dissolution process they observed may be distinct from that modeled by transition state theory. MacInnis et al. also observed some evidence of inhibition by aqueous Al, but they were unable to quantify this effect.

There is no single study providing rate data for analcime at more than one temperature. Lasaga, Ganor et al. (1994) determined the dissolution of analcime at 80°C with flow-through methods. Their rate equation is similar to that determined by MacInnis et al. (1995) in which the rate depends linearly on the degree of saturation:

$$R = -10^{-12.4} a_{Al(OH)_4^-}^{-0.27} \left(\left|\Delta G(\text{kcal mol}^{-1}\right|\right)^{105}, \qquad \text{(Eq. 6.1-11)}$$

where a is activity and the measurements were made at pH 8.6 to 8.9 and the degree of saturation is represented by the Gibbs free energy of the dissolution reaction. Typical values at 80°C for the net dissolution rate constant, $\log(k_{diss})$, are approximately -11. Again, these rate constants do not agree well with the batch-study values of W.M. Murphy et al. (1996) where log rates were -11 at 25°C.

In summary, the available kinetic data for both analcime and clinoptilolite are not consistent or well constrained and reflect the incomplete status of kinetic data measurement for these minerals. Based on existing data, the dissolution of clinoptilolite does appear to be slower than analcime, by a factor near 100.

6.1.7.2 Applicability of Dissolution/Precipitation Data to Yucca Mountain

The kinetic data in Table 6.1-25 and their referenced sources permit some interesting calculations to be performed on the expected longevity of the metastable silica polymorphs at Yucca Mountain. Where cristobalite and quartz coexist, a simple growth-and-dissolution process should have operated in which adjacent crystals of cristobalite and quartz dissolve and grow. Using the rate constant data of Rimstidt and Barnes (1980), the time necessary to completely dissolve a cristobalite grain of a given size can be calculated (see Table 6.1-25). These data indicate that cristobalite having a size consistent with observations (radius <50 μm), the maximum lifetime should have been less than 500,000 years. Thus, it is evident that dissolution and precipitation processes are not adequate to explain existing silica polymorph distributions (or that of clinoptilolite, because the thermodynamic data indicate the destabilization of clinoptilolite in the absence of metastable silica polymorphs). The silica polymorphs at Yucca Mountain are significantly less reactive than the predictions based on experimental dissolution rate data would indicate. The predictions are of dissolution rates that are at least 1 order of magnitude faster than is consistent with the known age of Yucca Mountain. Therefore, the rate data of Table 6.1-25 could perhaps be used as an upper bound on reaction kinetics but have an uncertain relevance to processes actually occurring at Yucca Mountain.

6.1.7.3 An Alternative Kinetic Model for Cristobalite and Opal-CT

The discrepancy between laboratory measured dissolution/precipitation data and some natural environments prompted Duffy (1993a, 1993b) to develop an alternative kinetic model for the transformation of opal-CT and cristobalite to quartz. Because the dissolution data of Rimstidt and Barnes (1980) yield unreasonably short times for the reaction, Duffy suggested that the rate of precipitation of quartz determines the rate of transformation of opal-CT and cristobalite to quartz.

An explanation for the retardation of quartz precipitation may be developed from experimental results on the behavior of quartz in silica supersaturated solutions. Baumann (1971) placed quartz in pH 8.5 solutions at 25°C that were saturated with respect to amorphous silica. The aqueous silica activity was observed to decrease with time. When fresh quartz crystals were used, the solution composition came to quartz saturation within 40 days. However, when the same crystals were repeatedly placed in the amorphous-silica-saturated solution, the final value of the aqueous silica activity was found to be higher with each repetition of the experiment. Iler (1979) suggested that the increase in solubility was caused by the deposition of successively less well-ordered surface layers. It appears that if quartz crystals are maintained in a supersaturated solution, layers that have successively higher defect concentrations are formed on the quartz. Additional layers cease to form when the surface of the disturbed layer comes into equilibrium with the solution. Further growth of the quartz occurs only as defects diffuse out-of or order-within the surface layer. Hydroxyl groups are probably the dominant type of defect in the surface layer because the initial attachment of silica takes place as $Si(OH)_4$ groups, although other foreign ion defects are certainly possible.

The migration of defects is, in general, a complex function of the chemical potential gradient, which may run counter to the defect concentration gradient causing defects to diffuse out of the surface layer. Because the defect concentration gradient may vary as a function of solution supersaturation, it is also possible that diffusion may be inward under some conditions and outward under others and that an intermediate condition exists in which the chemical potential of defects is constant throughout the disturbed zone and no diffusion occurs.

Such a situation would provide an explanation for the observation that quartz does not crystallize until opal-CT has become highly ordered. At higher aqueous silica activities than those in equilibrium with ordered opal-CT, Duffy (1993b) proposed that the chemical potential gradient drives defects to diffuse inward, inhibiting growth of or even destroying quartz crystals and that, at lower aqueous silica activities, diffusion of defects is outward and quartz precipitation proceeds. At aqueous silica activities substantially below ordered opal-CT saturation, the defect layer becomes insignificant, and the rate of quartz growth becomes proportional to the degree of supersaturation. The pH dependence of the rate probably results because the majority of defects are either hydrogen or hydroxide ions.

A kinetic model that is consistent with these experimental observations has two components. In the first stage, the kinetics of completely ordering opal-CT and lowering the aqueous silica activity are the most significant. Following the development of ordered opal-CT (essentially the same as cristobalite), the kinetics of the transformation of ordered opal-CT to quartz are dominant. The ordering of opal-CT may be a relatively simple process of bond rearrangement in the solid state. The ordering of opal-CT is directly reflected by its 101 interplanar spacing, $d(101)$, which varies from 4.13 Å for highly disordered opal-CT to 4.04 Å for the ordered form. The ordering is associated with a decrease in aqueous silica activity (for example, Lasaga and Blum 1986).

Mizutani (1977) examined the $d(101)$ of opal-CT in 0.077 N KOH solution as a function of time at temperatures between 117 and 278°C and 10 MPa pressure. Kano and Taguchi (1982) conducted similar experiments in 0.1 N KOH solution at 200, 270, and 300°C and 10 MPa pressure. They found that the rate of ordering could be expressed as

$$\frac{dS}{dt} = kS, \qquad \text{(Eq. 6.1-12)}$$

where $S = d(101) - 4.04$ Å, t is the reaction time, and k is the rate constant.

They found that the temperature dependence of the rate constant followed an Arrhenius equation. Kano (1983) used this rate constant and derived a frequency factor that closely describes the variation of $d(101)$ for opal-CT in MITI Hamayuchi, a borehole in the Tempoku district, western Hokkaido, Japan. In contrast to the expected behavior of a solid-state transformation, these workers observed the rate of ordering of opal-CT to proceed much more rapidly in a high-pH environment than in a more nearly neutral natural environment. This pH dependence is similar to what has been observed for the opal-CT to quartz reaction (e.g., Ernst and Calvert 1969).

The kinetics of the transformation of opal-CT to quartz was studied by Ernst and Calvert (1969) in pure water; they calculated an activation energy of 23.2 kcal/mol. Ernst and Calvert's results indicate that the opal-CT to quartz transition would take 36,000 years at 100°C. Mizutani (1966) studied the reaction in 0.077 N potassium hydroxide and found an activation energy of 14.3 kcal/mol. Mizutani (1970) suggested that the different activation energies are caused by the difference in solution composition. The experiments of Ernst and Calvert also show a much slower reaction rate at a given temperature than those of Mizutani, in agreement with Campbell and Fyfe (1960), who observed that the rate of formation of quartz from cristobalite increased with increasing hydroxyl-ion concentration.

This model appears to be consistent with observations of the transformation of biogenic opal (opal-A) in the Monterey Shale in a stepwise process of opal-A to opal-CT that was followed by ordering of the opal-CT. Quartz crystallized only after ordering of the opal-CT was essentially complete (Murata and Larson 1975; Murata et al. 1977). The nature of the Monterey Shale and the agreement between inferred reaction times (Murata et al. 1977) and those predicted by Ernst and Calvert (1969) suggest that conditions in the Monterey Shale were probably near neutral.

6.1.7.4 Summary Conclusions for Kinetic Data

- Dissolution/precipitation rates of silica polymorphs predicted on the basis of laboratory kinetic data are not consistent with the observation of persistent opal-CT and cristobalite below the water table.

- Kinetic data are consistent with the necessity for saturated conditions for any perceptible reaction to occur.

- The fact that rates of reaction of silica are slower than those for clinoptilolite, in combination with the thermodynamic data, suggests that silica activity may be the rate-limiting step in the transformation of clinoptilolite and mordenite to analcime + quartz assemblages.

- Rates of dissolution and precipitation are enhanced significantly at 100°C and would predict significant reaction of all metastable mineral phases during a repository-induced thermal pulse.

- Dissolution and precipitation rates can be used to apply upper bounds to the rate of reaction of the silica polymorphs and, hence, the rate of reaction of clinoptilolite and mordenite to analcime.

- An alternative model based on the kinetic study of Ernst and Calvert (1969) of the opal-CT to quartz reaction predicts much more reasonable reaction rates.

6.1.8 Geochemistry and Mineralogy of Radionuclide Mobility at the Site

General Background I: Nature of Samples Used in Sorption Experiment—As part of an effort to determine how radionuclides will interact with rocks at Yucca Mountain, the Chemical Science and Technology Division (formerly Isotope and Nuclear Chemistry Division) of Los Alamos National Laboratory has conducted numerous sorption experiments. The radionuclides chosen for study were isotopes of americium, cesium, neptunium, plutonium, thorium, uranium, strontium, technetium, tin, barium, radium, cerium, europium, and selenium (Thomas 1987). Early work was conducted mainly on whole-rock samples from Yucca Mountain. Uncertainties exist, however, because natural materials are multicomponent mixtures of minerals, and it is often difficult to determine which mineral or minerals were responsible for the observed sorption. Also, natural materials may contain potentially important and highly sorptive trace phases that may not have been detected in the whole-rock samples. To better address these concerns, the early sorption studies were expanded to include pure mineral specimens.

To understand better the interaction of radionuclides with the various rocks and minerals used in the Chemical Science and Technology Division's experiments, it is important to determine the mineralogy in the samples using quantitative X-ray diffraction methods. Detailed results of the quantitative X-ray diffraction analyses for the samples used in batch- and column- sorption experiments are summarized in Chipera and Bish (1989, 1995). Quantitative X-ray diffraction results show that the Chemical Science and Technology Division's sorption sample can be broken down into three basic rock types, although subdivisions of these three types should be considered in evaluating the results of sorption experiments, as discussed below. The first rock type is devitrified tuff, characterized by prominent feldspar associated with tridymite, cristobalite, and/or quartz, often with minor amounts of hematite and smectite. The second major rock type is altered zeolitic tuff, generally characterized by abundant clinoptilolite, less often by abundant mordenite, and rarely by chabazite and or one of several lesser zeolites. Zeolitic tuff may be partially vitric in the basal Topopah Spring, Calico Hills, and upper Prow Pass units and typically contain opal-CT with lesser amounts of feldspar, quartz, and smectite. The third major rock type is vitric tuff, which is distinguished by its glass component and lesser amounts of smectite, zeolites, silica polymorphs, and hematite. There is a fourth type of sample

used in sorption experiments, obtained from surface soils and distinguished by the presence of variable amounts of opaline material, calcite, sepiolite, smectite, quartz, and feldspar.

In the reports of mineral abundances in the Chemical Science and Technology Division's samples, "clinoptilolite" is used to designate that the zeolite is of the clinoptilolite-heulandite group. No testing was conducted to determine whether the zeolite species was clinoptilolite or heulandite. Some of the Exploratory Studies Facility samples contain a zeolite that has been tentatively listed as "clinoptilolite" although the intensity ratios between the peaks is more in accord with that of heulandite. A second possibility is that the zeolite could be stellerite. Testing this hypotheses would require concentrating the zeolite with heavy liquids to enable a more positive identification due to the significant peak overlaps between stellerite and clinoptilolite, cristobalite, tridymite, and feldspar, which also occur in the samples.

The pure mineral phases used in batch- and column-sorption experiments represent many of the phases that have either significant sorption coefficients or are present in significant abundance at Yucca Mountain. Some of the minerals analyzed include clinoptilolite, smectite, quartz, opal, hematite, magnetite, feldspar, calcite, and the Mn-oxides hollandite/cryptomelane and romanèchite. Sorption studies were conducted on the Mn-oxides because they are important as fracture-lining minerals, even though they are not common in the bulk rock at Yucca Mountain. The importance of the Mn-oxides in water-rock interactions is described above in Subsection 6.1.5.2.

The quantitative X-ray diffraction results for each of the aliquots for a given sample (for example, dry-sieved, pretreated with J-13 water, pretreated with synthetic Paleozoic water, and original chunk) are in excellent agreement with each other. In several cases, the same sample and size fraction was analyzed twice, or closely neighboring samples were analyzed. Results for these samples are also in excellent agreement with each other, demonstrating the reproducibility of the quantitative X-ray diffraction methods and the generally consistent nature of mineralogy over short-range distances (with some notable exceptions; see Subsection 6.1.3.5). Chipera and Bish (1989) and Rogers and Chipera (1994) reported that sieving the samples into several size fractions did not have a significant effect on the relative amounts of individual minerals, although smectite and zeolite abundance were often slightly greater in the finer-size fractions. Likewise, the samples that were pretreated and washed in the J-13 and synthetic Paleozoic carbonate waters did not show significant variation in mineral abundances, although once again, the smectite and zeolite abundance were often slightly greater in the nonwashed samples (Chipera and Bish 1995). This result is to be expected, because clays are very fine grained and zeolites are soft minerals susceptible to mechanical disintegration and would be expected to be preferentially removed with the fine material from a sample by sieving or washing.

During one flow-through experiment using sample UE-25 UZ#16 1,362.3/1,362.7 (zeolitic sample from the Calico Hills Formation, Tac), some fine material was washed out the end of the column. A portion of this sample was examined by X-ray diffraction to determine whether the fine materials being washed out represent a close approximation of the bulk sample or if they represented a preferential loss of mineral components. Comparison of the results from this fraction with those obtained for the original bulk sample showed that the fine materials are very representative of the bulk sample used in the experiment. Thus, preferential loss of mineral components should not be a factor affecting the results of column experiments. It should be

noted, however, that calcite may be forming in the column and washing out in the fines, as evidenced by the presence of 2 percent calcite in the fine material.

The X-ray diffraction results for each of the aliquots for a given sample (e.g., dry-sieved, J-13 pretreated, Ca-Mg pretreated, and original chunk) demonstrate that there are no significant differences in the mineralogy due to the sample treatment. Although the zeolites and clays may change their exchangeable cation and the surface chemistry may be slightly altered due to the pretreatments in the J-13 and synthetic Paleozoic carbonate waters (thereby affecting sorption behavior), the bulk mineralogy changes very little (some clay and zeolite may be removed from the sample during washing). This result suggests that quantitative X-ray diffraction analyses for each aliquot are not necessary. Chipera and Bish (1995) determined that a single pretreated/washed aliquot of the same material that is used for the sorption experiments should be sufficient for the determination of representative mineralogy.

Daniels et al. (1982), Bish, Ogard et al. (1984), and Thomas (1987) have discussed the effects of mineralogy on the batch-sorption experiments. Minerals such as zeolites and clays have high cation-exchange capacities and interact strongly with simple cations such as cesium, strontium, and barium. Thus, zeolitic and clay-rich tuffs generally have high sorption ratios for these cations. In addition, sorption of cerium and europium was greater in zeolitized and clay-rich samples. Selenium, neptunium, uranium, and plutonium showed slightly higher sorption in zeolitized samples although there are no trends with the degree of zeolitization. Technetium, americium, and thorium showed no correlation with mineralogy. Surface sorption can be important for minerals with high surface areas and depends on a mineral's zero-point-of-charge and the pH of the system. Redox conditions can greatly affect sorption of some radionuclides, especially the actinides, and can significantly alter the solubility of some elements. In particular, phases such as iron and manganese oxides can interact strongly with redox-sensitive species. The role of manganese oxides in this regard is evident both in the wider literature (e.g., Hem 1978) and in the evidence of Ce oxidation by fracture manganese oxides at Yucca Mountain (see Subsection 6.1.5.2.3). Daniels et al. (1982) found that technetium in a nitrogen atmosphere was sorbed significantly more than in an air (oxidizing) atmosphere. There is also some evidence to suggest that migration of some radionuclides may be retarded in rocks containing carbonate minerals, perhaps due to precipitation.

In general, sorption of the various species can be associated with a particular mineral or minerals. Several of the surface samples submitted for quantitative X-ray diffraction analyses were surface calcretes from Yucca Mountain (for example, OP-DS, OP-WS, and FR-F) These samples had elevated sorption coefficients (K_ds) for neptunium, an element which normally has low K_ds for most of the subsurface rock types studied. It was initially suspected that the elevated K_ds in these samples were due to the sepiolite contained in the samples. However, pure samples of sepiolite from Vallecas, Spain, and Eskihi-Sher, Asia Minor, (obtained from Ward's Natural Science Establishment, Inc.) showed very low K_ds for neptunium. At present, it is unknown why the calcrete samples had elevated K_d for neptunium.

General Background II–Importance of rock type in the descriptions of sorption-study samples provided below, we include information on stratigraphic horizon as well as lithology. Table 6.1-26 shows the Project lithologic stratigraphy and the number of different samples from each

unit that have been used in sorption studies. In addition, the geochemically distinct units that are quartz-latitic in composition are shaded. The quartz-latitic units stand out in comparison with the generally rhyolitic compositions of the other units (see Figure 6.1-1 and associated text). The importance of distinctions between rhyolitic and quartz-latitic units is discussed in Subsection 6.1.8.1.

6.1.8.1 Mineralogy of Batch- and Column-Sorption Experiments

6.1.8.1.1 Mineralogy and Petrology of Samples Used in Batch-Sorption Experiments

The samples used in batch-sorption experiments were crushed and separated to obtain the 75 to 500 μm-size fraction. These materials were then pretreated with the groundwater being studied and centrifuged to separate the solids from the pretreatment water. One-gram aliquots of the solids were then equilibrated with 20 mL of solution containing the radionuclide of concern and centrifuged to separate solids from solution. Activity of the radionuclide associated with the solids was then determined by measurement of the activity left in solution. Details of the method and results can be found in Triay, Meijer, Conca et al. (1997). The samples used in these experiments have included both rocks and pure minerals. The rock samples were chosen to represent the lithologies of major stratigraphic subunits at Yucca Mountain; the pure minerals were selected to provide information on the most important mineral constituents of these stratigraphic subunits and of the fractures that occur in these subunits.

The results of batch-sorption experiments have provided abundant information on the relative extents of interaction between radionuclides of greatest concern and the rocks and minerals that constitute natural barriers at Yucca Mountain (Triay, Meijer, Conca et al. 1997). In particular, it has been found that Np presents a problem in its particularly low degree of interaction with most rocks and minerals representative of Yucca Mountain. Because of this poor performance in regards to Np, a more extensive sample suite has been tested with this radionuclide. The list of batch-sorption samples used is therefore more extensive for Np than for most other radionuclides, as reflected in Table 6.1-27.

The samples used in the batch-sorption experiments are the most comprehensive of any sample suite used in any sorption studies. In general, the results of batch-sorption studies show that the lithologies at Yucca Mountain can be broadly considered as the three major types shown in Table 6.1-27: zeolitic, devitrified, and vitric (Triay, Meijer, Conca et al. 1997). However, the distinctions between these lithologies are blurred in the sorption affinities of some radionuclides (for example, Am, which sorbs readily regardless of lithology) and require finer subdivision to explain the sorption behavior of other radionuclides. As an example of the latter case, Np exhibits particularly complex behavior.

The "reduction factor" for Np concentrations, required to meet U.S. Environmental Protection Agency limits, is not large (~46) compared to radionuclides such as Am and Pu (~12,000 to 18,000; Oversby 1987). Nevertheless, the sorption of Np is much poorer than either Am or Pu, making the detailed knowledge of small differences in Np sorption behavior very important (Triay, Meijer, Conca et al. 1997). Examination of the batch-sorption results, and of the fracture flow experiments discussed below (Subsection 6.1.8.2), shows that the understanding of Np movement at Yucca Mountain requires a more detailed assessment of site lithology

and mineralogy than the simple tripartite "zeolitic-devitrified-vitric" distinction allows. Figure 6.1-81, from Triay, Meijer, Conca et al. (1997), shows the range of small but variable K_d values for Np in J-13 water. If these data are considered only in light of the tripartite "zeolitic-devitrified-vitric" distinction, it appears that the only consistently high K_d values (>1) are in the zeolitic samples. The devitrified and vitric samples may have K_d values > 1, but there are some devitrified or vitric samples with lower K_d. However, by splitting out the quartz-latitic from the rhyolitic devitrified and vitric samples it can be seen that the lowest K_ds (<0.5) are associated only with quartz-latitic compositions, whether vitric or devitrified. The reassessment of Np sorption along these lines, based on geochemistry as well as lithology, allows interpretation of the data in Figure 6.1-81 as follows:

- Np K_ds for zeolitic samples: ~1 to 5.
- Np K_ds for devitrified rhyolitic samples: ~1 to 2.
- Np K_ds for vitric rhyolitic samples: ~0.5 to 2.2.
- Any Np K_ds <0.5 are in quartz-latitic devitrified or vitric samples.

This analysis of the Np data provides an approach to assessments of Np transport that can be linked to the site stratigraphy as well as to lithology, because the quartz-latitic tuffs that are relevant to transport modeling are all *above* the potential repository horizon (Table 6.1-26). The exceptionally low Np K_d values determined for quartz-latitic compositions in batch-sorption experiments thus supply information on the nature of Np-rock interactions but are not a factor in calculating Np migration rates. This is because unsaturated zone and saturated zone transport beneath the potential repository will occur in tuffs that are rhyolitic and not quartz-latitic.

6.1.8.1.2 Dynamic-transport Column Experiments

For dynamic-transport sorption experiments with crushed-rock columns, plexiglass columns were packed with sample crush sizes comparable to those used in batch-sorption studies (75 to 500 μm). In the column experiments (Table 6.1-28), however, the exposure to radionuclide-bearing solution was not static. Instead, flow was established with either J-13 or synthetic carbonate water types and an aliquot of radionuclide solution was introduced into the input stream. Breakthrough curves were then measured for the radionuclides in the introduced solution. Solutions containing Np, Pu, and Tc were studied in this way.

It is important to note in these experiments that the devitrified lithologies tested are quartz-latitic, and the sorption results for Np can be expected to be poor in this rock type, as discussed above. This is in fact the result observed, with highest K_ds in the zeolitic samples (1.7 to 2.1) and K_ds of <0.1 in the devitrified quartz-latitic samples (using J-13 water; Triay, Meijer, Conca et al. 1997). The vitric rhyolitic samples also had relatively low K_ds in the column experiments (0.1 to 0.2), but these values were still higher than those recorded for the quartz-latitic samples. Results for Pu at different flow rates indicate significant sorption by vitric and zeolitic tuffs but with distinct kinetic effects. Pu breakthrough in the columns of devitrified quartz-latitic tuffs was rapid, but it is not known whether the breakthrough would have been any slower in columns of devitrified rhyolitic tuff.

6.1.8.2 Mineralogy of Fracture Transport Experiments

For fracture-flow experiments, fractures of devitrified tuff only were used (Table 6.1-29). In these samples, natural fractures were identified by their mineral coatings (stellerite, Fe oxides, hollandite, romanechite), although some apparently drilling-induced fractures were tested as well. Both J-13 and synthetic UE-25 p#1 waters were used. The goal of these experiments was to test Np transport through fractures in devitrified tuff in which fracture transport is likely to predominate over matrix diffusion. The results of the fracture transport experiments show high Np affinity for the Mn-oxide minerals hollandite and romanechite; these results were confirmed in batch-sorption studies using pure-mineral samples.

The most important results of the fracture-transport experiments are summarized in Figure 6.1-82. This figure shows the very rapid breakthrough of Tc (principally due to anion exclusion from matrix diffusion), the relatively rapid breakthrough of tritium (H) with somewhat more matrix retention across the hollandite + romanechite fracture lining, and the markedly strong retention of Np by hollandite + romanechite relative to stellerite + Fe oxides. The Np results are backed by batch-sorption results indicating very high Np K_ds (600 to 700) with pure-mineral experiments using hollandite and romanechite. These batch-sorption results are much higher than obtained with bulk-rock experiments (K_ds <5 in J-13 water; see Figure 6.1-45). The combined data make it evident that Mn-oxides provide an important component of the natural barrier against Np movement. These laboratory results should be considered in conjunction with the field evidence of significant interaction between groundwater and Mn oxides in Yucca Mountain fractures (see Subsection 6.1.5.2). The latter data provide a strong indication that the interactions observed in the laboratory will indeed occur on the field scale at Yucca Mountain, even with Mn-oxide minerals that are only thin and intermittent linings along fractures.

6.1.8.3 Mineralogy of Diffusion Experiments

Diffusion studies have been pursued to test the movement of radionuclides through matrix diffusion (Table 6.1-30). These experiments have been conducted in two forms. In the first, rock beakers were prepared with drilled-out cavities of 2.8 cm diameter and 2.5 cm depth. The beakers were surrounded with J-13 water and radionuclide-containing solutions of J-13 water were introduced into the drilled-out cavities. In the beaker experiments, the solution introduced into the drilled-out cavity was sampled over time to determine the progressive loss of radionuclide by diffusion through the rock beaker. Radionuclides used in the beaker experiments included H (tritium), Tc, Np, Am, Sr, Cs, and Ba. In the beaker experiments, only devitrified tuffs have been tested.

The second type of diffusion experiment uses diffusion cells that have a simpler geometry, measuring the diffusion across a planar slab of tuff. In these experiments, two chambers are separated by a slab of tuff ~1 cm thick. The radionuclide tracer solution is emplaced on one side and groundwater without radionuclides is introduced on the other side. Both J-13 and synthetic carbonate aquifer waters have been used. Aliquots are periodically sampled from the untraced solution and the radionuclide activity is measured. As aliquots are removed, the untraced side of the cell is replenished with groundwater to maintain volume. Radio-nuclides used in the diffusion cell experiments include H (tritium), Tc, U, Pu, and Np for devitrified and zeolitic tuffs using both groundwaters; mixed solutions of H-U-Pu and Tc-Np were studied with devitrified

and vitric tuffs. Results of these experiments show that diffusion is slower in devitrified than zeolitic tuff, but Pu is not observed in the sampled side of the cell for either lithology, over time spans > 2,000 hours.

Results of the diffusion experiments agree well with batch-sorption data. For sorbing traces, such as Cs, diffusion out of the rock beakers was faster than predicted from assumptions of reversible, instantaneous, and linear sorption (Triay, Meijer, Conca et al. 1997). The dispersal of sorbing species into the matrix thus appears to be more effective than these simplified assumptions would suggest. In the diffusion cell experiments, results indicate that diffusion of nonsorbing tracers (tritium) is more rapid in zeolitic than in devitrified tuff. Poorly sorbing species (U) also diffused more rapidly through the zeolitic tuff, but more highly sorbing species (Pu) were effectively blocked from diffusion into either rock type (Triay, Meijer, Conca et al. 1997).

6.1.8.4 Distributions of Sorptive Minerals Along Transport Pathways

As discussed at the beginning of Subsection 6.1.8, the principal mineral-stratigraphic units between the repository horizon and the water table are vitric tuffs (mostly nonwelded), zeolitized tuffs, and devitrified tuffs (poorly welded). The nature of the lateral and vertical transitions between zeolitized and vitric portions of the Calico Hills Formation is of fundamental importance to understanding the transport pathways from the potential repository to the saturated zone and the potential for thermal alteration or dehydration of existing zeolites and possible formation of new zeolites and/or clays from heated glass (Vaniman and Bish 1995). The principal barriers to radionuclide transport are the zeolitized horizons. The information on zeolite distributions across the exploration block at Yucca Mountain, as well as total mineral abundances and distributions, is contained in a 3-D Mineralogic Model of Yucca Mountain (Chipera, Vaniman, Bish et al. 1997; Carey, Chipera, Vaniman et al. 1997). The 3-D Mineralogic Model is based on X-ray diffraction determination of zeolite abundances in core and cuttings samples. As of early 1998, quantitative X-ray diffraction data from 21 drillholes was available for constructing the model (Table 6.1-31). Stratigraphic subdivisions within which the data are represented are based on the Yucca Mountain Project's Integrated Site Model, as shown in the lithologic stratigraphy of Table 6.1-32.

As of early 1998, the 3-D Mineralogic Model provides information based on both core and cuttings. Because core samples have more reliable depth assignments and are not prone to mixing during the drilling process, the most effective extrapolations of mineralogy between drill cores are based on core samples excluding drillholes with only cuttings samples or for which the sample suite has only limited cored intervals.

The current 3-D Mineralogic Model has a grid spacing of 243.8 m (800 feet) in a 47 x 61 grid that covers a ground area of approximately 1.7×10^8 m^2. A smaller subarea of the model contains the exploratory block and is well defined by the available drillhole data. This subarea extends from USW G-2 in the north to USW G-3 in the south and from the crest of Yucca Mountain in the west to UE-25 a#1 in the east. Each cell of the model contains 12 values, including a percent abundance for six phases (zeolites, smectite + illite, cristobalite + opal-CT, tridymite, glass, and analcime), cell volume, cell location (x, y), elevation (z), stratigraphic unit, and the unit sublayer. Any cell within the volume can be queried to determine any of these

values. Figure 6.1-83 shows a north-south cross section through Yucca Mountain showing the distribution and thickness of the stratigraphic units used as the framework for the preliminary 3-D Mineralogic Model.

The current 3-D Mineralogic Model is well constrained along midline, north-south cross-sections. The new data also help to improve the accuracy of the interpolation of mineralogic values in the exploratory block, particularly in the area of Drill Hole Wash and within the Topopah Spring Tuff across the block.

The current 3-D Mineralogic Model is not as well constrained along east-west cross-sections, particularly for the western region of the repository block. This results from a lack of mineralogic data to the west of the north-south midline. Drillhole USW H-6 has the potential to be particularly significant in this respect, as it provides the western-most mineralogic data. However, USW H-6 occurs on the western side of the Solitario Canyon fault zone, and it does not appear to be representative of rocks east of the fault. We have compared 3-D mineralogic models constructed with and without USW H-6. These results suggest that incorporation of USW H-6 modifies expected mineralogic trends in the western portion of the repository block in a manner which we believe is unrealistic. For example, zeolite abundances in the Calico Hills Formation and the Prow Pass Tuff are significantly lower at USW H-6 than extrapolations from the exploratory block would suggest. This result is due, in part, to the intervening fault zone, which is not adequately modeled as a zone of discontinuity. As a consequence, the current version of the 3-D Mineralogic Model does not include the data from USW H-6. This omission allows the mineralogic predictions for rocks in the western portion of the repository block to be governed by the abundant data from the repository midline.

We have included USW H-3 and H-5 in the model because of their key location in the western portion of the exploratory block. However, much of the data from these drillholes are in the form of cuttings and some of the mineralogic results show discrepancies with respect to other drillholes. This statement is illustrated by the results for zeolite on a cross-section from USW G-2 to G-3 that passes very near USW H-3 and H-5 (Figure 6.1-84). A comparison between two models, one constructed with USW H-3 and H-5, the other without, illustrates the unusual results for zeolite at these holes. The model constructed without USW H-3 and H-5 portrays a more smoothly varying zeolite abundance. These results illustrate some of the ambiguities that may be attributable to the cuttings, the limited amount of data, or to geological complexity. At present, we have inadequate data to resolve these possibilities. Additional data, such as that planned at USW SD-6, would greatly reduce the reliance on cuttings materials and provide much needed data to define the western region of the exploratory block.

Glass distributions at Yucca Mountain are a factor in both flow-transport modeling and in models of thermal stability. Glass dissolution and glass/fluid reaction are factors that need to be considered in assessing the impact of various thermal loads. Glassy tuffs also have their own set of mineral associations that need to be considered in transport modeling (see Subsection 6.1.8.6 below). Glasses, like tridymite, provide some constraints on possible past water table elevations. Past water tables are discussed in detail in Subsection 6.1.5.1, constraints on the vitric-to-zeolitic transition are considered more in terms of the impact of this boundary on transport. Changes in past elevations in static water level have implications for possible changes in repository to static water level distance under possibly wetter climates in the future. One of the potential

mineralogic indicators of past elevations in static water level beneath the exploration block is the distance between the top of the first major zeolitized horizon and the present static water level. Figure 6.1-89, modified from Chipera, Vaniman, Carlos et al. (1995), summarizes some estimates of this distance from several drillholes. Ideally, a direct correlation between the occurrence of the top of this horizon of abundant zeolitization and an ancient static water level would be seen in all drillholes as a surface occurring at a relatively fixed elevation above the present static water level. However, there are several reasons (Levy 1991) for this not to be the case:

- Even if the static water level were to rise, abundant zeolitization would not occur to the height of saturation if appropriate parent material (porous, nonwelded vitric tuff) were not present.

- More than one event of rise in the static water level can result in variable elevations of the zeolitization horizon because of possible tectonic offsets in parts of the exploration block between the timing of ancient and more recent rises in the static water level.

- The present static water level is relatively flat beneath the exploration block but rises sharply to the north and west (Ervin et al. 1993). Similar variable elevations may have occurred in an ancient static water level but not necessarily in the same locations as in the present static water level.

- Zeolitization can occur in unsaturated rocks, especially in situations of possible capillary draw, perched water, or lateral transmission from features that may be significant sources of recharge during pluvial episodes.

- Widely spaced sample collections, and in particular the need to rely on cuttings or intermittent core/sidewall samples in all H- and WT-series holes, place large uncertainties on the estimates of the top of the zeolitized horizon (generally at least ±10 m). The contact between vitric and zeolitic rocks is also gradational (Levy 1991), adding a further uncertainty in the location of the zeolitization front. This is a most important factor, emphasized by the overlap in glass and zeolite occurrences by many tens of meters in USW SD-7 and 12.

Given these caveats, there remains a significant number of drill cores with zeolitization horizons about 106 to 135 m above the present static water level (Figure 6.1-89). Unfortunately, all of these cores are closely clustered in one central area and are thus of uncertain regional significance. The search for ancient static water levels will require the examination of multiple lines of evidence. Combined studies of structural indications of fault displacements of the zeolitization horizon, of glass preservation, and of other mineral distributions (e.g., tridymite) have been interpreted to indicate that past rises in the static water level have been no greater than ~60 m (Levy 1991). Studies of Sr isotopes in calcite at Yucca Mountain suggest a possible ancient static water level ~85 m above the present static water level (Marshall, Peterman et al. 1993). Hydrologic modeling suggests a maximum static water level rise of 130 m (Czarnecki 1985). At present, it appears the modeled static water level maximum rise of 130 m may be closest to inferences of past static water level from zeolite occurrences. However, other

constraints such as tridymite distributions continue to cast doubt on the utility of zeolite occurrences as measures of past water-table rise.

It should be remembered that the horizon of concern is that of the vitric-to-zeolitic transition, and one may as readily define a possible surface of past water-table rise based on the deepest preservation of abundant (≥ 10 percent) nonwelded glass as on the shallowest occurrence of abundant zeolites. Using the depth of abundant glass as a criterion, a different set of "past water-table elevations" can be defined as shown in Figure 6.1-90. Divergences between the zeolite-based (Figure 6.1-89) and glass-based (Figure 6.1-90) model surfaces are in some cases caused by the inadequacies of dealing with widely spaced analyses of cuttings (e.g., ±34 m in USW H-5), but the more recent data show a real and large overlap of glassy and zeolitic samples across a dispersed vitric-to-zeolitic transition (±36 m in USW SD-7). In the most extreme example, the vitric-to-zeolitic transition in USW SD-12 is dispersed over a vertical range of 67 m if the slightly to moderately zeolitized samples of the Calico Hills Formation and the Topopah Spring Tuff are considered (note that these occurrences of ≤10 percent zeolite were not included when determining the top of the zeolitized horizon in Figure 6.1-89). This consideration is of more than passing interest, because the abundance at which zeolites become effective in sorption is an important factor to be considered in performance calculations. The Sr data indicate that the 67 m of slightly zeolitized tuff in USW SD-12 can be effective in sorbing those alkaline-earth radionuclides for which clinoptilolite is highly selective. Although the sorption of complex transuranics by clinoptilolite is minor (Robinson, B.A. et al. 1995), potentially greater permeability of partially zeolitized tuffs, in contrast to those that are fully zeolitized, may permit dispersed access of radionuclide-bearing solutions to zeolite surfaces.

6.1.8.5 Mineralogy of Colloids

Fine particulate materials called colloids are a distinct class of alteration product because they can behave differently than solutes and secondary minerals that are deposited from solution directly onto a fixed substrate. The relevance of natural colloids to the suitability of Yucca Mountain as a waste repository site falls within two areas of interest. The first area is the potential role of natural colloids in radionuclide transport. Studies of natural alteration can augment laboratory experiments and numerical modeling studies by providing natural analog information about the behavior of colloidal material and natural radionuclides in a variety of alteration environments. The second area of interest is the recognition of colloids in the geologic record as indicators of young geochemical alteration, fast or preferred-fluid flow paths, perched-water zones, and other processes or features pertinent to recent paleohydrology and water-rock interaction.

Colloid researchers define a variety of upper size limits, commonly less than 10 μm, for colloidal particles (Yariv and Cross 1979). The selection of a particular size limit is not so important for alteration history studies because the relict colloidal materials preserved in Yucca Mountain rocks have been texturally modified by recrystallization. For these studies, colloids are adequately defined as fine particulates that were transported and deposited in aqueous suspension. Most of the colloidal deposits identified in alteration history studies existed at some time as gels, semisolid colloid-water systems with the macroscopic appearance and behavior of a jelly or paste (Yariv and Cross 1979). Relict gels are much easier to identify than isolated, individual colloidal particles in the geologic record of Yucca Mountain because the gels

contained higher concentrations of colloidal material. Liquid-rich gels have been observed in underground workings at Rainier Mesa, north of Yucca Mountain, and dried or crystallized gels have been identified in drill cores and in the Exploratory Studies Facility at Yucca Mountain itself.

6.1.8.5.1 Sample Collection and Analysis

The Yucca Mountain materials available for study include cores from continuously cored drillholes and sidewall samples from other drillholes, as well as Exploratory Studies Facility samples. All pyroclastic units, including both altered and unaltered rocks, were studied. This section highlights the best examples of tuffs containing small amounts of material thought to be relict colloidal accumulations.

Two semitransparent fluid gel samples examined in this study were collected from tunnel exposures at Rainier Mesa during investigations supporting Defense Nuclear agency activities. No determinations of water or solid content were made at the time of collection. Sample U12t.02 Station 19+24, hereafter referred to as sample U12t, was collected in 1971 from a drift location that is no longer accessible (Levy, Carlos et al. 1986). The material had the consistency of a gel and was oozing from a fracture in the drift wall. About one-half cm^3 of material was available for study after having dried at room temperature. Sample MIEC-2 was collected from a fracture in tunnel U12n in 1988. At the time of collection, the sample had the consistency of a paste.

Samples were studied in thin section by petrographic microscope and by X-ray diffraction, scanning electron microscope, and electron microprobe analysis. A key objective in the study of the Yucca Mountain rocks is to develop textural criteria for recognition of relict gels. The basic criterion in all cases is preserved evidence of original fine grain size (≤10 μm) in possible relict gel deposit. Another textural criterion, not as easy to establish, is evidence that material behaved in a fluid or plastic manner during or after deposition.

6.1.8.5.2 Gels at Rainier Mesa

Rainier Mesa is located about 40 km northeast of Yucca Mountain. Like Yucca Mountain, it consists of Miocene ashflow and bedded tuffs resting in Paleozoic basement. The caprock of predominantly devitrified tuff about 100 m thick is underlain by 200 m of vitric Paintbrush Group Tuff altered to clays and zeolites in the lower 30 m. Below the Paintbrush Group Tuff are bedded tuffs extensively altered to zeolites, clays, and silica. The bedded tuffs are informally known as the tunnel beds for the tunnel complex mined in this interval (Claassen and White 1979). The tunnels are 400 m below the mesa top and 300 m above the regional static water level (Waddell et al. 1984). Local recharge into the mesa maintains saturated conditions in the tuffs, which are undergoing active zeolitic alteration. Some fractures intersected by the tunnels discharged water or gels for several days following excavation (for example, Thordarson 1965). Some areas of the tunnels have remained wet and were still discharging gels when examined in 1993. Gels observed at that time were nearly clear drip pendants distinguishable from ordinary dripping water by the greater temporal persistence and ≥1 cm length of the drips. The drip pendants existed on tunnel surfaces in zones of active fluid discharge (Levy, S.S. 1993c, Los Alamos Laboratory Field Notebook TWS-EES-1-3-93-6, p. 8).

The gel sample MIEC-2 was translucent and jelly-like when collected. X-ray diffraction of the dried gel revealed a very pure, well-crystallized smectite. The mineral component of most gels in the Rainier Mesa tunnels, including the drip pendants, is probably smectite.

Sample U12t.02 consists mostly of detrital rock and mineral fragments. The detrital grains include zeolitized nonwelded tuff, devitrified tuff, and individual phenocrysts of quartz and feldspar. Smectite is an interstitial and clast-coating material in this sample. The larger detrital clasts and clasts of secondary origin have laminated smectite coatings up to about 50 μm thick (Figures 6.1-91 and 6.1-92) that are typically the outermost coatings. Another locally abundant coating consists of net-like aggregates of fibrous crystals less than 20 μm long. The areas occupied by the fibrous mineral are mainly spaces created by the separation of larger detrital grains from adjacent fine-grained detrital material and by the formation of short open cracks in the fine detritus. The morphology of the fibrous material is similar to mordenite.

In addition to the smectite, fibrous material, and detrital grains, there are fragments and clast coatings of silica-rich dried gels. This material is texturally variable. In scanning electron microscope images, the texture varies from featureless and massive to spongy, granular, or faintly fibrous. The color in plane-polarized light varies from colorless to medium pink-brown. Many of the gel fragments contain sparse to dense aggregates of irregular round silica particles 2 to 5 μm across. The densest aggregates are also the largest, up to > 150 μm across. Silica particles delineate a variety of relict textural boundaries within the gel. The most prominent are lines of silica particles that mark the locations of former fractures where brittle gel cracked and the fractures were filled with more fluid gel (Figure 6.1-93). Cross-cutting relationships indicate multiple episodes of fracturing, with little or no development of silica particles along the youngest fractures. In addition to fracturing, some of the gel fragments were deformed in a plastic manner (Figure 6.1-94).

Silica-particle concentrations have also preserved the shapes of cavities left in the gel by dissolved crystals or fragments of some kind. The cavities are narrow and elongate, mostly about 25 to 100 μm long. After the original material dissolved, the cavities were infilled with gel. The gel fragments also contain a few irregular crystal-lined cavities about 10 to 50 μm across. Locally, this type of cavity is concentrated within the boundaries of infilled ghost crystals (Figure 6.1-95). There are also crystal-lined cavities in the fibrous material. Individual cavity-lining crystals are mostly < 1 μm. Mineral phases identified by morphology and energy-dispersive X-ray spectra include silica, barite, Cu-Fe sulfides or sulfates, and possible zeolites. Some elongate prismatic or fibrous crystals have bead-like coats of silica (Figure 6.1-96).

Electron microprobe analyses for silica-rich gel fragments and smectite from this sample are given in Table 6.1-33. The very low analysis total for A1-1 probably results from a combination of high water content and low material density. Analysis A1-2, of a round silica particle within a gel fragment, has a much higher total, probably because it is denser, less hydrous, and more crystalline than the featureless A1-1 fragment. The smectite has a moderately iron-rich composition, with potassium as the main exchangeable cation.

6.1.8.5.3 Gels at Yucca Mountain and Vicinity

6.1.8.5.3.1 Dried Gels in the Exploratory Studies Facility

Liquid-rich free gels (as distinguished from gel layers on hydrated glass surfaces) have not yet been found at Yucca Mountain, in either drill core or the Exploratory Studies Facility. Materials that were originally gels or colloids are present in altered tuffs, as fracture and void fillings in devitrified tuffs, and in fault zones. Dried equivalents of the smectite-water gels typical of Rainier Mesa have been observed in the Exploratory Studies Facility but have not been studied systematically. Typical occurrences are summarized below.

Tiva Canyon Tuff at the North Portal–Prominent dried smectite gels are present in the Tiva Canyon Tuff exposed by the Exploratory Studies Facility North Ramp box cut and starter tunnel. Laminated deposits of smectite up to several cm thick coat fractures and fill the bottoms of lithophysal cavities. The abundance of this material gradually diminishes inward from the portal. Although this diminution corresponds to increasing depth below the surface in the Exploratory Studies Facility, the smectite probably is not derived from present-day surficial deposits because clay coatings are absent from the Tiva Canyon Tuff exposed at the Exploratory Studies Facility South Portal.

Topopah Spring Tuff at Station 16+19–A clay-rich fracture filling from the Tptrn, collected for ^{36}Cl isotopic analysis, offers a dramatic example of particulate transport (Fabryka-Martin, Flint et al. 1997). The wall rock is densely welded, devitrified tuff, but the fracture filling consists of devitrified rock fragments in a fine-grained matrix of Topopah Spring glass pyroclasts. Several sequences of graded bedding are preserved within the fillings. The glassy constituents had to come from tens of meters higher in the stratigraphic section.

The abundance of clay-size material is ~10 to 20 percent. Centimeter-scale domains of the finest-grained material, without coarser components, show graded bedding from very fine sand to silt, capped with ≤ 1-mm thick layers of red-brown clay. The graded bedding was produced by settling of particles in a water-filled fracture. The red-brown clay layers are the dried remains of colloidal clay suspensions.

Despite the evidence of fluid flow sufficient to transport silt-size particulates tens of meters and produce transient saturation in the fracture, this sample does not have a bomb-pulse $^{36}Cl/Cl$ signature signifying movement of water from the surface in 50 years or less. A number of factors unrelated to the hydrologic properties of this specific fracture may be responsible. The most likely explanation is that the particulate fillings were deposited before the Paintbrush nonwelded tuffs (equivalent to the PTn hydrogeologic unit) were emplaced on top of the Topopah Spring Tuff. In numerical simulations of infiltration, the PTn dampens out the effects of episodic high-infiltration events (Fabryka-Martin, Turin et al. 1998) so that flow from the surface through the PTn sufficient to saturate a fracture in an underlying unit would be unlikely to occur. Also supporting an early age of particulate transport is the principle that remobilization of Topopah Spring nonwelded pyroclasts would have been more feasible before the tuff was compacted by the addition of new overburden. This one-time fast path may have lost its connection to the surface as a result of later pyroclastic deposition, and a throughgoing connection was never re-established.

Dune Wash Fault at Station 67+87–The Dune Wash fault is a block-bounding fault, locally expressed as a graben, juxtaposing the Topopah Spring and Tiva Canyon Tuffs across a complex 4 m wide rubble and broken-block zone. The rubble zone contains mostly equant, subangular clasts ranging from silt-size up to ~40 cm and is not notably clayey. The proportion of fine-grained material increases to the west. Near the western margin of the rubble zone, adjacent to the downdropped Tpcpv, there is a 3 to 5 cm-wide zone of pure to nearly pure smectite (Vaniman, Chipera, Bish 1997) occupying a formerly open fracture parallel to the rock fracture surface that forms the margin. A parallel zone of silt-rich material is located near the clay zone.

The purity of the clay zone, compared to the surrounding wall rock and rubble, indicates that this is translocated clay. The clay probably was deposited in multiple episodes by water moving down a zone of separation between the fault rubble and the wall rock.

6.1.8.5.3.2 Relict Gels of Hydrothermal Origin

Of the former gels and colloidal accumulations observed in altered rocks at Yucca Mountain, those in altered basal Topopah Spring vitrophyre are especially relevant because the alteration conditions may represent a natural analog to a waste-repository environment (Levy 1992). Alteration in the vitrophyre took place during the cooling of the pyroclastic deposit and probably lasted on the order of 10^2 years. Temperatures of rock alteration cover the entire range from pyroclastic emplacement temperatures to ambient conditions, but the alteration of interest occurred at temperatures in the 40 to 100°C range or lower (Levy and O'Neil 1989). Meteoric water moved downward along fractures in the cooling tuff and encountered the transition zone between the central, hotter part of the tuff where glass devitrification prevailed and the underlying, cooler vitrophyre where glass dissolution and hydrous-mineral precipitation dominated. In the transition zone, domains of devitrification and dissolution are discontinuous and intermingled on both a macroscopic and microscopic scale. Alteration tends to be localized around fractures, and field evidence indicates that some parts of the transition zone received greater input of water than others.

The chief hydrous products of glass alteration are smectite and heulandite-clinoptilolite. Smectite commonly crystallized as spherical aggregates, 2 to 50 μm across, adhering to each other, with a small amount of intergrown extremely fine-grained zeolite. Perhaps because of this growth habit, there is little evidence of free smectite gels in this altered zone. A few <1 mm-thick smectite fracture coatings are present in some places.

The most abundant gels crystallized to heulandite-clinoptilolite and zeolite-silica mixtures (Table 6.1-33). Additional minor gel products include hematite, manganese minerals, and mordenite. Fractures are filled with stratified and nonstratified accumulations of former colloidal particles. One example is known (VH-1 1694) of a nonlayered gel fracture filling that crystallized first Ca-K-rich heulandite-clinoptilolite (molecular Si/Al = 3.67) and then alkali-rich clinoptilolite (Si/Al = 5.14) in the interstices of the earlier, larger crystals. Relict colloidal accumulations of silica also fill dissolution cavities in altered vitrophyre and primary and secondary pores in moderately welded tuffs below the vitrophyre. Some of these are uraniferous opal deposits, and their relevance to radionuclide transport is described in a subsequent section.

6.1.8.5.3.3 Relict Gels of Diagenetic Origin

The most common examples of former gels are microscopic geopetal deposits in pores of the zeolitized nonwelded tuffs. The term geopetal refers to the gravitational settling of colloidal particles in water-filled pores. Typical deposits are shown in Figure 6.1-50. Pores containing deposits are either primary voids, such as vesicles, or secondary cavities created by dissolution of glass pyroclasts. Most of the pores containing relict gel deposits are less than 1 mm across. The deposits contain silica of variable crystallinity and heulandite-clinoptilolite. Planar layering is characteristic of many deposits (see Subsection 6.1.4.2.2.1). Layers within silica deposits are distinguished by color, by variations in incipient birefringence related to differences in crystallinity, or by differences in granularity. Zeolite and silica are commonly in separate layers with the zeolite lowermost. Some gel deposits crystallized as aggregates of mixed 3- to 5-μm cristobalite and heulandite-clinoptilolite crystals (H-5 1917). Microprobe analyses of silica-rich relict gels in H-5 1917 are included in Table 6.1-33.

Another variety of relict gel fills only primary pores and is a major cementing constituent in certain well-sorted bedded tuffs that originally contained little or no fine-grained ash. Heulandite-clinoptilolite and opal, in variable proportions, are the main constituents (for example, Figure 6.1-48). Internal layering is absent, but in a few incompletely filled pores, the free upper surface of the deposit is planar. The infilling of virtually all primary porosity, but only primary porosity, by gel in this kind of tuff indicates that the gel constituents were externally derived and transported into the bedded tuff by moving water before the tuff itself began to be altered.

6.1.8.5.3.4 Colloidal Silica and Actinide Transport

Secondary silica is a common and locally abundant product of the low- to moderate-temperature alteration that accompanied the cooling of the Topopah Spring Tuff. Many of the silica deposits exhibit a yellow-green fluorescence in short-wave ultraviolet light that indicates significant UO_2^{2+} content (Marfunin 1979). Actinide sorption by colloidal silica has been studied experimentally and in natural samples by Zielinski (1980, 1982) as a uranium exploration tool, but the studies are also relevant to a nuclear waste-repository environment. Experimental coprecipitation of dissolved uranium and silica gel showed that $[U]_{\text{dried silica gel}}/[U]_{\text{solution}}$ = 400 to 1000 at pH = 7.0 to 8.5, ΣCO_2 = 0.001 to 0.01 M, and T = 25 to 80°C, indicating that silica has a very strong affinity for uranium. Zielinski et al. (1986) also discuss the specific application of their studies to Yucca Mountain. The natural record of post-eruptive alteration that they summarize provides strong evidence of significant U mobilization, contrasted with relatively little mobilization of relatively insoluble Th. They also point to an association between U and leachable Mn, suggesting associations between U and Mn in the formation of fracture-lining Mn oxides. Studies of fracture minerals at Yucca Mountain (e.g. Carlos, Chipera et al. 1993) indicate a relatively early and probably higher-temperature regime of Mn oxide formation relative to opal deposition. Considering these studies, it is most likely that the interactions between opal and uranium will be most significant under potential repository heat loads.

Zielinski (1982) concluded from studies of U/Pb systematics in natural uraniferous opals that the uranium-opal demonstrated closed-system behavior. The immobility of uranium that is incorporated in opal was also suggested by the preservation of sharp gradients in uranium

concentration between zones of different uranium content and fluorescence intensity. This observation probably holds true for most of the ~2 m.y. post-depositional history of the opal, and it seems to be true for Yucca Mountain opals from the Topopah Spring Tuff in the Exploratory Studies Facility that have been dated by the U-Th disequilibrium technique (Paces, Neymark et al. 1996). Many of the ages of uraniferous opals associated with calcite fracture and void fillings are clustered at dates of 100 k.y. or more. This clustering, like the clustering of opal dates of Zielinski (1982), suggests closed-system behavior. However, the studies of relict colloidal silica deposits at Rainier Mesa and Yucca Mountain reported here identified strong indications that the early post-depositional history of such deposits cannot have occurred under closed-system conditions. The Rainier Mesa silicas, thought to be young, have very low densities compared to similar deposits at Yucca Mountain, thought to be >11 Ma old. These differences are evident in the analysis totals of Table 6.1-33. The slight granularity of the Rainier Mesa deposits is the beginning of a process of redissolution, reprecipitation, additional deposition, and crystallization that must eventually produce a three- or four-fold densification of the silica deposit. These are extremely unlikely to have been closed-system processes. The duration of this stage of opal evolution is unknown, but if it represents a significant portion of the "age" of the youngest opals, then it probably restricts the applicability of U-Th disequilibrium dating. It must also be a factor in the retention of actinides from a waste repository by the siliceous products of repository hydrothermal alteration.

Variations in uranium content of secondary silica also correlate with differences in silica crystallinity (Zielinski 1980, 1982). As amorphous silica crystallizes, its capacity to sorb uranium or to retain previously sorbed uranium is diminished. Silica deposited in a repository hydrothermal environment is likely to be converted to crystalline forms within perhaps 10^2 years because the bulk of silica deposited within the devitrified Topopah Spring Tuff and the devitrified-vitric transition zone below the candidate host rock during cooling of the tuff is chalcedony or quartz (Levy and O'Neil 1989; Levy and Valentine 1993). This material may incorporate and retain natural uranium dissolved in groundwater but may have lost its sorptive capacity through crystallization by the time radionuclides are released from a potential repository. Silica gel deposited at near-ambient temperatures near the outer margins of the repository thermal aureole may retain its near-amorphous state for tens to hundreds of thousands of years (Paces, Neymark et al. 1996), but it too is likely to have scavenged natural uranium. Field studies of fracture systems that have acted as conduits for secondary silica transport indicate that early high-angle syngenetic fractures crossing the devitrified Topopah Spring Tuff (and the candidate host rock) terminate in the underlying vitrophyre, perhaps because they were closed by viscous creep. In places where this is a typical fracture termination, silica moving away from the potential repository would tend to be trapped in the upper vitrophyre and be subjected to higher than ambient temperatures leading to rapid crystallization.

6.1.8.6 Microautoradiography and Rock Affinity for Actinides

Microautoradiography provides direct observations of those minerals within a rock that accumulate radionuclides from solution. The main goal of microautoradiography studies conducted for the YMP has been to examine the details of mineral-specific retardation of actinide elements in the three volumetrically most important rock types along transport pathways at Yucca Mountain: devitrified tuff, zeolitic tuff, and vitric nonwelded tuff. As end-member carrier fluids, aqueous solutions of actinides in J-13 (tuffaceous aquifer) and synthetic UE-25

p#1 (carbonate aquifer) waters were used for each lithology and for each radionuclide. It is important to consider, in this choice of fluids, that the "carbonate aquifer" composition may apply not only to the deep saturated zone but also to possible unsaturated-zone water compositions.

In addition to the microautoradiography studies of these three important lithologies, splits of the same rocks used in making thin sections were crushed for batch-sorption studies. The goal of this approach was to provide batch-sorption K_d data for direct comparison with the results to be obtained in microautoradiography studies. Sorption values, expressible as K_ds, can be inferred from batch-sorption experiments and from dynamic transport studies. Inferences about sorption behavior may also be made directly from microautoradiography studies, but direct derivation of a bulk K_d from microautoradiography data is problematic. Sorption of a radionuclide onto a thin section need not necessarily correspond to sorption on crushed rock; in particular, the epoxy stabilization process may mask large proportions of minerals with high surface area, removing critical surfaces from interaction with the radionuclide-bearing solution. In addition, the need to rinse the thin sections prior to counting, in order to count and subsequently view (via microautoradiography) only the affixed radionuclides, adds an additional process that is not used in batch sorption.

The radionuclides initially considered for use in these experiments included U, Np, Pu, and Am. Trial tests with Np, using ^{237}Np, indicated that ingrowth in solution of daughter ^{233}Pa, with a much shorter half-life, swamped the microautoradiography signal and obviated the use of this isotope. For this reason, only solutions with U, Pu, and Am were used for the microautoradiography experiments. Vaniman, Bish, Chipera et al. (1996) used optical microautoradiography pointed to significant Pu retention by some (but not all) oxide minerals, by Fe-rich amorphous products associated with altered orthopyroxenes in the devitrified Prow Pass Tuff, and most significantly by the smectites that are concentrated in some rocks at Yucca Mountain but are found in small amounts in almost all rocks at Yucca Mountain. That study was able to show that the relative smectite/clinoptilolite retention factor for Pu is >80 in the zeolitized Calico Hills Formation samples analyzed (Vaniman, Bish, Chipera et al. 1996).

In a later study (Kitten et al. 1997), microautoradiographic analysis of a wider variety of radionuclides with two different water compositions was pursued. In addition, batch-sorption data on splits of the same rocks were obtained. Samples used in the Kitten et al. (1997) study are described below.

Vitric Nonwelded Portion of the Lower Topopah Spring Tuff–(LANL Sample #1875, USW SD-12 at 1,399.2 to 1,399.3 foot [426.48 to 426.51 m] depth; batch-sorption data on LANL Sample #1874, USW SD-12 at 1,388.0 to 1,388.2 foot depth). The sample used for preparing thin sections is a poorly consolidated vitric, nonwelded tuff. This sample was selected to be representative of the vitric nonwelded tuffs that occur throughout most of the western and southern parts of the Yucca Mountain exploration block and above the principal zeolitic horizons. The composition of this rhyolitic lower Topopah Spring Tuff is generally similar to that of the Calico Hills Formation, which is also commonly vitric and nonwelded across the western and southern areas. Because there was insufficient material in LANL Sample #1875 for both thin sections and batch-sorption experiments, the nearby LANL Sample #1874 was used for

the batch-sorption experiments. As shown in Table 6.1-34, the mineralogic composition of these two samples is essentially identical.

Zeolitic Bedded Tuff From the Base of the Topopah Spring Tuff–(LANL Sample #1895; USW SD-9 at 1,465.9 to 1,466.1 foot [446.81 to 446.87 m] depth). There are many zeolitized horizons at Yucca Mountain. The uppermost significant horizon is commonly referred to as the Calico Hills zeolitized horizon, but this large and widely distributed zeolitic barrier includes much of the lower poorly welded to nonwelded parts of the Topopah Spring Tuff. As a representative of the upper part of this zeolitic barrier, and as a representative of the yet poorly studied zeolitic bedded tuffs at the site, it was decided to use LANL Sample #1895 for both batch-sorption and microautoradiography experiments (Table 6.1-35).

Devitrified Prow Pass Tuff–(LANL Sample #1286; UE-25 UZ#16 at 1638.7 to 1,639.2 foot [499.48 to 499.63 m] depth). Previous experiments with devitrified tuffs using Pu in synthetic p#1 water (Vaniman, Bish, Chipera et al. 1996) included samples of both the Topopah Spring Tuff and of the Prow Pass Tuff. In that study, it was found that altered orthopyroxene phenocrysts in the devitrified Prow Pass Tuff from 1,745 foot depth in drill core USW GU-3 were especially effective in retention of Pu. Unaltered orthopyroxenes did not have any effect. To test whether the altered orthopyroxenes of the Prow Pass Tuff are consistent in this effect, a sample of the devitrified Prow Pass Tuff from UE-25 UZ#16 was used in the present experiments (Table 6.1-36). More importantly, this unit in general is found consistently beneath the exploration block at Yucca Mountain as the first major body of devitrified tuff, other than the potential repository host rock (the devitrified Topopah Spring Tuff), that would be encountered in downward transport away from the potential repository.

The 18 experiments with the major tuff lithologies are summarized in Table 6.1-37. The first three columns summarize the results of the batch-sorption experiments, which were performed in duplicate. The last four columns summarize results of the microautoradiography experiments with brief notes on the principal results from optical analysis of the experimental results.

6.1.8.6.1 Results from Experiments with the Three Principal Tuff Lithologies

Optical analysis of these microautoradiography samples provides a relatively rapid corroboration of previous inferences relating Pu retention to specific mineralogies. In previous work, smectite-altered portions of devitrified, vitric, and zeolitic tuffs were found to be consistently higher in Pu retention than most other mineralogic zones (whether devitrified or zeolitic); unaltered glass has essentially no retention capability. The present study found this smectite effect to be common but not universal. Specific optical evidence of smectite retention by clay alteration is most evident in the Pu- and U-exposed thin sections of the devitrified Prow Pass Tuff, which contains 7 percent smectite. The vitric sample used has only trace amounts of smectite, yet even here the very localized smectite or smectite/oxide associations had visible affinity for Pu and U retention. The particular zeolitic sample used, from the bedded tuff below the Topopah Spring Tuff, contains smectite that is closely associated with the Mn-oxide mineral rancieite. The two minerals occur in thin coatings on phenocrysts and lithic fragments, in intergrowths so close that the microautoradiography results reflect the smectite/rancieite mixture rather than the individual phases. Nevertheless, significantly higher Pu concentrations (exceeding optical density limits)

occur where rancieite is most abundant in both the UE-25 p#1 and J-13 waters. A lesser but similar effect was found with Am, and with U in the p#1 but not with the J-13 water.

Electron microprobe analysis of Ag in the emulsions was used to quantify the relative actinide abundances in these associations. At present, the electron microprobe analysis has been used on all of the zeolitic samples (U, Pu, and Am exposed in both J-13 and p#1 waters) and on all of the Pu-exposed samples (vitric, devitrified, and zeolitic samples in both J-13 and p#1 waters). Detailed results are compiled in Kitten et al. (1997). The electron microprobe traces show a very strong variability in mineral/mineral actinide partitioning; in particular, Pu is exceptionally concentrated over the smectite + rancieite zones of the zeolitic lithology (sample #1895). When corrected for background Ag in emulsion without tracks, the concentrations of signal over background in Table 6.1-38 are observed.

From the table of signal/background ratios above, it is evident that exceptionally high-radionuclide retention (signal/background > 10 x) was observed for smectite exposed to Pu with synthetic p#1 water in the vitric tuff and for the smectite + rancieite association exposed to Pu with either the J-13 or the synthetic p#1 water in the zeolitic tuff.

6.1.8.6.2 Microautoradiography of Fracture Samples

In addition to these bulk-rock samples, fracture samples and samples of alteration features near fractures were chosen to represent a variety of fracture linings and near-fracture deposits from the unsaturated zone and the saturated zone. Combined petrographic and X-ray diffraction data for these samples are summarized below.

LANL Sample 996–Carbonate filling in breccia fracture from devitrified Tram Tuff, USW G-3 at 2,945.0 to 2,946.3 foot [897.64 to 898.03 m] depth.

LANL Sample 1900–Sections made across an orbicular 2 cm body from the same major transmissive interval as sample #1899, in the devitrified Tram Tuff of USW G-4 at 2,875.1 foot [876.33 m] depth.

The data from these fracture samples provide an important comparison with the bulk rock-matrix results shown in Table 6.1-38. One of the fracture samples is a mm-scale calcite fracture coating that provides a broad, polished surface much wider that the 10 mm beam used in electron microprobe analysis; the other fracture sample contains Mn-oxide (cryptomelane-hollandite), an orbicular feature transected by several small fractures. The Mn-oxide habit is acicular, providing mineral surfaces that are much smaller than the 10-μm beam used in electron microprobe analysis. Table 6.1-39 summarizes the results in a format similar to the table compiled above for bulk-lithology microautoradiography data.

The data in Table 6.1-39 show that the cryptomelane-hollandite Mn-oxide body analyzed has a strong affinity for Pu, as does the Mn-oxide mineral rancieite that occurs in the bulk zeolitic sample. However, the very small cross-sections of the acicular cryptomelane-hollandite grains in section #1900 provide only a limited surface for exposure to radionuclide-bearing solutions and for electron microprobe analysis, in contrast to the broad calcite surface analyzed in section #996. The breadth of the analytical surface in section #996 provides a large number of data

points that can be averaged for a more accurate assessment of the Pu retention factors; in contrast, the limited surfaces of the cryptomelane-hollandite grains in section #1900 always present a mixture of epoxy plus mineral to the electron beam, providing at best a minimum signal and, as a result, a minimum signal/background ratio.

6.1.8.6.3 Comparison of Batch Sorption Data with Microautoradiography Data

Comparisons of batch-sorption data with microautoradiography results are particularly difficult in Yucca Mountain samples for which many of the most active minerals are fine-grained (smectites and, especially, Mn-oxides). Although smectite masses can be found in some lithologies in thicknesses close to the diameter of the electron microprobe beam (10 μm), Mn-oxide occurrences in thin sections are seldom more than a mm in thickness. This problem is exacerbated by the acicular habit of some Mn oxides; such elongate grains have a much larger surface area than accessed by polished slices, in which most of the needle walls are coated by stabilizing epoxy during the sectioning process. The greater surface area of these acicular samples, however, is accessible to solution in batch experiments. As summarized in Vaniman, Bish, Chipera et al. (1996), the smaller grains that are especially active allow only a minimum retardation factor to be determined because the small grains are likely to provide fewer Ag particle tracks than would an absolutely pure mineral, larger than the analytical beam, without epoxy impregnation, and exposed to the same radionuclide-bearing solution. Nevertheless, minimum mineral/background retention ratios can be estimated from the microautoradiography.

If there were a simple correlation between the exposure of crushed tiffs to radionuclides, and the exposure of thin sections in the same manner, then one might expect a reasonable correlation between the activity ratios of (batch sample)/(solution) and (thin section)/(solution). There are a number of problems, however, that complicate such a correlation. These problems fall into two categories: those having to do with differences inherent in the two methods and those having to do with differences in the samples used. The batch method is elegant in its simplicity, exposing the crushed sample to a flow of fluid and comparing the activity in the extracted fluid with the initial activity. The microautoradiography method requires exposure to the solution followed by rinsing that may affect retention of radionuclides that are bound to mineral surfaces at exposure concentrations but not at rinse concentrations. The crushed samples used in batch sorption allow access to a much higher surface area, dominated by cleavage surfaces in most minerals. The thin sections also present fresh surfaces to the solution, but in a single plane of much lower surface area and with highly polished surfaces that are not cleavage planes. These differences (and others mentioned within this paper) lead to very different response of the two types of samples in exposure to actinide-bearing solutions.

Figure 6.1-97 compares the K_ds determined from batch-sorption experiments with an approximation of comparable measure for radionuclide affinity in the microautoradiography thin sections (activity in cpm of the exposed and rinsed thin section/activity in cpm of starting solution). As discussed in the paragraph above, it would be unreasonable to expect a simple near-linear correlation between the two methods. However, systematic deviations within and between the two methods provide some important information about the different mechanisms by which minerals interact with radionuclides in solution. The U and Pu data have two significant outliers in the batch-sorption data: one being an exceptionally high batch-sorption result in the U/zeolitic/J-13 experiment and the other an exceptionally high batch-sorption result

in the Pu/zeolitic/p#1 experiment. These values are not significantly higher in the activity ratios measured on thin sections. Both of the high batch-sorption values occur with zeolitic samples; one possible explanation would be an enhancement of cation exchange with zeolites that have been crushed (and hence have abundant cleavage surfaces). Alternatively, simple exposure of three-dimensional mineral forms may favor actinide retention in these particular experiments. The americium results are significantly different. With Am, the batch-sorption method readily distinguishes differences between the p#1 and J-13 solutions, but the thin-section method masks these differences while reflecting differences between the three lithologies. It is likely that these differences in sensitivity—one to solution, the other to mineralogy—reflect the major differences between the two methods. The Am results suggest that higher surface area and/or access to fresh cleavage faces affects Am retention in batch sorption regardless of the mineral substrate, whereas the polished mineral surfaces exposed in thin sections provide access to polished mineral surfaces with a hierarchy of Am retention (zeolites > glass > silica/feldspar).

Results of microautoradiography using three major lithologies from Yucca Mountain (devitrified, vitric, and zeolitic) exposed to three actinide elements (Am, Pu, U) in two different waters (tuffaceous and carbonate aquifers) provide some insight into the mechanisms that account for variability in batch-sorption results. Batch-sorption analysis of the three lithologies used shows a general ranking of effective retardation for all three actinides in all rock types and both waters with retention of Am >> Pu ≥ U. The use of electron microprobe analysis to measure differential retention of these actinides by specific minerals shows that Pu is particularly strongly concentrated over smectite + Mn-oxide associations in zeolitic rocks (regardless of water composition). However, Pu is concentrated over smectite in vitric samples only in the case that synthetic UE-25 p#1 water is used (J-13 water does not lead to any notable smectite preference in the vitric tuff). Phase preferences with Am and U were also tested in the zeolitic lithology. For both of these actinides, significantly higher preference for smectite + Mn-oxide bodies was observed in synthetic UE-25 p#1 water, but there was little or no discrimination of mineral sites with J-13 water. The implications of enhanced phase preference in p#1 water for explaining shifts in retardation factors may be best illustrated by the behavior of Am in p#1 versus J-13 water. All lithologies exposed to Am in p#1 water have batch-sorption values ranging from 5 to 7 times (in devitrified and vitric rocks) to 55 times (in zeolitic rocks) the batch-sorption values in J-13 water. The strong phase preference for trace but widely dispersed smectite and Mn-oxides in zeolitic rocks with UE-25 p#1 water may account for much of this shift, with the much larger shift in the zeolitic sample attributable principally to the presence of the Mn-oxide mineral rancieite. However, the solution/mineral mechanisms that favor this shift in p#1 rather than J-13 water are not known. The microautoradiography data provide a sensitivity test of how retardation operates with insights into phase preferences that may drive the sensitivity of particular lithologies to changes in water composition.

INTENTIONALLY LEFT BLANK

6.2 FLUID GEOCHEMISTRY

Fluid geochemistry data and models that are important for site characterization purposes and for evaluations of site performance are discussed in this subsection. Much of the available hydrochemical data are also presented in Section 5 (Hydrologic System), which discusses them from the perspective of their implications for the development and testing of hydrologic flow models. In the present subsection, geochemical and isotopic data are reviewed and evaluated with respect to the development and testing of models to explain variations in water chemistry at the site. Such models are required to derive bounds on future variations in the chemical compositions of waters in the Yucca Mountain flow system. These bounds are required to model the behavior of radionuclides in the flow system.

More specifically, this subsection will:

- Identify fluid geochemical parameters that are relevant to site characterization and repository evaluations (Subsection 6.2.1).
- Review the methods that were used in investigating fluid geochemistry (Subsection 6.2.2).
- Discuss available data on the geochemical and isotopic compositions of precipitation (Subsection 6.2.3), surface water (Subsection 6.2.4), unsaturated-zone pore waters and perched waters (Subsections 6.2.5), isotopic compositions of all waters (Subsection 6.2.6), unsaturated-zone gases (Subsection 6.2.7), and saturated-zone groundwaters (Subsection 6.2.8), including an overview of processes that control fluid compositions and the limitations of the existing data for each category.
- Summarize a conceptual model for the evolution of fluid geochemistry in Yucca Mountain (Subsection 6.2.9.1).
- Discuss how these data bear on several major site characterization and performance issues (Subsection 6.2.9.2).

Quality Assurance All of the Yucca Mountain Site Characterization Project (YMP) work or activities summarized in this section come under the control of the *Quality Assurance Requirements and Description* (DOE 1997). All data included in this section, except for referenced information from other sources outside the YMP, were collected under controls of the YMP *Quality Assurance Requirements and Description* (DOE 1997). This document is not an activity that generates data itself; rather, the material presented is a compilation/synthesis of data and other information that have been collected under other activities and reported elsewhere. The quality assurance status of the data in this section is determined by the activities and reports from which they were synthesized, with the specific controls noted in Scientific Notebooks associated with those activities.

6.2.1 Fluid Geochemical Parameters and Their Relevance to Site Characterization and Site Evaluations

Fluid geochemical parameters of importance to site characterization and repository evaluations include the following, although not necessarily in order of importance:

- Major, minor and trace species
- Redox-sensitive elements
- Oxidation/reduction potential (usually expressed as Eh, for Electrode potential, on the hydrogen scale)
- Colloids and particulates
- Dissolved organic carbon
- Microbial populations
- Gases (dissolved in aqueous phase as well as present in gas phase)
- Stable isotopes (H, C, O)
- Cosmogenic and atmospheric radionuclides (^{3}H, ^{14}C, ^{36}Cl)
- Radiogenic isotopes (isotopes of Sr and U)
- Temperature and pressure

Some of the parameters on this list are primarily pertinent to site characterization issues, others are primarily pertinent to radionuclide transport issues, and some are pertinent to both sets of issues. Data on stable isotopes, cosmogenic and atmospheric radionuclides, and radiogenic isotopes are used primarily for site characterization purposes. More specifically, data for these isotopes have been used to develop and calibrate models for the hydrologic flow system (Section 5). Most of the remaining parameters are primarily used in repository performance evaluations. The major constituent and trace-element concentration data are used in both areas. These parameters are discussed in this subsection.

The parameters pertinent to repository performance evaluations are used in various ways. For example, data on oxidation/reduction potentials, pH, major constituents, major species, gas concentrations, redox-sensitive elements, dissolved organic carbon, and microbial populations are all used to constrain predictions of the corrosion behavior of the waste packages and the solubility of the waste forms. Most of these parameters are also used to constrain predictions for the sorption behavior of the radionuclides released from the waste forms. The latter predictions also require data on trace-element concentrations in the waters in Yucca Mountain.

6.2.2 Methods Used in Investigations of Fluid Geochemistry

This subsection reviews the sampling or measurement locations and collection methods for the different types of fluid samples (or fluid characteristics in the case of in situ measurements such as temperature) analyzed in Yucca Mountain studies including precipitation, surface waters, pore waters, gases from the unsaturated zone, perched water, and saturated-zone waters. For detailed descriptions of sampling or measurement locations and collection methods, the original publications should be consulted (for example, Ogard and Kerrisk 1984; McKinley et al. 1991; Benson and McKinley 1985; Yang, Rattray et al. 1996; Yang, Yu et al. 1998; Fabryka-Martin, Wolfsberg et al. 1997).

Surface-based boreholes from which water and gas samples were collected in the Yucca Mountain area are shown in Figure 6.2-1. A summary of the types of unsaturated-zone geochemical and isotopic data available from the unsaturated zone of these boreholes is provided in Table 6.2-1. A map and table of wells sampled for groundwater analyses in the Yucca Mountain area is presented in Subsection 6.2.8 (Figure 6.2-46 and Table 6.2-17).

Gas samples have been collected from a limited set of boreholes in Yucca Mountain (Yang, Rattray et al. 1996). Borehole UZ-1 was instrumented for temperature and other probes at 33 levels and allows sampling of gas compositions from 15 distinct intervals (Montazer et al. 1985). Additional boreholes (that is, UZ-6, UZ-6S, UZ#16, NRG-6, NRG-7a, and SD-12) were cased from the surface down to some depth and are open below this depth. In boreholes UZ#16, NRG-6, and SD-12, packers were installed to isolate specified intervals for gas sampling. In addition, gases have been collected from radial boreholes drilled from alcoves driven from the Main Drift of the Exploratory Studies Facility. Sulfur hexafluoride, SF_6, was used in each of these boreholes as a gaseous tracer to identify drilling-air contamination of the rock gas. Based on ten years of records and the stabilized value in borehole UZ-1, the tracer (SF_6) concentration of less than 0.1 ppm in the borehole air is used to define uncontaminated rock gas. Gas samples were collected using a 500 cm^3-per-min peristaltic pump connected through short silicone tubing to within hole gas-sampling tubes as described by Yang, Rattray et al. (1996). Sampling tubes were pumped overnight to purge any atmospheric air. Two different methods were used to collect CO_2 for isotopic analysis: a molecular-sieve method and a whole-gas method as described by Yang, Rattray et al. (1996). $\delta^{13}C$ was measured by mass spectrometry and the precision of $\delta^{13}C$ analysis is about ±0.2‰. Carbon-14 analysis was accomplished by counting in a gas proportional counter by Krueger Enterprises, Inc., and uncertainty is reported as ±7 pmc. Gas data are discussed in Subsection 6.2.7.

Pore-water samples were obtained from core samples recovered from dry-drilled boreholes UZ#4, UZ#5, UZ-14, UZ#16, NRG-6, NRG-7a, SD-7, SD-9, and SD-12 (Yang, Rattray et al. 1996; Yang, Yu et al. 1998; Yang, Turner et al. 1988). Each core was wrapped in plastic, placed in a lexan liner, sealed inside an aluminum foil bag, and stored under cool conditions until ready for analysis. The method used to extract most of the pore-water samples from the cores was high-pressure uni-axial compression, applying an initial pressure of 103.4 MPa which was gradually increased to a final pressure of 827 MPa. To protect against atmospheric contamination, particularly with regard to carbonate species, the system is air tight throughout the extraction process. Additional pore water was extracted in some cases by injecting dry

nitrogen gas into the porespace and by forcing out pore water at the end of the compression (Yang, Yu et al. 1998).

Extracted pore waters were filtered through Nucleopore filters (0.45 μm) before chemical analysis (Yang, Yu et al. 1998). Cation concentrations were measured using inductively coupled plasma emission spectroscopy, and anion concentrations were measured using ion chromatography. Analytical errors were ±5% for all major ions except sulfate, for which the error was ±10%. Reported aluminum values contain both dissolved and particulate components < 0.45 μm. Yang, Turner et al. (1988) determined that the chemical composition of extracted water changed under increasing stress in a triaxial compression cell operating with an axial stress between 41 and 190 MPa and a lateral confining stress between 34 and 69 MPa. However, with a few exceptions, the range of variation was generally less than 20% for calcium, sodium, magnesium, potassium, chloride, sulfate and silica.

Centrifugation methods were used on some samples to test whether a compression method modified the chemistry of the pore-water samples. Yang, Davis et al. (1990) analyzed pore waters extracted from adjacent samples of nonwelded tuff using a triaxial compression system (operating up to 152 MPa axial stress and 62 MPa confining stress) and a high-speed centrifuge (operating up to 18,000 rpm). These authors concluded that both methods produced reliable data, with similar results from each under the operating conditions used in the test. In general, differences in chemical concentrations of the major ions (calcium, sodium, magnesium, chloride, and sulfate) within each pair were less than 15%. However, other chemical species were not analyzed in the study. For example, it is likely that *in-situ* concentrations of bicarbonate and carbonate would be influenced to different extents by the extraction methods used. In addition, the compression extraction method precludes accurate measurement of several other parameters of interest such as pH and the major species of redox-sensitive elements. Analyses of chloride, bromide and sulfate were performed on pore waters extracted from Exploratory Studies Facility drill core by ultracentrifugation (Fabryka-Martin, Wolfsberg et al. 1997). Pore-water data are discussed in Subsection 6.2.5 (Geochemistry) and 6.2.6 (Isotopes).

Samples of perched waters were obtained from shallow boreholes UZN#2 and UZ-N46 and from deep surface-based boreholes UZ-1, UZ-14, G-2, ONC#1, NRG-7a, SD-7, SD-9, and WT-24. These samples were collected with a bailer or from the surface output of a downhole pump. As with the pore-water extraction methods, these methods of sampling perched water make it very difficult to derive reliable values for some parameters of interest such as pH, ORP/Eh, and the major species of redox-sensitive elements. Geochemical and isotopic analyses of perched waters are discussed in Subsections 6.2.5 and 6.2.6, respectively.

Subsection 6.2.6 also provides additional details on sample processing methods for specific isotopes. Methods include leaching salts from unsaturated rock cores or cuttings for ^{36}Cl and Sr isotopic analysis, distillation or compression of core to extract water for analysis of tritium or stable isotopes of hydrogen and oxygen, and compression of core to extract water for carbon isotopic analysis. Tritium was analyzed by liquid scintillation, with a one-sigma uncertainty of 4 tritium units (TU). Stable hydrogen ($^2H/^1H$) and oxygen ($^{18}O/^{16}O$) isotope ratios were measured by gas source mass spectrometry and are reported as δD and $\delta^{18}O$, which expresses the sample's degree of enrichment or depletion of the heavy isotope relative to the Vienna Standard Mean Ocean Water (VSMOW) standard (Clark and Fritz 1997). Uncertainties were ±0.2 parts per mil

(‰) for $\delta^{18}O$ and ±1.0 ‰ for δD. Carbon-14 and stable carbon isotopes were analyzed by accelerator mass spectrometry, with uncertainties of ±0.7 pmc for ^{14}C and ±0.2 ‰ for $\delta^{13}C$ (Yang, Rattray et al. 1996). $\delta^{18}O$ is measured relative to the Vienna PDB (VPDB) standard ($^{13}C/^{12}C$ = 0.011237). Chlorine-36 was also analyzed by accelerator mass spectrometry (as $^{36}Cl/Cl$), with typical uncertainties of ±5%. Strontium isotope ratios ($^{87}Sr/^{86}Sr$) were done by solid source mass spectrometry and can be expressed as $\delta^{87}Sr$ relative to the ratio of reference seawater strontium ($^{87}Sr/^{86}Sr = 0.7092$).

Samples of saturated-zone waters were generally obtained with either a downhole pump or a bailer (Ogard and Kerrisk 1984; Benson and McKinley 1985). Geochemical and isotopic analyses of saturated-zone waters are discussed in Subsection 6.2.8.

6.2.3 Chemical Composition of Precipitation

6.2.3.1 Processes Controlling Precipitation Chemistry

The initial chemical and isotopic composition of Yucca Mountain groundwater is largely established by that of local precipitation and dry fallout. Once the precipitation enters the soil zone, absolute and relative concentrations of the various constituents are shifted to varying degrees by evapotranspiration and by interactions with minerals, organic matter, and the gas phase. The effects of these latter processes are described in subsequent sections. Isotopic data for precipitation are discussed in Subsection 6.2.6.

Several processes control the initial composition of precipitation or fallout. Some examples are:

- Salts from marine and terrestrial sources. For example, ions such as Na and Cl in precipitation derive predominantly from the ocean, whereas terrestrial sources contribute to Ca and Mg concentrations.

- Anthropogenic sources. Acid rain resulting from industrial releases of sulfur is an example of an anthropogenic source that impacts the chemical reactivity of precipitation. Other examples of anthropogenic sources are nitrates, freons, and fallout of radioactivity from above-ground nuclear tests. These species occur at such extremely low levels that they are useful as groundwater tracers but do not affect its chemistry. Global fallout nuclides in precipitation are discussed in Subsection 6.2.6.

- Wet and dry deposition processes. For example, between one-third and two-thirds of the Cl deposition in Southern Nevada is from dry fallout.

- Atmospheric processes (for example, chemical transformation of molecular species). Different chemical species have dramatically different residence times in the atmosphere. For example, the chloride ion is rapidly removed by precipitation or as dry fallout of aerosols, with an average residence time on the order of a couple weeks. In contrast, chlorinated organic compounds have residence times on the order of years.

- Season, frequency and cycles of precipitation events, and El Niño influences.

- Evaporation prior to deposition will concentrate many solutes, as well as affect the fractionation of hydrogen and oxygen isotopes in moisture.

- Air temperature affects H and O isotopic fractionation, with the greatest fractionation observed for cold temperatures. It also controls gas solubilities.

6.2.3.2 Present-Day Regional Characteristics

The largest database available for characterizing regional precipitation chemistry is that maintained by the National Atmospheric Deposition Program/National Trends Network (NADP/NTN 1997), which was established in 1978. The network is a cooperative effort between many different groups, including the State Agricultural Experiment Stations, U.S. Geological Survey, U.S. Department of Agriculture, and numerous other governmental and private entities. This network presently consists of 200 rural stations throughout the United States that monitor wet-only deposition. A limited number of stations also monitor dry deposition, but none of these stations are in Nevada. Chemical analyses on weekly precipitation samples are conducted by the Central Analytical Laboratory operated by the Illinois State Water Survey. Summary records are available for annual, quarterly, and monthly periods.

Within the Yucca Mountain Project, the NADP/NTN regional database has thus far only been used to characterize Cl deposition rates in the Southwestern United States. Cl is the most conservative dissolved chemical species in Yucca Mountain groundwaters, insofar as its origin is strongly dominated by atmospheric sources and the contribution from water-rock interactions generally appears to be negligible. Increases in its subsurface concentrations relative to that in precipitation (including dry fallout) are attributed to evapotranspiration in the soil zone. Because of this characteristic, various pore-water constituents are commonly plotted as a function of Cl concentration to assess the direction and magnitude of rock-water interactions in the subsurface (Subsection 6.2.5).

Chloride pore-water concentrations have also been used as a surrogate measure of infiltration rates, an approach called the chloride-mass-balance method (for example, Subsection 5.3.4.1.1.4). Total Cl deposition is a key parameter in the Cl-mass-balance method. In general, Cl concentrations in precipitation decrease with increasing distance from the ocean (Eriksson 1960) (Figure 6.2-2). Wet and total Cl deposition rates for NADP/NTN stations in the Southwestern United States show this same general trend (Figure 6.2-3). However, dry-deposition of Cl is quite variable, showing no clear trend (Figure 6.2-4), possibly because dry fallout is largely dependent upon local sources of Cl in addition to distance and wind patterns, which control the regional distribution of aerosol particles and their deposition rates (Winchester and Duce 1967). For the Southwestern NADP/NTN stations, dry fallout generally comprises between 30 and 60 percent of total Cl deposition. Eriksson (1960) studied the ratio of Cl concentrations in runoff to that in precipitation and suggested that, as a rule of thumb, about 67 percent of the total Cl deposition was contributed by dry fallout. In a local study of the Great Basin of Nevada and Utah, Dettinger (1989) estimated that dry deposition comprises 33 percent of the total Cl input.

A crude estimate of the contribution of dry fallout to total Cl deposition rates in Southern Nevada can also be derived by comparing the average annual Cl concentration in wet fallout at Red Rock

Canyon (0.16 mg/L, Table 6.2-4) to the average annual Cl concentration in precipitation at 3 Springs Basin, which includes both wet and dry fallout (0.36 mg/L, Table 6.2-3). This comparison indicates that dry fallout comprises about 60 percent of the total fallout in this area.

6.2.3.3 Present-Day Site Characteristics

The isotopic and chemical composition of precipitation at the Yucca Mountain site is largely inferred from measurements made at other local sites. Seven years of record (1985 to 1992) are available for precipitation chemistry in the semiarid 3 Springs Basin located east of Kawich Peak in the Kawich Range east of Tonopah, Nevada, and about 130 km due north of Yucca Mountain (McKinley and Oliver 1994, 1995). Major ion chemistries of precipitation for the two precipitation chemistry monitoring stations at this location (3 Springs Basin and Kawich Peak) are summarized in Table 6.2-2. These data are used later in this subsection to derive average annual weighted concentrations for major constituents, and regression lines for these constituents relative to Cl concentrations (Table 6.2-3). The regression lines are used to illustrate subsequent changes in water chemistry as it flows through the subsurface.

Chemical data for precipitation are also available for Red Rock Canyon, the desert observation station closest to Yucca Mountain in the NADP/NTN network. This site is about 120 km southeast of Yucca Mountain. Its record spans 11 years, from January 1985 to the present, which includes two El Niño episodes, one in 1986 to 1987, and a long episode from autumn 1989 through the summer of 1995. Annual and seasonal summaries of precipitation-weighted averages are shown in Table 6.2-4. Neither alkalinity nor carbonate species are reported in this database. Based on the Red Rock data (Table 6.2-4), Fabryka-Martin, Turin et al. (1998) concluded that the increased precipitation associated with El Niño years did not appear to lead to a significant increase in the Cl deposition rate. Its influence on other chemical parameters has not been evaluated.

The chemistry of precipitation is important for modeling the composition of waters at Yucca Mountain because precipitation represents the starting point in the evolution of groundwater chemistry. Subsequent changes in the water chemistry as it enters the subsurface are illustrated by three types of diagrams.

- *Tri-linear (Piper) diagrams* show the relative concentrations of major ionic species. Figure 6.2-5 is a tri-linear diagram for the precipitation samples from 3 Springs Basin, to be compared against other tri-linear diagrams for surface waters and subsurface waters in later sections. (Because bicarbonate concentrations are not available for the Red Rock Canyon data, these data are not presented on a tri-linear diagram. However, bicarbonate concentration could be estimated for these samples based on charge-balance calculations.)

- *Frequency distributions* of major elements illustrate how the concentrations change as the water enters and moves through the subsurface. Frequency distributions for precipitation data have been included on the figures in Subsection 6.2.5, in which they can be directly compared to those in surface and subsurface waters.

- *Scatterplots* of various major constituents as a function of some conservative species are a common method for evaluating the role of water-rock interactions in changing concentrations along a flow path. Chloride is usually considered to be the most conservative species, and a common assumption is that its concentration in surface and subsurface pore waters reflects increases due solely to evapotranspiration. Figure 6.2-6 presents a set of plots of sodium, calcium, sulfate, bicarbonate, and silica as a function of Cl. Only samples with less than 1 mg/L Cl have been included. The regression lines plotted for each constituent on this figure represent least-squares fits to the precipitation data from the two 3 Springs Basin sites. These lines have also been plotted on analogous figures in Subsection 6.2.5 (chemistry of waters from the unsaturated zone) as a basis for a discussion of the direction and magnitude of rock-water interactions in the subsurface.

Other than the monitoring studies at 3 Springs Basin and Red Rock Canyon, only a few studies of Yucca Mountain precipitation chemistry have been conducted, and the coverage of these studies was very limited in time, space, and/or analytical data. An analysis of a single precipitation sample collected near borehole UZ-N2 in March 1992 is reported in Table 6.2-10 (subsection on perched-water chemistry) and is plotted on the tri-linear diagram in Figure 6.2-5 (point labeled M). Chloride, bromide and sulfate were measured in a suite of about 100 samples collected from rain gauges at several neutron-monitoring boreholes at Yucca Mountain in the spring of 1995 (Fabryka-Martin, Turin et al. 1998). The purpose of these analyses was to provide independent corroboration for estimates of the Cl deposition rate, a parameter used in the Cl-mass-balance method, and to characterize the Cl/Br and SO_4/Cl ratios of precipitation because these ratios can be useful qualitative tracers of groundwater origins and flow paths. Histograms showing the frequency distributions of Cl and SO_4 from this work are presented in Subsection 6.2.5 (Figures 6.2-17 and 6.2-18), in which they are compared to the concentrations of these species in waters from the unsaturated and saturated zones.

6.2.3.4 Representativeness of the Available Data

An important issue to address is the extent to which these precipitation data are representative of precipitation at Yucca Mountain, both past and present. Monitoring at the site at the present time may not produce valid data because it may not be possible to separate out the effects of site disturbance from natural conditions. Present-day compositions may also not be representative of past (pre-industrial) compositions, for example, due to regional contaminant plumes emanating from Los Angeles. This raises the question, then, of which of the two available data sets is more representative of natural conditions at Yucca Mountain. The compositions differ in both absolute as well as relative concentrations of major ions (for example, compare annual average values for Na/Cl, SO_4/Cl, and Ca/Cl in Figure 6.2-6). The Red Rock Canyon data have the advantage of providing a comparatively long (13-year) record, with details available for individual storms if desired. However, the proximity of Las Vegas may influence the chemical compositions, and the lack of alkalinity analyses is a significant shortcoming that also makes it impossible to calculate a charge balance. In addition, only wet deposition chemistry is measured. The 3 Springs Basin data, although further removed from Yucca Mountain, have the advantages of being uninfluenced by local anthropogenic inputs and of including both wet and dry deposition. Consequently, preference has been given to the 3 Springs Basin data set.

Despite their shortcomings, these precipitation data are probably adequate for the purposes for which they are used. For the saturated zone, the geochemical evolution of the water is not very sensitive to uncertainties in the precipitation chemistry. However, for the unsaturated zone, the dominant input function is the composition of precipitation following evapotranspiration, and hence, the unsaturated-zone pore water compositions can be more sensitive to the precipitation uncertainties because errors may be magnified as the water becomes more concentrated. The approach taken in this assessment to address this problem is to bound the range in initial concentrations of critical parameters.

6.2.3.5 Scenarios for Future Trends in Precipitation Chemistry

Global climate change could be expected to influence the chemistry of precipitation in the future through its effects on carbon-dioxide levels, rainfall patterns, and dust levels and sources. No studies exist or are planned to assess possible future trends or to establish bounds on such factors controlling precipitation chemistry and the possible consequence for the various geochemical parameters in precipitation.

6.2.4 Chemical and Isotopic Composition of Surface Waters

This subsection describes the limited data available on the chemistry of surface water in the region. Three types of surface-water chemistry exist depending on the source of the water:

- Relatively dilute waters from runoff during precipitation or snowmelt
- Relatively saline waters from groundwater discharge at springs
- A mixture of the two preceding types

No studies with a description of surface water chemistry as the major objective exist or are planned. After an overview of the occurrence of surface water in the basin, the following discussion focuses on the chemical composition of the first category of surface waters, and particularly on surface waters from potential recharge areas and along flow paths through the Yucca Mountain area. Additional chemical data on spring discharges and channel flow down-gradient or away from Yucca Mountain are reported in Subsection 5.1.6. Isotopic data for surface waters are discussed in Subsection 6.2.6.

6.2.4.1 Regional and Local Surface-Water Bodies and Drainage Areas

Yucca Mountain lies within the Amargosa River drainage basin, which is a closed basin with Death Valley at the terminus (Figure 5.1-1). Subsection 5.1.1 provides a detailed description of the physiography of the regional and site drainage area, hydrographs of flood events at various locations, the distribution of spring discharges, and hydrologic and geochemical data. The following discussion is largely summarized from that in Subsection 5.1.

Local drainages on Yucca Mountain ultimately enter the Amargosa River. The eastern slope drains via Yucca Wash, Drill Hole Wash, and Dune Wash to Fortymile Wash; Fortymile Wash spreads out into a distributary system in the Amargosa Desert, joining the Amargosa River about 18 km north of Death Valley Junction, California. An unnamed ephemeral channel in Crater Flat collects drainage from the western and southern slopes of Yucca Mountain, draining to the

Amargosa River near its confluence with Fortymile Wash. In addition, the tributary Carson Slough enters the Amargosa River as it flows southward through the Amargosa Desert. Carson Slough drains spring flow from the Ash Meadows regional groundwater discharge area in the eastern portion of the Franklin Lake Playa (also known as Alkali Flat), a discharge area for Yucca Mountain regional groundwater. However, the Amargosa River and its tributaries are ephemeral streams except where spring discharges enter the channel system for short distances; flow throughout its entire reach occurs rarely (Malmberg and Eakin 1962; Walker and Eakin 1963) because of losses to infiltration and evaporation from the streambed.

Savard (1995, 1997) and Grasso (1996) discuss climatic and weather patterns responsible for Yucca Mountain area streamflow and associated flooding (Subsection 5.1.5). Winter/spring stream flow occurs during El Niño events when the track of Pacific cyclonic fronts crosses the Yucca Mountain area. Summer streamflow occurs from thunderstorms, often when the summer monsoon in the Southwestern United States extends into the Yucca Mountain area. Occasionally, remnant hurricanes from the Pacific move into the Yucca Mountain area, causing stream flow in the late summer and fall. These climatic factors control the initial chemical and isotopic composition of the local precipitation. Once the water contacts the ground, the chemistry of ephemeral surface waters evolves based upon surface characteristics that control either the type of geologic materials with which the water comes into contact or the length of time of the contact period:

- Site topography (for example, slope, ridgetop, terrace, sideslope, channel)
- Soil development (for example, depth of regolith, porosity, soil stratification/profile development, infiltration rates)
- Soil mineralogy and chemistry
- Biota and vegetative coverage
- Evaporative concentration of solutes during flow

In addition to ephemeral flows following precipitation events, perennial surface water in the Amargosa River drainage basin is associated with springs. Flowing water occurs in the Oasis Valley, Ash Meadows, Tecopa, and Badwater areas after infrequent precipitation/runoff events, as well as during winter months when evapotranspiration is at a minimum. Some of these areas dry up almost entirely during high evapotranspiration periods during the summer.

- Numerous permanent or nearly permanent springs discharge along or near the Amargosa River channel in Oasis Valley. Although the flow in the channel is ephemeral through the Amargosa Desert, short reaches of persistent flow occur between the desert and the channel entry into Death Valley. Wet playas occur in the eastern (Amargosa or Peters Playa) and southernmost (Franklin Lake Playa or Alkali Flat) parts of Amargosa Desert.
- The Ash Meadows regional groundwater system, which drains the region east of Yucca Mountain, discharges at several perennial springs that sustain small pools at Ash Meadows in Southeastern Amargosa Desert. Crystal Reservoir, a man-made structure,

captures discharge from Crystal Spring and several springs in the Point of Rocks area and drains to the Amargosa River by Carson Slough.

- Four small perennial ponds occur in the Amargosa Desert in former clay mining pits.
- Badwater is a spring discharge pool in the terminal area of the Amargosa River in Death Valley.

Chemical data for perennial surface waters are discussed in Subsection 5.1.6.

6.2.4.2 Relevance of Surface-Water Chemistry to Site Assessment

Chemical and isotopic compositions of some of the surface waters described above may be relevant to site assessment concerns for two major reasons. First, infiltration under large channels such as Fortymile Wash may contribute significantly to local recharge and may thereby influence the chemistry of saturated-zone fluids. Although such fluids do not have the potential to contact waste packages and are, furthermore, unlikely to lie along the direct flow path between the potential repository and the accessible environment, characterizing their chemical and isotopic compositions is nonetheless necessary to use these characteristics as groundwater tracers for the regional flow system. These aspects are discussed in Subsection 5.1.6. Secondly, infiltration from runoff events collected from small channels above the potential repository, at locations where soil cover is negligible, may contribute to seeps that have the potential to directly contact the repository backfill and the waste canisters. Runoff water chemistry is discussed in Subsection 6.2.4.3.

Chemical and isotopic compositions of waters from spring discharge areas may possibly be relevant to site assessment to the extent that they could be considered to represent the end-member geochemical environment of the flow system. These compositions then provide data suitable for developing and testing the alternative models of groundwater flow and of geochemical evolution along the flow path. Chemical and isotopic data for these samples, and their applicability to site assessment issues and geochemical modeling, are not currently discussed in this document.

6.2.4.3 Surface-Water Chemistry Data

A limited number of samples have been collected to document stream flow chemistry during the occasional runoff event as part of Yucca Mountain site characterization studies. Physical characteristics and chemical compositions of these surface runoff sites in the vicinity of Yucca Mountain and Fortymile Wash are summarized in Tables 6.2-5a and 6.2-5b. Sampling locations are plotted on the map in Figure 6.2-7.

Some of the data included in Tables 6.2-5a and 6.2-5b are taken from a compilation of hydrochemical data collected in the Death Valley region during the period from 1910 to 1990, which included baseline data from rivers and playas in addition to springs and wells (Perfect et al. 1995). Although the main objective of the 1995 report was to document groundwater quality in the Yucca Mountain area, surface-water quality is also documented. The chemical analyses in the compilation by Perfect et al. are taken from four general sources: USGS

unpublished data files, USGS National Water Information System database, published reports from Federal and State agency investigations, and unpublished data. A cation-anion balance was computed for each chemical analysis, which was then assigned to one of three categories: the analysis balances to within ±10 percent, not enough major ion information is available to calculate a balance, or the analysis balances over ±10 percent.

The following general observations are made from the chemical data for channel flow and surface runoff in Table 6.2-5. Major ion chemistry for these samples is plotted in the tri-linear diagram in Figure 6.2-8. The sampling sites fall into three general categories: channel flow fed by springs and seeps, channel flow from runoff events and surface runoff, and overland runoff mixed with spring discharge.

Nineteen samples were analyzed for major and minor ions between 1984 and 1995 from 15 locations within 15 km of Yucca Mountain along its eastern side (Table 6.2-5). These data were collected during three series of runoff events.

- Surface water samples collected in Fortymile Wash, Drill Hole Wash, and Busted Butte Wash in August 1984 were the first surface-water samples collected during site characterization studies in the Yucca Mountain area.

- Emett et al. (1994) document analyses from dip samples of surface water in the Amargosa River drainage basin from six sampling sites during stream flow conditions in 1993. Two of the sites (Stockade Wash at Airport Road and Yucca Wash near its mouth) represent local overland runoff during precipitation. (The other three sites [Amargosa River near Beatty, Carson Slough at Stateline Road, and Amargosa River near Eagle Mountain] represent spring discharge from groundwater or mixing of overland runoff and spring discharge and are not discussed here. Although the Cane Spring Wash sample represents runoff, it is not included here because of its distance from Yucca Mountain.)

- During periods of stream flow in 1995, surface-water quality samples were also collected on Yucca Mountain and Fortymile Canyon during overland runoff and channel flow following precipitation. Some of the overland runoff from the hill slopes in the drainage basins infiltrated soil and volcanic rock layers and then re-emerged as overland runoff. Some of the overland runoff also originated from disturbed areas in the drainage basins such as roads and drill pads where compaction of the surface material reduced infiltration and increased overland runoff. Some of the surface-water quality samples in Fortymile Canyon were taken during overland runoff of precipitation and or snowmelt, whereas others were taken during the recession period after peak discharge. All samples probably represent a mixing of overland runoff and shallow infiltration waters that discharge along the hillslopes.

Among these dilute runoff samples, total dissolved solids range from 45 to 122 mg/L. These waters have similar ionic chemistries to one another on a tri-linear diagram (Figure 6.2-8). The cation field is slightly dominated by calcium, which accounts for 50 to 60 percent of the cation charge, whereas the anion field is dominated by carbonate species, which account for 70 to

90 percent of the total anion charge. The average Cl content of these local runoff waters is 3.5 mg/L.

In addition to surface-water samples from the general vicinity of Yucca Mountain, water quality data are also available for 3 Springs Basin and East Stewart Basin, sites that are considered representative of potential recharge areas in Central Nevada (McKinley and Oliver 1994, 1995). 3 Springs Basin is a semiarid basin in the Kawich Range east of Tonopah; sampling locations are at elevations of 7,070 to 9,040 feet. East Stewart Basin is a subalpine basin in the Toiyabe Range north of Tonopah with sampling occurring at elevations of 9,455 to 10,240 feet. The two basins were being studied as analog sites to Yucca Mountain during wetter and cooler periods (Subsection 5.1.4.4). Water quality samples were collected from precipitation, springs, and other surface waters during the period 1986 to 1992. Physical characteristics and chemical compositions of the surface-water samples from their studies are tabulated in Tables 6.2-6 and 6.2-7; chemical data for precipitation at the 3 Springs Basin sites were presented previously in Subsection 6.2.3. Springs in the basins are probably above the regional groundwater system and do not represent discharge from large groundwater basins, in contrast to the case for springs at Ash Meadows in the Amargosa Desert. The water quality of the spring discharges does represent movement of water through unsaturated volcanic rock layers in the basins. Surface-water samples can represent overland runoff from precipitation or snow melt and also can represent mixing of spring discharge with overland runoff.

Major ion compositions of some of the 3 Springs Basin and Stewart Basin samples are plotted in the tri-linear diagram shown in Figure 6.2-9, and the major constituents are plotted versus chloride concentration in Figure 6.2-10. These waters are very similar to the Yucca Mountain runoff samples with respect to their relative proportions of the major ions, that is, they are Ca-bicarbonate waters with a significant component of Na. However, the Central Nevada samples have slightly higher proportions of Na and Cl, and lower proportions of Ca and carbonate species, than the Yucca Mountain waters.

Figure 6.2-10 shows various major constituents plotted against Cl concentrations for channel flow and surface runoff at Yucca Mountain and for surface waters from 3 Springs Basin and Stewart Basin. Also shown on the plots are the regression lines obtained for 3 Springs Basin precipitation chemistry from Subsection 6.2.3. The surface water plots illustrate the direction and magnitude of changes in water chemistry in response to evaporation, dissolution of dry-fall salts accumulated since the last infiltration event, and water-rock interactions. Sulfate in these waters increases to a similar extent as does Cl, as shown by the fact that the surface-water compositions cluster about the regression line. This observation suggests that sulfate concentrations in these waters are fairly conservative and are determined mostly by evaporation and dissolution of dry-fall salts. In contrast, both Na and Ca concentrations plot considerably above the precipitation regression lines, suggesting that their concentrations are increased by dissolution of carbonate minerals and weathering reactions of soil minerals. Dissolution of carbonate minerals also leads to a large gain in bicarbonate concentrations, which is also apparent in a comparison of the tri-linear plot of Figure 6.2-5 (precipitation) with those in Figures 6.2-8 (Yucca Mountain runoff) and 6.2-9 (surface waters from 3 Springs Basin and Stewart Basin). Finally, the most dramatic constituent increase is observed for silica, which increases by two orders of magnitude over its concentration in precipitation due to fast dissolution of unstable amorphous silica minerals in the soil.

Another source of chemical data for surface-water samples is the compilation of analyses of springs and tunnel seeps from Rainier Mesa (McKinley et al. 1991). Because of the similarity in geologic settings and soil cover for Yucca Mountain and Rainier Mesa, these samples expand the database used to develop a conceptual model for the early stages of the geochemical evolution of waters contacting tuff. A tri-linear plot of these data is presented in Figure 6.2-11, in which the similarity between some of the tunnel seeps (points 8, 9, A) and the Yucca Mountain runoff samples is apparent. In Subsection 6.2.5, these waters are also seen to be very similar in composition to perched waters at Yucca Mountain (Figure 6.2-16).

These surface-water chemical data are also included in the discussion on the geochemical evolution of Yucca Mountain waters (Subsection 6.2.5) in which frequency histograms for some of the major ion species are presented (Figures 6.2-17 to 6.2-21).

6.2.4.4 Representativeness of the Data

A key question is, to what extent are the Yucca Mountain runoff samples representative of surface water at this location? Surface waters under current climatic conditions at Yucca Mountain are an infrequent occurrence, thereby making it difficult to build a chemical database. Re-aeration of surface water as it proceeds down the channel may also affect the chemistry of the collected samples. Some samples were analyzed for bicarbonate in the laboratory instead of at the site during collection, such that the reported bicarbonate concentrations may not represent field conditions.

Some of the samples may also be affected by site activities because man-made disturbances influence sediment concentrations in surface water. Savard (see Subsection 5.1.6) noted runoff coming from the Exploratory Studies Facility pad and tunnel waste piles during light precipitation events and going down the Drill Hole Wash channel. Fine sediment probably originating from the Exploratory Studies Facility pad and tunnel waste piles was being transported down the channel system and clogging infiltration pathways in the channel alluvial material. Because of greatly reduced infiltration in the channel bottom, surface-water runoff and sediment were both transported much greater distances than they would have been under natural conditions. During some periods of runoff from the Exploratory Studies Facility pad, no other runoff was noted in the area, leading to the hypothesis that the Exploratory Studies Facility pad and tunnel waste piles were influencing water quality and runoff.

From a practical perspective, the current Yucca Mountain data set is the best available. Including the more extensive data from the 3 Springs Basin and Stewart Basin is useful to develop and test concepts about geochemical evolution in this environment. The surface geology at the two Central Nevada sites is similar to that at Yucca Mountain insofar as both are dominated by silicic volcanic rocks, and the precipitation chemistry is also expected to be quite similar. The prevailing climatic regime at the Central Nevada sites differs from that at Yucca Mountain, leading to differences in soil chemistry, in particular less calcic soils. The Central Nevada sites also have higher precipitation rates and higher infiltration rates, such that concentrations should be slightly lower for these surface waters than for the Yucca Mountain samples. However, taken together, these two data sets are believed to be adequately representative of site conditions for the purposes for which they are used.

6.2.5 Chemical Composition of Unsaturated-Zone and Perched Waters

6.2.5.1 Processes Controlling the Chemistry of Unsaturated-Zone Waters

The major processes that could influence the chemistry of waters in the unsaturated zone, including perched water, include the following.

Dry and Wet Deposition (Precipitation)–This refers to the compositions of rain, snow, and dust deposited on the surface of Yucca Mountain. These compositions provide the starting point (that is, input composition) for unsaturated-zone water chemistry. Chemical data available for wet and dry deposition were discussed in Subsection 6.2.3.

Surface-Water Chemistry–Under some conditions, surface waters may be a significant source of recharge to the unsaturated zone in the Yucca Mountain region (see Section 5). Therefore, the chemistry of surface waters is potentially an important factor in the control of unsaturated-zone water compositions. Chemical data available for surface waters were discussed in Subsection 6.2.4.

Soil-Zone Processes–Soil-zone processes of importance to unsaturated-zone water chemistry include evapotranspiration, deposition of pedogenic mineral horizons, reaction of infiltrating precipitation waters with soil minerals, and biogenic processes.

Infiltration Paths and Rates–The pathways by which waters infiltrate Yucca Mountain impact water chemistry not only because they determine the rock/mineral types that the waters contact but also because they determine the contact times for waters with the various rock/mineral types. These contact times in turn determine the extent of reaction between the waters and the rocks/minerals. Particularly significant to solute transport rates is the distribution of flow between fractures and matrices in each lithologic unit.

Rock-Water Interactions–The extent to which infiltrating waters react with the rocks/minerals with which they come into contact will have a major impact on water chemistry. These interactions can include rock/mineral-dissolution reactions, ion-exchange reactions, hydrolysis reactions, precipitation reactions, and possibly other alteration reactions.

Mineral-Substrate–Water Interactions–These interactions are a subset of rock/mineral interactions but are separated out here because of their potential significance with respect to radionuclide retardation reactions (for example, sorption).

Water-Air Interactions–The composition of the gas phase in the unsaturated zone is an important factor in the control of unsaturated-zone water chemistry. For example, the carbon-dioxide partial pressure influences the carbonic-acid system and the oxygen partial pressure influences the oxidation state of redox-sensitive elements such as carbon, sulfur, iron, manganese, and others.

Microbial Influences–The existence of various microbial populations in the unsaturated zone implies that water chemistry could be altered by microbial activity. For example, microbial

metabolic activity could influence pH, the concentrations of redox-sensitive species, and the concentrations of organic acids in unsaturated-zone waters.

Temperature and Pressure–Variations in temperature can influence the composition of unsaturated-zone waters by increasing or decreasing the rates of important reactions (for example, dissolution or precipitation reactions) and by changing the composition of the equilibrium assemblage in the system. Temperature variations in the ambient unsaturated-zone system are relatively minor and likely have minor impacts on water chemistry. During the repository heating phase, temperature will have a much more important impact on water chemistry. These aspects of unsaturated-zone chemistry are discussed in detail in the chapter on the near field (Subsections 7.4.2 and 7.5.3). The most significant impact of pressure on water chemistry will likely be through its effect on the dissolution of gases in water.

6.2.5.2 Present-Day Site Characteristics of Unsaturated-Zone Pore Waters and Perched Waters

This subsection discusses the data available on the chemistry of pore waters and perched waters in the unsaturated zone both above and below the potential repository horizon. It is based primarily on data presented in reports by Yang, Rattray et al. (1996), Yang, Yu et al. (1998), and Fabryka-Martin, Flint et al. (1997) and on the groundwater chemistry model presented in Triay, Meijer, Conca et al. (1997).

The compositions of pore waters above the potential repository horizon are of significance because they represent the types of waters that could enter the near-field of the potential repository. They are also significant because they can be used to constrain models for the rock/mineral-water-gas interactions that occur in the soil zone and the unsaturated zone above the potential repository horizon. Such models can be used to derive estimates of future variations in unsaturated zone water chemistry.

Available chemical data for the unsaturated zone are presented in Tables 6.2-8 (pore water from surface-based boreholes), 6.2-9 (pore water from Exploratory Studies Facility drillholes), 6.2-10 (shallow transient perched water), and 6.2-11 (deep perched water). Tri-linear (Piper) diagrams are used to characterize the relative distributions of major cations and anions in these waters as a function of their stratigraphic depths. Figures 6.2-12 through 6.2-15 present such plots for pore waters from the Paintbrush Tuff nonwelded hydrologic unit, the upper and lower parts of the Calico Hills unit, and the Prow Pass unit, respectively. Figure 6.2-16 presents a tri-linear plot for the shallow and deep perched-water samples. These plots are referenced in the subsequent discussion of the geochemical evolution of pore fluids in the unsaturated zone.

Frequency histograms of chloride concentration data are plotted in Figure 6.2-17 for pore waters from the PTn units, from the CHn hydrogeologic unit, and from the TCw and TSw hydrogeologic units. These concentrations are compared against data for precipitation, surface waters, perched waters, and saturated-zone waters. Nearly all pore waters in the unsaturated zone have chloride concentrations that are higher than those for other waters at Yucca Mountain, with PTn waters having the highest concentrations. As noted in Subsection 5.3.4.1.3.3, estimates of infiltration rates on Yucca Mountain derived from physical measurements are generally consistent with infiltration rates calculated using the chloride-mass-balance method. Thus, the

elevated chloride concentrations in the PTn pore waters would appear to reflect high degrees of evapotranspiration and small infiltration rates at most of the sampled locations. Figure 6.2-18 shows that sulfate concentrations are similarly elevated in PTn pore waters relative to those for the other waters plotted.

The higher proportions of chloride and sulfate concentrations in PTn pore waters relative to the other waters at the site are also evident by comparing the tri-linear plot in Figure 6.2-12 to the tri-linear plots in Figure 6.2-13 (upper Calico Hills pore waters), 6.2-14 (lower Calico Hills pore waters), 6.2-15 (Prow Pass pore waters), and 6.2-16 (perched waters).

The frequency distribution for silica shown in Figure 6.2-19 indicates that silica is low in precipitation but substantially higher in surface waters. By the time precipitation and surface waters infiltrate into the unsaturated zone, the silica concentrations have reached a limit. This limit is presumably the result of saturation with a silica phase as discussed further below.

The concentrations of sodium and calcium are also elevated in pore waters relative to other waters at the site as shown in Figure 6.2-20 and 6.2-21. Sodium is elevated in most of the pore-water samples whereas calcium is elevated only in the PTn and TSw samples. The tri-linear diagram for PTn pore waters (Figure 6.2-12) shows that PTn pore-water compositions extend to higher calcium proportions than observed in either precipitation compositions (Figure 6.2-5) or surface-water compositions (Figures 6.2-8 and 6.2-9). This presumably reflects water-soil/rock reactions that dissolve calcium preferentially to sodium and magnesium. The pore waters in the Calico Hills and Prow Pass units show high proportions of sodium (Figures 6.2-13, 6.2-14, and 6.2-15). This primarily reflects the ion-exchange reactions with zeolites in the CHn unit.

A convenient method for assessing the magnitude and direction of rock/mineral-water interactions experienced by percolating infiltration waters transported through the soil and unsaturated zones is to plot the concentrations of the major constituents in these waters relative to a conservative constituent (that is, highly soluble and nonsorbing), such as chloride, in an *x-y* plot (Scanlon 1991; Triay, Meijer, Conca et al. 1997). In the absence of other geochemical processes, evapotranspiration of a given water sample will result in proportional increases in all constituent concentrations, describing a linear trend in this plot starting at the origin. If processes other than evapotranspiration significantly influence the concentration of a particular constituent, the resulting data point will lie off the evapotranspiration trend. The selection of chloride as the normalizing constituent for such a plot assumes that its concentration is not affected significantly by leakage from fluid inclusions or by geochemical reactions along the flow path, such as exchange with hydroxy phases and glasses or halite dissolution.

Plots of this type showing the concentrations of calcium and bicarbonate versus chloride for various pore-water, perched-water, and saturated-zone samples are presented as Figures 6.2-22 and 6.2-23, respectively. Included on each plot is a regression line representing a least-squares fit to the weighted annual precipitation data from the 3 Springs Basin monitoring sites (Subsection 6.2.3). These plots show that both calcium and bicarbonate concentrations in PTn pore waters generally plot on or below the evapotranspiration lines (Figures 6.2-22a and 6.2-23a). This result implies that calcium and bicarbonate were lost from these waters relative to chloride. Given the fact that soils on Yucca Mountain contain abundant caliche horizons (Taylor, E.M. 1986), this loss likely reflects the precipitation of calcite in the soil zone. The

process of evapotranspiration of water in the soil zone presumably concentrated calcium and bicarbonate sufficiently to cause the precipitation of calcite.

Pore waters from the Calico Hills and Prow Pass units show even greater depletions of calcium relative to the precipitation trend (Figure 6.2-22b and c). These greater depletions likely reflect ion-exchange processes in which sodium in the ion-exchanger phase (for example, zeolite or clay) was replaced by calcium from the water and vice versa. Unlike the PTn pore waters, many of the Calico Hills and Prow Pass pore waters are enriched in bicarbonate relative to the precipitation trend (Figure 6.2-23b and c). This fact most likely reflects the carbonic acid weathering reactions, which start with the dissociation of carbonic acid in the water as follows:

$$H_2CO_3 \Leftrightarrow H^+ + HCO_3^- .$$

In the weathering of aluminosilicate rocks and minerals, the weathering reactions proceed with the exchange of the hydrogen ions produced in this reaction with sodium or other cations on the rock or mineral. This step leads to an increase in sodium as well as bicarbonate concentrations in the water. The overall reaction is approximated as follows:

$$>SO\text{–}Na + H_2CO_3 \Leftrightarrow >SO\text{–}H + Na^+ + HCO_3^- ,$$

where >SO is a mineral substrate with a surface-complexation site at which ions can be exchanged. A plot of sodium versus chloride concentrations for PTn pore waters is presented in Figure 6.2-24a. The fact that sodium concentrations plot below the evapotranspiration line in this figure is puzzling. As explained previously, sodium is generally leached from minerals and rocks during low-temperature weathering reactions. Such leaching would lead to compositions that plot above the evapotranspiration line, not below it. Similarly, dissolution of halite along the flow path also cannot account for the decrease in sodium relative to chloride because this process would cause pore water samples to plot close to the precipitation line. Analytical error is considered unlikely to be the sole explanation not only because of quality-control measures but also because nearly all the samples plot below the line, implying they would all have to be in error, and because the charge balances for the analyses generally agree within ±10 percent (Yang, Rattray et al. 1996; Yang, Yu et al. 1998). Another possibility is that the average Na/Cl ratios in precipitation were lower in the past than those measured in the 3 Springs Basin samples at the present day. This possibility is supported by the fact that the weighted-average ratio in precipitation at the Red Rock site near Las Vegas (Table 6.2-3) is much lower than the ratio for the 3 Springs Basin data. A final possibility is that sodium is taken up by some sort of rock-water interaction or biogenic process not generally considered. However, smectites in the PTn are generally low in sodium and high in potassium and calcium. Although present in the PTn, zeolites do not appear to be particularly common here, and limited analytical data also show them to be calcium rich.

As shown in Figure 6.2-24b and c, sodium concentrations in pore waters from the Calico Hills and Prow Pass units generally plot well above the precipitation trendline. This result is attributed to the sodium/hydrogen ion-exchange reaction and to ion-exchange reactions involving calcium, magnesium, and sodium ion exchange on zeolites and clays. Assuming the sodium/hydrogen ion-exchange reaction is accompanied by the formation of an equimolar amount of bicarbonate, the increase in bicarbonate levels over and above the amount predicted by the precipitation trend

line would imply a large proportion of the increase in sodium concentrations shown in Figure 6.2-24 is due to the sodium/hydrogen ion reaction.

Like chloride, sulfate is considered to be a generally conservative constituent in dilute oxidizing waters such as the unsaturated-zone pore waters in Yucca Mountain. However, as shown in Figure 6.2-25a, b, and c, unsaturated-zone pore waters show sulfate-to-chloride ratios consistently lower than the ratios observed in recent precipitation. Because all the unsaturated-zone pore-water analyses are grossly undersaturated with chloride phases and with gypsum and other possible sulfate phases involving the major cations, it is unlikely that solid chloride or sulfate phases are precipitated in the unsaturated zone (Triay, Meijer, Conca et al. 1997). Although anthropogenic sulfate may have elevated the modern-day SO_4/Cl ratio in precipitation, the data used to prepare the precipitation regression line do not appear to have been significantly influenced by this source because perched waters and saturated-zone waters plot near the precipitation regression line (Figure 6.2-25d).

Drever and Smith (1978) presented a model that offers one potential explanation for the low sulfate-to-chloride ratios in the unsaturated-zone pore waters (Triay, Meijer, Conca et al. 1997). Their model involves drying and wetting cycles in the soil zone. During the drying phase, concentrations of dissolved solutes are increased in soil waters by evapotranspiration to the degree that phases such as calcite, gypsum, silica, and the more soluble salts precipitate. During occasional heavy rains, the phases precipitated during the drying phase are partially redissolved. Because the dissolution rates for highly soluble salts, such as sodium chloride, are higher than the rates for less-soluble salts, such as calcite, gypsum, and silica, a portion of the less-soluble salts may remain undissolved after the occasional heavy rains infiltrate through the soil zone. In terms of sulfate and chloride concentrations, this process could lead to soil waters with lower sulfate-to-chloride ratios than those observed in precipitation. The actual concentrations of sulfate and chloride in these waters would depend on the details of the processes involved, including the dissolution kinetics of the sulfate and chloride phases, the residence time of the waters in the soil zone, and the original masses of sulfate and chloride in the soil zone.

An alternative hypothesis to account for the low sulfate-to-chloride ratio is the microbial reduction of sulfate ions in the soil (e.g., initially to hydrogen sulfide), or more likely to a mixture of organic sulfides such as methyl disulfide and dimethyl disulfide. These volatile compounds are commonly produced in soils and are readily lost to the atmosphere. The magnitude of this effect at Yucca Mountain is not known. However, decreased SO_4/Cl are not observed in local saturated-zone waters. Because these waters recharge in regions with more vegetation and wetter soils, one might expect the likelihood of microbial reduction of sulfate to be even greater for those waters than for infiltrating waters at Yucca Mountain.

Although differences in the dissolution kinetics of sulfate and chloride salts may be part of the explanation for the low sulfate-to-chloride ratios in pore waters from the unsaturated zone at Yucca Mountain, these differences are likely augmented, and perhaps even dominated, by crystallization-sequence effects. For example, it is possible that minerals, such as calcite and gypsum, that precipitate from evaporating pore waters early in a crystallization sequence are partially or completely sequestered by minerals that precipitate later in the sequence (such as being coated by opal-A and halite). Alternatively, early crystallized phases may completely fill smaller pores in the rocks and, therefore, be less accessible to infiltrating waters than minerals

crystallized later in the sequence in larger pores (for example, Chadwick et al. 1987). During subsequent infiltration events, the latest-formed phases in pores accessible to infiltrating waters would preferentially dissolve, leading to soil solutions enriched in the more soluble salts relative to the less soluble salts.

A plot of silica versus chloride concentrations in pore waters, perched waters, and saturated-zone waters is shown in Figure 6.2-26. Most of the water samples from the Yucca Mountain area plot above the precipitation trend line (Triay, Meijer, Conca et al. 1997). This result suggests that a process other than evapotranspiration is contributing to the increase in silica concentrations in these waters. According to Gifford and Frugoli (1964) and Chadwick et al. (1987), silica is added to soil waters as a result of the dissolution of unstable silica phases present in soil horizons in arid regions. This explanation would be consistent with the presence of amorphous silica in the soils of Yucca Mountain and opal deposits on fracture surfaces exposed in the Exploratory Studies Facility (Paces, Neymark et al. 1996). It is also consistent with the fact that surface waters have much higher silica concentrations than precipitation compositions (Figure 6.2-19).

Perched-water compositions are generally distinct from the compositions of pore waters, although they are very similar to saturated-zone water compositions. These relationships are readily seen by comparing the tri-linear plots of each category of water: perched water (Figure 6.2-16), unsaturated-zone pore waters (Figures 6.2-12, 6.2-13, 6.2-14, and 6.2-15), and groundwater from the saturated zone (Figure 6.2-48). The similarity of perched and saturated-zone water compositions suggests that these waters are subject to similar water-rock interactions. As discussed below in the saturated-zone subsection (6.2.8), these reactions predominantly involve mineral/rock dissolution and ion exchange.

Controls on pH in ambient unsaturated-zone pore waters and perched waters are dominated by the carbonic-acid system and the interaction of hydrogen ions with the host rock/mineral. As discussed above, hydrogen ions can replace sodium ions in the host rock/mineral (for example, volcanic glass, feldspar) under most conditions. As hydrogen ions are used up, carbonic-acid dissociation produces additional hydrogen ions and bicarbonate ions. If hydrogen/sodium exchange is inhibited, the pH of a given pore-water sample will depend primarily on the partial pressure of carbon dioxide in the gas phase in contact with the water and on whether or not the gas phase has equilibrated with the water phase. This process will buffer the pH of the (dilute) pore waters at near neutral levels. If both the carbonic-acid dissociation and hydrogen/sodium exchange reactions are important, the control of pH becomes a kinetic problem. For example, if the rate at which hydrogen ions react with the host rock is fast relative to the rate at which the carbon-dioxide partial pressure changes or the rate at which the carbon dioxide in the gas phase equilibrates with the water phase, the pH of the water phase could increase above the equilibrium level for the carbon-dioxide partial pressure of interest. Conversely, if the hydrogen reaction rate is slow relative to the carbon-dioxide equilibration rate, the pH of the water phase would more directly reflect the carbon-dioxide partial-pressure variations.

Because the sodium-versus-chloride concentration data for pore waters from units above the Calico Hills nonwelded (CHn) unit (Figure 6.2-24) suggest little or no evidence for the hydrogen/sodium ion-exchange reaction, the pH of these pore waters likely is controlled directly by the carbon-dioxide partial pressure with which they are in contact. According to Yang, Rattray et al. (1996), measured pH values in these pore waters average approximately 7.1. The

CHn pore waters and perched waters show clear evidence of sodium/hydrogen ion exchange. The pH values measured by Yang, Rattray et al. (1996) for these waters average approximately 8.3. Uncertainties in pH measurements are about 0.2 to 0.3 pH units. Whether this higher pH value reflects the cation/hydrogen-ion exchange rate or simply a lower partial pressure of carbon dioxide in the gas phase cannot be resolved with the existing data. It is also possible that the pore water pH changes when it is exposed to air during sample collection, or that it is affected by the compression of the rock during the pore water extraction process; both processes could vary according to rock type.

The oxidation/reduction state of unsaturated-zone waters are likely dominated by the presence of oxygen in the unsaturated-zone gas phase. At the one location where such measurements have been made, the unsaturated-zone gas phase has atmospheric levels of oxygen (Thorstensen et al. 1989; Subsection 6.2.7). This result would suggest that unsaturated-zone pore waters would generally be oxidizing. Measured Eh would typically be high (400 to 600 mV) even though in low-temperature natural systems they do not always indicate equilibrium insofar as some oxidation/reduction reactions may not have gone to completion. It is possible that lower oxidation/reduction potentials could be present locally (that is, in microenvironments) as a result of microbial activity or the presence of a reducing compound (for example, pyrite).

The influence of microbes on the chemistry of waters in the unsaturated zone is not well defined. At a minimum, microbes could produce organic acids and locally alter pH and oxidation/reduction states. Microbial activity could also affect concentrations of sulfate, bromide, and other dissolved species, as well as fractionate isotopes of light elements such as carbon. According to Kieft et al. (1997), microbial cell counts and microbial biomasses were low at all the locations sampled by these authors in the Exploratory Studies Facility. Kieft et al. (1997) suggest that this result was likely due to low water contents and low nutrient availability. However, they note that the potential for microbial activity was high. That is, microbial populations were present but not active. They concluded that if sufficient water and nutrients were added to the system, microbial populations could increase dramatically.

6.2.5.3 Representativeness of Available Data

The data available on pore-water and perched-water chemistry are limited in several ways. First, pore-water analyses are available mainly for those horizons in Yucca Mountain that contain nonwelded tuffs with relatively high porosities. Pore-water analyses are not available for well indurated, low-porosity rocks (for example, welded tuffs in the repository horizon). Second, pore-water and perched-water analyses are only available for samples from a limited number of boreholes (Table 6.2-8). Third, the procedure for extraction of water from the pores may have an impact on the water chemistry. For example, the release of carbon dioxide from pore-water samples could change the pH of the samples. Note that this caveat does not apply to perched-water samples.

In spite of these restrictions, the major ion chemistry of the pore waters is sufficiently consistent and the controls on this chemistry are sufficiently well understood that bounds can be placed on the likely range of variations to be expected. An important parameter in estimation of these bounds is the net infiltration rate (that is, the degree of evapotranspiration) over the period of interest. Bounds on the pH of the pore waters are more difficult to derive because the variations

in carbon-dioxide partial pressures within the unsaturated-zone gas phase are not well defined at the present time. However, model calculations assuming saturation with calcite would allow this parameter to be bounded. Bounds on the oxidation/reduction state cannot be derived without additional field data.

6.2.5.4 Scenarios for Future Trends in Pore-Water and Perched-Water Chemistry

As discussed in the previous subsection, the compositional variations of pore waters and perched waters in the unsaturated zone at Yucca Mountain reflect a variety of infiltration rates, rock-water interactions, gas-water interactions, and other effects. The range of these processes and effects will likely not change greatly within the potential range of climatic regimes likely to affect Yucca Mountain. What may change is the relative importance of these processes and effects. For example, under climatic regimes involving higher infiltration rates, the processes represented by pore waters from the Calico Hills nonwelded unit and by the perched waters may become more dominant. This scenario would result in more dilute pore waters with higher proportions of sodium ions and possibly higher pH. However, as these types of waters are present in the ambient system, they do not present an unanticipated change in water chemistry.

The potential impacts of the thermal pulse resulting from waste emplacement and components introduced into the repository horizon are discussed in Section 7.

6.2.6 Isotopic Composition of the Waters

The purpose of this subsection is to present aqueous-phase isotopic data for precipitation, surface waters, pore water recovered from the unsaturated zone, and groundwaters. These data provide constraints for water and solute transport rates and mechanisms. Examples of specific issues addressed by these data include spatial and temporal variability in net fluxes, lateral diversion in specific stratigraphic units, role of faults in controlling flow paths, fracture-matrix interactions, and distribution of water travel times.

Borehole designation and related information for samples from the unsaturated zone were presented previously in Table 6.2-1. Borehole locations are presented in Figures 6.2-1, 6.2-45, and 6.2-46.

6.2.6.1 Overview of Isotopic Methods

Isotopes measured in unsaturated-zone fluids as part of YMP site characterization activities fall into five general categories. It would be incorrect to assume that these various methods provide redundant information. Rather, each method yields very different types of information (IAEA 1983; Fritz and Fontes 1980; Davis, S.N. and Murphy 1987; Clark and Fritz 1997). Hence, a large suite of different approaches has been critical to the development and testing of conceptual models for flow and transport through the unsaturated zone at Yucca Mountain.

Anthropogenic Material–This category of environmental tracers includes radioactive species present in global fallout from nuclear weapons testing and from releases from nuclear-fuel reprocessing plants. Tritium, ^{14}C, and ^{36}Cl produced in the atmosphere during above-ground nuclear testing activities, primarily between 1952 and 1963, have been widely used in hydrologic

studies. The presence of these nuclides above background levels in subsurface fluids is generally accepted as a clear indication that some proportion of the water was transported to that depth in less than 50 years. If the sampled depth is more than a few meters, the presence of global fallout nuclides implies a component of fracture flow. Hence, these isotopic data provide a means for constraining the extent to which solute transport is retarded by diffusion from fractures into the adjacent matrix. Fission products ^{99}Tc and ^{129}I in a subsurface sample (above natural background) would also provide a clear indication of a component of recent water. However, a robust analytical protocol for these species in unsaturated-zone fluids has not yet been developed and the data available thus far are non-Q. Other radionuclides in global fallout, such as ^{137}Cs and plutonium isotopes, sorb strongly onto most mineral surfaces and hence are largely immobilized in the near-surface soil. Tritium, ^{36}Cl, and ^{14}C data acquired as part of the YMP site characterization activities are discussed in Subsections 6.2.6.2, 6.2.6.3, and 6.2.6.4, respectively. Fluorocarbon compounds have also been used as a tracer of recent water movement at Yucca Mountain.

Atmospheric Radionuclides–Tritium, ^{36}Cl, and ^{14}C also exist naturally in the atmosphere as the result of the interactions of cosmic rays with atmospheric gases. To the extent that the original concentrations at the surface can be reconstructed, these nuclides are useful indicators of water residence times, with water ages based on the extent of radioactive decay of the atmospheric component. All three nuclides have been widely used for dating in numerous studies published in the scientific literature. As part of YMP site characterization activities, ^{14}C and ^{36}Cl have been used to constrain water age estimates. Chlorine-36 and ^{14}C data acquired as part of the YMP site characterization activities are discussed in Subsections 6.2.6.3 and 6.2.6.4, respectively.

Climatic Reconstruction–Some aqueous constituents reflect climatic conditions at time of recharge, which allows a correlation to be made with known Pleistocene climate changes. Best known of these paleoclimate indicators are the stable isotopic compositions of hydrogen and oxygen, which generally are isotopically lighter under cooler climates and isotopically heavier under warmer ones. Hydrogen and oxygen isotopic analyses of water samples acquired under Yucca Mountain site characterization activities are summarized in Subsection 6.2.6.5. Noble gases are another indicator of the paleotemperature of recharge waters but are relevant mostly to saturated-zone water and have not been measured in the YMP site characterization activities.

Water-Rock Interactions–Groundwater is commonly out of chemical and isotopic equilibrium with the rocks through which it moves. The extent of disequilibrium provides a qualitative method for establishing flow paths and flow chronologies. Furthermore, if the kinetics of chemical or isotopic exchange between the water and minerals along its flow path are sufficiently well known, then semi-quantitative estimates of water travel times may be possible. This approach has been applied using isotopes of strontium (Subsection 6.2.6.6) and uranium (Subsection 6.2.6.7) in groundwater.

Dating of Secondary Fracture Minerals–Water percolating through the unsaturated zone at Yucca Mountain leaves secondary minerals within the fracture network and in lithophysal cavities, in areas where solutions exceed chemical saturation with respect to various mineral phases, most commonly calcite and opal. These minerals provide evidence of past percolation flow paths and preserve physical and isotopic records related to fracture solutions. An

understanding of the origins of calcite and opal in these settings provides a set of observational data that may provide constraints on the fracture flow through the mountain (Paces, Neymark et al. 1998). As part of site characterization activities, measurements of ^{14}C activities and $^{230}Th/U$ activity ratios have provided the basis for estimating mineral formation ages, which have been used as surrogate indicators of past water movement through these features (Subsection 6.2.6.8).

6.2.6.2 Tritium

Natural tritium is produced from cosmic radiation interacting with nitrogen in the upper atmosphere. Once produced, it oxidizes rapidly to tritiated water and enters the hydrologic cycle. HTO has a short residence time in the atmosphere (less than one year) and is eventually removed from the atmosphere in precipitation or through isotopic exchange. Historical concentrations in rain water in the middle latitudes have been estimated to be on the order of 10 tritium units (TU) (Davis, S.N. and Bentley 1982; Clark and Fritz 1997) with one TU being equal to one tritium atom per 10^{18} atoms of ^{1}H and corresponding to 3.2 pCi/L. Because of the relatively short half-life of tritium (12.4 years), groundwater infiltrating prior to 1952 with an initial tritium content of 10 TU would have a present-day (1998) tritium content of 0.7 TU or less.

Above-ground testing of nuclear devices in the Northern Hemisphere between 1952 and 1963 produced significant amounts of tritium in the Earth's atmosphere and overwhelmed natural background levels by as much as several orders of magnitude (Figure 6.2-27). Peak concentrations in precipitation, expressed as annual averages, were reached in 1963 when the average value measured near Salt Lake City, Utah, was 2,700 TU (Michael 1989). Seasonal variations in post-bomb tritium concentrations in precipitation are quite significant (Davis, S.N. and Murphy 1987; Clark and Fritz 1997). These variations are caused by changes in atmospheric circulation between the troposphere and the stratosphere, which is a major reservoir of tritium. During the early 1960's in the Northern Hemisphere, early summer maxima at many monitoring locations were ten times as large as the winter minima. Even in the early 1980s, 20 years after the cessation of atmospheric nuclear tests, summer maxima were still more than twice winter minima at many stations (Davis, S.N. and Murphy 1987). Consequently, the seasonal timing of precipitation is a critical determinant of the magnitude of the tritium signal introduced into the subsurface.

A nuclear-test ban treaty signed in 1963 largely stopped further nuclear testing activity in the atmosphere, although some small atmospheric releases of tritium continued from nuclear reactors and testing by countries that had not signed the treaty (Carter and Moghissi 1977). Tritium concentrations have gradually decreased since 1963 to about 10 to 40 TU measured in precipitation at the Nevada Test Site between November 1983 to June 1985 (Milne et al. 1987). Surface-water samples from 3 Springs Basin and Stewart Basin in Central Nevada, slightly north of the test site, had similar tritium concentrations in samples collected during 1984 to 1991, ranging from 41 to 140 pCi/L (13 to 44 TU) (Tables 6.2-6b and 6.2-7b). Annual mean values and monthly maximum values for monitoring stations in states surrounding Nevada likewise were in this range (i.e., still elevated above pre-1952 background levels) during 1988 to 1993 (Yang, Rattray, et al. 1996). In December 1992 to February 1993, the tritium content of surface runoff collected from several sites in the vicinity of Yucca Mountain ranged from 18 to 32 pCi/L

(6 to 10 TU) (Table 6.2-6); values of tritium during the winter are typically the lowest of the year.

It is possible that venting of tritium from subsurface nuclear detonations on the Nevada Test Site may also have contributed to tritium in precipitation at Yucca Mountain. For example, the Project Plowshare Schooner event on December 8, 1968, was a shallow cratering experiment conducted in Area 20 (Pahute Mesa) of the Nevada Test Site, about 40 km due north of Yucca Mountain, and was known to have vented tritium to the atmosphere (West and Kelly 1971). However, trajectories for this particular event were mostly northerly and northeasterly, such that Yucca Mountain precipitation was unlikely to have been influenced by it.

The extent to which detectable quantities of tritium enter the subsurface is dependent upon the spatial and temporal variations in precipitation. If precipitation is insufficient to lead to net infiltration following a storm event, then the tritium is lost back to the atmosphere by evapotranspiration. Consequently, because 1958 to 1964 experienced below-average levels of precipitation at Yucca Mountain (Precipitation Station 4JA), it is entirely possible that much of the peak tritium concentrations were never transported into the bedrock at Yucca Mountain. In this regard, the behavior of tritium as a tracer of modern water differs substantially from that of ^{36}Cl. In the latter case, all global fallout ^{36}Cl eventually is carried into the subsurface.

As part of YMP site-characterization activities, tritium has been analyzed in pore-water fluids extracted from unconsolidated material in shallow surface-based boreholes (Flint 1990), from drill core from deep surface-based boreholes (Yang, Rattray et al. 1996), and from Exploratory Studies Facility drillholes. Analyses are also available for water samples bailed and pumped from perched-water bodies and from the saturated zone (Yang, Rattray et al. 1996). Detectable levels of tritium have been observed along major structural features in Exploratory Studies Facility drillholes and in pore waters extracted from core samples from surface-based boreholes. These detections occur predominantly within the PTn unit, but also in some of the samples from the Topopah Spring Tuff and Calico Hills unit, and as deep as the Prow Pass member of the Crater Flat Tuff.

The largest concentrations of tritium found thus far within the unsaturated zone are those associated with the Bow Ridge fault. Samples were collected from drillhole HPF#1, which was drilled from the Bow Ridge fault alcove of the Exploratory Studies Facility into the fault. Values as great as 155 TU were found in pore waters 3.4 m west of the fault within the pre-Rainier Mesa Tuff. Values of approximately 120 and 130 TU were found in pore waters within the fault breccia. The high values, which indicate minimal mixing of the percolating fluids with older fluids, may be a consequence of the width of the fault zone at the surface, the lack of alluvium up-slope from the fault, and the shallow depth of the fault where sampled (approximately 20 to 30 m). Low but above-background tritium levels were also measured in Exploratory Studies Facility drillholes transecting the Ghost Dance fault in the Northern and Southern Access Drifts (Alcoves 6 and 7). Regardless of whether or not these data constitute evidence for post-bomb water at this location, they clearly indicate that at least a fraction of the water cannot be much older than 50 years because of the short half-life of tritium and its relatively low pre-bomb concentrations.

Tritium data for the unsaturated-zone boreholes show several inversions (larger tritium concentrations located below smaller tritium concentrations in a vertical profile) (Figures 6.2-28 and 6.2-29). These inversions suggest that vertical water percolation through the rock matrix may not be the predominant flow mechanism in the unsaturated zone for all stratigraphic units at Yucca Mountain. Post-bomb tritium concentrations were observed down to bedded tuff or Pah Canyon Tuff in many boreholes. The occurrence of detectable tritium in waters below non-tritium-bearing water (and hence older water) in a vertical profile is a strong evidence of fracture and lateral flow occurring at Yucca Mountain. An alternative hypothesis would be that the inversion results from piston flow of the atmospheric input signal, with the 1960's peak remaining higher than the 1980's input.

Many tritium values above 10 TU have been reported for Yucca Mountain pore waters from deep boreholes, but in general only those above 30 TU are considered to provide positive evidence of post-bomb water in this particular data set. Although the analytical detection limit is approximately 4 TU (or 8 TU, for 2-sigma uncertainties), the identification of levels above background is ambiguous for concentrations less than 30 TU "due to possible minor contamination from atmosphere during sample processing" (Yang, Yu et al. 1998). Present-day atmospheric tritium levels can still be elevated above natural background levels, depending on the latitude, season and storm direction. This concern for contamination during sample processing is not applicable to analyses of perched-water and saturated-zone samples, for which the analytical detection limit of 4 TU applies. Because of this uncertainty about contamination of pore-water samples, unambiguous levels of post-bomb ^{3}H in the deep unsaturated zone greater than 366 m (1,200 feet) were found only in borehole UE-25 UZ#16 (Figure 6.2-29). In support of this observation, the chemical composition of pore water at 501.5 m (1,645 feet) in Prow Pass Tuff of this borehole is similar to that at the shallower depth at 49.8 m (164 feet), insofar as it is a calcium-bicarbonate type water instead of the sodium-bicarbonate type commonly seen at this depth (for example, compare point 7 on the tri-linear plot in Figure 6.2-15 to point Y in Figure 6.2-12) (Yang, Rattray et al. 1996). The geochemical and isotopic data suggest fast fracture transport of younger water from the shallow depths with little cation exchange in the zeolitic unit of CHn unit.

The following is a summary of occurrences of tritium above 30 TU in the surface-based boreholes:

- UZ#4 and UZ#5 (Figure 6.2-28). A cluster of four samples with levels of 38 to 45 TU occurs in the interval of 45 to 50 m in UZ#4, within and below the Yucca Mountain unit. In UZ#5, a zone of samples with levels above 30 TU occurs in the interval of 28 to 37 m, at the base of the Tiva Canyon unit, with a peak of 75 TU. (These data are not qualified.)

- UZ#16 (Figure 6.2-29b). The maximum concentration (150 TU) occurs at a depth of 48 m, just above the bedded tuff unit. Several tritium peaks are observed in the Topopah Spring Tuff at depths of 80 m, 204 m, and the interval of 317 to 357 m. Other peaks occur in the Calico Hills Formation at depths of 426 m (44 TU) and 437 m (103 TU).

- UZ-14 (Figures 6.2-29a and c). Tritium concentrations between 30 to 40 TU are observed in intervals between 35 to 45 m in the Pah Canyon Tuff and at a depth of 385 m in the Topopah Spring Tuff.

- NRG-6 and NRG-7a (Figures 6.2-29g and h). Only small intervals of these two boreholes have been analyzed for tritium. A broad peak of high tritium concentrations between 30 to 150 TU was observed in NRG-6, from 53 to 75 m in the Pah Canyon Tuff and near the top of the Topopah Spring Tuff. A single large tritium concentration of 47 TU is observed at a depth of 109 m in NRG-7a.

- SD-7, SD-9, SD-12 (Figures 6.2-29d–f). All tritium analyses from SD-7 were less than 10 TU. All analyses from SD-9 and SD-12 were less than 15 TU.

Isotopic compositions have been measured in perched water from four Yucca Mountain boreholes. Post-bomb tritium was detected only in the sample from NRG-7a, with 10 TU; in other samples, it was indistinguishable from background levels (Table 6.2-12).

6.2.6.3 Chlorine-36

Measurements of chloride (Cl^-) concentrations and $^{36}Cl/Cl$ for salts extracted from water, soil, and rocks have been used to provide information on characteristics of water movement and solute transport through the unsaturated zone at Yucca Mountain (Fabryka-Martin, Wolfsberg et al. 1997; Fabryka-Martin, Turin et al. 1998). Chlorine-36 is a radioactive isotope of chlorine, with a half-life of 301,000 years, and in nature, it occurs primarily as the chloride anion. As such, it is relatively inert in the subsurface environment and behaves conservatively. This radionuclide is present in infiltrating waters as a natural tracer produced mainly by cosmic rays interacting with argon in the atmosphere. The relatively long half-life of ^{36}Cl theoretically permits the detection of travel times up to several hundred-thousand years. To normalize the data for the variable effects of evapotranspiration, the ^{36}Cl concentration is generally reported relative to that of stable Cl^-. Expressed in this manner, the present-day background level is $^{36}Cl/Cl$ of 500×10^{-15} (Fabryka-Martin, Turin et al. 1998). Global fallout from thermonuclear tests conducted primarily in the Pacific Proving Grounds resulted in a ^{36}Cl "bomb pulse" with maximum meteoric ratios in excess of $200{,}000 \times 10^{-15}$ (Figure 6.2-27). These extremely high values were diluted by mixing processes in the soil zone and subsurface and are not observable today. Nevertheless, high $^{36}Cl/Cl$ (those greater than about 1250×10^{-15}) indicate some bomb-pulse component, and their appearance in an environmental sample signals the presence of at least a small component of bomb-pulse ^{36}Cl. Present day $^{36}Cl/Cl$ in surface soils at Yucca Mountain are generally in the range of 1500×10^{-15} to 3000×10^{-15}. In groundwater, high ratios suggest travel times from the ground surface of 50 years or less (Fabryka-Martin, Wolfsberg et al. 1997; Levy, Sweetkind et al. 1997; Sweetkind et al. 1997).

Although the existence of bomb-pulse ^{36}Cl enables the study of solute transport with travel times of 50 years or less, the natural cosmogenic background permits analysis of much longer term transport processes. However, the use of $^{36}Cl/Cl$ for dating older waters is not as straightforward as the case for bomb-pulse signals due to the time-varying input signal. Both theoretical considerations as well as measurements of soil profiles and fossil urine from ancient pack-rat middens support the hypothesis that the present-day background ratio has remained relatively

constant during the Holocene (last 10 ka) (Fabryka-Martin, Turin et al. 1998; Plummer et al. 1997). Expected lower rates of stable Cl deposition during the Pleistocene (10 ka to 2 Ma), in combination with higher rates of cosmogenic ^{36}Cl deposition as a result of Southern shifts in the jet stream, would have led to higher local meteoric $^{36}Cl/Cl$, relative to those that were present throughout the Holocene (Plummer et al. 1997). Superimposed on this effect are varying atmospheric ^{36}Cl production rates caused by variations in the Earth's geomagnetic field. Based on these two factors, the meteoric $^{36}Cl/Cl$ at Yucca Mountain has been reconstructed for the last 1.8 Ma (Fabryka-Martin, Turin et al. 1998). Analyses of $^{36}Cl/Cl$ in pack-rat midden samples dated by the ^{14}C technique are generally consistent with the reconstruction, although these data can only cover the last 40 ka due to the comparatively short half-life of ^{14}C (Figure 6.2-30). Chlorine-36 is also produced in rocks due to a low but ubiquitous neutron flux resulting from the decay of uranium and thorium isotopes and their daughters, but these background levels are low relative to those that have been measured in Yucca Mountain water samples (Fabryka-Martin, Wolfsberg et al. 1997; Fabryka-Martin, Turin et al. 1998). Although uranium concentrations reach several hundred ppm in some silica deposits lining fractures in the unsaturated zone at Yucca Mountain, such concentrations do not elevate the local neutron flux (or ^{36}Cl production rates) because the flux is determined by uranium and thorium concentrations averaged on a much larger scale (e.g., 10^4 cm^3).

Together the bomb-pulse record and the long-term reconstruction allow $^{36}Cl/Cl$ observations in subsurface fluids at Yucca Mountain to be divided into four classes (Fabryka-Martin, Turin et al. 1998):

- Ratios over 1250×10^{-15} provide clear evidence of bomb-pulse influence, and indicate the presence of some rapid transport pathways.

- Ratios near the present-day value of 500×10^{-15} suggest Holocene precipitation of pre-nuclear-age (from 1950, extending back to about 10 ka before the present). A value of 500×10^{-15} is very unlikely to indicate extremely young (post-1980) precipitation because bomb-pulse ^{36}Cl is still widely prevalent in surface soils at Yucca Mountain, based on analyses of surface soils and surface runoff.

- Ratios that are elevated above present-day background but less than 1250×10^{-15} cannot be interpreted unambiguously in terms of water travel time, in the absence of additional geochemical or isotopic information. These may be attributed to Pleistocene-aged water that is not so old as to unequivocally demonstrate radioactive decay. Alternatively, these ratios may reflect the presence of a small component of bomb-pulse ^{36}Cl, possibly as low as a percent of the total flow.

- Ratios significantly less than 350×10^{-15} clearly show the effects of radioactive decay of ^{36}Cl. Actual estimates of water age will depend on the past meteoric ratios, which must be considered highly speculative for the period before the earliest packrat data (40 ka), but based on the current reconstruction, these ratios imply ages in excess of 200 ka.

Unfortunately, the interpretation of a given sample in one of the above categories is not always clear-cut. Only interpretation of the highest ratios (indicating bomb-pulse water) and the lowest ratios (indicating radioactively decayed ancient water) may usually be considered relatively

unequivocal. Intermediate ratios may represent Holocene or Pleistocene input with corresponding travel times or may represent mixtures of waters of different ages. Nonetheless, the intermediate ratios shed light on the interpretation of water ages when considered in conjunction with other independent lines of evidence, such as other isotopic measurements and infiltration studies and results of flow and transport simulations of alternative conceptual models.

Data Collection and Interpretation–Over 700 ^{36}Cl measurements have been conducted thus far for the Yucca Mountain Project (Fabryka-Martin, Wolfsberg et al. 1997; Fabryka-Martin, Turin et al. 1998; Levy, Sweetkind et al. 1997; Sweetkind et al. 1997). Analyzed samples include surface soils and soil profiles; rock samples collected from boreholes and within the Exploratory Studies Facility; water samples including surface runoff, unsaturated-zone pore water, perched water, and saturated-zone water; and fossilized urine from pack-rat middens.

Analyses of bomb-pulse ^{36}Cl and Cl^- profiles in soil and alluvial profiles show that thick alluvium is effective at reducing net infiltration to levels less than 1 mm/y (Fabryka-Martin, Turin et al. 1998). Similarly, borehole samples collected from rock units underlying such thick alluvium do not show any evidence for the presence of bomb-pulse ^{36}Cl (Fabryka-Martin, Turin et al. 1998) (Figure 6.2-31). In contrast, where alluvial cover is thin (for example, less than a few meters thick) or missing, water is able to readily enter fractures of the bedrock, as shown by the detection of bomb-pulse ^{36}Cl measurements in samples from such locations. For example, fast transport through the welded Tiva Canyon (TCw) is indicated by bomb-pulse $^{36}Cl/Cl$ ratios measured in several boreholes that intersect the nonwelded Paintbrush Tuff (PTn), which lies below the TCw (Figure 6.2-32).

Other evidence of fast pathways that persist into the TSw is provided by bomb-pulse $^{36}Cl/Cl$ ratios measured at locations in the Exploratory Studies Facility (Figure 6.2-33) (Fabryka-Martin, Wolfsberg et al. 1997; Levy, Sweetkind et al. 1997; Sweetkind et al. 1997). A suite of 247 samples has been analyzed from this 8 km tunnel, of which 31 had ^{36}Cl levels sufficiently elevated as to be interpreted as unambiguous evidence for the presence of bomb-pulse ^{36}Cl. The interpretation of the elevated ^{36}Cl signals as evidence for bomb-pulse is supported by the presence of bomb-pulse ^{99}Tc at two locations that also contained elevated ^{36}Cl: the Bow Ridge fault exposed at Exploratory Studies Facility Station 2+00 and UZ-N55 cuttings from the base of the PTn. (Note, however, that the ^{99}Tc data are non-Q.) The correlation of the elevated measurements in the Exploratory Studies Facility with the surface expression of faulting indicates that the pathway and travel time may involve locally modified PTn fracture properties (Fabryka-Martin, Wolfsberg et al. 1997; Levy, Sweetkind et al. 1997; Sweetkind et al. 1997). These data support the hypothesis that faulting or other disturbances increase PTn fracture permeability, thereby generating a local environment in the PTn that supports fracture flow and hence rapid transport of solutes. Once through the PTn, flux distributions favor fracture flow in the TSw, thereby providing a continuous pathway to the Exploratory Studies Facility.

Most of the Exploratory Studies Facility sample analyses had ratios less than the threshold for indicating bomb-pulse ^{36}Cl (Figure 6.2-33). In the southern part of the Exploratory Studies Facility, beyond station 45+00, most samples had $^{36}Cl/Cl$ ratios typical of Holocene water, which could suggest travel times less than 10 ka to this depth. (Averages of water with greater and lesser values provide a less likely explanation because the mixing proportions would have to be the same for the large number of samples). A number of samples from this part of the system

also had ^{36}Cl signals that were significantly below the present-day background value, suggesting the possible presence of zones of relatively stagnant water.

Many of the samples from the northern part of the Exploratory Studies Facility, up to station 45+00, had $^{36}Cl/Cl$ ratios variably above the present-day background and provide a striking contrast to the nearly-constant ratios measured in the southern part of the Exploratory Studies Facility (Figure 6.2-33). The largest signals–those above a ratio of $1250x10^{-15}$–are attributed to global fallout ^{36}Cl. Fabryka-Martin, Wolfsberg et al. (1997) discuss alternative hypotheses to account for these highly elevated signals and rule out sample contamination as well as in situ production of ^{36}Cl either at the surface or deeper in the profile. The favored hypothesis is that fast hydrologic paths capable of conducting bomb-pulse ^{36}Cl to the level of the Exploratory Studies Facility are more prevalent in the northern part of the Exploratory Studies Facility than in the southern part, due to a greater number of faults in the north that cut through the comparatively unfractured PTn where it overlies the Exploratory Studies Facility. With regard to those intermediate samples with ratios greater than present-day background but less than $1250x^{-15}$, it is not presently possible to assess whether or not these intermediate signals indicate the presence of a very small component of bomb-pulse ^{36}Cl or whether the elevated signals reflect travel times exceeding 10 ka, the most recent time when the signal in infiltrating water would have been high enough to provide the $^{36}Cl/Cl$ signatures found in water from this area.

Measured $^{36}Cl/Cl$ ratios for samples of moderately to densely welded tuff from boreholes are systematically lower than the values for Exploratory Studies Facility samples (for example, compare results for the TSw unit in Figure 6.2-34 to those in Figure 6.2-33). This apparent discrepancy is probably attributable to differences in the sample collection techniques (Fabryka-Martin, Turin et al. 1998). Borehole samples are obtained from ream cuttings. Rock Cl^- is released to the cuttings during drilling and, subsequently, is leached together with the pore-water Cl^- during sample preparation for ^{36}Cl analysis. This source of Cl has a $^{36}Cl/Cl$ ratio on the order of 40×10^{-15}. The extent to which rock Cl contributes to the total amount of Cl leached from the rock can be estimated from its Br/Cl ratio (Fabryka-Martin, Wolfsberg et al. 1997; Fabryka-Martin, Turin et al. 1998) Because of the low $^{36}Cl/Cl$ of the rock Cl, the $^{36}Cl/Cl$ calculated for the meteoric component of Cl in the borehole samples is always equal to or higher than the measured ratio. The Exploratory Studies Facility samples are not as greatly affected by rock Cl as are borehole samples because the manual method of collection used in the Exploratory Studies Facility does not pulverize the rock as does the ream bit. Borehole samples from nonwelded units (PTn, CHn, Prow Pass) also do not appear to be greatly affected by the release of rock Cl^-, probably because the concentration of leachable rock Cl^- in these particular units is negligibly small relative to that in the pore-water fluids. Differences between uncorrected $^{36}Cl/Cl$ ratios for borehole samples from welded units and those from the Exploratory Studies Facility demonstrate the importance of recognizing the magnitude of the influence of rock Cl to the $^{36}Cl/Cl$ values measured for borehole samples. After correcting for this effect, the two sets of analyses are consistent (Fabryka-Martin, Wolfsberg et al. 1997). None of the few $^{36}Cl/Cl$ measurements available for samples collected below the potential repository horizon are sufficiently high as to indicate the unambiguous presence of bomb-pulse ^{36}Cl (Figure 6.2-34).

The variation of input signal for $^{36}Cl/Cl$ over time enables $^{36}Cl/Cl$ measurements to be interpreted in support of ^{14}C ages. Figure 6.2-35(b) shows that co-variation of ^{14}C and $^{36}Cl/Cl$ is irregular but can be smoothed as a "meteoric water curve." This co-variation is most reliable in

supporting interpreted ^{14}C ages as being less than or greater than about 10,000 years. However, there is substantial uncertainty in attributing $^{36}Cl/Cl$ data to particular ages above 10,000 years, as well as uncertainty in the quantitative interpretation of ages from ^{14}C data.

Consistency of Data With Site-Scale Flow and Transport Models–A flow and transport model using the FEHM code was used to simulate transport of ^{36}Cl into the Exploratory Studies Facility tunnel (Fabryka-Martin, Wolfsberg et al. 1997; Robinson, B.A. et al. 1996). Modeling results show that observed ^{36}Cl signals are consistent with the above site conceptual model and with reasonable parameter estimates. The overall picture from these studies is that infiltration is spatially variable and on the average exceeds 1 mm/year over the potential repository block, that fracture transport can be critical, permitting rapid transport through otherwise low-conductivity materials, and that isolated fast paths associated with faults and fractures may penetrate deep into the mountain.

6.2.6.4 Carbon Isotopes ($\delta^{13}C$ and ^{14}C)

The best-developed isotopic method for dating groundwater is that using ^{14}C, an application that began with Munnich's study in 1957 (Davis, S.N. and Murphy 1987; Fritz and Fontes 1980; Clark and Fritz 1997). Carbon-14 is produced naturally in the atmosphere by cosmogenic neutrons interacting primarily with nitrogen. The natural atmospheric activity of ^{14}C is about 13.56 decays per minute per gram of carbon in the year A.D. 1950 (Karlen et al. 1966). Based on a half-life of 5,730 years, this specific activity corresponds to a $^{14}C/C$ ratio of 1.175×10^{-12} and is most often reported as 100 pmc. The effect of above-ground testing of nuclear devices was to temporarily increase the ^{14}C content by as much as a factor of two (Mook 1980). The decrease since 1964 is due to the exchange of ^{14}C for nonradioactive carbon from the biosphere and hydrosphere, predominantly the ocean (Figure 6.2-27). Other secondary influences on the atmospheric ^{14}C inventory are releases of ^{14}C from nuclear fuel reprocessing plants and dilution by releases of nonradioactive carbon from the burning of fossil fuels.

Despite its extensive use in hydrologic studies, numerous processes related to carbon geochemical reactions complicate the interpretation of ^{14}C analyses in water. These processes involve the isotopic exchange between carbonate species dissolved in pore water, and carbonates in soil and fracture minerals along the flow path, as well as with CO_2 in the gas phase. Hence, the successful use of ^{14}C to date groundwater is dependent upon a thorough understanding of geochemical reactions involving carbon species in the hydrologic system. Stable carbon isotope ratios ($\delta^{13}C$ values) are invaluable for evaluating the likelihood and magnitude of subsurface reactions involving carbon (Yang, Yu et al. 1998). Section 5 includes a detailed discussion of geochemical modeling of carbon reactions, and the implications for ^{14}C ages of Yucca Mountain pore waters.

As part of YMP site characterization activities, ^{14}C and stable carbon isotopes have been analyzed in pore-water fluids extracted from drill core from deep surface-based boreholes (Table 6.2-13) (Yang, Turner et al. 1988; Yang, Rattray et al. 1996; Yang, Yu et al. 1998) and from Exploratory Studies Facility drillholes. Analyses are also available for unsaturated-zone gas samples (Subsection 6.2.7, Table 6.2-15), water samples bailed and pumped from perched-water bodies (Table 6.2-12), and from the saturated zone (Subsection 6.2.8, Table 6.2-19). Results and interpretations of these analyses are also presented in Subsection 5.3.4.2.4. As is the

case for tritium, post-bomb levels of ^{14}C have been observed in a few samples collected above and within the PTn unit. The largest ^{14}C activity measured thus far within the unsaturated zone was a value of 117 pmc for pore water extracted from a drillhole sample in Exploratory Studies Facility Upper Paintbrush (nonwelded) Contact Alcove. Values above 100 pmc were also measured for samples from drillholes in Alcoves 1 and 2, associated with the Bow Ridge fault.

None of the pore-water samples from surface-based boreholes have shown post-bomb levels of ^{14}C (Table 6.2-13). For the 15 pore-water samples extracted from the PTn unit, ^{14}C activities range from 55 pmc (UZ#5) to 96 pmc (UZ-14). The 32 samples extracted from the CHn unit range from 53 pmc (UZ#16) to 98 pmc (UZ#16). A histogram distribution of the data from these two hydrogeologic units (Figure 6.2-36) shows that the PTn values cluster tightly about the range of 80 to 90 pmc, whereas the CHn values spread more evenly across the range, presumably reflecting a larger spread in groundwater travel times to this depth as would be expected if fracture flow were mixing to variable extents with slower matrix flow. Stable carbon isotope ratios for these same pore waters show a wide range in both hydrogeologic units (Figure 6.2-36), which may be a consequence of a variety of processes but which is also consistent with spatially and temporally variable infiltration rates and mixing between fast fracture flow and slow matrix flow.

The ^{14}C pore-water data do not show any trend with stratigraphic depth, with larger ^{14}C activities interspersed among smaller ^{14}C activities in a vertical profile (Figure 6.2-29). These irregular profiles are consistent with a conceptual model in which fracture flow and perhaps lateral flow occur in some of the stratigraphic units at Yucca Mountain (Yang, Rattray et al. 1996; Yang, Yu et al. 1998). In general, ^{14}C activities in pore waters from both the PTn and CHn suggest apparent ages that are less than 10,000 years. Apparent ages are based on the assumption that the initial ^{14}C activity is 100 pmc, and that the carbon isotopic composition of the sample has not been significantly altered by any geochemical processes such that changes relative to the initial atmospheric activity are solely the result of radioactive decay.

Detailed evaluations of the various processes that could affect ^{14}C activities and stable carbon isotope ratios in Yucca Mountain pore waters are presented in Yang, Rattray et al. (1996) and Yang, Yu et al. (1998). These processes include:

- Atmospheric contamination of pore-water samples during drilling could shift ^{14}C activities to higher values.
- $^{14}CO_2$ in the gaseous phase may exchange with bicarbonate species in the groundwater. However, this exchange apparently does not go to equilibrium (Subsection 6.2.7).
- The large amounts of cement used to seal off perched water in UZ-14 contain $Ca(OH)_2$, which absorbs atmospheric CO_2 during mixing with water and releases the CO_2 during curation.
- Seasonal variations in $\delta^{13}C$ in soil gas as a function of the stage of vegetative growth affect the isotopic signature in infiltrating waters.

- Dissolution of caliche and calcites in fractures, with their wide variations in ^{14}C ages, can dilute the initial ^{14}C activity of infiltrating pore water and shift its $\delta^{13}C$ value.

To some extent, the significance of these processes can be evaluated by examining the $\delta^{13}C$ and ^{14}C data for trends as a function of borehole, depth, and stratigraphic unit and by comparing pore-water data to those for the gas phase, perched water and groundwaters for which some of the above processes can be assumed to be negligible. Figure 6.2-37 plots $\delta^{13}C$ versus ^{14}C for these different categories. This plot suggests the idea that some of the high ^{14}C pmc values and young apparent ages may be the result of contamination from $^{14}CO_2$ in the drilling air (about 120 pmc, $\delta^{13}C$ about –8 ‰). Although carbon concentrations in pore water are orders of magnitude higher than those in air, it is possible that the injection of large volumes of drilling air may alter the carbon isotopic composition of pore waters under some conditions.

Gas samples were collected from boreholes following overnight pumping to remove atmospheric air from the well bore (these data are presented and discussed in greater detail in Subsection 6.2.7.2). Gas samples from UZ-14 had ^{14}C activities of 48 to 68 pmc, similar to the pore-water ^{14}C activities in CHn. Boreholes SD-9 and SD-12 exhibit significantly smaller ^{14}C activities in gas samples compared to activities in pore waters from the same zone. If the CO_2 in the gas phase were in isotopic equilibrium with CO_2 in the aqueous phase of the pore water, then the ^{14}C activities in the two phases should be comparable. The reason for the isotopic disequilibrium is not currently known. Because of these various unresolved issues, Yang, Rattray et al. (1996) conclude "it would be difficult to make a good age correction. However, a possible range of ages with some uncertainty can be assigned in the future when more data become available. At present, apparent ages will be used to make preliminary interpretation."

Carbon-14 activities and $\delta^{13}C$ values of perched waters are shown in Table 6.2-12. The ^{14}C values range from 67 to 27 pmc, corresponding to apparent ^{14}C residence times of about 3,500 to 11,000 years. Water ^{14}C ages can be affected by the dissolution of older carbon in the rocks, which would result in anomalously old apparent ages. Reaction with or incorporation of gas-phase CO_2 from deep in the unsaturated zone can also result in an anomalous apparent age. Recent input of post-bomb ^{14}C is expected to be minor because all perched-water samples contain background tritium concentrations. If post-bomb water is present in the perched bodies, the component is too small to be detectable.

The $\delta^{13}C$ values measured for perched water are quite variable, ranging from -9.2 to -16.6 ‰ (Table 6.2-12). A weak correlation is observed between these values and the surface material in which the drillhole is located. Perched water in SD-7, a borehole that is essentially started in bedrock, has heavy values of about -9.5 ‰, only slightly lighter than atmospheric CO_2. In contrast, perched water from NRG-7a, which was drilled through soil, has the lightest value of -16.6 ‰, presumably reflective of the isotopic composition of soil CO_2 gas. This observation is similar to that made for strontium isotopic data, which show a less radiogenic input for bedrock and fracture coatings where there is no soil and for pore waters from a drillhole that was started in bedrock (Subsection 6.2.6.6). In summary, $\delta^{13}C$ data show that most of the bicarbonate in unsaturated-zone pore fluids originated in the soil zone. Most of the perched-water bodies (Table 6.2-12) and groundwater in the Yucca Mountain area (Table 6.2-19) have heavier (less

negative) $\delta^{13}C$ values that do not show the same degree of soil influence as do the unsaturated-zone pore waters.

6.2.6.5 Stable Hydrogen and Oxygen Isotopes (δD and $\delta^{18}O$)

Large differences in hydrogen and oxygen isotopic ratios (δD and $\delta^{18}O$) in water arise from phase changes that do not go to completion, that is, partial evaporation, condensation, crystallization, or melting (Davis, S.N. and Murphy 1987). Such incomplete processes are typical of rainfall, snowfall, evapotranspiration, and melting of snow and ice. As a consequence, regional differences arise in surface waters as a function of elevation, distance from water sources (such as the ocean), orographic (rain shadow) effects, degree of evaporation, and air temperature during precipitation. If the first four of these factors stay relatively constant for a given location, then variations in δD and $\delta^{18}O$ in infiltrating water may be related to temperature variations during precipitation events. Factors that might complicate simple interpretations of such data at Yucca Mountain include shifts in $\delta^{18}O$ in pore waters due to: alteration, dissolution, or precipitation of minerals containing oxygen; isotopic exchange; and sorption of water by clays and zeolites.

The standard method for presenting stable isotope data is by plotting δD versus $\delta^{18}O$, as has been done in Figure 6.2-38 for precipitation, surface waters, perched water, and regional groundwater. The following observations are made from this figure:

- Precipitation data from 3 Springs Basin and Stewart Basin are plotted in Figure 6.2-38a. These data illustrate how fractionation of oxygen and hydrogen isotopes in atmospheric moisture results in a well-defined correlation line, called the "meteoric water line." Interpretations of isotopic data for other waters are all based upon the extent to which their compositions shift along or away from this line. Based upon its lower elevation and warmer temperatures, modern precipitation at Yucca Mountain is generally expected to fall along the upper end of the range shown, with heavier (less negative) compositions.

- Surface water data from 3 Springs Basin and Stewart Basin (Figure 6.2-38b) illustrate how stable isotopes reflect average climatic conditions prevailing during infiltration events. The cooler climate at Stewart Basin results in lighter (more negative) isotopic compositions. These surface waters have not undergone much evaporation, based on the fact that the isotopic data plot on the meteoric line. Such a conclusion is supported by the dilute chemical compositions of these waters (Subsection 6.2.3). Data for two Yucca Mountain surface runoff samples, both collected in February 1993, also show negligible evaporation. Their heavy isotopic signatures overlap with those of the four precipitation samples collected at Yucca Mountain in 1984 (Figure 6.2-38a).

- Stable isotopic data of the perched-water samples also lie close to the meteoric water line, indicating little evaporation occurred before infiltration.

- Groundwaters beneath Fortymile Wash (Figure 6.2-38d) have stable isotope values similar to that of the perched water. Both sets are consistent with recharge during the

Holocene (that is, post-glacial climate), as suggested by the ^{14}C data for these waters (Subsection 6.2.6.4; Figure 6.2-37c and d).

- Among the groundwaters in the Yucca Mountain area, the lightest waters are from wells in the southwestern most portion of the site (for example, VH-1, WT#10, H-3). Local groundwaters with the heaviest isotopic values overlap with the values measured for perched waters and for wells in Fortymile Wash.

- Groundwaters from Pahute Mesa have lighter isotopic values than do the perched waters and groundwaters from Fortymile Wash. This difference is consistent with recharge of the Pahute Mesa waters under colder climatic conditions than those that prevailed for the perched waters and samples from Fortymile Wash, and subsequent modification of the Pahute Mesa waters by water-rock interactions that shift $\delta^{18}O$ to heavier values. Although isotopic shifts due to evaporative loss cannot be altogether ruled out, this process seems unlikely to be significant for the Pahute Mesa recharge waters.

In contrast with the above types of samples, hydrogen and oxygen isotope data for unsaturated-zone pore waters are more difficult to interpret, presumably due to complications related to the methods used to extract the fluids for analysis. Vacuum distillation and compression extraction ("squeezing") were the two methods of pore-water extraction for stable-isotope analysis of δD and $\delta^{18}O$ used in the site-characterization investigation (Yang, Yu et al. 1998). Vacuum distillation involves heating the rock sample under vacuum in a distillation apparatus and collecting and condensing the evolved water vapor in a separate flask (Subsection 5.3.4.2.4). Compression extraction is similar to the procedures described previously for pore-water extraction for chemical compositions and ^{14}C analyses (Mower et al. 1991, 1994; Higgins et al. 1997). Water samples were collected in glass syringes attached to the compression cell. For both extraction methods, stable isotope ratios are determined by mass spectrometer.

Testing for isotopic effects resulting from the two different water-extraction procedures was accomplished by analyzing adjacent core samples (Yang, Yu et al. 1998). The two methods yielded comparable results for samples from the PTn (Figures 6.2-39). However, isotopic compositions of water obtained by vacuum distillation are more depleted in δD and $\delta^{18}O$ than water obtained by the compression method for cores containing clay or zeolite minerals, particularly for samples from CHn, Prow Pass Tuff, and Bull Frog Tuff (Yang, Yu et al. 1998). Subsequent tests have shown that vacuum distillation of pore waters for stable isotope analysis produced reliable results from tuffs free of clay and zeolite minerals but not for tuffs with large contents of hydrated minerals (Yu 1996). The compression-extraction process only extracts pore water, whereas the vacuum-distillation process extracts both pore water as well as water held by zeolites or clays. Percolating water can replace the water in the large pore spaces as well as undergo isotopic exchange with water in zeolites. Isotopic exchange rates range from days to months. Pore waters extracted from zeolitic core by compression may, therefore, reflect the most recently infiltrated water but may lose the record of past percolating water.

The oxygen and hydrogen isotopic composition of pore waters can yield information about infiltrating waters, provided that sampling has not disturbed the original compositions. Significant amounts of drilling air were injected into the formation during borehole drilling that could cause drying of the core samples. The potential magnitude of this effect can be examined

by plotting the stable isotope compositions of the pore water on the δD versus $\delta^{18}O$ diagram (Figures 6.2-39). Data for unsaturated-zone pore-water samples, obtained by squeezing UZ-14 core, plot on or slightly below the meteoric precipitation line, indicating minor evaporative loss. This evaporation may have occurred either prior to recharge or during drilling. Alternatively, the shift away from the meteoric water line may reflect oxygen isotopic exchange with the host rock (Subsection 6.2.8). The composition of the CHn pore waters by distillation in UZ-14 (Figure 6.2-39a) is significantly lighter than that of the PTn pore waters. The lighter values for CHn pore waters do not result from incomplete recovery by the distillation method because more than 98% of the water was recovered by vacuum distillation in laboratory tests in which tap water of known mass and isotopic composition was imbibed into an oven-dried core. These extremely light isotopic signatures are not representative of in-situ percolating water but rather are caused by fractionation of infiltrating water as the water moves from pore spaces into channel layers of zeolite minerals (Yang, Yu et al. 1998). Comparison of isotopic compositions of unsaturated-zone pore waters (Figures 6.2-39) with those of the saturated-zone groundwaters (Figures 6.2-38d) beneath Yucca Mountain show that the CHn pore waters are similar to the heaviest groundwaters in the Yucca Mountain area, whereas the PTn pore waters are significantly heavier than either of these data sets. Again, this difference is consistent with recharge of the CHn pore waters and Yucca Mountain groundwaters occurring under colder climatic conditions than recharge for the PTn pore waters.

6.2.6.6 Strontium Isotopes

Strontium isotopic signatures ($^{87}Sr/^{86}Sr$) of groundwater are principally derived from water-rock interaction (Paces, Marshall et al. 1997), and therefore, these isotopic data are not directly comparable to data for cosmogenic or bomb-pulse isotopes such as ^{36}Cl. Because the variations in strontium isotopic values of rock leachates reflect processes such as the interaction of water with rock whose isotopic signatures change very slowly as a result of *in situ* radioactive decay, strontium isotopic studies cannot be used to detect fast fluid flow. The data can, however, be used to test hypotheses about fluid sources or pathways and fluid mixing. Strontium isotopic studies of Yucca Mountain calcites were consequently undertaken to help place bounds on infiltration rates during the last 12 m.y. by assuming a proportional link between mineral deposition rates and fluid flux (Paces, Marshall et al. 1997). Additional goals include the development and testing of conceptual models of fluid infiltration, diversion, and mixing, and of water-rock interaction. This is an area of active research, in which conceptual models are being rapidly developed and modified.

The isotopic composition of strontium in pore waters varies less erratically than does the major ion chemistry and provides further evidence of rock-water interaction (Marshall, Futa et al. 1997). Strontium isotopic data have thus far been reported for drill core leachates from drillhole USW SD-7 (Paces, Marshall et al. 1997). Strontium was separated from coarsely crushed whole-rock samples by brief leaches with distilled water. The results show that water enters the surface at Yucca Mountain with a isotopic composition roughly equal to that of the wet- and dry-fall material and begins to become more radiogenic by reacting with strontium in the Tiva Canyon Tuff (Figure 6.2-40). Pore water within the PTn becomes markedly more radiogenic, possibly due to longer reaction times and/or ion exchange with minerals in this unit. Further rock-water interaction within the Topopah Springs Tuff increases the $^{87}Sr/^{86}$ Sr ratio slightly. Near the bottom of the sampled core, in the CHn, strontium isotope ratios are more erratic,

possibly due to either another source of pore fluids such as perched water or leaching of ancient, less radiogenic, strontium from zeolites.

These Sr isotopic data were interpreted as indicating enhanced water-rock interaction within the PTn units above the Topopah Spring Tuff, even though the pore-fluid strontium never achieves equilibrium with the rock strontium (Sonnenthal et al. 1997; Marshall 1997). High porosity and permeability and high glass content and reactive surface area are the factors contributing to increased rates of water-rock interaction in the nonwelded tuffs relative to overlying and underlying densely welded tuffs. Part of the isotopic shift occurring within the nonwelded tuffs may be attributable to their somewhat higher strontium content relative to the Tiva Canyon and Topopah Spring Tuffs (Peterman, Spengler, Singer et al. 1993), rather than to enhanced water-rock interaction.

The data necessary for rigorous numerical modeling of strontium geochemistry as an indicator of water-rock interaction and fluid flux do not exist at present. Preliminary modeling efforts are primarily intended to place bounds on the percolation flux, and the rock reaction (dissolution) rate is one of the parameters required for numerical simulations of pore-salt strontium isotopic profiles. Additional discussion of this aspect of the Sr isotopic data is contained in Subsection 6.1.4.5.

6.2.6.7 Uranium Disequilibria

Uranium Disequilibria in Unsaturated-zone Pore Fluids and Perched Water–Groundwaters carry a natural $^{234}U/^{238}U$ signal inherited in recharge areas and modified by interactions with minerals encountered along the flow path (Paces, Ludwig et al. 1998). Uranium-234 is a decay product of ^{238}U, which in a closed system, reaches a state of secular equilibrium after about a million years. Secular equilibrium is indicated by a $^{234}U/^{238}U$ activity ratio of 1.0. However, oxygenated groundwaters typically have $^{234}U/^{238}U$ ratios that are nearly always greater than those in surface runoff waters and associated soil-zone carbonates (activity ratios of 1.5 to 2.0 (Paces, Ludwig et al. 1998). These elevated signals develop because ^{234}U is released more effectively to pore fluids than is ^{238}U due to processes (called alpha recoil) related to the effects of radioactive decay in the adjacent wall rock (Clark and Fritz 1997). The amount of ^{234}U excess relative to ^{238}U is limited by rates of ^{234}U decay, water-rock ratios, flow path length, and the amount of bulk-rock dissolution in the aquifer. These factors typically restrict $^{234}U/^{238}U$ activity ratios in most Southern Nevada groundwaters to values between about 2 and 4 (Ludwig et al. 1993). At Yucca Mountain, these ratios in the saturated zone extend up to 8 (Paces, Ludwig et al. 1998).

Perched water pumped from USW UZ-14 and USW SD-7 have very different $^{234}U/^{238}U$ characteristics (Paces, Ludwig et al. 1998). Perched water from the welded Topopah Spring Tuff in UZ-14 has 0.01 to 0.03 ppb U and $^{234}U/^{238}U$ activity ratios of 7.4 to 7.6, whereas perched water from the nonwelded Calico Hills unit at SD-7 has normal groundwater uranium concentrations (1.0 to 1.9 ppb) and lower activity ratios (3.4 to 3.7). These differences may be due to different infiltration rates or to higher degrees of water-rock interaction with the nonwelded tuffs in the perched water body at SD-7.

Uranium Disequilibria in Saturated-Zone Fluids–Shallow saturated-zone water beneath Yucca Mountain has anomalous $^{234}U/^{238}U$ activity ratios relative to up-gradient waters to the

north (Paces, Ludwig et al. 1998). Elevated values of 6 to 8 are consistent with percolation through the thick volcanic unsaturated zone into the upper portions of a stratified saturated zone. Similar values are not observed in groundwaters from higher elevation recharge areas to the north. Possibly, the northern wells sample deeper zones, or the higher recharge rates led to greater water-rock ratios (and hence less time for interactions along the flow path) that persist through the volcanic units. It may be that the largest $^{234}U/^{238}U$ ratios are only attainable in areas of long travel times (such as beneath zones of low net flux) such that preferential incorporation of ^{234}U along flow paths is not overwhelmed by the greater relative amounts of ^{238}U in shallow infiltrating waters. However, interpretation of the data is not conclusive and alternative hypotheses are being developed.

Although these data suggest a component of recharge beneath Yucca Mountain, recharge volumes are likely to be small relative to those in adjacent areas (Paces, Ludwig et al. 1998). Anomalous $^{234}U/^{238}U$ ratios do not appear to extend down-gradient to areas South of Yucca Mountain (Paces, Ludwig et al. 1998).

6.2.6.8 Secondary Fracture Mineral Ages

Water percolating through the unsaturated zone at Yucca Mountain leaves secondary minerals within the fracture network and in lithophysal cavities, in areas where solutions exceed chemical saturation with respect to various mineral phases, most commonly calcite and opal. Given appropriate conditions favorable for deposition, these minerals provide evidence of past percolation flow paths and preserve physical and isotopic records related to fracture solutions, subject to the limitations discussed later in this section. An understanding of the origins of calcite and opal in these settings provides a set of observational data that may provide constraints on the fracture flow through the mountain (Paces, Neymark et al. 1998).

Measurement of the $^{230}Th/U$, $^{206}Pb/^{238}U$, and $^{207}Pb/^{235}U$ isotopic ratios provide the basis for estimating mineral formation ages, which can then be used as surrogate indicators of past water movement through these features. The record of calcite and opal deposition in fractures and voids of the Tiva Canyon Tuff and Topopah Spring Tuff is a subject of active research and is becoming increasingly well documented through studies of samples from the Exploratory Studies Facility (for example, Paces, Marshall et al. 1997; Paces, Neymark et al. 1996). The study results indicate that deposition of calcite and opal have been ongoing processes during at least the last 8 to 10 m.y. Most of the secondary minerals (opal and calcite) in the Exploratory Studies Facility have calculated U-series ages for outer mineral surfaces that range from 28 k.y. to more than 500 k.y., with no distinct clustering of mineral ages in either time or space (Figures 6.2-41 and 6.2-42a) (Paces, Marshall et al. 1997; Paces, Neymark et al. 1996). Secondary minerals from lithophysal cavities as well as from fractures have similar deposition-age distributions. A correlation is observed between sample size (milligram versus microgram sample quantities) and mineral deposition age. Larger samples are associated with older ages as an artifact of the sampling process, which leads to a homogenization of depositional growth zones and, thus, ages. To offset this sampling effect, sampling was done on the smallest sample possible to give the most accurate age for the latest period of mineral deposition.

Maximum initial uranium isotope compositions of secondary minerals generally increase with depth in the unsaturated zone (Figure 6.2-42b) (Paces, Neymark et al. 1998). Most notably,

mineralization in the shallow portions of the Exploratory Studies Facility within the Tiva Canyon Tuff contains low initial $^{234}U/^{238}U$ activity ratios similar to values observed in surface waters and soils, whereas occurrences deeper in the TSw have elevated initial $^{234}U/^{238}U$ ratios. Therefore, ^{234}U-enrichment is a function of the percolation process and contains information related to the history and mechanisms of unsaturated-zone flow. The $^{234}U/^{238}U$ composition of percolating solutions will represent a mixture of the ^{238}U that was acquired mostly at the surface through reaction with soil materials and the excess ^{234}U that is available along flow pathways. Large amounts of water with normal U concentrations (0.5 to 3 µg/l) will contain enough ^{238}U to overwhelm recoil ^{234}U, resulting in waters with low $^{234}U/^{238}U$ ratios. If the infiltrating waters have very low uranium concentrations, higher $^{234}U/^{238}U$ ratios may be obtained for the same amount of flux. Small amounts of flux that wash pathway surfaces continuously will remove gradually accumulating ^{234}U and also inhibit $^{234}U/^{238}U$ ratios from reaching elevated values. However, if only a small amount of intermittent flux is present in fractures, ^{234}U will gradually accumulate on surfaces to a level that will not be overwhelmed by the ^{238}U in migrating solutions. Under the latter conditions, $^{234}U/^{238}U$ ratios would become elevated to the high values that are typically observed in minerals throughout most of the Exploratory Studies Facility Main Drift and North and South bends. Quantitative analysis of isotope mass balance between ^{238}U and ^{234}U are required to place limits on the effectiveness of using $^{234}U/^{238}U$ ratios as a proxy for percolation volume. Boundaries between zones of low versus high $^{234}U/^{238}U$ values observed in the Exploratory Studies Facility correspond to shallower stratigraphic levels within the TSw or with areas of increased structural disruption of the PTn. These two conditions are broadly coincident in the Exploratory Studies Facility, complicating attempts to resolve the dominating influence.

The U-series data and associated mineral deposition ages do not capture evidence of the fast infiltrating fluids being recorded by the bomb-pulse signals seen in the ^{36}Cl data. Several plausible explanations can be advanced for this apparent discrepancy (Fabryka-Martin, Wolfsberg et al. 1997).

- The two data sets may be sampling different flow networks. Despite attempts to coordinate Exploratory Studies Facility sampling locations for these two activities, practical constraints on sample size requirements greatly limited the number of cases in which sampling for multiple isotopic analyses was actually feasible. Chlorine-36 samples were often collected from features where little or no secondary mineralization was visible; conversely, samples for U-series analysis were often collected as narrow fracture linings that could not provide the 1-kg sample size needed at that time for ^{36}Cl analysis.

- As a corollary to the above hypothesis, the U-series sample set may be biased toward older fluids if young fluids such as those transporting bomb-pulse ^{36}Cl are not actively depositing secondary minerals phases that can be measured by U-series disequilibrium methods. These faster-moving fracture fluids may be undersaturated with respect to calcite and silica, as indicated by calculations for matrix pore waters in Paces, Neymark et al. (1996, their Figure 6.2), in Triay, Meijer, Conca et al. (1997, Table 8), and in Figure 6.2-26 (for silica). Although pore waters are saturated with respect to calcite near the surface, as evidenced by widespread calcic deposits in soils and in fractures in the Tiva Canyon unit, several geochemical processes can drive fluid compositions toward

undersaturation at deeper depths. These processes include decreases in Ca concentrations by ion exchange with Na on clays or zeolites (Subsection 6.2.5), mixing with more dilute waters (for example, fracture flow), and decreases in CO_2 gas pressure (Subsection 6.2.7.2). Alternatively, the kinetics of mineral precipitation may be too slow relative to the flow rate to allow significant deposition at a specific location.

- In some cases at least, the mineral formation ages determined by the U-series analyses may actually record the time at which the sampled section of a fracture became closed to active water movement.

- Calculated average long-term mineral growth rates of 0.001 to 0.004 mm/ka (Paces, Marshall et al. 1997) would result in 0.05 to 0.2 mm of deposition on the outer surface of a crystal in 50 ka. The difficulty of sampling such thin layers means that evidence of most recent mineral deposition would be unobtainable from many or most mineral samples due to insufficient mass for analysis.

Carbon-14 Dating of Fracture Calcites–Carbon-14 studies on small (less than 20 mg) calcite samples has accompanied the $^{230}Th/U$ geochronologic studies of calcite and opal in the Exploratory Studies Facility dating activity described above (Paces, Marshall et al. 1997). The aim of this work was to determine the relative timing of calcite formation among different occurrences in the Exploratory Studies Facility. Some of the sampling focused on Exploratory Studies Facility sites that had shown elevated levels of ^{36}Cl and that had been interpreted as representing transport of bomb-pulse ^{36}Cl along fast pathways (Subsection 6.2.6.3).

Carbon-14 dating techniques only supply reliable information on the relative ages of secondary minerals. Accurate and precise age determinations of secondary carbonate minerals are compromised by the dynamics of the hydrologic system and the small size of the crystals that are analyzed. Several caveats render it difficult to calculate true ^{14}C ages from the secondary calcite (Paces, Marshall et al. 1997):

- Percolating fluids dissolve older calcite in the overlying soils and along their flow paths in the unsaturated zone, and the amount of dead carbon added to the solution is variable and cannot be precisely evaluated

- Secondary calcite crystal surfaces in the unsaturated zone have been exposed to atmospherically derived gases since their formation, and experiments have not been able to rule out exchange between calcite surfaces and these gases

- The ^{14}C geochronometer starts at the time of infiltration, not at the time of calcite precipitation, so percolation travel time from the surface to the site of deposition is unknown

- Fine growth laminations and relatively large sample sizes required for analysis result in apparent ^{14}C ages that represent a mechanical mixture of multiple layers within a wide range of ages

In spite of these caveats, ^{14}C measurements still provide a rough measure of the relative timing of calcite formation and permit recognition of the most recent sites of secondary mineral formation (Paces, Marshall et al. 1997).

Apparent ^{14}C ages from the latest calcite surfaces range from 16 to 52 ka, with a median between 30 and 35 ka (Figure 6.2-41) (Paces, Marshall et al. 1997). Ages for samples from sites at which bomb-pulse ^{36}Cl had been observed were not statistically different from those from sites having background ^{36}Cl levels. Either calcite was not formed during the most recent percolation episodes, or bulk samples contain too much old calcite for small amounts of young calcite to be detectable.

Stable Isotopic Analyses–Analyses of stable carbon and oxygen isotopes have been used to demonstrate that secondary calcite and opal in the unsaturated zone formed largely from percolating meteoric waters. These waters acquired their geochemical signature and dissolved components during infiltration through overlying soils and near-surface fracture systems containing pedogenic calcite and opal. As such, the distribution of secondary minerals in the unsaturated zone provides a physical record of percolation flow paths. In addition, subsurface calcites provide a proxy of prevailing climate at or near the time of their deposition caused by $\delta^{13}C$ values documenting variations in the makeup of the plant community at the surface, and $\delta^{18}O$ values recording changes in precipitation sources and temperatures (Whelan, Vaniman et al. 1994; Whelan, Moscati et al. 1996). Modern gas and porewater ^{13}C and $\delta^{18}O$ values for samples from the unsaturated zone (UZ) are consistent with the isotopic compositions of secondary calcite in the UZ. Carbon dioxide extracted from UZ gases generally ranges between -14 and -17‰ (Yang, Rattray et al. 1996; Yang, Peters et al. 1993). Assuming calcite precipitation temperatures of 15 to 35°C and using carbon isotopic fractionation factors from Deines et al. (1974), calcite deposited from percolating fluids in isotopic equilibrium with this CO_2 would have $\delta^{13}C$ values ranging from about -3.2‰ (highest $\delta^{13}C$ CO_2, lowest temperature) to about -8‰ (lowest $\delta^{13}C$ CO_2, highest temperature). Latest secondary calcite $\delta^{13}C$ values generally range between -8 and -4‰, in excellent agreement with the UZ pore gas isotopic compositions.

The $\delta^{18}O$ values of UZ porewaters distilled from the welded tuffs or squeezed from the non-welded tuffs generally range from -14 to -12‰ (Yang, Rattray et al. 1996). Again assuming temperatures of 15 to 35°C for calcite deposition and using the oxygen isotopic fractionation factors from Kim and O'Neil (1997), the porewater $\delta^{18}O$ values indicate that calcite should have $\delta^{18}O$ values ranging from about 18‰ (lowest T, highest $\delta^{18}O$ water) to about 12‰ (highest T, lowest $\delta^{18}O$ water). Unsaturated zone calcite $\delta^{18}O$ values range from about 13 to 21‰ (Fig. 3.4.2.5.2-2), in reasonable agreement with modern porewater. The somewhat larger spread of calcite $\delta^{18}O$ in the UZ, relative to the range predicted from modern porewater, reflects variability in the $\delta^{18}O$ of percolating water due to varying climate states in the past, and evaporative enrichment of ^{18}O in near-surface percolation where the largest calcite $\delta^{18}O$ values occur. For example, some calcite $\delta^{18}O$ values suggest warmer precipitation temperatures; in particular, those that formed during the earliest periods of secondary mineral formation. Similarly, only the earliest secondary calcite in the unsaturated zone appears to be incompatible

with precipitation from plant-generated carbon. Possible origins of this early, $\delta^{13}C$-enriched calcite are discussed in Paces, Marshall et al. (1997).

Relations between the stable C and O isotopic chemistry of percolation and secondary calcite and the effects of past climate variations are discussed in more detail in section 3.4.2.5, Site Records of Climate Change.

6.2.7 Chemical and Isotopic Composition of Gases in the Unsaturated Zone

6.2.7.1 Processes Controlling Gas Chemistry

The major processes that control the chemistry of the gas phase include:

Atmospheric Gas Chemistry–The composition of air is the primary control on unsaturated-zone gas chemistry.

Soil-Zone Processes–Soil-zone processes such as plant respiration can alter the chemistry of the gases that diffuse into the unsaturated zone. Carbon-dioxide partial pressures are particularly susceptible to modification by these processes.

Water-Air Interactions–Once gases diffuse from the soil zone into the unsaturated zone, the gas-phase composition will tend to equilibrate with the waters present in the unsaturated zone. For example, CO_2 will tend to dissolve or exsolve from the waters depending on the partial pressures of CO_2 in the soil zone versus the upper unsaturated zone.

Upward Flow–Gases can migrate upward through the unsaturated zone along various gradients including concentration gradients and temperature and pressure gradients. The gases migrating along these gradients may have a nonatmospheric composition. Therefore, as they mix with the indigenous gases in the unsaturated zone, they alter the overall gas composition in the unsaturated zone.

Matrix, Fractures, and Fault Structures–Because gas permeabilities of matrix, fractures, and faults are very different, the composition of the gas phase in a certain part of Yucca Mountain at a given time may deviate from the average composition.

Microbial Influences–As noted in Subsection 6.2.5, microbial metabolic activity may locally influence the composition of the gas phase in the unsaturated zone.

Temperature and Pressure–Temperature can influence the composition of the gas phase in the unsaturated zone primarily through its influence on the kinetics of the various reactions involved controlling the composition of the gas phase. Variations in total gas pressure can influence the composition of unsaturated-zone waters through their effect on the partial pressures of separate gases in the gas phase. For example, the partial pressure of carbon dioxide in the gas phase varies directly with total gas pressure. Such variations in the CO_2 partial pressure directly affect the concentration of CO_2 in water, which in turn, affects the dissociation of carbonic acid and, thereby, the pH. In addition, temperature controls the equilibrium fractionation of light stable isotopes, particularly oxygen.

6.2.7.2 Present-Day Site Characteristics

Data exist on the abundances of the major atmospheric gases in the unsaturated-zone gas phase at Yucca Mountain, including data obtained from the open borehole UZ-1 (Yang, Rattray et al. 1996; Table 6.2-14) and data from several other boreholes. To a depth of 368 m in UZ-1, the concentrations of oxygen, nitrogen, and argon are within analytical error of atmospheric compositions. Carbon-dioxide partial pressures were elevated above atmospheric levels (0.035 percent by volume) in the soil zone (0.8 to 1.3 percent by volume). Halfway down the hole in the 1994 data set, carbon dioxide dropped to 0.08 percent by volume but increased with increasing depth to 0.36 percent by volume at the lowest sampling point in the hole (367.9 m). Yang, Rattray et al. (1996) published several analyses for the partial pressure of CO_2 in NRG-6 and NRG-7a, in which CO_2 concentrations ranged from 0.05 to 0.19 percent by volume. These data are listed in Table 6.2-15. Note that essentially all the data indicate that the partial pressure of CO_2 in the unsaturated-zone gas phase is higher by factors of three or more than that in the atmosphere.

According to Thorstenson et al. (1989), all samples of gases from UZ6S, UZ6, and the neutron boreholes collected to date show concentrations of O_2, N_2, and Ar that are identical to the concentrations of these gases in atmospheric air to the limits of precision of the analyses. The gas analyses on which this statement is based are not published. The authors report that all soil gases sampled on and near Yucca Mountain showed methane concentrations that were depleted relative to the atmospheric value of about 1.7 ppm by volume (ppmv), but still greater than 0.5 ppmv. In contrast, neutron hole and UZ6S gases generally showed methane concentrations near zero, ranging up to a maximum value of 0.5 (± 0.1) ppmv, suggesting that methane consumption occurs in the subsurface, even below the soil zone. Similar to the data in Table 6.2-15, CO_2 gas concentrations in these boreholes ranged from 0.10 (± 0.01) to 0.71 (± 0.01) percent by volume compared to an atmospheric value of approximately 0.035 percent by volume.

Carbon isotopes were monitored at the different sampling depths in UZ-1 over time (Yang, Rattray et al. 1996; Yang, Peters et al. 1993). Early data are believed to show the effects of contamination by drilling air. For the most recent data, from 1986 through 1994, most values for $\delta\ ^{13}C$ were in the range of -14 to -17 ‰. A similar range was obtained for gas samples from three radial boreholes drilled from the upper Tiva Contact alcove of the Exploratory Studies Facility. Boreholes within the upper Paintbrush Contact alcove tend to be slightly heavier ($\delta\ ^{13}C$ of generally -12 to 13 ‰), but this tendency is not noted in the shallower reaches of UZ-1. In fact, the earliest gas samples tend to be anomalously light ($\delta\ ^{13}C$ less than -20 ‰) at shallow depth, reflecting a biogenic (plant root respiration) component. Subsection 5.3.4.2.4 contains additional discussion of CO_2-concentration and $\delta\ ^{13}C$ profiles as a function of time in UZ-1.

The ^{14}C data for UZ-1 have been very consistent for the last seven years of monitoring, with a gradual decrease in ^{14}C activity with depth to about 23 pmc at 368 m (Figure 6.2-43). The ^{14}C profile shows an abrupt change in the slope within the PTn unit (Yang, Peters et al. 1993). The gas transport velocity (^{14}C concentration gradient over distance) within the PTn unit is smaller than the transport velocity in the TSw unit. The smaller transport velocity may be due to greater degree of water saturation in this unit. An estimate of the minimum travel time of gas in the TSw unit based on the apparent ^{14}C ages and depths in the borehole yields gas movement of

3.26 cm/year. This rate, as well as results of gas-transport modeling (Yang, Rattray et al. 1996), is consistent with downward movement of atmospheric CO_2 by simple Fickian diffusion. The fact that the ^{14}C values of rock gas in the closed (i.e., instrumented) borehole decrease steadily with depth indicates that inhalation and exhalation of gases in response to changes in atmospheric pressure, as observed in open boreholes, is not a significant process under undisturbed conditions. If such a topographic effect were to be significant, then ^{14}C values would not decrease steadily as seen in UZ-6 and UZ-6s. Although diffusion may not be the only mechanism for gas movement in the TSw unit at UZ-1, it seems to be the dominant mechanism and can account for the observed distribution of gaseous ^{14}C with depth.

There is no evidence that the rock gas is in isotopic equilibrium with the pore waters. The isotopic composition of pore waters is highly variable, with $\delta\ ^{13}C$ ranging from -9 to -27 ‰ (Table 6.2-13). At equilibrium, carbon in bicarbonate in water should be about 8.5 ‰ heavier than carbon in CO_2 in the gas phase at 25°C (Clark and Fritz 1997). There are no data for gas and pore water from the same sample, but Table 6.2-16 compares a few samples that were collected from the same general depth ranges. For these, the differences for $\delta\ ^{13}C$ in gas and pore water are much less than 8.5 ‰. The larger range for $\delta\ ^{13}C$ in pore water than for gas in a given borehole also argues against large-scale equilibrium of carbon isotopes in the two phases.

Although the data sets are less extensive, data for NRG-6 and NRG-7a yield different results from those for UZ-1 (Figure 6.2-44). In these drillholes, ^{14}C activity does not appear to decrease with depth, and in fact, all three gas analyses from NRG-7a show post-bomb carbon.

The ^{14}C activity of gas in borehole SD-12 (Table 6.2-15) is similar to that of UZ-1 in that there is a decrease from surface to depth, but with some irregularly large deviations from the trend. Another striking difference is the markedly lighter carbon in SD-12 and the strong correlation between $\delta\ ^{13}C$ and ^{14}C activities (Figure 6.2-44c).

Rousseau et al. (J.P. Rousseau et al., Eds., *Hydrogeology of the Unsaturated Zone, North Ramp Area of the Exploratory Studies Facility, Yucca Mountain, Nevada*, Milestone Report 3GUP667M, U.S. Geological Survey, in press, MOL.19980220.0164) noted a gas pressure deficiency in the two deepest stations of SD-12 (both within the CHn), which they postulated could be due to the presence of hydrocarbons. The oxidation of hydrocarbons, such as methane, could account for the anomalously light carbon in the drillhole, and assuming that the methane is older than 50,000 years, this source would also account for the low ^{14}C activity of the sample at 407 m. Because the postulated methane would be affecting both carbon isotopes, the two isotopic compositions would tend to be correlated.

The smooth trends within SD-12 are consistent with the data obtained from UZ-1, indicating gas transport by diffusion mechanism as previously concluded (Yang, Rattray et al. 1996). However, the large fluctuations towards greater percentages of modern carbon probably represent a fracture-flow component. The component in the bottom of the hole could be modern atmospheric carbon, given the sharp increase in both $\delta\ ^{13}C$ and ^{14}C.

6.2.7.3 Scenarios for Future Variations in Gas-Phase Chemistry

It is most likely that in the future, the composition of the gas phase in the unsaturated zone will remain very near atmospheric except possibly for carbon dioxide and methane which are controlled by vegetation and soil-zone processes. Without a better model of the causes for the variations in CO_2 partial pressures in UZ-1, it is difficult to predict what future variations there might be in these parameters. It is also difficult to estimate past variations in these parameters.

6.2.7.4 Representativeness of Available Data

The degree to which available unsaturated-zone gas phase data are representative of *in situ* conditions is a problematic issue. Most of the gas samples for which data have been reported were integral samples in that they were obtained from open boreholes. This approach makes it difficult to associate a given gas analysis with a pore water from a specific depth interval. The data reported for borehole UZ-1 are the exception. This borehole was instrumented with gas sampling ports isolated at 15 different levels in the hole (Yang, Peters et al. 1993).

Data obtained in annual sampling events of borehole UZ-1 for gas compositions over a decade have established that variability in gas compositions (that is, CO_2 partial pressure and isotopic compositions) tends to decrease with time in instrumented boreholes. This fact suggests that reported gas compositions reflect distinct zones in the borehole and that the compositions reflect in situ (that is, natural) compositions. This type of data is not available for most of the other boreholes that have been sampled.

The number of boreholes for which gas data are available is limited in terms of both areal coverage and depth. This fact makes it difficult to realistically evaluate the potential variations in gas compositions in the unsaturated zone of Yucca Mountain.

Gas-phase sampling in open boreholes (for example, UZ-6S; Thorstensen et al. 1989) is subject to contamination from atmospheric gas as a result of the drilling of the borehole. This possibility must be taken into account when using these data.

6.2.8 Chemical and Isotopic Composition of Saturated-Zone Groundwater

6.2.8.1 Processes That Control Saturated-Zone Water Chemistry

The chemistry of saturated-zone waters is determined by a series of processes that are linked in space and time. In this section, the primary focus will be on processes that control the chemistry of groundwaters along flow paths from recharge areas north of Yucca Mountain, through Yucca Mountain, and downgradient from Yucca Mountain to the accessible environment. The main processes that determine groundwater chemistry along these flowpaths are:

- Precipitation quantities and compositions (Subsection 6.2.3)
- Surface-water quantities and compositions at recharge areas and along flow paths between recharge areas and the accessible environment (Subsection 6.2.4)

- Soil-zone processes at recharge areas and along flow paths between recharge areas and the accessible environment, including the effects of evapotranspiration
- Rock-water-gas interactions in the unsaturated zone at recharge areas
- Rock-water-gas interactions in the unsaturated zone at Yucca Mountain (Subsection 6.2.5)
- Rock-water interactions in the saturated zone along flowpaths between the recharge areas and the accessible environment
- Temperature and pressure along flow paths between recharge areas and the accessible environment
- Mixing of groundwaters from different flow systems

According to the regional hydrologic model for the Nevada Test Site (D'Agnese et al. 1997), the recharge areas for saturated-zone waters in Yucca Mountain are located to the northeast of Yucca Mountain in the direction of Buckboard Mesa, Rainier Mesa, and the eastern-most portion of Pahute Mesa. The rock types dominating the recharge areas are silicic and basaltic volcanic units (Byers et al. 1976). Although Paleozoic limestones and other sedimentary units are present at great depth, they do not appear to influence the compositions of waters that occur in the volcanic units in the saturated zone beneath Yucca Mountain.

Climatic conditions in the recharge areas are somewhat different from those that prevail at Yucca Mountain. Specifically, they receive more precipitation and are cooler on average than the Yucca Mountain area and support a greater abundance of vegetation (Spaulding 1985). Based on the data presented by Blankennagel and Weir (1973) and in Section 5 of this report, infiltration rates on Pahute Mesa are higher on average than infiltration rates on Yucca Mountain. Higher infiltration rates imply that dissolved salts and other constituents that may accumulate in the soil zone as a result of evapotranspiration of infiltrating waters (that is, precipitation) have shorter residence times in this zone. This process is likely the reason soils on Pahute Mesa and adjacent areas contain much less pedogenic calcite and/or silica than is the case at Yucca Mountain. The higher infiltration rates also imply that waters infiltrating into the saturated zone will have lower salt and silica concentrations than is the case at Yucca Mountain. This dilute composition makes these waters more reactive with respect to the rock units through which they may subsequently migrate.

As discussed in Subsection 6.2.5, water-rock reactions that recharging waters encounter in the soil zone or the unsaturated zone include dissolution reactions, mineral precipitation reactions, alteration reactions, and ion-exchange reactions. Because the waters percolating downward from the soil zones in recharge areas are likely more reactive than soil waters percolating into the unsaturated zone in Yucca Mountain, dissolution reactions are likely more important in the unsaturated zones of the recharge areas. The dominant changes to the water compositions that result from these reactions are major increases in silica, sodium, and bicarbonate (White, Claassen et al. 1980).

Once the water has undergone the initial dissolution reactions, the rate of change in water composition would likely decrease. This decrease is because the rate of dissolution is a function of the degree to which the water has approached thermodynamic equilibrium with the rock units with which it is in contact. The closer the water is to thermodynamic equilibrium with the host rock, the slower the rate of reaction.

Actual calculation of the degree to which the reaction approaches thermodynamic equilibrium is difficult because the reactions involved are commonly incongruent. For example, in the case of feldspar equilibration with a given water composition, the feldspar crystals do not simply dissolve into the solution. It appears that the cation/hydrogen ion-exchange reaction discussed previously (Subsection 6.2.5.2) causes the feldspar surface layers to be converted (that is, hydrolyzed) into a poorly structured hydrogen aluminosilicate solid "phase." Sodium, potassium and calcium are the major cations that participate in this exchange. The solubility of this solid "phase" would then control the rate of disappearance of the feldspar crystal (Brantley and Stellings 1996). Unfortunately, the thermodynamic properties of this solid "phase" are not well defined. The same situation occurs with the hydrolysis of volcanic glass at ambient temperatures.

The dominant water-rock reactions that impact the water chemistry after the initial dissolution reactions are silica precipitation reactions and ion-exchange reactions involving minerals such as zeolites and clays. The cation/hydrogen ion-exchange reaction will also continue to be of significance. The ion-exchange reactions will tend to lead to increased sodium concentrations and decreased calcium, magnesium, and potassium concentrations in the waters. However, changes in the concentrations of these ions will only occur if zeolites and/or clays are present in adequate quantities in rock units through which the waters migrate. The sodium/hydrogen ion-exchange reaction will continue to increase the sodium content of the waters until thermodynamic equilibrium is achieved with the host rock.

The degree to which alteration reactions involving silicates and aluminosilicates in the host rock control water compositions is unclear. For example, volcanic glass is thermodynamically unstable in contact with water at ambient conditions, and given enough time, it will alter to secondary minerals such as clays, zeolites, silica polymorphs, and other minerals. However, glass is still present in great abundance in the volcanic units that make up Pahute Mesa and Rainier Mesa (Byers et al. 1976). Without doubt, glass alteration reactions are taking place at some rate. However, this rate appears to be much slower than the rate of the initial dissolution reactions and ion-exchange reactions. For purposes of predicting water compositions, restricting the discussion to the latter reaction is probably adequate given the current state of knowledge.

Controls on the pH of groundwaters in the saturated zone are similar to those discussed in Subsection 6.2.5.2. In brief, the primary controls on pH are the partial pressure of CO_2 and the rate at which hydrogen ions are consumed by the rock/mineral matrix. In the saturated zone, access to the CO_2 reservoir in the gas phase of the unsaturated zone becomes progressively more difficult with depth. Therefore, unless a secondary source of carbonic acid or another source of acidity (for example, sulfide minerals) exist in the saturated zone, the reaction of hydrogen ions with the rock/mineral matrix will eventually consume the available acidity, leading to increased pH. The high pH value observed in H-3 (pH 9.0 in Table 6.2-18) (Ogard and Kerrisk 1984) likely reflects this process.

Controls on reduction/oxidation (redox) states in the saturated zone are more difficult to define. Potential redox reactions in the saturated zone include various redox couples such as oxygen/water, ferrous/ferric iron, sulfide/sulfate, nitrite/nitrate, and other couples. The methane/CO_2 couple is not likely to be of significance where methane abundances are very low because this redox couple only becomes active at low temperatures if it is microbially mediated. If dissolved oxygen is higher than approximately 0.1 mg/L, it could produce a relatively high redox potential (Eh > 600 mV). The redox state of saturated-zone waters as calculated from the concentrations or activities for respective couples may or may not be at equilibrium. Lindberg and Runnels (1984) have argued that ground and surface waters are rarely in equilibrium in terms of redox couples and that different couples may give different redox potentials (that is, Eh). However, this conclusion is based primarily on measurements on young groundwaters. Deep groundwaters such as those in the saturated zone at Yucca Mountain have had longer time frames over which to reach equilibrium.

In summary, the dominant processes that are likely to control water compositions along the flow paths from recharge areas to the saturated zone beneath Yucca Mountain are dissolution reactions, silica and calcite precipitation reactions, and ion-exchange reactions. The pH of these waters will be controlled primarily by the partial pressure of carbon dioxide and the rate at which the rocks consume hydrogen ions. Controls on the redox state are poorly defined at the present time.

6.2.8.2 Present-Day Regional Characteristics

This section summarizes the available data for groundwater chemistry in volcanic aquifers and tuffaceous valley fill in the saturated zone in the Yucca Mountain region extending from recharge areas north of Yucca Mountain along flow paths through Yucca Mountain and to the accessible environment boundary south of Yucca Mountain. For a discussion of saturated-zone water chemistry in carbonate regional aquifers see Subsection 5.2.4.

Figure 6.2-45 shows the locations of several wells on Pahute Mesa from which water samples have been obtained. All of these wells were completed in Tertiary volcanic rocks (McKinley et al. 1991). Full identifiers for these wells are shown in Figure 6.2-47. Based on the flow models discussed in Section 5, only those wells in the eastern part of Pahute Mesa are likely to lie along flow paths that pass through the Yucca Mountain area. Those wells located in the western part of Pahute Mesa apparently lie along flow paths that pass through Oasis Valley. Water samples from springs located in the area of Rainier Mesa (locations also plotted in Figure 2-45) may reflect the compositions of waters recharging the saturated zone in the Pahute Mesa area.

The available data on saturated-zone waters from the recharge areas consist primarily of analyses of the major constituents, although a limited number of isotopic analyses have been reported. A plot of the relative abundances in saturated-zone waters from eastern Pahute Mesa and southern Rainier Mesa is shown in Figure 6.2-47. The data indicate that the waters are dominated by sodium bicarbonate. These waters have pH values ranging from 7.4 to 8.2 and total dissolved solids ranging from 169 to 578 mg/L. Claassen (1985) noted that these waters are chemically relatively evolved. By this he was apparently referring to the fact that the ratio of

sodium to other major cations was high. Because these waters occur in the recharge area (that is, they are the youngest waters in the flow system), this is an important observation.

The locations of wells in the vicinity of Yucca Mountain from which groundwater samples were taken to obtain geochemical data are shown in Figure 6.2-46. Physical data for these wells are listed in Table 6.2-17. Corresponding chemical and isotopic analyses are presented in Tables 6.2-18 and 6.2-19. The relative abundances of major ionic constituents in saturated-zone waters from wells in the vicinity of Yucca Mountain and from wells down-gradient of Yucca Mountain in the Amargosa Valley are plotted in Figures 6.2-48 and 6.2-49, respectively. Comparison of Figures 6.2-47 to 6.2-49 shows saturated-zone waters from volcanic aquifers to be very similar in all three areas. Data for down-gradient waters were not plotted in the cations/anions versus chloride plots (Figures 6.2-22 to 6.2-26) because they directly overlap data points for Yucca Mountain area saturated-zone waters. The down-gradient waters show a pH range from 7.5 to 8.2 and a range in total dissolved solids from 217 to 233 mg/L, depending on where the southern boundary is placed. The fact that the down-gradient waters are even further from the recharge areas than those in the Yucca Mountain area again suggests these waters are close to equilibrium with their host rocks. The isotopic characteristics of the regional saturated-zone waters are discussed in Subsections 5.2.4 and 6.2.6.

6.2.8.3 Present-Day Characteristics of Groundwaters in the Yucca Mountain Area

As pointed out in the last section, saturated-zone waters from volcanic aquifers in the recharge area are compositionally very similar to saturated-zone waters from the Yucca Mountain area. Analyses of groundwater from drillholes that penetrate the host rock and other volcanic units in the area of the exploration block indicate that they are principally sodium-bicarbonate waters (Benson et al. 1983; Ogard and Kerrisk 1984) with low contents of total dissolved solids (200 to 400 mg/L). Compared to waters in the recharge areas, the Yucca Mountain area waters show a greater range in pH values from 6.6 to 9.2 and total dissolved solids ranging from 181 to 887 mg/L.

Plots of the major cations versus chloride show that saturated-zone waters (and perched waters) are generally distinct from unsaturated-zone pore waters in the Yucca Mountain area. First, saturated-zone waters (and perched waters) have much lower chloride concentrations than the pore waters (Figure 6.2-17). This result suggests the saturated-zone waters were subject to less evapotranspiration than the pore waters. An alternative explanation, loss of chloride from solution by reactions with glass or hydroxy phases in tuff, is improbable for unsaturated-zone pore waters at Yucca Mountain. Second, saturated-zone waters are either on or above the precipitation trend line in a sulfate versus chloride plot suggesting they gained sulfate, perhaps by dissolving some sulfate mineral(s) such as gypsum (Figure 6.2-25). Third, unlike unsaturated-zone waters, the saturated-zone waters plot both above and below the precipitation trend line in a calcium-versus-chloride plot (Figure 6.2-22). This result suggests some of these waters gained calcium while others lost calcium. The fact that nearly all of these waters gained bicarbonate (Figure 6.2-23) suggests the calcium gained may have come from the dissolution of calcite. The loss of calcium likely reflects ion-exchange reactions on clays and zeolites. This possibility is supported by the fact that these waters have all gained sodium (Figure 6.2-24). Finally, silica concentrations in these waters are slightly lower than those measured in pore waters. However, most of these waters are oversaturated with alpha-cristobalite (Figure 6.2-26).

The relative abundances of cations in saturated-zone waters show considerable variation from east to west across Yucca Mountain. Wells on Yucca Mountain and just to the west (USW H-3, USW H-5, and USW H-6) plot nearest the sodium apex of Figure 6.2-48. Wells on the eastern slopes and washes (USW H-1, USW H-4, USW G-4, J-13, and UE-25 b#1) show increasing levels of calcium. The Na+K/Ca+Mg ratio increases from 3.8 in J-12 to 263 in H-3. This result most likely reflects ion-exchange reactions involving the zeolites and clays in the saturated-zone units beneath Yucca Mountain and the sodium/hydrogen ion-exchange reaction. The fact that bicarbonate concentrations also increase from east to west suggests a significant contribution from the latter reaction. The anionic constituents of the Yucca Mountain groundwaters show a relatively uniform distribution in all the wells, with about 80 percent bicarbonate and the remainder as sulfate and chloride (usually present in nearly equal molar concentrations) and fluoride (in varying concentrations).

Oxidation/reduction states in saturated-zone waters at the site appear quite variable. Although most groundwaters at the site are oxidizing, as indicated by high Eh values, some evidence suggests that reducing conditions may exist in some wells. Field measurements at some of the site wells tested by Ogard and Kerrisk (1984) had lower Eh values (less than 200 mV with a Pt electrode), little if any dissolved oxygen, and ferrous iron. Additional measurements are required to map out the reducing zones if present. Since the gas phase in the unsaturated zone has levels of oxygen near that of the atmosphere, the upper part of the saturated zone is conservatively constrained to be oxidizing until shown otherwise. Work is ongoing and will be reported in the future.

Organic Content and Microbial Activity–Naturally-occurring organic compounds(carboxylic acids, humic and fulvic acids, and lipids) are produced by microbial degradation of plant tissue (including photosynthetic algae) and animal tissue, or by the degradation of material produced by autotrophic microorganisms (e.g., those that use H_2, Fe(II), or S° as energy sources). Pore water from a well-developed soil environment usually contains dissolved organic carbon (DOC) at levels greater than 20 mg/L in top soil and at about 5 mg/L in subsoils. DOC concentrations in groundwaters are usually below 2 mg/L (Drever 1988). *In situ* organic contents of waters from drillhole UE-25 b#1 and well J-13 were measured by Means et al. (1983). Total organic-carbon (TOC) contents were 0.14 mg/L (+/- 0.05 mg/L) in well J-13 water and 0.58 mg/L (+/-0.06 mg/L) in drillhole UE-25 b#1 water, respectively. The lower carbon content in well J-13 water is probably representative of the in situ content because the well is a producing well for the Nevada Test Site, and all drilling fluids have been removed by extensive pumping. Because of the low concentrations, little can be said about the individual organic compounds other than that organics with high molecular weight (higher than 1,000) constitute 50 percent of the organic content present in J-13 water and 33 percent in UE-25 b#1 water. Subsection 6.3.3.2 discusses the potential role of organic matter for radionuclide sorption and transport.

The nature of microbial activity in saturated-zone waters at the site is unknown at the present time. Early in the YMP Site Characterization, groundwater was considered to be part of the "accessible environment" and as such, beyond the charter of Site Characterization activities. Thus, microbial analysis of Yucca Mountain was limited to unsaturated-zone environments. Microorganisms are certain to exist in groundwater, and could be a major player in groundwater chemistry.

Naturally-Occurring Colloids–Colloid concentrations are a function of pH, oxidation/reduction states, concentrations of major cationic species (Na, K, Ca, Mg) and organic carbon. Data have been compiled for a variety of saturated systems reported in the literature, as well as for J-13 groundwater at Yucca Mountain, in order to develop a general understanding of colloid formation and stability that would be suitable for establishing bounds on the potential role of colloids in radionuclide transport. These data and the resulting model are presented in detail in Subsection 6.3.6.1. The colloid concentration of J-13 groundwater was on the order of 10^6 particles/mL.

The isotopic characteristics of the Yucca Mountain area saturated zone waters are discussed in Subsections 5.2.4 and 6.2.6.

6.2.8.4 Representativeness of Available Data

Because the analyses of major constituents in saturated-zone groundwaters from volcanic aquifers in the Yucca Mountain region show only limited variability (compare Figures 6.2-47 to 6.2-49), the available data are sufficiently representative for characterization and modeling purposes. In terms of other parameters such as pH, oxidation/reduction states, colloid abundances, and microbial populations, it is less clear that the available data are representative. For pH, bounds can be placed on the likely variability to be expected based on observations and hydrochemical models. For oxidation/reduction states and microbial populations, additional characterization data are required.

6.2.8.5 Scenarios for Future Trends in Saturated-Zone Water Chemistry

The consistency in saturated-zone water chemistry discussed previously suggests that climatic influences on saturated-zone water chemistry are damped in the flow system. Future climatic change could involve higher infiltration rates in the recharge areas but would not likely involve lower rates. Higher rates would result in more dilute water compositions (lower chloride, etc.). Such changes to water compositions would not lead to greater transport of waste radionuclides compared to transport rates that would occur under current conditions.

What effect variations in climatic regimes would have on oxidation/reduction states and microbial populations is uncertain given the present database. However, it is unlikely that higher infiltration rates would negatively affect these parameters in terms of transport behavior of important radionuclides.

The potential impacts of the thermal pulse resulting from waste emplacement and components introduced into the repository horizon are discussed in Section 7.

6.2.9 Geochemical Model for the Geochemical Evolution of Water at Yucca Mountain

6.2.9.1 Model Overview

The available data on the chemistry of waters at Yucca Mountain indicate the existence of two basic types of waters in volcanic units in the Yucca Mountain region. Type I is found as pore water above the Calico Hills nonwelded hydrogeologic unit. Type II is found as perched water

and saturated-zone groundwater. The pore waters in the Calico Hills nonwelded unit appear to be mixtures of these two water types.

The chemistry of Type I waters will be controlled primarily by soil-zone processes, including evapotranspiration and the precipitation/dissolution of calcite, gypsum, and amorphous silica. Evapotranspiration is important in concentrating the solutes deposited on the soil at the site as wet-fall and dry-fall. Soil-zone hydrology influences the ionic strength and chemical composition of subsurface waters because these characteristics are a strong function of the flux and residence time of infiltrating waters in the soil zone prior to percolation into the unsaturated zone. Because our understanding of soil-zone hydrology at Yucca Mountain is not fully developed, the impact of soil-zone hydrology on the composition of unsaturated-zone pore waters can only be approximated with the data presently available.

The pH and oxidation/reduction states of unsaturated-zone pore waters will be regulated primarily by the composition of the gas phase in the pores. As discussed in Subsection 6.2.5, Type I pore waters show only limited evidence of water-rock interaction in the unsaturated zone. Therefore, the pH of these waters is controlled primarily by the CO_2 partial pressures in the gas phase. At shallow levels (for example, < 30 m), these pressures are elevated well above the atmospheric partial pressure (Subsection 6.2.7). This fact causes the pore waters at these levels to have pH values less than 7.0 with some exceptions.

At intermediate levels, the CO_2 partial pressures are lower, resulting in higher pH values in the range 7.0 to 8.0. At the deepest levels, the situation is more complicated because pore waters at these levels show the effects of water-rock interactions as well as soil-zone processes. The water-rock interactions tend to consume hydrogen ions, driving the pH higher. If there are no additional sources of CO_2 at depth, the pH values would likely exceed 8.0.

The measured field Eh of unsaturated-zone pore waters will generally be oxidizing (> 400 mV) because this gas phase usually has an oxygen partial pressure equal to that observed in the atmosphere (Thorstenson et al. 1989; Yang, Rattray et al. 1996). This assumption that gaseous oxygen exerts a dominant control on redox conditions assumes that pore solutions are effectively buffered by exchange with the gas phase everywhere in the system. However, apparent lack of isotopic equilibrium with respect to stable carbon isotopes in some gas and pore fluids from Yucca Mountain suggests that this assumption may not always be valid.

The compositions of Type II waters are dominated by rock/mineral-water reactions. These reactions involve the exchange of cations (dominantly sodium) with hydrogen ions on the surfaces of aluminosilicate phases in the rocks. Hydrogen ions are supplied by the dissociation of carbonic acid. Therefore, the partial pressure of CO_2 is a critical parameter because it has a major influence on the pH of the waters. Prediction of the future variations in perched and saturated-zone groundwater compositions requires that the rock/mineral-water reactions be modeled. This approach requires knowledge of the secondary phase(s) involved in the reactions and kinetic rate constants for the most important reactions. These data are generally not available at the present time.

Lacking the data required to perform realistic reaction-path modeling, an alternative approach is to compare saturated-zone water compositions in volcanic units along flow paths from the

recharge areas through the site area and into the Amargosa Valley. Such a comparison indicates that water compositions in volcanic units are very similar along these flow paths. This similarity implies that these compositions are attained early in the recharge history of these waters. The main reactions involved are likely dissolution reactions. Once the waters become saturated with respect to secondary phases, their compositions appear to remain fairly constant (in the absence of mixing with waters from other flow systems). The main alterations to these compositions are the sodium/hydrogen ion-exchange reaction involving carbonic acid and other ion-exchange reactions involving zeolites and clays. The eventual product of these reactions is a sodium-bicarbonate water with a relatively high pH (8 to 9). The oxidation/reduction potentials of these waters cannot be modeled with currently available data.

Although the waters between the recharge areas and the saturated zone underlying Yucca Mountain are theoretically oversaturated with respect to various phases (for example, silicates and aluminosilicates), evidence for the net loss of constituents from solution through precipitation reactions is meager. For example, the concentration of silica in these waters is well over the saturation level (concentration) for quartz and cristobalite. This oversaturation would suggest these mineral phases should precipitate, leading to a down-gradient decrease in the silica concentrations. The fact that silica concentrations remain high down-gradient suggest these phases do not control the silica activity in solution. More likely, the silica concentration in a given groundwater sample results from a balance between the rate of dissolution of a silica-rich phase (for example, opal, amorphous silica, volcanic glass) and the rate of crystallization of a silica polymorph or, perhaps, more than one silica polymorph. The identity of the silica polymorph(s) is uncertain but may be poorly crystalline cristobalite.

6.2.9.2 Implications for Radionuclide Transport

The chemistry of water is a potentially important factor in radionuclide transport because it influences the solubilities of radionuclide compounds that form and because it influences the sorption behavior of the radionuclides. In addition, the chemistry of waters that may infiltrate the potential repository will be determined in part by the chemistry of water present in the unsaturated zone above the potential repository horizon. Therefore, the model for unsaturated-zone water compositions developed in this section can be used as input to the near-field corrosion and transport models discussed in Section 7.

Variations expected in water compositions that intersect the near-field environment will be strongly dependent on the climatic regime and on flow paths. Because most flow paths that would produce water in the repository horizon will likely represent fast flow paths, the water compositions are likely to be relatively dilute, similar to the ambient perched-water compositions. If infiltration rates are increased in the site area as a result of a climatic shift, these compositions would likely become even more dilute. The pH of these waters should be near neutral.

The compositions of waters in the saturated zone beneath the potential repository horizon will influence the sorption behavior of the radionuclides transported out of the potential repository horizon. The expected compositional variation of these waters is limited. The main fluid-phase parameters that could significantly influence the sorption behavior are pH, oxidation/reduction states of redox couples, and carbonate speciation which itself varies with pH. The range in pH to

be expected is from 6.5 to 9.0. Because this range is accommodated in the sorption experiments that have been performed (Subsection 6.3), the potential impact of this parameter has been bounded. The range in oxidation/reduction states to be expected remains to be determined. Experiments to-date have largely been carried out under oxidizing conditions. Waters down-gradient from the repository could be more reducing than has been presumed to-date. Reducing conditions in saturated-zone waters could result in substantially higher retardation of certain radionuclides of interest such as technetium, plutonium and neptunium.

6.2.10 Conclusions

The hydrochemical data available for the Yucca Mountain area include pore-water compositions, gas-phase compositions, saturated-zone-water compositions, and isotopic data. These data provide a basis for understanding the controls on water chemistry in the site area and a basis for predictions of future variations in water chemistry in the unsaturated zone and the saturated zone. Unsaturated-zone-water compositions at Yucca Mountain are dominated by soil-zone processes, including evapotranspiration and the precipitation of pedogenic calcite and silica horizons. Saturated-zone-water compositions show a greater influence of water-rock interactions in the unsaturated zone below recharge areas. These water-rock interactions are dominated by dissolution reactions and ion-exchange reactions. Controls on the pH and oxidation/reduction states of these waters include the unsaturated gas phase and cation/hydrogen ion-exchange reactions.

Models for the prediction of future variations in unsaturated and saturated-zone-water compositions are sufficiently advanced to allow bounds to be placed on the potential variations in major constituents. Models for variations in pH and oxidation/reduction states will require additional study. Currently, data on the microbial activity in saturated-zone waters is non-existent. Sample analysis, plus a complete review of the literature, will be required to assess the effects of these organisms on water chemistry and radionuclide transport.

6.3 GEOCHEMISTRY GOVERNING RADIONUCLIDE MOBILITY

Radionuclide migration from a potential repository would be mitigated by several barriers, including the geochemical barriers of solubility and sorption described in this section. One of the initial barriers is the solubility of the radionuclides themselves in any water that infiltrates the potential repository. The solubility of key radionuclides (for example, Np, Pu, Am, and Tc) has been shown to be controlled by solution speciation and by the solubility-limiting actinide-bearing solid. Bulk solubility experiments provided empirical data directly, but because they were long-term experiments, only a limited amount of data were collected over a limited range of conditions. To determine solubility for general conditions, the system was modeled thermodynamically. Models were tested against the solubility found from the bulk experiments prior to being used in the general cases for performance assessment. The approach used was to calculate/measure the solubility of the most stable observed radionuclide solid phases that might precipitate under conditions anticipated in and near a high-level radioactive waste repository (Nitsche 1991; Nitsche, Roberts et al. 1995). This approach is conservative in that, besides U, the concentrations of the radionuclides are likely to be so low relative to the concentrations of the major elements that coprecipitation within solid solutions of the major elements will occur rather than precipitation as pure phases, which are usually more soluble (Gnanapragasam and Lewis 1995; Langmuir 1997). Subsection 6.3 will summarize the results of the following investigations: radionuclide solubility and speciation, sorption, transport diffusion, and the conceptual models that can describe these phenomena in transport codes. Subsection 7.4.2.5 considers the interactions of radionuclides with the products of canister corrosion such as iron oxides and cementaceous materials that might be generated from concrete tunnel liners.

DATA TRACEABILITY AND QUALITY

All work performed to collect data and test, analyze, model, or describe the natural system under study has been done under the YMP QA program at Los Alamos. This report and the analyses included herein are considered "Q". However, the computer codes used for the interpretive analyses were not developed or tested under a YMP QA program. Q reports/analyses/models include non-Q data that are clearly defined as such. Based on this assumption, all of the field data developed at Los Alamos and most of the laboratory data discussed in this report are Q data.

The following outlines the Q or non-Q status and data tracking numbers relevant to the data included in this report or used to summarize the current state of knowledge:

Sorption (Subsection 6.3.3)

Neptunium data:
LA000000000090.001 * (TBV); Q data
LA00000000104.001* (TBV); Q data
Plutonium data:
LA000000000104.001* (TBV); Q data
Uranium data:
LA000000000104.001* (TBV); Q data
All other radionuclides
Data tracking numbers are not applicable; non-Q data

Transport (Subsections 6.3.4 and 6.3.6)

Solid Rock Columns (all isotopes)
LA000000000127.001* (TBV); Q data
Fractures (all isotopes)
LAIT831361AQ95.003 (TBV); Q data
LAIT831361DQ95.004 (TBV); Q data
LAIT831361AQ97.004 (TBV); Q data
Colloids
Stability data and concentration determinations in J-13 water
LA000000000128.001 (TBV); Q data
Transport
LAIT831341AQ97.002 (TBV); Q data
Reversibility of Radionuclide Sorption onto Colloids
LAIT831341AQ97.001 (TBV); Q data
Rest of data
Data tracking numbers are not applicable; non-Q data

Diffusion (Subsection 6.3.5)

All isotopes
LAIT831362AQ95.001 (TBV); Q data
LAIT831362DQ95.002 (TBV); Q data
*Superseded by LAIT831341AQ96.001 (TBV)

6.3.1 Radionuclides of Concern

Although the fission products ^{90}Sr and ^{137}Cs will dominate the radioactive inventory at the start of the repository's life (Choi and Pigford 1981), the half lives of ~30-years means that these radionuclides will be essentially decayed away by the time the metal-waste packages could fail due to corrosion a minimum of 1,000 years) (Langmuir 1997). Therefore, little emphasis is placed on these elements. For spent fuel, the chief sources of radioactivity from 1,000 years up to 10,000 years are Am and Pu isotopes (Langmuir 1997). From roughly 10^4 to 10^7 years, ^{237}Np contributes the most to radioactivity of the waste (Langmuir 1997). Therefore, scientific study has concentrated on the geochemical mobility of Am, Pu, and Np as the successively dominant contributors to radioactivity. In addition to these actinides, $^{233,234}U$, ^{129}I, and ^{99}Tc have received attention in TSPA exercises (Rechard 1995), principally because there is little demonstrated geochemical retardation from solubility or sorption for these radioactive isotopes. The radionuclides singled out here as those of concern (Np, Pu, Am, Tc, and U) were chosen from the most important species for the first 10^7 years from the water-dilution figures of Choi and Pigford (1981) and from Langmuir (1997).

Therefore, brief coverage of the geochemistry and thermodynamic solubility of the long-lived radionuclides will be reviewed in this section, followed by more extensive review of Np, Pu, and Am and their relevance to Yucca Mountain in subsequent sections.

Technetium–Technetium is a priority radionuclide due to its high solubility and low sorption. It is also the most important β emitter in radioactive waste in the $>10^3$ year time frame (CRWMS M&O 1994). Thermodynamic data for solids and solutions are being evaluated critically by scientists collaborating through the Nuclear Energy Agency (NEA), and this review is scheduled to be published shortly. It is presumed by the TSPA that the waters at Yucca Mountain are oxidizing waters and that Tc will therefore exist in the Tc(VII) state as TcO_4^-. The tetrahedral arrangement of coordinating oxygens prevents the formation of stable solid precipitates and shields the Tc from mineral sorption sites. Solubility would be essentially limited by the inventory and not from precipitation equilibrium. However, interaction with reduced minerals or in more reducing waters may reduce the Tc to lower oxidation states (i.e., Tc(IV)), which would be orders of magnitude less soluble and more sorptive (Lieser and Bauscher 1988). In reducing neutral waters, the predominant aqueous species would be $TcO(OH)_2^0(aq)$ in equilibrium with $TcO_2 \cdot 2H_2O(c)$ with a solubility of $\sim 10^{-8}$ M (Rard 1983; Langmuir 1997). (Note: throughout this section, (c) indicates crystalline, (aq) indicates aqueous, and (am) indicates amorphous. At higher values of pH (>10), amphoteric behavior starts to increase the solubility to $\sim 10^{-7}$ at a pH of 11. In the presence of high carbonate concentrations, carbonate complexes can form at pH values >8.5, raising solubility to $\sim 10^{-6}$ M by a pH of 11 for $P_{CO_2} = 10^{-2}$ bar (that is, ~31 times standard atmospheric CO_2 pressure). Little is known about the temperature effects on the Tc(VII)/Tc(IV) equilibrium, so extrapolation to 90 to 95°C in the near field of the repository is not possible. Furthermore, the intervening oxidation states (VI and V) are considered to be unstable with respect to disproportionation, but their stability under very dilute conditions or different temperatures is also not known. These comments on the effect of temperature on speciation, redox barriers, and ultimately thermodynamic solubilities can be made almost across the board for all the radionuclides discussed here (although Yucca Mountain water-specific solubility experiments will be described below for Np, Pu, and Am). At this point, the only conservative, nonreproachable course of action is not to use solubility as a limiting factor in Tc release.

Iodine–Iodine occurs as iodate (IO_3^-) in highly oxidizing waters and iodide (I^-) under less oxidizing conditions, including most groundwaters (Pourbaix 1966; Langmuir 1997). Iodide salts are less soluble than iodate salts but are still too soluble to limit maximum possible iodine concentrations in groundwaters. Therefore, the concentration will be limited by the amount of iodine available from the inventory.

Uranium–Uranium has been studied extensively for over a century, and the relevant thermodynamics that control uranium solubility has been critically evaluated by Grenthe et al. (1992) under the auspices of the Nuclear Energy Agency. Spent fuel from nuclear power plants to be disposed in a repository is largely in the form of UO_2, so the discussion here starts with U(IV) complexes. Note that only U(IV) and U(VI) are considered to be important oxidation states of uranium, with U(V) quickly disproportionating (Newton 1975). Uranium(IV) is stable only at very reducing potentials, with the principal minerals being uraninite (crystalline UO_2), pitchblende (amorphous UO_2), and the ominously named coffinite ($USiO_4$) (Langmuir 1997). In the absence of carbonates, the principle solution species in equilibrium with uraninite/pitchblende (various degrees of crystallinity found experimentally) at pH values >4 is $U(OH)_4^0(aq)$, with a uranium solubility of $<10^{-8}$ M to pH values >12 (Ryan and Rai 1983; Parks

and Pohl 1988; Rai, Felmy et al. 1990; Yajima et al. 1995). Given the formation constant of coffinite, its solubility should also be comparable to these values (Langmuir 1997). Under Yucca Mountain conditions, the most important other ligand, besides OH^-, for uranium is carbonate. At very reducing conditions, the tetrahydroxide U(IV) complex is more stable in solution than the carbonates (Grenthe et al. 1992), so U(IV) carbonates do not need to be considered further.

In the more oxidizing regions of uraninite (but not pitchblende) stability, the solution species in equilibrium over the U(IV) solid can be a U(VI) solution species, either a uranyl aquo/hydroxide species or a carbonate species (Langmuir 1997). In fact, several mixed-oxidation-state solids predominate at groundwater-relevant pH's before the U(VI) solid phases (schoepite (β-$UO_3 \cdot 2H_2O$) and/or secondary uranyl solid phases such as carbonates) predominate in the higher Eh values of the Eh/pH stability diagram. In ascending order of Eh values, important uranium solids formed in carbonate-free near-neutral pH water include UO_2, β-U_4O_9, β-U_3O_7, U_3O_8, and UO_3 (Langmuir 1997). Important uranyl solution species under Yucca Mountain waters such as J-13 include, with increasing importance with pH, UO_2^{2+}, UO_2OH^+, $UO_2CO_3^0$, $(UO_2)_3(OH)_5^+$, $(UO_2)_2(CO_3(OH)_3^-$, $UO_2(CO_3)_2^{2-}$, and $UO_2(CO_3)_3^{4-}$ (Grenthe et al. 1992; Waite et al 1994). Langmuir (1997) has plotted the uranyl solubility as a function of pH with schoepite as the solubility-controlling solid for two P_{CO_2} cases. With no carbonate present, the solubility reaches a minimum of just over 10^{-7} M at a pH value just over of 7. By a pH of 8.5 and, on the other side of the minimum, a pH of 5.5, the solubility has increased to 10^{-6} M. With $P_{CO_2} = 10^{-2.0}$ bar (31 times more than atmospheric CO_2), the minimum has shifted to a pH of ~6.3 and to a value of about 10^{-6} M. The solubility has increased from this value by an order of magnitude by a pH of 5 and of 8. Typical Yucca Mountain waters such as J-13 would produce solubilities intermediate between these two P_{CO_2} cases. The presence of other potential solid uranyl phases, such as rutherfordine or $Na_2(UO_2)(CO_3)_2$, was not considered. This fact implies that the present estimate is conservative, as a more stable uranyl carbonate solid would lower the solubility values and less stable phases would convert to the schoepite.

Although the other actinides also exhibit oxide solubility-limiting solids rather than carbonates in J-13 water conditions (see below), schoepite has been reported to be a nonterminal phase: it dehydrates in dried-out conditions possible in the vadose zone and, thereby, its crystal structure is compromised allowing it to be dissolved (Finch and Ewing 1992; Finch et al. 1992). Secondary uranium mineralization subsequently occurs with weathering to form uranyl silicates (uranophane and soddyite), phosphates (autunite), vanadates (carnotite), or carbonates (for example, rutherfordine), depending on what anions are available. Because many uranium deposits start out as uraninite and show these weathering/oxidation patterns, they can be used as natural analog systems for a nuclear-waste depository to show mobility patterns of uranium over long periods of time (Curtis et al. 1994). An example of an analogue for Yucca Mountain is the Peña Blanca deposit in northern Mexico, which occurs in an unsaturated and oxidized tuff located in an arid region (Pearcy et al. 1994). The formation of some of these secondary phases would limit the solubility of uranium further from that of schoepite. For instance, the formation of uranophane as the solubility-limiting phase, as is seen at Peña Blanca, should limit the uranium solubility to ~10^{-7} M (Langmuir 1997). Wilson (1990) produced similar Ca-U(VI) silicate solids by leaching spent fuel with J-13 water.

Neptunium–Total System Performance Assessment (TSPA) results have shown that the inventory of Np from stored nuclear waste under current scenarios would be sufficient to consider Np a potential problem contaminant, with ^{237}Np being the largest contributor to the radioactivity of a nuclear-waste repository at times between 10^4 to 10^7 years (CRWMS M&O 1994; Wilson et al. 1994; Rechard 1995; Langmuir 1997). Neptunium is considered to be the most hazardous radionuclide for repository times beyond 10^4 years in the most recent TSPA for the Yucca Mountain site (Rechard 1995). Under Yucca Mountain conditions, the final oxidation state of Np is not known, but the solubility-limiting solid is predicted to be either Np(IV) or Np(V), depending on the redox of the infiltrating water and on the source of the database (Wilson and Bruton 1990; Hakanen and Lindberg 1991; Janecky, Duffy et al. 1994; Janecky, Enter et al. 1995). The solubility of the two oxidation states is quite different, with Np(IV) having a solubility several orders of magnitude less than Np(V). Although Np(IV) is expected to be the dominant oxidation state under reducing conditions in natural groundwaters, Np(V) is the most common oxidation state in oxygen-rich natural waters (Katz et al. 1986; Lieser and Muhlenweg 1988; Hobart 1990). As described in Subsections 6.2.7 and 6.2.8, reducing conditions may exist in the saturated zone or locally in the near field (at least temporarily). For Np(IV), solubility-controlling solids include $Np(OH)_4(am)$ and, especially, $NpO_2(c)$. Important solution species include $Np(OH)_4^0$ in low carbonate solutions (for pH>3) and $Np(OH)_3CO_3^-$ in higher carbonate solutions (for example, total carbonate = 10^{-2} M, similar to UE-25 water, and a pH range from 5 to 11). Under conditions for the Np(IV) redox state, the solubility in water to at least a total carbonate concentration of up to 10^{-2} M is expected to be lower than 10^{-8} M (Langmuir 1997).

As for uraninite described above, the stability field for $NpO_2(c)$ may extend into the Eh region in which Np(V) solution species may also exist (Langmuir 1997). This extension depends critically upon the database used. Np(V) solubility-limiting solids include $Np_2O_5(c)$, $NpO_2OH(am)$, and in high ionic-strength carbonate media, the so-called double carbonate salts $Na_{1-2x}NpO_2(CO_3)_x$ (where x = 1 to 3) (Volkov et al. 1979, 1981; Neck, Runde, Kim et al. 1994; Neck, Runde, Kim 1995). In the absence of carbonates, the solution speciation of Np(V) is dominated by the highly soluble NpO_2^+, which does not hydrolyze readily below a pH of 10 (Moskin 1971; Rosch et al. 1987; Itagaki et al. 1992; Neck, Kim et al. 1992; Tait, Palmer et al. 1995). In J-13 type waters, where the higher carbonate complexes are not strong enough to be predominant, even at higher temperatures, the carbonate-complexed Np(V) species of importance includes $NpO_2CO_3^-$ (Tait, Palmer et al. 1995).

Plutonium–Plutonium is a priority radionuclide because much of it will exist in the inventory of a nuclear repository and in oxidized form it can be quite mobile. Unlike most metal cations, Pu can exist in multiple oxidation states simultaneously. The III, IV, V, and VI states of Pu are readily attainable under environmentally relevant conditions, and therefore, redox conditions do not necessarily preclude a low release. In general, the solid state is dominated by Pu(IV), specifically $PuO_2(c)$, $Pu(OH)_4(am)$, and radiocolloids (suspended PuO_2 polymer). The aging of Pu solubility-limiting solids may start with the formation of radiocolloids, which gradually dehydrate/polymerize to mixtures of $Pu(OH)_4(am)$ and/or $PuO_2(am)$, which, in turn, eventually go on to $PuO_2(c)$ (Hobart et al. 1989; Clark 1994). The final aged form should be $10^{6.6}$ times less soluble than $Pu(OH)_4(am)$, but recent modeling suggests that even aged $PuO_2(c)$ contains

$Pu(OH)_4(am)$ units on its surface, lessening this effect (Efurd, D.W. et al., "Measured Solubilities and Speciation of Neptunium and Plutonium in J-13 Groundwater," *Environmental Science and Technology*, unpublished). Mobility of the suspended radiocolloid and Pu-particle sorption (pseudocolloids) form can be significant, especially in highly fractured matrices in which filtration, redox reactions, and so forth are of diminished importance (Penrose et al. 1990; Triay, Simmons et al. 1995). Oxidation states can redistribute through disproportionation (for example, Pu(V) disproportionates to Pu(IV) and Pu(VI) in acidic conditions at a rate inversely proportional to $(pH)^4$ (Newton 1975)) and from radiolysis effects. These radiolysis effects can cause either reduction (Cleveland 1979a, 1979b) or oxidation (Runde 1993), depending on the initial plutonium oxidation state and the chemical composition of the solution. As with Am, radiolysis can also complicate the solubility measurements due to radiation damage of the solubility-limiting solid.

In the solution phase, dilute Pu solutions expected in the environment are likely to have a distribution of oxidation states dominated by the +5 oxidation state, although Langmuir (1997) shows a large region of predominance for $Pu(OH)_4^0(aq)$ in the Eh-pH diagram for dilute Pu. As for Np(V), PuO_2^+ does not readily hydrolyze (Bennet et al. 1992), in sharp contrast to the other oxidation states (Lemire and Tremaine 1980; Lemire and Garisto 1989; Langmuir 1997). Hydrolysis of the other Pu oxidation states is high, occurring by a pH of 5 for PuO_2^{2+}, a pH of ~1.5 for Pu(IV), and a pH of ~8 for Pu(III). Pu(IV) undergoes extremely strong hydrolysis, leading to the universally seen formation of radiocolloids at neutral pHs and Pu concentrations $>\sim 10^{-7}$ M (Nitsche, Gatti et al. 1993). All oxidation states have strong complexes with carbonate (Langmuir 1997), cutting into the Pu^{3+} and $Pu(OH)_4^0$ predominance zones even at relatively low total carbonate concentration (10^{-2} M).

Americium–As noted above, in the 10^3 to 10^4 year period, americium is, for awhile, the largest contributor to the radioactivity of the nuclear waste. Unlike other transuranic species, Am exists primarily in one oxidation state, namely as Am(III) (Silva et al. 1995). The NEA database for Am has been published recently (Silva et al. 1995), putting Am and U alone as the actinides whose databases could be agreed upon. At least two complicating factors do exist for interpreting Am data. Like Pu, Am can also exist in colloidal form (Penrose et al. 1990; Bates, Bradley et al. 1992), so phase separation of truly soluble species is problematic, and there is another route for radionuclide migration. Furthermore, because ^{241}Am is intensely radioactive, it is difficult if not impossible to form a good crystalline solid as the solubility-controlling phase.

Americium(III) forms strong hydroxo, carbonato, and for solids, mixed hydroxo-carbonato species (Silva et al. 1995). Important solution species at a P_{CO_2} of $10^{-3.5}$ bar (atmospheric CO_2, producing water similar to J-13 at pH values between 7 and 9) include, with increasing pH from a pH of 6, Am^{3+}, $AmOH^{2+}$, $AmCO_3^+$, $Am(OH)_2^+$, $Am(CO_3)^{2-}$, and beyond a pH of 9, $Am(CO_3)_3^{3-}$ (Silva et al. 1995). The only solid found in Yucca Mountain experiments in J-13 water was $AmOHCO_3$ (Nitsche, Gatti et al. 1993), consistent with the large stability field of this solid over different values of pH and P_{CO_2} (Silva et al. 1995). Other important solids include $Am(OH)_3(c)$ ($\log P_{CO_2}$ <–4, pH > 7.5) and $Am_2(CO_3)^3$ ($\log P_{CO_2}$ > –1, neutral pH) (Runde et al. 1992). Solubilities in Yucca Mountain specific waters will be discussed below. Thermodynamic studies of $AmOHCO_3(c)$ at room temperature and $P_{CO_2} = 10^{-3.5}$ bar by Felmy et al. (1990) show a

solubility of $10^{-7.5}$ M to $10^{-8.5}$ M for pH values from 6.5 to 9. Above a pH of 9, the solubility is increasing due to the formation of $Am(CO_3)_3^{3-}$ in solution.

6.3.2 Solubility Studies and Speciation

Recent measurements (Efurd et al. 1996; D.W. Efurd et al., "Measured Solubilities and Speciation of Neptunium and Plutonium in J-13 Groundwater," *Environmental Science and Technology*, unpublished) have shown that the bulk solubility of neptunium in J-13 water ranges from 6×10^{-6} to 1×10^{-3} M. These results are generally an order of magnitude lower than earlier reports (Nitsche, Gatti et al. 1993). This difference has been attributed to the artificially higher ionic strength in the earlier studies caused by continual pH control. Some models, depending on the Np database employed, have predicted Np(IV) as the predominant oxidation state in Yucca Mountain waters, which if true, would lower the ultimate solubility of Np by several orders of magnitude. However, the oxidation state of neptunium in the later study still points to Np(V) as the predominant species (Efurd et al. 1996; D.W. Efurd et al., "Measured Solubilities and Speciation of Neptunium and Plutonium in J-13 Groundwater," *Environmental Science and Technology*, unpublished), albeit a different solid than reported in the earlier study (Nitsche, Gatti et al. 1993). Whether this Np(V) solid is the equilibrium state or a kinetically controlled state has not been determined. Similarly, the more refined solubility measurements of Efurd et al. (1996; D.W. Efurd et al., "Measured Solubilities and Speciation of Neptunium and Plutonium in J-13 Groundwater," *Environmental Science and Technology*, unpublished), found lowered variability and lowered Pu solubility in J-13 water, although the difference between the two studies was less pronounced than for neptunium. The solubility data for neptunium and plutonium from Efurd et al. (1996; D.W. Efurd et al., "Measured Solubilities and Speciation of Neptunium and Plutonium in J-13 Groundwater," *Environmental Science and Technology*, unpublished), are considered more reliable than those of Nitsche, Gatti et al. (1993) because they have an ionic strength closer to that expected for ground water at Yucca Mountain and because the solids were better characterized.

For americium, the existing solubility and sorption data are difficult to interpret, at least partly because they have been performed in Yucca Mountain conditions using Am as a tracer in Nd/Am solutions (Nitsche, Gatti et al. 1993; Nitsche, Roberts et al. 1994). Radiation damage of a pure Am solid may preclude the formation of the stable solid indicated in the Yucca Mountain studies. Trivalent actinides are known to be more soluble than the analogous lanthanide(III) compounds (Runde et al. 1992).

6.3.2.1 Solubility in Yucca Mountain Relevant Waters

The YMP requires "studies to provide the information required on radionuclide retardation by precipitation processes along flow paths to the accessible environment" before licensing and construction of the project (DOE 1988). The purpose of this study is to summarize data for calculating radionuclide transport along potential transport pathways from the repository to the accessible environment. In selecting these experiments, the generic U.S. Nuclear Regulatory Commission (NRC) technical position entitled "Determination of Radionuclide Solubility in Groundwater for Assessment of High-Level Waste Isolation" were considered (Brooks and Corrado 1984). This technical position served as guidance for experiments to determine radionuclide solubility. It requires that if radionuclide solubility is used as a factor in limiting

radionuclide release, experiments must be designed to determine solubility under site-specific conditions. To predict behavior at higher temperatures expected in the near field of a potential repository, databases used for modeling calculations must contain data on thermodynamic functions at elevated temperatures. To date, many of these data are unavailable and are therefore estimated by extrapolation from lower temperature data.

Radionuclide concentrations in water passing through the emplacement area can be limited by two mechanisms, low dissolution rates of the solid waste form or solubility of individual radionuclides. If solid waste dissolution rates are low enough, it may not be necessary to depend on the solubility to limit radionuclide concentrations. In other words, the amount of a radionuclide dissolved in solution could be limited by the amount of that radionuclide freed from the solid waste form by the dissolution of the waste form. Alternatively, determination of radionuclide solubility limits provides an upper bound on radionuclide concentrations in solution and a basis for "extrapolation to long-term behavior." The rate of groundwater flow through the waste is expected to be sufficiently slow to permit saturation of water with radionuclides freed from the waste form. Dissolution limited by saturation will provide maximum concentration limits. Therefore, an assessment of radionuclide release rates using a saturation-limited dissolution model represents the most conservative approach possible for solution transport (Dozol and Hageman 1993).

The range of water conditions at Yucca Mountain (dominating solubility and speciation) is generally anticipated to be in the pH range from 6 to 8.5, but contact with cement or backfill may push the pH higher (up to 11). This is examined in detail in Subsection 7.4.2.4. Ionic strength of groundwaters in the western U.S. is generally low, and J-13 and UE-25p #1 waters are low ionic-strength waters that are considered to be representative of potential Yucca Mountain waters (Ogard and Kerrisk 1984). Future considerations of repository loading (for example, thermal loading) may cause groundwaters to be refluxed and, hence, affect the ultimate ionic strength that could contact the waste. This is discussed in Subsection 7.4.2.1. The effects on canisters of salts from such waters combined with humidity as the repository cools is considered in Subsection 7.6.1.

The solubilities of neptunium and plutonium in J-13 groundwater from the Yucca Mountain region at three temperatures and three hydrogen-ion concentrations have been studied best by Efurd et al.(1996; D.W. Efurd et al., "Measured Solubilities and Speciation of Neptunium and Plutonium in J-13 Groundwater," *Environmental Science and Technology*, unpublished). The actinide solubilities were determined from oversaturation at 25°C, 60°C, and 90°C and initial pH values at 6.0, 7.0, and 8.5. Tables 6.3-1 and 6.3-2 summarize the results. Sample evaporation was minimized to maintain the ionic strength of the solutions as close to that of J-13 water as practical for the duration of the experiments. The pH of each solution was initially adjusted at the start of the solubility experiments; no pH adjustments were performed during the year that the solubility experiments were conducted. In general, the neptunium solubilities decreased with increasing pH and temperature. The steady-state solids were greenish brown in color. X-ray diffractometry identified a mixture of neptunium compounds. Crystalline Np_2O_5 and a salt of neptunium were identified. Plutonium was less soluble than neptunium. In general, plutonium solubility decreased with pH and temperature. The solubility-controlling steady-state solids were dense green crystals that produced x-ray diffraction patterns that were indicative of a mixture of

amorphous and crystalline materials. The relative amount of crystalline solid (PuO_2) increased with temperature.

The solution behavior of the element plutonium is the most complicated of all the elements of interest and the least understood, particularly in near-neutral solutions representative of water compositions expected within the Yucca Mountain flow system. Plutonium can have several oxidation states in a given solution, and it can form complexes with a variety of ligands.

According to Nitsche, Gatti et al. (1992) and Nitsche, Roberts, Prussin et al. (1994), plutonium will be present in the +3, +4, +5, and +6 oxidation states in solutions representative of water compositions expected within Yucca Mountain. The +5 and +6 oxidation states should predominate in solution at redox potentials in the range of 230 to 350 mV. In J-13 and UE-25p #1 waters, the +5 oxidation states should be dominant (60 to 80 percent) at 25°C. Most of the remaining plutonium in solution is in the +6 oxidation state in J-13 water and the +4 oxidation state in UE-25p #1 water.

Experimentally determined solubilities range from 3.0×10^{-7} to 1.0×10^{-6} M at 25°C. The solubility-controlling solids were found to be mixtures of polymeric Pu(IV) and smaller amounts of plutonium carbonates. The solubilities measured at pH values of 6 and 7 are consistent with the data reported by Rai, Serne et al. (1980). However, the solubilities measured for a pH of 8.5 exceed those reported by Rai, Serne et al. for amorphous $Pu(OH)_4$ in 0.0015 M $CaCl_2$. This result suggests that carbonate complexation of plutonium is significant at a pH of 8.5 in the Yucca Mountain groundwaters.

At 60°C, the +6 oxidation state was dominant (> 80 percent) in the UE-25p #1 water at all three pH values. In J-13 water, the +5 and +6 oxidation states were present in nearly equal amounts (50 percent) at a pH of 7, whereas the +5 state dominated (60 percent) at a pH of 8.5 and the +6 state dominated (70 percent) at a pH of 6.

Experimentally determined solubilities at 60°C in J-13 water ranged from 2.7×10^{-8} M at a pH of 6 to 1.2×10^{-7} M at a pH of 8.5. For UE-25p #1 water, the solubilities ranged from 4.5×10^{-7} M at a pH of 7 to 1.0×10^{-6} M at a pH of 8.5. The solubility-controlling solids at 60°C were found to be amorphous Pu(IV) polymer and PuO_2.

Finally, there are americium solubility values for Yucca Mountain site-specific conditions as well (Nitsche, Gatti et al. 1993). As noted above, these experiments were done ultimately at high ionic strength and with Am as a tracer in a Nd/Am mixture. Given that the solubility-limiting solid state is $AmOHCO_3$, the effect of the ionic-strength differences should be relatively small, and these numbers (Table 6.3-3) are the best site-specific values available. However, some outliers, especially at 60°C, should be viewed with caution. In general, though, these site-specific numbers are similar to slightly less than the thermodynamic values measured by Felmy et al. (1990) for $P_{CO_2} = 10^{-3.5}$ atm.

According to Nitsche, Gatti et al. (1992) and Nitsche, Roberts, Prussin et al. (1994), the solubilities of americium compounds in solutions representative of water compositions expected within Yucca Mountain are approximately 1 to 2×10^{-9} M in J-13 water and 3 to 30×10^{-7} M in

UE-25p #1 water as a function of pH at 25°C. At 60°C, the solubilities of americium compounds were 1 x 10^{-8} to 2.5 x 10^{-6} M in J-13 water and 7 x 10^{-10} to 3 x 10^{-9} M in UE-25p #1 water as a function of pH. The solubility-controlling solids were found to be hexagonal and orthorhombic forms of $AmOHCO_3$. The speciation of americium in these solutions could not be determined due to the low solubilities of americium in these water compositions relative to the detection limits of the available spectroscopic techniques. Preliminary modeling calculations with the speciation code EQ3 suggest that carbonate complexes dominate in both J-13 and UE-25p #1 waters at 25° and 60°C (Ogard and Kerrisk 1984).

6.3.2.2 Solid State and Solution Speciation

Measurements of the solubility-limiting solid of Yucca Mountain solubility experiments have been performed with x-ray diffraction (XRD), Raman vibrational, and x-ray absorption (XAS) techniques. For neptunium, the sodium neptunyl carbonates found in earlier studies (Nitsche, Gatti et al. 1993) are unlikely to be formed in the low ionic-strength J-13 water. Other Np(V) solids such as Np_2O_5 and/or NpO_2OH(am) have been indicated to be the solubility-limiting solid phase in J-13 (Efurd, D.W. et al. 1996; Efurd, D.W. et al., "Measured Solubilities and Speciation of Neptunium and Plutonium in J-13 Groundwater," *Environmental Science and Technology*, unpublished). No evidence for Np(IV) solids, such as NpO_2, have been observed yet, even though thermodynamic modeling suggests this is the most stable solid (see Subsection 6.3.2.3). The solution species are dominated by two species, NpO_2^+ and $NpO_2CO_3^-$, at about equal proportions for a pH of 8.5 in J-13 water. For plutonium, the solid phase is best described as poorly crystalline PuO_2, with higher crystallinity for the higher-temperature solutions Efurd et al.(1996; Efurd, D.W. et al., "Measured Solubilities and Speciation of Neptunium and Plutonium in J-13 Groundwater," *Environmental Science and Technology*, unpublished). The presence of $Pu(OH)_4$(am) is also possible, especially on the surface of the precipitate (Efurd, D.W. et al., "Measured Solubilities and Speciation of Neptunium and Plutonium in J-13 Groundwater," *Environmental Science and Technology*, unpublished; see modeling in Subsection 6.3.3), as is the presence of a binary oxide containing Pu(VI) (Stakebake et al. 1993; Haschke and Ricketts 1997). The solution phase contains the suite of oxidation states (Nitsche, Gatti et al. 1993), including the plutonium colloid. Much of the colloid was filtered out of the solution before counting and was, therefore, not included in the soluble Pu concentration figures. Finally, the americium precipitation solid has been reported to be $AmOHCO_3$ (Nitsche, Gatti et al. 1993), although the presence of two different phases (orthorhombic and hexagonal) may require further scrutiny. Also, the trace nature of the americium in these experiments must always be kept in mind: the Nd phase was what was really determined. The suite of americium hydroxides and carbonates discussed above in the Am section applies here as well.

6.3.2.3 Thermodynamic Modeling

Different databases for Np exist. Using the Lemire-based data accepted into GEMBOCHS by the Yucca Mountain Project, NpO_2 is always the most thermodynamically stable solid in J-13 for pH values from 6 to 9 and temperatures from 20°C to 90°C (Janecky, Duffy et al. 1994; Janecky, Enter et al. 1995; Efurd et al. 1996; Efurd, D.W. et al., "Measured Solubilities and Speciation of Neptunium and Plutonium in J-13 Groundwater," *Environmental Science and Technology*, unpublished). This stability extends to an ionic strength of 0.1 M, at which point the sodium

neptunyl carbonate becomes stabilized. Other solids of calculated importance include (in decreasing importance) $Np(OH)_4$ (the hydrated amorphous form of NpO_2), NpO_2OH (am), and Np_2O_5 (the actually observed bulk solid). More recent calculations show that Np_2O_5 is a more reasonable choice for the solubilities actually measured and that Np(IV) solids do not have to be invoked to explain the solubility data (Efurd, D.W. et al., "Measured Solubilities and Speciation of Neptunium and Plutonium in J-13 Groundwater," *Environmental Science and Technology*, unpublished). The predicted solubility of PuO_2(c) is orders of magnitude below what is actually measured (Efurd, D.W. et al., "Measured Solubilities and Speciation of Neptunium and Plutonium in J-13 Groundwater," *Environmental Science and Technology*, unpublished), but the predicted solubility of $Pu(OH)_4$(am) is about right. It may be that although the bulk of the precipitate is PuO_2(c), the surface is coated to some extent with $Pu(OH)_4$, and this latter solid is the solubility-controlling one. Radiation damage to any real Am solid would make the predictions for Am difficult to compare to the actual data. However, modeling shows that $AmOHCO_3$(c) is just about at saturation for the experimental conditions reported by Nitsche, Gatti et al. (1993), whereas $Am(OH)_3$(c) and $Am(OH)_3$(am) are both significantly undersaturated (Janecky, Duffy et al. 1994).

The databases for the key aqueous radionuclide species are given in an appendix at the end of Subsection 6.3 (GEMBOCHS Thermodynamic Data). Because the NEA has published critically reviewed data for uranium and americium and soon will publish them for technetium, this tabulation includes only the GEMBOCHS data for neptunium and plutonium, with the neptunium section modified only slightly in recognition of YMP work on Np(V)-carbonate thermodynamic constants. The appendix lists the standard Gibb's free energy of formation, enthalpy of formation, and entropy for each species.

Abstracts to Performance Assessment–The values quoted in the above Tables 6.3-1 through 6.3-3 represent the best available site-specific numbers for performance assessment to use for Np, Pu, and Am. The values chosen were from NEA sources (Grenthe et al. 1992; Silva et al. 1995), YMP quality assurance sources tested with specific-ion interaction theory (e.g., Tait, Clark et al. 1996), and literature sources (e.g., Langmuir 1997). Note that the use of Efurd et al. 1996 (Efurd, D.W. et al. "Measured Solubilities and Speciation of Neptunium and Plutonium in J-13 Groundwater," *Environmental Science and Technology*, unpublished) values for Np and Pu give more consistent and smaller values than those of Nitsche, Gatti et al. (1993), which have been used in performance-assessment calculations to date. For oxidizing waters such as those expected at Yucca Mountain, radionuclide mobility cannot conservatively be limited by solubility for Tc and I. Uranium is an interesting case, and the solubility depends on the secondary phase that will precipitate. Langmuir (1997) favors the view that uranium solubility will be limited by the formation of uranophane ($Ca(H_3O)_2(UO_2)_2(SiO_4)_2{\cdot}3H_2O$(c)) to be about 10^{-7} M at Yucca Mountain. Other phases could also be suggested as potential controls on uranium. For example, in the high-silica groundwaters of Yucca Mountain, the solubility-controlling compound for uranium could be haiweeite ($Ca(UO_2)_2(Si_6O_{15})$ $(H_2O)_5$), according to available thermodynamic data (Bruton 1990, 1991). Interestingly, leaching experiments on uranium-oxide pellets (Bates, Tani et al. 1990) at 90°C using J-13 water produced a variety of phases on reacted surfaces that did not include haiweeite.

Ultimately, TSPA requires that radionuclide solubilities be extracted to simple terms that can be dealt with efficiently. Table 6.3-4 abstracts solubility values for radionuclides of concern. The elements listed include relevant radionuclides whose source terms could be solubility limited. The values used are from expert elicitations, primarily as cited by Triay, Meijer, Conca et al. (1997) and Langmuir (1997) but also Rechard (1995), and some new data are from Efurd et al. (1996).

6.3.3 Sorption And Sorption Modeling Studies

6.3.3.1 Batch-Sorption Data

Introduction–The solubility limits of radionuclides can act as an initial barrier to radionuclide migration from the potential repository at Yucca Mountain. However, once radionuclides have dissolved in water infiltrating the site, sorption of these radionuclides onto the surrounding tuffs becomes a potentially important second barrier. Thus, the study of the retardation of actinides and other key radionuclides is of major importance in assessing the performance of the potential repository.

Sorption actually comprises several physicochemical processes, including ion exchange, adsorption, and chemisorption. Determining whether sorption will occur requires knowledge of the likely flow paths of the groundwater and the spatial and temporal distribution of sorbing minerals along these paths. Evaluating the retardation effectiveness of sorption for repository design and licensing requires theoretical and quantitative understanding of sorption. Thus, experimental measurements of sorption with modeling of the data were combined in an attempt to identify key sorption mechanisms.

The use of batch-sorption experiments to obtain sorption distribution coefficients and to identify sorption mechanisms is fast, easy, and inexpensive compared to other types of sorption experiments. A disadvantage is the fact that such experiments are static in nature, whereas transport of radionuclides through the site is, obviously, a dynamic process. However, batch-sorption experiments are useful for bounding more detailed and mechanistic sorption studies, and a major part of the experimental effort was devoted to such measurements.

In the experiments, batch-sorption distribution coefficients were determined as a function of variables representing conditions expected beyond the region disturbed by waste emplacement. The variables included mineralogy, groundwater chemistry, sorbing element concentration, atmospheric conditions, and temperature. Batch-sorption results are very sample specific and, therefore, difficult to generalize and apply throughout the mountain. Deconvolution of sorption isotherms provides much greater detail about sorption sites (kind, number, specificity, and so forth), and this analysis was done for a number of the actinides. Such information is correlated with crystallographic data and related to specific sorption sites in the crystal structure. All sites are not equally selective for all sorbing species.

Also examined was the sorption behavior of individual pure minerals, such as zeolites and manganese or iron oxyhydroxides found in Yucca Mountain tuffs. This approach can help predict sorption coefficients along flow paths of known mineral content.

Linear Versus Nonlinear Sorption–The sorption distribution coefficient, K_d, for the species being sorbed, is the ratio of its concentration in the solid phase, F, to its concentration in the solution phase, C, which implies a linear relationship between the concentrations:

$$F = K_d C \quad . \qquad \text{(Eq. 6.3-1)}$$

Besides linearity, the valid use of sorption distribution coefficients in transport calculations also requires the sorption to be instantaneous and reversible, conditions that may or may not be met for the sorption of radionuclides onto Yucca Mountain tuffs.

Nonlinear adsorption isotherms have been reviewed by de Marsily (1986, p. 258). A useful nonlinear relationship, Freundlich's isotherm, is given by the equation

$$F = KC^{1/n} \quad , \qquad \text{(Eq. 6.3-2)}$$

where K and n are positive constants (with $n \geq 1$).

Another nonlinear relationship is Langmuir's isotherm, given by

$$F = \frac{K_1 C}{1 + K_2 C} \quad , \qquad \text{(Eq. 6.3-3)}$$

where K_1 and K_2 are positive constants. Part of the research was an attempt to assess the validity of using the linear distribution coefficients as opposed to other isotherm functional forms to describe retardation by sorption in transport calculations.

Mechanistic Models–A better understanding of the sorption of radionuclides onto tuff is possible if the data can be related to mechanistic models. Two general mechanisms are important: ion-exchange reactions that are primarily electrostatic in nature and surface complexation in which a relatively covalent chemical bond forms with the mineral surface. Ion exchange does not have the same degree of selectivity between aqueous ions of like charge as does surface complexation. The adsorption of metal ions via cation exchange will only occur on surfaces of opposite charge and so is affected by such common components of groundwater as sodium. Surface complexation, on the other hand, can occur even when the mineral surface charge is the same as the aqueous ion. Both of these processes can, in principle, be modeled using a triple-layer surface-complexation model. However, there are significant differences between the cation exchange in zeolites and clays and the formation of surface complexes on metal oxides, so cation exchange and surface complexation have been treated separately.

Physiochemical processes that might accelerate radionuclide migration relative to groundwater flow rates must also be quantified. For example, mineral surfaces in rock pores are predominantly negatively charged, so anions are typically repelled and can actually migrate through the rock faster than the average rate for the water. Such acceleration processes depend largely on the molecular complexation or speciation that occurs in solution. Accordingly,

detailed assessment of this possibility is needed to fully evaluate the potential for transport retardation by geochemical processes.

Experimental Procedures–All batch-sorption experiments were performed at room temperature. The procedure first involved pretreating the solid phase with the groundwater being studied (J-13 or UE-25p #1 well water or a synthetic bicarbonate groundwater) in the ratio of 1 g of solid to 20 mL of solution. The pretreated solid phase was then separated from the groundwater by centrifugation and exposed to 20 mL of a radionuclide solution (in the groundwater being studied) for approximately 3 weeks. After sorption, the phases were again separated by centrifugation.

The amount of radionuclide in solution initially and then after sorption was either determined with a liquid-scintillation counter (such as for neptunium and plutonium) or with inductively coupled plasma mass spectrometry (such as for uranium). The amount of radionuclide in the solid phase was determined by difference.

The liquid-scintillation counting technique that was used can discriminate alpha activity from beta activity. Consequently, no interference from beta emitters (such as ^{233}Pa, the daughter of ^{237}Np) is expected. Because the efficiency of this liquid-scintillation counter is approximately 100 percent, the counts per minute measured are approximately equivalent to disintegrations per minute.

As controls, container tubes without solid phases in them were used to monitor radionuclide precipitation and sorption onto the container walls during the sorption experiment. The difference in the concentration of the radionuclide in the initial solution and in the solution in the control tube generally was only a few percent, and then in either a plus or a minus direction.

Results for the plutonium solution did show a small amount of sorption onto the container walls. Even here, the difference in concentration between the initial plutonium solution and the plutonium solution in the control tube never exceeded 7 percent for the experiments reported. Nevertheless, in the case of plutonium, the amount of radionuclide sorbed in the solid phase was calculated by taking the difference of the final plutonium solution concentration both with the initial solution concentration and with the solution concentration in the control tube. The latter approach is conservative because plutonium may sorb to container walls only in the absence of the geologic material.

Batch-sorption experiments were performed under atmospheric conditions and inside glove boxes with a carbon-dioxide overpressure. The pH of the J-13 and UE-25p #1 waters under atmospheric conditions was approximately 8.5 and 9, respectively, and inside the glove boxes was 7 (the CO_2 overpressure was adjusted to bring the pH of both waters down to 7). Details of the experimental setup and the analytical techniques that were used in the sorption experiments are given in the YMP Detailed Procedures of the Los Alamos National Laboratory.

The Distribution Coefficient–The batch-sorption distribution coefficient, K_d, was calculated using

$$K_d = \frac{F}{C} = \frac{\text{moles of radionuclide per g of solid phase}}{\text{moles of radionuclide per mL of solution}} \quad \text{(Eq. 6.3-4)}$$

K_d thus has units of mL/g.

Determination of very small or very large batch-sorption distribution coefficients results in large uncertainties in the K_d values calculated. When very little sorption occurs, calculations can yield negative K_d values; the error results from subtracting two large numbers (the initial radionuclide concentration in solution and the radionuclide concentration after sorption) to obtain a small number (the amount of radionuclide left in the solid phase). Therefore, small K_d values not significant. On the other hand, when a great deal of sorption occurs, calculations can yield large uncertainties associated with measuring the small amount of radioactivity left in solution after sorption. Because of these uncertainties, most K_d values are only reported to one significant figure.

Plutonium

Behavior In Solutions Representative Of Yucca Mountain Groundwater–The speciation of plutonium in J-13 and UE-25p #1 waters could not be determined due to the low solubilities of plutonium in these water compositions relative to the detection limits of the available spectroscopic techniques. Modeling calculations with the EQ3 speciation computer code suggest that in J-13 water at 25°C the plutonyl ion and various carbonate complexes are most important at pH values from 6 to 7, whereas carbonate complexes and hydrolysis products are most important at a pH of 8.5 (Nitsche 1991). Speciation in the UE-25p #1 water has not been modeled.

It is noteworthy that the experimentally determined redox behavior of plutonium in solution was quite distinct from the behavior predicted on the basis of EQ3 calculations (Nitsche 1991). The causes for the differences in measured and calculated behavior have not been defined. They could involve various types of kinetic effects, including radiolysis effects, as well as the quality of the literature data in the EQ3 database. In any case, the uncertainties in our knowledge of the solution behavior of plutonium will make it difficult to properly interpret the sorption behavior of that element.

Qualitative Evidence For Behavior In The Surficial Environment–Although naturally occurring plutonium has been detected at ultratrace levels in the environment, there is little documentation of the chemical controls on the mobility of this plutonium. However, anthropogenic plutonium has been present in the environment for decades. Data on the environmental behavior of this plutonium provide some indications of the behavior to be anticipated for plutonium emplaced in the proposed repository at Yucca Mountain.

Various papers in the literature discuss the transport of plutonium in the surficial environment around process stream outfalls or burial sites (for example, Means et al. 1978; Price and Ames 1978; Polzer et al. 1983). Unfortunately, the data on plutonium transport discussed in these papers are difficult to apply to the Yucca Mountain site because the waste streams included various types of organic ligands (for example, EDTA (ethylenediaminetetraacetic acid) that tend to enhance the transport of plutonium at these sites). In addition, the initial pH of many of these waste streams was in the acid range (2–4). Low pH conditions are not expected in the Yucca Mountain flow system. Organic ligands may be present at trace levels in this flow system, but they are not expected to play a major role in radionuclide transport.

The results of studies of plutonium transport in areas exposed to physical dispersal processes (for example, safety tests of nuclear weapons) are also difficult to interpret because of subsequent disturbances of the surface soils by wind, burrowing animals, construction activities, and so forth (for example, Essington et al. 1978).

More pertinent perhaps are the measurement of plutonium concentrations in oceanic sediments and their associated pore waters (Buesseler and Sholkovitz 1987). Such studies invariably yield sorption coefficients for plutonium in the range of 10^3 to 10^5 mL/g with the lower values observed in the more oxidized sediments. Given the high ionic strength of seawater (that is, the pore waters), these data suggest that ionic-strength effects are not an issue in the plutonium sorption behavior in natural systems. However, complexation of plutonium by carbonate can be significant and appears to be the cause for elevated plutonium activities in several high alkalinity (0.3 to 3.0 M) lakes in the western United States (Sanchez et al. 1985). Because alkalinity values are expected to be orders of magnitude lower within the Yucca Mountain flow system relative to the levels found in these lakes, carbonate complexation in the solution phase should not be an issue at this site.

The question of concern to the present study is how groundwater compositional parameters will effect this redox disequilibrium and, in turn, the sorption behavior of plutonium. In the disproportionation experiments reported by Newton et al. (1986) and in the solubility experiments reported by Nitsche, Gatti et al. (1992) and Nitsche, Roberts, Prussin et al. (1994), plutonium concentrations in the experiments were sufficiently high that radiation effects were evident. An important question is "If plutonium is present at trace levels and not in contact with a 'pure' plutonium compound, are disproportionation reactions still a factor?" If they are not, then the next question would be "What is the stable oxidation state of plutonium when it is present at trace levels in Yucca Mountain groundwaters?" If the +5 or +6 oxidation states of plutonium are the dominant stable states in groundwaters such as those found within Yucca Mountain, as suggested by the experiments of Nitsche, Gatti et al. (1992) and Nitsche, Roberts, Prussin et al. (1994), then plutonium might be as mobile as neptunyl in the far-field of the potential repository, assuming it is present as the plutonyl ion or its complexes. On the other hand, if the +4 or +3 oxidation states are the dominant stable states in these groundwaters, this element would likely behave as other +3 and +4 actinides and be strongly sorbed with minimal migration potential.

Data From Laboratory Sorption Experiments–The data discussed in this section are provided to show trends for the sorption of plutonium. The data used in relation to the YMP are on Yucca Mountain tuffs only. Allard (1982) reported results on experiments involving plutonium

sorption on quartz, apatite, attapulgite, montmorillonite, and various minerals rich in ferrous iron in a dilute groundwater containing plutonium at 1.8×10^{-11} M. For all the minerals, the sorption coefficients were greater than 10^3 mL/g over a pH range from 4 to 9. Apatite, attapulgite, biotite, and montmorillonite showed sorption coefficients greater than 10^4 mL/g over this pH range. Torstenfelt et al. (1988) presented data for plutonium sorption on feldspars, clays, and granite in contact with J-13 water. The sorption coefficients reported by them are generally between 100 to 200 mL/g in neutral to alkaline solutions. These authors emphasized the importance of proper experimental technique in the determination of sorption coefficient values for plutonium and noted the potential for colloid formation in these types of experiments. Data indicating high affinity of plutonium for ferric oxyhydroxide, manganese oxide, and carbonate mineral surfaces were presented by Means et al. (1978), Keeney-Kennicutt and Morse (1985), and Sanchez et al. (1985). Means et al. noted that manganese oxides sorb plutonium more strongly than ferric oxyhydroxides in natural environments (presumably as a result of redox reactions on the manganese-oxide surface).

Measurements of plutonium sorption coefficients involving Yucca Mountain rock samples and J-13 groundwater were summarized by Thomas (1987). The following observations are considered the most significant. First, the values measured for the plutonium sorption coefficient range from 20 to greater than 4,500 mL/g with most values lying between 100 to 2,000 mL/g at a pH of from 8.2 to 8.8. Second, the coefficients determined during the desorption experiments were occasionally in the range of the sorption coefficient values, but more typically, they were 10 to 20 times larger, reflecting the irreversibility of the sorption reactions. Third, zeolitic samples typically had lower sorption-coefficient values than vitric or devitrified samples. It appears that rocks that have essentially no reduction capacity remaining (that is, samples lacking ferrous iron or sulfide) show the lowest sorption coefficients for plutonium. Fourth, samples with calcite or clay showed the largest sorption coefficients (> 4,500 mL/g for samples with 30 percent calcite). Fifth, based on the six to eight experiments for which data are available, there was up to a factor of twelve variation in sorption coefficients as a function of groundwater composition. Water from Well UE-25p #1 was associated with the largest values (240 to 540 mL/g, sorption-desorption) with waters from Wells H-3 and J-13 showing the lowest values (20 to 230 mL/g). The higher values obtained with UE-25p #1 water may reflect calcite precipitation. Sixth, there did not appear to be a dependence of the sorption coefficient on pH over the range from 7 to 9, although the available data are limited on this issue. Seventh, there was less than a factor of four dependence of the sorption coefficient on radionuclide concentration over the range from 10^{-9} to 10^{-12} M.

Conclusions that can be drawn from these data include:

The plutonium sorption coefficient will be greater than 100 mL/g for most of the groundwater and rock compositions likely to be encountered within Yucca Mountain.

- Calcite and clay promote plutonium sorption/co-precipitation and may retard plutonium migration in fractures.

- The redox state of the groundwaters and of the rock units in which they occur may be critical to the sorption behavior of plutonium.

The sorption of plutonium onto the three main types of tuff in J-13 water was studied (under oxidizing conditions) using a carbon-dioxide overpressure (to obtain a pH of 7). To identify the sorbing minerals in the tuffs, sorption onto the pure minerals hematite, clinoptilolite, albite, and quartz was also studied. The results of the batch-sorption experiments for plutonium are summarized in Figure 6.3-1. Because plutonium sorbs onto nongeologic media, the batch-sorption distribution coefficients reported in Figure 6.3-1 are based on the concentration of plutonium in the control solutions. The affinity of tuffs for plutonium at a pH of 7 in decreasing order is zeolitic > vitric > devitrified. The affinity of minerals for plutonium in decreasing order is hematite > clinoptilolite > albite > quartz. Inspection of Figure 6.3-1 indicates that plutonium sorption is nonlinear in the concentration range from 6×10^{-9} to 2×10^{-7} M.

Nitsche, Gatti et al. (1993) report that even when a plutonium solution in J-13 or UE-25p #1 water is prepared starting in the +4 oxidation state, the predominant final oxidation state is +5, or Pu(V). The solution used for plutonium sorption experiments was prepared from a well-characterized Pu(V) acidic stock in J-13 well water. Consequently, it would be reasonable to assume that, during the short time of the sorption experiment, the plutonium would have remained predominantly in the +5 oxidation state, although over the long term, the plutonium may not remain in that state.

Comparison of the data in Figure 6.3-1 with the results of similar experiments with neptunium and uranium indicates that significant plutonium sorption occurred in tuffs and minerals that exhibit very small sorption of Np(V) and U(VI). This result is very puzzling; if plutonium in J-13 well water is predominantly Pu(V) and Pu(VI), it is expected that its sorption behavior would have been similar to that observed for Np(V) and U(VI). Several possible explanations of the plutonium sorption results are:

- Nitsche's data for the oxidation states are incorrect, and the predominant plutonium oxidation state in J-13 well water at a pH of 7 is Pu(IV), not Pu(V) and Pu(VI).
- The Pu(IV) species is what sorbs from J-13 water but a re-equilibration in the solution phase produces more Pu(IV) to maintain equilibrium (which implies that the kinetics of plutonium speciation in solution are fast).
- Pu(V) and Pu(VI) reduce to Pu(IV) at solid surfaces (as a result of changes in the solution redox potential in the presence of the solid phases).

The sorption of plutonium onto tuffs and minerals in J-13 and synthetic UE-25p #1 water under atmospheric conditions was studied as a function of time and initial plutonium solution concentration (Figure 6.3-2 shows an example). Inspection of this figure indicates that plutonium sorption is extremely slow (possibly due to a redox reaction at the solid surface). Even after 32 days of sorption, equilibration had not been achieved. The sorption of plutonium onto the tuffs and minerals is very substantial.

Table 6.3-5 summarizes the ranges for sorption distribution coefficients in Yucca Mountain groundwaters for plutonium. The sorption isotherms for plutonium (Figure 6.3-3 to 6.3-18) indicate that plutonium sorption as a function of radionuclide concentration cannot be expressed using a K_d; the isotherms are generally nonlinear. However, given the high affinity of Yucca

Mountain tuffs for plutonium and the other observations made in this study, it appears that using a K_d to predict plutonium radionuclide transport in performance-assessment calculations will provide conservative predictions for the release of radionuclides.

Conclusions Regarding Sorption Behavior With Respect To Expected Variations In Groundwaters–On the basis of the discussion in the previous subsections, it appears the most important groundwater compositional parameter in relation to plutonium sorption is the redox potential. Closely related to this parameter is the abundance of ferrous iron in the rock units. Note that redox potentials in groundwaters may not reflect equilibrium with the host rock (Lindberg and Runnells 1984). Complexation reactions with inorganic ligands in solution and variations in solution pH appear to have less significant impacts on the sorption behavior of plutonium in Yucca Mountain rock-water systems.

Cesium, Radium, and Strontium

Behavior In Solutions Representative Of Yucca Mountain Groundwaters–These elements show relatively simple solution behavior in typical groundwaters. They are not subject to changes in oxidation state in the groundwater compositions expected in Yucca Mountain. Radium and cesium are invariably present as the simple Ra^{2+} and Cs^{+} cations in the expected groundwater compositions (Ogard and Kerrisk 1984). Strontium exists primarily as the Sr^{2+} ion in these waters but may also be present as the neutral aqueous species $SrSO_4$ at concentrations of a few percent of the total strontium solution concentration (Ogard and Kerrisk 1984). The data of Langmuir and Riese (1985) indicate that $RaSO_4/Ra^{2+}$ will be greater or equal to 0.6 when the sulfate ion concentration is greater than 10^{-3} M. These numbers suggest that $RaSO_4$ will be a significant species ($RaCO_3$ and $SrCO_3$ may also be significant).

Qualitative Evidence For Behavior In The Surficial Environment–The literature on the behavior of cesium, radium, and strontium in the surficial environment is voluminous and will not be reviewed here. Their sorption behavior is fairly well understood and is largely controlled by ion-exchange reactions (Bolt and Bruggenwert 1976), although surface-complexation reactions involving these elements have also been discussed (for example, Balistrieri and Murray 1982). The dominant controls on the ion-exchange reactions are the cation-exchange capacities of the minerals in the system, the abundances of these ion-exchanging minerals, their selectivity coefficients for the various cations in the solution phase, and the concentrations of the competing cations in the solution phase. The selectivity of most clays and zeolites for cesium, radium, and strontium is greater than the selectivities for the major cations in solution. Further, pH does not have a significant effect on the sorption behavior of these elements over the pH range of interest. Because their sorption behavior is fairly well understood and because this behavior depends strongly on local conditions, data from sites other than Yucca Mountain will not be reviewed here.

Data From Laboratory Sorption Experiments–Sorption coefficients for cesium, radium, and strontium were reviewed by Daniels et al. (1983), Thomas (1987), and Meijer (1990). For cesium at low concentrations (10^{-8} M), sorption coefficients are greater than 100 mL/g for all water-rock combinations tested except UE-25p #1 water in contact with vitric tuff (Knight and Thomas 1987). Cesium sorption coefficients for the devitrified-tuff/J-13-water system show a

clear concentration dependence that has been modeled with a Fruendlich isotherm (Polzer and Fuentes 1988). The coefficients for this particular rock-water system are greater than 100 mL/g for cesium solution concentrations below 5 x 10^{-5} M. For UE-25p #1 water in contact with this rock type, the coefficient would be 100 mL/g at somewhat lower solution concentrations. In any case, in the higher ionic-strength waters (0.02 eq/L), including unsaturated-zone waters, the sorption coefficients for cesium on devitrified and vitric samples may be less than 100 mL/g if solution concentrations of cesium exceed 10^{-6} M. For zeolitic tuffs, cesium sorption coefficients are greater than 100 mL/g for all water compositions and cesium concentrations anticipated in the potential repository environment.

Radium appears to have a somewhat higher affinity for sorption onto Yucca Mountain tuffs than cesium. In addition, the solubility of $RaSO_4$ limits the concentrations in solution to trace levels (1027–1028 M; Ogard and Kerrisk 1984). At concentrations below the solubility limit for RaSO4, sorption coefficients for radium are greater than 100 mL/g in essentially all rock-water combinations tested, using barium as an analog for radium (Knight and Thomas 1987). This fact suggests that a minimum sorption coefficient of 100 mL/g can be used for radium in all rock-water systems. For zeolitic samples, minimum values of 1,000 mL/g can be used.

Strontium sorption behavior is more sensitive to mineral and water compositions than the other two elements discussed in this subsection. For devitrified and vitric tuffs, sorption coefficients for the higher ionic-strength waters (such as UE-25p #1) are in the range of 10 to 30 mL/g (Knight and Thomas 1987). These sorption coefficients will decrease as the solution concentration of strontium is increased above approximately 10^{-5} M (Thomas 1987). However, this concentration is close to the solubility limit for $SrCO_3$ in these waters so that the 10 to 30 mL/g range is likely appropriate for use in performance-assessment calculations in the devitrified or vitric tuffs. For zeolitic tuffs, a minimum value of 1,000 mL/g would be appropriate (Knight and Thomas 1987).

Conclusions Regarding Sorption Behavior With Respect To Expected Variations In Groundwaters–The existing sorption-coefficient database for cesium, radium, and strontium should be adequate for performance-assessment calculations. The main concern would be the concentration of cesium in the solution phase in contact with devitrified and vitric tuffs. If this concentration is over 10^{-5} M, the appropriate value for the sorption coefficient may be less than the minimum recommended value of 100 mL/g. The sorption coefficients for strontium in devitrified and vitric tuffs will be as low as 10 to 30 mL/g in higher ionic-strength waters. If additional experiments were to be carried out for this group of elements, they should focus on strontium in contact with devitrified and vitric tuffs in the higher ionic-strength waters.

Nickel and Lead

Behavior In Solutions Representative Of Yucca Mountain Groundwaters–The aqueous solution behavior of nickel and lead is relatively simple. Within the range of groundwater compositions expected in the Yucca Mountain flow system, these elements are present in solution primarily as simple divalent cations. Several percent of the total nickel concentration will be present as the $NiSO_4^+$(aq) complex. [NOTE: Take charge off NiSO4]. $NiCO_3$ may also be a significant

aqueous species. Similarly, several percent of the total lead concentration will be present as the $PbCl^+$ complex.

Qualitative Evidence For Behavior In The Surficial Environment–The behavior of nickel and lead in the surficial environment has been studied in some detail (for example, Snodgrass 1980). These elements are generally quite particle-reactive. The dominant mechanisms that control their sorption behavior are ion exchange on clay minerals (for example, Bowman and O'Conner 1982) and adsorption onto various oxides (for example, Theis and Richter 1980). The selectivities of clay minerals for nickel and lead are large relative to the major cations (such as Mg^{2+}) in typical groundwaters (Decarreau 1985). Solution compositional parameters that can influence this adsorption behavior include pH, ionic strength, concentrations of competing ions, and concentrations of complexing agents (see review by Rai and Zachara 1984).

Data From Laboratory Sorption Experiments–Data on the sorption behavior of nickel in Yucca Mountain rock-water systems were reported by Knight and Lawrence (1988). Sorption and desorption ratios were determined in several water compositions in the pH range from 8.3 to 9.0 with nickel concentrations in solution of approximately 10^{-8} M. For devitrified and zeolitic samples, sorption coefficients were in the range of 200 to 400 mL/g. Sorption coefficients obtained in the desorption step were generally a factor of two larger than the sorption coefficients. In the only vitric sample analyzed, sorption coefficients ranged from approximately 30 to 70 mL/g. For the desorption step, the coefficients were in the range of 33 to 72 mL/g for this rock type. References to the adsorption behavior of lead on tuffaceous or even granitic rock samples were not found.

Data on sorption of transition metals on synthetic zeolites suggest that Pb^{2+} has a high affinity for ion exchange compared with Sr^{2+}, whereas Ni^{2+} has a lower affinity relative to Sr^{2+} (Barrer and Townsend 1976; Obeng et al. 1981; Blanchard et al. 1984). This result suggests the zeolitic zones within Yucca Mountain could be significant barriers to lead migration.

Conclusions Regarding Sorption Behavior With Respect To Expected Variations In Groundwaters–Based on information in the literature, the sorption behavior of these elements will be determined largely by the free-ion activities in solution and the cation-exchange capacity of the host rock (for example, Bowman and O'Connor 1982; Rai and Zachara 1984). Solution pH and oxide-mineral abundances may be a factor in rocks in which nickel and lead sorb primarily by surface-complexation mechanisms. In any case, lead appears to sorb more strongly than nickel in most surficial environments, and both elements appear to sorb more strongly than strontium (Bowman and O'Connor 1982). The nickel sorption coefficients discussed in the previous subsection could reasonably be used as default values for lead in performance-assessment calculations. For nickel, a minimum sorption coefficient of 100 mL/g could be used in the devitrified and zeolitic zones. For the vitric zones, the performance-assessment calculations could be done using random sampling and a normal distribution ranging from 0 to 50 mL/g.

Neptunium, Protactinium, Selenium, and Uranium

The main factor that neptunium, protactinium, selenium, and uranium have in common is that they all tend to show small values for sorption coefficients in the rock-water systems expected

within Yucca Mountain under oxidizing conditions. Under more reducing conditions, they would all have much lower solubilities and higher sorption affinities in Yucca Mountain groundwaters. As the solution and sorption behavior is somewhat different for each of these elements, they will be discussed separately.

Neptunium

Behavior In Solutions Representative Of Yucca Mountain Groundwaters–In solutions representative of water compositions expected within the Yucca Mountain flow system, neptunium will be predominantly in a +5 oxidation state. Unlike pentavalent niobium and protactinium, Np(V) compounds are relatively soluble (Nitsche, Roberts, Prussin et al. 1994). This result appears to be due to the formation of the oxocation NpO_2^+ in solution. Pentavalent niobium and protactinium apparently do not form analogous oxocations (that is, NbO_2^+ and PaO_2^+) in near-neutral solutions to an appreciable degree. Instead they hydrolyze and form insoluble precipitates. The NpO_2^+ ion appears to be quite stable in aqueous solutions (Cotton and Wilkinson 1988).

Nitsche, Gatti et al. (1992) and Nitsche, Roberts, Prussin et al. (1994) studied the solubilities and speciation of neptunyl compounds in solutions representative of water compositions expected within Yucca Mountain. The results at 25°C and several pH values are summarized in Table 6.3-6. The solubility-controlling solids were found to be hydrated sodium neptunyl carbonates, and the primary species for the water compositions expected at Yucca Mountain were NpO_2^+ and $NpO_2(CO_3)^-$. The speciation results of Table 6.3-6 for J-13 water are similar, although not identical, to those calculated using the EQ3 speciation code (Nitsche 1991).

At higher temperatures (60° and 90°C), neptunium was less complexed by carbonate at pH values of 6 and 7 but more highly complexed with carbonate at a pH of 8.5. The solubilities at 60°C were similar to those in Table 6.3-6, although they were somewhat higher at a pH of 8.5 relative to the 25°C results.

The neptunium solubility experiments were repeated by D.W. Efurd et al. 1996 (D.W. Efurd et al. "Measured Solubilities and Speciation of Neptunium and Plutonium in J-13 Groundwater," *Environmental Science and Technology*, unpublished) from oversaturation using an experimental approach that limited the amount of Na^+ in solution and maintained the ionic strength as close to that of J-13 water as practical. This approach resulted in lower solubilities for neptunium (see Table 6.3-1) and in steady-state solids containing Np_2O_5 and a salt of neptunium. There is a possibility, however, that the correct long-term solubility-limiting solid in waters typical of Yucca Mountain should be Np in the +4 rather than the +5 oxidation state, and experiments are continuing in an attempt to settle this uncertainty.

Qualitative Evidence For Behavior In The Surficial Environment–Although ^{237}Np has been detected in the surficial environment (for example, Sakanoue 1987), essentially no information has been found on its transport behavior in this environment.

Data From Laboratory Sorption Experiments–Laboratory experiments have been carried out on neptunium sorption with a variety of rock and mineral types and solution compositions. The

results of neptunium sorption experiments with pure mineral separates have been reported by Allard (1982), Meijer, Triay et al. (1989), Triay, Robinson, Lopez et al. (1993), and others. On the basis of these results, it is evident that neptunium has a high affinity for ferric oxides and oxyhydroxides, apatite, and attapulgite (a magnesium-rich clay). It has a somewhat lower affinity for carbonates (such as calcite), sulfates (for example, anhydrite) and manganese minerals (for example, cryptomelane). It has a low affinity for most silicate minerals. Neptunium also shows high affinities for minerals that contain ferrous iron (such as pyrite, olivine, augite, magnetite, hornblende, epidote, biotite, and chlorite). This affinity is likely due to the reduction of Np^{5+} to Np^{4+} by Fe^{2+} on the surfaces of these minerals. Although ferrous iron-bearing minerals are, at best, minor species in Yucca Mountain tuffs (Bish and Chipera 1989), they could be of considerable significance to neptunium sorption.

In addition to the nature of the available mineral surfaces, it is also evident that pH is a critical parameter. In general, neptunium sorption increases with increasing pH. This effect is particularly evident in the experiments with iron oxyhydroxides (for example, Combes et al. 1992). However, similar behavior is evident in the sorption experiments with silicate minerals. In the latter case, the sorption edge (as a function of pH) is located at a higher pH (8–9) than the edge associated with the ferric oxyhydroxides (a pH of 6–7). Data reported by Combes et al. (1992) suggest neptunium is sorbed as an inner-layer complex on ferric oxyhydroxide.

Neptunium does not appear to have a high affinity for ion-exchange reactions on clays and zeolites (Allard 1982; Triay, Robinson, Lopez et al. 1993). This phenomenon may be due to the small charge-to-radius ratio and the large size of the neptunyl ion.

The results of neptunium sorption experiments involving Yucca Mountain rock and water samples have been reported by Daniels et al. (1982), Thomas (1987, 1988), and Triay, Robinson, Lopez et al. (1993). These experiments indicate that neptunium has a low affinity (for example, K_d values of 0 to 5 mL/g) for the surfaces in Yucca Mountain tuffs over most of the pH range and water compositions expected in the Yucca Mountain flow system. The sorption mechanisms are apparently not entirely reversible as coefficients obtained from desorption experiments are commonly larger than those obtained from sorption experiments even though the isotherms are linear in the concentration range covered by these experiments. There is some indication of increased sorption coefficients (5 to 40 mL/g) at the highest pH values (8.5 to 9.0). Torstenfelt et al. (1988) suggest that this result reflects increased hydrolysis of the neptunyl ion, resulting in an increase in surface-adsorption reactions. However, in Yucca Mountain rock-water systems, it could also reflect increased potential for calcite precipitation at high pH.

In the pH range from 6.5 to 8.5, the small but consistent affinity of neptunium for the tuffs most likely reflects the existence of a limited number of favorable adsorption sites for neptunium. This number apparently does not involve ion-exchange sites because zeolitic rock samples also show low sorption coefficients. For example, Thomas (1988) describes a case in which a zeolitic tuff sample (G4-1608) with a cation-exchange capacity of approximately 1.5 meq/g appears to have essentially the same affinity for neptunium as a devitrified tuff sample (GU3-433) with an exchange capacity of approximately 0.02 meq/g. These sites are apparently not present in the same abundance on all tuff samples. That is, some zeolitic, vitric, and devitrified tuff samples have almost no affinity for neptunium over the pH range from 6.5 to 8.5, whereas other samples with similar proportions of major minerals show sorption coefficients in the range of

5 to 10 mL/g. This result suggests, but does not prove, that the favorable sites are associated with some minor primary or secondary phase that has variable abundance. Hematite and calcite are candidates for this phase based on pure mineral studies. Because ferric oxides are present at trace levels in most of the rock units within Yucca Mountain, they could be the source of the low but consistent values (0.5 to 2 mL/g) observed in experiments on devitrified and zeolitic tuffs. Alternatively, neptunium may be sorbed (through reduction to Np^{4+}) by the small amounts of ferrous-iron-bearing minerals present in the rock samples used in the sorption experiments.

The increased sorption of neptunium on tuffaceous samples known to contain calcite suggests this mineral is of considerable potential significance to neptunium sorption on Yucca Mountain tuffs. If so, prediction of the adsorption behavior of neptunium will depend on knowledge of the surface areas of calcite in the various hydrologic units or on the saturation state of calcite in groundwaters present in these units.

Because even small amounts of calcite appear to significantly increase neptunium sorption coefficients, current mineral identification techniques may not be adequate for prediction of neptunium sorption behavior. A more viable approach may be to determine the calcite saturation level in the various groundwater compositions expected within Yucca Mountain. If calcite is saturated or oversaturated in a given groundwater, the upper end of the range of experimentally determined sorption coefficients could be used with the assumption that neptunium will either co-precipitate with calcite or adsorb to calcite surfaces. Alternatively, if calcite is undersaturated in a given water, the lower end of the range could be used under the assumption that neptunium is sorbed on oxides, such as ferric or ferrous oxides. For vitric units lacking iron oxides and calcite, neptunium may not be sorbed at all.

The sorption of Np(V) onto samples of the three types of tuff in J-13 water (under oxidizing conditions) was studied at two pH values (7 and 8.5). However, to identify the sorbing minerals in the tuffs, sorption onto the pure minerals hematite, clinoptilolite, albite, and quartz was also studied. It was found that neptunium in J-13 water does not sorb onto devitrified and vitric tuffs, albite, and quartz (Table 6.3-7).

The initial neptunium concentrations for the data reported in Table 6.3-7 ranged from 1×10^{-7} to 3×10^{-5} M. Wet-sieved tuffs, albite, and quartz samples with particle sizes in the range from 75 to 500 μm, were used. The pretreatment period lasted 2 to 3 days, and the sorption period, 2 to 4 days. The negative values reported in the table are a result of the analytical error for the case of very little sorption (that is, a small number is obtained as the difference of two large numbers).

For the experimental conditions cited earlier, the sorption of neptunium onto zeolitic tuffs and clinoptilolite appears to be linear in the concentration range from 1×10^{-7} to 3×10^{-5} M and can be fitted using a K_d (Figure 6.3-19 and 6.3-20). The sorption of neptunium onto zeolites is higher at a pH of 7 than a pH of 8.5, which might be explained by the larger amount of NpO_2^+ relative to $NpO_2CO_3^-$ in J-13 well water at a pH value of 7 than at a pH value of 8.5.

As has been pointed out, one surprise for neptunium is the relatively small amount of sorption (values of K_d ranging from 1.5 to 3 mL/g) compared to the large amount expected for a cation-exchange sorption mechanism in a zeolite with a large cation-exchange capacity (such as

clinoptilolite). This result indicates that the sorption mechanism for neptunium onto clinoptilolite is a surface reaction rather than cation exchange where only the accessible cations within the zeolite surface are involved. One possible explanation is steric: the shape and large size of the neptunyl cation prevents cation exchange. This ion likely has a trans-dioxol configuration normal to a puckered equatorial ring containing six bound water molecules.

The experiments with pure clinoptilolite indicate that sorption increases with decreasing pH for Np(V). Because the major constituent of tuff G4-1510 is clinoptilolite, predictions of the K_a (K_d divided by the solid-phase surface area) were made for neptunium sorption onto this tuff by assuming that clinoptilolite is the only sorbing phase. Table 6.3-8 shows measured and predicted values of K_a for the clinoptilolite-rich tuff G4-1510 at two different pH values. Because sorption is correlated with surface area, similar calculations (Table 6.3-9) were made for a series of tuff samples containing various amounts of clinoptilolite for which the surface area had been measured. The values in the two tables indicate that reasonable predictions can be made based on neptunium sorption data for pure clinoptilolite (assuming clinoptilolite is the only sorptive mineral).

The sorption of neptunium onto pure iron oxides is very large (measured values of K_d for hematite range from 100 to 2000). Although the sorption onto the pure iron oxide hematite is very large, neptunium sorption onto devitrified tuffs, which appear to have traces of hematite (1 percent ± 1), is essentially zero. This result could be due to differences in the surface of pure hematite compared to hematite in tuff. It could be due to passivation of the hematite surfaces in the tuff by elements (such as the rare earths) that have a higher affinity for hematite than neptunium and, thus, occupy the sorption sites. Also, perhaps the sorption is not occurring because there is no hematite present in the tuffs (concentrations are within experimental error).

Sorption was investigated as a function of sieving procedure for devitrified (G4-270) and zeolitic (G4-1506) tuffs in J-13 and UE-25p #1 well waters. Data presented in Figure 6.3-21 indicate that wet-sieving probably eliminates small particles that cause artificially high K_d values. As previously determined by Rogers and Chipera (1994), the optimal batch-sorption procedure involves wet-sieving the tuff samples to a size of 75 to 500 μm. Figure 6.3-22 illustrates the problem that could arise when sorption experiments are performed with pure minerals consisting of very finely divided particles that cannot be wet-sieved. The neptunium batch-sorption coefficients determined vary by more than an order of magnitude between the dry- and the wet-sieved natural calcite. The potential differences in surface area and particle size between a pure mineral and that same mineral in the tuff samples may make predictions of sorption behavior on whole rock impossible when the basis of those predictions is pure mineral work. As illustrated in Figure 6.3-22, the trends in sorption as a function of concentration and groundwater chemistry stay the same regardless of whether dry- or wet-sieved calcite is used.

Consequently, the most effective use of pure mineral sorption data is the identification of trends in the sorptive behavior of a mineral. Figures 6.3-21 and 6.3-22 also illustrate the effect of water chemistry on neptunium sorption; for example, the sorption of neptunium onto zeolitic tuffs decreases considerably with the increasing carbonate content and ionic strength of the UE-25p #1 water. The reverse trend is observed for calcite samples.

The kinetics of neptunium sorption onto tuffs and pure minerals were investigated and it was found that the sorption of neptunium onto tuffs and clinoptilolite appears to be fast (Figure 6.3-23). Although the data are scant, they can be used as guidelines. No significant differences are observed in neptunium sorption as a function of time for the tuffs studied and for clinoptilolite. This is not the case for pure minerals that tend to sorb by means of a co-precipitation mechanism (such as calcite) or by surface complexation (such as hematite). Figures 6.3-24 and 6.3-25 show the sorption dependence with time for calcite and hematite in waters from the Wells J-13 and UE-25p #1. The dissolution/precipitation reactions that may accompany the co-precipitation of neptunium with calcite may be slow compared with other sorption mechanisms. Future experiments will address this issue by monitoring the chemistry of the groundwater as it is being equilibrated with these minerals.

Figures 6.3-26 and 6.3-27 give further data from the investigation of the dependence of neptunium sorption on pH in J-13 water. The figures show that for vitric tuffs (such as samples G2-767 and GU3-1407), pH does not seem to make a significant difference in the amount of neptunium sorption measured. Likewise, the sorption of neptunium onto devitrified tuffs (such as sample G4-270) in J-13 is not affected by pH. Samples G2-1813, G2-1951, G2-2000, and G2-2222 are zeolitic tuffs, but until the X-ray powder diffraction analyses of these samples become available, it is difficult to know the relative amounts of clinoptilolite versus mordenite in each. However, tuff samples G4-1510 and G4-1395 consist of 59 percent and 22 percent clinoptilolite, respectively, and exhibit the same trend as clinoptilolite itself: an increase in sorption as the pH is decreased from 8.5 to 7, probably because of the increase of neptunyl cation concentration. As discussed earlier, these results seem to indicate that neptunium sorption onto clinoptilolite may follow an ion-exchange mechanism, but the fact that neptunium sorption on pure clinoptilolite is so small favors a surface-complexation reaction, even for this zeolite. Again, the reason may be that the hydrated neptunyl cation is too large to fit in the zeolite cages.

Also studied was the sorption of neptunium in UE-25p #1 water and it was found that, regardless of the conditions, neptunium sorption onto tuffs and zeolites is negligible (K_d <1 mL/g) in this water (Figure 6.3-28). If clinoptilolite is the only mineral affecting neptunium sorption, and if ion exchange at the surface is the dominating mechanism, it may be concluded that the reason for the lack of neptunium sorption on clinoptilolite is the formation of the neptunium carbonado complex ($NpO_2CO_3^-$) in UE-25p #1 water to the exclusion of the neptunyl cation. The data reported by Nitsche, Roberts, Prussin et al. (1994) do not support this conclusion (Table 6.3-6); the relative amount of neptunyl in UE-25p #1 water is larger than that in J-13 water at a pH of 7. If the data of Nitsche et al. are correct, another possible reason for the lack of neptunium sorption on clinoptilolite in UE-25p #1 water is competitive effects due to the larger ionic strength of that water compared with J-13 water, which has a smaller ionic strength by nearly an order of magnitude.

As mentioned earlier, iron oxides have a high affinity for neptunium (Combes et al. 1992). Figure 6.3-29 shows further data on the sorption of neptunium onto hematite, this time in both J-13 and UE-25p #1 waters as a function of pH. It is important to note that the trends observed in this figure (sorption increasing with increasing pH and larger sorption in UE-25p #1 water than in J-13 water) are not followed by the neptunium sorption reported for clinoptilolite-rich tuff samples. Also once again, the neptunium sorption in the rest of the tuff samples is so small

(even in the samples that contain traces of hematite) that the iron oxides appear to be passivated in the tuffs.

As illustrated in Figure 6.3-30, regardless of the tuff studied, neptunium sorption onto tuffaceous materials is extremely limited. One exception is tuff sample G2-723 (not shown), which contains a large amount of calcite, a good sorber for neptunium. This sample will be discussed later.

Figure 6.3-31 is a plot both of neptunium sorption data in J-13 water and of surface area for tuffs for which BET-surface-area and X-ray powder diffraction analyses exist. The surface-area data correspond to the surface area for the tuffs sieved in J-13 water with the following exceptions: the surface area used for sample G4-2077 was for dry-sieved tuff; the surface area used for tuffs G4-268 and G4-272 was the same as that measured for tuff G4-270; the surface area plotted for tuffs G4-1505 and G4-1510 was the same as that measured for tuff G4-1506; and the surface area plotted for tuff GU3-1405 was the same as that measured for tuff GU3-1407. Figure 6.3-32 shows a reasonable correlation between sorption and surface area. The surface areas that are larger than 18 m^2/g correspond to clinoptilolite-rich tuffs.

Figures 6.3-32 and 6.3-33 summarize the sorption of neptunium under atmospheric conditions for tuffs and minerals as a function of water type. Sorption onto zeolitic tuffs decreases considerably with increasing carbonate content and ionic strength of the water. Figure 6.3-33 also shows the calcite-rich tuff G2-723 (34 percent calcite), which exhibits considerable sorptive capacity for neptunium. Assuming that the calcite in the tuff sample has the same surface area as the natural calcite used for these experiments (and that calcite is the only sorptive mineral in the tuff), one would predict from neptunium sorption on pure calcite a $\log K_d$ for tuff G2-723 of 1.5. This prediction agrees well with the measured K_d (Figure 6.3-33).

As the neptunium concentration is increased towards the solubility limit for neptunium in the J-13 and UE-25p #1 groundwaters, the observed sorption decreases, but the general trends remain the same (as seen by comparing Figure 6.3-31 and 6.3-34). The extremely low neptunium sorption reported for devitrified tuffs in J-13 and UE-25p #1 waters is supported by the sorption data plotted for albite (Figure 6.3-35), which appears to be a very poor sorber for neptunium (in both waters). The nonlinearity of neptunium sorption in the high-concentration region (approaching the solubility limits for neptunium) is further illustrated in Figures 6.3-36 and 6.3-37 (for J-13 and UE-25p #1 waters under a carbon-dioxide atmosphere at a pH of 7).

Conclusions Regarding Sorption Behavior With Respect To Expected Variations In Groundwaters–The mechanisms by which neptunium appears to sorb onto mineral surfaces in the Yucca Mountain flow system appear to be surface complexation on oxide phases and co-precipitation and surface adsorption involving carbonate minerals. The surface-complexation mechanism appears to be relatively insensitive to variations in ionic strength, detailed groundwater composition, and pH over the range from 6.5 to 8.5. This mechanism is likely responsible for the 0.5 to 5.0 mL/g range in sorption-coefficient values consistently measured in many different rock samples. The high end of this range may reflect secondary mechanisms, such as the reduction of Np(V) to Np(IV) on mineral surfaces containing ferrous iron. Regardless of the details of the mechanisms, performance-assessment calculations could use a

probability distribution for sorption-coefficient values, as was done for the 1993 total-system performance assessment (Wilson et al. 1994).

For hydrologic units in which calcite is known to be present or in which groundwaters are oversaturated in calcite, higher neptunium sorption coefficients could be used in the calculations if it could be established through laboratory experiments that such coefficients are appropriate. To date, most neptunium sorption coefficients have been obtained using samples from the unsaturated zone, many of which came from levels above the repository horizon. According to the mineralogic studies, calcite is more common at depths below the potential repository horizon than it is at the intermediate depths. Many of the samples used in sorption experiments to date have been obtained from intermediate depths.

Protactinium

Behavior In Solutions Representative Of Yucca Mountain Groundwaters–In aqueous systems, protactinium appears to exist dominantly in the +5 oxidation state although the +4 state may occur in reducing environments (Brookins 1988). In both oxidation states, protactinium is strongly hydrolyzed and forms highly insoluble compounds (Cotton and Wilkinson 1988). This result implies that the +5 solution chemistry of protactinium is more akin to that of Nb(V) than to other actinides in +5 oxidation states, such as PuO_2^+ or NpO_2^+. If this interpretation is correct, then the solution parameter of greatest importance to protactinium sorption behavior would be pH.

Qualitative Evidence For Behavior In The Surficial Environment–Information on behavior of protactinium in the surficial environment is sparse. Because protactinium forms such insoluble compounds, it is generally assumed to be immobile in the surficial environment.

Data From Laboratory Sorption Experiments–Batch-sorption experiments with protactinium have yielded some interesting results. In dilute to intermediate ionic-strength solutions, Allard et al. (1982) report large values (10^4 mL/g) for the protactinium sorption coefficient on alumina and silica at pH values greater than 6 to 7 but much lower values (90 to 500 mL/g) at pH values less than 7. Rundberg, Ogard et al. (1985) report protactinium sorption coefficients in the range from 3.7 to 8.2 mL/g for a zeolitic tuff in contact with J-13 water spiked with 10^{-11} to 10^{-14} M protactinium at pH values of 6.3 to 6.7. Together, these data suggest that protactinium sorbs by a surface-complexation mechanism and that there is a rather steep sorption edge for protactinium as a function of pH at a pH value of approximately 7.

Conclusions Regarding Sorption Behavior With Respect To Expected Variations In Groundwaters–Batch-sorption data for protactinium suggest that sorption coefficients for this element will be small (<10 mL/g) at lower pH values. Because protactinium sorption experiments on rock samples from Yucca Mountain have only been carried out in the low pH range, it would be prudent to carry out several experiments using a Yucca Mountain water at several pH values from 7 to 9.

Selenium

Behavior In Solutions Representative Of Yucca Mountain Groundwaters–Selenium will occur as anionic species in all water compositions expected at Yucca Mountain. Although the two oxidation states of +4 and +6 (Howard, III, J.H. 1977) are found for selenium in surficial waters in contact with atmospheric oxygen, the +4 state predominates under the conditions expected for groundwaters at Yucca Mountain (Howard, III, J.H. 1977; White, Benson et al. 1991). In that state, selenium is found as the SeO_3^{2-} and $HSeO_3^-$ selenite ions. In the +6 oxidation state, selenium occurs as the SeO_4^{2-} and $HSeO_4^-$ selenate ions.

Qualitative Evidence For Behavior In The Surficial Environment–Selenium behavior in the surficial environment is very closely tied to the redox potential of different parts of the near-surface environment. Under reducing conditions, selenium is immobilized as $FeSe_2$ at low pH (<5) and as native selenium at higher pH (Howard, III, J.H. 1977). The stability range for native selenium extends nearly to surface redox conditions. When in contact with atmospheric oxygen levels, selenium is apparently stabilized as the selenite ion (SeO_3^{2-}). At higher redox potentials, selenium is oxidized to the selenate ion (SeO_4^{2-}), which appears to be more mobile in the surficial environment than the selenite ion (Howard, III, J.H. 1977).

Data From Laboratory Sorption Experiments–Because selenium occurs as anionic species in the surficial environment, its adsorption behavior is controlled primarily by surface-complexation reactions on oxide minerals including iron oxides and oxyhydroxides (Balistrieri and Chao 1987), manganese oxides and oxyhydroxides, clays (Bar-Yosef and Meek 1987), and other minerals with affinities for anionic species. These surface-complexation reactions are quite sensitive to pH. For example, adsorption on iron oxyhydroxides decreases for both selenite and selenate ions with increasing pH (Balistrieri and Chao 1987). Selenate ions appear to sorb dominantly in the outer layer of the electrical double layer present on oxide surfaces, whereas selenite tends to sorb in the inner layer (Hayes et al. 1987). Selenate ions are subject to ionic-strength effects as well as competitive effects with sulfate and other anions in solution, presumably because they sorb in the outer layer. Selenite ions are not subject to ionic-strength effects but may be subject to competition from other anions sorbing on inner-layer sites (Hingston et al. 1971).

Studies of selenite adsorption on soils in the pH range expected for Yucca Mountain groundwaters indicate relatively limited adsorption (<30 percent) from 0.05 N chloride solutions containing 0.16 to 0.63 mg/L selenium (Neal et al. 1987). This limited sorption potential will likely be further decreased in natural waters containing high concentrations of competing anions.

Data for selenium sorption coefficients on Yucca Mountain rock samples in contact with J-13 water have been summarized by Thomas (1987). Most measured values are less than 5 mL/g, and they do not appear to correlate with rock type. A puzzling feature of the data is that, for a given rock sample, sorption coefficients are larger in the higher pH experiments (pH of 8.8) compared to the lower pH experiments (pH of 6.0). This result is contrary to the pH dependence predicted on the basis of double-layer theories. Neal et al. (1987) noted a similar effect for selenium sorption on soils for a solution phase enriched in calcium. They suggested the effect may be due to the formation of a calcium-rich surface precipitate or, alternatively, a change in

surface charge due to the adsorption of divalent calcium cations. M.M. Benjamin (1983) made similar observations involving other divalent cations. These data suggest that in groundwaters relatively enriched in calcium, and perhaps other divalent cations, selenium adsorption may be somewhat enhanced in the alkaline pH range.

Conclusions Regarding Sorption Behavior With Respect To Expected Variations In Groundwaters–Sorption coefficients for selenium on Yucca Mountain rock samples have only been measured in J-13 water. These experiments do not show the expected decrease in sorption coefficient with pH. Therefore, variations in pH over the range expected in Yucca Mountain groundwaters do not appear to be the most important groundwater compositional parameter in the sorption behavior of this element. Based on the data obtained in other studies, divalent cations may have a significant impact on the sorption behavior of this element in Yucca Mountain rock-water systems. Additional experiments with waters enriched in divalent cations (such as UE-25p #1 water) may be productive and may enlarge the range of selenium sorption-coefficient values appropriate for use in performance-assessment calculations.

Uranium

Behavior In Solutions Representative Of Yucca Mountain Groundwaters–Under the redox potentials expected in Yucca Mountain groundwaters, particularly in the unsaturated zone, uranium should be in the +6 oxidation state. In this oxidation state, uranium will be present in solution in a variety of complexes including $(UO_2)_2CO_3(OH)_3^-$, $UO_2(CO_3)_2^{2-}$, $UO_2(CO_3)_3^{4-}$, $UO_2(OH)_2(aq)$, $UO_2(CO_3)(aq)$, and other minor species. Phosphate, fluoride, or sulfate species will not be significant within the concentration ranges for these anions and the pH range expected in Yucca Mountain groundwaters.

Qualitative Evidence For Behavior In The Surficial Environment–Data on the behavior of uranium in the surficial environment are available from various sources. Several types of uranium ore deposits have been studied as natural analogs to repository settings. Other sources of data include studies of uranium mill-tailings piles, waste-stream outfalls, and other uranium ore deposits. Only the natural analog studies will be discussed in this subsection.

The deposits that have been studied as natural analogs include the deposits at Oklo, Gabon, the Alligator Rivers region in Australia, Cigar Lake in Canada, Poças de Caldas in Brazil, and Peña Blanca in Mexico. Each of these deposits has been studied in considerable detail to define the geochemical behavior of uranium and its daughter products in the environments in which the ore deposits are found. Although none of the environments are completely analogous to the Yucca Mountain site, the Peña Blanca deposit is at least situated in Tertiary volcanic tuffs similar to those present at Yucca Mountain.

A critical aspect of any analog to potential uranium migration at the Yucca Mountain site is that the uranium source must be subject to redox potentials similar to those expected at Yucca Mountain, particularly in the unsaturated zone. This fact eliminates from detailed consideration data from the Cigar Lake and probably the Oklo deposits (Goodwin et al. 1989; Cramer and Sargent 1994; Brookins 1983).

The Alligator Rivers deposits are exposed to oxidizing conditions in a surficial environment (Gilbin and Snelling 1983). Uranium isotope-disequilibrium studies at this site indicate that uranium migration has occurred relatively recently (Snelling and Dickson 1979). However, evidence for recent transport does not by itself provide an estimate of the rate of transport and, more importantly, of the chemical controls on this rate. The latter type of information could be very useful to the YMP.

At the Koongarra deposit, uranium migration is significantly retarded by the precipitation of uranyl phosphate minerals (Snelling 1980). Although phosphate concentrations in local groundwaters are not high (0.01 to 0.1 mg/L), significant phosphate concentrations are found in the country rocks in minerals such as apatite. The phosphate in the rocks is apparently redistributed locally by groundwater, resulting in the precipitation of uranyl phosphate minerals within the zone of weathering (Snelling 1980). This retardation mechanism is not expected to be important at Yucca Mountain, given the low phosphate concentrations found in Yucca Mountain rock units (Broxton, Warren, Hagan et al. 1986).

Uranium in the zone of weathering at Alligator Rivers also appears to be associated with and is probably retarded by ferric-iron compounds (Payne et al. 1991). Sorption experiments have been carried out involving uranium sorption on whole-rock samples and on pure mineral samples (Payne et al. 1991). The results of these experiments suggest that ferric hydroxides are strong sorbers of uranium in this system over a pH range of 5 to 9. This result is not particularly new as similar results on ferric oxyhydroxides have been reported by others (for example, Hsi and Langmuir 1985). A potentially important result from these studies would be the derivation of some defensible estimate of the rate of transport of uranium in this system using the experimentally derived chemical constraints on uranium adsorption behavior and a valid groundwater flow model. Unfortunately, hydrologists who are knowledgeable about the site suggest the complicated nature of the flow system may preclude the development of defensible flow models (S.N. Davis cited in Curtis, D.E. and Fabryka-Martin 1988).

The Peña Blanca uranium deposits in Mexico provide a potentially more appropriate analog site in relation to Yucca Mountain. The primary uranium deposits at this site are hydrothermal in origin and were emplaced in structural features associated with Tertiary silicic volcanic tuffs that overlie Mesozoic calcareous basement (George-Aniel et al. 1991). In addition to the hydrothermal deposits, which contain sulfide minerals as well as uranium oxides, supergene deposits have formed locally through the leaching of uranium from the volcanic rocks and subsequent precipitation as uranyl silicate minerals, including uranophane (Murphy, W.M. 1992). The supergene deposits are hosted by kaolinitized and silicified rhyolite and do not appear to contain sulfide minerals. The absence of sulfide minerals is important because sulfides, such as pyrite, oxidize readily in the surficial environment to produce acidic conditions unlike those expected within Yucca Mountain. The supergene deposits are thought to have formed in the surficial environment (George-Aniel et al. 1991), and their study may offer useful insight into the potential for migration of uranium from the proposed repository within Yucca Mountain. No data on the present-day sorption behavior or rate of migration of uranium in these deposits has been reported to date. However, several geochemical studies are currently underway to provide such data (Murphy, W.M. 1992).

A qualitative study by Rosholt et al. (1971) established that uranium was leached from devitrified tuff samples but not from hydrated glassy samples obtained from a given geologic unit. This and other data presented suggest devitrification makes the uranium in tuffs more mobile in the surficial environment. Zielinski et al. (1986) and Flexser and Wollenberg (1991) observed that uranium in Yucca Mountain devitrified tuffs was commonly associated with manganese oxides. This fact suggests that, although uranium may be mobile in the unsaturated devitrified tuffs in Yucca Mountain, it could be retarded to the extent that there are manganese oxides present along the flow path with sufficient capacity to sorb the potential flux of uranium from the proposed repository horizon. Given the amount of uranium to be emplaced in the potential repository, it would seem the sorption capacity of the manganese oxides present in the mountain (Bish and Chipera 1989) would be rapidly saturated. Nonetheless, manganese oxides may significantly retard the movement of uranium in some of the fracture-flow scenarios.

Data From Laboratory Sorption Experiments–Data have been presented on the adsorption of uranium as U(VI) onto a variety of pure mineral phases in simple electrolytes. Among the solid phases investigated are goethite (for example, Hsi and Langmuir 1985), hematite (Ho and Miller 1986), silica gel (Zielinski 1980), clays (Tsunashima et al. 1981), and zeolites (Ames et al. 1983). The results reported are sometimes difficult to reconcile. For example, Hsi and Langmuir report that hematite sorbs very little of the uranium in solutions with 5×10^{-5} M uranium and 10^{-3} M total carbonate, whereas Ho and Miller report that hematite sorbs up to 100 percent of the uranium in their experiments with similar uranium and bicarbonate solution concentrations. Both sets of experiments had similar hematite surface areas. The main difference was that the solution phase in the Hsi and Langmuir experiments also contained 0.1 M $NaNO_3$. However, $NaNO_3$ is generally considered to be a nonreactive electrolyte, and nitrate does not form complexes with uranium in the pH range addressed in these experiments. Why there is a difference in these results is unclear. One possibility is that the surface characteristics of the solid phases used were not the same in the two sets of experiments.

Silica gel appears to have a clear affinity for uranium as established by the results of laboratory experiments and by observations on the association of uranium with opals in nature (Zielinski 1980). According to Maya (1982), the uranium is adsorbed to silica gel as the uranyl ion, free of carbonate ligands. Zielinski has shown that sorption of uranium onto silica gel is sensitive to the total carbonate concentration of the solution phase when this concentration is above 0.01 M. Interestingly, experiments carried out at elevated temperatures (65 to 80°C) resulted in somewhat higher sorption coefficients. Data regarding competitive effects on silica gel between uranium and other constituents in groundwaters at near-neutral pH have not been found in the literature.

Sorption of uranium by clays has been investigated in some detail. Borovec (1981) has presented data that indicate montmorillonite has a high selectivity for uranyl ions relative to divalent ions of zinc, manganese, calcium, magnesium, cobalt, cadmium, and nickel at a pH of 6 in chloride solutions. However, Tsunashima et al. (1981) found montmorillonite has a greater selectivity for calcium, magnesium, and barium ions than for uranyl ions in nitrate solutions over the pH range from 4.0 to 4.5. Montmorillonite was found to have a greater selectivity for the uranyl ion than for sodium and potassium ions in the same solutions. Ames et al. (1983) found that uranium was strongly sorbed to montmorillonite from 0.01 M NaCl solutions but weakly sorbed from 0.01 M $NaHCO_3$ solutions in the pH range from 8 to 9.

Because groundwaters in Yucca Mountain contain significant concentrations of bicarbonate, calcium, and magnesium ions, these data suggest overall that uranyl ions may not compete favorably for exchange sites on clay minerals in Yucca Mountain, although quantitative prediction of the extent of exchange would require more detailed analysis.

Data available on uranium sorption on zeolitic minerals are very limited. Ames et al. (1983) report that clinoptilolite has a low affinity for trace levels of uranium in the pH range from 8 to 9 in 0.01 M $NaHCO_3$. Doi et al. (1975) found that uranium at concentrations of 10^{-6} g per g of solution was strongly sorbed onto clinoptilolite from perchlorate solutions in the pH range from 4 to 8.5.

Data on uranium sorption coefficients for Yucca Mountain rock-water systems were reported by Thomas (1987) and discussed by Meijer (1990, 1992). The affinity of the devitrified and vitric tuffs for trace levels of uranium is generally small (K_d <5 mL/g) over the pH range from 6 to 9 in J-13 water. For zeolitic tuffs, the K_d is near zero at a pH of 9 but increases with decreasing pH to values of approximately 25 mL/g at a pH of 6 in J-13 water. This behavior suggests uranyl ions can exchange with the major cations in zeolites.

In UE-25p #1 water, uranium batch-sorption experiments were only carried out in the pH range from 8.3 to 9.3 with the result that the measured sorption coefficients were small (0 to 2.7 mL/g; Thomas 1988). The devitrified sample showed the largest sorption coefficient. In the pH range from 6 to 8, it is expected that the sorption coefficients for uranium in UE-25p #1 water will increase with decreasing pH (because of predominance by $UO_2CO_3^0$ at higher pH values), but they will likely be smaller than the coefficients obtained for the same rock samples in J-13 water over this pH range. In H-3 groundwater, sorption coefficients were also low for zeolitic and devitrified rock types over the pH range from 9.2 to 9.3, presumably reflecting the elevated carbonate content of this water. However, data for a vitric sample showed a value of 6.2 mL/g for the uranium sorption coefficient at a pH of 9. This relatively high value has not been explained.

The sorption of U(VI) onto samples of the three types of tuff in J-13 water (under oxidizing conditions) at the two pH values (7 and 8.5) was studied. However, to identify the sorbing minerals in the tuffs, sorption onto the pure minerals hematite, clinoptilolite, albite, and quartz was also studied. It was found that uranium in J-13 water does not sorb onto devitrified and vitric tuffs, albite, and quartz (Table 6.3-10).

Wet-sieved tuffs, albite, and quartz samples with particle sizes in the range from 75 to 500 μm were used. Initial uranium concentrations ranged from 8×10^{-8} to 1×10^{-4} M. The pretreatment period was 2 to 4 days, and the sorption period, 3 to 4 days. The negative values reported in Table 3.6-10 are the result of analytical error for the case of very little sorption (that is, a small number obtained as the difference of two large numbers). For the experimental conditions cited, uranium sorption onto zeolitic tuffs and clinoptilolite is nonlinear and can be fitted with Freundlich and Langmuir isotherms (Figure 6.3-38 and 6.3-39).

For the clinoptilolite-rich zeolitic tuff sample G4-1510, the scatter in the data makes it impossible to conclude whether there is a significant difference between the experiments

performed under a carbon-dioxide overpressure and a pH of 7 or at atmospheric conditions and a pH of 8.5 (Figure 6.3-38). However, the experiments with pure clinoptilolite indicate that sorption increases with decreasing pH for U(VI) (Figure 6.3-39), as is the case for Np(V). Because the major constituent of tuff sample G4-1510 is clinoptilolite, predictions of the K_a (K_d divided by the solid-phase surface area) were made for uranium sorption onto this tuff by assuming that clinoptilolite is the only sorbing phase. Inspection of Table 6.3-11 indicates that reasonable predictions are obtained with this assumption for a pH of 7 but not for a pH of 8.5. In all cases, predictions based on clinoptilolite sorption are conservative.

The sorption of uranium onto pure iron oxides (such as hematite) is very large (and large uncertainties in the K_d values result from measuring the small amounts of radionuclide left in solution after sorption). Although the measured sorption of uranium onto pure hematite is very large, sorption onto devitrified tuffs, which appear to have traces of hematite (1 percent ± 1), is essentially zero. As with neptunium, this result could be due to differences in the surface of pure hematite compared to hematite in tuff, or it could be due to passivation of the hematite surfaces in the tuff by elements (such as the rare earths) that have a higher affinity for hematite than uranium and, thus, occupy the sorption sites.

Conclusions Regarding Sorption Behavior With Respect To Expected Variations In Groundwaters–The dominant groundwater compositional controls on the sorption behavior of uranium on Yucca Mountain rock samples will likely be pH, carbonate content, and the concentrations of calcium and magnesium ions in solution. The pH and carbonate contents influence the sorption largely as a result of the decrease in carbonate complexation of uranium with decreasing pH. These two parameters are therefore not entirely independent. However, different water compositions can have different carbonate contents at a given pH. The expectation is that waters with higher carbonate contents will be associated with lower sorption coefficients. This trend would apply to both ion-exchange and surface-complexation sorption mechanisms. However, decreasing pH will have different effects on uranium sorption behavior in zeolitic and clay-rich samples versus devitrified and vitric samples. In the former samples, the uranium sorption coefficient will likely increase with decreasing pH due to the increase in uranyl ion concentrations with decreasing pH. For a given rock-water system, the magnitude of this increase will depend on the concentrations of competing ions such as calcium and magnesium in the water. For high calcium and magnesium waters, the competition effects will be substantial. Because unsaturated-zone waters are relatively enriched in calcium and magnesium, uranium sorption coefficients in the unsaturated zone may be on the low end of the range reported to date (Thomas 1987, 1988) unless the low total carbonate concentrations in these waters balance the effect of the elevated calcium and magnesium concentrations.

It will be important to carry out experiments on representative rock samples using a high-calcium-and-magnesium, low-carbonate, unsaturated-zone water composition with pH controlled over a range from 6 to 9. Similar experiments should be carried out with a high total-carbonate and high calcium-and-magnesium water composition, such as UE-25p #1 water, over the pH range from 6 to 8.

Carbon, Chlorine, Iodine, and Technetium–Because carbon, chlorine, iodine, and technetium are unlikely to have significant sorption affinity in the rock-water systems expected at Yucca

Mountain, their sorption behavior will not be discussed in detail. For carbon, the most robust retardation mechanism will be isotopic exchange with stable carbon isotopes in groundwater and on carbonate mineral surfaces (Meijer 1993).

Chloride and iodide ions will have no significant retardation in Yucca Mountain rock-water systems and may even have slightly enhanced migration rates due to anion-exclusion effects (Ogard and Vaniman 1985). If conditions were to become sufficiently oxidizing to convert iodide to iodate, some retardation of iodine might occur in the flow system. Although such conditions might occur locally, for example, due to radiolysis effects, it is considered unlikely that such conditions would be present over a significant volume of the flow system for an extended period of time.

Technetium appears to show nonzero, although minimal, retardation in Yucca Mountain rock-water systems (Ogard and Vaniman 1985; Rundberg, Ogard et al. 1985; Thomas 1988). However, the cause of this retardation has not been identified, and it may simply be an experimental artifact. Because the minimal values obtained for technetium sorption coefficients to date will not result in significant retardation of technetium, it does not seem prudent to expend funds on the detailed investigation of potential sorption mechanisms for this element. More significantly, if sufficiently reducing conditions could be shown to exist in portions of the flow system down-gradient of the proposed repository, retardation of technetium by the precipitation and sorption of Tc^{4+} species might occur.

6.3.3.2 Effects of Organics on Actinide Sorption

Naturally occurring organic compounds generated during the transformation of plant and animal debris over time and as a result of the synthetic activities of microorganisms are ubiquitous in surface and subsurface environments. For example, pore water from a well-developed soil environment usually contains dissolved organic carbon in quantities greater than 20 mg/L in top soils and in quantities of about 5 mg/L in subsoils. Dissolved organic carbon concentrations in groundwaters typically depend on the environment and are usually below 2 mg/L (Drever 1988). The decrease in concentrations of organic materials with increasing depth is attributed to chemical and biological degradation as well as to sorption on mineral surfaces. Sorption of organic materials onto mineral surfaces is considered the dominant contributing factor to the removal of organics from solution during percolation through the subsurface.

The interaction between organic materials and mineral surfaces in the natural environment is important to mineral surface geochemistry. Sorption of organic material onto mineral surfaces affects not only the solubility and charge of the organic materials in solution but also the properties of the mineral surfaces, such as their charge and hydrophobicity, thereby altering the reactivity of the mineral toward metal ions. A clear understanding of the effects of the organic materials that frequently coat mineral surfaces in natural environments will lead to improvements in the sorption models used to predict the mobility of radionuclides in natural aquatic environments (Choppin 1992).

The objective of this subsection is to summarize the laboratory results for the effect of organic materials on the sorption of plutonium and neptunium on selected mineral oxides and tuff material.

6.3.3.2.1 Experimental Procedures

Preparation of Tuff and Oxide Minerals–Synthetic boehmite, goethite, hematite, ferrihydrite, and a crushed natural tuff material from Yucca Mountain, Nevada, served as model sorbents (boehmite served as an end member in relation to Yucca Mountain tuffs). Details of the methods for preparing the oxides are described in the literature (Kung and McBride 1989a, 1989b, 1991). In brief, iron oxide was synthesized by reacting ferric chloride with dilute NaOH under slightly acidic conditions and was then aged at raised temperature for several days. X-ray powder diffraction analysis confirmed the material to be pure goethite. The surface area of the goethite, calculated from N_2 adsorption by the three-point BET method, was about 89.5 m^2/g.

The ferrihydrite preparation involved the overnight hydrolysis of ferric salt at low pH followed by raising the pH with dilute NaOH and, finally, aging the mixture for two weeks at raised temperature. The surface area of the freeze-dried material was 91.5 m^2/g. X-ray powder diffraction analysis indicated a poorly crystalline product containing ferrihydrite. Hematite was prepared by aging ferric nitrate solution at raised temperature for 3 days. The surface area of the freeze-dried material was 39.4 m^2/g. X-ray powder diffraction analysis confirmed that this material was well-crystallized hematite.

Boehmite was prepared by fast hydrolysis of aqueous aluminum chloride with NaOH, followed by mixing and aging. The surface area of the freeze-dried material was 324 m^2/g. X-ray powder diffraction analysis confirmed that this aluminum oxide was poorly crystallized boehmite, an aluminum oxyhydroxide. The metal oxides were stored either in a freeze-dried state or in suspensions containing 0.1 M KCl. For those in suspensions, solid concentration of these oxide suspensions was less than 20 mg/mL. X-ray powder diffraction analysis of the crushed tuff material (USW G-4 270), obtained from S. Chipera, indicated that it was about 30 percent quartz and 69 percent feldspar, the remainder consisting of trace amounts of layer silicates and iron oxide. Part of the tuff material was treated with a 15 percent hydrogen-peroxide solution to remove any natural organic material from the tuff surface.

Preparation of Organics and Radionuclides–Catechol, alanine, DOPA (dihydroxyphenylalanine), and NAFA (Nordic aquatic fulvic acid) were used as model organic materials. Alanine is an amino acid that will complex with the hard acid type of metal ions in solution. Catechol is a phenolic compound that may chelate with metal ions and undergo redox reaction with the metal. DOPA, a naturally occurring amino acid commonly found in plant seedlings, pods, and broad beans, was chosen because it contains well-defined organic functional groups such as carboxylic acid, amine, and phenols. The catechol, alanine, and DOPA, purchased from Fluca Chemical Company with purity greater than 99 percent, were used as received. The NAFA, obtained from the IHSS (International Humic Substances Society), is identified by IHSS as a reference fulvic acid with the code number 1R105F and is prepared and homogenized from a designated aquatic source by IHSS.

Neptunium-237 was obtained from Amersham International (product code NGZ-44). The ^{239}Pu stock solution was prepared in the Pu(V) oxidation state. This concentrated stock solution was obtained from P. Parmer, CST-7. The desired concentrations of neptunium and plutonium were diluted and stored in 0.1 M KCl solutions. Under the experimental conditions used in this work,

the plutonium and neptunium are expected to exist as the chemical species PuO_2^+ and NpO_2^+, respectively.

Radionuclides Sorption Measurements–Sorption isotherms were obtained by mixing the desired sorbent suspension and sorbate in Teflon and/or polycarbonate centrifuge tubes. The initial DOPA concentrations ranged from 20 to 100 μM. The pH was adjusted by adding 0.05 M NaOH or HCl immediately after mixing. The tubes were capped and shaken for at least 20 hours at 22 ± 1°C. The solid phase was separated from suspension by centrifugation. The supernatant was analyzed for unsorbed DOPA by UV spectrometry (Hewlett-Packard 8450A), and the amount of sorption was calculated by determining the difference between the initial and final concentrations. Potassium chloride was used as a background electrolyte to maintain an essentially constant ionic strength of 0.1 M.

A similar method was used for obtaining plutonium and neptunium sorption isotherms. The amount of radionuclide in solution was determined by liquid scintillation counting (Packard 2550-TR/AB). The metal ions were introduced into the tubes after the pH in each suspension was adjusted. For the multisorbate systems, the organic sorbate was added before the radionuclides sorbate. Solution pH was measured after shaking. The carbon dioxide was not controlled in all the systems studied. About 3 to 50×10^{-8} M plutonium solutions were used for the initial plutonium sorption isotherms. About 1 to 40×10^{-7} M neptunium solutions were used for the initial neptunium sorption isotherms. Standard sorbate solutions to which no sorbent was added and which were subjected to the same shaking treatment were used to generate the standard curves. No sorbate sorption onto the centrifuge tubes was detected.

6.3.3.2.2 Results and Discussion

6.3.3.2.2.1 Neptunium

Sorption as a Function of Tuff and Oxide Minerals–The isotherms for neptunium sorption on different iron oxides are shown in Figure 6.3-40. In this experiment, hematite, goethite, and ferrihydrite were used as sorbents. Results show that, on a weight basis, hematite was the most adsorptive whereas goethite was the least adsorptive. The sorption of neptunium on model iron oxides follows the order hematite > ferrihydrite > goethite.

Two things should be noted in this study. First, the surface areas of these iron oxides were different. The sorptivity of neptunium on these iron oxides was not compared on a unit surface area basis. For ferrihydrite and goethite, the surface areas are around 90 m^2/g. The surface area of hematite is about 40 m^2/g. Higher surface areas are expected to have higher sorptions. Secondly, the sorption experiments were not conducted at the same pH. Sorption on ferrihydrite was conducted at pH 6.2. Sorption on hematite and goethite were conducted at pH 6.9. The pH may affect the sorptivity of neptunium on iron oxides, and this effect will be presented in the next subsection.

The effect of oxide surface areas on neptunium sorption was replotted in Figure 6.3-41. In this figure, the amount of neptunium sorption was normalized on the basis of unit surface area (m^2). Results again showed that the sorption of neptunium follows the order hematite > ferrihydrite >

goethite. Evidently, hematite has the highest sorptivity for neptunium on the basis of both weight and unit surface area.

Effect of pH on Sorption–To quantify organic sorption, it is required that the effect of organics on radionuclide sorption is understood. Experiments were conducted to study organic sorption, and the results are presented in this subsection. The isotherms for DOPA adsorption on goethite and boehmite at different pH levels are shown in Figure 6.2-42. On a weight basis, boehmite was more adsorptive than goethite. The linear sorption curves for these materials suggest a low degree of coverage of the surface reactive sites by the organic material in the presence of excess potassium chloride. This finding is consistent with the theoretical calculation of coverage, which suggests that the amount of DOPA sorption is much less than a monolayer, based on BET surface area.

Increasing the solution pH resulted in a higher organic sorptivity for all oxides. Under neutral and slightly acidic conditions (pH 5.5 to 7), iron and aluminum oxides were expected to have positive surface charges (Sposito 1989). However, the sorption of DOPA on all sorbents was found to increase as solution pH increased despite the fact that the surface charge of silicon oxide is opposite that of iron and aluminum oxides. Although the sorption of DOPA is apparently not dependent on surface-charge effects such as electrostatic attraction, it may be controlled by the deprotonation process of the organic material. DOPA is expected to be dominated by neutral species under neutral and slightly acidic conditions, but raising the pH level will increase the concentration of deprotonated DOPA species, which are expected to have a stronger affinity for oxide surfaces in direct surface complexation. Therefore, it is reasonable to assume that DOPA forms direct surface bidentate complexes on the oxide surfaces. The isotherms for neptunium sorption on goethite at different pH levels are shown in Figure 6.3-43. Increasing the solution pH from 6.2 to 6.9 resulted in a higher neptunium sorptivity.

Effect of Model Organics on Sorptive Behavior–The study examined the effect of natural organics on radionuclide sorption onto natural tuff material that may have been precoated with natural organic material. The standard method for removing the natural organic material from mineral samples is to use hydrogen peroxide to oxidize the organic matter (Kunze and Dixon 1986). In these experiments, a 15 percent hydrogen-peroxide solution was used to remove the possibly presorbed natural organic from the crushed tuff material collected from Yucca Mountain, Nevada. In sorption experiments conducted to study the effect of the naturally presorbed organics on neptunium sorption on tuff materials, half of the samples were treated with hydrogen peroxide, half were not.

Figure 6.3-44 shows the sorption isotherms of neptunium on both types of tuff samples. The results suggest that treatment with hydrogen peroxide had little or no effect on the sorption of neptunium onto the tuff material.

The lack of effect of hydrogen peroxide treatment on neptunium sorption on tuff materials is attributable to three factors. First, untreated tuff may contain very little or no organic material on its surface. Low organic content on the untreated tuff surface could be expected because crushed tuff material is generated from bedrock that may have little exposure to natural organic materials. New surfaces generated during the crushing process would not contain organic materials, in which case untreated tuff would be expected to behave essentially the same as tuff treated with

hydrogen peroxide. Second, neptunium has intrinsically low sorptivity on tuff material. No observable difference in sorption on both treated and untreated tuff is attributed to the low sorption of neptunium on both sorbents. Any minute differences in sorption are likely to occur below the level of detection. Third, the sorption of neptunium may be unaffected by organic material, assuming that organic materials such as DOPA do not influence neptunium sorption on tuff, goethite, or boehmite.

To explore the possibility that the untreated tuff contained little organic material, 4 to 50 μM of DOPA was purposely added to both treated and untreated crushed tuff materials, and the sorption isotherms of neptunium on these systems were compared. As Figures 6.3-45 and 6.3-46 illustrate, the addition of DOPA had no effect on neptunium sorption on either treated or untreated crushed tuff materials. These data thus support the premise that the presence of organic material does not affect neptunium sorption on tuff materials.

Because this experiment did not rule out the possibility that the lack of an observable effect was a result of the intrinsically low sorptivity of tuff materials, the sorption of neptunium on iron and aluminum oxides in the absence and presence of DOPA was examined. The sorption of neptunium is expected to be much higher on iron and aluminum oxides than on tuff material. Thus, any effect of DOPA on neptunium sorption ought to appear in the oxide systems. To verify this assumption, sorption isotherms were measured for neptunium on iron and aluminum oxides and tuff material in the absence of organic materials with 0.1 M KCl at pH 6.2. The results presented in Figure 6.3-47 indicate that the sorptivity of boehmite and goethite is approximately one and two orders of magnitude higher, respectively, than the sorptivity of tuff material. Thus, any effect of DOPA on neptunium sorption should be easily detectable in these oxide systems.

Neptunium sorption isotherms on iron and aluminum oxides in the presence of DOPA are shown in Figures 6.3-48 and 6.3-49. In these experiments, 0.1 M KCl was used to maintain an essentially constant ionic strength, and the final pH of the suspensions was adjusted to 6.2. The initial neptunium concentration ranged from 0.2 to 2 μM, and the initial DOPA concentration ranged from 4 to 50 μM. The sorption isotherms of neptunium on aluminum and iron oxides suggest that DOPA does not significantly affect the sorption of neptunium. The relatively weak complexation of the pentavalent neptunium ion is a result of its relatively low effective charge on the cation (Choppin and Rao 1984). These results imply that there is no significant influence of DOPA on neptunium sorption on aluminum and iron oxides.

The occurrence of surface complexation between DOPA and oxide surfaces is supported by the observed sorption of catechol on metal oxide, which indicates that catechol chemisorbs on metal oxide by forming a bidentate complex with surface metal. DOPA is an organic with functional groups like catechol (phenols) and alanine (amino acids). Thus, the effect of simple organics such as catechol and alanine on the sorption of neptunium was studied. Both catechol and alanine are expected to complex with metal ions in solution. Besides the formation of metal-organic complexation, catechol readily undergoes redox reactions with some metal and metal oxides (McBride and Wesselink 1988). For example, catechol at high concentrations may undergo electron transfer reactions with manganese and iron oxides. The effect of catechol and alanine on neptunium sorption was quantified by sorption isotherms.

Neptunium sorption isotherms on goethite, ferrihydrite, and hematite in the presence and absence of catechol and alanine are shown in Figures 6.3-50 to 6.3-52. In these experiments, 0.1 M KCl was used to maintain an essentially constant ionic strength. The final pH of the suspensions was adjusted to 6.2 for ferrihydrite and to 6.9 for goethite and hematite. The initial neptunium concentration ranged from 0.2 to 2 μM, and the initial catechol and alanine concentrations were 1 μM. The sorption isotherms of neptunium on iron oxides suggest that catechol and alanine does not significantly affect the sorption of neptunium. The implication of these results is that there is no significant influence of catechol and alanine on neptunium sorption on different iron oxides.

Although both catechol and alanine may complex with neptunium in solution, the organic-metal complexes are apparently not strong enough to affect the neptunium sorption. These results are consistent with the data obtained from Figure 6.3-48, which indicate that DOPA has no effect on neptunium sorption.

In another set of experiments to study the effect of naturally occurring organic material on neptunium sorption, NAFA served as the model fulvic material. The sorption isotherms of neptunium on boehmite in the presence and the absence of NAFA are shown in Figure 6.3-53. The sorption isotherms of neptunium on goethite in the presence and the absence of NAFA are shown in Figure 6.3-54. Sorption isotherms of neptunium on untreated tuff materials are shown in Figure 6.3-55. Sorption isotherms of neptunium on treated tuff materials are shown in Figure 6.3-56. In these experiments, 0.1 M KCl was used as the background electrolyte, and the final pH was adjusted to 6.2. Initial neptunium concentrations ranged from 0.2 to 3 μM, and NAFA concentrations ranged from 0.1 to 0.4 ppm. As shown in Figures 6.3-53 to 6.3-56, NAFA had little effect on neptunium sorption in all systems. Thus, it is concluded that organics do not affect the sorption of neptunium in both simple, low-molecular-weight organics and naturally occurring fulvic organic material. The lack of detectable effects of organics on neptunium sorption is possibly attributed to the stable redox state of Np(V) in solution and to low complexation between neptunium ions and organic chemicals.

6.3.3.2.2.2 Plutonium

Sorption as a Function of Tuff and Oxide Minerals–Plutonium sorption on different materials is shown in Figure 6.3-57. On a weight basis, hematite was the most adsorptive whereas goethite was the least adsorptive. The sorption of plutonium follows the order hematite > ferrihydrite > goethite. Two things should be noted in this result. First, the surface areas of these iron oxides were not the same. For ferrihydrite and goethite, the surface areas are around 90 m^2/g; for hematite, the surface area is about 40 m^2/g. Second, the sorption experiments were not conducted at the same pH. The sorption on ferrihydrite was conducted at pH 6.1; the sorption on goethite was conducted at pH 6.6; and the sorption on hematite was conducted at pH 6.9. The effect of oxide surface areas on plutonium sorption was replotted in Figure 6.3-58, with the amount of plutonium sorption normalized to unit surface area (m^2). Results again showed that the sorption of neptunium follows the order hematite > ferrihydrite > goethite. The effect of pH on plutonium sorption is presented in the next subsection.

Effect of pH on Sorption–The isotherms for plutonium sorption on goethite at two different pH levels are shown in Figure 6.3-59. Increasing the solution pH from 6.6 to 6.9 resulted in a higher

plutonium sorptivity. It should be noted that the initial plutonium concentration was the same for both isotherms; however, the amount of goethite was different. The linear sorption curves suggest a low degree of coverage of the surface reactive sites by plutonium ions in the presence of excess potassium chloride. This finding is consistent with the theoretical calculation of coverage, which suggests, based on BET surface areas, that the amount of plutonium sorption is much less than a monolayer.

Increasing the solution pH resulted in a higher plutonium sorptivity. Under neutral conditions (pH 7), goethite is expected to have positive surface charges. However, the sorption of plutonium on goethite was found to increase as solution pH increased. The sorption of plutonium is apparently not dependent on ion exchange because iron oxide should have no cation exchange capacity. The sorption is believed to be controlled by a surface-complexation process because plutonium is expected to be dominated by the cationic species PuO_2^+ under neutral and slightly acidic conditions.

Effect of Model Organics on Sorptive Behavior–The isotherms for plutonium sorption on ferrihydrite in the presence of catechol and alanine are shown in Figure 6.3-60, and the isotherms for plutonium sorption on goethite and hematite in the presence of catechol and alanine are shown in Figure 6.3-61. These sorption isotherms clearly demonstrate that the sorption of plutonium onto goethite and ferrihydrite was affected by the presence of the organic materials. The amount of plutonium sorption on goethite and ferrihydrite was lower in systems that contained alanine than in systems that contained no alanine. Apparently, the presence of alanine suppressed the plutonium sorption on goethite and ferrihydrite. The inhibition of plutonium sorption on the iron-oxide surface in the presence of alanine is probably caused by the lowering of the free plutonium ion activity in solution by formation of an alanine-plutonium complex.

Conversely, the amount of plutonium sorption on goethite and ferrihydrite was higher in the presence of catechol than it was in the absence of catechol. Evidently, catechol enhanced the sorption of plutonium on goethite and ferrihydrite.

However, the effect of catechol and alanine on plutonium sorption was not found in the hematite system. The presence of catechol and alanine had little effect on the sorption of plutonium on hematite (Figure 6.3-61). The lack of an observable effect from the presence or absence of catechol and alanine on plutonium sorption on hematite is probably a result of the intrinsically high sorptivity of plutonium on hematite. Any small enhancement or suppression of sorption that might be attributed to catechol and alanine under such a high sorptivity would not be detected. Results of this study suggest that the model organic materials catechol and alanine do affect the sorption of plutonium on iron oxides.

The isotherms for sorption of plutonium on ferrihydrite and goethite in the absence of DOPA and in its presence at three concentration levels (1×10^{-6}, 1×10^{-7}, and 1×10^{-8} M) clearly demonstrate (Figures 6.3-62 and 6.3-63) that such sorption was affected by the presence of the organic material DOPA. Plutonium sorption was higher in systems that contained DOPA than in systems that contained no DOPA. Furthermore, sorptivity increased as initial DOPA concentration increased from 1×10^{-8} to 1×10^{-6} M. Evidently, the presence of DOPA enhanced plutonium sorption on goethite and ferrihydrite. This result is likely attributed to the formation of stable surface DOPA-plutonium ternary complexes and a redox reaction between DOPA and

plutonium. Reduction of Pu(V) to lower oxidation states will enhance the sorption/precipitation of plutonium. However, the effect of DOPA on neptunium sorption was not found in goethite (Figure 6.3-48), boehmite (Figure 6.3-49), and tuff material (Figure 6.3-46). The presence of DOPA had little effect. It is possible that DOPA does not complex with neptunium in solution and/or that DOPA cannot reduce Np(V) to lower oxidation states. Such relatively weak complexation is possibly a result of the relatively low effective charge on the cation (Choppin and Rao 1984), consistent with the fact that neptunium complexed weakly with a natural humic material extracted from a groundwater (Kim and Sekine 1991).

6.3.3.2.3 Summary

From the sorption data, the following conclusions can be drawn concerning the effect of natural organic materials on neptunium and plutonium sorption by iron and aluminum oxides and crushed tuff material:

- The sorption of model organic material DOPA on oxide surfaces follows the order aluminum oxide > iron oxide. For a given sorbent, the higher the pH, the more DOPA is sorbed. Surface complexation is the most likely sorption mechanism.

- The sorption of plutonium generally follows the order hematite > ferrihydrite > goethite. The sorption of neptunium on iron oxide is higher than that on aluminum oxide. The sorption of neptunium on crushed tuff material was much lower than that on oxide surfaces.

- The sorption of plutonium and neptunium on iron oxides increases as the solution pH is raised. The sorption of plutonium is much higher than that of neptunium on hematite, goethite, and ferrihydrite.

- The amount of neptunium sorption was not affected by any of the organic materials that were studied. The presence of the model organic materials alanine, catechol, DOPA, and NAFA did not influence the sorption of neptunium on tuff or on iron and aluminum oxides. This lack of an observable effect is presumably a result of the weak complexation between neptunium and the model organics.

- The sorption of plutonium was influenced by the presence of DOPA on goethite and ferrihydrite. Increasing the amount of DOPA resulted in higher sorption of plutonium on goethite and ferrihydrite. Alanine decreased the sorption of plutonium.

However, in the system containing catechol, plutonium sorption was increased. The enhancement of plutonium sorption in the presence of catechol is probably due to the reduction of Pu(V) to Pu(IV) by the organic. The inhibition of plutonium sorption in the presence of alanine is probably caused by the lowering of the free plutonium-ion activity in solution by formation of an alanine-plutonium complex. No observable effect of organics on plutonium sorption was found in the hematite system, which is probably due to a relative high sorptivity of plutonium on the hematite surface.

6.3.3.3 Models That Can Explain The Sorption Data

Radionuclides are known to be adsorbed by mineral surfaces in rocks and soils. The strongest interactions between aqueous species and mineral surfaces are the formation of electrostatic and covalent bonds. Ion-exchange reactions are primarily electrostatic interactions (outer electronic sphere and diffuse layer). Inner-sphere surface complexes form a chemical bond (to the mineral surface) that is more covalent. The electrostatic interaction does not have the same degree of selectivity between aqueous ions of like charge as does the more covalent inner-sphere surface complex. Stable inner-sphere complexes can be formed even when the mineral surface charge is the same as the aqueous ion. On the other hand, the adsorption of metal ions via cation exchange will only occur on surfaces of opposite charge and is affected by such common components of groundwater as sodium. Both of these processes can, in principle, be modeled using a triple-layer surface-complexation model. There are significant differences between the cation exchange in zeolites and clays and the formation of outer-sphere complexes on metal oxides. For this reason, cation exchange and surface complexation will be treated separately.

Cation Exchange

Description Of The Process–The cation exchange capacity of aluminosilicates is often high. Zeolites, such as clinoptilolite and mordenite, and clays, such as montmorillonite, have enormous surface areas because of their channeled and layered structures, respectively. The surfaces are negatively charged because they are composed of tetrahedrally bound silica and alumina. Aluminum requires an additional electron in order to share electrons equally between four oxygen atoms in a tetrahedral structure. The excess negative charge is balanced by an alkali-metal or alkaline-earth cation. These cations can be exchanged for cationic radionuclides. The extent to which a radionuclide is adsorbed depends on the selectivity for that cation. The equilibrium reaction can be represented, for example, as follows:

$$t\text{-}AlO^-Na^+ + Cs^+ \leftrightarrow t\text{-}AlO^-Cs^+ + Na^+ \quad , \qquad \text{(Eq. 6.3-5)}$$

where t-AlO^- represents a tetrahedrally bound aluminum site. The equilibrium expression for this reaction is

$$K = \frac{[AlO^-Cs^+][Na^+]}{[AlO^-Na^+][Cs^+]} \quad , \qquad \text{(Eq. 6.3-6)}$$

where K is the selectivity coefficient. For a mineral with one type of cation exchange and a binary aqueous salt, this expression can be rewritten in terms of the solid-phase concentration, q, of one of the cations of interest (here, cesium). The result is

$$q = \frac{KQc}{(K-1)c} \quad , \qquad \text{(Eq. 6.3-7)}$$

where, in this case, $q = [AlO^-Cs^+]$, c is the solution-phase concentration of the cation, $[Cs^+]$, c_o is the total solution-phase cation concentration ($[Cs^+] + [Na^+]$), and Q is the cation exchange

capacity of the solid phase ([AlO$^-$Cs$^+$] + [AlO$^-$Na$^+$]). Equation 6.3-7 is nearly identical to the Langmuir isotherm (derived for the adsorption of gases on solids) and will be referred to as such in the remainder of this report.

Factors Affecting Cation Exchange–There are many factors affecting cation exchange in natural systems, such as competition between multiple cation exchange sites, selectivity between cations in groundwater and the radionuclide of interest, and aqueous speciation of the radionuclide, to name a few. Competition between multiple cation exchange sites leads to nonlinear adsorption isotherms. The selectivity between cations depends on the geometry of the cation exchange site and the relative degree of hydration of the aqueous cations. In clays and zeolites, the selectivity coefficient increases from more- to less-hydrated cations, so that the order for alkali metal cations is lithium < sodium < potassium < rubidium < cesium (see McBride 1994, for example). Aqueous speciation can change the charge and the net size of the ions. In addition, there are sites in minerals, such as analcime, that can exclude larger ions, like cesium, entirely.

In principle, an equilibrium code, such as EQ3/EQ6 (Wolery 1983), could predict cation exchange if selectivity coefficients for all the significant cationic constituents of groundwater were known for each cation exchange site in each mineral contained in tuff. In practice, few selectivity coefficients are known for single minerals, let alone individual exchange sites.

Experimental Methods–The most useful experiment for determining sorption thermodynamic data is the adsorption isotherm. The adsorption isotherm is a measurement of the solid-phase concentration versus the aqueous-phase concentration at constant temperature. If the behavior of the isotherm is ideal, it can be described by a Langmuir isotherm (Equation 6.3-7), which can be the case only if there is one type of cation exchange site and if outer-sphere surface complexation is not significant.

Pure cation exchange cannot be measured in a system also capable of surface complexation, whether that system is a whole rock or a clay mineral. By varying the pH and electrolyte concentration, either surface complexation or cation exchange can be enhanced, which allows information about both mechanisms to be extracted from the data. The Swiss nuclear waste program has made great progress in developing such methods (Baeyens and Bradbury 1995a, 1995b; Bradbury and Baeyens 1995).

Ion-exchange Models–One approach that allows the determination of the free energy of exchange in even non-ideal systems is that of Gaines and Thomas (1953). This approach requires that the adsorption isotherm be taken from one end member (for example, sodium saturated) to the other end member. In this case, the free energy of exchange, ΔG°, is related to the definite integral over the mole ratio of cations from one end member to the other as follows:

$$\Delta G^\circ = -\frac{RT}{Z_1 Z_2}\left[(Z_2 - Z_1) + \int_0^1 \ln K \, dA\right], \qquad \text{(Eq. 6.3-8)}$$

where Z_1 and Z_2 are the charges on the original and incoming cations, respectively, A is the mole ratio of the incoming cation, R is the gas constant, and T is absolute temperature. This approach

cannot, in general, be used to calculate distribution coefficients because it cannot describe nonideal solid solutions.

Ion exchange arises from two distinctly different chemical structures on the surfaces of minerals. One is the incorporation of aluminum (with a valence of 3) in a tetrahedrally bonded silicate structure. The other is the amphoteric reaction of metal oxides with acids and bases. The former is a negatively charged surface of a fixed nature with the charge compensated by cations. The latter can be either negatively or positively charged depending on the pH of the aqueous phase. The exchange capacity of the former structure is fixed, whereas the exchange capacity of the latter depends on pH, ionic strength, and the concentration of specific inner-sphere complexing ligands. The adsorption of exchangeable ions on an activated metal-oxide surface is a form of outer-sphere surface complexation.

The selectivity in aluminosilicates for a given radionuclide over another has been shown to be not a simple binary exchange process, even when the solution is a simple binary aqueous solution, because not all positions in aluminosilicate are equivalent with respect to crystallographic structure (for example, there can be differences due to steric crowding). These differences have been studied by deconvolving the ion-exchange isotherm.

The method of deconvolution has been shown to be effective in studying structural effects on ion selectivities in synthetic zeolites (Triay and Rundberg 1989a). In that study, the shape of the ion-exchange isotherm was shown to be due to differences in the crystallographic structure at the ion exchange sites. This interpretation could not be made on the basis of the deconvolution of adsorption isotherms without spectroscopic data. However, the method of deconvolution does allow a quantitative correlation of the ion-exchange data with the spectroscopic data.

The method of analysis assumes ion exchange. The thermodynamics of ion exchange have been reviewed by Cremers (1977). The selectivity coefficient K for the hypothetical ion-exchange process in the reaction

$$AlO\text{–}M_1 + M_2^+ \leftrightarrow M_1^+ + AlO\text{–}M_2 \qquad \text{(Eq. 6.3-9)}$$

is given by

$$K = \frac{q_2 a_1}{q_1 a_2} \quad , \qquad \text{(Eq. 6.3-10)}$$

where a_1 and a_2 are the activities in solution of the cation to be exchanged and the entering cation, respectively, and q_1 and q_2 are the corresponding concentrations of these cations in the solid phase expressed as moles of cation per gram of the exchanger.

As a result of mass-balance considerations, Equation 6.3-10 can be rewritten as

$$q_2 = \frac{KQ\gamma_2 C_2}{C_o\gamma_1 + (K\gamma_2 - \gamma_1)C_2} \quad , \qquad \text{(Eq. 6.3-11)}$$

where Q is the total moles of exchangeable sites per gram of exchanger ($Q = q_1 + q_2$), C_2 is the concentration of the entering cation in the liquid phase, C_o is the total concentration of cations in the liquid phase ($C_1 + 1\ C_2$), and γ_1 and γ_2 are the activity coefficients in the solution phase of the cation to be exchanged and the entering cation, respectively (that is, $a_1 = \gamma_1 C_1$ and $a_2 = \gamma_2 C_2$).

Equation 6.3-11 represents the dependence of the solid-phase concentration on the liquid-phase concentration. It has the mathematical form of the Langmuir isotherm. In general, adsorption isotherms do not follow the Langmuir isotherm. Many authors have successfully described cation exchange in terms of multiple sites (Barrer and Klinowksi 1972; Barrer and Munday 1971; Brouwer et al. 1983). The underlying assumption of the deconvolution method is that the nonideality of the adsorption isotherm is due to adsorption at multiple sites. Consequently, one may consider a set of simultaneous equilibria

$$\begin{aligned} A^1\text{–}M_1 + M_2^+ &\leftrightarrow A^1\text{–}M_2 + M_1^+ \\ A^2\text{–}M_1 + M_2^+ &\leftrightarrow A^2\text{–}M_2 + M_1^+ \\ &\vdots \\ A^n\text{–}M_1 + M_2^+ &\leftrightarrow A^n\text{–}M_2 + M_1^+ \ , \end{aligned} \qquad \text{(Eq. 6.3-12)}$$

where $A^1, A^2, \ldots, A^n$ represent different sites in the ion exchanger.

The solid-phase concentration of the cation M_2^+ in site i is given by

$$q_2^i = \frac{K^i Q^i \gamma_2 C_2}{C_o\gamma_1 + (K\gamma_2 - \gamma_1)C_2} \quad , \qquad \text{(Eq. 6.3-13)}$$

and the total solid-phase concentration of M_2^+ is given by the sum

$$q_2 = \sum_{i=1}^{n} q_2^i = \sum_{i=1}^{n} \frac{K^i Q^i \gamma_2 C_2}{C_o\gamma_1 + (K^i\gamma_2 - \gamma_1)C_2} \quad . \qquad \text{(Eq. 6.3-14)}$$

This approach is further generalized by replacing the sum in Equation 6.3-14 with the integral equation

$$q_2(C_2) = \int q_2(C_2, K) \cdot f(K) \cdot dK \ , \qquad \text{(Eq. 6.3-15)}$$

where $f(K)$ is a distribution function for the selectivity coefficient of the exchange.

The idea of expressing the heterogeneity of the exchanger in terms of a distribution function has been previously presented (Brouwer et al. 1983; Adamson 1982; Sposito 1979, 1980, 1984; Kinniburgh, Barker et al. 1983). Equation 6.3-15 is a Fredholm integral of the First Kind, and the methodology used here to solve for $f(K)$ has been described by the authors (Triay and Rundberg 1987, 1989b) and others (Butler et al. 1981; Britten et al. 1983). The computer code INVPOS has been written (Brown, L.F. and Travis 1984) to solve Equation 6.3-15. INVPOS uses the method of Butler, Reeds, and Dawson (1981) to find an optimal solution using regularization with a positivity constraint.

Semiempirical adsorption isotherms, such as the Freundlich isotherm, are derived by evaluating the integral (Equation 6.3-15) using closed-form approximations and assuming some arbitrary site energy distribution. These approaches are only valid for data interpolation because they do not provide insight into the actual mechanism of adsorption.

Description Of Cation Exchange Sites In Yucca Mountain Tuff–Detailed adsorption isotherms adequate for the analysis described above have not been done for the Yucca Mountain Project. Measurements of the mineralogy of Yucca Mountain tuffs have shown an abundance of minerals known to have both pH-independent cation exchange sites (that is, tetrahedral aluminum sites) and surface complexation sites (for example, clay edge sites) for outer-sphere surface-complex formation. The most abundant minerals found in Yucca Mountain tuffs (Bish, Vaniman et al. 1983; Daniels et al. 1982) with a high cation exchange capacity are listed in Table 6.3-12.

In addition to the minerals listed in that table, feldspars may be important cation exchangers in the devitrified tuffs. Cation exchange capacity for a feldspar is not an intrinsic property because only the external surfaces are available for exchange. Thus, the number of sites depends on the crystal size and morphology.

State Of Knowledge Of Cation Exchange With Respect To Yucca Mountain Tuffs–As early as 1983 (Daniels et al. 1982), it was shown that the sorption distribution coefficient, K_d, for the adsorption of cesium onto Yucca Mountain tuffs could be predicted to within a factor of three using literature data for the cation exchange on the minerals in Table 6.3-12 with the addition of analcime. These predictions only considered competition with sodium. This simplification was made because there were no data for the cation exchange of the other alkali metals and alkaline earths present in J-13 well water. Some of the observed scatter could possibly be reduced with these additional data. Unfortunately, over the years since then, the situation has not changed. Thus, there is no predictive model based on mineralogy for cation exchange for radionuclides other than cesium.

The relative contribution of cation exchange to the adsorption of neptunyl onto the zeolitic tuff sample G4-1506 from a sodium-bicarbonate solution, was determined. The experiment was based partly on the method of Baeyens and Bradbury. Crushed tuff G4-1506 was equilibrated with 1 M sodium perchlorate to remove alkali metals and alkaline earths by mass action. Solutions containing 0.0022 M sodium bicarbonate (as a pH buffer) were prepared with sodium perchlorate added to provide sodium concentrations that varied from 0.0022 M to 0.22 M. Distribution coefficients for neptunium were determined using the standard procedure (Figure 6.3-64).

The surface complexation of neptunyl has been shown to be inner sphere and noncharging. Therefore, the surface complexation of neptunium is expected to be largely independent of sodium-ion concentration. The results show a linear decrease in K_d with sodium concentration at low sodium concentrations that is consistent with cation exchange (see Equation 6.3-10). At high sodium concentrations, the K_d asymptotically approaches 2.5 mL/g, consistent with surface complexation. The ion-exchange component is larger than the surface-complexation component, which corresponds to a K_d of about 10 in 0.0022 M sodium bicarbonate. The relatively low K_d for neptunyl in a zeolitic tuff is likely due to the large ion size and high hydration number. The K_d in pure sodium-bicarbonate solution is larger than that observed in J-13 water; this effect is due to competition with the additional cations in J-13 water of calcium, magnesium, and potassium. A model that describes these data and predicts neptunium sorption in the zeolitic tuff of Calico Hills will be described in the next subsection.

Surface Complexation

Description Of Surface-Complexation Process–The model that will be used to interpret the results of the experiments is the triple-layer surface-complexation model (Davis, J.A. et al. 1978). The most important difference between this model and conventional chemical equilibria is the effect of surface charge on the activity of ions in the triple layer. This effect is calculated by multiplying the bulk-solution concentration, $[M^+]_{bulk}$, by a Boltzmann factor

$$[M^+] = [M^+]_{bulk}\, e^{-\left(\frac{e\psi_o}{kT}\right)}, \qquad \text{(Eq. 6.3-16)}$$

where k is the boltzmann constant, T is the absolute temperature, e is electronic charge, and ψ_o is the potential of the ion in the inner Helmholtz layer.

The charge on the metal-oxide surface is produced by the amphoteric reaction of the metal-oxide surface with acids and bases. The basic charge-producing reactions are with Brönsted acids and bases:

$$MOH_2^+ + H_2O \leftrightarrow MOH + H_3O^+ \text{ and} \qquad \text{(Eq. 6.3-17)}$$

$$MOH + H_2O \leftrightarrow MO^- + H_3O^+ , \qquad \text{(Eq. 6.3-18)}$$

for which the equilibrium constants are

$$K_{a_1}^{\text{int}} = \frac{[\text{MOH}][\text{H}_3\text{O}^+]}{[\text{MOH}_2^+]} e^{-\left(\frac{e\psi_o}{kT}\right)} \quad \text{and} \qquad \text{(Eq. 6.3-19)}$$

$$K_{a_2}^{\text{int}} = \frac{[\text{MO}^-][\text{H}_3\text{O}^+]}{[\text{MOH}]} e^{-\left(\frac{e\psi_o}{kT}\right)} \; . \qquad \text{(Eq. 6.3-20)}$$

Cations and anions can interact with the electric field near the metal-oxide surface by forming outer-sphere complexes. Ions can also be repelled from the aqueous phase near the metal-oxide surface, as illustrated by Equation 6.3-3, which can lead to what appears to be a negative sorption distribution coefficient. This phenomenon is a result of the increase in tracer concentration in the bulk solution due to repulsion of ions from the solution within the double layer. This effect is always small, $K_d > -1$ mL/g. The strict definition of K_d does not allow for negative values because that would imply a negative concentration (which is meaningless). The negative K_d arises because, experimentally, it is impossible to separate the solid phase without including the thin layer of water close to its surface.

Negative K_d values can be used in the same way as positive K_d values and lead to the correct prediction of more rapid migration of excluded tracer with respect to tritiated water, that is, retardation factors less than 1. This phenomenon has been used by van den Hul and Lykelma (1968) to measure the specific surface area of suspended materials. Outer-sphere surface complexation can account for this phenomenon and is represented by the following equations:

$$\text{MOH}_2^+ + \text{An}^- \leftrightarrow \text{MOH}_2^+\text{An}^- \quad \text{and} \qquad \text{(Eq. 6.3-21)}$$

$$\text{MO}^- + \text{Cat}^+ \leftrightarrow \text{MO}^-\text{Cat}^+ \; , \qquad \text{(Eq. 6.3-22)}$$

where An^- is the anion and Cat^+ is the cation. The equilibrium constants corresponding to these equations are

$$K_{\text{an}}^{\text{int}} = \frac{[\text{MOH}_2^+\text{An}^-]}{[\text{MOH}_2^+][\text{An}^-]} e^{-\left(\frac{e\psi_\beta}{kT}\right)} \quad \text{and} \qquad \text{(Eq. 6.3-23)}$$

$$K_{\text{cat}}^{\text{int}} = \frac{[\text{MO}^-\text{Cat}^+]}{[\text{MO}^-][\text{Cat}^+]} e^{\left(\frac{e\psi_\beta}{kT}\right)} \; , \qquad \text{(Eq. 6.3-24)}$$

where ψ_β is the potential of the ion in the outer Helmholtz layer. The ions adsorbed in the outer layer can be exchanged for other ions. The ion-exchange process would be expected to have selectivity differences due to factors such as ion size.

Factors Affecting Surface Complexation–Surface-complexation models are equilibrium models and, therefore, account for speciation reactions explicitly. It is inherently difficult to characterize whole rock, however. This difficulty arises from the very surface nature of the reactions described. The number of available sites depends on the crystal size and morphology. The identity of available sites depends on the availability of mineral surfaces to the pore water and can be changed by weathering. Given these inherent difficulties, an attempt will be made to develop a simplified model of surface complexation, including cation exchange.

HSAB (Hard-Soft Acid-Base) Theory–The surface-complexation coefficients for monodentate surface complexes have been shown to be proportional to the first hydrolysis constant of the aqueous metal ion. This relationship is the natural consequence of the Lewis acid-base theory. The Lewis definition of an acid is an electron-pair acceptor and of a base, an electron donor. The hydrolysis of metal ions in aqueous solution proceeds by reacting with a water molecule displacing a hydrogen ion (an Arrhenius acid) yielding a monohydroxide:

$$M^{n+} + H_2O \leftrightarrow MOH^{(n-1)+} + H^+ \quad . \qquad \text{(Eq. 6.3-25)}$$

This reaction is analogous to the formation of a monodentate surface complex on a metal oxide, for example, alumina:

$$Al_{surf}\text{–}OH + M^{n+} \leftrightarrow Al_{surf}\text{–}OM^{(n-1)+} + H^+. \qquad \text{(Eq. 6.3-26)}$$

The principal difference between these reactions is that the hydroxide ion is the Lewis base in the aqueous hydrolysis reaction (Equation 6.3-25) and the surface oxygen is the Lewis base in the surface-complexation reaction (Equation 6.3-26). The strength of the Lewis acid M^{n+} in both reactions is related to the first hydrolysis constant, K_{11}. The basicity of the surface oxygen is related to the second acid-dissociation constant, K_{a2}, of the metal oxide. This relationship can be tested by comparing the sum of the logarithms of the surface-complexation constant and the second acid-dissociation constant against the logarithm of the first hydrolysis constant of the metal ion. The log K_a values for the first and second acid-dissociation constants of metal oxides expected to be found in Yucca Mountain tuffs are listed in Table 6.3-13, along with the point of zero charge (the pH at which surface in equilibrium with that solution has no net charge). The comparison of literature values (Dzombak and Morel 1990; Kinniburgh, Jackson et al. 1976; Huang and Stumm 1973; Schindler 1985) for surface complexation (log K_s + log K_{a2}), of metal ions on alumina, silica, and iron oxide are shown in Figure 6.3-65.

The results of this comparison demonstrate that the surface-complexation constant can be estimated to within an order of magnitude, for most metals, given the first hydrolysis constant. A similar comparison for bidentate attachment has yet to be developed, primarily because of the lack of reliable data for bidentate surface complexes.

Description Of Surface Complexation Sites In Yucca Mountain Tuffs–Although surface complexation has just begun to be studied on Yucca Mountain tuffs, there are a number of mineral surfaces having known surface complexation sites. These are hematite and related iron oxides, silica, and the edge sites of clays. The clay edge sites have been studied and found to be

most similar to octahedral alumina (Wieland 1988; Stumm 1992). Although there is no supporting data to determine the relative abundance of these sites, the hard-soft acid-base approach described above allows one to predict the surface-complexation mechanisms in terms both of stoichiometry and of equilibrium constants.

Modeling Of Yucca Mountain Tuff–A surface-complexation model for neptunium adsorption onto the zeolitic tuff sample G4-1506 was developed to fit the sodium-concentration dependence. The model considered a simple ion-exchange mechanism:

$$AlO^-Na^+ + NpO_2^+ \leftrightarrow AlO^-NpO_2^+ + Na^+ , \qquad \text{(Eq. 6.3-27)}$$

and the formation of an inner-sphere surface complex with octahedral alumina (edge sites) or hematite:

$$AlOH + NpO_2^+ \leftrightarrow AlONpO_2 + H^+ . \qquad \text{(Eq. 6.3-28)}$$

The number of cation exchange sites available to neptunium (Table 6.3-14) was based on the apparent saturation of sites observed in a neptunium adsorption isotherm measured for tuff sample G4-1608 in a carbon-dioxide atmosphere (Thomas 1987). The neptunium exchange capacity is four orders of magnitude smaller than the cation exchange capacity of clinoptilolite (Table 6.3-12). This difference can be explained by the large size of the hydrated neptunyl ion. If no sorption occurs in the intracrystalline channels of the clinoptilolite, the maximum exchange capacity will be on the order of a μmole per gram, assuming a 3-μm crystal diameter. The selectivity for neptunium was used as an adjustable parameter, and the model was fit to the results of the sodium-ion dependence of neptunium adsorption onto tuff sample G4-1506.

The inner-sphere surface complexation of neptunium was modeled assuming that surface complexation occurs primarily on clay edge sites or iron-oxide surfaces. The constant for inner-surface complexation of neptunium onto iron oxide was used because the analogous constant for alumina is expected to be nearly equal on the basis of the hard-soft acid-base theory shown above. Thus, the second adjustable parameter was the edge-site density.

To extend this model to the empirical measurements done under the project's geochemistry program, additional assumptions were made. The competition of cations in groundwater for cation exchange sites was based on the selectivities derived from measurements on the mineral tobermorite (Tsuji and Komarneni 1993). This approach was the result of the argument explaining the reduced cation exchange capacity for neptunium. If exchange occurs only on the exterior of the zeolite crystal, then steric effects must be avoided. Tobermorite offers an open structure that could be expected to have less steric effects than a zeolite. Furthermore, that work showed little difference between magnesium and calcium so that both magnesium and calcium were treated as one competitor. There were no data for potassium, so competition with potassium was not considered.

The surface-complexation constant for calcium was taken from the hard-soft acid-base theory. Thus, there were no additional adjustable constants. The concentrations used for J-13 and UE-25p #1 well water are shown in Table 6.3-15. The calculations were made using the

FITEQL equilibrium code in the forward mode only, that is, no fitting. The results of the modeling are shown in Figures 6.3-66 and 6.3-67. The correct pH dependence was predicted for the dry-sieved samples; the wet-sieved samples agreed better with a calculation that had no surface complexation sites. The implications of these results are not yet fully understood. Two possibilities are that either the clay particles are washed out, reducing the available edge sites, or that a trace component of J-13 water is forming a strong surface complex that competes with neptunium. The model also predicted the observed reduction in the sorption distribution coefficient, K_d, due to the components of UE-25p #1 water. In this water, the higher carbonate concentration eliminates the contribution of surface complexation observed in J-13 water at pH values above 7.

A model was also developed for pH dependence of uranium adsorption onto crushed devitrified tuff. This treatment was similar to that used to model neptunium adsorption except that the cation exchange capacity for uranium was not known (i.e., there was no adsorption isotherm) and a cation exchange with the monohydroxy-uranyl complex was included. The parameters used are listed in Table 6.3-16. The number of sites used to model these data was much greater than for the zeolitic tuff. The possible reason for this is the exposure of fresh surfaces of feldspar and quartz combined with the lack of exposure to a complex groundwater.

The results of this exercise are shown in Figure 6.3-68 and are in excellent agreement with the results of Leckie and his students (Davis, J.A. et al. 1978). The equilibrium concentration of uranium at pH values of 9 and above are above the solubility limit for uranium hydroxide. The effect of precipitation was evident in the experimental data. The solubility product was not included in this model.

State Of Knowledge Of Surface Complexation With Respect To Yucca Mountain–Surface-complexation reactions with Yucca Mountain tuffs have just begun to be studied. The pH dependence of actinide adsorption can be readily explained with a combined surface-complexation and ion-exchange model. The effect of changing groundwater composition on neptunium adsorption has also been successfully modeled using a surface-complexation model. There are significant gaps in the knowledge base, however. From a fundamental standpoint, a hard-soft acid-base model for bidentate inner-sphere complexes needs to be developed. The consequences of a bidentate attachment mechanism, as was included in the uranium adsorption model, is an increased sensitivity to competition with metal ions favoring monodentate attachment (for example, calcium). From an experimental standpoint, the effects of wet-sieving needs to be better understood. If wet-sieving removes all of the clay minerals, the resulting distribution coefficients may be too low (overly conservative). On the other hand, if a trace component of groundwater is responsible for the decrease in surface complexation, it must be identified and measured in groundwaters and in pore waters.

The modeling of actinide sorption shows that high carbonate concentrations will severely reduce the ability to form surface complexes on tuff. The ion exchange of actinides appears to dominate under normal conditions over surface complexation. Furthermore, divalent cations are found to be strong competitors for cation exchange sites found in Yucca Mountain tuffs.

6.3.3.4 Sorption Results Recommended for Performance Assessment

Sorption is a function of water chemistry and the type of tuff at Yucca Mountain. The water chemistry at Yucca Mountain was reviewed by Meijer (1992) and is discussed in Subsection 6.2, "Fluid Geochemistry." The concentration of the major cations and anions in unsaturated-zone groundwaters appears to be intermediate between the saturated-zone tuffaceous waters (for example, from Well J-13) and waters from the Paleozoic carbonate aquifer (from Well UE-25p #1) see Subsections 6.2.5 and 6.2.8 for further discussions of the major ions in these waters). Consequently, the first assumption made for the performance-assessment recommendations was that the waters from Wells J-13 and UE-25p #1 bound the chemistry of the groundwaters at Yucca Mountain.

The second assumption made dealt with grouping all strata on the basis of rock type. This assumption reduced the number of sorption-coefficient distributions elicited to four per radionuclide: iron oxides, devitrified tuff, vitric tuff, and zeolitic tuff (Wilson et al. 1994). The basis for this grouping is the fact that sorption of radionuclides is the result of a chemical reaction between the radionuclide in the groundwater and the minerals in the tuff. The mineralogy of the different strata of the same rock group is very similar, and the sorption coefficients can be grouped in terms of these rock types (Thomas 1987).

The containers to be used in the repository were added to the list after consideration of whether the corrosion by-products of the massive multipurpose container could become a substrate for sorption. Actinides are sorbed strongly by iron oxides. However, although hematite is found in the tuffs at Yucca Mountain, the iron-oxide minerals in the tuffs appear to be "passivated"–that is, all of the sorption sites could be occupied by other metals (Triay, Robinson, Lopez et al. 1993)–and the sorption of the radionuclides onto tuff (containing iron oxides as trace minerals) is not as large as predicted on the basis of the sorption of radionuclides onto synthetic pure iron oxides. (It should be noted that passivation is only a hypothesis to explain the observation that Np does not sorb significantly with respect to Yucca Mountain tuffs.) Because the sorption sites on the degraded container material would not necessarily be occupied by other metals, the experts agreed to add iron oxides to the list of "rock" types.

The effect of temperature on sorption coefficients was reviewed by Meijer (1990). Measured sorption coefficients onto tuffs were higher at elevated temperatures for all elements studied: americium, barium, cerium, cesium, europium, plutonium, strontium, and uranium. Consequently, the third assumption made was that sorption coefficients measured at ambient temperatures should be applicable and generally conservative when applied to describing aqueous transport from a hot repository. (This assumption is meaningful provided that high temperatures, that will be sustained for long time periods due to potential high thermal loads, do not result in changes in the mineralogy and water chemistry at Yucca Mountain that are not predictable by short-term laboratory and field experiments.)

Table 6.3-17 shows the parameters for the sorption-coefficient probability models recommended for performance assessment for the unsaturated-zone units, and Table 6.3-18 shows the same parameters for saturated-zone units. The source of these values for each of the elements is discussed separately in the following paragraphs.

Americium–Americium sorbs strongly to most materials (Triay, Meijer, Cisneros et al. 1991). The potential mechanisms for actinide sorption onto mineral surfaces has been reviewed by Meijer (1992). The sorption-coefficient distributions for americium in Yucca Mountain tuffs and iron oxides given in Tables 6.3-17 and 6.3-18 were inferred from the data presented by Thomas (1987), Triay, Meijer, Cisneros et al. (1991), and Meijer (1992).

Plutonium–One of the problems of interpreting sorption data for plutonium is that this element can exist in multiple oxidation states under oxidizing conditions at near-neutral pH values (Nitsche, Gatti et al. 1993). Plutonium can also exist as a polymer (Triay, Hobart et al. 1991). The lack of information on the speciation of plutonium in the groundwaters at Yucca Mountain makes it difficult to assess the sorption mechanism for this element. However, the empirical data obtained in Yucca Mountain tuffs indicate that plutonium sorbs strongly. The sorption-coefficient distributions for plutonium in Yucca Mountain tuffs given in Tables 6.3-17 and 6.3-18 were inferred from the data presented by Thomas (1987) and Meijer (1992).

Uranium–No additional data for uranium have been collected for Yucca Mountain tuffs since the 1991 total-system performance-assessment effort (Barnard et al. 1992). Consequently, no change was made for the sorption-coefficient distributions used for this element. As previously discussed (Meijer 1992), uranium sorbs strongly to synthetic iron oxides.

Thorium–The information elicited for americium was also used for thorium. This approach is due both to the lack of sorption information available for thorium and to the similarities exhibited by the sorption behavior of these two elements (Thomas 1987).

Radium–Barium has been used as an analog for radium in the experiments performed at Los Alamos (Thomas 1987). These elements sorb to Yucca Mountain tuffs via an ion-exchange mechanism and surface-adsorption reactions (Meijer 1992). The sorption-coefficient distributions for radium in Yucca Mountain tuffs and iron oxides given in Tables 6.3-17 and 6.3-18 were inferred from the data presented by Thomas (1987), Meijer (1992), and Triay, Mitchell et al. (1991).

Lead–The sorption-coefficient distributions for lead in Yucca Mountain tuffs and iron oxides given in Tables 6.3-17 and 6.3-18 were inferred from the data presented by Meijer (1990).

Neptunium–Sorption-coefficient distributions for neptunium in tuff are the same as those used in TSPA-1991. Recently obtained data (Triay, Robinson, Lopez et al. 1993) agree with previous observations. Neptunium is a poorly sorbing radionuclide in tuff even when the tuffs are known to have iron oxides because the iron oxides in the tuff appear to be passivated. The neptunium sorption-coefficient distribution for sorption onto iron oxides given in Tables 6.3-17 and 6.3-18 was inferred from data presented by Meijer (1992) and Triay, Robinson, Lopez et al. (1993) for sorption onto synthetic iron oxides.

Protactinium–Very little information exists for protactinium sorption onto tuffs (Thomas 1987), so, for this element, the experts decided to use the same sorption coefficients elicited for neptunium.

Tin–There is very little information for the sorption of tin onto tuffs (Thomas 1987). Based on the data available, Meijer (1992) suggested that tin exhibited large values of K_d in the devitrified tuffs (larger than 1000 mL/g). The sorption-coefficient distributions given in Tables 6.3-17 and 6.3-18 were inferred from the work by Andersson (1988); the uniform distributions chosen were the result of the expert's uncertainty about the sorption of tin.

Nickel–For devitrified, vitric, and zeolitic tuffs, the nickel sorption-coefficient distributions given in Tables 6.3-17 and 6.3-18 were inferred from data presented by Meijer (1992). For iron oxides, the nickel sorption-coefficient distribution was inferred from the data presented by Siegel, Hopkins et al. (1992) and Siegel, Ward et al. (1993)

Cesium–Cesium sorption-coefficient distributions for tuff and iron oxides were inferred from the data presented by Thomas (1987), Meijer (1992), and Triay, Mitchell et al. (1991). Cesium has one of the highest selectivity coefficients for zeolites among all chemical elements (Meijer 1992). Cesium sorption onto devitrified and vitric samples could be the result of ion exchange onto clays or feldspars in the tuff samples or surface-adsorption reactions (Meijer 1992).

Strontium–Strontium sorption-coefficient distributions for tuff and iron oxides were inferred from the data presented by Thomas (1987) and Triay, Mitchell et al. (1991). Strontium sorbs strongly onto zeolites by ion exchange. This element's sorption onto other types of tuff may be dominated by the amount of clay in the tuff units. The values given in Tables 6.3-17 and 6.3-18 are generally conservative.

Selenium–There are limited data on tuff for selenium sorption (Thomas 1987), so the experts decided to use the same sorption-coefficient distributions for selenium as the ones elicited for uranium. This decision is a conservative one because uranium can be oxidized much more readily than selenium in Yucca Mountain groundwaters.

Carbon–Carbon is a special case because transport is expected to occur primarily in the gaseous phase as carbon dioxide. The major retardation mechanism is exchange of carbon-14 with the carbon in the carbon dioxide dissolved in the groundwater.

Actinium, Samarium, Niobium, and Zirconium–All these elements are strongly sorbing (Meijer 1992). The experts advised using for these elements the same sorption-coefficient distributions as those elicited for americium.

Iodine, Technetium, and Chlorine–Iodine and chlorine have anions that do not sorb onto tuffs. Technetium exists as pertechnetate under oxidizing conditions and does not sorb either (Triay, Birdsell et al. 1993).

6.3.4 Dynamic Transport Studies

6.3.4.1 Crushed-Rock Columns

Generally, batch-sorption experiments, which were discussed in Subsection 6.3.3, are used to identify sorption mechanisms and to obtain sorption distribution coefficients (Triay, Cotter, Huddleston et al. 1996; Triay, Cotter, Kraus et al. 1996). Such experiments are fast, easy, and

inexpensive compared to other types of sorption experiments. This section, contains discussion of the attempts to verify the results of earlier batch-sorption measurements by performing crushed-tuff column studies under flowing conditions without significantly changing the surface properties of the tuff. By comparing differences with the batch-sorption measurements, such studies would be most sensitive to multiple-species formation, colloid formation, and any other geochemical reactions (such as changes in surface reactivity due to agitation) not adequately described by batch-sorption distribution coefficients. In these crushed-tuff column experiments, mass-transfer kinetics were investigated by studying radionuclide migration as a function of water velocity.

Column elution curves can be characterized by two parameters: the time of arrival of the radionuclide eluted through the column and the broadness (dispersion) of the curve. The arrival time depends on the retardation factor, Rf, which, for soluble radionuclides, depends, in turn, on the sorption distribution coefficient, Kd. Significant deviations (those larger than expected based on sampling variability) in arrival time from that predicted on the basis of the batch-sorption distribution coefficients indicate one of the following problems:

- The presence of more than one chemical species that are not readily exchanged and that have different selectivities in tuff minerals
- The presence of the radionuclide as a colloid
- Extremely slow sorption kinetics
- Nonreversibility of the sorption process
- Solubility effects due to the presence of solids
- Hydrologic parameters (conductivity and porosity)
- Experimental artifacts

The broadness, or apparent dispersion, of the curve depends on:

- The kinetics and reversibility of sorption
- The linearity of the isotherm that describes the dependence of sorption on radionuclide concentration

The main goal of the study was to test the necessary assumptions made in using values of the sorption distribution coefficient, Kd, (determined by batch-sorption measurements) to describe hydrologic transport (see Eq. 6.3-29 that follows for the relationship between the retardation coefficient and the sorption distribution coefficient). These assumptions are:

1. Microscopic equilibrium is attained between the solution species and the adsorbate.

2. Only one soluble chemical species is present (or if more than one is present, they interchange rapidly).

3. The radionuclides in the solid phase are adsorbed on mineral surfaces (that is, they are not precipitated).

4. The dependence of sorption on concentration is described by a linear isotherm.

The importance of verifying these assumptions can be demonstrated by the following hypothetical cases. If equilibrium were not attained in the batch experiments (violation of assumption 1, the retardation of radionuclides could be dependent on groundwater velocity. If a radionuclide were present in solution as an anionic and a cationic species and solution equilibrium were not maintained (violation of assumption 2, the batch measurement would predict a single retardation factor, whereas in a flowing system, the anion could move unimpeded (its size and charge excluding it from the pores of the Yucca Mountain tuffs) compared to movement of the cation. If the radionuclide had precipitated in the batch experiments (violation of assumption 3, the value of the Kd thus determined would be meaningless, and depending on the precipitation mechanism, colloid transport could be important. If the isotherm was nonlinear (violation of assumption 4, the migration front of the radionuclides in a column study would usually broaden, appearing as increased dispersion over that observed for nonsorbing tracers.

Experimental Procedures

Groundwaters and Solutions–Because the J-13 and UE-25p #1 well waters that bound the Yucca Mountain groundwaters are both oxidizing (Ogard and Kerrisk 1984), all the batch-sorption and column experiments were performed under oxidizing conditions. In the batch-sorption experiments, both groundwaters (filtered by a 0.05-μm filter) were used, but in the column experiments, J-13 water (filtered) and a sodium-bicarbonate buffer that simulated UE-25p #1 groundwater (because of the unavailability of water from this well) were used. The synthetic UE-25p #1 water was prepared by dissolving 0.39 g of Na2CO3 and 8.90 g of NaHCO3 in 10 L of deionized water, which duplicates the larger amount of bicarbonate in reference, or on-site, UE-25p #1 water.

In the column experiments, neptunium and plutonium solutions were prepared in the same way as the batch-sorption experiments (by taking an aliquot of a well-characterized ^{237}Np(V) or ^{239}Pu(V) acidic stock and diluting it in the water being studied). Also used were tritium and pertechnetate solutions, which were similarly prepared by adding an aliquot of 3H or 95mTc acidic stock to the groundwater being studied.

Crushed-Rock Column Procedure–The details of the crushed-rock column experimental setup and procedure are illustrated in Figures. 6.3-69 and 6.3-70. Plexiglas columns were packed with crushed tuff by using a continuously agitated wet slurry, a technique that provides a relatively homogeneous packing nearly free of stratification. As in the batch-sorption experiments, all tuff samples had previously been crushed and wet-sieved (with the groundwater being used in the experiment) to obtain particle sizes ranging from 75 to 500 μm.

After establishing the desired flow rate in the tuff column using the desired groundwater, an aliquot of the radionuclide solution was injected and a syringe pump was used to elute the radionuclide through the column. The breakthrough or elution curve was measured. Tritiated water was used to measure the free volume of the column, which excludes dead-end pore volume. The concentration of tritium, pertechnetate, ^{239}Pu, or ^{237}Np in the eluent was measured by liquid-scintillation counting. The crushed-rock column dimensions and flow velocities that were used followed the guidelines provided by Relyea (1982).

Relationship Between Column and Batch Experiments–The batch-sorption distribution coefficients were measured under static conditions by equilibrating a solution containing the radionuclides with a sample of crushed tuff. If it is assumed that equilibrium is achieved between a single aqueous chemical species and the species adsorbed on the solid phase, the rate at which a radionuclide moves through a column can simply be related to the sorption distribution coefficient, K_d. The relationship between the retardation factor, R_f, obtained from column-transport experiments, and the values of K_d, obtained from batch-sorption experiments, is generally given by

$$R_f = 1 + \frac{\rho_b}{\varepsilon} K_d \ , \qquad \text{(Eq. 6.3-29)}$$

where ρ_b is the dry bulk density (including pores) and ε is the porosity of the column. Hiester and Vermeulen (1952) derived this equation and carefully described its underlying assumptions. To test these assumptions, the radionuclide solution used in the batch-sorption measurements was eluted through columns containing tuff samples that came from the same drillhole and depth interval and that had been crushed and sieved to the same size fraction as samples used in the batch-sorption studies.

Results and Discussion–The most comprehensive explanation of the fate of reactive and nonreactive solutes and suspended particles in porous and fractured media has been presented by de Marsily (1986, Chapter 10). The transport of radionuclides in porous media is governed by advection, diffusion, or kinematic dispersion. Advection is the mechanism in which dissolved species are carried along by the movement of fluid. Diffusion causes species to be transferred from zones of high concentration to zones of low concentration. Kinematic dispersion is a mixing phenomenon linked to the heterogeneity of the microscopic velocities inside the porous medium. The migration of a solute in a saturated porous medium is described by the following transport equation

$$\nabla \cdot (\mathbf{D} \nabla C - C\mathbf{U}) = \varepsilon \frac{\partial Q}{\partial t} + Q \ , \qquad \text{(Eq. 6.3-30)}$$

where **D** is the dispersion tensor, C is the concentration of solute in the solution phase, **U** is the filtration velocity (Darcy's velocity), ε is the porosity, t is time, and Q is a "net source or sink term" that accounts for such things as reactivity or adsorption.

For the case of a sorbing, nonreactive solute, the equation becomes

$$\nabla \cdot (\mathbf{D}\nabla C - C\mathbf{U}) = \varepsilon \frac{\partial Q}{\partial t} + \rho_b \frac{\partial F}{\partial t} \quad , \qquad \text{(Eq. 6.3-31)}$$

where ρ_b, again, is the dry bulk density of the medium and F is the mass of solute sorbed per unit mass of solid.

Dispersion has three components: the longitudinal dispersion coefficient in the direction of the flow, D_L, and the transverse dispersion coefficient, D_T, in the two directions at right angles to the velocity of the flow. These components are given by

$$D_L = \varepsilon d + \alpha_L |U| \text{ and} \qquad \text{(Eq. 6.3-32)}$$

$$D_T = \varepsilon d + \alpha_T |U| \quad ,$$

where d is the effective diffusion coefficient in the medium and α is dispersivity.

The characteristics of the sorption determine the actual relationship between F and C. For the case in which sorption is linear, reversible, and instantaneous, the ratio between F and C is simply equal to the sorption distribution coefficient:

$$\frac{F}{C} = K_d \quad . \qquad \text{(Eq. 6.3-33)}$$

Substitution of Equation 6.3-33 into Equation 6.3-31 yields

$$\nabla \cdot (\mathbf{D}\nabla C - C\mathbf{U}) = \varepsilon \left[1 + \frac{\rho_b}{\varepsilon} K_d \right] \frac{\partial C}{\partial t} \quad , \qquad \text{(Eq. 6.3-34)}$$

The expression in brackets in Equation 6.3-34 corresponds to the retardation factor, R_f, given earlier (Equation 6.3-29). Thus, there is a way to compare sorption coefficients obtained under advective, diffusive, and dispersive conditions with sorption coefficients obtained from batch-sorption experiments. However, this approach is valid only if sorption is linear, reversible, and instantaneous.

Neptunium Results–Elution of Np(V) was measured as a function of water velocity through zeolitic, devitrified, and vitric crushed tuff in columns with J-13 well water and with synthetic UE-25p #1 water. The elution curves have been previously published (Triay, Furlano et al. 1996). Porosity was calculated as the free column volume divided by the total column volume (free volume was defined as the volume of tritium solution that had to be eluted to recover 50 percent of the injected tritium). Values of R_f were then calculated for the column experiments by dividing the free column volume into the volume of neptunium solution that had to be eluted to recover 50 percent of the injected ^{237}Np. From these values of R_f, Equation 6.3-29 was used to calculate the column sorption-distribution coefficients listed in Table 6.3-19.

How do the earlier results of batch-sorption experiments (Triay, Cotter, Huddleston et al. 1996; Triay, Cotter, Kraus et al. 1996) compare with the results of the crushed-tuff column experiments? Inspection of Table 6.3-19 indicates good agreement between the values of K_d obtained by the two approaches, which means that the arrival time of ^{237}Np can be predicted from a value for K_d. On the other hand, the broad, dispersive shape of the elution curves indicates that sorption of neptunium onto zeolitic and vitric tuffs appears to be nonlinear, nonreversible, or noninstantaneous. Previous work has found that sorption of neptunium onto clinoptilolite-rich tuffs is rapid (Triay, Cotter, Huddleston et al. 1996) and can be fit with a linear isotherm (Triay, Cotter, Kraus et al. 1996). Consequently, the degree of reversibility of neptunium sorption onto zeolitic and vitric tuffs may be the most likely reason for the apparent dispersivity in the tuff-column elution curves.

The elution curves also reveal that, regardless of the water being studied, the elution of ^{237}Np does not precede the elution of tritium for any of the tuffs. This observation is extremely important because if charge-exclusion effects were to cause the neptunyl-carbonato complex (an anion) to elute faster than neutral tritiated water molecules, significant neptunium releases could occur at Yucca Mountain. Another important observation that can be drawn from these experiments is that values of K_d can be used to obtain accurate or conservative estimates for the performance-assessment calculations of neptunium transport through Yucca Mountain tuffs. This conclusion assumes that transport of radionuclides through the unsaturated zone from the repository will occur homogeneously through tuff; the transport and retardation of radionuclides heterogeneously through fractures is deal with in Subsection 6.3.4.3.

Neptunium Summary–

- Using crushed-rock columns, the retardation of ^{237}Np by zeolitic, devitrified, and vitric tuffs in sodium-bicarbonate waters under oxidizing conditions (at room temperature, under atmospheric conditions, and using different water velocities) was studied.

- The sorption distribution coefficients obtained from the column experiments under flowing conditions were compared to those obtained from batch-sorption experiments under static conditions.

- The column and batch distribution coefficients agreed well for all tuffs regardless of the groundwater studied and the water velocity used for the column experiments.

- It was found that batch-sorption distribution coefficients predict well the arrival time for neptunium eluted through a crushed-rock column.

- The apparent dispersivity of the neptunium elution curves through the zeolitic and vitric tuffs indicates that the sorption is either nonlinear, irreversible, or noninstantaneous, which means the transport cannot be completely described using a sorption distribution coefficient. The reversibility of neptunium sorption onto tuff will be studied as the most likely reason for the apparent dispersivity of the elution curves.

- The use of a batch-sorption distribution coefficient to calculate neptunium transport through Yucca tuffs would result in conservative values for neptunium release.

- Neptunium never eluted prior to the nonsorbing radionuclide (tritiated water) used in the column experiments. Thus, charge exclusion does not appear to exclude neptunium from the tuff pores.

- Corroborated by these column experiments were the general trends previously observed for neptunium sorption using batch-sorption experiments: neptunium sorption onto devitrified and vitric tuffs is minimal, and neptunium sorption onto zeolitic tuffs decreases as the amount of sodium and bicarbonate/carbonate in the groundwaters increases.

Plutonium and Technetium Results–The elution of Pu(V) through zeolitic, devitrified, and vitric crushed tuff was measured in columns with J-13 well water and with synthetic UE-25p #1 water. The elution curves for these experiments (Figures 6.3-71 to 6.3-73) indicate that vitric and zeolitic tuffs sorb plutonium significantly, which is probably due to their clay content. The shape of the elution curves for plutonium indicates that use of K_d values to predict plutonium transport through Yucca Mountain tuffs will predict plutonium releases conservatively. Results by Triay, Cotter, and Harrigan (1995) indicate that plutonium sorption onto tuffs is a slow process and probably due to a redox reaction occurring at the tuff surfaces. To verify these batch-sorption results, which suggest that plutonium sorption, even to the lowest sorbing tuff type (devitrified), could be significant, the migration of plutonium as a function of flow velocity was measured in devitrified tuff using J-13 and UE-25p #1 waters. Inspection of these elution curves (Figures 6.3-74 and 6.3-75) confirms the trends observed using batch-sorption techniques; the elution curves observed for these columns are consistent with slow sorption kinetics.

The elution of pertechnetate was also studied in devitrified, vitric, and zeolitic tuffs in J-13 and synthetic UE-25p #1 waters as a function of flow velocity. Inspection of the elution curves (Figures 6.3-76 to 6.3-78) indicate that anion-exclusion effects for pertechnetate in crushed tuff are essentially negligible except in the case of technetium transport through zeolitic tuff in J-13 well water (Figure 6.3-78). In this case, the anion-exclusion effect is small but measurable.

6.3.4.2 Solid-Rock Columns

Direct measurements of transport parameters in actual subsurface materials under subsurface conditions are necessary for defensible modeling of contaminant transport in host rocks and engineered barriers surrounding nuclear and hazardous waste repositories. The hydraulic conductivity, K, and the retardation factor, R_f, along with the associated distribution coefficient, K_d, are poorly known transport parameters for real systems but are key input parameters to existing and developing contaminant release models. Unsaturated R_f and K were experimentally determined for core samples of Yucca Mountain vitric-member tuff and zeolitic nonwelded tuff from G-Tunnel, Bed 5, with respect to J-13 well water with a selenium concentration (as selenite) of 1.31 mg/L (ppm) at 23°C. The intent was to demonstrate that a method in which flow is induced with an ultracentrifuge (the UFA™ method) could rapidly and directly measure R_f and K in whole-rock tuff cores and then to compare these directly measured unsaturated R_f

values with those calculated from K_d values obtained through traditional batch tests on the same materials.

Methodology

Retardation–Retardation factors can be determined in flow experiments where R_f for a particular species is the ratio of the solution velocity to the species velocity. The retardation factor for that species is given by:

$$R_f = \frac{V_{gw}}{V_{sp}} = 1 + \rho_d \frac{K_d}{\varepsilon} \quad , \qquad \text{(Eq. 6.3-35)}$$

where V_{gw} is the velocity of carrier fluid, V_{sp} is the velocity of the species, ρ_d is the dry bulk density, ε is the porosity, and K_d is defined as the moles of the species per g of solid divided by the moles of the species per mL of solution. If none of a particular species is lost to the solid phase, then $K_d = 0$ and $R_f = 1$ for that species. In column experiments, a breakthrough curve is obtained for the particular species and R_f is determined as the pore volume at which the concentration of the species in the solution that has passed through the column is 50 percent of the initial concentration ($C/C_0 = 0.5$). It is now generally assumed that, for unsaturated systems, $\varepsilon = \theta$, where θ is the volumetric water content (Bouwer 1991; Conca and Wright 1992a). The study described in this section experimentally addresses this concern under unsaturated conditions in whole rock and evaluates the use of data from batch experiments in determining R_f in whole rock.

Solutions were prepared using J-13 well water with a selenite concentration of 1.31 ppm and determined the selenium concentrations with an inductively coupled, argon-plasma, atomic-emission spectrometer (Jarrell-Ash Model 976 Plasma Atomcomp). An ion chromatograph (Dionex Series 4000i) was used to determine the speciation of selenium in solution. All selenium in the starting and effluent solutions was found to exist as selenite.

Hydraulic Conductivity–One way to drive fluid through rock is to use centripetal acceleration as the driving force. This approach was used with a new technology (UFA) to produce hydraulic steady-state, to control temperature, degree of saturation, and flow rates in all retardation experiments, and to measure the hydraulic conductivity. A specific advantage of this approach is that centripetal acceleration is a whole-body force similar to gravity that acts simultaneously over the entire system and independently of other driving forces, such as gravity or matrix suction. It has been shown that capillary bundle theory holds in the UFA method (Conca and Wright 1992a, 1992b).

The UFA instrument consists of an ultracentrifuge with a constant, ultralow flow-rate pump that provides fluid to the sample surface through a rotating seal assembly and microdispersal system (Figure 6.3-79). Accelerations up to 20,000 g are attainable at temperatures from 220° to 150°C and flow rates as low as 0.001 mL/hr. The effluent is collected in a transparent, volumetrically calibrated container at the bottom of the sample assembly. The effluent collection chamber can be observed during centrifugation using a strobe light.

The current instrument has two different rotor sizes that hold up to 50 and 100 cm^3 of sample, respectively. Three different rotating-seal assemblies facilitate various applications and contaminant compatibilities; they are a face seal, a mechanical seal, and a paramagnetic seal. Figure 6.3-79 shows the large-sample option with the paramagnetic seal, a configuration that is optimal for adsorption and retardation studies.

Numerous studies have compared use of the UFA approach with traditional methods of doing this type of analysis in soils and clays, and the agreement is excellent (Conca and Wright 1992b; Nimmo et al. 1987). Good agreement is expected because the choice of driving force does not matter provided the system is Darcian (see next paragraph) and the sample is not adversely affected by a moderately high driving force ($\leq$ 1000 g for all samples run in these experiments); both of these provisions hold for most geologic systems. Additionally, all techniques for estimating hydraulic conductivity, $K(\theta)$, are extremely sensitive to the choice of the rock or soil residual water content, θ_r, and to the saturated hydraulic conductivity, K_s; minor variations in θ_r or K_s produce order-of-magnitude changes in $K(\theta)$ (Stephens and Rehfeldt 1985).

The UFA technology is effective because it allows the operator to set the variables in Darcy's Law, which can then be used to determine hydraulic conductivity. Under a centripetal acceleration in which water is driven by both the potential gradient, $d\psi/dr$, and the centrifugal force per unit volume, $\rho\omega^2 r$, Darcy's Law is

$$q = -K(\psi)\left[\frac{d\psi}{dr} - \rho\omega^2 r\right] , \qquad \text{(Eq. 6.3-36)}$$

where q is the flux density into the sample; K, the hydraulic conductivity, is a function of the matric suction, ψ, and, therefore, of water content, θ; r is the radius from the axis of rotation; ρ is the fluid density; and ω is the rotation speed. When multicomponent and multiphase systems are present in the UFA instrument, each component reaches its own steady-state with respect to each phase, as occurs in the field. Appropriate values of rotation speed and flow rate into the sample are chosen to obtain desired values of flux density, water content, and hydraulic conductivity in the sample. Above speeds of about 300 rpm, depending upon the material and providing that sufficient flux density exists, $d\psi/dr << \rho\omega^2 r$. Under these conditions, Darcy's Law is given by $q = -K(\psi)\,[-\rho\omega^2 r]$. Rearranging the equation and expressing hydraulic conductivity as a function of water content, Darcy's Law becomes

$$K(\theta) = \frac{q}{\rho\omega^2 r} . \qquad \text{(Eq. 6.3-37)}$$

As an example, a whole-rock core of Topopah Spring Member Tuff accelerated to 7,500 rpm with a flow rate into the core of 2 mL/hr achieved hydraulic steady-state in 30 hours with a hydraulic conductivity of 8.3 x 10^{-9} cm/s at a volumetric water content of 7.0 percent. Previous studies have verified the linear dependence of K on flux and the second-order dependence on rotation speed (Conca and Wright 1992a; Nimmo et al. 1987), and several comparisons between the UFA method and other techniques have shown excellent agreement (Conca and Wright 1992a, 1992b). Because the UFA method can directly and rapidly control the hydraulic

conductivity, fluid content, temperature, and flow rates, other transport properties can then be measured as a function of fluid content by associated methods either inside or outside the UFA instrument during the overall run.

Fundamental physics issues involving flow in an acceleration field have been raised and successfully addressed by previous research and in numerous forums (Conca and Wright 1992a, 1992b; Nimmo et al. 1987; Nimmo and Akstin 1988; Nimmo and Mello 1991). These studies have shown, first, that compaction from acceleration is negligible for subsurface soils at or near their field densities. Bulk density in all samples remains constant because a whole-body acceleration does not produce high point pressures. A notable exception is surface soils, which can have unusually low bulk densities; special arrangements must be made to preserve their densities. Whole-rock cores are completely unaffected.

The studies have also shown that three-dimensional deviations of the driving force with position in the sample are less than a factor of 2, but moisture distribution is uniform to within 1 percent in homogeneous systems because water content depends only upon ψ, and unit gradient conditions are achieved in the UFA instrument in which $d\psi/dr = 0$. Hydraulic steady-state is not as sensitive to changes in rotation speed as to flux density. In heterogeneous samples or multicomponent systems such as rock, each component reaches its own hydraulic steady-state and water content, as occurs for such materials under natural conditions in the field. This last effect cannot be reproduced with pressure-driven techniques but only under a whole-body force field, such as with gravity columns or centrifugal methods. The ratio of flux to rotation speed is always kept high enough to maintain the condition of $d\psi/dr = 0$.

Results and Discussion for Vitric and Zeolitic Tuff

Column Breakthrough Test Results–For these experiments, the rotation speed was set at 2,000 rpm with a flow rate into each sample of 0.2 mL/hr. The experiment was run for 9 days with an initial selenium concentration of 1.31 ppm. Figure 6.3-80 shows the breakthrough curves for selenite in the Yucca Mountain vitric member at 62.6 percent saturation and in the zeolitic nonwelded tuff at 52.8 percent saturation. The experiment was stopped before full breakthrough in the zeolitic nonwelded tuff, but the C/C_o = 0.5 point was reached. The retardation factor for each tuff sample is only 2.5, giving a K_d of 0.9 mL/g for the Yucca Mountain vitric-member tuff and 0.8 mL/g for the zeolitic nonwelded tuff.

During these experiments, the unsaturated hydraulic conductivity, K, for each sample at these water contents was 2.5 x 10^{-8} cm/s for the Yucca Mountain vitric-member tuff and 1.2 x 10^{-8} cm/s for the zeolitic nonwelded tuff. Figure 6.3-81 gives the characteristic curves, $K(\theta)$, for these tuffs determined in separate experiments, as well as measurements for other tuffs and materials for comparison. As in most whole-rock cores studied (Conca and Wright 1992a, 1992b), the characteristic curves for the tuffs are steep, almost linear functions of the volumetric water content and are displaced according to the degree of welding and alteration.

Batch Test Results–We conducted Batch-adsorption tests were conducted using the same J-13 well water with the slightly lower selenium concentration of 1.1 ppm and the same zeolitic nonwelded tuff from G-Tunnel, Bed 5, as in the UFA column breakthrough test. The batch-

adsorption tests consist of crushing and wet-sieving the tuff, pretreating the tuff with J-13 water, placing the selenium solution in contact with the tuff, separating the phases by centrifugation, and determining the amount of selenium in each phase by difference using inductively coupled plasma mass spectrometry. Control samples were used to determine the sorption of selenium onto the walls of the sorption containers. The control procedure consisted of following the described batch-sorption procedure with a sample containing the selenium solution, except with no tuff added. The results of the control experiments indicate no loss of selenium due to precipitation or sorption onto the walls of the container during the batch-sorption experiment. The sorption distribution coefficients obtained are given in Table 6.3-20. The Eh of all solutions, measured after the sorption experiments, varied from 140 to 150 mV.

The data presented in Table 6.3-20 and Figure 6.3-81 indicate agreement between the column and the batch-sorption experiments. At a selenium concentration of ~1 ppm, no sorption of the selenium by the tuff is observed for the zeolitic tuff used in batch experiments, and minimal sorption (K_d of 0.8 mL/g) is observed for the zeolitic tuff used in the unsaturated column experiments. The method used for the batch-sorption experiments to determine K_d values (by difference) involves subtracting the selenium concentration in solution after equilibration with the solid phase from the initial selenium concentration in solution. This method yields large scatter in the data when the batch-sorption distribution coefficient is small because two large numbers are subtracted to get a small number. Inspection of Table 6.3-20 also suggests that the kinetics of selenium sorption onto tuff are fast.

***Conclusions*–**This study demonstrated the feasibility of using the UFA technology to rapidly and directly measure retardation factors and hydraulic conductivities in whole-rock cores of tuff under the unsaturated conditions that exist in the field. In UFA column breakthrough tests, the retardation factor for the selenite species was only 2.5 in both Yucca Mountain vitric member tuff at 62.6 percent saturation and zeolitic nonwelded tuff from G-tunnel at 52.8 percent saturation for a selenium concentration in J-13 water of 1.31 ppm. In batch tests on the same material with an initial selenium concentration of 1.1 ppm, the average K_d was 0.08 ± 0.2 mL/g, which gives retardation factors that are slightly lower than those from the UFA column breakthrough experiments. This finding suggests that using batch-sorption coefficients to predict radionuclide transport through unsaturated tuff will yield conservative results.

Future experiments will use initial selenium concentrations smaller than the ones used in these experiments to further assess the validity of batch-sorption distribution coefficients to predict transport under unsaturated conditions. The unsaturated hydraulic conductivities during the experiments were 2.5 x 10^{-8} cm/s for the Yucca Mountain vitric-member tuff and 1.2 x 10^{-8} cm/s for the zeolitic nonwelded tuff.

6.3.4.3 Radionuclide Transport Through Fractures

Yucca Mountain was chosen as a potential site for a high-level nuclear-waste repository because its geochemistry is believed to form both a physical as well as chemical barrier to radionuclide migration. However, the Yucca Mountain region has undergone significant deformation with the most recent tectonic activity occurring during the development of the Basin and Range geologic province and silicic volcanic activity. As a result of the tectonics and volcanism, many faults

and fractures were produced within the tuffaceous units as well as the entire region. In addition, volcanic tuffs are often fractured as a result of cooling. The numerous fractures present at Yucca Mountain potentially represent a breach in the natural barrier, providing a fast pathway for contaminant migration.

Radionuclide transport calculations often assume that radionuclides can travel through fractures unimpeded; this assumption is too simplistic and leads to overconservative predictions of radionuclide releases to the accessible environment. The assumption ignores two main mechanisms by which retardation of radionuclides migrating through fractures can occur: diffusion of the radionuclides from the fractures into the rock matrix and sorption of radionuclides onto the minerals coating the fractures.

Minerals coating the fracture walls are generally different from the host-rock mineralogy due to a variety of factors ranging from precipitation of hydrothermal waters or meteoric waters to alteration of the pre-existing minerals. A review of the literature (Carlos 1985, 1987, 1989, 1990, 1994; Carlos, Chipera, Bish et al. 1993) has provided a list of the minerals lining the fractures found at Yucca Mountain (Table 6.3-21).

The transport of radionuclides through fractures from Yucca Mountain was examined to assess the retardation that can be provided by radionuclide diffusion into the matrix and sorption onto the minerals coating the Yucca Mountain fractures.

Experimental Procedures

Groundwaters–The groundwaters used for the experiments presented in this section were waters from Well J-13 (filtered through a 0.05-μm filter) and two sodium-bicarbonate buffers that simulated the water chemistry of the groundwaters from Wells J-13 and UE-25p #1The synthetic J-13 water was prepared by dissolving 0.03 g of Na_2CO_3 and 1.92 g of $NaHCO_3$ in 10 L of deionized water; the synthetic UE-25p #1 water by dissolving 0.39 g of Na_2CO_3 and 8.90 g of $NaHCO_3$ in 10 L of deionized water. The reasons for having to use synthetic waters for the fracture-column experiments was the unavailability of water from Well UE-25p #1 and the prevention of microbial activity in the columns.

Fractured-Tuff Samples–Tuff samples with natural fractures from drillholes at Yucca Mountain chosen from the YMP Sample Management Facility in Mercury, Nevada. The tuff matrix of all samples consisted of devitrified tuff, and the minerals lining the fractures were stellerite, magnetite, hollandite, and romanechite. The sampling criteria were confined to cores with natural fractures, determined by the presence of secondary mineral coatings; and fractures with removable fracture walls that could be repositioned to their original orientation. Based on this criteria, it was concluded that of the fractured-tuff cores selected (USW G1-1941, UE-25 UZ-16 919, USW G4-2981, and USW G4-2954) all consisted of natural fractures except G1-1941, the only core sample that did not have secondary minerals coating its fracture. The fracture in sample G1-1941 is apparently induced.

Radionuclide Solutions–The radionuclide solutions used in the experiments (tritium, pertechnetate, and neptunium) were prepared in the same manner as for the crushed-tuff column experiments.

Fractured-Column Procedure–The experimental setup that was used for the fractured-tuff column is shown in Figure 6.3-82 (the flowchart for the experiments is the same as for the crushed-tuff column experiments (Figure 6.3-70), except the crushed-rock column is replaced with a fractured-tuff column). The column was submerged in a beaker ontaining either synthetic UE-25p #1 or synthetic J-13 water. The beakers were subjected to a vacuum for a minimum of two weeks until all evacuating gas bubbles had ceased. After saturation, the fracture columns were connected, via one of the two outflow ports, to a syringe pump, and the second outflow port was to connect to a pressure transducer. The tracer was injected through the bottom. A constant flow rate was established, and a radionuclide tracer was introduced into the system through an injection valve. The column elutions were collected as a function of time and analyzed, using standard radiometric techniques, for the percentage of radionuclide tracer recovered. The aperture of the fractures has not yet been determined, but Table 6.3-22 gives the other characteristics of the four columns.

Batch-Sorption Experiments–For comparison with the fractured-column experiments, batch-sorption tests of neptunium onto the fracture minerals stellerite, hollandite, romanechite, and magnetite were conducted. These tests were performed under atmospheric conditions using J-13 well water with a Np(V) concentration of 6.7×10^{-7} M. The batch-sorption tests consisted of:

- Crushing and wet-sieving the minerals to a size of 75 to 500 μm
- Pretreating the minerals with J-13 water
- Placing the neptunium solution in contact with the minerals for a period of three days (using a solid to solution ratio of 1 g to 20 mL)
- Separating the phases by centrifugation
- Determining the amount of neptunium in each phase by difference using liquid scintillation counting

Control samples were used to determine the sorption of neptunium onto the walls of the sorption containers. The control samples consisted of following the described batch-sorption procedure with a sample containing the neptunium solution only with no solid added. The results of the control experiments indicate no loss of neptunium due to precipitation or sorption onto the walls of the container during the batch-sorption experiment. The pH of the water in these experiments was approximately 8.5.

Results and Discussion–As discussed earlier, neptunium does not sorb onto devitrified tuff (Triay, Cotter, Huddleston et al. 1996), which constitutes the matrix of all the fractures studied. Retardation during fracture flow occurs by diffusion of the radionuclides into the tuff matrix or by sorption of the radionuclides onto the minerals coating the fractures. Table 6.3-23 lists the results of batch-sorption experiments describing the sorption of neptunium onto natural minerals.

Although the extrapolation from these experiments to Yucca Mountain tuffs containing the same minerals is not immediate, the data of Table 6.3-23 show some important trends. Neptunium has a high affinity for hollandite and romanechite, whereas sorption onto the zeolite stellerite is not

significant. If ion exchange is the main mechanism for neptunium sorption onto stellerite, changing the water from J-13 to UE-25p #1 will only result in less sorption (due to the formation of a larger amount of the neptunyl carbonado complex and competitive effects as a result of the higher ionic strength in the UE-25p #1 water). The sorption of neptunium onto magnetite does not appear to be significant either. As shown in Table 6.3-23, the magnetite sample studied contains hematite and goethite, which could account for the entire observed sorption (Triay, Cotter, Huddleston et al. 1996).

Because no secondary minerals coating the fractures were observed for the G1-1941 fractured sample (column #1 of Table 6.3-22 and Figure 6.3-83), it can be concluded that the retardation of neptunium observed for that column is due to diffusion into the matrix.

The total neptunium recovery of 70 percent in the UE-25 UZ-16 919 fractured sample (column #2 of Table 6.3-22 and Figure 6.3-84) could be due to minimal sorption onto the stellerite and magnetite coating that fracture or due to diffusion into the matrix. It is important to note that in changing the water for this column from synthetic J-13 to synthetic UE-25p #1, the speciation of neptunium changes from a mixture of neptunyl and carbonado complex to almost 100 percent carbonado complex (which can be excluded from tuff pores due to size and charge).

Neptunium seems to be significantly retarded even during fracture-flow in the G4-2981 fractured sample (Figure 6.3-85) that is coated with hollandite and romanechite. The recovery of neptunium in this fracture is less than 10 percent, and its first appearance is delayed with respect to tritium and technetium.

Inspection of Figures 6.3-85 and 6.3-86 (columns #3 and #4 of Table 6.3-22) indicates that diffusion from the fracture into the matrix has taken place because recovery of tritium was only 80 percent compared to 90 percent for technetium. This trend agrees with diffusion data that were previously obtained for ^{3}H and ^{95m}Tc in devitrified tuff and water from Well J-13. These data were fitted to the diffusion equation using the transport code TRACRN (Triay, Birdsell et al. 1993), which yielded diffusion coefficients for saturated devitrified tuffs that were of the order of 10^{-6} cm^2/s for tritiated water and 10^{-7} cm^2/s for technetium. Thus, anion exclusion, in which the large pertechnetate anion is excluded from tuff pores due to its size and charge, has been previously observed.

Continuing with the explanation by de Marsily (1986, Chapter 10) of the fate of reactive and nonreactive solutes in porous and fractured media, that was started in the earlier section on crushed-rock columns, the equation for a sorbing, nonreactive solute (Equation 6.3-31) can be expanded to account for a solute that also undergoes radioactive decay:

$$\nabla \cdot (\mathbf{D} \nabla C - C\mathbf{U}) = \varepsilon\left(\frac{\partial Q}{\partial t} + \lambda C\right) + \rho_b\left(\frac{\partial F}{\partial t} + \lambda F\right) , \qquad \text{(Eq. 6.3-38)}$$

where λ is related to the half-life, $t_{1/2}$, of the decaying radionuclide by the relationship $\lambda = 0.693/t_{1/2}$.

As was pointed out earlier, the mechanism of sorption determines the relationship between F and C. If the linear, reversible, and instantaneous relationship for sorption is substituted, that is $F = K_d C$, Equation 6.3-38 becomes

$$\nabla \cdot (\mathbf{D} \nabla C - C\mathbf{U}) = \varepsilon \left(1 + \frac{\rho_b}{\varepsilon} K_d\right)\left(\frac{\partial C}{\partial t} + \lambda C\right) \quad . \qquad \text{(Eq. 6.3-39)}$$

The expression inside the first set of parentheses in Equation 6.3-39 is the retardation factor, R_f, which, of course, is only valid if sorption is linear, reversible, and instantaneous.

For radionuclide elution through fractures, two transport equations (like Equation 6.3-38) are considered, one for the porous medium and one for the fractured medium, each with its own Darcy's velocity and porosity (de Marsily 1986). The two transport equations for the porous and the fractured media can be coupled by a convection and a dispersion-exchange term.

The radionuclide elution data through fractured media was reduced and analyzed using the transport code FEHM and reported on by B.A. Robinson et al. (1995). Their analyses of ^{237}Np elution through fractured rock made it clear that the data are consistent with very large values of K_d, at least compared to the typical value of 2.5 for $^{-237}$Np on zeolitic tuff. They also felt it possible that minerals present in trace quantities in the bulk rock that appear to contribute insignificantly to sorption may be quite effective at retarding ^{237}Np transport when concentrated on fracture surfaces.

The most significant conclusion of the work presented here is that, contrary to previous assumptions about the role of fractures in radionuclide retardation, preliminary results from these experiments indicate that fracture flow does not necessarily result in a fast pathway for actinide migration through fractures. As can be seen in the experiments described above, the migration of actinides through fractures could be significantly retarded by sorption onto minerals coating the fractures and by diffusion into the tuff matrix.

6.3.5 Diffusion Transport

A model for matrix and fracture flow regimes in unsaturated, fractured porous media at Yucca Mountain was developed by Nitao (1991). This model provides a framework for assessment of the importance of matrix diffusion at Yucca Mountain. Solute transport in fractured rock in a potential radionuclide waste repository has been discussed by Neretnieks (1990) who concluded that most rocks (even dense rocks such as granites) have small fissures between the crystals that interconnect the pore system containing water. Small molecules of radioactive materials can diffuse in and out of this pore system. The inner surfaces in the rock matrix are much larger than the surfaces in the fractures on which the water flows. The volume of water in the microfissures is much larger than the volume in fractures. Therefore, over a long time scale, diffusion can play an important role in radionuclide retardation.

The objective of diffusion experiments was to provide diffusion information for nonsorbing neutral molecules and anions and sorbing radionuclides. Because the uptake of radionuclides by

tuff is measured as a function of time, the experiments also yield information on kinetics of sorption.

6.3.5.1 Rock-Beaker Experiments

Experimental Procedure–The experimental technique used involved fabricating rock-beakers of tuff. The beaker sits inside a Plexiglas™ container surrounded by groundwater (Figure 6.3-87). A stopper is used to prevent evaporation. The cavity in the rock-beaker has a radius of approximately 1.4 cm and a length of 2.5 cm. The beaker itself has a length of approximately 5 cm and a radius of 3.1 cm.

The radionuclides used in these experiments were ^{3}H, ^{95m}Tc, ^{237}Np, ^{241}Am, ^{85}Sr, ^{137}Cs, and ^{133}Ba. A solution (prepared with groundwater from Well J-13) containing the radionuclide of interest was placed in the rock cavity and then aliquots of the solution from the beaker for the remaining radionuclide concentration were analyzed as a function of time. Also performed were batch-sorption experiments with J-13 water and the tuffs under study using the batch-sorption procedures described in Subsection 6.3.3.1.

Data Analysis–The results of the rock-beaker experiments were modeled using TRACRN, a 3-D geochemical/geophysical-model transport code (Travis and Birdsell 1991). Because the geometry of the rock beaker is complex, an analytical solution is not available for this system. The concentration profiles of the diffusing tracer are fitted to the transport equation (de Marsily 1986, Chapter 10):

$$\nabla \cdot (\varepsilon d \nabla C) = \varepsilon \frac{\partial C}{\partial t} + Q \quad , \qquad \text{(Eq. 6.3-40)}$$

where ε is the total porosity of the tuff, d is the diffusion coefficient through the tuff, C is the concentration of the diffusing tracer in solution, and the source term, Q, is zero for a nonreactive tracer but for a sorbing solute

$$Q = \rho_b \frac{\partial F}{\partial t} \quad , \qquad \text{(Eq. 6.3-41)}$$

where F is the amount of tracer sorbed per unit mass of solid and ρ_b is the bulk tuff density ($\rho_b = (1 - \varepsilon)\rho_s$, where ρ_s is the density of the solid particles).

As discussed in previous chapters, the mechanism of sorption determines the relationship between F and C. When sorption is linear, reversible, and instantaneous, the relationship between F and C is given by the sorption distribution coefficient

$$K_d = \frac{F}{C} \quad . \qquad \text{(Eq. 6.3-42)}$$

Substitution of this equation and Equation 6.3-41 into Equation 6.3-40 yields

$$\nabla \cdot (\varepsilon d \nabla C) = \varepsilon R_f \frac{\partial C}{\partial t} \quad , \qquad \text{(Eq. 6.3-43)}$$

where, once again, the retardation factor, R_f, is given by

$$R_f = 1 + \frac{\rho_b}{\varepsilon} K_d \quad , \qquad \text{(Eq. 6.3-44)}$$

Equation 6.3-44 provides a means of comparing results for sorption coefficients obtained under diffusive conditions with sorption coefficients obtained from batch-sorption experiments and is valid only if sorption is linear, reversible, and instantaneous (the Langmuir and the Freundlich isotherms are examples of nonlinear relationships between F and C).

Consequently, the diffusion coefficient can be determined by fitting concentration profiles for the nonsorbing tracers, and sorption parameters, such as K_d, can be determined by fitting concentration profiles for the sorbing tracers.

Results and Discussion–Figure 6.3-88 shows an example of a set of diffusion data for a rock beaker experiment in which the feldspar-rich tuff G4-737 and solutions of tracers in J-13 water were used. The concentration of tracer, C, remaining in the solution inside the cavity of the rock-beaker divided by the initial concentration, C_o, is plotted as a function of elapsed time.

The solid lines in Figure 6.3-89 are a fit of these same data to the diffusion equation (Equation 6.3-40) using the TRACRN transport code for the two nonsorbing radionuclides, tritium and technetium-95m. The diffusion coefficients obtained in this manner for these radionuclides for all the tuff samples studied (Table 6.3-24) agree well with previous results (Rundberg, Partom et al. 1987). These two tracers diffuse essentially as tritiated water and the pertechnetate anion, TcO_4^-. Large anions are excluded from tuff pores because of their size and charge, which can account for the lower diffusivity of TcO_4^-.

If sorption is linear, reversible, and instantaneous, then F/C is equal to a sorption coefficient, K_d. To test this assumption, values of K_d in batch-sorption experiments using the tuffs under study (Table 6.3-25) were determined. An expected diffusion curve was calculated using, for each tuff, the diffusion coefficient measured for tritiated water and the batch-sorption coefficient measured for each sorbing radionuclide. Figure 6.3-90 shows these calculated diffusion curves for devitrified tuff G4-737. Comparison of the calculated curves with the actual measured data (see the example in Figure 6.3-91) shows that the concentration of the sorbing radionuclides remaining in the rock-beaker drops faster than predicted on the basis of a linear K_d. This result indicates that the diffusion of the sorbing radionuclides could not be fitted by assuming reversible, instantaneous, and linear sorption. These results also indicate that transport calculations using a batch-sorption K_d value and the diffusion coefficient measured for tritiated water will result in conservative predictions for the transport of sorbing radionuclides. (It should be noted that Cs appears to diffuse much faster than the tritium in tritiated water (mostly HTO))

The results obtained from rock-beaker experiments agree with previous results (Rundberg 1987). Experiments were performed on the uptake of sorbing radionuclides by tuff and it was found that rate constants for uptake of the sorbing cations from solution onto tuff were consistent with a diffusion-limited model in which diffusion occurs in two stages. In the first stage, the cations diffuse into rock through water-filled pores; in the second stage, they diffuse into narrower intracrystalline channels. This diffusion model yielded sorption coefficients for cesium, strontium, and barium that agree well with the sorption coefficients determined by batch techniques.

6.3.5.2 Diffusion-Cell Experiments

Experimental Procedures and Data Analysis–Diffusion cells were constructed with two chambers containing groundwater separated by a slab of tuff. After radioactive tracers were added to one of the chambers, the untraced chamber was periodically monitored for the presence of radioactivity by taking an aliquot of the solution in the chamber and then replenishing that chamber with groundwater. The dimensions of the diffusion cells used are given in Table 6.3-26.

The only driving force in this experimental setup is the chemical concentration gradient; thus, the solute flux is purely diffusive. The apparent time of arrival depends on the porosity, the heterogeneity of the pore structure, the retardation factor for a given radionuclide, and the sensitivity of radionuclide measurements. The rate of concentration increase in the untraced chamber depends on the ionic diffusivity, the tuff porosity, and the tuff tortuosity/constrictivity factor. Thus, by measuring the movement of sorbing and nonsorbing tracers through tuff slabs as a function of time, the rock-dependent diffusion parameters can be measured.

The two major rock types used for the diffusion-cell experiments were zeolitic (UE-25 1362) and devitrified (G4-287). The zeolitic tuff has a porosity of 0.4 and a bulk density of 1.5 g/mL. The devitrified tuff has a porosity of 0.2 and a bulk density of 2.3 g/mL. The major component of the zeolitic tuff is clinoptilolite; the major component of the devitrified tuff is alkali feldspar.

The solutions used for the diffusion-cell experiments were prepared by taking an aliquot of a ^{3}H, ^{95m}Tc, natural U(VI), $^{237}Np(V)$, or $^{239}Pu(V)$ acidic stock and diluting it in the water being studied. The actinide concentration of the solutions used for the diffusion experiments was very close to the solubility limit of the actinides in the groundwaters. The experimentally determined solubilities (Nitsche, Gatti et al. 1993; Nitsche, Roberts, Prussin et al. 1994) of plutonium range from 2×10^{-7} (J-13 water at a pH of 7) to 1×10^{-6} M (UE-25p #1 water at a pH of 8.5) and of neptunium range from 7×10^{-6} (UE-25p #1 water at a pH of 8.5) to 5×10^{-3} M (J-13 water at a pH of 6). Table 6.3-6 in Subsection 6.3.3.1 summarizes the solubilities and speciation of neptunium in these groundwaters.

The experimental setup for the diffusion cells can be described by a 1-D diffusion model. Thus, Equation 6.3-43 (on rock-beaker experiments) can be rewritten as

$$D_e \frac{\partial^2 C}{\partial x^2} = \alpha \frac{\partial C}{\partial t} \quad , \qquad \text{(Eq. 6.3-45)}$$

where x is the axis along the direction of tracer diffusion, D_e is the effective diffusivity ($= \varepsilon d$), and α is the rock-capacity factor ($= \varepsilon R_f$). This equation yields an analytic solution to diffusion through a slab.

Bradbury et al. (1986) solved Equation 6.3-45 for a porous rock. For the experimental setup, the boundary conditions can be taken to be:

- At $x = 0$, a constant source concentration, C_o, is maintained
- At $x = L$, where L is the tuff-slab thickness, the concentration measured at the initially untraced cell, C_t, is much smaller than the source concentration ($C_t << C_o$).

For these conditions, the total quantity, Q_t, diffused through a tuff slab of area A after a time t is given by the equation

$$\frac{Q_t}{ALC_o} = \frac{D_e t}{L^2} - \frac{\alpha}{6} - \frac{2\alpha}{\pi^2} \sum_{n=1}^{\infty} \frac{(-1)^n}{n^2} e^{-\left(\frac{D_e n^2 \pi^2 t}{L^2 \alpha}\right)} \quad . \qquad \text{(Eq. 6.3-46)}$$

As $t \rightarrow \infty$, the asymptotic solution becomes

$$Q_t = \frac{AC_o D_e}{L} t - \frac{AC_o L \alpha}{6} \quad . \qquad \text{(Eq. 6.3-47)}$$

Consequently, a plot of Q_t versus t yields the effective diffusivity, D_e, from the slope and the rock-capacity factor, α, from the intercept on the time axis of the extrapolated linear region. For a nonsorbing species, $K_d = 0$, $R_f = 1$, and $\alpha = \varepsilon$; for a sorbing species, K_d may be calculated from the value of α.

The diffusion coefficient, d, can be calculated from the effective diffusivity ($D_e = \varepsilon d$). The difference between the diffusion coefficient, d_s, for a tracer diffusing in the solution phase and the diffusion coefficient, d, for a tracer passing through tuff pores is given by

$$d = \frac{\delta}{\tau^2} d_s \quad , \qquad \text{(Eq. 6.3-48)}$$

where δ is the constrictivity and τ is the tortuosity of the tuff pore structure.

Results and Discussion–The diffusion of ^{3}H, ^{95m}Tc, natural U(VI), $^{237}Np(V)$, and $^{239}Pu(V)$ through devitrified and zeolitic tuffs was studied using water from Well J-13 and synthetic UE-25p #1 water. The radionuclides ^{3}H, natural U(VI), and $^{239}Pu(V)$ were studied together in four diffusion cells (devitrified and vitric tuff cells, each with both types of water). Likewise, the radionuclides ^{95m}Tc and $^{237}Np(V)$ were studied together in another four diffusion cells. Typical results for these experiments are shown in Figures 6.3-92 to 6.3-94.

The results indicate that the diffusion of nonsorbing radionuclides into saturated tuff (illustrated by the diffusion of tritiated water in Figures 6.3-92 to 6.3-94) is slower in devitrified tuffs than in zeolitic tuffs. Large anions such as pertechnetate (which are excluded from the tuff pores by size and charge) diffuse slower through the pores than tritium regardless of the groundwater or tuff type (as also observed in the rock-beaker experiments). The migration of plutonium through tuff under diffusive conditions is dominated by sorption (as shown by Figures 6.3-92 to 6.3-94). The migration of Np(V) and U(VI) through tuff depends on tuff type and water chemistry. In cases, such as tuff G4-287, for which the reported sorption of neptunium is essentially zero (Triay, Cotter, Huddleston et al. 1996; Triay, Cotter, Kraus et al. 1996), the diffusion of neptunium through the tuff is slower than the diffusion of tritium but comparable to the diffusion of a nonsorbing, large anion, such as pertechnetate (Figure 6.3-93).

The analysis of data described in Subsection 6.3.5.2 has some problems with respect to the assumptions required to find an analytical solution. The assumptions do not allow for a changing concentration in the traced chamber, for a concentration in the untraced chamber that is not much smaller than the initial concentration in the traced chamber, and for the addition of groundwater to the untraced chamber each time an aliquot was taken.

Therefore, future analysis of these data will involve fitting the diffusion profiles using a transport code (such as the TRACRN code used in the rock-beaker diffusion experiments) to obtain diffusion coefficients. The concentration profiles of the diffusing radionuclides would be fitted to the same equation as Equation 6.3-45 but using the algebraic form given in the section on rock-beaker experiments (Equations 6.3-40 to 6.3-42).

6.3.6 Colloid-Facilitated Radionuclide Transport

This subsection presents an overview of the models that can be incorporated into transport codes to assess the role of colloids at Yucca Mountain. Subsection 6.3.6.1 describes a global approach for the stability of natural colloids (developed by Degueldre) that can be applied to Yucca Mountain waters. Subsection 6.3.6.2 describes available colloid transport models and the effectiveness of those models to fit laboratory data obtained for an idealized system that describes the role of silica colloids facilitating cesium transport through glass-bead columns. Subsection 6.3.6.3 illustrates a methodology for the determination of sorption parameters needed for colloid transport models. Subsection 6.3.6.4 employs this methodology to determine sorption parameters needed for colloid transport calculations involving actinide colloids.

6.3.6.1 Global Approach to Colloid Stability

This subsection presents groundwater colloid results from various geological formations ranging from crystalline to sedimentary, saturated to unsaturated, and organic rich to organic depleted.

Colloid presence and their potential mobility are justified on the basis of stability properties in the investigated groundwater. The colloid concentration is a function of pH, potential redox, the concentrations of Na, K, Ca, Mg, and organic carbon, as well as the status of the chemical and physical steady state of the hydrogeochemical system. The colloid properties are discussed with a non-site-specific approach.

Introduction–Groundwater colloids are investigated for their potential role in subsurface systems. Contaminants can be transported either in true solution or associated with colloidal particles whose sizes range from some nm to μm. In natural groundwaters, there is a continuum between inorganic colloids (clay, oxide), inorganic colloids coated with organic material, organic colloids associated with inorganic phases, and organic colloids. A first list of colloid data (for example, concentration) was published recently (McCarthy and Degueldre 1993). Colloid studies are important to understand the behavior of trace concentrations of strongly sorbing or insoluble elements in groundwater systems. Key factors affecting colloid stability are pH, redox potential, salt (Na, Ca) concentrations (Degueldre, Pfeiffer et al. 1996), the presence of dissolved organics (O'Melia and Tiller 1993), and the status of the system steady state (for example, Fauré et al. 1994).

The conceptual model describing the colloid occurrence takes into account their generation and disappearance, their aggregation and desegregation, as well as their attachment and detachment on the rock. In the aquifer, the balance between production and disappearance may be postulated for the undisturbed saturated zone. However, it is considered that the stability of the colloid phase is a function of the disappearance rate by attachment, which justifies the colloid concentration in the aquifer. Because attachment parameters are defined in stationary conditions, this concept must be extended for perturbed aquifers. This extension may justify larger colloid concentrations during hydrogeochemical transients in the aquifer.

The general consensus about contaminant transport by colloid-facilitated process is the need to understand the colloid generation mechanisms to evaluate contamination hazard or to design remediations when required. The purpose here is to discuss and define rules for evaluating colloid properties in natural systems or systems modified by the presence of contaminant and to sketch a conclusion on a non-site-specific basis. This general study, based on recent results obtained from selected hydrogeochemical systems, should allow us to draw a global approach.

Systems–Data have been collected for systems ranging from various crystalline to sedimentary geological formations. Table 6.3-27 summarizes the minerals composing the rocks of the considered formations. The crystalline systems comprise recent granitic systems (such as the Central European Basement with studies in the Black Forest, South Germany, and the Northern part of Switzerland, as well as in the Alpine area, Grimsel, Switzerland) and older granitic systems (such as the Scandinavian or Canadian shield). The rock in these systems is mainly composed of quartz, feldspar, and mica. Minerals currently found in the granitic fractures are illite, muscovite, quartz, chlorite, calcite, iron oxyhydroxides, and some pyrite. Their organic content is rather low.

The Swiss Crystalline studies (Degueldre, Pfeiffer et al. 1996; Degueldre, Grauer et al. 1996) selected systems ranging from shallow to deep aquifers. The sites are the Menschenchwand uranium prospect, the Bad Säckingen spring, the Zurzach thermal well, the Leuggern borehole,

and in the Alps, both the Grimsel Test Site and the Transitgas Tunnel. The depth ranges from about 100 to 1680 m in 600 m.y.-old granite. In Sweden, two systems were considered in the 2 By-old granite: Äspö, the Experimental Underground Laboratory at a depth of 70 m below the surface (Laaksoharju et al. 1995), and the Laxemar deep borehole with a 1420–1705 m depth. Both sites are located on the Baltic coast about 350 km south of Stockholm. In Canada, Vilks, Miller et al. (1991) investigated waters at the Whiteshell Research Area, underlain by the Lac du Bonnet granite batholith and located in the southeastern part of Manitoba Zones, at depths down to 1150 m.

Yucca Mountain consists of a 1,500-m-thick accumulation of Miocene silicic ashflow tuffs of volcanic origin. The rocks can be generally characterized as alternating layers of highly porous nonwelded tuff and low-porosity densely welded tuff. The original rock constituents were predominantly volcanic glass, but high-temperature devitrification and lower-temperature alteration have produced mineral assemblages dominated by feldspar, zeolites, and various silica polymorphs with low organic content. Crystallized accumulations of former colloidal material, produced during rock alteration, are present in the pores of some rock layers (Levy 1992).

Morro do Ferro, Brazil, is an altered (weathered) formation with some organic content that issued from volcanic activities in a subtropical area. Morro do Ferro is located in the caldera of Poços de Caldas, Minerais Generai. The rocks are predominantly carbonitites deeply weathered to laterites (gibbsite, illite, and kaolinite-rich). As its name suggests, Morro do Ferro is characterized by magnetite dikes and breccia, which are believed to comprise the most hydraulically conductive zones (Miekeley et al. 1992).

Partially and nonmetamorphosed sedimentary systems were also considered. They generally contain more organic compounds than the previous studied formations.

The Wellenberg (Degueldre et al. 1994) system is located in central Switzerland and comprises a marl formation slightly metamorphosed. The investigated aquifer lies in this marl formation at a 360-m depth, but another system of interest lies at a depth of 1,600 m below the marl formation in a chalk (limestone) layer. In Markham, U.K., Longworth et al. (1989) investigated colloids from the Triassic Sandstone aquifer (120 m depth) of a site 50 km north of Nottingham. At Gorleben, Central Germany, Kim et al. (1992) investigated a system composed of porous sediments with lignite intercalations. The aquifers there are located between 50- and 300-m depth and are composed of glacial sand, silt, marl, and clay. Elevation has caused rupturing and folding of the overlying and surrounding Miocene "Brown-Coal" sand and clay.

The Cigar Lake uranium deposit is a sandstone-hosted ore body located in the Athabasca Sandstone Basin of northern Saskatchewan, Canada (Vilks, Cramer et al. 1993). The ore is located at the contact between sandstone and altered basement rock and is separated from the sandstone host by zones of clay-rich altered sandstone. The sandstone formation lies at a depth of 432 m below the surface. Finally, the Bagombé fossil reactor zone, Gabon, discovered in 1980, is located some 30 km south of the Oklo deposit. The sedimentary formation of sandstones is overdecked by a thick series of marine-derived, organic-rich pelites associated with limestones. These formations were also slightly metamorphosed (Pedersen et al. 1996).

Waters–Prior to comparing colloid properties, the hydrochemical properties of the studied groundwaters must be well described and understood. Table 6.3-28 shows the most important hydrogeochemical parameters. The individual water properties may be summarized as follows:

- In the Transitgas tunnel, zone 1, nine springs were investigated with mixed Na-Ca-SO_4-HCO_3 waters at pH values from 7.8 to 9.4 that were mostly oxic (5–9°C). Locally, in zone 2 (springs 10–14), hydrothermal (18–28°C) Na-SO_4 waters with pH of 8.8 to 9.2 were sampled that were reducing. Finally, in zone 3 (springs 15–16), shallow groundwaters of the Ca-HCO_3 type with oxic character, pH of 9.2 to 9.6, and temperature around 4 to 6°C were sampled. At the Grimsel Test Site a deep Na-Ca-HCO_3-F groundwater was collected at a depth of 450 m below the surface. From the boreholes in Leuggern and Zurzach, crystalline waters of a Na-SO_4-HCO_3-Cl type were sampled from depths of 1860 and 450 m, respectively.

- At Whiteshell, Na-Ca-HCO_3 waters were studied in the upper zones down to 400 m, and Ca-Na-Cl waters were collected at depths down to 1100 m below the surface. In Äspö, mixed waters of Na-Ca-Cl-HCO_3 type were studied at a depth of 70 m below the surface, and at Laxemar, deep Na-Ca-Cl water was pumped from a depth of 1400 m.

- In Yucca Mountain, the J-13 oxic water of a Na-HCO_3-SiO_2 type is pumped from a depth 300 m below the surface. At Morro do Ferro, the K-SO_4-F water was also pumped, but from a depth of 30 m only.

In the sedimentary aquifers, the water properties may be summarized as follows:

- At Gorleben, both GOHY532 and 1271, deep Na-HCO_3-OC waters are sampled from depths of 60 and 80 m below the surface. At Wellenberg, deep Na-HCO_3 waters flow artesically from depths of 350 and 1,350 m below the surface.

In Markham, the oxic municipal water of a Mg-Ca-Na-HCO_3 type is pumped from a depth 100 m below the surface. At Cigar lake, the Ca-Na-HCO_3 groundwaters were sampled from depths down to 435 m. Finally, in Bagombé, complex Ca-Mg-Na-HCO_3 (relatively demineralized) waters were pumped from depths of about 20 m below the surface. The considered anaerobic aquifers are rather shallow but not oxidized.

These groundwaters range from oxic to anoxic, Na (Bad Säckingen) or Na-Ca-rich (Äspö) to K-rich (Poços de Caldas) or with large Mg contribution (Markham, Wellenberg), and organic depleted (Zurzach) to organic rich (Gorleben). Their type goes from shallow Ca-HCO_3 (Transitgas tunnel, zone 3) to more complex Na-SO_4-HCO_3-Cl (Zurzach) or K-SO_4-F (Poços de Caldas). For the water considered, the salt concentrations range over 4 orders of magnitude, the total hardness of the water over 2 orders of magnitude, and the pH from 6 to 10. Total organic carbon (TOC) is low in most of the groundwater and is $<10^{-5}$ M in the Swiss crystalline and of the order of 6×10^{-5} M in the sedimentary (for example, Wellenberg). Its concentration in the

Gorleben system may reach the 10^{-2} M level because the waters originate from the brown coal formation (nonmetamorphosed system).

The steady state in the aquifer is broken in some cases. For example, mixing of Na-Ca-HCO_3-Cl and Na-Ca-(Mg)-Cl-HCO_3 waters is observed at Äspö. A similar situation is also locally observed at Bad Säckingen. An important assessment of the status of the aquifer is comparison of water temperature with the temperature estimated by the geothermometer ($T\&T_{geo}$ in Table 6.3-28), which may give information about the status of the thermal steady state of the water. For example, large differences between temperature at the source and that evaluated from the geothermometer are noted in the hydrothermal waters collected in zone 2 of the Transitgas Tunnel.

Colloid Characterization–Colloids have been characterized by various techniques, including detection of a single-particle unit by scattering of laser light, filtration and ultrafiltration techniques (see Buffle et al. (1992) for limitations of this technique), Scanning Electron Microscopy investigation and counting (McCarthy and Degueldre 1993), and gravimetry (Vilks, Miller et al. 1991).

Colloid concentration results obtained for various sizes may be modeled. When a size distribution is studied in detail and accurately, it can be described by a Pareto power law:

$$\delta[coll] \cdot \delta d^{-1} = A \cdot d^{-b} \quad , \quad \text{with } [coll] = A \cdot (1-b)^{-1} d^{1-b} \quad , \qquad \text{(Eq. 6.3-50)}$$

and with A and b constant for given size ranges. The parameter b can then be easily determined when plotting the log of the normalized colloid concentration as a function of the log of their size. The slope of the plot, b, reflects the stability such that the value of b is large for a small stable colloid population. The colloid concentration given in mass units is then deduced by taking into account an average density for the size range and by considering spherical colloids.

Measurement of the colloid attachment factors, a, was performed with model colloids of montmorillonite with size of 100 nm. The effect of Ca, Mg, Na, and K concentrations and of pH changes was studied in batch experiments. The attachment factors were obtained by measuring the colloid concentration during the coagulation process and elimination by sedimentation in static batches.

Results and Discussion–Colloid occurrence in the aquifer is postulated to be a consequence of the colloid stability in the hydrogeochemical system. The system is first supposed to be constant in time (no hydrogeochemical changes).

Colloid phases range from clay (Grimsel Test Site, Wellenberg), to SiO_2 (Yucca Mountain), Fe-organic-rich phases (Morro do Ferro), clay-coated with organics (Äspö), and clay associated with organic phases (Gorleben).

Comparison of all results was performed at the 100-nm size for accuracy reason. Factors decreasing the colloid stability are an increase of salt (Na^+, K^+) concentration and of water total hardness (Ca^{2+}, Mg^{2+}). The trend of colloid concentrations as a function of salt and hardness of

the water is shown in Figure 6.3-95. Strong flocculent (for example, Fe^{3+}, Al^{3+}) are quasi-insoluble in the groundwater, limiting their action in the aquifer. The effect of calcium may be reversed on a charge basis (Seaman et al. 1995), mostly in weakly acidic oxic water loaded with positively charged iron-oxyhydroxy colloids for which cations are not able to act as a coagulant. This effect was observed in the Poços de Caldas mine where iron-oxyhydroxo colloids are stabilized at pH values from 3 to 5 in the surface water in which pyrite oxidation decreases the pH, locally increasing the stability of these positively charged iron colloids. The calcium does not act as a coagulant for iron-rich colloids in these waters. It must also be noted that artifacts such as calcite particles are generated during water sampling; consequently, colloid concentrations from calcium-rich water are sometime affected by these artifacts. This fact explains the absence of Laxemar, Whiteshell, and Äspö data in Figure 6.3-95.

The apparent observed in Figure 6.3-95 must be justified on the basis of the physicochemical properties of alkali and alkaline-earth elements on the stability of model colloids. This basis was tested for montmorillonite colloids, selected as an example of clay colloids. The attachment factor of these colloids increases towards 1 with increasing alkali and alkaline-earth element concentrations (Figure 6.3-96). This test clearly demonstrates that the salinity and the hardness of the water play an important role on the colloid stability and that the attachment factor of these clay colloids reaches about 1 for salt concentrations around 10^{-2} M and alkaline-earth element concentrations around 10^{-4} M.

Factors increasing colloid stability and their transport include the presence of organics or changes in the hydrogeochemical state in the aquifer. The effect of organics on the colloid phase stability was studied in detail by O'Melia and Tiller (1993). These authors confirm that the specific increase of dissolved organic concentration and of pH enhances colloid stability. This result justifies the large colloid concentration observed in Gorleben. Their presence stabilizes the small colloids and, consequently, increases the value of *b* in the Pareto law (Figure 6.3-97). The dissolved organics originate from the rock and the groundwater colloids are potentially transportable through the formation. The next cases studied were systems subject to chemical or dynamic changes that are not in steady state with a hydrothermal signature (for example, zone 2 in the Transitgas tunnel, Bad Säckingen, and Yucca Mountain) or with phases that include amorphous components (vitrified tuff from Yucca Mountain) or in which the chemistry is variable (such as the mixing waters at Äspö). In zone 2 from the Transitgas tunnel, the colloid concentration remains large because the hardness of these waters is low.

A model of contaminant transport by colloids may be better adapted to describe reality on the basis of these properties. Colloid stability may be described first as a function of the water chemistry and not of the rock itself, because groundwater chemistry is already driven by rock properties on the basis of rock-water interactions. The colloid stability limits their presence and mobility.

Conclusions–Colloid concentration in a given aquifer is a function of the colloid phase stability in the hydrochemical system. Stability is a function of the chemical composition of the water as well as of the hydrogeochemical steady state of the aquifer. For an aquifer in a steady-state situation, decreases of the concentration of alkali element below 10^{-2} M and of alkali-earth elements below 10^{-4} M contribute to an increase in the colloid stability and concentration. However, water mixing and large concentrations of organic carbon contribute to an increase in

the colloid stability and concentration. Generally, the presence of transient situations, such as changes of T, flow rate, or chemistry (pH, salt, or redox potential) in the aquifer, also induces larger colloid concentrations. The values of b obtained from the distribution law are indicative of the system's situation with regard to chemical or dynamic steady state, and these values are also a function of pH and the presence of organic carbon.

6.3.6.2 Modeling of Colloid Transport

Experimental Study–Groundwater colloids can act as a vector that enhances the migration of contaminants. While sorbed to mobile colloids, contaminants can be held in the aqueous phase, which prevents them from interacting with immobile aquifer surfaces. As a result, an important aspect of the modeling effort for the Yucca Mountain Site Characterization Project is to describe colloid transport.

In this study (Noell, Thompson et al. 1997), an idealized laboratory setup was used to examine the influence of amorphous silica colloids on the transport of cesium. Synthetic groundwater and saturated glass-bead columns were used to minimize the presence of natural colloidal material. The columns were assembled in replicate, some packed with 150- to 210-µm glass beads and others packed with 355- to 420-µm glass beads. The colloids used in the experiments were 100-m amorphous silica colloids.

The retardation factor for cesium in the two types of glass-bead columns was determined both in the absence of the silica colloids and in the presence of a constant flux of colloids. Also, the influence of anthropogenic colloids was tested by injecting pore-volume slugs of an equilibrated suspension of cesium and colloids into the colloid-free columns. Finally, a model developed by Corapcioglu and Jiang (1993) was compared with the experimental elution data. Both equilibrium sorption expressions using an effective retardation coefficient and fully kinetic simulations were used to describe the colloid-facilitated transport of cesium.

Summary of Results–The intent of these experiments was to establish data, under ideal circumstances, that show the influence of silica colloids on the migration of radionuclides through porous media. This goal was accomplished by using synthetic groundwater and saturated glass-bead columns so that the amount of natural colloidal material in the columns was minimized. Cesium-137 was used as a model radionuclide because of its detectability and simple chemistry. Colloidal silica was examined because of its abundance in many groundwaters.

The sorption of cesium to the amorphous silica colloids was found to be significant and fully reversible. In independent batch-sorption experiments, it was determined that a Freundlich isotherm with the partitioning coefficient, K, equal to 0.111 x/÷ 1.17 mL/mg and with the empirical order, m, equal to 0.882 ± 0.013 adequately described the partitioning of cesium to the amorphous silica colloids at equilibrium. Nonlinear Freundlich isotherms also best described the sorption of cesium to the glass beads. The nonlinear least-squares approximations of Freundlich parameters for the sorption of cesium to the 150- to 210-µm glass beads were $K = 1.58 \times 10^{-4}$ x/÷ 3.18 mL/mg and $m = 0.828 \pm 0.007$, whereas for the sorption of cesium to the 355- to 420-µm glass beads were $K = 9.86 \times 10^{-5}$ x/÷ 9.23 mL/mg and $m = 0.821 \pm 0.014$.

The impact of amorphous silica colloids on the transport of cesium was assessed in saturated glass-bead columns. Independently calculated column parameters were verified using tritiated water as a groundwater tracer. The retardation of cesium in colloid-free water was initially examined. The migration of cesium through the columns with the smaller glass beads was more retarded than it was in the larger glass-bead columns. Linear Freundlich partitioning coefficients determined from these column experiments agreed with the sorption data determined in batch experiments. The flow of colloids was also examined independently. Because the surface charges of the silica colloids and the glass beads were similar, the colloids were repelled from the surface of the media and were able to migrate easily through the glass-bead columns. The slight retardation of the colloids was mainly due to physical interactions between the silica colloids and glass beads. To simulate the effect of anthropogenic colloids, an equilibrated suspension of cesium and silica colloids was injected into colloid-free columns as a 0.09 pore-volume pulse. In the smaller glass-bead columns, the colloid front traveled eight times faster than the cesium front. Because the sorption of cesium to the colloids is reversible, this effect resulted in little noticeable colloid-facilitated transport of cesium. In the larger glass-bead columns, however, there was a slight reduction in the retardation of cesium. This reduction was probably due to the fact that the colloid front only traveled 3.6 times as fast as the cesium front. When silica colloids had a continuous presence and a constant flux through the columns, silica colloids significantly enhanced the migration of cesium. In the smaller glass-bead columns, the silica colloids reduced the retardation of cesium by 14 to 32 percent, whereas in the larger glass-bead columns, they reduced the retardation of cesium by 38 to 51 percent.

To simulate the colloid-facilitated transport of cesium, a model based on work by Corapcioglu and Jiang (1993) was used. Models with equilibrium sorption and with first-order kinetic sorption were compared with colloid-facilitated transport experiments of cesium. For the equilibrium case, when the flux of colloids was constant, the transport of cesium was able to be modeled using an effective retardation coefficient, R^*_f. This relation is expressed by the equations:

$$R^*_f \frac{\partial C_D}{\partial t} = \frac{D}{1+K_c C_c} \nabla^2 C_D - V \nabla C_D \quad , \qquad \text{(Eq. 6.3-51)}$$

$$R^*_f = \frac{R_f + R_c K_c C_c}{1+K_c C_c} \quad , \qquad \text{(Eq. 6.3-52)}$$

where C_D is the mass concentration of dissolved contaminant, D is the hydrodynamic dispersion coefficient, K_c is the equilibrium coefficient used to express the sorption of contaminant to the mobile colloids, C_c is the mass concentration of the suspended colloids in the aqueous phase, V is the aqueous phase velocity, R_f is the retardation coefficient for the contaminant, and R_c equals the retardation coefficient for the colloids. As the partitioning of cesium to the colloids and the concentration of colloids approaches zero, the effective retardation of cesium approaches the retardation of cesium in the absence of colloids. As the partitioning of cesium to the colloids and the concentration of colloids increases, the effective retardation of cesium approaches the retardation of the silica colloids. Equation 6.3-51 also reveals that the continuos presence of colloids decreases the effective dispersion of the contaminant.

The equations used for the kinetic simulations start with the net rate of contaminant sorption to the soil media, Q_m, given by

$$Q_m = \frac{\partial(\rho_b \sigma_D)}{\partial t} = k_3(\phi - \sigma_c)C_D - k_4 \rho_b \sigma_D \ , \qquad \text{(Eq. 6.3-53)}$$

where ρ_b is the bulk density, σ_D is the mass fraction of contaminant sorbed to the soil media, ϕ is the porosity, σ_c is the volumetric fraction of captured colloids (volume of captured colloids per unit volume of porous media), and k_3 and k_4 are the first-order adsorption and desorption rate coefficients, respectively, for the sorption of contaminant to the media.

Next, the governing equations developed to express the colloid-facilitated transport of contaminants for the fully kinetic sorption case are a set of first-order sorption expressions. First, the transport and sorption of colloids is described by

$$\frac{\partial(\theta C_c)}{\partial t} = D^* \theta \nabla^2 C_c - V \theta \nabla C_c - k_1 \theta C_c + k_2 \rho_c \sigma_c \ , \text{ and} \qquad \text{(Eq. 6.3-54)}$$

$$\frac{\partial(\rho_c \sigma_c)}{\partial t} = k_1 \theta C_c - k_2 \rho_c \sigma_c \ , \qquad \text{(Eq. 6.3-55)}$$

where $\theta = \phi - \sigma_c$, D^* signifies the gradient of D, k_1 and k_2 are the first-order adsorption and desorption rate coefficients, respectively, for the sorption of colloid to the media, and ρ_c is the density of colloidal particles. Likewise, the transport of contaminants is described by

$$\frac{\partial(\theta C_D)}{\partial t} = D\theta \nabla^2 C_D - V\theta \nabla C_D - k_3 \theta C_D + k_4 \rho_b \sigma_D - 2k_5 \theta C_D + k_6 \theta \sigma_{cm} C_c + k_7 \rho_c \sigma_c \sigma_{cc} \ , \qquad \text{(Eq. 6.3-56)}$$

where k_5 is the first-order adsorption rate coefficient, k_6 and k_7 are the first-order desorption rate coefficients from the mobile and captured colloids, respectively, and σ_{cm} and σ_{cc} are mass fractions of contaminant sorbed to colloid per unit mass of that colloid for mobile colloid surfaces and captured colloids, respectively.

The sorption of contaminant with the soil media is described by

$$\frac{\partial(\rho_b \sigma_D)}{\partial t} = k_3 \theta C_D - k_4 \rho_b \sigma_D \ ; \qquad \text{(Eq. 6.3-57)}$$

the sorption of contaminant to mobile colloids is described by

$$\frac{\partial(\theta \sigma_{cm} C_c)}{\partial t} = [D^* \theta \nabla C_c - V\theta C_c]\nabla \sigma_{cm} + [D^* \theta \nabla^2 C_c - V\theta \nabla C_c - (k_1 + k_6)\theta C_c]\sigma_{cm} + k_5 \theta C_D + k_2 \rho_c \sigma_c \sigma_{cc} \ ; \qquad \text{(Eq. 6.3-58)}$$

and the sorption of contaminant to captured colloids is given by

$$\frac{\partial(\rho_c \sigma_c \sigma_{cc})}{\partial t} = k_5 \theta C_D - (k_2 + k_7)\rho_c \sigma_c \sigma_{cc} + k_1 \theta \sigma_{cm} C_c \ . \qquad \text{(Eq. 6.3-59)}$$

Fully kinetic simulations using the above equations were found to more accurately describe the colloid-facilitated transport of cesium in these experiments.

6.3.6.3 Determination of Sorption Parameters for Colloid Transport Model

When natural colloidal material is present, stable, and mobile in groundwater, colloids can facilitate the transport of contaminants. When the sorption of contaminants to colloids is irreversible, the transport of the contaminant can become solely a function of the transport of colloids. The failure to account for the role of colloids in facilitating the transport of contaminants can lead to a serious underestimation of the distances that groundwater contaminants migrate (McCarthy and Zachara 1989).

Experimental Study–In this study (Noell, Triay et al. 1997), the kinetics for the adsorption and desorption of cesium to amorphous silica colloids was examined in batch experiments. The partitioning of cesium between the water and the colloids was determined after many different time periods.

A sorption rate equation was developed for the reaction. Because the number of sorption sites overwhelmed the number of sorbents, this rate equation was able to be expressed with first-order adsorption and desorption rates. The ordinary differential equation was solved, which allowed calculation of the forward and reverse first-order sorption rates. It was also found that a Freundlich isotherm adequately described the sorption of cesium to these amorphous silica colloids in the given synthetic water.

Summary of Results–The sorption of cesium to amorphous silica colloids occurred very rapidly and was completely reversible. This fact allowed the reaction to be approximated with sorption isotherms. The sorption of cesium to amorphous silica colloids in a synthetic water resembling UE-25p #1 groundwater under atmospheric conditions was best approximated using a Freundlich isotherm with partitioning coefficient K equal to 0.0224 x/÷ 1.21 and empirical order m equal to 0.955 ± 0.023. A linear Freundlich isotherm also suitably described this sorption reaction. Although the sorption of cesium to amorphous silica colloids was slightly underestimated at lower cesium concentrations, a K_d equal to 0.0219 ± 0.0022 mL/mg adequately described sorption of cesium to the amorphous silica colloids for most of the regions examined.

Although the sorption of cesium to amorphous silica colloids appeared to be rapid and completely reversible, a methodology was established to determine first-order kinetic sorption rate coefficients from batch experiments. To find these coefficients uniquely, batch-sorption experiments must be performed at multiple time intervals both before and after sorption equilibrium occurs. The first-order sorption of cesium to silica colloids is described by

$$\frac{d(CsOSi(OH)}{dt} = k_f [Cs^+] - k_r [CsOSi(OH)] \qquad \text{(Eq. 6.3-60)}$$

where k_f and k_r are the first-order forward and reverse reaction rates, respectively, and brackets denote number concentrations. Ordinarily, the forward reaction should be described as second order, but when the sorbed contaminant does not influence the sorption of additional contaminants (as is the case when the number of sorption sites overwhelms the number of sorbents), it is valid to use a first-order adsorption rate coefficient.

The analytical solution of Equation 6.3-60, in terms of the ratio of the number concentration of colloidally sorbed cesium to the number concentration of dissolved cesium ions, is

$$\frac{[Cs \cdot OSi(OH)]}{[Cs^+]} = \frac{k_f - k_f \exp\left[-(k_f + k_r)t\right]}{k_r + k_f \exp\left[-(k_f + k_r)t\right]} \; . \qquad \text{(Eq. 6.3-61)}$$

It was determined that the first-order desorption rate coefficient for cesium on silica colloids was approximately eight times greater than the first-order adsorption rate coefficient. Because equilibrium was achieved in all of the samples, only minimum values of the sorption rate coefficients were determined. These values were

$$k_f > 0.005 \text{ sec}^{-1} \text{ and } k_r > 0.04 \text{ sec}^{-1} \; . \qquad \text{(Eq. 6.3-62)}$$

By finding batch kinetic sorption rates between various radionuclides and naturally occurring colloidal material, it might be possible to determine which radionuclides have the lowest desorption rates from natural colloids. This information could aid in predicting their migration because radionuclides that are irreversibly sorbed to colloids are most likely to be transported by colloids.

6.3.6.4 Reversibility of Radionuclide Sorption Onto Colloids

Subsection 6.3.6.1 presented a global approach to colloid stability. Subsections 6.3.6.2 and 6.3.6.3 reviewed colloid transport models, their effectiveness in fitting laboratory data, and a methodology to determine the parameters needed for the colloid models. Subsections 6.3.6.2 and 6.3.6.3 deal with an idealized system involving silica colloids and glass beads as the transport medium. Applied in this subsection is the methodology developed for an idealized system to the colloids expected at Yucca Mountain, namely plutonium sorbed onto iron-oxide colloids.

Sorption of ^{239}Pu onto iron-oxide colloids in groundwater plays an important role for the transport of Plutonium along potential flow paths from radionuclide contaminated areas and the

release to the accessible environment. A natural groundwater and a carbonate-rich synthetic groundwater, filtered through a 0.05-μm membrane, were used as media in this subsection. Laboratory batch-sorption experiments were performed to evaluate sorption of Pu as a function of different iron-oxide colloids and different oxidation states of Pu and to examine the sorption kinetics of Pu(IV) colloids (hydrous plutonium oxide) and soluble Pu(V) onto these iron-oxide colloids.

The preliminary results show that adsorption of Pu exhibits different patterns between Pu(IV) colloid and soluble Pu(V), hematite and goethite, and natural and synthetic J-13 groundwaters. Adsorption of both the Pu(IV) colloid and soluble Pu(V) onto the hematite and goethite colloids occurs as a function of time. Iron-oxide colloids sorbed more soluble Pu(V) than Pu(IV) colloids and also sorbed more Pu in the synthetic J-13 groundwater than in the natural J-13 groundwater. The results also show that the hematite colloids sorbed more Pu than the goethite colloids. This result was due to differences in their surface characterization. Preliminary results indicate that Pu(IV) colloids, as well as soluble Pu(V), can be rapidly adsorbed by hematite or goethite colloids in natural or synthetic groundwater. Desorption of Pu(IV) colloids as well as soluble Pu(V) is slower than the sorption processes. To confirm the results from these experiments, additional experiments are being conducted to examine sorption of Pu onto iron-oxide colloids in nanopure deionized water under carbon-dioxide-free environments, desorption of Pu from Pu-loaded iron-oxide colloids as a function of time over a long period (~1 year), and the identification of the species of Pu(IV) and Pu(V) on the surface of iron-oxide colloidal particles after the sorption process.

Introduction–Traditionally, the transport of metal contaminants in groundwater has been predicted by evaluating their distribution between two phases: a dissolved, mobile phase and a sorbed or precipitated, stationary phase associated with aquifer solids. Most models of metal contaminant transport processes assume that groundwater is a two-phase system with contaminants partitioning between the immobile solid phase and the mobile aqueous phase (McCarthy and Zachara 1989). However, components of the solid phase may exist in groundwater in the colloidal size range (1 nm to 1 μm, or to a few μm for organic colloids). These colloidal particles have compositions and surface characteristics similar to the immobile aquifer solids but are mobile within aquifers. In porous media, the size of colloids is smaller than the pores that allow colloids to migrate over long distances. Generally, the same processes that control adsorption of radionuclides to aquifer solids also affect their association with colloidal materials. Colloids are capable of associating with radionuclides (Penrose et al. 1990; Vilks and Degueldre 1991). The very large surface area of colloids (10 to 500 m^2 g^{-1}) can significantly sorb radionuclides even for relatively low mass concentrations of colloidal particles in the aquifer (McCarthy and Degueldre 1993). These mobile colloids may enhance the transport of the strongly sorbing radionuclides along flow paths and release these radionuclides to the accessible environment. Triay, Degueldre et al. (1996) studied the generation and stability of colloids in Yucca Mountain groundwater and found that colloids of clays, silicon, and iron oxides were generated in the groundwater and irreversible sorption of radionuclides onto these colloids occurred. The stability of clay and silica colloids is a function of the ionic strength. Ryan and Geschwend (1990) reported that anoxic conditions induce mobilization of clay colloids in groundwater by dissolving the ferric oxyhydroxide coatings cementing the clay particles to the aquifer solids. Champ et al. (1982) observed that when groundwater was pumped through

undisturbed aquifer cores, plutonium was rapidly transported, and almost 75 percent of the plutonium was associated with colloidal particles. At the Nevada Test Site, transition metals and lanthanide radionuclides were associated with inorganic colloids recovered from groundwater 300 m from a nuclear detonation cavity (Buddemeier and Hunt 1988). Plutonium and americium were associated with siliceous colloids in an alluvial aquifer at Los Alamos National Laboratory (Penrose et al. 1990). Uranium and its daughter species were found associated with iron- and silica-rich colloids downgrade from a uranium deposit in Australia (Short et al. 1988).

Mineral oxides/hydroxides, especially those of Si, Fe, and Al, are important in natural water systems. These oxides and hydroxides exhibit variable charged surfaces; the net charge changes with pH and is positive at low pH and negative at high pH. Metal sorption kinetics on oxides and hydroxides depend on the type of surface and metal being studied but generally are rapid (Sparks 1995). The mechanism that dominates the sorption of metal onto oxide or hydroxide colloids in a solid-aqueous interface system is surface complexation (reaction of cations with surface hydroxyl groups) (Liang and McCarthy 1995).

Thermodynamic calculations show that Pu(V) is a stable oxidation state in the pH range of 5 to 7 at a pE of 12 and that Pu(VI) is the most stable oxidation state at higher pH values (Sanchez et al. 1985). It was assumed that adsorption of Pu(IV) onto suspended particulate matter is due to the interaction of the strongly hydrolyzable Pu(IV) oxidation state with the surfaces of natural particulate matter (Sanchez et al. 1985). Keeney-Kennicutt and Morse (1985) found that $Pu(V)O_2^+$ can be adsorbed from diluted solution and seawater on goethite, aragonite, calcite and δ-MnO_2. The sorption behavior of $Pu(V)O_2^+$ is influenced by oxidation-reduction reactions occurring on the mineral surface. Adsorption of $Pu(V)O_2^+$ on goethite results in a reaction in which Pu(IV) and Pu(VI) are formed on the mineral surface. The Pu(VI) is slowly reduced to Pu(IV), leaving Pu(IV) as the dominant surface Pu species (Keeney-Kennicutt and Morse 1985). Sanchez et al. (1985) studied adsorption of soluble Pu(IV) and Pu(V) on goethite from a sodium-nitrate solution and found that redox transformations are an important aspect of Pu adsorption chemistry. The adsorption behavior of Pu on goethite is related to the different hydrolytic character of these two oxidation states in the solution. The adsorption edge of the more strongly hydrolyzable Pu(IV) occurred in the pH range 3 to 5 whereas that for Pu(V) is at pH 5 to 7 (Sanchez et al. 1985).

However, information on affinity, kinetics, and reversibility critical to the evaluation of the significance of colloids to Pu transport, is largely unavailable for groundwater particles. There is no information on the adsorption of radionuclide colloids (for example, Pu(IV) colloids) onto iron oxide, silica, and clay colloids in groundwater. Studies, performed in three phases, focus on the adsorption affinity, kinetics, and reversibility of the sorption of soluble Pu(V) and Pu(IV) colloids onto iron oxide, silica, and clay colloids and on the effect of different Pu oxidation states with different forms (for example, colloidal or soluble form) on their behavior in natural and synthetic groundwater. In this phase of the study, laboratory batch-sorption experiments were performed using a natural groundwater and a carbonate-rich synthetic groundwater as media, to evaluate:

The sorption of Pu as a function of two different iron oxide colloids (hematite and goethite)

Sorption of Pu as a function of two different oxidation states with different forms (Pu(IV) colloid and soluble Pu (V))

Sorption kinetics of Pu(IV) colloid and soluble Pu(V) onto these iron-oxide colloids

Desorption of Pu from Pu-loaded iron oxide colloids as a function of time over a long period (~1 year)

Adsorption of Pu(IV) and Pu(V) onto Hematite Colloids–The preliminary results show that sorption of Pu onto the hematite and goethite colloids is a function of time. The amounts of Pu adsorbed varied among the two iron oxides and two solutions. The adsorption of Pu also exhibits different patterns between the Pu(IV) colloid and the soluble Pu(V).

Hematite sorbed more soluble Pu(V) than Pu(IV) colloids (Table 6.3-29). Adsorption of Pu also shows different patterns for the two solutions (natural J-13 groundwater and synthetic J-13 groundwater). In the synthetic groundwater, the adsorption of Pu(IV) colloids shows a one-step mechanism. After a 10-minute contact period, about 66 percent of Pu(IV) colloids were adsorbed onto hematite colloids, and from then on, the percentage of adsorbed Pu(IV) remained constant over time.

Additional contact time between Pu(IV) colloids and hematite colloidal particles did not affect the amount of Pu(IV) colloids adsorbed onto the hematite colloidal particles. The adsorption rate is 11.36 pCi/mg/min during the first 10 min (Figure 6.3-98).

In the natural groundwater, although the amounts of adsorbed Pu(IV) colloids increased slightly as the contact time extended from 10 min to 60 min, the adsorption of Pu(IV) colloids also shows a one-step mechanism. The percentage of adsorbed Pu(IV) colloids remained constant with additional time (Table 6.3-28). After 10 min of contact period, about 60 percent of the Pu(IV) colloids was adsorbed by hematite colloids. The adsorption rate is 10 pCi/mg/min in the natural groundwater (Figure 6.3-98). At the end of the experiments (5760 min), about 60 percent to 66 percent of the Pu(IV) colloids was adsorbed by hematite colloids in both natural and synthetic groundwater. These results indicate that Pu(IV) colloids can be rapidly adsorbed by hematite colloid in natural or synthetic groundwater.

With soluble Pu(V), adsorption patterns of Pu(V) onto hematite colloids varied between the two solutions. Generally, hematite colloids sorbed more Pu(V) in the synthetic groundwater than in the natural groundwater.

In the synthetic groundwater, the adsorption of soluble Pu(V) shows a two-step mechanism. The first step is a fast process that occurred in the 10-min contact period. About 82 percent of the Pu(V) was sorbed during this short period (Table 6.3-29). The adsorption rate is 14.18 pCi/mg/min in the natural groundwater during this period (Figure 6.3-98). The second step is a slow process that continued for 5750 minutes. Only 5 percent additional Pu(V) was adsorbed during this period.

The results of Figure 6.3-98 indicate that soluble Pu(V) and Pu(IV) colloids can be rapidly adsorbed by hematite colloids in natural or synthetic groundwater. In natural groundwater, the

adsorption of Pu(V) shows a positive correlation with time. The amounts of Pu(V) adsorbed gradually increased from 44 percent to 76 percent as the sorption time increased from 10 to 5760 min (Table 6.3-29). However, these data were not adequate to determine if the adsorption of Pu(V) in natural water is a one-step or a two-step mechanism. The adsorption of Pu(V) may be a one-step mechanism.

Desorption of Pu from Pu-loaded hematite colloids did not occur during the first 3 days of desorption process. After 30 days of desorption, Pu(V) was not desorbed from hematite, and less than 0.01 percent of Pu(IV) colloid was desorbed from hematite. Desorption of Pu is much slower than sorption.

Adsorption of Pu(IV) and Pu(V) onto Goethite Colloids–Generally, goethite sorbed less amounts of Pu(IV) and Pu(V) than hematite did in both natural and synthetic groundwater. Adsorption of Pu onto goethite colloids also exhibits different patterns between Pu(IV) colloids and soluble Pu(V). Adsorption of Pu also shows different patterns between the two solutions (natural groundwater and synthetic groundwater).

In the synthetic groundwater, adsorption of Pu(IV) onto goethite colloids is slower than onto hematite colloids. After a 10-min contact period, only 34 percent of the Pu(IV) was adsorbed. The adsorption rate is 5.6 pCi/mg/min (Figure 6.3-99). Although the amounts of Pu(IV) adsorbed increased with increasing contact time, only 52 percent of Pu(IV) was adsorbed after 5760 min of sorption (Table 6.3-30).

In the natural groundwater, about 29 percent of the Pu(IV) colloids was adsorbed during the first 10-min period; after 10 min, the amounts of Pu(IV) colloids adsorbed reached a maximum (45 percent) at 60 min, then the sorption of Pu(IV) colloids decreased with additional time. The adsorption rate is 4.5 pCi/mg/min during the first 10-min contact period (Figure 6.3-99).

With Pu(V), goethite also sorbed the more soluble Pu(V) in the synthetic groundwater than in the natural groundwater. In the synthetic groundwater, about 63 percent of the soluble Pu(V) was sorbed during the first 10-min period. The adsorption rate is 10.6 pCi/mg/min during this period (Figure 6.3-99). Thereafter, there is a small but significant increase in the adsorption of soluble Pu(V) with time.

In the natural groundwater, the adsorption of soluble Pu(V) onto goethite also shows a positive correlation with time. Amounts of Pu(V) adsorbed gradually increased from 19 percent to 62 percent as the sorption time increased from 10 to 5,760 min (Table 6.3-30).

These results indicate that Pu(IV) colloids and soluble Pu(V) can be rapidly adsorbed by goethite colloids in natural or synthetic groundwater. However, desorption of Pu(V) and Pu(IV) from Pu-loaded goethite colloids did not occur during the first 3 days of the desorption process. After 30 days of desorption, less than 0.01 percent of Pu(V) and less than 0.1 percent of Pu(IV) desorbed from the goethite. Desorption of Pu is much slower than sorption.

The results show that hematite colloids sorbed more Pu than goethite (Tables 6.3-29 and 6.3-30). This result was due to differences in their surface characteristics and the purification of the mineral materials. The hematite material contained 99.6 percent Fe_2O_3; the goethite material

contained 86 percent Fe_2O_3. Chwertmann and Taylor (1977) reported that the usual crystal morphology of synthetic hematite particles is hexagonal plates and the crystal morphology of synthetic goethite particles is an aciculate. Therefore, hematite colloids may have larger surface areas than goethite when the particle sizes of both iron oxide colloids are the same.

Both iron-oxide colloids sorbed more Pu in the synthetic groundwater than in the natural groundwater. The zero point of charge of synthetic hematite and goethite ranged in pH value from 7.95 to 8.01 in both groundwaters, indicating a similar surface activity with regard to the Fe-OH groups for the two iron oxides. However, the surface electrical potential of iron-oxide colloids in the synthetic groundwater was higher than in the natural groundwater.

Adsorption of soluble Pu(V) may be a chemisorption process in which the soluble Pu(V) or its hydrolysis species bind to hydroxyl (OH^-) groups on the hematite or goethite surface (see Subsection 6.3.3.2.2.2). Assuming that Pu(V) binds to hematite or goethite surface (OH^-) groups analogous to aqueous coordination reactions, the adsorption of Pu(V) to both iron-oxide colloids can be chemically described by the following equation (Liang and McCarthy 1995).

$$\equiv SOH + Pu^{5+} \Leftrightarrow \equiv SO\text{-}Pu^{4+} + H^+ \qquad K_{1,\,app} \qquad \text{(Eq. 6.3-63)}$$

where ≡SOH denotes a surface site of hematite or goethite and $\equiv SO\text{-}Pu^{4+}$ is the concentration of Pu(V) adsorbed on the surface sites of the colloids. $K_{1,app}$ is the apparent surface equilibrium constant and is defined as:

$$K_{1,\,app} = \{\equiv SO\text{-}Pu^{4+}\}[H^+] / [\equiv SOH]\,[Pu^{5+}] \qquad \text{(Eq. 6.3-64)}$$

Because of the charge characteristics of the surface of iron-oxide colloidal particles, the activity of ions at the surface needs to be corrected to obtain the intrinsic equilibrium constant, which can be calculated by the following equation:

$$K_{1,\,int} = K_{1,\,app} \exp\,[(z-1)F\Psi/RT] \qquad \text{(Eq. 6.3-65)}$$

where Ψ is the potential difference between the binding site and the bulk solution, F is the Faraday constant, R is the gas constant, T is temperature in absolute degrees, and z is the ionic charge of the sorbing metal ion. The exponential term accounts for the coulombic contribution to the intrinsic equilibrium constants.

Theoretically, from the reaction equation, after soluble Pu(V) adsorbs onto iron oxide, Pu(V) is reduced to Pu(IV) on the surface of colloidal particles. To confirm this possibility, the Pu oxidation species on the surface of iron-oxide colloidal particles will be experimentally determined. It will also be determined whether Pu(V) in the natural or the synthetic groundwaters remains stable. The hydrolysis constants for adsorption of Pu(V) onto iron oxides are not well known (Sanchez et al. 1985).

However, sorption of Pu(IV) colloids onto iron oxide colloids may have different mechanisms; the adsorption mechanism of Pu(IV) colloids onto hematite or goethite colloids is not well

understood. During the experiment, precipitation of Pu(IV) colloids did not occur. The sorption of Pu(IV) colloids onto iron oxide colloids may have happened by an electrical or other binding force. In the natural or the synthetic groundwater with pH ranges of 8.4 to 8.6, the surface electrical potential of hematite and goethite colloids ranged from 27.1 to 35. 4 mV. Therefore, the negatively charged surfaces of iron oxide colloids may electrostatically sorb (or bind) positively charged Pu(IV) colloids.

Sanchez et al. (1985) studied the sorption of soluble Pu(IV) species onto goethite. They found that soluble Pu(IV) species was chemically described by three reactions involving the adsorption of Pu(IV) hydrolysis species.

$$\equiv SOH + Pu^{4+} + 2H_2O \Leftrightarrow \equiv SOPu(OH)_2^{2+} + 3H^+ \qquad {}^*K_{1,\,int} \qquad \text{(Eq. 6.3-66)}$$

$$\equiv SOH + Pu^{4+} + 3H_2O \Leftrightarrow \equiv SOPu(OH)_3^{+} + 4H^+ \qquad {}^*K_{2,\,int} \qquad \text{(Eq. 6.3-67)}$$

$$\equiv SOH + Pu^{4+} + 4H_2O \Leftrightarrow \equiv SOPu(OH)_4^{0} + 5H^+ \qquad {}^*K_{3,\,int} \qquad \text{(Eq. 6.3-68)}$$

It is not known whether the sorption of Pu(IV) colloids onto hematite or goethite follows the same reactions described by Sanchez et al. (1985).

Because of the presence of carbonate and bicarbonate ions in both natural and synthetic groundwater, the formation of Pu(V)-carbonate complexes may occur, which may influence the adsorption of Pu(V). To confirm this, the experiments are being conducted with deionized water under carbon-dioxide-free conditions. The ionic strength of deionized water was brought to 0.005 M using sodium nitrate ($NaNO_3$) (same ionic strength as the natural and the synthetic groundwater). The alkalinity of the natural and synthetic groundwater used in the study ranged from 22.5 to 25 meq/L. At these values, it was predicted that the adsorption of both Pu(IV) and Pu(V) should not be affected. Sanchez et al. (1985) reported that adsorption of soluble Pu(IV) and Pu(V) was not affected by alkalinity values less than about 100 meq/L, where the amount of adsorbed Pu on goethite was similar to that obtained at the same pH in 0.1 M sodium-nitrate solution.

Conclusions–Preliminary results show that both hematite and goethite colloids sorbed more soluble Pu(V) than Pu(IV) colloids in the natural and synthetic groundwaters. Iron oxide sorbed more Pu in the synthetic groundwater than in the natural groundwater. The percentage of Pu adsorbed varied with the two iron oxides and the two solutions. Adsorption of Pu(IV) is a time-independent process whereas adsorption of Pu(V) is a time-dependent process. After a 10-minute contact period, hematite sorbed about 57 percent to 66 percent of Pu(IV) colloids and 44 percent to 82 percent of soluble Pu(V), whereas goethite sorbed 29 percent to 34 percent of Pu(IV) colloid and 19 percent to 63 percent of Pu(V). However, the process of Pu desorption from Pu-loaded iron-oxide colloidal particles is slow. After 30 days of desorption, Pu(V) was not desorbed from hematite, and less than 0.01 percent of Pu(V) desorbed from goethite. Less than 0.01 percent of Pu(IV) colloids was desorbed from hematite and less than 0.1 percent of Pu(IV) was desorbed from goethite.

6.4 HEALTH-RELATED MINERAL ISSUES

Introduction–A thorough knowledge of the airborne particulates generated through site characterization, ECRB, and construction activities is crucial to worker and environmental safety. It is important to identify any potential hazards related to airborne materials that could impact the safety of workers during mining, drilling, excavation, and other future activities in the area of the potential repository. These materials might be generated during drilling or excavation or released from muck piles. The concern is addressed in this subsection by providing background information on mineral health hazards, surveying the distribution of potentially hazardous minerals at Yucca Mountain, and describing the implications of such mineral hazards for construction and operation.

Anthropogenic activities at Yucca Mountain have the potential to release to the environment airborne minerals, some of which pose health risks following inhalation. They can pose an immediate risk to humans (for example, through direct exposure to workers) or a delayed risk to humans (for example, through releases to the environment that may cause future exposures). Most of the minerals of concern occur naturally at the surface throughout Nevada and other regions of the United States, and these naturally derived dusts contribute to the eolian burden. This natural component provides a useful baseline for assessing the potential impact of anthropogenic sources of eolian dusts (for example, dusts generated by drilling, excavation, etc.). The project currently monitors dust levels generated by operations to ensure worker safety (for example, the effort by those involved in the safety and health oversight role). The potential long-term exposure can be evaluated by investigating the mineral content of dusts deposited in the vicinity of operations at Yucca Mountain. An important aspect of such a study is the comparison of dusts potentially released by operations with the dusts released by natural processes (that is, background dusts). Therefore, the mineralogy of eolian-deposited dusts in the vicinity of Yucca Mountain has also been investigated to evaluate the potential impact of site activities on the environment. These efforts are intended to determine the natural mineral-dust input and its variability, and to estimate the changes to the natural mineral-dust load brought about by site activities.

Three-dimensional information on the bulk-rock mineralogy of Yucca Mountain is available from the extensive mineralogy-petrology studies conducted at Yucca Mountain. These data are the basis for the 3-D Mineralogic Model. Los Alamos National Laboratory staff have worked since the late 1970s to characterize and to understand the mineralogy and petrology of the rocks at and surrounding Yucca Mountain. The information from this research, including studies of fracture mineralogy, is summarized in Section 6.1 and in the Min-Pet summary and synthesis report (Bish, Carey et al. 1996). This section focuses on the distribution of minerals that are present in the subsurface and in eolian-deposited dusts and that may be potential health hazards. Numerous minerals have been suggested as potentially hazardous following inhalation, and some of these occur in the subsurface at Yucca Mountain. Subsection 6.4.1 (Background Information on Mineral Health Hazards) summarizes the published biological data for minerals that are known to occur at Yucca Mountain. Based on these data, the minerals at Yucca Mountain are divided into three groups. The distributions of the minerals in these groups are discussed in Subsection 6.4.2 (Survey of Potential Mineral Health Hazards at Yucca Mountain). Finally, Subsection 6.4.3 (Implications of Mineral Health Hazards for Construction and Operation), the

implications of the known mineral health hazards at Yucca Mountain for construction and operation of a repository are discussed.

6.4.1 Background Information on Mineral Health Hazards

Numerous minerals have been suggested as potentially hazardous following inhalation, and some of these occur in the subsurface and at the surface at Yucca Mountain. This subsection focuses on biological data on mineral toxicity for minerals known to occur at Yucca Mountain. Based on available data, the minerals at Yucca Mountain may be divided into three groups: minerals that clearly represent potential health hazards; minerals that do not represent potential health hazards; and minerals that are probably not health hazards, but data on their biological activities are extremely limited so they can not be reliably discounted at present. The minerals will be discussed in the first group because these minerals are extremely important to consider in any risk assessments. Also discussed will be the minerals of the third group because they cannot be eliminated from concern as potential health hazards. The distributions of the minerals in the first and third groups are discussed in Subsection 6.4.1.2. However, the minerals of the second group will not be discussed in this report.

The concern with hazardous minerals began at Yucca Mountain when erionite was discovered in samples analyzed by the Mineralogy-Petrology team. Before 1959, the fibrous zeolite erionite was considered extremely rare and was known only from a deposit at Durkee, Oregon (Gottardi and Galli 1985). It was not until Deffeyes (1959) reported erionite from several sedimentary occurrences in the Western United States that erionite was recognized as a relatively common zeolite. Since then, it has been found in numerous sedimentary zeolite deposits throughout the world, including Western United States localities in Idaho, New Mexico, California, Oregon, Wyoming, Nevada, and Arizona (Surdam and Sheppard 1978). In the past 15 years, additional attention has been focused on the natural occurrence of erionite because of its association with incidences of malignant mesothelioma in Turkey.

Erionite was first discovered in Yucca Mountain Tuffs in a fracture from drillhole UE-25 a#1 at 395 depth (1,296.2 feet) on February 14, 1985 (Bish and Vaniman 1985). A description of the techniques specially developed at Los Alamos shortly thereafter to detect very small quantities of erionite in mixtures with other minerals is reported above in the Subsection 6.1 and in Bish and Chipera (1987). When erionite was first identified in tuffs at Yucca Mountain, its health effects were not well known, and erionite was not listed by regulatory agencies. Since that time, YMP scientists have learned considerably more about the occurrence and distribution of erionite at Yucca Mountain and about its health effects. Furthermore, erionite is now listed as a Group-1 carcinogen by the International Agency for Research on Cancer, a listing that signifies it is a known human carcinogen.

After a link was identified between erionite and malignant mesothelioma, the YMP intensified and focused mineralogical studies to include routine analyses for erionite. A wide assortment of samples was analyzed to assess the distribution and abundance of erionite at Yucca Mountain. Some studies were done in response to requests on the part of the YMP for information on possible erionite occurrence in newly drilled boreholes. The urgency arose out of the finding in late fiscal year 1994/early fiscal year 1995 of large concentrations of erionite in a section of core from borehole USW UZ-14 closely underlying the potential repository horizon.

Because erionite is a known human carcinogen, it is imperative that the YMP know its distribution at Yucca Mountain. The project has determined this information primarily through highly specialized X-ray powder diffraction analyses of core samples. However, because erionite is such a potent biological hazard, techniques have also been developed to allow prediction of where erionite may occur at Yucca Mountain before it is encountered. For example, thermodynamic modeling has been used in an attempt to predict the factors that control the distribution of zeolites at Yucca Mountain. This study involved searching for a unique set of geochemical conditions that would give rise to the formation of erionite. This information will provide the YMP with a better ability to predict where erionite occurs throughout Yucca Mountain. The most common zeolites at Yucca Mountain are clinoptilolite-heulandite and mordenite (Bish and Chipera 1989), although sporadic occurrences of chabazite, erionite, phillipsite, and stellerite have been identified, mainly in fractures (Carlos, Chipera, Bish et al. 1995). It appears that subtle differences in geochemical conditions must have existed locally over short distances to give rise to the formation of these unusual zeolites. For example, fractures in drillhole UE-25 a#1 contain a sequence with increasing depth in which clinoptilolite and mordenite coexist, then only clinoptilolite, then erionite-clinoptilolite, then phillipsite-clinoptilolite, and then back to coexisting clinoptilolite-mordenite, all within a depth range of approximately 21.6 m (71 feet) (Table 6.4-1). Likewise, a similar sequence exists in drillhole USW GU-3 (Table 6.4-1). A report predicting the distribution of erionite in drillhole SD-6 used all available criteria, including the 3-D Mineralogic Model, to guide drilling and sample analysis during drilling. This section summarizes the current state of knowledge concerning the biological effects of erionite and its occurrence and distribution at Yucca Mountain. The report also presents preliminary modeling results to aid in developing a capability to predict erionite distributions.

As a result of the recent work on erionite distribution at Yucca Mountain, the YMP also gained an awareness of the importance of airborne mineral hazards in general, not just those limited to erionite. Therefore, this subsection of the site description will address all of the potentially hazardous minerals occurring at Yucca Mountain.

6.4.1.1 Introduction to Biological Activity

The biological activities of minerals are generally evaluated using one of three approaches: epidemiological studies, *in-vivo* studies, and *in-vitro* studies. Epidemiological studies evaluate the health risks associated with a particular agent (mineral in this case) by determining the relationships between human exposure to the agent and observable health effects. *In-vivo* studies evaluate an agent's health risks by testing the agent on living animals. *In-vitro* studies evaluate an agent's activity in simplified systems, such as individual cell types. A more detailed discussion of these methods is given by Guthrie (1992) and Guthrie and Mossman (1993). Data from these three types of studies can be used to evaluate the biological activities of minerals at Yucca Mountain. Biological activity is used as a measure of a mineral's potential to affect a biological system, and a biologically active mineral may induce a specific response when introduced to cells or animals. However, biological activity does not necessarily imply that a mineral is carcinogenic. Some minerals appear biologically active but do not appear to be carcinogenic in humans. A carcinogenic response in humans results from complex mechanisms that are affected by numerous processes and mineralogical properties, including (but not limited

to) biological activity, particle size and morphology, biodurability, exposure levels and conditions, concurrent exposures to other agents, and genetic factors.

The International Agency for Research on Cancer is part of the World Health Organization and is recognized by the Hazard Communication Standard (29 CFR 1910) as an authority on carcinogenic substances. Periodically, the International Agency for Research on Cancer publishes monographs on the evaluation of the carcinogenicity of various substances to humans. Several of these monographs (IARC 1971, 1987a, 1987b, 1997) explicitly address minerals that occur at Yucca Mountain. The International Agency for Research on Cancer classifies the biological data for a mineral with respect to carcinogenicity to humans and animals, based on epidemiological and experimental data, respectively. A mineral's carcinogenic potential for humans or animals is classified as follows (IARC 1987a):

- Sufficient Evidence of Carcinogenicity–A causal relationship has been established between exposure to the agent and cancer induction.

- Limited Evidence of Carcinogenicity–A positive association has been observed between exposure to the agent and cancer induction for which a causal relationship is possible but for which chance, bias, or confounding cannot be ruled out.

- Inadequate Evidence of Carcinogenicity–Available studies are of insufficient quality to permit a conclusion regarding the presence or absence of a causal relationship between exposure to the agent and cancer induction.

- Evidence Supporting a Lack of Carcinogenicity–Adequate studies show no relationship between exposure to the agent and cancer induction.

Using these summaries, the International Agency for Research on Cancer groups each agent based on its carcinogenic potential. The groups indicate the following:

- Group 1–the agent or mixture is carcinogenic to humans
- Group 2A–the agent or mixture is probably carcinogenic to humans
- Group 2B–the agent or mixture is possibly carcinogenic to humans
- Group 3–the agent or mixture is not classifiable as to its carcinogenicity to humans
- Group 4–the agent or mixture is probably not carcinogenic to humans

Table 6.4-2 lists the minerals known to occur at Yucca Mountain and summarizes the conclusions of the International Agency for Research on Cancer monographs. No minerals at Yucca Mountain are listed as Group 4. Minerals in Groups 1 and 2 should be treated as human carcinogens, and a conservative approach would be to treat minerals in Group 3 as carcinogens unless other factors (as discussed below) suggest otherwise.

When reviewing the summary of carcinogenicity data presented in Table 6.4-2 and in the remainder of this section, it is important to consider several factors, particularly the fact that although a mineral may be shown to be carcinogenic under some conditions, the same mineral may not pose a cancer risk under other conditions. This results because minerals induce carcinogenic responses only under specific conditions. It is generally believed that most

minerals are only of concern if they remain in contact with the respiratory tract for extended periods. Consequently, only minerals occurring as respirable particles (that is, < ~10 μm) can pose a potential risk. Furthermore, the respiratory tract possesses numerous defense mechanisms against inhaled particles, and most of these involve removal or isolation of a particle. These defense mechanisms can fail, however, if the particle has a fibrous shape or if the respiratory tract is overloaded with particles. This latter condition does not usually result from modern mining practices. Finally, a particle must possess specific physical and chemical properties so that it does not dissolve rapidly and it induces the biochemical responses that lead to carcinogenesis. These criteria can eliminate concern over a given mineral under some conditions, regardless of whether the mineral poses a risk under other conditions.

For example, consider the risk posed by exposure to quartz. Quartz is ubiquitous at the earth's surface (for example, in beach sand, soils, and airborne dusts), so each of us is exposed to quartz daily. Cancer induction by quartz is generally believed to require high prolonged exposures and, possibly, concurrent exposure to other agents. Although quartz may be carcinogenic under some conditions, one can be exposed to quartz under most conditions and not be at risk. In other words, the typical level of precaution applied to exposures to other carcinogens may not be appropriate for quartz. This statement is not meant to ignore the data suggesting that quartz is carcinogenic, but rather, it is to acknowledge that minerals induce a carcinogenic response by mechanisms that are very different from the mechanisms for other carcinogens, such as benzo[*a*]pyrene (a carcinogenic component of coal tar and cigarette smoke). These caveats on risk posed by exposure to quartz (and cristobalite) are now reflected in the International Agency for Research on Cancer's classification, which modifies their Group-1 classification with the phrase "inhaled in the form of quartz or cristobalite from occupational sources." Finally, it is important to remember that human systems are capable of handling exposures to some levels of dusts, and risk due to exposures to minerals may be maintained at acceptable levels by minimizing (but not necessarily eliminating) dust levels. Furthermore, carcinogenic minerals induce their response by a physical contact with the respiratory tract, and a dissolved or suspended form of the mineral would not be expected to induce the same response.

6.4.1.2 Biological Data on Mineral Toxicity

This subsection briefly discusses the biological information available for those minerals occurring at and around Yucca Mountain that represent potential health hazards including:

- Quartz
- Tridymite
- Cristobalite
- Opal-CT
- Volcanic glass
- Erionite
- Mordenite
- Clinoptilolite/heulandite
- Phillipsite
- Palygorskite
- Sepiolite

- Smectite
- Mica
- Feldspar
- Calcite
- Mn-oxides

For those minerals not listed by the International Agency for Research on Cancer, this information is used to develop an evaluation consistent with those in the International Agency for Research on Cancer monographs, and the final analysis is given in Table 6.4-2 in parentheses. A more detailed discussion of the biological data on many of these minerals is given by Guthrie (1992).

6.4.1.2.1 Silica

Crystalline Silica–The biological activities of several of the crystalline silica polymorphs have been evaluated, although most of the research has focused on quartz, cristobalite, and tridymite. The data for quartz and cristobalite are now sufficient for the International Agency for Research on Cancer to list these minerals as Group 1 (IARC 1997). The remaining silica minerals are listed as Group 2A, although two of the polymorphs (stishovite and coesite) exhibit at most minor biological activities (for example, Stalder and Stöber 1965; Brieger and Gross 1966, 1967; Driscoll 1993). Quartz, tridymite, and cristobalite have been the focus of numerous epidemiological, in-vitro, and in-vivo studies, which have demonstrated a link between the exposure to silica-bearing dusts and fibrosis and tumors in humans and laboratory animals (for reviews, see Heppleston 1984; Holland, L.M. 1990; Saffiotti 1992; Saffiotti et al. 1993). Generally, however, silica represents a significant risk only at high exposures, and epidemiological data suggest that, in humans, concurrent exposures to silica and other agents (for example, radon) are important determinants of actual risk (for example, McLaughlin et al. 1992). The fact that high exposures are generally required is reflected in the International Agency for Research on Cancer classification of quartz and cristobalite, which includes the statement "inhaled in the form of quartz or cristobalite from occupational sources." Consequently, crystalline silica minerals at Yucca Mountain will generally pose a health hazard at high dust levels for prolonged periods, particularly in poorly ventilated areas.

Opal-CT–Opal-CT is not discussed explicitly in the International Agency for Research on Cancer monographs, nor has it been studied extensively with respect to biological activity. As a conservative approach, opal-CT has been treated as a form of crystalline silica in Table 6.4-2. In fact, the International Agency for Research on Cancer defines "crystalline" as any material exhibiting structural periodicity that can be detected by X-ray diffraction; this would apply to opal-CT.

Volcanic Glass–The glassy material in the tuffs at Yucca Mountain is difficult to categorize with respect to biological activity. A conservative estimate for the biological activity of this material can be derived from the International Agency for Research on Cancer's evaluations for amorphous silica (Group 3, IARC 1997) and glasswool (2B), because the compositions of these two categories bracket the compositions for the glassy-tuff material. This estimate would imply that the glassy-tuff material would be Group 2B, at most. However, the glassy-tuff material from Yucca Mountain is nonfibrous, particularly when compared with the material used to determine

the biological activities of amorphous silica and glass wool. Consequently, the conclusion is that the potential cancer risk associated with the glassy material in the tuffs of Yucca Mountain is indeterminate but probably lower than Group 2B (that is, Group 3).

6.4.1.2.2 Zeolites

The biological activity of erionite (a fibrous zeolite) has been studied extensively, and all data indicate that it is extremely active in humans, both *in-vivo* and *in-vitro*. Limited data on other zeolites are less conclusive, particularly in light of the poor quality of the samples studied. The International Agency for Research on Cancer (IARC 1997) recently classified clinoptilolite, phillipsite, and mordenite into Group 3.

Erionite–The International Agency for Research on Cancer first listed erionite in Group 1 (the agent is carcinogenic to humans) in 1987, and the data for human and animal carcinogenicity are presently determined to be sufficient. When evaluating the International Agency for Research on Cancer classification, it is important to consider several factors, as outlined above. Clearly erionite fulfills these criteria because it is probably relatively insoluble in physiological fluids, it is clearly biologically active, and it is fibrous.

Epidemiological data suggest that exposure to erionite-bearing dusts increases the risk of mesothelioma (a rare, asbestos-related cancer) in humans, even at much lower exposure levels than required for any of the common asbestos minerals. Early epidemiological studies in the Cappadocian region of Turkey revealed outbreaks of "asbestos-related" respiratory diseases, including mesothelioma (Ross et al. 1993). Mumpton (1979) showed that, although erionite is found in the villages where mesothelioma occurs, erionite is also found in a Turkish village (Sarihidir) that (at the time) had no reported cases of mesothelioma. This report caused many to doubt the association between erionite and mesothelioma. However, Baris et al. (1987) re-examined the population of Sarihidir and found several cases of mesothelioma, although the incidence they found in Sarihidir (compared with incidences found in other villages) did not correlate with the current ambient levels of erionite (see Guthrie 1992 for a more detailed discussion). Several factors influence the incidences of diseases like mesothelioma, including genetic factors, which may vary between villages, so one would not necessarily expect a straightforward relationship between current fiber levels and disease. Nevertheless, it is now universally accepted in the health-effects-of-minerals community that erionite causes mesothelioma and that erionite is a much more potent carcinogen than any other mineral yet investigated, including the worst type of asbestos.

The most disturbing implication of the observations in Turkey is that erionite is capable of inducing mesothelioma in humans at low exposures. Baris et al. (1987) reported total fiber levels in the villages from 0.004 to 0.175 fibers/mL, and these measurements included other dusts in addition to zeolite. Simonato et al. (1989) reported newer estimates of fiber levels in Karain and Sarihidir (two of the affected villages) and found levels to be 0.002 to 0.010 fibers/mL (~80 percent zeolite) and 0.001 to 0.029 fibers/mL (~60 percent zeolite), respectively. The current regulatory standard for occupational asbestos exposure in the United States is <0.1 fiber/mL. In other words, the above studies suggest that erionite can induce mesotheliomas at fiber levels 1 to 2 orders of magnitude lower than the United States regulatory limits for occupational exposure to asbestos. The estimated rate per year (I) of a given cancer

per one million people has been modeled empirically using the formula $I = (K)(\text{exposure})(\text{time})^n$ (Health Effects Institute-Asbestos Research 1991), where K is a constant related to the mineral, exposure is the fiber level, time is in years, and n is a factor relating to the exposure model (usually 3 to 4) (Peto et al. 1982). Using a K value of 2×10^{-8} (average of three values for asbestos; Health Effects Institute-Asbestos Research 1991), an n value of 4 (conservative), and the fiber levels (exposures) reported by Ross et al (1993) corrected to 100 percent zeolite, the mesothelioma rates in Table 6.4-3 are obtained. This simplified but conservative exposure model for the rate of mesothelioma in these Turkish villages strongly suggests that erionite is at least comparable in toxicity to asbestos. This result is consistent with other attempts to assess the relationship between mesothelioma and exposure to erionite (for example, Simonato et al. 1989).

In-vivo experiments have further demonstrated the high biological activity of erionite-bearing dusts (see review by Davis, J.M.G. 1993). For example, Wagner et al. (1985) induced mesotheliomas in 100 percent (40 out of 40) of the rats they exposed to Oregon erionite, with a mean survival time of 390 days. For comparison, in the same experiment, they induced mesotheliomas in 47.5 percent (19 in 40) of the rats exposed to chrysotile (a type of asbestos), with a mean survival time of 678 days. With respect to erionite, they stated "No other dusts we have investigated have produced this high incidence of tumors particularly following inhalation." Suzuki and Kohyama (1988) studied the carcinogenic and fibrogenic effects of erionite, mordenite, and synthetic zeolite 4A. Their results show that erionite produced malignant tumors at a high rate after considerable latency and suggest that long-term persistence of the fibrous erionites in the mesothelial tissue is important in the development of mesothelioma. In light of the epidemiological and in-vivo studies, exposure to airborne erionite in Yucca Mountain operations should be minimized and eliminated if possible, and samples in zones of concern should be analyzed for erionite, ensuring that detection limits are as low as reasonably achievable.

Mordenite–No epidemiological studies have been published on the effects of human exposure to mordenite. However, several experimental studies have investigated the biological activities of this mineral. In general, these studies concluded that mordenite is much less biologically active than erionite. In-vivo experiments by Suzuki and Kohyama (Suzuki 1982; Suzuki and Kohyama 1984, 1988) suggest that a mordenite-bearing dust is fibrogenic but noncarcinogenic following intraperitoneal injection in mice. (In the same experiments, Suzuki and Kohyama found erionite to be both fibrogenic and carcinogenic.) However, they described the mordenite sample as consisting of both granular and fibrous morphologies, implying that their sample contains more than one mineral species. Indeed, quantitative X-ray diffraction of this mordenite-bearing sample has shown that it contains ~63.5 percent impurities, including clinoptilolite, feldspar, opal–CT, and gypsum (Guthrie 1993). Hence, the biological data published by Suzuki and Kohyama apply to an impure mordenite sample.

In-vitro experiments by two groups suggest that mordenite-bearing dust is relatively inactive in a variety of assays (Hansen and Mossman 1987; Mossman et al. 1989). However, the mordenite sample used in these experiments is highly impure. Quantitative X-ray diffraction of this mordenite-bearing sample has shown that it contains ~50.5 percent impurities, including clinoptilolite, feldspar, and opal–CT (Guthrie 1993). Hence, the biological data on the in-vitro activity of mordenite apply to an impure mordenite sample.

No published studies have concluded mordenite to be carcinogenic, although some studies have shown it to be fibrogenic and mildly biologically active. Nevertheless, because the two mordenite samples that account for all published biological data are highly impure, the biological activity and carcinogenic potential of pure samples of mordenite remain unreported. In light of the extreme biological activity of erionite, the fibrous nature of mordenite, and the uncertainties associated with pure mordenite's biological activity, it appears that:

- The biological activity of mordenite warrants more investigation, particularly using pure samples of mordenite.

- The potential cancer risk associated with mordenite exposure at Yucca Mountain is indeterminate.

These inferences are consistent with the International Agency for Research on Cancer's (IARC 1997) recent classification of mordenite in Group 3. However, although mordenite at Yucca Mountain has a fibrous habit (Figure 6.4-1), limited scanning electron microscope examination of air filters obtained during the cutting of mordenite-rich Yucca Mountain Tuff revealed no fibrous material (Figure 6.4-2), despite the presence of mordenite on the filters (as determined by X-ray diffraction analysis). This result suggests that the mordenite in the tuff at Yucca Mountain might be released in nonfibrous aggregates during cutting (and, possibly, drilling and boring), which would minimize any risk posed by mordenite exposure at Yucca Mountain.

Clinoptilolite and Heulandite–No epidemiological studies have been published on the effects of human exposure to clinoptilolite or heulandite. Limited data have been published on the experimental investigation of the biological activities of these minerals (for example, Guthrie, McLeod et al. 1992), and no in-vivo data have been published in the western literature. Several Russian articles reported data on clinoptilolite, but no published studies have concluded clinoptilolite or heulandite to be carcinogenic. However, the biological data suggest that clinoptilolite is much less biologically active than erionite on a mass or particle basis, although it may be as cytotoxic as erionite on a surface-area basis (Guthrie, McLeod et al. 1992). Nevertheless, these minerals have nonfibrous morphologies. In agreement with earlier assessments of clinoptilolite/heulandite, the International Agency for Research on Cancer (IARC 1997) recently classified these minerals as Group 3. It appears that the potential cancer risk associated with clinoptilolite and heulandite exposure at Yucca Mountain is indeterminate but probably low (due to their particle morphology).

Phillipsite–No epidemiological studies have been published on the effects of human exposure to phillipsite, and no experimental data have been published in the western literature on its biological activity. The particle morphology of phillipsite is generally nonfibrous, and the abundance of this mineral at Yucca Mountain is low (only two known occurrences, thus far). The International Agency for Research on Cancer (IARC 1997) recently classified phillipsite as Group 3, and the conclusion is that the potential cancer risk associated with phillipsite exposure at Yucca Mountain is indeterminate but probably low (due to its particle morphology and low abundance).

6.4.1.2.3 Other Silicates

Palygorskite and Sepiolite–Epidemiological data suggest that exposure to palygorskite-bearing dusts may increase the risk of lung cancer among some ethnic groups. Waxweiler et al. (1988) studied a cohort of 2,302 miners and millers from a United States "attapulgite" company and reported slight excesses of lung cancers for whites only. Other epidemiological studies have confirmed the little-to-no risk associated with exposure to palygorskite, particularly for those with, at most, moderate exposures for short terms (see review by Ross et al. 1993). In-vivo experiments have suggested that palygorskite-bearing dusts are mildly active in the lung, though some samples can be very active. For example, Wagner (1982) observed mesothelioma rates of 12.5 to 25 percent for palygorskite in rats compared with a rate of 22.5 percent for chrysotile asbestos, and Pott, Bellman et al. (1990) and Pott, Huth et al. (1974) found that palygorskite is carcinogenic at rates from 3.5 to 40 percent following intrapleural injection in rats. In contrast, Jaurand et al. (1987) found that palygorskite is nontumorigenic in rats, whereas in the same experiments, chrysotile asbestos induces tumors at a rate of 19 to 52 percent, depending on particle size. In other words, the biological activity of palygorskite (as determined by in-vivo techniques) appears to vary between samples. In general, however, most studies report much lower activities for palygorskite than for asbestos. Although palygorskite appears to be carcinogenic under some conditions in vivo, the epidemiological data suggest that the risk of lung cancer is still relatively low, even following exposure to quantities larger than expected at Yucca Mountain. In light of the variation between different types of palygorskite, International Agency for Research on Cancer (IARC 1997) listed long-fiber (>5 μm) palygorskite as Group 2B and short-fiber (<5 μm) palygorskite as Group 3. Sepiolite is listed as Group 3 (IARC 1997). In general, the conclusion is that the potential cancer risk associated with palygorskite and sepiolite exposure at Yucca Mountain is probably low. Nevertheless, due to the limited amount of biological data available on the biological activity of these two minerals, exposure to airborne palygorskite and/or sepiolite dust should probably be minimized.

Smectite and Mica–Smectite and mica are common minerals at the earth's surface, occurring in many soil and rock types. Most published studies on the biological activities of 2:1 layer silicates (including smectite and micas) suggest that these minerals can be extremely active at the cellular level. In addition, in-vivo experiments suggest that these minerals are fibrogenic but noncarcinogenic (for example, Pott, Bellman et al. 1990; Pott, Huth et al. 1974; Rosmanith et al. 1990; Schyma 1990). Epidemiological studies confirm this; however, the epidemiological studies also suggest that exposures resulting from modern mining conditions may not pose a significant risk. These minerals have tabular morphologies, so they may be cleared more rapidly from the lung than fibrous minerals. Hence the following conclusions:

- An evaluation of the published smectite/mica data using the approach followed by the International Agency for Research on Cancer would result in a classification of these minerals in Group 3 (due to the relatively limited epidemiological and in-vivo data).

- The potential cancer risk associated with exposure to these minerals is indeterminate but probably low (due to their particle morphologies and the lack of evidence showing carcinogenicity in animals).

These evaluations for smectite and mica are consistent with the International Agency for Research on Cancer's evaluation for talc (another 2:1 layer silicate).

Kaolinite–Although this mineral may be cleared rapidly from the lung (and, hence, is not pathogenic in humans), its in-vivo and in-vitro activities may provide clues to the mechanisms of mineral-induced pathogenesis. Epidemiological studies suggest that kaolinite is fibrogenic only under extraordinary conditions—that is, high dust conditions or exposure combined with another respiratory disease, such as tuberculosis (for example, Kennedy et al. 1983; Oldham 1983; Sepulveda et al. 1983). In-vivo experiments reported thus far on the fibrogenic potential of kaolinite are inconclusive (see Guthrie 1992 for reviews). Most recent in-vivo studies of the pulmonary effects of kaolinite suggest that kaolinite is not carcinogenic (for example, Mossman and Craighead 1982; Wagner 1990), although it may be mildly fibrogenic (Wastiaux and Daniel 1990). Finally, in-vitro experiments suggest that kaolinite can be highly active at the cellular level (for example, Low et al. 1980; Dubes and Mack 1988). The apparent discrepancy between the in-vivo and in-vitro data probably reflects kaolinite's nonfibrous morphology (that is, kaolinite's tabular morphology may facilitate its clearance from the lung and prevent it from being highly pathogenic in humans). Hence, it is concluded that an evaluation of the published data using the approach followed by International Agency for Research on Cancer would result in a classification of kaolinite in Group 3. Indeed, the International Agency for Research on Cancer has not even listed kaolinite, despite kaolinite's widespread use in industrial settings. Furthermore, it is concluded that the potential cancer risk associated with exposure to kaolinite is probably low.

Feldspar–Feldspar is the most common group of minerals at the earth's surface, and the most abundant mineral group in nonzeolitized Yucca Mountain Tuffs. Limited data on the biological activities of feldspars (for example, Marks and Nagelschmidt 1959; Pott and Friedrichs 1972) suggest that minerals of this group are mildly active, at most. No published studies suggest that feldspars are carcinogenic in either humans or animals. If exposure to feldspars represented a major carcinogenic risk, an epidemiological link would likely have already been recognized, considering the widespread distribution of feldspar. The morphology of feldspar is nonfibrous. The conclusion is that:

- An evaluation of the published feldspar data using the approach followed by the International Agency for Research on Cancer would result in a classification of this mineral group in Group 3 (due to the paucity of biological data).

- The potential cancer risk associated with feldspar exposure at Yucca Mountain is indeterminate but probably low (due to its particle morphology and its apparent biological inertness).

6.4.1.2.4 Other Minerals

Calcite–The paucity of published data on the biological activity of calcite makes an evaluation of its carcinogenic potential impossible. However, no published studies have suggested that calcite is carcinogenic in either humans or animals. If exposure to calcite represented a major carcinogenic risk, an epidemiological link would likely have already been recognized,

considering calcite's widespread distribution the earth's surface. The morphology of calcite is generally nonfibrous. The conclusion is that:

- An evaluation of carcinogenic risk due to calcite using the approach followed by the International Agency for Research on Cancer would result in a classification of this mineral group in Group 3 (due to the paucity of biological data).

- The potential cancer risk associated with calcite exposure at Yucca Mountain is indeterminate, but is probably low (due to its particle morphology and its apparent biological inertness).

Mn Oxides–Most studies of oxide-bearing dusts suggest that some samples can produce fibrosis in vivo but are relatively inactive minerals (for example, hematite, Group 3). Exceptions may include oxides containing Cr (not necessarily mineral samples). The International Agency for Research on Cancer does not list Mn oxides, nor does it list any Mn compounds. The paucity of published data on the biological activity of the Mn oxides makes an evaluation of their carcinogenic potential impossible. The abundance of these minerals at Yucca Mountain is so low that even if they were carcinogenic, their occurrence would probably present only a low risk, at most. We conclude that:

- An evaluation of carcinogenic risk due to Mn oxides, using the approach followed by the International Agency for Research on Cancer, would result in a classification of this mineral group in Group 3 (due to the paucity of biological data).

- The potential cancer risk associated with exposure to Mn oxides at Yucca Mountain is indeterminate but probably low (due to their low abundance).

6.4.2 Survey of Potential Mineral Health Hazards at Yucca Mountain

The potential hazards of a particular airborne phase hinge directly on its distribution in the rocks at Yucca Mountain, that is, whether or not it is present and, if present, what its abundances are. Thus, it is important to outline how rocks are analyzed for their mineral content, how both qualitative and quantitative analyses are performed, what the detection limits are for a particular phase, and how precision and accuracy are determined. Many surface, Exploratory Studies Facility, and drill-core samples have been analyzed using the techniques outlined below, and the results are usually quantitative. Because of the limitations inherent in sampling fractures, their mineralogy is necessarily qualitative and we report here only the presence or absence of a given mineral in a fracture. These limitations include:

- Field and laboratory sampling of fracture minerals is limited and sporadic (for example, most information is obtained from limited amounts of drill core).

- Vertical sampling of vertical fractures provides a poor statistical estimation of fracture characteristics.

- The total amount of material along a fracture is extremely small compared with the matrix.

- Coverage of fracture surfaces by minerals is sporadic.

Consequently, quantitative estimates of a mineral's abundance in a fracture would be meaningless.

The natural eolian input is a critical piece of information if we are to determine the effect that operations at Yucca Mountain have on the airborne dust budget. The YMP has used dusts that accumulate in natural dust traps (which include boulder deposits and vertical fractures in rock outcrops) as a measure of such natural eolian input. Natural dust traps should receive a dominant input from aeolian processes, a negligible contribution from sediment transported by water, and a negligible direct contribution from alteration products of the bedrock. Using these criteria, two types of sampling locations were chosen:

- Under boulders in boulder fields, and only those boulders that were well above soil were used

- In vertical fractures within large boulders that were well above the ground level

At each site, the overlying boulder was removed, and the aeolian-derived sediment was collected by scooping or brushing the dust into a bag. We selected Only natural dust traps located sufficiently above the surface to exclude material transported by fluvial processes, were selected. Particles transported by surface saltation, however, would be included in these traps. These dusts were also compared with vesicular A-horizons of soils at Yucca Mountain. The material in the vesicular A-horizon is mostly of eolian origin, although some local reworking of detritus may occur prior to incorporation in the A-horizon. The sampling area includes ~1,400 km^2 in the vicinity of Yucca Mountain. Dusts were size separated by dry sieving and analyzed as described below. A sample was also taken from the cyclone attached to the UZ-16 drilling rig, which should be representative of the dusts generated by drilling operations at the time of sample collection. Samples were collected on February 11, 1993, and the drill was reported at 441.7 m depth the previous day.

6.4.2.1 Methods of Analysis

6.4.2.1.1 X-ray Diffraction Analyses

X-ray data for Yucca Mountain whole-rock and core samples are discussed in Subsection 6.1.3 and were obtained using the methods described there. In the examination of rocks for the presence of erionite, more than 200 samples were analyzed from more than 20 drillholes and the Exploratory Studies Facility at the Yucca Mountain site over the course of these studies. Samples were chosen from stratigraphic levels most likely to contain erionite, and welded, devitrified tuffs were generally not analyzed. Present-day drilling is accompanied by immediate X-ray diffraction analysis of samples from suspect erionite-bearing zones (for example, WT-24). All of these samples were also prepared as described in Subsection 6.1.3, and X-ray powder diffraction mounts were prepared either as powders pressed into a cavity in a glass or metal plate

or as water-smears on an off-axis-cut (zero-background) quartz plate. The water-smear mounts yielded greater preferred orientation than the cavity mounts, and because of transparency effects, these mounts were used only for detection and not for quantification. Smectite-bearing samples were glycolated to shift any smectite peaks to lower 2θ values, thus reducing overlap of the smectite 001 reflection on the erionite 100 reflection. The glycolated mounts were X-rayed in an ethylene-glycol-saturated atmosphere using an enclosed sample cell fitted with X-ray-transparent windows. Data were obtained and analyzed as described in Subsection 6.1, *Background Methods*.

6.4.2.1.2 Microchemical and Chemical Analyses

Scanning electron microscope images and energy-dispersive spectra were obtained using a Tracor ADEM scanning electron microscope. Images were collected using both backscattered electrons and secondary-electron imaging, using accelerating voltages between 19 and 20 keV. Images were collected from both sample chips and thin sections; energy-dispersive spectra line scans for signal and epoxy background were collected only from thin sections. A Cameca SX-50 electron microprobe was used to analyze zeolites in thin section. A defocused, rastered beam with an accelerating potential of 10 keV and a beam current of 9 nA was used.

Chemical data on vitrophyre, smectite, and erionite-bearing samples from USW UZ-14 were obtained through instrumental neutron activation analysis. Samples were analyzed at the trace-element geochemistry laboratory of Washington University, St. Louis, Missouri, using methods described in Korotev (1991).

6.4.2.1.3 Thermodynamic Modeling

As emphasized in Subsection 6.4.1, the YMP has used thermodynamic modeling in an attempt to predict the factors that control the distribution of zeolites at Yucca Mountain. In particular, a search was made for a unique set of geochemical conditions that would give rise to the formation of erionite, and thermodynamic modeling was performed to provide insight into such conditions. The thermodynamic calculations presented in this study used estimated zeolite thermodynamic data as outlined in Chipera, Bish, and Carlos (1995). The primary reason for using estimated thermodynamic data, even though data have been measured for many natural zeolites, is that the chemistry of zeolites is highly variable. Thermodynamic properties measured for a zeolite in one sample may not be representative of the thermodynamic properties of the same zeolite in another sample. For example, analcime at Yucca Mountain is more Si rich (Si:Al ratios of 2.4 to 2.8) than the analcimes used for calorimetric studies (Johnson, Flotow et al. 1982; Si:Al = 2.15). Recent solubility measurements on a stoichiometric analcime and a Si-rich sedimentary analcime yielded standard free energies of formation at 25°C of -3090 ± 5 and -3036 ± 5 kJ/mol, respectively (Wilkin and Barnes 1995). Likewise, Si:Al ratios for clinoptilolite show considerable variation at Yucca Mountain, ranging from 4 to 5. Clinoptilolite has the added complexity that the exchangeable cation composition can vary considerably, and compositions close to the Na, Ca, or K end members and all combinations in between are possible.

Various empirical routines have been formulated for estimating thermodynamic data for minerals. The more recent methods, however, represent mineral phases as a set of elemental building blocks composed of unique polyhedra (Robinson, Jr., G.R. and Hass 1983; Berman and

Brown 1985; Hazen 1985; Chermak and Rimstidt 1989; Holland, T.J.B. 1989). By adding the contributions from each polyhedron, the thermodynamic properties can be estimated for the complete mineral unit. In the present studies, thermodynamic data for the zeolites were estimated using the methods proposed by Berman and Brown (1985) for heat capacity, Chermak and Rimstidt (1989) for Gibbs free energies and enthalpies of formation at 298 K, and T.J.B. Holland (1989) for entropy. Holland's method to estimate entropy from individual polyhedra further improves on previous methods in that it also considers phase volumes. This improvement is important because entropy depends not only on the individual polyhedra composing the phase but, also, on how tightly the polyhedra are assembled. Because Holland proposed only two choices for entropy contributions of water in the polyhedrally derived structure (20.74 kJ/mol·K for structurally bonded and 30.03 kJ/mol·K for "loosely bonded" water), a value for "zeolitic" water was determined for use in the present calculations (in this treatment, "zeolitic" water is more weakly bonded than "loosely bonded" water). An average value of 59.1 kJ/mol·K for zeolitic water was determined by comparing calculated entropies of anhydrous forms of analcime, heulandite, mordenite, phillipsite, clinoptilolite, and stilbite (phases representative of those at Yucca Mountain) with the measured hydrous entropy values for these phases (Johnson, Flotow et al. 1982, 1985; Johnson, Tasker et al. 1992; Hemingway and Robie 1984; Howell et al. 1990) and then determining the average difference on a per-mole-of-water basis. This value (59.1 J/mol·K) compares well with values measured by others for zeolitic water (55.0 J/mol·K for analcime, Johnson, Flotow et al. 1982; 57.0 J/mol·K for clinoptilolite, Hemingway and Robie 1984; 54.05 J/mol·K for mordenite, Johnson, J.W., Oelkers et al. 1991; and 52.0 J/mol·K for Ca-clinoptilolite, Carey and Bish 1996).

Thermodynamic data for zeolites that occur at Yucca Mountain, calculated using representative chemical formulae, are given in Carey, Bish, Chipera (1996). Actual chemical analyses of Yucca Mountain zeolites were used whenever possible and were normalized to form balanced structural formulae when the individual atom abundances were rounded to the first decimal place. Inasmuch as zeolites at Yucca Mountain range widely in chemical composition, some constraints on chemical formulae were imposed. Broxton, Bish, Warren (1987) showed that clinoptilolite/heulandites in diagenetic Zone I have uniform Ca-rich compositions (60 to 90 mole% Ca) and Si:Al ratios mainly between 4.0 and 4.6. Diagenetic zone-II clinoptilolites, however, show considerably more variability. Clinoptilolites in the eastern part of Yucca Mountain are calcic-potassic, becoming more calcic with depth, whereas clinoptilolites in the western part of Yucca Mountain are sodic-potassic, becoming more sodic with depth. The Si:Al ratios of the diagenetic zone-II clinoptilolites are generally between 4.4 and 5.0. Chemical constraints were formulated for mordenite from coexisting mordenite-clinoptilolite assemblages, which show that mordenite contains more Na and K and less Ca than clinoptilolite (Caporuscio et al. 1982; Carlos 1987). In contrast to clinoptilolite, analcime at Yucca Mountain has a more uniform chemical composition consisting of an almost pure Na end member with Si:Al ratios between 2.4 and 2.8, considerably different from stoichiometric end-member analcime (2.0). Obtaining a representative analysis for erionite proved to be somewhat more difficult and is discussed in the results subsection. In addition to exchangeable and tetrahedral cation compositional variability, zeolites exhibit wide variations in water content, readily responding to changes in environmental conditions such as temperature and humidity. For the present calculations, all zeolites were assumed to be in a fully hydrated state as would be expected of a zeolite below the water table or above the water table at 100 percent relative humidity.

Thermodynamic calculations in this study were conducted using the Ge0-Calc PTA-System software (Brown, T.H., Berman et al. 1989). Thermodynamic data for quartz, cristobalite, and tridymite were obtained from the B88.MIN (Berman 1988) thermodynamic database supplied with the Ge0-Calc software package. Thermodynamic data for amorphous silica were obtained from the SUPCRT92 database (Johnson, J.W., Oelkers et al. 1991). Values for aqueous species (aqueous SiO_2, Ca^{2+}, Na^{+}, K^{+}, H^{+}) were taken from the HKF81.AQU database (Helgeson et al. 1981) also supplied with the Ge0-Calc software. To simplify the calculations, the chemical system was constrained to the system Na-K-Ca-Al-Si-O-H. Because thermodynamic data were calculated specifically for each solid phase and included any variability in exchangeable cation and Si:Al ratios, the activities of both clinoptilolite and analcime were assumed to be 1. The calculations were conducted projecting from water (activity = 1), and any reaction or product cations were exchanged with the liquid phase.

In the present calculations, cation concentrations in the fluid phase were assumed to approximate the current concentrations measured in Yucca Mountain groundwater (Kerrisk 1987), although as discussed below, present-day water compositions are probably not representative of water compositions existing during zeolite formation. Pressure was constrained such that all calculations were conducted on the liquid side of the water liquid-vapor curve. pH values used for the calculations were constrained to approximately 7.6, a value that is representative of present-day waters at Yucca Mountain (Kerrisk 1987). This constraint does not affect the results significantly because H^{+} is involved only peripherally in these reactions. For the calculations in this study, only zeolites known to exist at Yucca Mountain were used. Although other mineral phases may be in true equilibrium with respect to zeolites, zeolites often form metastably due to kinetic limitations on the formation of more stable species (Moncure et al. 1981). Consequently, phases that may potentially be more stable under the given conditions (for example, feldspars, mica, etc.) were not included in the calculations.

6.4.2.2 Mineral Distributions at Yucca Mountain

Quantitative whole-rock and fracture mineral analyses are discussed in Subsection 6.1.3, including the distribution of those phases identified above as potentially important. In addition, the occurrence of potentially important phases in bulk-rock samples and in fractures is indicated on the figures in Subsection 6.1.3. These figures illustrate the mineralogy as a function of depth in each drillhole for which there is sufficient data. It is important to note, however, that analysis of fracture-filling minerals was limited by the availability of appropriate samples. The absence of a particular mineral as a fracture filling is, therefore, not necessarily diagnostic. The following subsection presents details of the distributions for those phases that have been identified as potentially important based on the biological data discussed above.

6.4.2.2.1 Silica

Crystalline Silica–Three crystalline silica polymorphs, quartz, cristobalite, and tridymite, are abundant in the rocks at Yucca Mountain. Tridymite is common only in relatively shallow rocks, often associated with devitrification features and always above the static water level. It is absent in the north end of Yucca Mountain, where mineralogical evidence suggests that a high heat flow existed in the past (Bish and Aronson 1993). There appears to be a correlation between the loss of tridymite and the first appearance of abundant groundmass quartz with

increasing depth. This transition in part reflects the passage from zones of common high-temperature vapor-phase crystallization (tridymite) to zones of lower-temperature devitrification (quartz) within the Topopah Spring Member. Tridymite occurs in many fracture samples above the static water level (Carlos 1985). In samples in which cristobalite was distinguished from opal-CT, cristobalite is present in virtually every shallow sample examined above 400-m depth but it is very restricted in rocks below the static water level. Because of overlap of the major cristobalite peak with significant feldspar peaks in X-ray diffraction patterns, the precision of analysis of cristobalite when present in amounts below 10 percent is poor. Thus, the deeper samples identified as containing small amounts of cristobalite may in fact contain no cristobalite. The presence of cristobalite at shallow depths probably reflects the unsaturated nature of these rocks over much, if not all, of their history. Ernst and Calvert (1969) showed that an aqueous fluid is necessary for rapid recrystallization of cristobalite to quartz, and the recrystallization is accelerated in alkaline solutions. They concluded that conversion of the Monterey Formation porcellanite (cristobalite) to quartz in relatively pure water at 50°C would take between 4 and 5 m.y. Cristobalite occurs in most fracture samples above the static water level (Carlos 1985).

With depth, cristobalite gives way to opal-CT in zeolitized rocks in several drillholes. Quartz is present in most samples examined at Yucca Mountain, but it is typically less abundant at shallow depths and in glass-, clinoptilolite-, and mordenite-containing samples. It generally increases in abundance below the depth where clinoptilolite and mordenite disappear (that is, where cristobalite and opal-CT are no longer important silica phases). Quartz is nearly ubiquitous in fracture samples above the static water level (Carlos 1985).

Opal-CT–Early analyses of Yucca Mountain Tuffs did not distinguish opal-CT from cristobalite, but our most recent analyses include separate determinations of opal-CT, a disordered silica phase containing both cristobalite- and tridymite-like structural units (Jones and Segnit 1971). Almost without exception, opal-CT occurs in samples containing clinoptilolite and/or mordenite. Thus, the presence of opal-CT may be linked genetically to the formation of these two zeolites. Most of the opal-CT samples exhibit evidence for cristobalite- and tridymite-like stacking, but some more closely resemble opal-C (predominantly cristobalite-like stacking). As noted above, opal-CT was grouped with the crystalline silica polymorphs because most samples analyzed from Yucca Mountain show evidence for some 3-D order.

6.4.2.2.2 Zeolites

Erionite–As reported by Bish and Vaniman (1985), none of the earliest reports of erionite in Yucca Mountain rocks has been verified. However, Bish and Vaniman reported that one sample of erionite was conclusively identified in a fracture from UE-25 a#1 at 1,296 feet (395 m). Analyses since that time have expanded the known occurrences of erionite to samples from the altered zone immediately above the Topopah Spring Tuff lower vitrophyre, in the moderately welded subzone underlying the lower vitrophyre, or in the upper PTn just below the Tpcplnc/Tpcpv2 boundary in the lower Tiva Canyon Tuff. The altered zone immediately above the Topopah Spring Tuff lower vitrophyre contains a variety of zeolites that are either rare or absent in other Yucca Mountain Tuffs. It appears that erionite is restricted in this zone to fractures and must have formed under unusual and very localized conditions in this altered zone.

Drill cores analyzed by quantitative X-ray powder diffraction for erionite are graphically depicted in Figure 6.4-3, showing the stratigraphic distribution of erionite in these drillholes relative to the potential repository horizon and the static water level. The areal distribution of erionite in drillholes is also depicted in Figure 6.4-4. These data show clearly that when erionite exists in the potential repository horizon, it occurs either in the altered zone immediately above the Topopah Spring Tuff lower vitrophyre or in the moderately welded subzone underlying the lower vitrophyre. It has also recently been identified in the upper PTn, just below the Tpcplnc/Tpcpv2 boundary in the lower Tiva Canyon Tuff. Samples from suspect zones in drillhole USW WT-24 were recently also analyzed, and no erionite was detected in any samples.

Figure 6.4-5 and Table 6.4-4 show the distribution of erionite determined by X-ray powder diffraction in samples from drillhole USW UZ-14. Erionite occurs in significant abundances (up to 34 w%) over a limited depth range of approximately 2.3 m (7.6 feet), from 415.9 to 418.2 m depth (1,364.4 to 1,372.0 feet), in the moderately welded subzone beneath the Topopah Spring Tuff lower vitrophyre and above the Calico Hills Formation. Because of its thickness and high erionite content, this zone poses a significant risk. The limited amount of data in this zone show that erionite abundance is greatest at the top of the zone, decreasing significantly toward the bottom of the zone. Whether this distribution has a genetic implication is unknown, although the greater abundance at the top of the zone may be related to the proximity to the glassy vitrophyre. Visual examination of this interval indicates that it begins at the bottom of the densely welded basal vitrophyre (about 415.1 m, 1,362 feet depth, just above the first X-ray powder diffraction sample) and is most prominently developed in the moderately welded basal vitrophyre, dying out in the nonwelded vitric tuffs (about 418.5 m, 1,373 feet depth) at the base of the Topopah Spring Tuff. Beneath this, a more typical vitric-to-clinoptilolite transition occurs in the interval from 422.8 to 426.1 m (1,387 to 1,398 feet). The surprising upside-down "erionite-to-vitric" transition at the bottom of the Topopah Spring Tuff is unusual and will require further study for complete understanding. Textural relations in the USW UZ-14 samples suggest that erionite formed after clinoptilolite. Comparable alteration, producing large amounts of erionite, has not been observed in any other drill core. However, it is important to note that the restricted sampling intervals used in the past on the YMP, with samples often taken at 15 m (50 feet) intervals, do not allow the project to conclude that erionite does not occur in earlier sampled drillholes.

The instrumental neutron activation analysis data for erionite-bearing samples from USW UZ-14 can be compared with data for the unaltered vitrophyre to determine the geochemical environment and the extent of chemical exchange involved in zeolitization. The alkali and alkaline-earth elements have proven particularly useful in estimating the amount of exchange involved in zeolitization. Table 6.4-5 summarizes these data for the vitrophyre, for a smectite concentrate, and for the erionite-rich tuff beneath the vitrophyre. The smectite sample is a relatively pure mineral separate from sample LANL#1876p1 (see Table 6.4-4). The mineral compositions of the vitrophyre sample (LANL#1714p1, 88 percent glass) and of the erionite-rich sample (LANL#1715p1, 34 percent erionite) are listed in Table 6.4-4.

If one assumes that the vitrophyre is a good compositional analog to the vitric tuff that altered to create the smectite- and zeolite-rich samples, the data in Table 6.4-5 indicate strong depletions of Na and moderate depletions of K in zeolites (erionite/heulandite) resulting from alteration of glass, with associated strong Ca enrichment. Changes in Rb, Cs, and Ba are minor, but both the smectite and the zeolitic tuff are enriched in Sr. Although volume corrections for alteration will

affect these trends somewhat, these corrections are minor compared with the amount of change seen in Na, K, Ca, and Sr. Particularly notable in the chondrite-normalized lanthanide-element patterns for these three samples is the absence of a Ce anomaly in the vitrophyre sample, the positive Ce anomaly in the erionite-rich sample, and the negative Ce anomaly in the smectite sample. Cerium separates from the other lanthanide elements only under oxidizing conditions, in which Ce is in the +4 oxidation state and the other lanthanides are +3. These data are used in Subsection 6.4.2.2.6 to infer the presence of both closed-system and open-system behavior.

Mordenite–Several studies have emphasized the occurrence of at least four distinct zones of clinoptilolite plus mordenite beneath Yucca Mountain (Bish, Ogard et al. 1984; Vaniman, Bish, Broxton et al. 1984). These zones occur primarily where glassy material remained outside the zones of devitrification in the centers of ashflows. There is thus a correlation between zeolitized material and the nonwelded tops, bottoms, and distal edges of ashflows. Exceptions to this correlation occur, including the zeolitized interval at the boundary between the devitrified zone and the vitrophyre of the Topopah Spring Member. In general, however, the thicker zeolitized horizons tend to correlate with those intervals that retained glass following early tuff devitrification.

Because the significant zeolitized horizons at Yucca Mountain occur near or below the static water level, there are few matrix (bulk-rock) occurrences of mordenite above the static water level. However, mordenite occurs with or without clinoptilolite as a common fracture-filling mineral between the static water level and the surface.

6.4.2.2.3 Other Silicates

Palygorskite–The distribution of palygorskite was not described by Bish and Chipera (1989). However, this fibrous mineral has since been identified in numerous fractures above the static water level, but it has not been identified as matrix mineral. This mineral is a major constituent of fracture fillings shallower than ~80 feet depth in USW G4 and shallower than ~830 feet depth in USW GU3, and it occurs at depths between 700 and 1,691 feet in USW VH1 and between 1,972 and 3,384 feet on USW VH2 in Crater Flat. It is not a common phase on or adjacent to Yucca Mountain but could be of concern in fractures.

6.4.2.2.4 Mineral Occurrences in the Exploratory Studies Facility

Rock and dust samples from the Exploratory Studies Facility have been analyzed in an effort to understand dust compositions and exposures. In addition, some mineralogical studies were done in association with other project investigations. All Exploratory Studies Facility samples were analyzed at Los Alamos by the methods outlined above. Silica polymorph and feldspar mineralogy in whole-rock samples was compared with that in the dust collected from a wall placard in the Exploratory Studies Facility. As might have been expected, the crystalline silica abundances in the dust were within the same range as within the bulk rock as evidenced by the ratios of the crystalline silica polymorphs to feldspar. The dust contains additional phases probably introduced during the mining operations (for example, material wearing from the conveyor belts, exhaust). These results suggest that the elevated crystalline silica concentrations observed on February 21 and 22 in the Exploratory Studies Facility, and those observed in the thermal test alcove, were not due to unusual wall-rock mineralogy, that is, they should have been

expected based on knowledge of the wall-rock mineralogy. Studies of the host-rock mineralogy indicate that it is remarkably constant, particularly the ratio of total crystalline silica polymorphs to total feldspar (the major crystalline phases in the host rock). The primary difference observed in crystalline silica mineralogy of fracture samples was an increase in tridymite and a decrease in cristobalite relative to wall-rock mineralogy. Thus, fracture-coating minerals need not be invoked to explain elevated airborne cristobalite and/or quartz concentrations in the Exploratory Studies Facility. Such elevated airborne crystalline silica concentrations should be expected from the host rock unless controls are in place to minimize dust.

Size fractionations were conducted on a dust smear (#2289) removed from the wall just behind the head of the tunnel-boring machine to determine if any mineral segregation occurs during the mining/grinding operation. From the resultant quantitative X-ray diffraction data, there does not appear to be any significant segregation/concentration of crystalline silica polymorphs in the finer fractions (although a slight increase in tridymite abundance may be possible). These results suggest that the dust generated during the mining operation does not deviate significantly in mineralogy from that of the bulk rock being mined. Thus a direct conclusion from this is that the YMP should be able to predict fairly accurately the concentrations of the mineral constituents in the dust phase simply by knowing the concentrations in the rock being mined. Another conclusion is that there are very large quantities of crystalline silica polymorphs being encountered by the tunnel-boring machine and potentially being released to the atmosphere.

Recently, a specific portion of a sample collected at station 75+20, right rib, in the Exploratory Studies Facility was found to contain about 1 w% erionite. The sample is from a breccia zone with secondary mineral deposition and alteration of the adjacent bedrock, located just below the Tpcplnc/Tpcpv2 boundary in the lower Tiva Canyon Tuff. After the initial discovery of erionite in the Exploratory Studies Facility, follow-up sampling and subsequent quantitative X-ray diffraction analyses were conducted to clarify the nature of this erionite occurrence. The results of quantitative X-ray powder diffraction analysis showed that erionite occurs at this location primarily outside of the breccia zone in the wall rock adjacent to the breccia and fracture zone. Samples spanning the breccia zone also contain erionite. Thus, it is apparent that erionite is not restricted to the breccia or fracture zone. The maximum amount of erionite in this location is about 1 wt%. Erionite was not found in breccia or in wall-rock samples above the Tpcpv2-Tpcplnc contact (it was found only in the Tpcpv2 unit), an interesting observation, but one that is based on only three samples. No further sampling for erionite was conducted in the Exploratory Studies Facility.

6.4.2.2.5 Eolian-Deposited Minerals Around Yucca Mountain

The similarity of mineral content for the various samples from around drillhole USW SD-9 indicates that the natural background contribution to the eolian dusts in the vicinity of Yucca Mountain appears to be relatively uniform over hundreds of km^2. The dusts are dominated by feldspar, quartz, and smectite, with a small but consistent contribution from several other minerals (particularly clinoptilolite). The same mineral content is present in the soil A-horizons at these locations. This uniformity in mineral content appears to be relatively unaffected by the lithology of the adjacent outcrops: for example, the 13.5 km sample is underlain by basalt (Red Cone), whereas the remaining samples were underlain by tuff. None of the dusts investigated

contained erionite, mordenite, or palygorskite at the detection limits (~0.05 to 0.5 wt% depending on the conditions of the X-ray powder diffraction runs).

The primary source of dust from drilling activity at USW SD-9 appears to be the release of material during the transfer of dusts from the cyclone to the disposal containers. The mineral content of this material varies, depending on the particular lithologies being drilled at the time. However, in general, the drilling dusts have a mineralogical signature that distinguishes them from the natural eolian dusts. For example, the dust from ~1,288 feet at drillhole USW SD-9 contains more cristobalite than the natural dusts, and the dust from ~1,449 feet at drillhole UE-25 UZ-16 contains more clinoptilolite and opal-CT. Hence, a significant input of drilling dusts to the local environment would likely be reflected in the mineral content of the eolian material. Some of this released material is sufficiently fine to be transported from the vicinity of the drill pad, but much is deposited in the local eolian-dust traps. Evaluation of post-drilling eolian dusts near UE-25 UZ-16 suggests that drilling activities do not significantly affect the mineral content of the trapped eolian dusts.

The Summary and Synthesis Report summarized the results of the quantitative X-ray powder diffraction analyses of each of the dust samples from around UZ-16. The mineral content of the background components of the dusts was evaluated from several samples, and only minor variation in the mineral content of each size fraction <425-μm was discovered. The weight percents of each mineral in the samples representing background contributions are identical within statistical error, suggesting a homogeneous source for background dusts over many kilometers. These results suggested that the dusts in the vicinity of UZ-16 have a mineral content consistent with the mineral content of the background dusts in the area. Furthermore, the analyses show that the mineral content of the dusts generated by drilling at UZ-16 could be significantly different from the background-dust mineral content. The composition of the UZ-16 dusts reflects the lithology being penetrated by the drill at any given time, so the results are not representative of all dusts generated by UZ-16 operations. Nevertheless, if significant amounts of dust were released to the local environment by operations at UZ-16, the mineral content of nearby dusts should be significantly different from background dusts. It is not surprising that the mineral content of dusts near UZ-16 were not significantly affected by drilling operations, because no dusts were visibly released during a visit to the site (February 11, 1993) despite the active drilling. In addition, the mineral content of the local dusts provides confirmation of the pristine nature of the local, background dusts. A small amount of mordenite (~1 wt%) was detected in cuttings from UZ-16, but similar analyses on dust samples revealed no mordenite. No palygorskite or erionite was observed in the X-ray powder diffraction patterns from any of the dusts.

The mineral content of the background dust is principally quartz, feldspar, and smectite/mica with minor amounts of clinoptilolite and several other minerals (including amphibole). Secondary-electron images of these samples revealed several elongate and/or fibrous particles. Energy-dispersive spectra analysis showed that the most common composition for fibrous particles in these samples was probably SiO_2 (only Si in spectrum; detector is insensitive to elements lighter than Na). These particles may be silicophytoliths derived from local plants. Other elongate particles in the background dusts include amphibole particles; these particles exhibit typical prismatic amphibole habits.

6.4.2.2.6 Factors Controlling the Distribution of Erionite at Yucca Mountain

Previous to about 1959, erionite was considered a rare mineral, found as woolly masses in only one locality near Durkee, Oregon (Mumpton and Ormsby 1976). Since then, it has been found in numerous saline-lake zeolite deposits (Surdam and Sheppard 1978) associated with the common sedimentary zeolites, clinoptilolite, mordenite, analcime, chabazite, and phillipsite.

Most zeolite occurrences can be assigned to one of several types of geologic environments or hydrologic systems (Hay 1978). They are: saline, alkaline lakes; saline, alkaline soils and land surfaces; marine sediments; percolating water in an open hydrologic system; hydrothermal alteration; and burial diagenesis or metamorphism. Erionite is not known to form as a weathering mineral or in soils, nor has it been found in deep-sea sediments; its rare presence in deep-sea samples is due to hydrothermal deposition in basalts (Gottardi and Galli 1985). It is also more common in sedimentary rocks than in hydrothermal deposits (Gottardi and Galli 1985).

In a study of an active saline-alkaline lake zeolite deposit at Lake Magadi in Kenya, Surdam and Eugster (1976) found that erionite was the most common zeolite present, with lesser amounts of chabazite, clinoptilolite, mordenite, and phillipsite. They postulated that erionite formed directly from trachytic glass solely through the addition of H_2O. To understand why erionite is the dominant zeolite phase found at Lake Magadi, Surdam and Eugster offered the following observations:

- The trachytic glass starting material is rich in alkalis and poor in alkaline-earth elements.
- There is an abundance of silica and silicate phases, indicating high silica activities.
- The inflow waters into the Magadi basin and the brines in the basin are rich in sodium and silica and poor in alkaline earths, especially calcium.

They used these observations to infer that erionite will form as the initial zeolite phase in an environment characterized by high silica, high sodium, and extremely low calcium activities. They stated that erionite can form directly from trachytic glass solely by the addition of water. However, this water is unlikely to be dilute surface or groundwater because such water would probably contain calcium obtained from either the weathering of plagioclase or the dissolution of carbonates.

There is little information available on the paragenesis of erionite at Yucca Mountain, although some data are contained in Levy (1984c), who conducted petrographic analyses on drill cores USW H-3, H-4, and H-5 from Yucca Mountain. She reported the occurrence of smectite, heulandite, and an unidentified fibrous/bladed zeolite in a side-wall sample from drillhole USW H-5 at 507.8 m depth (1,666 feet) located in the lower vitrophyre of the Topopah Spring Tuff. The unidentified zeolite was recently reinvestigated using X-ray powder diffraction methods and has been identified as erionite. Levy concluded that pumice fragments and the nondevitrified portions of the matrix had been replaced by smectite, heulandite, and the unidentified zeolite. Smectite was the earliest-formed alteration product, and in some parts of the rock, glass shards were completely altered to smectite. In areas where the smectite alteration was incomplete, the

glass was replaced inward from the smectite-lined cracks by heulandite. The unidentified zeolite (erionite) appeared to be partially intergrown with and draped over the heulandite, suggesting that it was the later phase to form. Levy concluded that, although the unidentified zeolite may be locally more abundant than heulandite, its overall abundance is ~1 to 2 percent.

Because of the unique nature of the erionite occurrence in drillhole USW UZ-14, the YMP investigated erionite-rich samples from ~415.4 m (1,364 feet) depth using scanning electron microscope to determine the morphology, distribution, and compositional variations between clinoptilolite/heulandite and erionite in the sample. Electron microprobe analyses were obtained for a zeolite, believed to be heulandite, from sample USW UZ-14 1,364.4. The erionite and heulandite in that sample are not readily discernible from each other. Although erionite is finely fibrous, its fibers are often clustered in bundles such that the thin-section view of erionite appears more blocky or tabular than fibrous. For those cases in which it appeared that an analysis was being obtained from a blocky heulandite crystal, increased magnification often showed that the "block" was composed of (or coated by) a bundle of fibers. If the analysis is assumed to be of heulandite, an approximate chemical analysis of the companion erionite can be formulated from semiquantitative scanning electron microscope energy-dispersive spectra analyses of the fibrous mineral. Although scanning electron microscope energy-dispersive spectra analyses show that erionite has somewhat lower Al/Si and higher K/Ca ratios, the differences in composition are not large. In both the USW UZ-14 and H-5 samples, the erionite is very potassic. However, the similarity in Al/Si ratios of erionite and heulandite in the USW UZ-14 sample (with the ratio in erionite being slightly lower) is quite distinct from USW H-5 samples in which aluminous erionite coexists with more siliceous clinoptilolite/heulandite.

The instrumental neutron activation analysis data for samples from USW UZ-14, in which erionite is exceptionally abundant and closely associated with the vitrophyre, indicate the existence of both closed-system and open-system behavior. Clearly, K and especially Na were lost from this system, whereas Ca and Sr were accumulated. The lanthanide elements, however, indicate possible closed-system behavior, with complementary Ce depletion in smectites and Ce accumulation in the erionite-rich tuff. The net indications from the instrumental neutron activation analysis data are that the erionite alteration was connected with other portions of the hydrologic system and that this system was oxidizing (to account for the Ce segregations).

6.4.2.2.7 Thermodynamic Modeling Results

As described in section 6.4.2.1.3, thermodynamic modeling of zeolite stability was conducted in order to formulate a set of conditions conducive to erionite formation at Yucca Mountain. If the geochemical conditions leading to the formation of erionite in Yucca Mountain tuffs can be understood through modeling, then the YMP can better predict where in the mountain erionite may be encountered. Figure 6.4-6a through d shows the results of modeling zeolite stability in $\log[(a_{K^+})^2/a_{Ca^{2+}}]$ versus $\log[(a_{Na^+})^2/a_{Ca^{2+}}]$ space at various temperatures and silica activities. The figure demonstrates the influence of groundwater composition on the formation of individual zeolite species. Although attempts were made to use "representative" chemical analyses, chemical compositions of the zeolites have been shown to vary considerably depending on drillhole locations and depth (for example, Broxton, Bish et al. 1987). Therefore, several calculations were conducted to determine sensitivity of the stability fields to variable input cation ratios for the phases. The exact stability fields for phases that exhibit significant variations in

cation ratios, however, can differ markedly in response to the cation ratios used for the calculations. These calculations showed that those zeolites that exhibit a large variation in cation composition (for example, clinoptilolite, mordenite, and erionite) were most sensitive to changes in input cation ratios. For example, although mordenite retains its central position on the activity-activity diagrams with changes in exchangeable-cation composition, its stability field has a strong negative correlation with that of clinoptilolite, that is, the mordenite stability field expands as that for clinoptilolite shrinks, and vice versa. A similar, less-dramatic effect was noted for the stability field of erionite with respect to the stability fields for clinoptilolite and mordenite. Bowers and Burns (1990) also noted that cation composition had an effect on stability and modeled the effects of Ca-Na-K-Mg substitution in clinoptilolite to determine its stability with respect to mordenite and heulandite. They found that increased K or Ca significantly increased the clinoptilolite stability field.

The effect of silica activity is clearly illustrated by comparing the calculations conducted at amorphous silica saturation (Figure 6.4-6a), at cristobalite saturation (Figure 6.4-6b), and at quartz saturation (Figure 6.4-6c). The stability fields for the more siliceous zeolites (for example, mordenite and clinoptilolite) dominate the figures at high silica activity (amorphous silica saturation), they decrease in size at cristobalite saturation, and they disappear almost entirely at quartz saturation. Silica activity during zeolite formation can be constrained by the SiO_2 polymorphs coexisting with the zeolites. Erionite is observed to occur in USW UZ-14 with opal-CT, indicating that it formed at a high silica activity. Opal-CT is generally intergrown with mordenite and clinoptilolite-heulandite at Yucca Mountain (Bish and Chipera 1989). For comparison, analyses of fracture minerals suggest that stellerite is associated with tridymite and that heulandite is associated with cristobalite (Carlos, Chipera, Bish et al. 1995).

The present-day water chemistry (Kerrisk 1987) may also provide some constraints on past chemical conditions under which zeolites formed at Yucca Mountain. An area representing the present-day water chemistry has been superimposed on the activity-activity diagrams. Calculations using a representative present-day silica activity ($10^{-3.1}$) and water temperature (~35°C) suggest that clinoptilolite-mordenite is the stable assemblage with respect to other zeolites at Yucca Mountain today (Figure 6.4-6d). However, only a small reduction in silica activity or increase in aqueous Ca concentration is required to cross into the stellerite stability field, which may explain the occurrence of stellerite in fractures above the static water level in drillholes USW G-1, USW G-2, and UE-25 a#1 (Carlos, Chipera, Bish et al. 1995). Figure 6.4-6a through d shows that an erionite stability field occurs only with aqueous K concentrations considerably more potassic than present Yucca Mountain water compositions.

Calculated equilibria between heulandite and erionite from drillholes USW UZ-14 1364 and USW H-5 1666 are shown in Figure 6.4-7a and b, respectively, as a function of temperature and $\log[(a_{K^+})^2/a_{Ca^{2+}}]$ for silica activities in equilibrium with quartz, cristobalite, and amorphous silica. An erionite stability field for both sets of mineral compositions exists only at elevated aqueous K-concentrations. Heulandite-erionite equilibrium, however, is very sensitive to the Al/Si ratio in the two phases. Assuming the Al/Si ratios from the analyses of the USW UZ-14 heulandite and erionite, an increase in silica activity expands the erionite stability field (Figure 6.4-7a). However, if the chemical compositions of the USW H-5 zeolites are used, in which case the Al/Si ratios are reversed (heulandite is more siliceous than erionite), increasing silica activity

expands the heulandite stability field (Figure 6.4-7b). Assuming a more siliceous clinoptilolite, representative of the compositions occurring at Yucca Mountain (Broxton, Bish et al. 1987), clinoptilolite stability increases significantly, such that substantially elevated aqueous K^+/Ca^{2+} ratios are required to stabilize erionite (for example, $\log[(a_{K^+})^2/a_{Ca^{2+}}]$ values of -1.8 for quartz saturation at 30°C and +1.0 for cristobalite saturation at 30°C). The effects of temperature are difficult to quantify. Although increasing temperature increases the stability of heulandite relative to erionite, $(a_{K^+})^2/a_{Ca^{2+}}$ also increases due to the removal of aqueous Ca^{2+} via carbonate formation. Nevertheless, it appears that an elevated aqueous-K concentration was an important requirement for the formation of erionite at Yucca Mountain, along with conditions that resulted in high Al/Si ratios in clinoptilolite/heulandite. Blacic, Pettit et al. (1996) found that erionite-bearing samples in USW UZ-14 have markedly higher Li/Na ratios compared with erionite-free clinoptilolite samples from the same core. It is still uncertain why this is the case or how widespread this chemical signature may be in other erionite occurrences, but this observation, coupled with the indications of a high-K environment for erionite formation, suggest that alkali-element concentrations play a significant role in erionite formation. It is readily apparent from Figure 6.4-7a and b that more accurate mineral compositions are required to predict the geochemical conditions resulting in erionite formation.

6.4.2.2.8 Stratigraphic Considerations in Predicting Erionite Distribution

In fiscal year 1997, the project undertook a program involving predictions of potential erionite-bearing zones in upcoming drillholes. For the first time, a detailed prediction was developed for drillhole USW SD-6, scheduled to be drilled in fiscal year 1998. This report (Bish, Carey et al. 1997) assembled all available data on erionite distribution and, in particular, included a variety of stratigraphic considerations to predict the distribution of erionite in the drillhole. Available data for Yucca Mountain Tuffs show clearly that the primary potential erionite-bearing zones in Yucca Mountain rocks are either in the altered zone immediately above the Topopah Spring Tuff lower vitrophyre or in the moderately welded subzone underlying the lower vitrophyre. At present, erionite has never been seen in the Topopah Spring Tuff more than 1.5 m (5 feet) above the Tptpln/Tptpv3 contact; therefore, a safety buffer zone above the vitrophyre can be reasonably thin. The deepest erionite occurrences found to date are within the moderately welded Topopah Spring Tuff immediately underlying the vitrophyre (Tptpv2); erionite has not been found in or beneath the lowest parts (nonwelded, Tptpv1) of the Topopah Spring Tuff. The nonwelded tuff or bedded tuff at the bottom of the Topopah Spring Tuff signal a return to erionite-free rock. Erionite has not been found in or below the Calico Hills Formation. Based on the project's substantial data for the Topopah Spring Tuff occurrences, including a known erionite occurrence in H-5, the report concluded with reasonable certainty that erionite was most likely to be encountered near the lower Topopah Spring Tuff vitrophyre in SD-6. Of course, the exact placement of such a buffer zone was directly tied to the accuracy of stratigraphic contacts as drilling proceeded.

In addition, the recent data from the Exploratory Studies Facility emphasize the possibility of erionite occurrences in the upper PTn, just below the Tpcplnc/Tpcpv2 boundary in the lower Tiva Canyon Tuff. However, the extremely limited amount of data concerning erionite distribution in the Tiva Canyon Tuff greatly limits the certainty with which a prediction could be made for this unit. As noted above, the existing data indicate the presence of erionite alteration

in the intact or broken wall rock adjacent to fractures and breccia zones with secondary-mineral deposition other than erionite.

This report (Bish, Carey et al. 1997) also illustrated the distributions of glass, smectite, and zeolite in the form of east-west cross sections through the location of drillhole SD-6 (Figure 6.4-8a, b, and c). A common feature of most erionite occurrences is the association of abundant smectite plus zeolite at the tops of vitric horizons. For the glassy interval at the base of the Tiva Canyon Tuff (Tpcpv), smectite and glass abundances were predicted to be moderately high whereas zeolites were predicted to be absent. For the glassy interval at the base of the Topopah Spring Tuff (Tptpv), smectite and zeolite were both predicted to occur but their abundances were predicted to be low. However, the data available from analyzed drillhole and Exploratory Studies Facility occurrences indicated that erionite occurrence does not require high abundances of clay and zeolite; small amounts of erionite can be associated with small amounts of alteration. Nevertheless, the absence of zeolites predicted in Tpcpv and the low predicted abundances of clay and zeolite in Tptpv indicate that large abundances of erionite (as in UZ-14) are unlikely in SD-6.

6.4.3 Implications of Mineral Health Hazards for Construction and Operation

By combining quantitative analyses of mineral distributions with information on mineral toxicity/carcinogenicity, potential hazards associated with airborne particles released by operations at Yucca Mountain can be evaluated. There are several minerals that may be of potential concern as airborne particles, but the risk posed by most of these can be minimized by safe, modern mining practices (for example, by maintaining low dust levels and adequate ventilation). The crystalline silica minerals (quartz, tridymite, cristobalite, and opal-CT) fall into this category. These minerals are classed by the International Agency for Research on Cancer as probable human carcinogens, and they are ubiquitous at Yucca Mountain. Nevertheless, the risk posed by these minerals can probably be mitigated by proper dust control. No additional "asbestos" type precautions would necessarily need to be taken to address concerns with the silica minerals. All of the excavations in vitric tuff—for example, the nonwelded tuff occurring at the base of the Topopah Spring Tuff and the lower Topopah Spring vitrophyre—will involve rocks with inherently low abundances of crystalline silica. Of the three crystalline silica phases (quartz, cristobalite, and tridymite), only small amounts of quartz (<1 to 7 wt%) and cristobalite (0 to 4 wt%) with no occurrences of tridymite in such vitric tuffs have been found. Total crystalline silica abundances in these vitric tuffs are all 7 percent or less; typical abundances are ~4 wt%. These low abundances of crystalline silica contrast with abundances in devitrified rhyolitic Topopah Spring Tuff (in which the Exploratory Studies Facility and the potential repository horizon are located). In these devitrified rocks the total crystalline silica abundances are typically ~30 to 40 wt%. The silica minerals in these devitrified rocks are generally quartz/cristobalite with more variable and generally lesser occurrences of tridymite.

Some minerals (for example, palygorskite and sepiolite) have occurrences limited to fractures, so exposures to these minerals will likely be very small, particularly if low dust levels are maintained. Consequently, most of these minerals probably do not pose a risk at Yucca Mountain. In addition, palygorskite, in particular, is usually at depths shallower than the repository horizon. Erionite may pose a risk if encountered in sufficient quantity even when standard - modern mining practices are followed, due to its apparently extremely high

carcinogenic potential. However, erionite occurrence at Yucca Mountain appears to be restricted to zones immediately below the potential repository horizon and in limited quantities just below the Tpcplnc/Tpcpv2 boundary in the lower Tiva Canyon Tuff. Consequently, it may only be a concern where the repository workings may penetrate into the basal vitrophyre of the Topopah Spring Member. However, given erionite's high apparent toxicity, great care should be exercised when penetrating such horizons during construction. Furthermore, it will be prudent to consider the possible horizons to be encountered before any new drilling or excavation, as is currently being done with drilling of WT-24 and SD-6 and construction of the east-west drift via predictive reports.

Only limited information is available on the toxicity and carcinogenicity of mordenite, so although the published data suggest that mordenite is not carcinogenic, a prudent approach would be to minimize exposures to airborne mordenite until additional biological data have been collected. These additional biological data should address the possible relationships between various mineralogical properties and biological activity, so that the biological activity of mordenite can be evaluated on a sample-by-sample basis. The precautions taken in response to the occurrence of the silica minerals may be sufficient to address mordenite occurrence at Yucca Mountain and would likely be considered conservative. However, the concern over erionite's extreme biological potential will probably focus attention on the potential risk posed by any fibrous zeolite, due to the poor understanding of mineralogical aspects relevant to mineral-induced diseases. If this were to occur, the approach to dealing with fibrous zeolites will probably be based on erionite's toxicity/carcinogenicity, regardless of whether or not other fibrous zeolites are as biologically active as erionite. The only way to avoid this type of inappropriate blanket approach is through more extensive biological evaluations of other fibrous zeolites, provided that mineralogical and geochemical concerns are properly addressed by the experiments.

6.4.4 Summary and Conclusions

By combining YMP quantitative X-ray diffraction analyses of mineral distributions at Yucca Mountain with published information on mineral toxicity/carcinogenicity, the YMP has evaluated health-related mineral issues associated with airborne particles released by operations at Yucca Mountain. There are several minerals that may be of potential concern as airborne particles during construction or operation, but the risk posed by most of these can be minimized by safe, modern mining practices (for example, by maintaining low dust levels and adequate ventilation). The crystalline silica minerals (quartz, tridymite, cristobalite, and opal-CT) fall into this category. These minerals are classed by the International Agency for Research on Cancer as probable human carcinogens, and it must be recognized that they are ubiquitous at Yucca Mountain. Apart from vitric and vitrophyre zones at Yucca Mountain, amounts of the crystalline silica minerals are typically 3 to 40 wt%. The potential repository horizon in the lower portion of the Topopah Spring Tuff contains typically 30 to 40 percent of these minerals. Other minerals (for example, palygorskite and sepiolite) have occurrences limited to fractures, usually at depths shallower than the repository horizon, so exposures to these minerals will likely be very small, particularly if low dust levels are maintained. Consequently, these minerals probably do not pose a risk at Yucca Mountain, and occasional penetration of shallower units containing these minerals can minimize exposure through the use of modern mining practices. Mordenite occurs in fractures in the Topopah Spring Tuff and in the zeolitized units below the repository horizon.

Although published data suggest that mordenite is not carcinogenic, a prudent approach will be to minimize exposures to airborne mordenite, using methods appropriate for crystalline silica.

Erionite is a natural fibrous zeolite that occurs in the rocks at Yucca Mountain and that is listed as a known human carcinogen by recognized international agencies such as the International Agency for Research on Cancer. There have been concerns about the occurrence of erionite at Yucca Mountain for almost a decade, and some individuals have suggested that erionite at Yucca Mountain should be treated as if it were asbestos (for example, R.. McDaniel, Yucca Mountain Project memorandum to Frances Stephenson, re: Zeolites, January 19, 1993). No safe exposure levels have been established for erionite and no federal health and safety standards are in place that specifically regulate exposure to erionite (aside from 29 CFR 1910, the Hazard Communication Standard). Although United States regulatory agencies do not specifically address erionite, its morphology and the International Agency for Research on Cancer classification strongly suggest that it be treated at least as carefully as asbestos. Furthermore, Nevada State Occupational Safety and Hazard Administration regulations specify that if an international agency such as the International Agency for Research on Cancer lists a material as carcinogenic, the material shall be considered by Occupational Safety and Hazard Administration to be carcinogenic and shall be treated as such. Erionite may pose a risk if encountered in sufficient quantity even when standard modern mining practices are followed due to its apparently extremely high carcinogenic potential. Erionite occurrence at Yucca Mountain appears to be restricted to zones immediately below the potential repository horizon and just below the Tpcplnc/Tpcpv2 boundary in the lower Tiva Canyon Tuff. Thus, it may only be a concern where underground workings penetrate into the basal vitrophyre of the Topopah Spring Member or when tunneling from the surface and penetrating the Tpcplnc/Tpcpv2 boundary.

Many methods have been proposed to deal with erionite, including those that attempt to make erionite non-hazardous. However, proposed processing such as heat treatments to dehydrate erionite would not make the mineral nonhazardous. Available data suggest that dehydration of erionite to temperatures in excess of 500°C (932°F) is reversible and does not destroy the mineral or make it less harmful. The only acceptable mitigation method for erionite at Yucca Mountain is to minimize exposures to workers and the public. Hence, it is critical that the distribution of erionite at Yucca Mountain be known accurately (and that acceptable mitigation methods be understood).

The ongoing Mineralogy-Petrology effort to determine the distribution of erionite using specially developed X-ray diffraction techniques has proved very successful, but new information on erionite distribution at Yucca Mountain continues to be obtained. Until 1997, all documented occurrences of erionite at Yucca Mountain were consistent and suggested that erionite, when it occurs, is restricted to the transition zone in the lower Topopah Spring Tuff where alteration occurs a few meters above, within, and a few meters below the basal vitrophyre. However, erionite has now also been identified just below the Tpcplnc/Tpcpv2 boundary in the lower Tiva Canyon Tuff at Yucca Mountain. In addition, it is important to note that, until very recently, it was believed that erionite occurrence at Yucca Mountain was restricted to fractures above the vitrophyre, and the high concentrations of erionite in the matrix below the vitrophyre in USW UZ-14 were totally unexpected. It is also important to note that restricted sampling intervals used in the past on the YMP, with samples often taken at 15 m (50 feet) intervals, do not allow the project to conclude that erionite does not occur in earlier sampled drillholes or in other

portions of the Exploratory Studies Facility. In fact, such broadly spaced sampling was the rule, rather than the exception, for most sampling done prior to 1996. For example, erionite could well occur over a narrow depth range beneath the Topopah Spring Tuff lower vitrophyre in drillholes such as USW G-1 and UE-25 a#1.

Given these caveats, the mineralogical data available to date allow the YMP to predict with some certainty the stratigraphic horizons in which erionite may be encountered during drilling or tunneling. Although occurrences similar to the one in USW UZ-14 have not been found in corresponding sections of other cores that have subsequently been analyzed, it is important to continue to examine new core and new sections of tunnels in the Exploratory Studies Facility for erionite, so that any new occurrences of erionite are detected quickly. Systematic sampling in suspect zones in the Exploratory Studies Facility has not yet been undertaken, and only limited zones were analyzed for erionite in the Exploratory Studies Facility. Encountering an erionite-rich zone such as that found in USW UZ-14 during drilling or construction would be particularly dangerous. Prudence requires that the project put protective measures in place when approaching the Topopah Spring Tuff lower vitrophyre, either when drilling or operating the tunnel-boring machine.

As an alternative approach to direct detection of erionite, modeling of the factors that controlled formation of erionite at Yucca Mountain has been done so that a better predictive model can be developed for where it might occur in newly encountered core or within Exploratory Studies Facility tunnels. The current thermodynamic approach shows promise for providing the basis of a predictive model, but further work on erionite formation is needed before such a model can be developed with confidence. Currently, the best approach for evaluating erionite occurrence at Yucca Mountain is by direct detection using methods such as X-ray diffraction that can provide unambiguous identification.

INTENTIONALLY LEFT BLANK

ACKNOWLEDGMENTS AND DATA TRACEABILITY

The project data reported for surface samples and for drillholes USW NRG-6, SD-7, SD-9, and UE-25 UZ#16 are the only Q data available; all other mineralogical data in this subsection are non-Q as they were obtained from non-Q core and cuttings. The accession numbers related to these data are NNA.890412.0062, NNA.891019.0029, MOL.19941220.0125 and NNA.490427.0099. Data tracking numbers are LA000000000018.001 (TBV), LA000000000086.002 (TBV), and LA000000000054.001 (TBV). The record packages containing traceability information are TWS-EES-1-3-89-21, TWS-EES-1-09-93-009, LA-EES-1-TIP-94-009, and LA-EES-1-03-94-003.

The Los Alamos data tracking number for the studies of Eolian-Deposited Minerals Around Drill Hole USW SD-9 is LA-000000000109.001 (TBV), and all data in that section are Q data. The record package containing traceability information is LA-EES-1-TIP-94-012.

IDENTIFICATION OF Q AND NON-Q DATA

The designation of Q data acquisition for the Yucca Mountain Site Characterization Project at Los Alamos National Laboratory begins with the acceptance of the Los Alamos National Laboratory Q program on January 22, 1991. All samples analyzed by group EES-1 at LANL are assigned sequential tracking numbers, using a sample tracking procedure (DP-101) that is an integral part of the LANL Q program. Therefore, the 3- or 4-digit LANL tracking numbers assigned on or after 1/22/91 permit the recognition of Q data. Some of the data collected at LANL after 1/22/91 were obtained from core materials for which the Q status of core records is yet to be determined by the Project. Because the Los Alamos National Laboratory data collected for these samples does fall under LANL Q control, these data are still considered to be Q data. The LANL EES-1 records show that all samples with LANL EES-1 tracking numbers • 310 represent Q data; any sample with a LANL EES-1 tracking number < 310 *or listed without a LANL EES-1 tracking number* represents non-Q data. The use of Q and non-Q data is discussed below for this subsection.

Q data, LA000000000018.001 (TBV), LA000000000086.002 (TBV), LA000000000054.001 (TBV), and LA000000000109.001 (TBV).

Accession Numbers:

NNA.890412.0062 [Chipera and Bish (1989)]

NNA.891019.0029 [Bish and Chipera (1989)]

MOL.19941220.0125 [Guthrie, Bish et al. (1995)]

NNA.94104.0054 [Guthrie (1992)]

NNA.94104.0056 [Guthrie, McLeod et al. (1992)]

NNA.490427.0099 [Chipera, Vaniman et al. (1995)]

Data tracking numbers:

LA000000000018.001 (TBV) [Bish and Chipera (1989)]

LA000000000086.002 (TBV) [quantitative XRD and zeolite stability modeling component of Chipera, Vaniman et al. (1995)]

LA000000000054.001 (TBV) [Guthrie, Bish et al. (1995)]

LA000000000109.001 (TBV) [Guthrie, Raymond et al. (1995)]

6.5 REFERENCES

NOTE: For each reference either a document accession number (NNA.19xxxxxx.xxxx) or a technical information center number (TIC xxxxxx) is provided. If a number is not currently available, it is noted by TBD (to be determined). All DTNs should be considered TBV (to be verified).

6.5.1 Documents Cited

Adamson, A.W. 1982. *Physical Chemistry of Surfaces*, 372. New York, New York: John Wiley and Sons. TIC 236950.

Ahn, J.H. and Buscheck, P.R. 1990. "Layer-Stacking Sequences and Structural Disorder in Mixed-Layer Illite/Smectite: Image Simulations and HRTEM Imaging." *American Mineralogist, 75*, 267–275. Washington, D.C.: Mineralogical Society of America. TIC 236922.

Allard, B. 1982. *Sorption of Actinides in Granitic Rock.* SKBF Teknisk Rapport (Technical Report) 82-21. Stockholm, Sweden: Svensk Kärnbränsleförsörjning AB/Avdelning KBS. TIC 205892.

Allard, B.; Olofsson, U.; Torstenfelt, B.; Kipatsi, H.; and Andersson, K. 1982. "Sorption of Actinides in Well-Defined Oxidation States on Geologic Media." *Scientific Basis for Radioactive Waste Management V*, 775-782. Pittsburgh, Pennsylvania: Materials Research Society. TBD

Altaner, S.P. and Grim, R.E. 1990. "Mineralogy, Chemistry, and Diagenesis of Tuffs in the Sucker Creek Formation (Miocene), Eastern Oregon." *Clays and Clay Minerals, 38*, 561–572. Long Island City, New York: Pergamon Press. TIC 235395.

Ames, Jr., L.L. 1961. "Cation Sieve Properties of the Open Zeolites Chabazite, Mordenite, Erionite, and Clinoptilolite." *American Mineralogist, 46*, 1120-1131. Washington, D.C.: Mineralogical Society of America. NNA.19930409.0077.

Ames, Jr., L.L. 1964a. "Some Zeolite Equilibria with Alkali Metal Cations." *American Mineralogist, 49*, 127–145. Washington, D.C.: Mineralogical Society of America. TIC 236905.

Ames, Jr., L.L. 1964b. "Some Zeolite Equilibria with Alkaline-Earth Metal Cations." *American Mineralogist, 49*, 1099–1110. Washington, D.C.: Mineralogical Society of America. TIC 236904.

Ames, Jr., L.L.; McGarrah, J.E.; and Walker, B.A. 1983. "Sorption of Trace Constituents from Aqueous Solutions onto Secondary Minerals: 1. Uranium." *Clays and Clay Minerals, 31(5)*, 321-334. Long Island City, New York: Pergamon Press. TIC 238914.

Anderson, L.A. 1981. *Rock Property Analysis of Core Samples from the Yucca Mountain UE25a-1 Borehole, Nevada Test Site, Nevada.* USGS-OFR-81-1338. Denver, Colorado: U.S. Geological Survey. NNA.19870406.0031.

Anderson, L.A. 1984. *Rock Property Measurements on Large-Volume Core Samples from Yucca Mountain USW GU-3/G-3 and USW G-4 Boreholes, Nevada Test Site, Nevada.* USGS-OFR-84-552. Denver, Colorado: U.S. Geological Survey. NNA.19870325.0105.

Andersson, K. 1988. *SKI Project-90: Chemical Data.* Swedish Nuclear Power Inspectorate Report SKI TR 91:21. Stockholm, Sweden: Swedish Nuclear Power Inspectorate. NNA.19940303.0040.

Armbruster, T. 1993. "Dehydration Mechanism of Clinoptilolite and Heulandite: Single-Crystal X-Ray Study of Na-Poor, Ca-, K-, Mg-Rich Clinoptilolite at 100 K." *American Mineralogist, 78*, 260–264. Washington, D.C.: Mineralogical Society of America. TIC 236906.

Aronson, J.L. and Hower, J. 1976. "Mechanism of Burial Metamorphism of Argillaceous Sediment: 2." *Radiogenic Argon Evidence.* Geological Society of America Bulletin, *87*, 738–744. Boulder, Colorado: Geological Society of America. TIC 236907.

Aronson, J.L. and Lee, M. 1986. "K/Ar Systematics of Bentonite and Shale in a Contact Metamorphic Zone, Cerrillos, New Mexico." *Clays and Clay Minerals, 34*, 483–487. Long Island City, New York: Pergamon Press. TIC 236819.

Baeyens, B. and Bradbury, M.H. 1995a. "A Quantitative Mechanistic Description of Ni, Zn, and Ca Sorption on Na-Montmorillonite: Part I." *Physico-Chemical Characterization and Titration Measurements.* Report PSI Bericht Nr. 95-10. Villigen, Switzerland: Paul Scherrer Institute. TIC 237271.

Baeyens, B. and Bradbury, M.H. 1995b. "A Quantitative Mechanistic Description of Ni, Zn, and Ca Sorption on Na-Montmorillonite: Part II." *Sorption Measurements.* Report PSI Bericht Nr. 95-11. Villigen, Switzerland: Paul Scherrer Institute. TIC 237272.

Balistrieri, L.S. and Chao, T.T. 1987. "Selenium Adsorption by Goethite." *Soil Science Society of America Journal, 51*, 1145–1151. Madison, Wisconsin: Soil Science Society of America. TIC 223172.

Balistrieri, L.S. and Murray, J.W. 1982. "The Adsorption of Cu, Pb, Zn, and Cd on Goethite from Major Ion Seawater." *Geochimica et Cosmochimica Acta, 46*, 1253–1265. Oxford/New York: Pergamon Press. TIC 238913.

Bargar, K. and Beeson, M. 1981. "Hydrothermal Alteration in Research Drill-Hole Y-2, Lower Geyser Basin, Yellowstone National Park, Wyoming." *American Mineralogist, 66*, 473–490. Washington, D.C.: Mineralogical Society of America. TIC 217376.

Baris, I.; Simonato, L.; Artvinli, M.; Pooley, F.; Saracci, R.; Skidmore, J.; and Wagner, C. 1987. "Epidemiological and Environmental Evidence of the Health Effects of Exposure to Erionite Fibres: A Four-Year Study in the Cappadocian Region of Turkey." *International Journal of Cancer, 39*, 10–17. Geneva, Switzerland: International Union Against Cancer. TIC 221880.

Barnard, R.W.; Wilson, M.L.; Dockery, H.A.; Gauthier, J.H.; Kaplan, P.G.; Eaton, R.R.; Bingham, F.W.; and Robey, T.H. 1992. *TSPA 1991: An Initial Total-System Performance*

Assessment for Yucca Mountain. SAND91-2795. Albuquerque, New Mexico: Sandia National Laboratories. NNA.19920630.0033.

Barrer, R.M. and Klinowski, J. 1972. "Ion Exchange Involving Several Groups of Homogeneous Sites." *Journal of the Chemical Society: Faraday Transactions I, 68*, 73–87. London, England: Chemical Society (Great Britain). TIC 236882.

Barrer, R.M. and Klinowski, J. 1974. "Ion-Exchange Selectivity and Electrolyte Concentration." *Journal of the Chemical Society: Faraday Transactions, 70*, 2080–2091. London, England: Chemical Society (Great Britain). TIC 235115

Barrer, R.M. and Munday, B.M. 1971. "Cation Exchange in the Synthetic Zeolite K-F." *Journal of the Chemical Society A 1971*, 2914–2921. London, England: Chemical Society (Great Britain). TIC 237502.

Barrer, R.M. and Townsend, R.P. 1976. "Transition Metal Ion Exchange in Zeolites: Part 1. Thermodynamics of Exchange of Hydrated Mn^{2+}, Co^{2+}, Ni^{2+}, Cu^{2+}, and Zn^{2+} Ions in Ammonium Mordenite." *Journal of the Chemical Society: Faraday Transactions I, 72*, 661–673. London, England: Chemical Society. TIC 239144.

Barrer, R.M. and Vaughan, J.H. 1969. "Sorption and Diffusion of Rare Gases in Heulandite and Stilbite." *Surface Science, 14*, 77–92. Amsterdam, Netherlands: North Holland Publishing Company. TIC 236820.

Barth, T.F.W. 1969. *Feldspars.* London, England: Wiley-Interscience. TIC 239857.

Bar-Yosef, B. and Meek, D. 1987. "Selenium Sorption by Kaolinite and Montmorillonite." *Soil Science, 144*, 11–19. Madison, Wisconsin: Soil Science Society of America. TBD

Bates, J. K.; Bourcier, W.L.; Bradley, C.R.; Brown, N.R.; Buck, E.C.; Carroll, S.A.; Cunnane, J.C.; Dietz, N.L.; DiSanto, T.; Ebert, W.L.; Emery, J.W.; Feng, X.; Gerding, T.J.; Gong, G.; Hafenrichter, L.D.; Hoh, J.C.; Mazer, J.J.; Newton, L.; Phillips, B.L.; Pletcher, R. and Wronkiewicz, D.J. 1994. *ANL Technical Support Program for DOE Environmental Restoration and Waste Management Annual Report, October 1992–September 1993.* ANL-94/19. Argonne, Illinois: Argonne National Laboratory. TIC 211863.

Bates, J.K.; Bradley, J.P.; Teetsov, A.; Bradley, C.R.; and Buchholtz ten Brink, M. 1992. "Colloid Formation During Waste Form Reaction: Implications for Nuclear Waste Disposal." *Science, 256*, 649–652. Washington, D.C.: American Association for the Advancement of Science. TIC 239138.

Bates, J.K.; Tani, B.S.; Veleckis, E. and Wronkiewicz, D.J. 1990. "Identification of Secondary Phases Formed During Reaction of UO2 With EJ-13 Water." *Materials Research Society Symposium Proceedings, 176*, 499–506. Pittsburgh, Pennsylvania: Materials Research Society. TIC 224105.

Baumann, V.H. 1971. "Herstellung Reiner und Gestörter Quarzoberflächen und ihr Verhalten Nach Unterschiedlicher Behandlung." *Fortschrittsberichte uber Kolloide und Polymere, 55,* 37-44. Bochum, Germany. TIC 223897.

Benjamin, M.M. 1983. "Adsorption and Surface Precipitation of Metals on Amorphous Iron Oxyhydroxide." *Environmental Science and Technology, 17,* 686–692. Easton, Pennsylvania: American Chemical Society. TIC 239143.

Benjamin, T.M.; Arndt, N.T.; and Holloway, J.R. 1977. "Instrumental Techniques for B-Track Mapping." *Annual Report of the Director, Geophysics Laboratory, Carnegie Institute, Washington, 1976–1977,* 658-660. Washington, D.C.: Carnegie Institute. TIC 237909.

Bennett, D.A.; Hoffman, D.; Nitsche, H.; Russo, R.E.; Torres, R.A.; Baisden, P.A.; Andrews, J.E.; Palmer, C.E.A.; and Silva, R.J. 1992. "Hydrolysis and Carbonate Complexation of Dioxoplutonium(V)." *Radiochimica Acta, 56,* 15–19. München, Germany: Verlag. TIC 224778.

Benson, L. and Klieforth, H. 1989. "Stable Isotope in Precipitation and Groundwater in the Yucca Mountain Region, Southern Nevada: Paleoclimatic Implications." Peterson, D.H., Ed. *AGU Geophysical Monograph, 55,* 41-59. Washington, D.C.: American Geophysical Union. TIC 224413.

Benson, L.V. and McKinley, P.W. 1985. *Chemical Composition of Groundwater in the Yucca Mountain Area, Nevada, 1971-84.* USGS-OFR-85-484. Denver, Colorado: U.S. Geological Survey. GS920408312321.003; NNA.19900207.0281.

Benson, L.V.; Robison, J.; Blankennagel, R.; and Ogard, A. 1983. *Chemical Composition of Groundwater and the Locations of Permeable Zones in the Yucca Mountain Area, Nevada.* USGS-OFR-83-854. Denver, Colorado: U.S. Geological Survey. NNA.19870610.0028.

Bentley, C.; Robison, J.; and Spengler, R. 1983. *Geohydrologic Data for Test Well USW H-5, Yucca Mountain Area, Nye County, Nevada.* USGS-OFR-83-853. Denver, Colorado: U.S. Geological Survey. GS91090831232.002; NNA.19870519.0098.

Berman, R.G. 1988. "Internally Consistent Thermodynamic Data for Minerals in the System Na_2O-K_2O-CaO-MgO-FeO-Fe_2O_3-Al_2O_3-SiO_2-TiO_2-H_2O-CO_2." *Journal of Petrology, 29(2),* 445-522. Oxford, England: Oxford University Press. TIC 236892.

Berman, R.G. and Brown, T.H. 1985. "Heat Capacity of Minerals in the System Na_2O-CaO-MgO-FeO-Fe_2O_3-Al_2O_3-SiO_2-TiO_2-H_2O-CO_2: Representation, Estimation, and High-Temperature Extrapolation." *Contributions to Mineralogy and Petrology, 89,* 168–183. New York, New York: Springer Verlag. TIC 235118.

Bish, D.L. 1984. "Effects of Exchangeable Cation Composition on the Thermal Expansion/Contraction of Clinoptilolite." *Clays and Clay Minerals, 32*(6), 444–462. Long Island City, New York: Pergamon Press. TIC 212510.

Bish, D.L. 1988. *Evaluation of Past and Future Alterations in Tuff at Yucca Mountain, Nevada, Based on the Clay Mineralogy of Drill Cores USW G-1, G-2, and G-3.* LA-10667-MS. Los Alamos, New Mexico: Los Alamos National Laboratory. TBD

Bish, D.L. 1989. *Evaluation of Past and Future Alterations in Tuff at Yucca Mountain, Nevada, Based on the Clay Mineralogy of Drill Cores USW G-1, G-2, and G-3.* LA-10667-MS. Los Alamos, New Mexico: Los Alamos National Laboratory. LA000000000040.001; NNA.19890126.0207.

Bish, D.L. and Aronson, J.L. 1993. "Paleogeothermal and Paleohydrologic Conditions in Silicic Tuff from Yucca Mountain, Nevada." *Clays and Clay Minerals, 41*, 148–161. Long Island City, New York: Pergamon Press. TIC 224613.

Bish, D.L. and Chipera, S.J. 1986. *Mineralogy of Drill Holes J-13, UE-25 a#1, and USW G-1 at Yucca Mountain, Nevada.* LA-10764-MS. Los Alamos, New Mexico: Los Alamos National Laboratory. MOL.19950412.0044.

Bish, D.L. and Chipera, S.J. 1987. "Detection of Trace Amounts of Erionite in Samples Using X-Ray Powder Diffraction and Profile Refinement." *Proceedings of the Clay Minerals Society 24th Annual Meeting, Socorro, New Mexico*, 32. Socorro, New Mexico: New Mexico Insitute of Mining and Technology. TIC 235124.

Bish, D.L. and Chipera, S.J. 1988. "Problems and Solutions in Quantitative Analysis of Complex Mixtures by X-Ray Powder Diffraction." *Advances in X-Ray Analysis, 31*, 295–308. New York, New York: Plenum Press. TIC 224050.

Bish, D.L. and Chipera, S.J. 1989. *Revised Mineralogic Summary of Yucca Mountain, Nevada.* LA-11497-MS. Los Alamos, New Mexico: Los Alamos National Laboratory. LA000000000018.001; NNA.19891019.0029.

Bish, D.L. and Chipera, S.J. 1991. "Detection of Trace Amounts of Erionite Using X-Ray Powder Diffraction: Erionite in Tuffs of Yucca Mountain, Nevada, and Central Turkey." *Clays and Clay Minerals, 39*, 437–445. Long Island City, New York: Pergamon Press. TIC 203789.

Bish, D.L. and Duffy, C.J. 1990. "Thermogravimetric Analysis of Minerals in Thermal Analysis." *Clay Science – Workshop Lectures, 3*, 96-157. Stucki, J.W. and Bish, D.L., Eds. Bloomington, Indiana: Clay Minerals Society. TBD

Bish, D.L. and Howard, S.A. 1988. "Quantitative Phase Analysis Using the Rietveld Method." *Journal of Applied Crystallography, 21*, 86–91. Copenhagen, Denmark: International Union of Crystallography. TIC 223712.

Bish, D.L. and Reynolds, Jr., R.C. 1989. "Sample Preparation for X-Ray Diffraction." *Modern Powder Diffraction, 20*, 73–99. Bish, D.L. and Post, J.E., Eds. Washington, D.C: Mineralogical Society of America. TIC 237913.

Bish, D.L. and Semarge, R.E. 1982. "Mineralogic Variations in a Silicic Tuff Sequence: Evidence for Diagenetic and Hydrothermal Reactions." *Program and Abstracts, 19th Annual*

Meeting, Clay Minerals Society, Hilo, Hawaii, 42. Bloomington, Indiana: Clay Minerals Society. TIC 222174.

Bish, D.L. and Vaniman, D.T. 1985. *Mineralogic Summary of Yucca Mountain, Nevada.* LA-10543-MS. Los Alamos, New Mexico: Los Alamos National Laboratory. LA000000000110.002; MOL.19950412.0041.

Bish, D.; Brown, L.; Broxton, D.; Byers, F.; Carlos, B.; Chipera, S.; Levy, S.S.; Stringer, P.; Travis, B.; and Vaniman, D.T. (compilers) 1987. *Research by ESS Division, for the Nevada Nuclear Waste Storage Investigations January-June, 1985.* LA-10987-PR. Los Alamos, New Mexico: Los Alamos National Laboratory. TIC 208727.

Bish, D.L.; Caporuscio, F.A.; Copp, J.F.; Crowe, B.M.; Purson, J.D.; Smyth, J.R.; and Warren, R.G. 1981. *Preliminary Stratigraphic and Petrologic Characterization of Core Samples from USW G-1, Yucca Mountain, Nevada.* LA-8840-MS. Los Alamos, New Mexico: Los Alamos National Laboratory. NNA.19870406.0099.

Bish, D.L.; Carey, J.W.; Carlos, B.A.; Chipera, S.J.; Guthrie, Jr., G.D.; Levy, S.S.; Vaniman, D.T.; and WoldeGabriel, G. 1996. *Summary and Synthesis Report on Mineralogy and Petrology Studies for the Yucca Mountain Site Characterization Project: Volume I. Introduction.* Los Alamos National Laboratory Geology and Geochemistry Group Report on Milestone 3665. Los Alamos, New Mexico: Los Alamos National Laboratory. MOL.19961230.0037.

Bish, D.; Carey, J.W.; Chipera, S.; Levy, S.; and Vaniman, D. 1997. *Predictive Report: Horizons of Potential Erionite Occurrence in Drill Hole USW SD-6.* YMP Deliverable Report SP32A2M4. Los Alamos, New Mexico: Los Alamos National Laboratory. MOL.19980213.0129.

Bish, D.L.; Ogard, A.E.; Vaniman, D.T.; and Benson, L. 1984. "Mineralogy-Petrology and Groundwater Geochemistry of Yucca Mountain Tuffs," in "Scientific Basis for Nuclear Waste Management VII." McVay, G.L. Ed. *Materials Research Society Symposium Proceedings,* 283-291. Pittsburgh, Pennsylvania: Materials Research Society. TIC 221127.

Bish, D.L.; Vaniman, D.T.; Rundberg, R.S.; Wolfsberg, K.; Daniels, W.R.; and Broxton, D.E. 1983. "Natural Sorptive Barriers in Yucca Mountain, Nevada, for Long-Term Isolation of High-Level Waste." *Radioactive Waste Management: Proceedings of the IAEA International Conference on Radioactive Waste Management, Seattle, Washington, 16–20 May 1983,* IAEA-CN-43/461, 415–432. Vienna, Austria: International Atomic Energy Agency. TBD

Blacic, J.; Carter, J.; Halleck, P.; Johnson, P.; Shankland, T.; Anderson, R.; Spicochi, K.; and Heller, A. 1982. *Effects of Long-Term Exposure of Tuffs to High-Level Nuclear Waste-Repository Conditions: Preliminary Report.* LA-9174-PR. Los Alamos, New Mexico: Los Alamos National Laboratory. NNA.19870406.0245.

Blacic, J.D.; Pettit, D.R.; and Cremers, D.A. 1996. *Final Report on Feasibility of Real-Time Geochemical Analysis at Yucca Mountain, Nevada, Using LIBS Technology.* LA-13190-MS. Los Alamos, New Mexico: Los Alamos National Laboratory. MOL.19980217.0068.

Blanchard, G.; Maunaye, M.; and Martin, G. 1984. "Removal of Heavy Metals from Waters by Means of Natural Zeolites." *Water Research, 18*, 1501–1507. Oxford/New York: Pergamon Press. TIC 239004.

Blankennagel, R.K. and Weir, Jr., J.E. 1973. *Geohydrology of the Eastern Part of Pahute Mesa, Nevada Test Site, Nye County, Nevada.* USGS Professional Paper 712-B. Denver, Colorado: U.S. Geological Survey. NNA.19870406.0202.

Bodvarsson, G.S.; Bandurraga, T.M.; and Wu, Y.S., Eds. 1997. *The Site-Scale Unsaturated-Zone Model of Yucca Mountain, Nevada, for the Viability Assessment.* LBNL-40376. Berkeley, California: Lawrence Berkeley National Laboratory. MOL.19971014.0232.

Boettinger, J.L. and Southard, R.J. 1990. "Micromorphology and Mineralogy of a Calcareous Duripan Formed in Granitic Residuum, Mojave Desert, California, USA." *Soil Micromorphology: A Basic and Applied Science,* 409-415. Amsterdam, Netherlands: Elsevier Scientific Publishing Company. TIC 224379

Boles, J.R. 1971. "Synthesis of Analcime from Natural Heulandite and Clinoptilolite." *American Mineralogist, 56*, 1724–1734. Washington, D.C.: Mineralogical Society of America. TIC 236668.

Bolt, G.H. and Bruggenwert, M.G.M. 1976. *Soil Chemistry Basic Elements.* Amsterdam, Netherlands: Elsevier. TBD

Borovec, Z. 1981. "The Adsorption of Uranyl Species by Fine Clay." *Chemical Geology, 32*, 45–58. Amsterdam/New York: Elsevier. TIC 237323.

Bottinga, Y. and Javoy, M. 1973. "Comments on Oxygen Isotope Geothermometry." *Earth and Planetary Science Letters, 20*, 250–265. Amsterdam, Netherlands: Elsevier Science Publishing Company. TIC 224380.

Bouwer, H. 1991. "Simple Derivation of the Retardation Equation and Application to Preferential Flow and Macrodispersion." *Ground Water, 29*, 41. Columbus, Ohio: Water Well Publishing Company. TIC 224079.

Bowers, T.S. and Burns, R.G. 1990. "Activity Diagrams for Clinoptilolite: Susceptibility of this Zeolite to Further Diagenetic Reactions." *American Mineralogist, 75*, 601–619. Washington, D.C.: Mineralogical Society of America. TIC 235378.

Bowman, R.S. and O'Connor, G.A. 1982. "Control of Nickel and Strontium Sorption by Free Metal Ion Activity." *Soil Science Society of America Journal, 46*, 933–936. Madison, Wisconsin: Soil Science Society of America Special Publication Series. TIC 236910.

Boyle, R.W. 1979. "Biogeochemistry of Gold." *The Geochemistry of Gold and its Deposits*, Geological Survey of Canada, Bulletin 280, 79–88. Canada: Geological Association of Canada. TBD

Bradbury, M.H. and Baeyens, B. 1995. *A Quantitative Mechanistic Description of Ni, Zn, and Ca Sorption on Na-Montmorillonite: Part III. Modelling.* Report PSI Bericht Nr. 95-12. Villigen, Switzerland: Paul Scherrer Institute. TIC 237271.

Bradbury, M.H.; Green, A.; Lever, D.; and Stephen, I.G. 1986. *Diffusion and Permeability-Based Sorption Measurements in Sandstone, Anhydrite, and Upper Magnesian Limestone Samples.* March, Harwell report AERER 11995. Oxfordshire, England. TIC 237243.

Brantley, S.L. and Stellings, L. 1996. "Feldspar Dissolution at 25°C and Low pH." *American Journal of Science, 296*, 101–127. New Haven, Connecticut: Kline Geology Laboratory, Yale University. TIC 239822

Brieger, H. and Gross, P. 1966. "On the Theory of Silicosis: I. Coesite." *Archives of Environmental Health, 13*, 38–43. Washington, D.C.: Heldref Publications. TIC 236822.

Brieger, H. and Gross, P. 1967. "On the Theory of Silicosis: III. Stishovite." *Archives of Environmental Health, 15*, 751–757. Washington, D.C.: Heldref Publications. TIC 236821.

Brindley, G.W. and Brown, G. 1980. *Crystal Structures of Clay Minerals and Their X-Ray Identification.* London, England: Mineralogical Society. TBD

Britten, J.A.; Travis, B.J; and Brown, L.F. 1983. *Calculation of Surface Site-Energy Distributions from Adsorption Isotherms and Temperature-Programmed Desorption Data.* LA-UR-83-1654. Los Alamos, New Mexico: Los Alamos National Laboratory. TBD

Brookins, D.G. 1983. "Migration and Retention of Elements at the Oklo Natural Reactor." *Environmental Geology, 4*, 201–208. New York, New York: Springer-Verlag. TIC239003.

Brookins, D.G. 1988. *Eh-pH Diagrams for Geochemistry.* New York, New York: Springer-Verlag. TIC 237943.

Brooks, D.J. and Corrado, J.A. 1984. *Determination of Radionuclide Solubility in Groundwater for Assessment of High-Level Waste Isolation.* Washington, D.C.: U.S. Nuclear Regulatory Commission. HQS.19880517.2024.

Brouwer, E.; Baeyens, B.; Maes, A.; and Cremers, A. 1983. "Cesium and Rubidium Ion Equilibria in Illite Clay." *Journal of Physical Chemistry, 87*, 1213–1219. Washington, D.C.: American Chemical Society. TIC 226332.

Brown, L.F. and Travis, B.J. 1984. "Optimal Smoothing of Site-Energy Distributions from Adsorption Isotherms." Meyers, A.L. and Belfort, G., Eds. *Fundamentals of Adsoprtion*, 125-134. New York, New York: Engineering Foundation. TBD

Brown, T.H.; Berman, R.G.; and Perkins, E.H. 1989. "PTA-SYSTEM: A Geo-Calc Software Package for the Calculation and Display of Activity-Temperature-Pressure Phase Diagrams." *American Mineralogist, 74*, 485–487. Washington, D.C.: Mineralogical Society of America. TIC 239006.

Broxton, D.E.; Bish, D.L.; and Vaniman, D.T. 1982. *Distribution and Character of Sorptive Zeolites in the Yucca Mountain Block, Nevada Test Site.* Geological Society of America, Abstracts with Programs, 14, 453. Boulder, Colorado: Geological Society of America. TIC 237363.

Broxton, D.E.; Bish, D.L.; and Warren. R.G. 1987. "Distribution and Chemistry of Diagenetic Minerals at Yucca Mountain, Nye County, Nevada." *Clays and Clay Minerals, 35*, 2, 89–110. Long Island City, New York: Pergamon Press. TIC 203900.

Broxton, D.E.; Byers, Jr., F.M.; Warren, R.G.; and Scott, R.B. 1985. "Trends in Phenocryst Chemistry in the Timber Mountain-Oasis Valley Volcanic Field, SW Nevada: Evidence for Episodic Injection of Primitive Magma Into an Evolving Magma System." *Geological Society of America, Abstracts with Programs 1985, 17*(6), 345. Boulder, Colorado: Geological Society of America. TIC 217806.

Broxton, D.E.; Chipera, S.J.; Byers, Jr., F.M.; and Rautman, C.A. 1993. *Geologic Evaluation of Six Nonwelded Tuff Sites in the Vicinity of Yucca Mountain, Nevada for a Surface-Based Test Facility for the Yucca Mountain Project.* LA-12542-MS. Los Alamos, New Mexico: Los Alamos National Laboratory. TIC 208615.

Broxton, D.E.; Warren, R.G.; Byers, F.M.; and Scott, R.B. 1989. "Chemical and Mineralogic Trends Within the Timber Mountain-Oasis Valley Caldera Complex, Nevada: Evidence for Multiple Cycles of Chemical Evolution in a Long-Lived Silicic Magma System." *Journal of Geophysical Research, 94*, 5961–5985. Washington, D.C.: American Geophysical Union. GS930508314214.005; TIC 225928.

Broxton, D.E.; Warren, R.G.; Hagan, R.C.; and Luedemann, G. 1986. *Chemistry of Diagenetically Altered Tuffs at a Potential Nuclear Waste Repository, Yucca Mountain, Nye County, Nevada.* LA-10802-MS. Los Alamos, New Mexico: Los Alamos National Laboratory. TIC 202366.

Bruton, C.J. 1990. *Solubility Controls on Radionuclide Concentrations in Solution: Preliminary Results for U, Np, Pu, and Am.* Lawrence Livermore National Laboratory Report. Livermore, California: Lawrence Livermore National Laboratory. TBD

Bruton, C.J. 1991. *Equilibrium Controls of Radionuclide Concentrations in Nevada Test Site Waters: Preliminary Results for Th, U, Np, Pu, Am, Sr, Ra, and Pb.* Appendix D in SAND91-0170-UC-902 (Chu, M.S.Y. and Bernard, E.A. "Waste Inventory and Preliminary Source Term Model for the Greater Confinement Disposal Site at the Nevada Test Site."). Albuquerque, New Mexico: Sandia National Laboratories. TBD

Bruton, C.; Glassley, W.E.; and Viani, B.E. 1993. "Geochemistry." *Preliminary Near-Field Environment Report: Volume II. Scientific Overview of Near-Field Environment and Phenomena.* Wilder, D.G., Ed. Report UCRL-LR-107476, Vol. 2. Livermore, California: Lawrence Livermore National Laboratory. MOL.19980326.0015.

Buddemeier, R.W. and Hunt, J.R. 1988. "Transport of Colloidal Contaminants in Groundwater: Radionuclide Migration at the Nevada Test Site." *Applied Geochemistry, 3*(5), 535–548. Elmsford, New York: Pergamon Press. TIC 224116.

Buesch, D.C.; Dickerson, R.P.; Drake, R.M.; and Spengler, R.W. 1994. "Integrated Geology and Preliminary Cross Section along the North Ramp of the Exploratory Studies Facility, Yucca Mountain." *High Level Radioactive Waste Management, Proceedings of the Fifth Annual International Conference, Las Vegas, Nevada, May 22-26, 1994*, 1055–1065. La Grange Park, Illinois: American Nuclear Society. TIC 211733.

Buesch, D.C.; Spengler, R.W.; Moyer, T.C.; and Geslin, J.K. 1996. *Proposed Stratigraphic Nomenclature and Macroscopic Identification of Lithostratigraphic Units of the Paintbrush Group Exposed at Yucca Mountain, Nevada.* USGS-OFR-94-469. Denver, Colorado: U.S. Geological Survey. MOL.19970205.0061.

Buesseler, K.O. and Sholkovitz, E.R. 1987. "The Geochemistry of Fallout Plutonium in the North Atlantic: I," in "A Pore Water Study in Shelf, Slope, and Deep-Sea Sediments." *Geochimica et Cosmochimica Acta, 51*, 2605–2622. Oxford/New York: Pergamon. TIC 239005.

Buffle, J.; Perret, D.; and Newman, M. 1992. "The Use of Filtration and Ultrafiltration for Size Fractionation of Aquatic Particles, Colloids, and Macromolecules." *Environmental Particles, 1*(6), 171–230." Environmental Analytical and Physical Chemistry Series. Chelsea, Michigan: Lewis Publishing. TIC 237396.

Burst, J.F. 1959. "Post-Diagenetic Clay Mineral-Environmental Relationships in the Gulf Coast Eocene in Clays and Clay Minerals." *Clays and Clay Minerals, 6*, 327–341. Long Island City, New York: Pergamon Press. TIC 236951.

Buscheck, T.A., and Nitao, J.J. 1992. "Impact of Thermal Loading on Repository Performance at Yucca Mountain." *High Level Radioactive Waste Management, Proceedings of the Third Annual International Conference, Las Vegas, Nevada, April 12-16, 1992,* 1003–1017. La Grange Park, Illinois: American Nuclear Society. TIC 233024.

Buscheck, T.A. and Nitao, J.J. 1993. "Analysis of Repository-Heat-Driven Hydrothermal Flow at Yucca Mountain." *High Level Radioactive Waste Management, Proceedings of the Fourth Annual International Conference, Las Vegas, Nevada, April 26-30, 1993*, 847–867. La Grange Park, Illinois: American Nuclear Society. TIC 235542.

Buscheck, T.A.; Nitao, J.J.; and Saterlie, S.F. 1994. "Evaluation of Thermo-Hydrological Performance in Support of Thermal Loading Systems Study." *High Level Radioactive Waste Management, Proceedings of the Fifth Annual International Conference, Las Vegas, Nevada, May 22-26, 1994*, 592-610. La Grange Park, Illinois: American Nuclear Society. TIC 226487.

Butler, J.P.; Reeds, J.A.; and Dawson, S.V. 1981. "Estimating Solutions of First-Kind Integral Equations with Nonnegative Constraints and Optimal Smoothing." *SIAM Journal on Numerical Analysis, 18*, 381–397. Philadelphia, Pennsylvania: Society for Industrial and Applied Mathematics (SIAM, Inc.). NNA.19900302.0040.

Byers, Jr., F.M. 1985. *Petrochemical Variation of Topopah Spring Tuff Matrix with Depth (Stratigraphic Level), Drill Hole USW G-4, Yucca Mountain, Nevada.* LA-10561-MS. Los Alamos, New Mexico: Los Alamos National Laboratory. NNA.19890804.0031.

Byers, Jr., F.M. and Moore, L.M. 1987. *Petrographic Variation of the Topopah Spring Tuff Matrix Within and Between Cored Holes, Yucca Mountain, Nevada.* LA-10901-MS. Los Alamos, New Mexico: Los Alamos National Laboratory. NNA.19870716.0010.

Byers, Jr., F.M.; Carr, W.J.; Christiansen, R.L.; Lipman, P.W.; Orkild, P.P.; and Quinlivan, W.D. 1976. Geologic Map of the Timber Mountain Caldera Area. USGS Miscellaneous Geologic Inventory Map I-891. Denver, Colorado: U.S. Geological Survey. TIC 204573.

Byers, Jr., F.M.; Carr, W.J.; and Orkild, P.P. 1989. "Volcanic Centers of Southwestern Nevada: Evolution of Understanding, 1960–1988." *Journal of Geophysical Research, 94*, 5908–5924. Washington, D.C.: American Geophysical Union. TIC 224013.

Byers, Jr., F.M.; Carr, W.J.; Orkild, P.P.; Quinlivin, W.D.; and Sargent, K.A. 1976. *Volcanic Suites and Related Cauldrons of Timber Mountain-Oasis Valley Caldera Complex, Southern Nevada.* USGS Professional Paper 919. Denver, Colorado: U.S. Geologic Survey. TIC 201146.

Bystrom-Brusewitz, A.M. 1975. "Studies on the Li Test to Distinguish Between Beidellite and Montmorillonite." *Proceedings of the International Clay Conference*, 419–428. Bloomington, Indiana: Clay Minerals Society. TIC 237735.

Campbell, A.S. and Fyfe, W.S. 1960. "Hydroxyl-Ion Catalysis of the Hydrothermal Crystallization of Amorphous Silica; A Possible High-Temperature pH Indicator." *American Mineralogist, 45*, 464–468. Washington, D.C.: Mineralogical Society of America. TIC 224642.

Caporuscio, F.A. and Vaniman, D.T. 1985. *Iron and Manganese in Oxide Minerals and in Glasses: Preliminary Consideration of Eh Buffering Potential at Yucca Mountain, Nevada.* LA-10369-MS. Los Alamos, New Mexico: Los Alamos National Laboratory. NNA.19870407.0331.

Caporuscio, F.A.; Vaniman, D.T.; Bish, D.L.; Broxton, D.E.; Arney, C.B.; Heiken, G.H.; Byers, F.M.; Gooley, R.; and Semarge, E. 1982. *Petrologic Studies of Drill Cores USW G-2 and UE-25b-1H, Yucca Mountain, Nevada.* LA-9255-MS. Los Alamos, New Mexico: Los Alamos National Laboratory. NNA.19870519.0041.

Carey, J.W. and Bish, D.L. 1996. "Equilibrium in the Clinoptilolite-H_2O System." *American Mineralogist, 81*, 952–962. Washington, D.C.: Mineralogical Society of America. TIC 233145.

Carey, J.W.; Bish, D.L.; and Chipera, S.J. 1996. "Kinetics and Thermodynamics of Mineral Evolution at Yucca Mountain." *Summary and Synthesis Report on Mineralogy and Petrology Studies for the Yucca Mountain Site Characterization Project, Volume III.* Report Milestone 3665. Los Alamos, New Mexico: Los Alamos National Laboratory. MOL.19961230.0039.

Carey, J.W.; Chipera, S.J.; and Bish, D.L. 1997. "Calculating Mineral Stabilities in the Absence of Adequate Thermodynamic Data: Application to Yucca Mountain, Nevada, USA." *Proceedings of the 11th International Clay Conference*, A13. Calgary, Alberta: Geological Survey of Canada. TIC 237007.

Carey, J.W.; Chipera, S.J.; Vaniman, D.T.; Bish, D.L.; Viswanathan, H.S.; and Carter-Krogh, K. 1997. *Three-Dimensional Mineralogic Model of Yucca Mountain, Nevada.* Milestone Report Deliverable SP344BM4. Los Alamos, New Mexico: Los Alamos National Laboratory. MOL.19971117.0110.

Carey, J.W.; Robinson, B.A.; and Henderson, S. 1995. "Consequences of the Dehydration and Hydration of Clinoptilolite-Rich Rocks on the Thermo-Hydrologic Evolution of a Model Radioactive Waste Repository." *Geological Society of America Abstracts With Programs 1995.* Boulder, Colorado: Geological Society of America. TIC 236094.

Carlos, B.A. 1985. *Minerals in Fractures of the Unsaturated Zone From Drill Core USW G-4, Yucca Mountain, Nye County, Nevada.* LA-10415-MS. Los Alamos, New Mexico: Los Alamos National Laboratory. NNA.19920506.0037.

Carlos, B.A. 1987. *Minerals in Fractures of the Saturated Zone from Drill Core USW G-4, Yucca Mountain, Nye County, Nevada.* LA-10927-MS. Los Alamos, New Mexico: Los Alamos National Laboratory. NNA.19900222.0149.

Carlos, B.A. 1989. *Fracture-Coating Minerals in the Topopah Spring Member and Upper Tuff of Calico Hills from Drill Hole J-13.* LA-11504-MS. Los Alamos, New Mexico: Los Alamos National Laboratory. TIC 202383.

Carlos, B.A. 1990. *Manganese-Oxide Minerals in Fractures of the Crater Flat Tuff in Drill Core USW G-4, Yucca Mountain, Nevada.* LA-11787-MS. Los Alamos, New Mexico: Los Alamos National Laboratory. NNA.19900206.0163.

Carlos, B.A. 1994. *Field Guide to Fracture-Lining Minerals at Yucca Mountain, Nevada.* LA-12803-MS. Los Alamos, New Mexico: Los Alamos National Laboratory. MOL.19950717.0113.

Carlos, B.A.; Bish, D.L.; and Chipera, S.J. 1991. "Fracture-Lining Minerals in the Lower Topopah Spring Tuff at Yucca Mountain." *High Level Radioactive Waste Management, Proceedings of the Second Annual International Conference, Las Vegas, Nevada, April 28-May 3, 1991,* 486–493. La Grange Park, Illinois: American Nuclear Society. TIC 234965.

Carlos, B.A.; Chipera, S.J.; and Bish, D.L. 1995. *Distribution and Chemistry of Fracture-Lining Zeolites at Yucca Mountain, Nevada.* LA-12977-MS. Los Alamos, New Mexico: Los Alamos National Laboratory. MOL.19960306.0564.

Carlos, B.A.; Chipera, S.J.; Bish, D.L.; and Craven, S.J. 1993. "Fracture-Lining Manganese Oxide Minerals in Silicic Tuff, Yucca Mountain, Nevada, USA." *Chemical Geology, 107,* 47-69. Amsterdam/New York: Elsevier. TIC 208629.

Carlos, B.A.; Chipera, S.J.; Bish, D.L.; and Raymond, R. 1995. "Distribution and Chemistry of Fracture-Lining Zeolites at Yucca Mountain, Nevada." *Natural Zeolites '93: Occurrence, Properties, Use.* Ming, D.W. and Mumpton, F.A., Eds. 547–563. Brockport, New York: International Committee on Natural Zeolites. TIC 217193.

Carlos, B.A.; Chipera, S.J.; and Snow, M.G. 1995. "Multiple Episodes of Zeolite Deposition in Fractured Silicic Tuff." *Proceedings of the Eighth International Symposium on Water-Rock Interaction—WRI-8*, 67–71. Kharaka, Y.K and Chudaev, O.V., Eds. Rotterdam, Netherlands: Balkema. TIC 222321.

Carr, W.J. 1984. *Regional Structural Setting of Yucca Mountain, Southwestern Nevada, and Late Cenozoic Rates of Tectonic Activity in Part of the Southwestern Great Basin, Nevada and California.* USGS-OFR-84-854. Denver, Colorado: U.S. Geological Society. NNA.19870325.0475.

Carter, M.W. and Moghissi, A.A. 1977. "Three Decades of Nuclear Testing." *Health Physics, 33*, 55-71. New York, New York: Health Physics Society. TIC 239141.

Chadwick, O.A.; Hendricks, D.M.; and Nettleton, W.D. 1987. "Silica in Duric Soils: I.A Depositional Model." *Soil Science Society of America Journal, 51*, 975-982. Madison, Wisconsin: Soil Science Society of America Special Publication Series. TIC 236964.

Chadwick, O.A.; Hendricks, D.M.; and Nettleton, W.D. 1989. "Silicification of Holocene Soils in Northern Monitor Valley, Nevada." *Soil Science Society of America Journal, 53*, 158–164. Madison, Wisconsin: Soil Science Society of America Special Publication Series. TIC 224385.

Chafetz, L. and Folk, R.L. 1984. "Travertines: Depositional Morphology and the Bacterially Constructed Constituents." *Journal of Sedimentary Petrology, 54*(#1), 289-316. Tulsa, Oklahoma: Society of Economic Paleontologists and Mineralogists. TIC 224387.

Champ, D.R.; Merritt, W.P.; and Young, J.L. 1982. "Potential for the Rapid Transport of Plutonium in Groundwater as Demonstrated by Core Column Studies." *Scientific Basis for Radioactive Waste Management V Proceedings of the Materials Research Society Fifth International Symposium, 11,* 745-754. Lutze, W., Ed. New York, New York: North Holland Publishing Company. TIC 218415.

Chermak, J.A. and Rimstidt, J.D. 1989. "Estimating the Thermodynamic Properties (G_f and H_f) of Silicate Minerals at 298 K from the Sum of Polyhedral Contributions." *American Mineralogist, 74*, 1023–1031. Washington, D.C.: Mineralogical Society of America. NNA.19910109.0351.

Chipera, S.J. and Bish, D.L. 1988. *Mineralogy of Drill Hole UE-25 p#1 at Yucca Mountain, Nevada.* LA-11292-MS. Los Alamos, New Mexico: Los Alamos National Laboratory. NNA.19880607.0036.

Chipera, S.J. and Bish, D.L. 1989. *The Occurrence and Distribution of Erionite at Yucca Mountain, Nevada.* LA-11663-MS. Los Alamos, New Mexico: Los Alamos National Laboratory. NNA.19890412.0062.

Chipera, S.J. and Bish, D.L. 1995. "Multi-Reflection RIR and Intensity Normalizations for Quantitative Analyses: Applications to Feldspars and Zeolites." *Powder Diffraction, 10,* 47–55. Woodbury, Long Island, New York: American Institute of Physics. TIC 222001.

Chipera, S.J. and Bish, D.L. 1997. "Equilibrium Modeling of Clinoptilolite-Analcime Equilibria at Yucca Mountain, Nevada." *Clays and Clay Minerals, 45,* 226–239. Long Island City, New York: Pergamon. MOL.19971105.0669.

Chipera, S.J.; Bish, D.L.; and Carlos, B.A. 1995. "Equilibrium Modeling of the Formation of Zeolites in Fractures at Yucca Mountain, Nevada." *Natural Zeolites '93: Occurrence, Properties, Use,* 565–577. Ming, D.W. and Mumpton, F.A., Eds. Brockport, New York: International Committee on Natural Zeolites. TIC 217196.

Chipera, S.J.; Guthrie, Jr., G.D.; and Bish, D.L. 1993. "Preparation and Purification of Mineral Dusts." *Health Effects of Mineral Dusts,* Guthrie, G.D. and Mossman, B.T., Eds. *Reviews in Mineralogy, 28,* 235–249. Washington, D.C.: Mineralogical Society of America. TIC 235091.

Chipera, S.J.; Vaniman, D.T.; and Bish, D.L. 1996. *Zeolite Abundances and the Vitric-to-Zeolitic Transition in Drill Holes USW SD-7, 9, and 12, Yucca Mountain, Nevada.* Milestone Report LA4240, LA-EES-1-TIP-96-005. Los Alamos, New Mexico: Los Alamos National Laboratory. MOL.19970407.0339.

Chipera, S.J.; Vaniman, D.T.; Bish, D.L.; and Carey, J.W. 1997. *Mineralogic Variation in Drill Holes USW NRG-6, NRG-7/7A, SD-7, SD-9, SD-12, and UZ#14: New Data from 1996-1997 Analyses.* YMP Level 4 Milestone Report SP321BM4. Los Alamos, New Mexico: Los Alamos National Laboratory. TIC 214889.

Chipera, S.J.; Vaniman, D.T.; Carlos, B.A.; and Bish, D.L. 1995. *Mineralogic Variation in Drill Core UE-25 UZ#16, Yucca Mountain, Nevada.* LA-12810-MS. Los Alamos, New Mexico: Los Alamos National Laboratory. NNA.19940427.0099.

Choi, J.S. and Pigford, T.H. 1981. "Water-Dilution Volumes for High-Level Wastes." *Transactions of the American Nuclear Society, 39,* 176–177. Winter meeting, San Francisco, California, 1981. La Grange Park, Illinois: American Nuclear Society. TIC 236930.

Choppin, G.R. 1992. "The Role of Natural Organics in Radionuclide Migration in Natural Aquifer Systems." *Radiochimica Acta, 58/59,* 113–120. München, Germany: Verlag. TIC 222387.

Choppin, G.R. and Rao, L.F. 1984. "Complexation of Pentavalent and Hexavalent Actinides by Fluoride." *Radiochimica Acta, 37,* 143–146. München, Germany: Verlag. MOL.19950118.0150; MOL.19950131.0009.

Chung, F.H. 1974a. "Quantitative Interpretation of X-Ray Diffraction Patterns of Mixtures: I. Matrix-Flushing Method for Quantitative Multicomponent Analysis." *Journal of Applied Crystallography, 7,* 519–525. Copenhagen, Denmark: International Union of Crystallography. TIC 224051.

Chung, F.H. 1974b. "Quantitative Interpretation of X-Ray Diffraction Patterns of Mixtures: II. Adiabatic Principle of X-Ray Diffraction Analysis of Mixtures." *Journal of Applied Crystallography, 7*, 526–531. Copenhagen, Denmark: Munksgaard International Booksellers and Publishers. TIC 224051.

Claassen, H.C. 1983. *Sources and Mechanisms of Recharge for Groundwater in the West-Central Amargosa Desert, Nevada: A Geochemical Interpretation.* USGS-OFR-83-542. Denver, Colorado: U.S. Geological Survey. TIC 219336.

Claassen, H.C. 1985. *Sources and Mechanisms of Recharge for Groundwater in the West-Central Amargosa Desert, Nevada: A Geochemical Interpretation.* USGS Professional Paper 712-F. Denver, Colorado: U.S. Geological Survey. TIC 204574.

Claassen, H.C. and White, A.F. 1979. "Application of Geochemical Kinetic Data to Groundwater Systems: A Tuffaceous-Rock System in Southern Nevada." *Chemical Modeling in Aqueous Systems, American Chemical Society Symposium Series, 93*, 771–793. Washington, D.C.: American Chemical Society. TIC 222177.

Clark, D.L. 1994. *Letter Report on the Status of Pu (VI) Colloid Studies.* Los ALamos National Laboratory Yucca Mountain Letter Report 4026. Los Alamos, New Mexico: Los Alamos National Laboratory. MOL.19951002.0234.

Clark, I.D. and Fritz, P. 1997. *Environmental Isotopes in Hydrogeology.* Boca Raton, Florida: CRC Press. TIC 233503.

Clayton, R.; O'Neil, J.; and Mayeda, T. 1972. "Oxygen Isotope Exchange Between Quartz and Water." *Journal of Geophysical Research, 77*, 3057–3067. Washington, D.C.: American Geophysical Union. TIC 225264.

Cleveland, J.M. 1979a. "Critical Review of Plutonium Equilibria of Environmental Concern." *Chemical Modeling in Aqueous Systems*, 321–338. Jenne, E.A., Ed. Washington, D.C.: American Chemical Society. TIC 236752.

Cleveland, J.M. 1979b. *The Chemistry of Plutonium.* La Grange Park, Illinois: American Nuclear Society. TIC 10231.

Combes, J.M.; Chisholm-Brause, C.J.; Brown, Jr., G.E.; Parks, G.A.; Conradson, S.D.; Eller, P.G.; Triay, I.R.; Hobart, D.E.; and Meijer, A. 1992. "EXAFS Spectroscopic Study of Neptunium(V) Sorption at the α-FeOOH/Water Interface." *Environmental Science and Technology, 26*, 376–382. Easton, Pennsylvania: American Chemical Society. TIC 222228.

Conca, J.L. and Wright, J.V. 1992a. "A New Technology for Direct Measurements of Unsaturated Transport." *Proceedings of the Nuclear and Hazardous Waste Management Spectrum '92 Meeting, 2*, 1546. La Grange Park, Illinois: American Nuclear Society. MOL.19950516.0011

Conca, J.L. and Wright, J.V. 1992b. "Flow and Diffusion in Unsaturated Gravel, Soils, and Whole Rock." *Applied Hydrogeology, 1*, 5–24. Hanover, Germany: Verlag. TIC 224081.

Corapcioglu, M.Y. and Jiang, S. 1993. "Colloid-Facilitated Groundwater Contaminant Transport." *Water Resources Research, 29*(7), 2215–2226. Washington, D.C.: American Geophysical Union. TIC 222362.

Cotton, F.A. and Wilkinson, G. 1988. *Advanced Inorganic Chemistry*, fifth edition. New York, New York: John Wiley and Sons. TIC 236867.

Cox, A. and Dalrymple, G.B. 1967. "Statistical Analysis of Geomagnetic Reversal Data and the Precision of Potassium-Argon Dating." *Journal of Geophysical Research, 72*, 2603–2614. Richmond, Virginia: William Byrd Press. TIC 236834.

Craig, H. 1961. "Isotopic Variations in Meteoric Waters." *Science, 133*, 1702–1703. Washington, D.C.: American Association for the Advancement of Science. TIC 236943.

Craig, R.W.; Reed, R.L.; and Spengler, R.W. 1983. *Geohydrologic Data for Test Well USW H-6, Yucca Mountain Area, Nye County, Nevada.* USGS-OFR-83-856. Denver, Colorado: U.S. Geological Survey. NNA.19870406.0058.

Cramer, J.J. and Sargent, F.P. 1994. "The Cigar Lake Analog Study: An International R&D Project." *High Level Radioactive Waste Management: Proceedings of the Fifth Annual International Conference, Las Vegas, Nevada, May 22–26, 1994*, 2237–2242. La Grange Park, Illinois: American Nuclear Society. TIC 236751.

Cremers, A. 1977. "Ion Exchange in Zeolites," Chapter 16 of *Molecular Sieves—II, American Chemical Society Symposium Series 40*, 179. Katzer, J.R, Ed. Washington, D.C.: American Chemical Society. TIC 237908.

CRWMS M&O (Civilian Radioactive Waste Management System Management and Operating Contractor) 1994. *Total System Performance Assessment—1993: An Evaluation of the Potential Yucca Mountain Repository.* INTERA, Inc. B00000000-01717-2200-000990 REV 01. Las Vegas, Nevada: Author. NNA.19940406.0158.

CRWMS M&O 1996. *A 3D Geological Framework and Integrated Site Model of Yucca Mountain Version ISM 1.0.* B00000000-01717-5700-00002 REV 01. Las Vegas, Nevada: Author. MOL.19970122.0053.

CRWMS M&O 1997. *ISM2.0: A 3D Geologic Frameworkand Integrated Site Model of Yucca Mountain.* B00000000-01717-5700-00004 REV 00. Las Vegas, Nevada: Author. MOL.19970625.0119.

Curtis, D.B.; Fabryka-Martin, J.; Dixon, P.; Aguilar, R.; and Cramer, J. 1994. "Radionuclide Release Rates from Natural Analogues of Spent Nuclear Fuel." *High Level Radioactive Waste Management: Proceedings of the Fifth Annual International Conference, Las Vegas, Nevada, May 22–26, 1994*, 2228–2236. La Grange Park, Illinois: American Nuclear Society. TIC 235157.

Curtis, D.E. and Fabryka-Martin, J. 1988. "Report on Trip to Alligator River Analogue Project." Workshop held in Tucson, Arizona, November 21–22, 1988. TBD.

Czarnecki, J.B. 1985. "Simulated Effects of Increased Recharge on the Groundwater Flow System of Yucca Mountain and Vicinity, Nevada-California." USGS Water Resources Investigation Report 84-4344. Denver, Colorado: U.S. Geological Survey. HQS.19880517.1750.

D'Agnese, F.A.; Faunt, C.C.; Turner, A.K.; and Hill, M.C. 1997. *Hydrogeologic Evaluation and Numerical Simulation of the Death Valley Regional Groundwater Flow System, Nevada and California.* USGS Water Resources Investigations Report 96-4300. Denver, Colorado: U.S. Geological Survey. MOL.19980306.0253.

Dalrymple, G.B. and Lanphere, M.A. 1969. *K-Ar Dating.* San Francisco, California: Freeman. TIC 238887.

Daniels, W.R.; Wolfsberg, K.; Rundberg, R.S.; Ogard, A.E.; Kerrisk, J.F.; Duffy, C.J. et al. 1982. *Summary Report on the Geochemistry of Yucca Mountain and Environs.* LA-9328-MS. Los Alamos, New Mexico: Los Alamos National Laboratory. NNA.19870406.0243.

Daniels, W.R.; Erdal, B.R.; and Vaniman, D.T. (compilers) 1983. *Research and Development Related to the Nevada Nuclear Waste Storage Investigations, July 1-September 30, 1982.* LA-9577-PR. Los Alamos, New Mexico: Los Alamos National Laboratory. TIC 202344.

Davis, B.L. and Smith, D.K. 1988. "Tables of Experimental Reference Intensity Ratios." *Powder Diffraction, 3,* 205–208. Woodbury, Long Island, New York: American Institute of Physics. TIC 237490.

Davis, B.L.; Smith, D.K.; and Holomany, M.A. 1989. "Tables of Experimental Reference Intensity Ratios: Table No. 2, December 1989." *Powder Diffraction, 4,* 201–205. Woodbury, Long Island, New York: American Institute of Physics. TIC 237700.

Davis, J.A.; James, R.O.; and Leckie, J.O. 1978. "Surface Ionization and Complexation at the Oxide-Water Interface." *Journal of Colloid and Interface Science, 63*(3), 480–499. New York: Academic Press. TIC 223904.

Davis, J.M.G. 1993. "In-Vivo Assays to Evaluate the Pathogenic Effects of Minerals in Rodents." *Health Effects of Mineral Dusts,* 471–487. Guthrie, Jr., G.D. and Mossman, B.T., Eds. Washington, D.C.: Mineralogical Society of America. TIC 236750.

Davis, S.N. and Bentley, H.W. 1982. "Dating Groundwater." "Nuclear and Chemical Dating Techniques, Interpreting the Environmental Record." Currie, L.A., Ed. *American Chemical Society Symposium Series, 176,* 187–222. Washington, D.C.: American Chemical Society. TIC 237670.

Davis, S.N. and Murphy, E. 1987. *Dating Groundwater and the Evaluation of Repositories for Radioactive Waste.* NUREG/CR-4912. Washington, D.C.: U.S. Government Printing Office. TIC 216635.

de Marsily, G. 1986. *Quantitative Hydrogeology: Groundwater Hydrology for Engineers.* Orlando, Florida: Academic Press, Inc. TIC 208450.

de Pablo-Galán, L. 1986. "Geochemical Trends in the Alteration of Miocene Vitric Tuffs to Economic Zeolite Deposits, Oaxaca, Mexico." *Applied Geochemistry, 1*, 273–285. New York, New York: Pergamon Press. TIC 236933.

Decarreau, A. 1985. "Partitioning of Divalent Transition Metals Between Octahedral Sheets of Trioctahedral Smectites and Water." *Geochimica et Cosmochimica Acta 49*, 1537–1544. Oxford/New York: Pergamon Press. TIC 237522.

Deer, W.A.; Howie, R.A.; and Zussman, J. 1966. *An Introduction to the Rock-Forming Minerals*. London, England: Longmans. TIC 234769.

Deffeyes, K.S. 1959. "Zeolites in Sedimentary Rocks." *Journal of Sedimentary Petrology, 29*, 602–609. Tulsa, Oklahoma: Society of Economic Paleontologists and Mineralogists. TIC 237557.

Degueldre, C.; Grauer, R.; Laube, A.; Oess, A.; and Silby, H. 1996. "Colloid Properties in Granitic Groundwater Systems: Part II. Stability and Transport Study." *Applied Geochemistry, 11*, 697–710. New York, New York: Pergamon Press. TIC 236569.

Degueldre, C.; Laube, A.; and Scholtis, A. 1994. "WLB: A Study of Colloids in Groundwaters at the Wellenberg Site: Status Report." *Nagra Interner Bericht 94-41*. Switzerland: PSI Bericht. TIC 224100.

Degueldre, C.; Pfeiffer, H-R; Alexander, W.; Wernli, B.; and Bruetsch, R. 1996. "Colloid Properties in Granitic Groundwater Systems: Part I. Sampling and Characterization." *Applied Geochemistry, 11*, 677–695. New York, New York: Pergamon Press. TIC 236886.

Deines, P.; Langmuir, D.L.; and Harmon, R.S. 1974. "Stable Carbon Isotope Ratios and the Existence of a Gas Phase in the Evolution of Carbonate Ground Waters." *Geochimica et Cosmochimica Acta, 38*, 1147-1164. Oxford/New York: Pergamon Press. TIC 224390.

Delany, J.M. 1985. *Reaction of Topopah Spring Tuff With J-13 Water: A Geochemical Modeling Approach Using the EQ3/6 Reaction Path Code*. UCRL-53631. Livermore, California: Lawrence Livermore National Laboratory. TIC 203439.

Denniston, R.F. 1995. "Trace and Minor Element Distributions in Fracture Calcites from Yucca Mountain, Nevada: Reconstructing Calcite Growth Histories." Master's thesis. Albuquerque, New Mexico: University of New Mexico. TIC 239253.

Dettinger, M.D. 1989. "Reconnaissance Estimates of Natural Recharge to Desert Basins in Nevada, U.S.A., by Using Chloride-Balance Calculations." *Journal of Hydrology, 106*, 55-78. Amsterdam, Netherlands: Elsevier Science Publishers. TIC 236967.

Dibble, W.E. and Tiller, W.A. 1981. "Kinetic Model of Zeolite Paragenesis in Tuffaceous Sediments." *Clays and Clay Minerals 29*, 323–330. Long Island, New York: Pergamon Press. TIC 221129.

DOE (U.S. Department of Energy) 1988. *Yucca Mountain Site Characterization Plan, Yucca Mountain Site, Nevada Research and Development Area, Nevada.* DOE/RW-0199. Washington, D.C.: U.S. Department of Energy, Office of Civilian Radioactivity Waste Management. TIC 223856 through TIC 223864.

DOE 1993. *Yucca Mountain Site Characterization Project Technical Data Catalog, Quarterly Supplement.* December 31, 1993. Washington, D.C.: U.S. Department of Energy, Office of Civilian Radioactive Waste Management. TIC 210473.

DOE 1997. *Quality Assurance Requirements and Description.* DOE/RW-0333P, Revision 7. Washington, D.C.: Office of Civilian Radioactive Waste Management. MOL.19970731.0427.

Doi, K.; Hirono, S.; and Sakamaki, Y. 1975. "Uranium Mineralization by Groundwater in Sedimentary Rocks, Japan." *Economic Geology, 70*, 628–646. El Paso, Texas: Economic Geology Publishing Company. TIC 236987.

Dozol, M. and Hageman, R. 1993. "Radionuclide Migration in Groundwaters: Review of the Behavior of Actinides." *Pure and Applied Chemistry, 65*, 1081–1102. Boston/Oxford: Blackwell Scientific Publications. TBD

Drever, J.I. 1988. *The Geochemistry of Natural Waters*, 437. Englewood, New Jersey: Prentice Hall. TIC 208530.

Drever, J.I. and Smith, C.L. 1978. "Cyclic Wetting and Drying of the Soil Zone as an Influence on the Chemistry of Groundwater in Arid Terrains." *American Journal of Science, 278*, 1448-1454. New Haven, Connecticut: Kline Geology Laboratory, Yale University. TIC 237357.

Driscoll, Jr., K.E. 1993. "In-Vitro Evaluation of Mineral Cytotoxicity and Inflammatory Activity." *Health Effects of Mineral Dusts,* 489–511. Guthrie, Jr., G.D. and Mossman, B.T., Eds. Washington, D.C.: Mineralogical Society of America. TIC 237362.

Dubes, G.R. and Mack, L.R. 1988. "Asbestos-Mediated Transfection of Mammalian Cell Cultures." *In Vitro Cellular and Developmental Biology, 24*, 175–182. Baltimore, Maryland: Tissue Culture Association. TIC 235667.

Duffy, C.J. 1983a. *Hydrothermal Stability Studies.* LA-9577-PR. Los Alamos, New Mexico: Los Alamos National Laboratory. TIC 237802.

Duffy, C.J. 1983b. *Permeability, Porosity, and Hydrothermal Reactions.* LA-9793-PR. Los Alamos, New Mexico: Los Alamos National Laboratory. TIC 237804.

Duffy, C.J. 1984. *Hydrothermal Geochemistry.* LA-10032-PR. Los Alamos, New Mexico: Los Alamos National Laboratory. TIC 237805.

Duffy, C.J. 1993a. *Preliminary Conceptual Model for Mineral Evolution in Yucca Mountain.* LA-12708-MS, UC-811. Los Alamos, New Mexico: Los Alamos National Laboratory. NNA.19900117.0152.

Duffy, C.J. 1993b. *Kinetics of Silica-Phase Transitions.* LA-12564-MS. Los Alamos, New Mexico: Los Alamos National Laboratory. NNA.19900112.0346.

Dzombak, D.A. and Morel, F.M.M. 1990. *Surface Complexation Modeling Hydrous Ferric Oxide*, Chapter 10. New York, New York: John Wiley and Sons. TIC 224089.

Eastman Whipstock 1982. "Report of Sub-Surface Directional Survey, USW G-4, Nevada Test Site, Nevada." Job number P1182-G-1208. TBD

Eberl, D. and Hower, J. 1976. "Kinetics of Illite Formation." *Geological Society of America Bulletin 87*, 1326–1330. Boulder, Colorado: Geological Society of America. TIC 223629.

Efurd, D.W.; Runde, W.; Banar, J.C.; Roensch, F.R.; Palmer, P.D.; Clark, D.L.; and Tait, C.D. 1996. *Measured Solubilities and Speciation of Neptunium and Plutonium in J-13 Groundwater.* Los Alamos National Laboratory Yucca Mountain Milestone Report 3411. Los Alamos, New Mexico: Los Alamos National Laboratory. TBD

Elliott, W.C. 1988. "Bentonite Illitization in Two Contrasting Cases: Denver Basin and the Southern Appalachian Basin." Doctoral dissertation. Cleveland, Ohio: Case Western Reserve University. TBD .

Elliott, W.C. and Aronson, J.L. 1987. "Alleghanian Episode of K-Bentonite Illitization in the Southern Appalachian Basin." *Geology, 15*, 735–739. Boulder, Colorado: Geological Society of America. TIC 237494.

Elliott, W.C.; Aronson, J.L.; Matisoff, G.; and Gautier, D.L. 1991. "Kinetics of the Smectite to Illite Transformation in the Denver Basin: Clay Mineral, K-Ar Data, and Mathematical Model Results." *American Association of Petroleum Geologists Bulletin, 75*, 436–462. Tulsa, Oklahoma: American Association of Petroleum Geologists. TIC 236845.

Emett, D.C.; Hutchinson, D.D.; Jonson, N.A.; and O'Hair, K.E. 1994. "Water Resources Data, Nevada, Water Year 1993." USGS Water-Data Report NV-93-1. Denver, Colorado: U.S. Geological Survey. TBD

Engstrom, D.A. and Rautman, C.A. 1996. *Geology of the USW SD-9 Drill Hole, Yucca Mountain, Nevada.* SAND96-2030 UC-814. Albuquerque, New Mexico: Sandia National Laboratories. MOL.19970508.0288.

Eriksson, E. 1960. "The Yearly Circulation of Chloride and Sulfur in Nature: Part II. Meteorological, Geochemical, and Pedalogical Implications." *Tellus, 12*, 63-109. Copenhagen, Denmark: Munksgaard International Publishers Ltd. TIC 236893.

Ernst, W.G. and Calvert, S.E. 1969. "Experimental Study of the Recrystallization of Porcelanite and its Bearing on the Origin of Some Bedded Cherts." *American Journal of Science, 267A*, 114–133. New Haven, Connecticut: Kline Geology Laboratory, Yale University. TIC 224645.

Ervin, E.M.; Luckey, R.R.; and Burkhardt, D.J. 1993. "Summary of Revised Potentiometric-Surface Map for Yucca Mountain and Vicinity, Nevada." *High Level Radioactive Waste*

Management, Proceedings of the Fourth Annual International Conference, Las Vegas, Nevada, April 26-30, 1993, 2, 1554–1558. La Grange Park, Illinois: American Nuclear Society; and New York, New York: American Society of Nuclear Engineers. TIC 225018.

Eslinger, E.V. and Savin, S.M. 1973. "Mineralogy and Oxygen Isotope Geochemistry of the Hydrothermally Altered Rocks of the Ohaki-Broadlands, New Zealand, Geothermal Area." *American Journal of Science, 273,* 240–267. New Haven, Connecticut: Kline Geology Laboratory, Yale University. TIC 237356.

Essington, E.H.; Fowler, E.B.; Gilbert, R.O.; and Eberhardt, L.L. 1978. "Plutonium, Americium, and Uranium Concentrations in Nevada Test Site Soil Profiles." *Transuranium Nuclides in the Environment* (IAEA publication SM-199/87), 157–173. Vienna, Austria: International Atomic Energy Agency. TIC 236913.

Fabryka-Martin, J.T.; Flint, A.L.; Sweetkind, D.S.; Wolfsberg, A.V.; Levy, S.S.; Roemer, G.J.C.; Roach, J.L.; Wolfsberg, L.E.; and Duff, M.C. 1997. *Evaluation of Flow and Transport Models of Yucca Mountain, Based on Chlorine-36 Studies for FY97.* YMP Milestone Report SP2224M3. Los Alamos, New Mexico: Los Alamos National Laboratory. MOL.19980204.0916.

Fabryka-Martin, J.T.; Turin, H.R.; Brenner, D.; Dixon, P.R.; Liu, B.; Musgrave, J.; and Wolfsberg, A.V. 1998. *Summary Report of Chlorine-36 Studies.* Yucca Mountain Project Milestone Report 3782M. Los Alamos, New Mexico: Los Alamos National Laboratory. MOL.19971111.0609.

Fabryka-Martin, J.T.; Wolfsberg, A.V.; Dixon, P.R.; Levy, S.S.; Musgrave, J.; and Turin, H.J. 1997. *Summary Report of Chlorine-36 Studies: Systematic Sampling for Chlorine-36 in the Exploratory Studies Facility.* LA-13352-MS. YMP Milestone Report 3783M. Los Alamos, New Mexico: Los Alamos National Laboratory. MOL.19980812.0254.

Faure, G. 1986. *Principles of Isotope Geology,* second edition. New York, New York: John Wiley and Sons. TIC 237212.

Fauré, M.-H.; Sardin, M.; and Vitorge, P. 1994. "Transport of Clay Particles and Radioelements in a Salinity Gradient: Experiments and Simulations." *Radiochimica Acta: Special Issue, Proceedings of the Fourth International Conference on the Chemistry and Migration Behaviour of Actinides and Fission Products,* 451–457. München, Germany: Oldenbourg Verlag. TBD

Felmy, A.R.; Rai, D.; and Fulton, R.W. 1990. "The Solubility of $AmOHCO_3(c)$ and the Aqueous Thermodynamics of the System Na^+-Am^{3+}-HCO_3^--CO_3^{2-}-OH^--H_2O." *Radiochimica Acta 50,* 193–204. München, Germany: Oldenbourg Verlag. TIC 236870.

Feng, X. and Savin, S.M. 1993. "Oxygen Isotope Studies of Zeolites—Stilbite, Analcime, Heulandite, and Clinoptilolite: II," in "Kinetics and Mechanisms of Isotopic Exchange Between Zeolites and Water Vapor." *Geochimica et Cosmochimica Acta, 57,* 4219–4238. Oxford/New York: Pergamon Press. TIC 235399.

Finch, R.J. and Ewing, R.C. 1992. "Alteration of Natural UO_2 Under Oxidizing Conditions from Shinkolobwe, Katanga, Zaire: A Natural Analogue for the Corrosion of Spent Fuel." *Radiochimica Acta 53/54*, 391. München, Germany: Oldenbourg Verlag. TIC 237035.

Finch, R.J.; Miller, M.L.; and Ewing, R.C. 1992. "Weathering of Natural Uranyl Oxide Hydrates: Schoepite Polytypes and Dehydration Effects." *Radiochimica Acta, 53/54*, 433–443. München, Germany: Oldenbourg Verlag. TIC238032.

Fitch, B. 1979. "Sedimentation of Flocculent Suspensions: State of the Art." *AIChE Journal, 25*, 913–930. New York, New York: American Institute of Chemical Engineers. TIC 237876.

Flexser, S. and Wollenberg, H.A. 1992. "Radioelements and their Occurrence with Secondary Minerals in Heated and Unheated Tuff at the Nevada Test Site." *High Level Radioactive Waste Management: Proceedings of the Third Annual International Conference, Las Vegas, Nevada, April 12–13, 1992*, 1593–1598. La Grange Park, Illinois: American Nuclear Society. TIC 239302.

Flint, A.L. 1990. *Study Plan for Study 8.3.1.2.2.1, Characterization of the Unsaturated-Zone Infiltration.* USGS Report YMP-USGS-SP 8.3.1.2.2.1. Prepared for the U.S. Department of Energy, Office of Civilian Radioactive Waste Management. Denver, Colorado: U.S. Geological Survey. NNA.19901203.0019.

Flint, A.L. and Flint, L.E. 1994. "Spatial Distribution of Potential Near-Surface Moisture Flux at Yucca Mountain." *High Level Radioactive Waste Management: Proceedings of the Fifth Annual International Conference, Las Vegas, Nevada, May 22–26, 1994, 4*, 2352–2358. La Grange Park, Illinois: American Nuclear Society; and New York, New York: American Society of Civil Engineers. TIC 224142.

Flint, A.L.; Hevesi, J.A.; and Flint, L.E. 1996. *Conceptual and Numerical Model of Infiltration for the Yucca Mountain Area, Nevada.* Milestone Report 3GUI623M, DTN GS960908312211.003. USGS Water Resources Investigations Report 96-4123. Denver, Colorado: U.S. Geological Survey. MOL.19970409.0087.

Forster, C. and Smith, L. 1990. "Fluid Flow in Tectonic Regimes." *Fluids in Tectonically Active Regimes of the Continental Crust.* Nesbitt, B.E., Ed., 1–47. Short Course Volume 18. Ottawa, Canada: Mineralogical Association of Canada. TIC 236877.

Friedman, I. and Long, W. 1984. "Volcanic Glasses, their Origins and Alteration Processes." *Journal of Non Crystalline Solids, 67*, 127-133. Amsterdam, Netherlands: Elsevier Science Journals. TBD

Friedman, I. and Smith, R.L. 1958. "The Deuterium Content of Water in Some Volcanic Glasses." *Geochimica et Cosmochimica Acta, 15*, 218-228. Oxford/New York: Pergamon Press. TBD

Fritz, P. and Fontes, J.C. Eds. 1980. *Handbook of Environmental Isotope Geochemistry, Vol 1. The Terrestrial Environment.* New York, New York: Elsevier Press. TBD

Gaines, Jr., G.L. and Thomas, H.C. 1953. "Adsorption Studies on Clay Minerals: II. A Formulation of the Thermodynamics of Exchange Adsorption." *Journal of Chemical Physics, 21*, 714. College Park, Maryland: American Institute of Physics. TIC 238308.

Galli, E. and Alberti, A. 1975. "The Crystal Structure of Stellerite." *Bulletin Soc. Fr. Miner. Crist. 98*, 11–18. TIC 235393.

Geldon, A.L. 1993. *Preliminary Hydrogeologic Assessment of Boreholes UE-25 c#1, UE-25c #2, and UE-25c #3, Yucca Mountain, Nye County, Nevada, 1993.* USGS Water Resources Investigation Report 92-4016. DTN: GS930308312313.002. Denver, Colorado: U.S. Geological Survey. MOL.19960808.0136.

George-Aniel, B.; Leroy, J.L.; and Poty, B. 1991. "Volcanogenic Uranium Mineralizations in the Sierra Peña Blanca District, Chihuahua, Mexico: Three Genetic Models." *Economic Geology, 86*, 233–248. El Paso, Texas: Economic Geology Publishing Company. TIC 237050.

Gibbons, A.B.; Hinrichs, E.N.; and Botinelly, T. 1960. "The Role of Impermeable Rocks in Controlling Zeolitic Alteration of Tuff." USGS Professional Paper 400-B, B473-B475. Denver, Colorado: U.S. Geological Survey. TIC 217750.

Gifford, R.O. and Frugoli, D.M. 1964. "Silica Source in Soil Solutions." *Science, 145*, 386-388. Washington, D.C.: American Association for the Advancement of Science. TIC 239118.

Gilbin, A.M. and Snelling, A.A. 1983. "Application of Hydrogeochemistry to Uranium Exploration in the Pine Creek Geosyncline, Northern Territory, Australia." *Journal of Geochemical Exploration, 19*, 33–55. Amsterdam, Netherlands: Elsevier Press. TIC 237423.

Gnanapragasam, E.K. and Lewis, B.G. 1995. "Elastic Strain Energy and the Distribution Coefficient of Radium in Solid Solutions and Calcium Salts." *Geochimica et Cosmochimica Acta 59*, 5103–5111. Oxford/New York: Pergamon. TIC 236660.

Goldstein, R.H. 1986. "Re-Equilibration of Fluid Inclusions in Low-Temperature Calcium-Carbonate Cement." *Geology, 14*, 792–795. Boulder, Colorado: Geological Society of America. TIC 237435.

Goodwin, B.W.; Cramer, J.J.; and McConnell, D.B. 1989. "The Cigar Lake Uranium Deposit: An Analogue for Nuclear Fuel Waste Disposal." Appendix B in *Natural Analogues in Performance Assessments for the Disposal of Long-Lived Radioactive Wastes*, IAEA Technical Reports Series No. 304, 37–50. Vienna, Austria: International Atomic Energy Agency. TIC 224104.

Gottardi, G. and Galli, E. 1985. *Natural Zeolites*. New York, New York: Springer-Verlag. TIC 235315.

Govindaraju, K., Ed. 1989. Special Issue of *Geostandards Newsletter* XIII: 21. Vandoeuvre, France. TIC 237458.

Grasso, D.N. 1996. *Hydrology of Modern and Late Holocene Lakes, Death Valley, California.* USGS Water-Resources Investigations Report 95-4237. Denver, Colorado: U.S. Geological Survey. MOL.1970204.0218.

Greene-Kelly, R. 1955. "Dehydration of the Montmorillonite Minerals." *Mineralogy Magazine, 30,* 604–615. London, England: Oxford University Press. TIC 218582.

Grenthe, I.; Fuger, J.; Konings, R.J.M.; Lemire, R.J.; Muller, A.B.; Nguyen-Trung, C.; and Wanner, H. 1992. *Chemical Thermodynamics of Uranium: Chemical Thermodynamics Series, 1.* Amsterdam, Netherlands: Elsevier Science Publications. TIC 224074.

Gundogdu, M.N.; Bonnet-Courtois, C.; and Clauer, N. 1989. "Isotope and Chemical Signatures of Sedimentary Smectite and Diagenetic Clinoptilolite of Lacustrine Neogene Basin Near Bigadic, Western Turkey." *Applied Geochemistry, 4,* 635–644. New York, New York: Pergamon Press. TIC 237608.

Guthrie, Jr., G.D. 1992. "Biological Effects of Inhaled Minerals." *American Mineralogist, 77,* 225–243. Washington, D.C.: Mineralogical Society of America. TIC 222995; TIC 235506.

Guthrie, Jr., G.D. 1993. "Mineral Characterization in Biological Studies." *Health Effects of Mineral Dusts,* 251–273. Guthrie, Jr., G.D. and Mossman, B.T., Eds. Washington, D.C.: Mineralogical Society of America. TIC 210393.

Guthrie, Jr., G.D. and Mossman, B.T. 1993. "Health Effects of Mineral Dusts." *Reviews in Mineralogy 28,* 584. Ribbe, P.H., Ed. Washington, D.C.: Mineralogical Society of America. TIC 210393.

Guthrie, Jr., G.D.; Bish, D.L.; Chipera, S.J.; and Raymond, Jr., R. 1995. *Distribution of Potentially Hazardous Phases in the Subsurface at Yucca Mountain, Nevada.* LA-12573-MS. Los Alamos, New Mexico: Los Alamos National Laboratory. TIC 216043.

Guthrie, Jr., G.D.; McLeod, K.; Johnson, N.; and Bish, D. 1992. "Effect of Exchangeable Cation on Zeolite Cytotoxicity." Abstract in *Goldschmidt Conference Abstracts with Program, A-46.* Washington, D.C.: Geochemical Society. TIC 235666.

Guthrie, Jr., G.D.; Raymond, Jr., R.; and Chipera, S.J. 1995. "Eolian-Deposited Minerals Around Drill Hole USW SD-9, Yucca Mountain, Nevada." *High Level Radioactive Waste Management, Proceedings of the Sixth Annual International Conference, Las Vegas, Nevada, April 30-May 5, 1995,* 135-136. La Grange Park, Illinois: American Nuclear Society. MOL.19950711.0380.

Guthrie, Jr., G.D.; Raymond, Jr., R.; Chipera, S.J.; and Bish, D.L. 1993. *The Distribution of Airborne Minerals Around UZ-16.* Letter Report TWS-EES-1-09-93-009. Los Alamos, New Mexico: Los Alamos National Laboratory. TBD

Hakanen, M. and Lindberg, A. 1991. "Sorption of Neptunium Under Oxidizing and Reducing Groundwater Conditions." *Radiochimica Acta 52/53,* 147–151. München, Germany: Verlag. TIC 237041.

Hampton, C.M. and Bailey, D.K. 1984. "Gas Extraction Experiments on Volcanic Glasses." *Journal of Non Crystalline. Solids, 67*, 147-168. Amstedam, Netherlands: Elsevier Science Journals. TBD

Hansen, K. and Mossman, B.T. 1987. "Generation of Superoxide (O_2) from Alveolar Macrophages Exposed to Asbestiform and Nonfibrous Particles." *Cancer Research 47*, 1681-1686. Baltimore, Maryland: Waverly Press. TIC 234178.

Haschke, J.M. and Ricketts, T.E. 1997. "Adsorption of Water on Plutonium Dioxide." *Journal of Alloys and Compounds, 252*, 148-156. Lausanne, Switzerland: Elsevier Science Journals. TBD

Hay, R.L. 1963. "Stratigraphy and Zeolitic Diagenesis of the John Day Formation of Oregon." *University of California Publications in Geological Sciences, 42*, 199–262. Berkeley, California: University of California Press. TIC 237979.

Hay, R.L. 1966. "Zeolites and Zeolitic Reactions in Sedimentary Rocks." *Geological Society of America Special Paper, 85*. Boulder, Colorado: Geological Society of America. TIC 238294.

Hay, R.L. 1978. "Geologic Occurrence of Zeolites." *Natural Zeolites, Occurrence, Properties, Use*. Sand, L.B. and Mumpton, F.A., Eds. 135-143. New York, New York: Pergamon Press. TIC 221136.

Hay, R.L.; Pexton, R.E.; Teague, T.T.; and Kyser, T.K. 1986. "Spring-Related Carbonate Rocks, Mg Clays, and Associated Minerals in Pliocene Deposits of the Amargosa Desert, Nevada and California." *Geological Society of America Bulletin, 97*, n. 12, 1488–1503. Boulder, Colorado: Geological Society of America. TIC 201804.

Hayes, K.F.; Roe, A.L.; Brown, Jr., G.E.; Hodgson, K.O.; Leckie, J.O.; and Parks, G.A. 1987. "In-Situ X-Ray Absorption Study of Surface Complexes: Selenium Oxyanions on α-FeOOH." *Science, 238*, 783–786. Washington, D.C.: American Association for the Advancement of Science. TIC 237033.

Hazen, R.M. 1985. "Comparative Crystal Chemistry and the Polyhedral Approach," in "Microscopic to Macroscopic: Atomic Environments to Mineral Thermodynamics." Kieffer, S.W. and Navrotsky, A., Eds., *Reviews in Mineralogy, 14*, 317–345. Washington D.C.: Mineralogical Society of America. TIC 235143.

Health Effects Institute-Asbestos Research 1991. *Asbestos in Public and Commercial Buildings: A Literature Review and Synthesis of Current Knowledge.* Cambridge, Massachusetts: Health Effects Institute. TBD .

Heiken, G. and Goff, F. 1983. "Hot Dry Rock Geothermal Energy in the Jemez Volcanic Field, New Mexico." *Journal of Volcanism and Geothermal Research, 15*, 223–246. Amsterdam, Netherlands: Elsevier. TIC 237042.

Helgeson, H.C.; Kirkham, D.H.; and Flowers, G.C. 1981. "Theoretical Prediction of the Thermodynamic Behavior of Aqueous Electrolytes at High Pressures and Temperatures: IV. Calculation of Activity Coefficients, Osmotic Coefficients, and Apparent Molal and Standard

and Relative Partial Molal Properties to 600°C and 5 kb." *American Journal of Science, 281*, 1249–1516. New Haven, Connecticut: Kline Geology Laboratory, Yale University. TIC 238264.

Hem, J.D. 1978. "Redox Processes at Surfaces of Manganese Oxide and their Effects on Aqueous Metal Ions." *Chemical Geology, 21*, 199-218. New York, New York: Elsevier Scientific Publishing Company. TBD

Hemingway, B.S. and Robie, R.A. 1984. "Thermodynamic Properties of Zeolites: Low-Temperature Heat Capacities of Thermodynamic Functions for Phillipsite and Clinoptilolite: Estimates of the Thermochemical Properties of Zeolitic Water at Low Temperature." *American Mineralogist, 69*, 692–700. Washington, D.C.: Mineralogical Society of America. TIC 235353.

Henisch, H.K. 1986. "Liesegang Ring Formation in Gels." *Journal of Crystal Growth, 76*, 279-289. Amsterdam, Netherlands: North Holland Publishing Company. TBD

Heppleston, A.G. 1984. "Pulmonary Toxicology of Silica, Coal, and Asbestos." *Environmental Health Perspectives, 55*, 111–127. Research Triangle Park, North Carolina: National Institute of Environmental Health Sciences. TIC 235613.

Hevesi, J.A.; Flint, A.L.; and Flint, L.E. 1994. "Verification of a One-Dimensional Model for Predicting Shallow Infiltration at Yucca Mountain." *High Level Radioactive Waste Management, Proceedings of the Fifth Annual International Conference, Las Vegas, Nevada, May 22-26, 1994,* 2323-2332. La Grange Park, Illinois: American Nuclear Society. TIC 238118.

Hevesi, J.A.; Flint, A.L.; and Flint, L.E. 1996. "The Effect of Bedrock Properties on the Spatial Variability of Infiltration at Yucca Mountain, Nevada" *Geological Society of America - Abstracts with Program 28*, A-522. Boulder, Colorado: Geological Society of America. TBD

Hiester, N.K. and Vermeulen, T. 1952. "Saturation Performance of Ion-Exchange and Adsorption Columns." *Chemical Engineering Progress, 48*(10), 505–516. Philadelphia, Pennsylvania: American Institute of Chemical Engineers. TIC 224052.

Higgins, J.D.; Burger, P.A.; and Yang, I.C. 1997. *The One-Dimensional Compression Method for Extraction of Pore Water From Unsaturated Tuff and Effects on Pore-Water Chemistry.* USGS Water Resources Investigations Report 96-4281. Denver, Colorado: U.S. Geological Survey. MOL.19980219.0818.

Hill, R.J. and Howard, C.J. 1987. "Quantitative Phase Analysis from Neutron Powder Diffraction Data Using the Rietveld Method." *Journal of Applied Crystallography, 20*, 467–474. Copenhagen, Denmark: International Union of Crystallography. TIC 237039.

Hingston, F.J.; Posner, A.M.; and Quirk, J.P. 1971. "Competitive Adsorption of Negatively Charged Ligands on Oxide Surfaces." *Discussions of the Faraday Society, 52*, 334–351. London, England: Gurney and Jackson. TIC 237679.

Ho, C-H. and Miller, N.H. 1986. "Adsorption of Uranyl Species from Bicarbonate Solution onto Hematite Particles." *Journal of Colloid and Interface Science, 110*, 165–171. New York, New York: Academic Press. TIC 226326.

Hobart, D.E. 1990. "Actinides in the Environment." *Fifty Years with Transuranium Elements: Proceedings of the Robert A. Welch Foundation Conference on Chemical Research XXXIV, October 22–12, 1990, Houston, TX*, Chapter XIII, 379–436. Houston, Texas: The Foundation. TIC 237030.

Hobart, D.E.; Morris, D.E.; Palmer, P.D.; and Newton, T.W. 1989. "Formation, Characterization, and Stability of Pu(IV) Colloid." *Proceedings of the Topical Meeting on Nuclear Waste Isolation in the Unsaturated Zone: FOCUS '89*, 118–124. La Grange Park, Illinois: American Nuclear Society. TIC 221879.

Hoffman, J. and Hower, H. 1979. "Clay Mineral Assemblages as Low-Grade Metamorphic Geothermometers: Application to the Thrust-Faulted Disturbed Belt of Montana, U.S.A." *Society of Economic Paleontology and Mineralogy, Special Publication, 26*, 55–79. Tulsa, Oklahoma: Society of Economic Paleontologist and Mineralogists. TIC 238312.

Holland, L.M. 1990. "Crystalline Silica and Lung Cancer: A Review of Recent Experimental Evidence." *Regulatory Toxicology and Pharmacology, 12*, 224–237. New York, New York: Academic Press. TIC 234127.

Holland, T.J.B. 1989. "Dependence of Entropy on Volume for Silicate and Oxide Minerals: A Review and a Predictive Model." *American Mineralogist, 74*, 5–13. Washington, D.C.: Mineralogical Society of America. TIC 235381.

Honda, A. and Muffler, L.J.P. 1970. "Hydrothermal Alteration in Core from Research Drill Hole Y-1, Upper Geyser Basin, Yellowstone National Park, Wyoming." *American Mineralogist, 55*, 1714–1737. Washington, D.C.: Mineralogical Society of America. TIC 219076.

Hoover, D.L. 1968. "Genesis of Zeolites, Nevada Test Site." *Nevada Test Site.* Eckel, E.B., Ed. *Geological Society of Amererica Memoir, 110*, 275–284. Boulder, Colorado: Geological Society of America. TIC 221109.

Horton, D.G. 1985. "Mixed-Layer Illite/Smectite as a Paleotemperature Indicator in the Amethyst Vein System, Creede District, Colorado, USA." *Contributions to Mineralogy and Petrolology, 91*, 171–179. New York, New York: Springer Verlag. TIC 237566.

Howard, III, J.H. 1977. "Geochemistry of Selenium: Formation of Ferroselite and Selenium Behavior in the Vicinity of Oxidizing Sulfide and Uranium Deposits." *Geochimica et Cosmochimica Acta, 41*, 1665–1678. Oxford/New York: Pergamon Press. TIC 239142.

Howard, J.J. 1981. "Lithium and Potassium Saturation of Illite/Smectite Clays from Interlaminated Shales and Sandstones." *Clays and Clay Minerals, 29*, 136–142. Long Island City, New York: Pergamon Press. TIC 237555.

Howell, D.A.; Johnson, G.K.; Tasker, I.R.; O'Hare, P.A.G.; and Wise, W.S. 1990. "Thermodynamic Properties of the Zeolite Stilbite." *Zeolites, 10*, 525–531. Guildford, Surrey, England: Elsevier. TIC 238583.

Hower, J. and Altaner, S.P. 1983. "The Petrologic Significance of Illite/Smectite." *Program and Abstracts, 20th Annual Meeting, Clay Minerals Society, Buffalo, New York*, 40. Bloomington, Indiana: Clay Minerals Society. TIC 237032.

Hower, J.; Eslinger, E.V.; Hower, M.E.; and Perry, E.A. 1976. "Mechanism of Burial Metamorphism of Argillaceous Sediments: 1" in "Mineralogical and Chemical Evidence." *Geological Society of America Bulletin, 87*, 725–737. Boulder, Colorado: Geological Society of America. TIC 235953.

Hsi, C.K.D. and Langmuir, D. 1985. "Adsorption of Uranyl onto Ferric Oxyhydroxides: Application of the Surface Complexation Site-Binding Model." *Geochimica et Cosmochimica Acta, 49*, 1931–1941. Oxford/New York: Pergamon Press. TIC 224090.

Huang, C.-P. and Stumm, W. 1973. "Specific Adsorption of Cations on Hydrous γ-Al_2O_3." *Journal of Colloid and Interface Science, 43*(2), 409–420. New York, New York: Academic Press. TIC 238483.

Hubbard, C.R.; Evans, E.H.; and Smith, D.K. 1976. "Reference Intensity Ratio I/Ic for Computer-Simulated Powder Patterns." *Journal of Applied Crystallography, 9*, 169–174. Copenhagen, Denmark: International Union of Crystallography. TIC 237040.

IAEA (International Atomic Energy Agency) 1983. *Isotope Techniques in the Hydrogeological Assessment of Potential Sites for the Disposal of High-Level Radioactive Wastes.* Technical Report Series 228. Vienna, Austria: International Atomic Energy Agency. TIC 238099.

IARC (International Agency for Research on Cancer) 1971. *IARC Monographs on the Evaluation of the Carcinogenic Risk of Chemicals to Man: Volume 1.* Lyons, France: World Health Organization, International Agency for Research on Cancer. TBD

IARC 1987a. "Overall Evaluations of Carcinogenicity: An Updating of IARC Monographs Volumes 1 to 42." *IARC Monographs on the Evaluation of the Carcinogenic Risk of Chemicals to Humans: Supplement, 7.* Lyons, France: World Health Organization, International Agency for Research on Cancer. TIC 237223.

IARC 1987b. *Silica and Some Silicates: IARC Monographs on the Evaluation of the Carcinogenic Risk of Chemicals to Humans: Volume 42.* Lyons, France: World Health Organization, International Agency for Research on Cancer. TIC 226502.

IARC 1988. *Man-Made Mineral Fibres and Radon: IARC Monographs on the Evaluation of the Carcinogenic Risk of Chemicals to Humans: Volume 43.* Lyons, France: World Health Organization, International Agency for Research on Cancer. TBD

IARC 1992. *Occupational Exposures to Mists and Vapors From Strong Inorganic Acids and Other Industrial Chemicals: IARC Monographs on the Evaluation of the Carcinogenic Risk of*

Chemicals to Humans: Volume 54. Lyons, France: World Health Organization, International Agency for Research on Cancer. TIC 237837.

IARC 1997. *Silica, Some Silicates, Coal Dust and Para-Aramid Fibrilss: IARC Monographs on the Evaluation of the Carcinogenic Risk of Chemicals to Humans: Volume 68.* Lyons, France: World Health Organization, International Agency for Research on Cancer. TIC 236833.

Iijima, A. 1975. "Effect of Pore Water on Clinoptilolite-Analcime-Albite Reaction Series." *Journal of the Faculty of Science, University of Tokyo, Section II, 19,* 133–147. Tokyo, Japan: University of Tokyo. TIC 223497.

Iijima, A. 1978. "Geological Occurrences of Zeolite in Marine Environments." *Natural Zeolites: Occurrence, Properties, Use*, 175–198. Sand, L.B. and Mumpton, F.A., Eds. New York, New York: Pergamon Press. TIC 235955.

Iijima A. 1980. "Geology of Natural Zeolites and Zeolitic Rocks." *Proceedings of the Fifth International Conference on Zeolites*, 103–118. Rees, L.V., Ed. London, England: Heyden. TIC 235591.

Iler, R.K. 1979. *The Chemistry of Silica: Solubility, Polymerization, Colloid and Surface Properties, and Biochemistry.* New York, New York: John Wiley and Sons. TIC 236710.

Inoue, A. 1985. "Conversion of Smectite to Chlorite in Acidic Pyroclastic Rocks in the Hokuroku Kuroko District, Northeast Japan." *Proceedings of the International Clay Conference, Denver, Colorado*, 109. Bloomington, Indiana: Clay Minerals Society. TIC 237031.

Inoue A.; Minato, H.; and Utada, M. 1978. "Mineralogical Properties and Occurrence of Illite/Montmorillonite Mixed Layer Minerals Formed from Miocene Volcanic Glass in Waga-Omono District." *Clay Science, 5*, 123-136. Evergreen, Colorado: Clay Minerals Society. TBD

Itagaki, H.; Nakayama, S.; Tanaka, S.; and Yamawaki, M. 1992. "Effect of Ionic Strength on the Solubility of Neptunium(V) Hydroxide." *Radiochimica Acta 58/59*, 61–66. München, Germany: Verlag. MOL.19950202.0003.

Jackson, M.R. 1988. *The Timber Mountain Magmato-Thermal Event: An Intense Widespread Culmination of Magmatic and Hydrothermal Activity at the Southwestern Nevada Volcanic Field.* Master's thesis. Reno, Nevada: University of Nevada, Reno. TIC 222749.

Jaillard, B.; Guyon, A.; and Maurin, A. F. 1991. "Structure and Composition of Calcified Roots, and their Identification in Calcareous Soils." *Geoderma, 50,* 197-210. Amsterdam, Netherlands: Elsevier Scientific Publishing Company. NNA.19940523.0002.

Janecky, D.R.; Duffy, C.J.; Tait, C.D.; and Clark, D.L. 1994. *Thermochemical Data on Actinides for Modeling.* YMP Letter Report 4025. Los Alamos, New Mexico: Los Alamos National Laboratory. TBD

Janecky, D.R.; Enter, J.; Duffy, C.J.; Tait, C.D. 1995. *Modeled Actinide Solubilities and Speciation.* YMP Letter Report 3463. Los Alamos, New Mexico: Los Alamos National Laboratory. MOL.19960417.0131.

Jaurand, M-C.; Fleury, J.; Monchaux, G.; Micheline, N.; and Bignon, J. 1987. "Pleural Carcinogenic Potency of Mineral Fibers (Asbestos, Attapulgite) and their Cytotoxicity on Cultured Cells." *Journal of the National Cancer Institute, 79,* 797–804. Washington, D.C.: U.S. Department of Health, Education, and Welfare, Public Health Service, available through U.S Government Printing Office. TIC 238288.

Johnson, G.K.; Flotow, H.E.; O'Hare, P.A.G.; and Wise, W.S. 1982. "Thermodynamic Studies of Zeolites: Analcime and Dehydration Analcime." *American Mineralogist, 67,* 736–748. Washington, D.C.: Mineralogical Society of America. NNA.19920529.0018.

Johnson, G.K.; Flotow, H.E.; O'Hare, P.A.G.; and Wise, W.S. 1985. "Thermodynamic Studies of Zeolites: Heulandite." *American Mineralogist, 70,* 1065–1071. Washington, D.C.: Mineralogical Society of America. TIC 238576.

Johnson, G.K.; Tasker, I.R.; Flotow, H.E.; O'Hare, P.A.G.; and Wise, W.S. 1992. "Thermodynamic Studies of Mordenite, Dehydrated Mordenite, and Gibbsite." *American Mineralogist, 77,* 85–93. Washington, D.C.: Mineralogical Society of America. TIC 238577.

Johnson, J.W.; Oelkers, E.H.; and Helgeson, H.C. 1991. *SUPCRT92: A Software Package for Calculating the Standard Molal Thermodynamic Properties of Minerals, Gases, Aqueous Species, and Reactions from 1 to 5000 Bars and 0° to 1000°C.* Report, Earth Sciences Department, L-219. Livermore, California: Lawrence Livermore National Laboratory. TBD .

Johnson J.W.; Oelkers, E.H.; and Helgeson, H.C. 1992. "SUPCRT92: A Software Package for Calculating the Standard Molal Thermodynamic Properties of Minerals, Gases, Aqueous Species, and Reactions from 1 to 5000 Bars and 0°C to 1000°C." *Computers and Geosciences, 18,* 899-947. Oxford/New York: Pergamon Press. TIC 234273.

Joint Committee on Powder Diffraction Standards 1986. *Mineral Powder Diffraction File Data Book.* Swarthmore, Pennsylvania: International Centre for Diffraction Data. TBD

Jones, J.B. and Segnit, E.R. 1971. "The Nature of Opal: I," in "Nomenclature and Constituent Phases." *Journal of the Geological Society of Australia, 18,* 57–68. Sydney, Australia: Geological Society of Australia. TIC 223242.

Junge, C. 1979. "The Importance of Mineral Dust as an Atmospheric Constituent." *Saharan Dust: Mobilization, Transport, Deposition,* 49–60. Morales, C., Ed. New York, New York: John Wiley and Sons. MOL.19940927.0001.

Kano, K. 1983. "Ordering of Opal-CT in Diagenesis." *Geochemical Journal, 17,* 87–93. Nagoya, Japan: Geochemical Society of Japan. TIC 226647.

Kano, K. and Taguchi, K. 1982. "Experimental Study on the Ordering of Opal-CT." *Geochemical Journal, 16,* 33–41. Nagoya, Japan: Geochemical Society of Japan. TIC 224648.

Karlen, I.; Olsson, I.U.; Kallberg, P.; and Kilicci, S. 1966. "Absolute Determination of the Activity of Two C-14 Dating Standards." *Arkiv Geofysik,* 6, 465-471. Denmark. TIC 238506.

Katz, J.J.; Seaborg, G.T.; and Morss, L.R., Eds. 1986. *The Chemistry of the Actinide Elements.* London, England: Chapman and Hall. TBD

Keeney-Kennicutt, W.L. and Morse, J.W. 1985. "The Redox Chemistry of Pu(V)O21 Interaction with Common Mineral Surfaces in Dilute Solutions and Seawater." *Geochimica et Cosmochimica Acta, 49,* 2577–2588. Oxford/New York: Pergamon Press. TIC 237000.

Keith, T.E.C.; White, D.E.; and Beeson, M.H. 1978. *Hydrothermal Alteration and Self-Sealing in Y-7 and Y-8 in Northern Part of Upper Geyser Basin, Yellowstone National Park, Wyoming.* USGS Professional Paper 1054-A. Denver, Colorado: U.S. Geological Survey. TIC 219043.

Kennedy, G.C. 1955. "Some Aspects of the Role of Water in Rock Melts, in Crust of the Earth." Poldervaart, A., Ed. *Geological Society of America – Special Paper 62,* 489-504. Boulder, Colorado: Geological Society of America. TBD

Kennedy, T.P.; Rawlings, W. Jr.; Baser, M.; and Tockman, M. 1983. "Pneumoconiosis in Georgia Kaolin Workers." *American Review of Respiratory Disease, 127,* 215–220. Baltimore, Maryland: National Tuberculosis Association. TIC 234119.

Kerrisk, J.F. 1983. *Reaction-Path Calculations of Groundwater Chemistry and Mineral Formation at Rainier Mesa, Nevada.* LA-9912-MS, UC-70. Los Alamos, New Mexico: Los Alamos National Laboratory. NNA.19870310.0007.

Kerrisk, J.F. 1987. *Groundwater Chemistry at Yucca Mountain, Nevada, and Vicinity.* LA-10929-MS, UC-70. Los Alamos, New Mexico: Los Alamos National Laboratory. NNA.19870507.0017.

Kieft, T.L.; Kovacik, W.P; Ringleberg, D.B.; White, D.C.; Haldeman, D.L.; and Hersman, L.E. 1997. "Limiting Factors to Microbial Activity in Volcanic Tuff at Yucca Mountain." *Applied and Environmental Microbiology, 63*(8), 3128-3133. Washington, D.C.: American Society for Microbiology. TIC 236444.

Kim, S.T. and O'Neil, J.R. 1997. "Equilibrium and Nonequilibrium Isotope Effects in Synthetic Carbonates." *Geochimica et Cosmochimica Acta, 61,* 3461-3475. Oxford/New York: Pergamon Press. TIC 236999.

Kim, J.I. and Sekine, T. 1991. "Complexation of Neptunium(V) with Humic Acid." *Radiochimica Acta, 55,* 187–192. München, Germany: Verlag. MOL.19950118.0149; MOL.19950202.0023.

Kim, J.I.; Zeh, P.; and Delakovitz. 1992. "Chemical Interactions of Actinide Ions with Groundwater Colloids in Groleben Aquifer Systems." *Radiochimica Acta 58/59,* 147–154. München, Germany: Verlag. TBD

Kinniburgh, D.G.; Barker, J.A.; and Whitfield, M.J. 1983. "A Comparison of Some Simple Adsorption Isotherms for Describing Divalent-Cation Adsorption by Ferrihydrite." *Journal of Colloid and Interface Science, 95*, 370–384. New York, New York: Academic Press. TIC 236980.

Kinniburgh, D.G.; Jackson, M.L.; and Syers J.K. 1976. "Adsorption of Alkaline-Earth, Transition, and Heavy-Metal Cations by Hydrous Oxide Gels of Iron and Aluminum." *Soil Science Society of America Journal, 40*, 796–799. Madison, Wisconsin: Soil Science Society of America. TIC 239884.

Kitten, J.; Vaniman, D.T.; Triay, I.; and Thompson, J. 1997. *Comparative Microautoradiography and Batch Sorption Experiments on Three Principal Lithologies from Yucca Mountain, Nevada.* Milestone Report SP341CM4. Los Alamos, New Mexico: Los Alamos National Laboratory. TBD

Klappa, C.F. 1979. "Calcified Filaments in Quaternary Calcretes: Organo-Mineral Interactions in the Subaerial Vadose Environment." *Journal of Sedimentary Petrology, 49*, 955-968. Tulsa, Oklahoma: Society of Economic Paleontologists and Mineralogists. TIC 224402.

Klappa, C.F. 1980. "Brecciation Textures and Tepee Structures in Quaternary Calcrete (Caliche) Profiles from Eastern Spain: the Plant Factor in their Formation." *Geological Journal, 15*, 81-89. New York, New York: John Wiley and Sons, Ltd. TIC 224403.

Klug, H.P. and Alexander, L.E. 1974. *X-ray Diffraction Procedures for Polycrystalline and Amorphous Materials.* New York, New York: John Wiley and Sons. TBD

Knauss, K.G. and Beiriger, W.B. 1984. *Report on Static Hydrothermal Alteration Studies of Topopah Spring Tuff Wafers in J-13 Water at 150°C.* UCRL-53576. Berkeley, California: Lawrence Livermore National Laboratory. HQS.19880517.2007.

Knauss, K.G. and Peifer, D. 1986. *Reaction of Vitric Topopah Spring Tuff and J-13 Groundwater Under Hydrothermal Conditions Using Dickson-Type Gold-Bag Rocking Autoclaves.* UCRL-53795. Livermore, California: Lawrence Livermore National Laboratory. NNA.19891102.0117.

Knight, S.D. and Lawrence, F.O. 1988. *Sorption of Nickel and Neptunium in Tuff Using Groundwaters of Various Compositions.* Letter Report on Nevada Nuclear Waste Storage Investigations Milestone R505. Los Alamos, New Mexico: Los Alamos National Laboratory. NNA.19881028.0004.

Knight, S.D. and Thomas, K.W. 1987. *Sorption of Radionuclides Using Different Groundwater Compositions.* Letter Report on Nevada Nuclear Waste Storage Investigations Milestone M316. Los Alamos, New Mexico: Los Alamos National Laboratory. MOL.1998.06250236; NNA.19870902.0098.

Kononov, V. and Polyak, B. 1982. "Identification of the Juvenile Component in Modern Hydrothermal Systems." *Geochemistry International, 19*, 119–133. Washington, D.C.: American Geophysical Union. TIC 237028.

Korotev, R.L. 1991. "Chemical Stratigraphy of Two Regolith Cores from the Central Highlands of the Moon." *Proceedings of the 21st Lunar and Planetary Science Conference, Houston, Texas, V*, 229–289. Sharpton, L. and Ryder, G. Eds. Houston, Texas: Lunar and Planetary Institute. TIC 224404.

Kung, K.S. and McBride, M.B. 1989a. "Adsorption of Para-Substituted Benzoates on Iron Oxides." *Soil Science Society of America Journal, 53*, 1673–1678. Madison, Wisconsin: Soil Science Society of America. TIC 237036.

Kung, K.S. and McBride, M.B. 1989b. "Coordination Complexes of Para-Hyroxybenzoate on Iron Oxides." *Clays and Clay Minerals, 37*, 333–340. Bloomington, Indiana: Clay Minerals Society. TIC 236863.

Kung, K.S. and McBride, M.B. 1991. "Bonding of Chlorophenols on Iron and Aluminum Oxides." *Environmental Science and Technology, 25*, 702–709. Washington, D.C.: American Chemical Society. TIC 236864.

Kunze, G.W. and Dixon, J.B. 1986. "Pretreatment for Mineralogical Analysis." *Method of Soil Analysis*, Part 1. Klute, A., Ed. Madison, Wisconsin: Soil Science Society of America. TIC 236860.

Laaksoharju, M.; Degueldre, C.; and Skårman, C. 1995. *Study of Colloids and their Importance for Repository Performance Assessment.* SKB Technical Report 95-24. Stockholm, Sweden: Svensk Karnbransleforsojning AB/Avdelning KBS. TIC 223428.

Landmark Graphics Corporation 1995. *Stratigraphic Geocellular Modeling Reference Guide, December 1995.* TBD

Langmuir, D. 1997. *Aqueous Environmental Geochemistry.* Upper Saddle River, New Jersey: Prentice Hall. TIC 237107. TBD

Langmuir, D. and Riese, A.C. 1985. "The Thermodynamic Properties of Radium." *Geochimica et Cosmochimic Acta, 49,* 1593-1601. Oxford/New York: Pergamon Press. TBD

Lappin, A.R.; VanBuskirk, R.G.; Enniss, D.O.; Butters, S.W.; Prater, F.M.; Muller, C.B.; and Bergosh, J.L. 1982. *Thermal Conductivity, Bulk Properties, and Thermal Stratigraphy of Silicic Tuffs from the Upper Portion of Hole USW-G1, Yucca Mountain, Nye County, Nevada.* SAND81-1873. Albuquerque, New Mexico: Sandia National Laboratories. TIC 202545.

Lasaga, A.C. 1984. "Chemical Kinetics of Water-Rock Interactions." *Journal Geophysical Research, 89*, 4009–4025. Washington, D.C.: American Geophysical Union. TIC 224110.

Lasaga, A.C. and Blum, A.E. 1986. "Surface Chemistry, Etch Pits, and Mineral-Water Reactions." *Geochimica et Cosmochimica Acta, 50*, 2363–2379. Oxford/New York: Pergamon Press. TIC 235388.

Lasaga, A.C.; Ganor, J.; and MacInnis, I.N. 1994. *Progress Report on the Kinetic Measurements of the Reactions of the Silicates at the Yucca Mountain Potential Repository Site* (August, 1994). Los Alamos, New Mexico: Los Alamos National Laboratory. TBD .

Lasaga, A.C.; Soler, J.M.; Ganor, J.; Burch, T.E.; and Nagy, K.L. 1994 . "Chemical Weathering Rate Laws and Global Geochemical Cycles." *Geochimica et Cosmochimica Acta, 58*, 2361-2386. Oxford/New York: Pergamon Press. TIC 237441.

Lawrence, J. 1970. *$^{18}O/^{16}O$ and D/H Ratios of Soils, Weathering Zones, and Clay Deposits.* Pasedena, California: California Institute of Technology. TIC 237238.

Lee, M.; Aronson, J.L.; and Savin, S.M. 1989. "Timing and Conditions of Permian Rotliegende Sandstone Diagenesis, Southern North Sea: K/Ar and Oxygen Isotope Data." *American Association of Petroleum Geologists Bulletin, 73*, 195–215. Tulsa, Oklahoma: American Association of Petroleum Geologists. TIC 237058.

Lemire, R.J. and Garisto, F. 1989. *The Solubililty of U, Np, Pu, Th, and Tc in a Geological Disposal Vault for Used Nuclear Fuel.* Atomic Energy of Canada Report ROE 1LO, AECL-10009. Pinawa, Manitoba, Canada: Atomic Energy of Canada. TIC 213161.

Lemire, R.J. and Tremaine, P.R. 1980. "Uranium and Plutonium Equilibria in Aqueous Solutions to 200°C." *Journal of Chemical and Engineering Data, 25*, 361–370. Washington, D.C.: American Chemical Society. TIC 222175.

Levy, S.S. 1984a. "Studies of Altered Vitrophyre for the Prediction of Nuclear Waste Repository-Induced Thermal Alteration," in "Scientific Basis for Nuclear Waste Management VII". McVay, G.L., Ed. *Materials Research Society Symposium Proceedings, 26*, 959–966. New York, New York: Elsevier Science Publishing Company. TIC 210392.

Levy, S.S. 1984b. "Petrofabric Constraints of the Age of Zeolitization at Yucca Mountain." *Research and Development Related to the Nevada Nuclear Waste Storage Investigations, July 1-Sep. 30, 1983.* Bryant, E.A. and Vaniman, D.T., Eds, 67–76. Progress Report LA-10006-PR. Los Alamos, New Mexico: Los Alamos National Laboratory. HQS.19880517.1962.

Levy, S.S. 1984c. *Petrology of Samples from Drill Holes USW H-3, H-4, and H-5, Yucca Mountain.* LA-9706-MS. Los Alamos, New Mexico: Los Alamos National Laboratory. NNA.19870519.0048.

Levy, S.S. 1985. "Episodic Zeolitization of Silicic Volcanic Tuff at Yucca Mountain, Nye County, Nevada." *Geological Society of America, Abstracts with Programs, 17*(6), 366. Boulder, Colorado: Geological Society of America. TIC 236911.

Levy, S.S. 1991. "Mineralogic Alteration History and Paleohydrology at Yucca Mountain, Nevada." *High Level Radioactive Waste Management, Proceedings of the Second Annual International Conference, Las Vegas, Nevada, April 28-May 3, 1991*, 477–485. La Grange Park, Illinois: American Nuclear Society; and New York, New York: American Society of Civil Engineers. TIC 217642.

Levy, S.S. 1992. "Natural Gels in the Yucca Mountain Area, Nevada, USA." *Applied Clay Science, 7*, 79–85. New York, New York: Elsevier. TIC 225196.

Levy, S.S. 1993a. "Surface-Discharging Hydrothermal Systems at Yucca Mountain—Examining the Evidence," in "Scientific Basis for Nuclear Waste Management XVI," Interrante, C.G. and Pabalan, R.T., Eds. *Materials Research Society Symposium Proceedings, 294*, 543–548. Pittsburgh, Pennsylvania: Materials Research Society. TIC 224597.

Levy, S.S. 1993b. Los Alamos National Laboratory Notebook TWS-ESS-1-10-82-19, p. 262. Los Alamos, New Mexico: Los Alamos National Laboratory. TBD

Levy, S.S. 1993c. Los Alamos National Laboratory Notebook TWS-EES-1-3-93-6, p. 8. Los Alamos, New Mexico: Los Alamos National Laboratory. TBD

Levy, S.S. 1996a. Los Alamos National Laboratory Field Notebook LA-EES-1-NBK-96-001, p. 46. Los Alamos, New Mexico: Los Alamos National Laboratory. TBD

Levy, S.S. 1996b. Los Alamos National Laboratory Field Notebook LA-EES-1-NBK-96-002, p. 8. Los Alamos, New Mexico: Los Alamos National Laboratory. TBD

Levy, S.S. and Chipera, S.J. 1997. *Updated Mineralogic and Hydrologic Analysis of the PTn Hydrogeologic Unit, Yucca Mountain, Nevada, as A Barrier to Flow.* YMP Milestone Report SP321DM4. Los Alamos, New Mexico: Los Alamos National Laboratory. MOL.19980520.0150.

Levy, S.S. and O'Neil, J.R. 1989. "Moderate-Temperature Zeolitic Alteration in a Cooling Pyroclastic Deposit." LA000000000067.001. *Chemical Geology, 76*, 321–326. Amsterdam/New York: Elsevier. TIC 223793.

Levy, S.S. and Valentine, G. 1993. "Natural Alteration in the Cooling Topopah Spring Tuff, Yucca Mountain, Nevada, as an Analog to a Waste-Repository Hydrothermal Regime." *Focus '93: Proceedings of the Topical Meeting on Site Characterization and Model Validation, Las Vegas, Nevada*, 145–149. La Grange Park, Illinois: American Nuclear Society. TIC 222055.

Levy, S.S.; Carlos, B.A; and Claassen, H.C. 1986. "Smectite-Zeolite Fracture Filling Caught in the Act?" *Transactions of the American Geophysical Union,* 67, 1253. Washington, D.C.: American Geophysical Union. TIC 238347.

Levy, S.S.; Norman, D.I.; and Chipera, S.J. 1996. "Alteration History Studies in the Exploratory Studies Facility, Yucca Mountain, Nevada, USA" in "Scientific Basis for Nuclear Waste Management XIX." Murphy, W.M. and Knecht, D.A., Eds. *Materials Research Society Symposium Proceedings 412*, 783–790. Pittsburgh, Pennsyvlania: Materials Research Society. TIC 225198.

Levy, S.S.; Sweetkind, D.; Fabryka-Martin, J.; Dixon, P.; Roach, J.; Wolfsberg, L.; Elmore, E.; and Sharma, P. 1997. *Investigations of Structural Controls and Mineralogic Associations of Chlorine-36 Fast Pathways in the ESF.* YMP milestone report SP2301M4. Los Alamos, New Mexico: Los Alamos National Laboratory. TIC 233991.

Liang, L. and McCarthy, J.F. 1995. "Colloidal Transport of Metal Contaminants in Groundwater." *Metal Speciation and Contamination of Soil*, 86–112. Hung, P.; Bailey, G.W.; and Boweres, A.R., Eds. Boca Raton, Florida: Lewis Publishers. TIC 236979.

Lieser, K.H. and Bauscher, C. 1988. "Technetium in the Hydrosphere and in the Geosphere. II. Influence of pH, of Complexing Agents, and of Some Minerals on the Sorption of Technetium." *Radiochimica Acta, 44/45*, 125–128. München, Germany: R. Oldenbourg Verlag. TIC 237071.

Lieser, K.H. and Muhlenweg, U. 1988. "Neptunium in the Hydrosphere and in the Geosphere: 1. Chemistry of Neptunium in the Hydrosphere and Sorption of Neptunium from Groundwaters on Sediments Under Aerobic and Anaerobic Conditions." *Radiochimica Acta, 43*, 27–35. München, Germany: R. Oldenbourg Verlag. TIC 236783.

Lindberg, R.D. and Runnells, D.D. 1984. "Groundwater Redox Reactions: An Analysis of Equilibrium State Applied to Eh Measurements and Geochemical Modeling." *Science, 225*, 925-927. Washington, D.C.: American Association for the Advancement of Science. TIC 224111.

Liou, J.G. 1971. "Analcime Equilibria." *Lithos, 4*, 389-402. New York/Amsterdam: Elsevier Scientific Publishing Company. TIC 235954.

Lipman, P.W. 1966. "Water Pressures During Differentiation and Crystallization of Some Ash-Flow Magmas from Southern Nevada." *American Journal of Science, 264*, 810–826. New Haven, Connecticut: Kline Geology Laboratory, Yale University. TIC 236812.

Lipman, P.W. 1971. "Iron-Titanium Oxide Phenocrysts in Compositionally Zoned Ash-Flow Sheets from Southern Nevada." *Journal of Geology*, 79, 438–456. Chicago, Illinois: University of Chicago Press. TIC 235394.

Lipman, P.W. and McKay, E. 1965. Geologic Map of the Topopah Spring SW Quadrangle. USGS Map GQ-439. Denver, Colorado: U.S. Geological Survey. TIC 212352.

Lipman, P.W.; Christiansen, R.L.; and O'Connor, J.T. 1966. *A Compositionally Zoned Ash-Flow Sheet in Southern Nevada*. USGS Professional Paper 524-F. Denver, Colorado: U.S. Geological Survey. TIC 219972.

Loeven, C. 1993. *Summary and Discussion of Hydrologic Data from the Calico Hills Nonwelded Hydrologic Unit at Yucca Mountain, Nevada*. LA-12376-MS. Los Alamos, New Mexico: Los Alamos National Laboratory. NNA.19921116.0001

Longworth, G.; Cross, C.; Degueldre, C.; and Ivanovich, M. 1989. *Interlaboratory Study of Sampling and Characterisation Techniques for Groundwater Colloids*. Harwell Laboratory Report AERE R 13393. England: Harwell Laboratory. TBD

Low, R.B.; Leffingwell, C.M.; and Bulman, C.A. 1980. "Effects of Kaolinite on Amino-Acid Transport and Incorporation into Protein by Rabbit Pulmonary Alveolar Macrophages." *Archives of Environmental Health, 35*, 217–223. Washington, D.C.: Heldref Publications. TIC 235614.

Lu, N.; Amter, S.; and Ross, B. 1991. "Effect of a Low-Permeability Layer on Calculated Gas Flow at Yucca Mountain" *Proceedings of the Second International Conference on High Level Waste Management*, 853-860. La Grange Park, Illinois: America Nuclear Society. TIC 234923.

Ludwig, K.R.; Peterman, Z.E.; Simmons, K.R.; and Gutentag, E.D. 1993. "$^{234}U/^{238}U$ Ratios as a Groundwater Flow Tracer, SW Nevada–SE California." *High Level Radioactive Waste Management, Proceedings of the Fourth Annual International Conference, Las Vegas, Nevada, April 26-30, 1993,* 1567–1572. La Grange Park, Illinois: American Nuclear Society; and New York, New York: American Society of Civil Engineers. TIC 224405.

Machette, M.N. 1985. *Calcic Soils of the Southwestern United States.* Geological Society of America Special Paper 203, 1-21. Weide, D.L., Ed. Las Vegas, Nevada: University of Nevada. TIC 223206.

MacInnis, I.N.; Wilkin, R.T.; Mercy, M.A.; Barnes, H.L.; and Lasaga, A.C. 1995. *A Rate Law for Clinoptilolite Dissolution/Precipitation at 50–125°C in Basic Solutions.* YMSCP Milestone Report LA3445, LA-EES-1-TIP-95-017. Los Alamos, New Mexico: Los Alamos National Laboratory. MOL.19970625.0088.

Mack, G.H. and James, W.C. 1992. "Calcic Paleosols of the Plio-Pleistocene Camp Rice and Palomas Formations, Southern Rio Grande Rift, USA." *Sedimentary Geology, 77,* 89-109. Amsterdam/New York: International Association of Sedimentologists. NNA.19940523.0007.

Maldonado, F. and Koether, S.L. 1983. *Stratigraphy, Structure and Some Petrographic Features of Tertiary Volcanic Rocks at the USW G-2 Drill Hole, Yucca Mountain, Nye County, Nevada.* USGS-OFR 83-732. Denver, Colorado: U.S. Geological Survey. NNA.19870506.0143.

Malmberg, G.T. and Eakin, T.E. 1962. *Groundwater Appraisal of Sarcobatus Flat and Oasis Valley, Nye and Esmeralda Counties, Nevada.* Groundwater Resources-Reconnaissance Series Report 10. Carson City, Nevada: Nevada Department of Conservation and Natural Resources. TIC 208666.

Marfunin, A.S. 1979. *Spectroscopy, Luminescence and Radiation Centers in Minerals.* Berlin, Germany: Springer-Verlag. TBD

Marks, J. and Nagelschmidt, G. 1959. "Study of the Toxicity of Dust with Use of the In Vitro Dehydrogenase Technique." *A.M.A. Archives of Industrial Health, 20,* 37,383–43,389. Chicago, Illinois: American Medical Association. TIC 235615.

Marshall, B.D. 1997. "Hydrologic Inferences from Strontium Isotopes in Pore Water from the Unsaturated Zone at Yucca Mountain, Nevada." *EOS, 78*(46), F308, 1997 Fall Meeting Supplement, Transactions. Washington, D.C.: American Geophysical Union. TIC 237795.

Marshall, B.D.; Futa, K.; and Peterman, Z.E. 1997. "Hydrologic Inferences from Strontium Isotopes in Pore Water from the Unsaturated Zone at Yucca Mountain, Nevada." *EOS: Transactions, American Geophysical Union, 1997 Fall Meeting, San Francisco, California, December 8-12, 1997, 78,* F308. Washington, D.C.: American Geophysical Union. TIC 237795.

Marshall, B.D.; Peterman, Z.E.; and Stuckless, J.S. 1993. "Strontium Isotopic Evidence for a Higher Water Table at Yucca Mountain, Nevada." *High Level Radioactive Waste Management, Proceedings of the Fourth Annual International Conference, Las Vegas, Nevada, April 26-30, 1993,* 1948–1952. La Grange Park, Illinois: American Nuclear Society. TIC 225324.

Matyskiela, W. 1997. "Silica Redistribution and Hydrologic Changes in Heated Fractured Tuff." *Geology, 25,* 1115–1118. Boulder, Colorado: Geological Society of America. TIC 236809.

Maya, L. 1982. "Sorbed Uranium(VI) Species on Hydrous Titania, Zirconia, and Silica Gel." *Radiochimica Acta, 31,* 147–151. München, Germany: Verlag. TIC 236887.

Mazaud, A.; Laj, C.; Bard, E.; Arnold, M.; and Tric, E. 1991. "Geomagnetic Control of ^{14}C Production Over the Last 80 ky: Implications for the Radiocarbon Time Scale." *Geophysical Research Letters, 18,* 1885–1888. Washington, D.C.: American Geophysical Union. TIC 236813.

McBride, M.B. 1994. *Environmental Chemistry of Soils,* 71–72. New York, New York: Oxford University Press. TIC 236919.

McBride, M.B. and Wesselink, B. 1988. "Chemisorption of Catechol on Gibbsite, Boehmite, and Noncrystalline Alumina Surfaces." *Environmental Science and Technology, 22,* 703–708. Easton, Pennsylvania: American Chemical Society. TIC 237431.

McCarthy, J. and Degueldre, C. 1993. "Sampling and Characterisation of Groundwater Colloids for Studying their Role in Subsurface Transport of Contaminants." *Environmental Particles, II.* Buffle, J. and Van Leeuwen, H., Eds., Chapter 6, 247–315. Boca Raton, Florida: Lewis Publishers. NNA.19930607.0075.

McCarthy, J.F. and Zachara, J.M. 1989. "Subsurface Transport of Contaminants: Mobile Colloids in the Subsurface Environment May Alter the Transport of Contaminants." *Environmental Science and Technology, 23*(5), 496–502. Easton, Pennsylvania: American Chemical Society. TIC 224876.

McCubbin, D.G. and Patton, J.W. 1981. "Burial Diagenesis of Illite/smectite: The Kinetic Model." *Annual Meeting of the American Assocociation of Petroleum Geologists, San Francisco, California.* Tulsa, Oklahoma: American Association of Petroleum Geologists. TBD

McKinley, P.W. and Oliver, T.A. 1994. *Meteorological, Stream-Discharge, and Water-Quality Data for 1986-1991 from Two Small Basins in Central Nevada.* USGS-OFR-93-651. Denver, Colorado: U.S. Geological Survey. NNA.19940114.0099.

McKinley, P.W. and Oliver, T.A. 1995. *Meteorological, Stream-Discharge, and Water-Quality Data for 1992 from Two Small Basins in Central Nevada.* USGS-OFR-94-456. Denver, Colorado: U.S. Geological Survey. MOL.19950124.0284.

McKinley, P.W.; Long, M.P.; and Benson, L.V. 1991. *Chemical Analyses of Water From Selected Wells and Springs in the Yucca Mountain Area, Nevada, and Southeastern California.* USGS-OFR-90-355. Denver, Colorado: U.S. Geological Survey. NNA.19901031.0004.

McLaughlin, J.K.; Jing-Qiong, C.; Dosemeci, M.; Rong-An, C.; Rexing, S.H.; Zhien, W.; Hearl, F.J.; McCawley, M.A.; and Blot, W.J. 1992. "A Nested Case-Control Study of Lung Cancer Among Silica Exposed Workers in China." *British Journal of Industrial Medicine, 49*, 167–171. England. TIC 234118.

Means, J.L.; Crerar, D.A.; and Borcsik M.P. 1978. "Adsorption of Co and Selected Actinides by Mn and Fe Oxides in Soils and Sediments." *Geochimica et Cosmochimica Acta, 42*, 1763–1773. Oxford, England: Pergamon Press. TIC 218336.

Means, J.L.; Maest, A.S.; and Crerar, D.A. 1983. *Organic Geochemistry of Deep Groundwaters and Radionuclide Partitioning Experiments Under Hydrothermal Conditions.* Office of Nuclear Waste Isolation Report ONWI-448. Columbus, Ohio: Battelle Memorial Institute. TIC 209098.

Meijer, A. 1987. *Investigations of Natural Geologic and Geochemical Analogs in Relation to a Potential Nuclear Waste Repository at Yucca Mountain, Nevada.* Los Alamos National Laboratory Report. Los Alamos, New Mexico: Los Alamos National Laboratory. NNA.19900112.0350.

Meijer, A. 1990. *Yucca Mountain Project Far-Field Sorption Studies and Data Needs.* LA-11671-MS. Los Alamos, New Mexico: Los Alamos National Laboratory. MOL.19980508.1113.

Meijer, A. 1992. "A Strategy for the Derivation and Use of Sorption Coefficients in Performance Assessment Calculations for the Yucca Mountain Site." *Proceedings of the DOE/Yucca Mountain Site Characterization Project Radionuclide Adsorption Workshop at Los Alamos National Laboratory, September 11–12, 1990*, 9–40. LA-12325-C. Los Alamos, New Mexico: Los Alamos National Laboratory. NNA.19920421.0117.

Meijer, A. 1993. "Far-Field Transport of Carbon Dioxide: Retardation Mechanisms and Possible Validation Experiments." *Proceedings of the Topical Meeting on Site Characterization and Model Validation, Focus '93, September 26–29, 1993, Las Vegas, Nevada.* La Grange Park, Illinois: American Nuclear Society. TIC 210958.

Meijer, A.; Triay, I.; Knight, S.; and Cisneros, M. 1989. "Sorption of Radionuclides on Yucca Mountain Tuffs. *Proceedings of the Topical Meeting on Nuclear Waste in the Unsaturated Zone, Focus '89: September 17–21, 1989, Las Vegas, Nevada*, 113–117. La Grange Park, Illinois: American Nuclear Society. TIC 222552.

Merchant, S. and Rosauer, E. 1969. "Layering Phenomena in Colloidal Suspensions." *Clays and Clay Minerals, 17*, 289–299. London, England: Pergamon Press. TIC 237511.

Michael, R.L. 1989. *Tritium Deposition in the Continental United States, 1953-1983.* USGS Water Resources Investigation Report 89-4072. Denver, Colorado: U.S. Geological Survey. TBD

Miekeley, N. Counthinho de Jesus, H.; Porto da Silveira, C.; and Degueldre, C. 1992. "Chemical and Physical Characterization of Suspended Particles and Colloids in Waters from the Osamu Utsumi Mine and Morro-do-Ferro Analog Study Sites, Poços-de-Caldas, Brasil." *Journal of Geochemical Exploration, 45*, 409–437. Amsterdam/New York: Elsevier. TIC 206355.

Miller, H. 1941. *Descriptive Geometry.* London, England: John Wiley and Sons, Inc. TBD

Milne, W.K.; Benson, L.V.; and McKinley, P.W. 1987. *Isotope Content and Temperature of Precipitation in Southern Nevada, August 1983-August 1986.* USGS-OFR-87-463. Denver, Colorado: U.S. Geological Survey. NNA.19900601.0002.

Mizutani, S. 1966. "Transformation of Silica Under Hydrothermal Conditions. *Journal of Earth Sciences, Nagoya University, 14*, 56–88. Japan: Nagoya University. TIC 223899.

Mizutani, S. 1970. "Silica Minerals in the Early Stage of Diagenesis." *Sedimentology, 15*, 419-436. Oxford/Boston: Blackwell. TIC 222325.

Mizutani, S. 1977. "Progressive Ordering of Cristobalitic Silica in the Early Stages of Diagenesis." *Contributions to Mineralogy and Petrology, 61*, 129-140. New York, New York: Springer Verlag. TIC 224653.

Moncure, G.K.; Surdam, R.C.; and McKaque, H.L. 1981. "Zeolite Diagenesis Below Pahute Mesa, Nevada Test Site." *Clays and Clay Minerals, 29*, 385–396. Long Island City, New York: Pergamon Press. TIC 221552.

Monger, H.C.; Daugherty, L.A.; Lindemann, W.C.; and Liddell, C.M. 1991. "Microbial Precipitation of Pedogenic Calcite." *Geology, 19*, 997-1000. Boulder, Colorado: Geological Society of America. NNA.19940523.0010.

Montazer, P.; Weeks, E.P.; Thamir, F.; Yard, S.N.; and Hofrichter, P.B. 1985. "Monitoring the Vadose Zone in Fractured Tuff, Yucca Mountain, Nevada." *Proceedings of the National Water Well Association Conference on Characterization and Monitoring of the Vadose (Unsaturated) Zone, Denver, Colorado, November 19-21, 1985*, 439-469. Denver, Colorado: National Water Well Association. TIC 201366.

Mook, W.G. 1980. "Carbon-14 in Hydrological Studies." *Handbook of Environmental Isotope Geochemistry: Vol. 1. The Terrestrial Environment*, Chapter 2, 49-74. Fritz, P. and Fontes, J.C., Eds. New York, New York: Elsevier Press. TIC 225816.

Moskin, A.I. 1971. "Hydrolytic Behavior of Neptunium(IV,V,VI)." *Soviet Radiochemistry, 13*, 700. MOL.19950202.0016.

Mossman, B.T. and Craighead, J.E. 1982. "Comparative Cocarcinogenic Effects of Crocidolite Asbestos, Hematite, Kaolin, and Carbon in Implanted Tracheal Organ Cultures." *The Annals of Occupational Hygiene, 26*, 553–567. Oxford: Elsevier. MOL.19940927.0003.

Mossman, B.T.; Hansen, K.; Marsh, J.P.; Brew, M.E.; and Petruska, J. 1989. "Mechanisms of Fibre-Induced Superoxide Release from Alveolar Macrophages and Induction of Superoxide

Dismutase in the Lungs of Rats Inhaling Crocidolite." *Non-Occupational Exposure to Mineral Fibres, 90*, 81-92. Bignon, J., Peto, J., and Saracci, R., Eds. Lyons, France: International Agency for Research on Cancer. TIC 237364.

Mower, T.E.; Higgins, J.D.; and Yang, I.C. 1991. "Pore-Water Extraction from Unsaturated Tuffs Using One-Dimensional Compression." *High Level Radioactive Waste Management, Proceedings of the Second Annual International Conference, Las Vegas, Nevada, April 28-May 3, 1991, 2*, 989-1006. La Grange Park, Illinois: American Nuclear Society, and New York, New York: American Society of Civil Engineers. TIC 234969.

Mower, T.E.; Higgins, J.D.; Yang, I.C.; and Peters, C.A. 1994. *Pore-Water Extraction from Unsaturated Tuff by Triaxial and One-Dimensional Compression Methods, Nevada Test Site.* USGS Water Resources Investigations Report 93-4144. Denver, Colorado: U.S. Geological Survey. NNA.19940621.0002.

Moyer, T.C. and Geslin, J.K. 1995. *Lithostratigraphy of the Calico Hills Formation and the Prow Pass Tuff (Crater Flat Group) at Yucca Mountain, Nevada.* USGS-OFR-94-460. Denver, Colorado: U.S. Geological Survey. GS940608314211.028; MOL.19941208.0003.

Moyer, T.C.; Geslin, J.K.; and Flint, L.E. 1996. *Stratigraphic Relations and Hydrologic Properties of the Paintbrush Tuff Nonwelded (PTn) Hydrologic Unit, Yucca Mountain, Nevada.* USGS-OFR-95-397. Denver, Colorado: U.S. Geological Survey. GS950708314211.033; MOL.19970204.0216.

Mumpton, F.A. 1960. "Clinoptilolite Redefined." *American Mineralogist, 45*, 351–369. Washington, D.C.: Mineralogical Society of America. TIC 218695.

Mumpton, F.A. 1979. *A Reconnaissance Study of the Association of Zeolites with Mesothelioma Occurrences in Central Turkey.* USGS-OFR-79-954. Denver, Colorado: U.S. Geological Survey. TBD

Mumpton, F.A. and Ormsby, W.C. 1976. "Morphology of Zeolites in Sedimentary Rocks by Scanning Electron Microscopy." *Clays and Clay Minerals, 24*, 1–23. Long Island City, New York: Pergamon Press. NNA.19890405.0182.

Murata, K.J. and Larson, R.R. 1975. "Diagenesis of Miocene Siliceous Shales, Temblor Range, California." *Journal of Research, U.S. Geological Survey, 3*, 553–566. Denver, Colorado: U.S. Geological Survey. TIC 224655.

Murata, K.J.; Friedman, I.; and Gleason, J.D. 1977. "Oxygen Isotope Relations Between Diagenetic Silica Minerals in Monterey Shale, Temblor Range, California." *American Journal of Science, 277*, 259–272. New Haven, Connecticut: Kline Geology Laboratory, Yale University. TIC 224654.

Murphy, W.M. 1992. "Natural Analog Studies for Geologic Disposal of Nuclear Waste." *Technology Today* (June), 16–21. San Antonio, Texas: Southwest Research Institute. TIC 238853.

Murphy, W.M.; Pabalan, R.T.; Prikryl, J.D.; and Goulet, C.J. 1996. "Reaction Kinetics and Thermo-Dynamics of Aqueous Dissolution and Growth of Analcime and Na-Clinoptilolite at 25°C." *American Journal of Science, 296*, 128–186. New Haven, Connecticut: Kline Geology Laboratory, Yale University. TIC 235949.

Myers, C.W. et al. (Exploratory Shaft Test Plan Committee) 1983. *Test Plan for Exploratory Shaft at Yucca Mountain.* NVO-244, Revision 0. Las Vegas, Nevada: U.S. Deptartment of Energy, Nevada Operations Office. NNA.19900427.0404.

NADP/NTN (National Atmospheric Deposition Program, NRSP-3/National Trends Network) 1993. *Precipitation Data for Stations CA34, CA42, CA45, CA68, CA75, CA76, CA88, CA98, CA99, NV00, NV01, NV03, NV05, AZ01, AZ03, AZ06, AZ99, UT01, UT08, UT98, UT99, NM01, NM07, NM08, NM09, NM12, 1985-1993. NADP/NTN Coordination Office.* Fort Collins, Colorado: Natural Resource Ecology Laboratory, Colorado State University. TBD

NADP/NTN 1997. *Data for Station NV00 (Red Rock Canyon), 1985-1997.* NADP/NTN Coordination Office. Fort Collins, Colorado: Natural Resource Ecology Laboratory, Colorado State University. TBD

Nagy, K.L.; Blum, A.E.; and Lasaga, A.C. 1991. "Dissolution and Precipitation Kinetics of Kaolinite at 80°C and pH 3: The Dependence on Solution Saturation State." *American Journal of Science, 291*, 649–686. New Haven, Connecticut: Kline Geology Laboratory, Yale University. TIC 236096.

Nasedkin, V.V. 1964. "Volatile Components of Volcanic Glasses." *Geochem. Int., 2*, 317-330. TIC 238433.

Neal, R.H.; Sposito, G.; Holtzclaw, K.M.; and Traina, S.J. 1987. "Selenite Adsorption on Alluvial Soils: I," in "Soil Composition and pH Effects." *Soil Science Society of America Journal, 51*, 1161–1165. Madison, Wisconsin: Soil Science Society of America Special Publication Series. TIC 237059.

Neck, V.; Kim, J.I.; and Kanellakopulos, B. 1992. "Solubility and Hydrolysis Behavior of Neptunium(V)." *Radiochimica Acta, 56*, 25. München, Germany: Verlag. TIC 224093.

Neck, V.; Runde, W.; and Kim, J.I. 1995. "Solid-Liquid Equilibria of Neptunium(V) in Carbonate Solutions of Different Ionic Strengths: II. Stability of the Solid Phases." *Journal of Alloys and Compounds, 225*, 295–302. Lausanne, Switzerland: Elsevier. TIC 237061.

Neck, V.; Runde, W.; Kim, J.I.; and Kanellakopulos, B. 1994. "Solid-Liquid Equilibrium Reactions of Neptunium(V) in Carbonate Solution At Different Ionic Strengths." *Radiochimica Acta 65*, 29–37. München, Germany: R. Oldenbourg Verlag. TIC 237467.

Neretnieks, I. 1990. "Solute Transport in Fractured Rock: Applications to Radionuclide Waste Repositories." SKB Technical Report 90-38. Stockholm, Sweden: Svensk Karnbransleforsojning AB/Avdelning KBS. TIC 208618.

Newton, T.W. 1975. *The Kinetics of the Oxidation-Reduction Reactions of Uranium, Neptunium, Plutonium, and Americium in Aqueous Solutions: ERDA Critical Review Series.* Available as TID-26506. Oak Ridge, Tennessee: ERDA Technical Information Center. TIC 239297.

Newton, T.W.; Hobart, D.E.; and Palmer, P.D. 1986. "The Formation of Plutonium(IV)-Colloid by the Alpha-Reduction of Pu(V) or Pu(VI) in Aqueous Solutions." *Radiochimica Acta, 39,* 139–147. München, Germany: Verlag. TIC 222593.

Nimick, F.B. and Schwartz, B.M. 1987. *Bulk, Thermal, and Mechanical Properties of the Topopah Spring Member of the Paintbrush Tuff, Yucca Mountain, Nevada.* SAND85-0762. Albuquerque, New Mexico: Sandia National Laboratories. NNA.19870723.0015.

Nimmo, J.R. and Akstin, K.C. 1988. "Hydraulic Conductivity of a Sandy Soil at Low Water Content After Compaction by Various Methods." *Soil Science Society of America Journal, 52,* 303. Madison, Wisconsin: Soil Science Society of America. TIC 224083.

Nimmo, J.R. and Mello, K.A. 1991. "Centrifugal Techniques for Measuring Saturated Hydraulic Conductivity." *Water Resources Research, 27,* 1263. Washington, D.C.: American Geophysical Union. TIC 224084.

Nimmo, J.R.; Rubin, J.; and Hammermeister, D.P. 1987. "Unsaturated Flow in a Centrifugal Field: Measurement of Hydraulic Conductivity and Testing of Darcy's Law." *Water Resources Research, 23,* n. 1, 124–134. Washington, D.C.: American Geophysical Union. TIC 216671.

Nitao, J.J. 1991. "Theory of Matrix and Fracture Flow Regimes in Unsaturated, Fractured Porous Media." *High Level Radioactive Waste Management: Proceedings of the Second Annual International Conference, Las Vegas, Nevada, April 28–May 3, 1991.* La Grange Park, Illinois: American Nuclear Society. TIC 234964.

Nitsche, H. 1991. "Basic Research for Assessment of Geologic Nuclear Waste Repositories: What Solubility and Speciation Studies of Transuranium Elements Can Tell Us." *Materials Research Society Symposium Proceedings (Scientific Basis of Nuclear Waste Management XIV), 212,* 517–529. Pittsburgh, Pennsylvania: Materials Research Society. TIC 222597.

Nitsche, H.; Gatti, R.C.; Standifer, E.M.; Lee, S.C.; Muller, A.; Prussin, T.; Deinhammer, H.; Mauer, H.; Becraft, K.; Leung, S.; and Carpenter, S.A. 1992. *Measured Solubilities and Speciations of Neptunium, Plutonium, and Americium in a Typical Groundwater (J-13) from the Yucca Mountain Region: Milestone Report 3010.* Report 30958. Berkeley, California: Lawrence Berkeley National Laboratory. MOL.19960701.0272.

Nitsche, H.; Gatti, R.C.; Standifer, E.M.; Lee, S.C.; Müller, A.; Prussin, T.; Deinhammer, R.S.; Maurer, H.; Becraft, K.; Leung, S.; and Carpenter, S.A. 1993. *Measured Solubilities and Speciations of Neptunium, Plutonium, and Americium in a Typical Groundwater (J-13) from the Yucca Mountain Region.* YMP Milestone Report 3010-WBS 1.2.3.4.1.3.1. LA-12562-MS. Los Alamos, New Mexico: Los Alamos National Laboratory. TIC 206976.

Nitsche, H.N.; Roberts, K.; Beacraft, K.; Prussin, T.; Keeney, D.; Carpenter, S.A.; and Hobart, D.E. 1995. *Solubility and Speciation Results from Over and Undersaturation Experiments on Neptunium, Plutonium, and Americium in Water from Yucca Mountain Region Well UE-25 p#1.* LA-13017-MS. Los Alamos, New Mexico: Los Alamos National Laboratory. MOV.19980501.0078.

Nitsche, H.N.; Roberts, K.; Prussin, T.; Muller, A.; Becraft, K.; Keeny, D.; Carpenter, S.A.; and Gatti, R.C. 1994. *Measured Solubilities and Speciations from Oversaturation Experiments of Neptunium, Plutonium, and Americium in UE-25 p#1 Well Water from the Yucca Mountain Region.* LA-12563-MS. YMP Milestone Report 3329. Los Alamos, New Mexico: Los Alamos National Laboratory. MOL.19951006.0171.

Noell, A.L.; Thompson, J.L.; Corapcioglu, M.Y.; and Triay, I.R. 1997. "The Role of Silica Colloids on Facilitated Cesium Transport Through Glass-Bead Columns and Modeling." Submitted to *Journal of Contaminant Hydrology.* Amsterdam, Netherlands: Elsevier. TBD

Noell, A.L.; Triay, I.R.; and Thompson, J.L. 1997. "Determination of Sorption Parameters Between Cesium and Amorphous Silica Colloids." Submitted to *Radiochimica Acta.* München, Germany: Verlag. TBD

Obeng, L.A.; Carrondo, M.J.T.; Perry, R.; and Lester, J.N. 1981. "The Influence of Zeolite Type A on Metal Concentrations in Water and Waste Water." *Journal of the American Oil Chemists' Society, 58,* 81–85. Champagne, Illinois: American Oil Chemists' Society. TIC 237902.

Odin, G.S., et al. (35 others) 1982. "Interlaboratory Standards for Dating Purposes." *Numerical Dating in Stratigraphy,* 124–150. Odin, G.S., Ed. Chichester, England: Wiley. TIC 236973.

Ogard, A.E. and Kerrisk, J.F. 1984. *Groundwater Chemistry Along Flow Paths Between a Proposed Repository Site and the Accessible Environment.* LA-10188-MS. Los Alamos, New Mexico: Los Alamos National Laboratory. HQS.19880517.2031.

Ogard, A.E. and Vaniman, D.T., compilers. 1985. *Research and Development Related to the Nevada Nuclear Waste Storage Investigations: July 1–September 30, 1984.* LA-10299-PR. Los Alamos, New Mexico: Los Alamos National Laboratory. TIC 202357.

Oldham, P.D. 1983. "Pneumoconiosis in Cornish China Clay Workers." *British Journal of Industrial Medicine* 40: 131–137. England. TIC 234185.

Oliver, T. and Root, T. 1997. *Hydrochemical Database for the Yucca Mountain Area, Nye County, Nevada.* USGS Level-4 Milestone Report SPH34BM4. Denver, Colorado: U.S. Geological Survey. TIC 238148.

O'Melia, C. and Tiller, C. 1993. "Physicochemical Aggregation and Deposition in Aquatic Environment." *Characterisation of Environmental Particles,* vol. II. Buffle, J. and van Leeuwen, H.P., Eds. IUPAC Environmental Analytical Chemistry Series. Chelsea, Michigan: Lewis Publishers, Inc. TIC 238504.

O'Neil, J. and Silberman, M. 1974. "Stable Isotope Relations in Epithermal Au-Ag Deposits." *Economic Geology, 69*, 902–909. El Paso, Texas: Economic Geology Publishing Co. TIC 222136.

Oversby, V. 1987. "Important Radionuclides in High-Level Nuclear Waste Disposal: Determination Using a Comparison of the U.S. EPA and NRC Regulations." *Nuclear Chem. Waste Management, 7*, 149-161. TIC 220003.

Pabalan, R.T. 1994. "Thermodynamics of Ion Exchange Between Clinoptilolite and Aqueous Solutions of Na^+/K^+ and Na^+/Ca^{2+}." *Geochimica et Cosmochimica Acta 58*, 4573–4590. Oxford/New York: Pergamon Press. TIC 234005.

Pabalan, R.T. and Bertetti, F.P. 1994. "Thermodynamics of Ion Exchange Between Na^+/Sr^{2+} Solutions and the Zeolite Mineral Clinoptilolite," in "Scientific Basis for Nuclear Waste Management XVII," Barkatt, A. and Van Konynenburg, R.A., Eds. *Materials Research Society Symposium Proceedings, 333*, 731–738. Pittsburgh, Pennsylvania: Materials Research Society. TIC 213541.

Paces, J.B.; Ludwig, K.R; Peterman, Z.E.; Neymark, L.A.; and Kenneally, J.M. 1998. "Anomalous Groundwater $^{234}U/^{238}U$ Beneath Yucca Mountain: Evidence of Local Recharge?" *High Level Radioactive Waste Management, Proceedings of the Eighth Annual International Conference, Las Vegas, Nevada, May 11-14, 1998.* La Grange Park, Illinois: American Nuclear Society. TIC 237806.

Paces, J.B.; Mahan, S.A.; Ludwig, K.R.; Kwak, L.M.; Neymark, L.A.; Simmons, K.R.; Nealey, L.D.; Marshall, B.D.; and Walker, A. 1995. "Progress Report on Dating Quaternary Surficial Deposits." *Dating Surface Deposits.* USGS, Yucca Mountain Project Branch, 1995 Milestone Report 3GCH510M. Denver, Colorado: U.S. Geological Survey. TIC 233988.

Paces, J.B.; Marshall, B.D.; Whelan, J.F.; and Neymark, L.A. 1997. *Progress Report on Unsaturated Zone Stable and Radiogenic Isotope Studies.* USGS Level 4 Milestone Report SPC23FM4. Denver, Colorado: U.S. Geological Survey. TIC 238068.

Paces, J.B.; Neymark, L.A.; Marshall, B.D.; Whelan, J.F.; and Peterman, Z.E. 1996. *Ages and Origins of Subsurface Secondary Minerals in the Exploratory Studies Facility (ESF).* USGS Yucca Mountain Project Branch 1996 Milestone Report 3GQH450M. DTN GS960908315215.011. Denver, Colorado: U.S. Geological Survey. MOL.19970324.0052.

Paces, J.B.; Neymark, L.A.; Marshall, B.D.; Whelan, J.F.; and Peterman, Z.E. 1998. "Inferences for Yucca Mountain Unsaturated-Zone Hydrology from Secondary Minerals." *High Level Radioactive Waste Management, Proceedings of the Eighth Annual International Conference, Las Vegas, Nevada, May 11-14, 1998.* La Grange Park, Illinois: American Nuclear Society. TIC 238482.

Parks, G.A. and Pohl, D.C. 1988. "Hydrothermal Solubility of Uraninite." *Geochimica et Cosmochimica Acta, 52*, 863–875. Oxford/New York: Pergamon Press. NNA.19910821.0003.

Payne, T.E.; Davis, J.A.; and Waite, T.D. 1991. "Modeling of Uranium Sorption to Substrates from the Weathered Zone in the Vicinity of the Koongarra Ore Body." *Alligator Rivers Analogue Project, First Annual Report, 1988–89*, 39–46. Menai, Australia: Australian Nuclear Science and Technology Organization. TBD

Pearcy, E.C.; Prikryl, J.D.; Murphy, W.M.; and Leslie, B.W. 1994. "Alteration of Uraninite From the Nopal I Deposit, Pena Blanca District, Chihuahua, Mexico, Compared to Degradation of Spent Nuclear Fuel in the Proposed U.S. High-Level Nuclear Waste Repository at Yucca Mountain, Nevada." *Applied Geochemistry, 9*, 713–732. London, England: Elsevier Science Publishing Company. TIC 236934.

Pedersen, K.; Arlinger, J.; Bruetsch, R.; Degueldre, C.; Hallbeck, L.; Laaksoharju, M.; Lutz, T.; and Pederson, C. 1996. *Bacteria, Colloids, and Organic Carbon in Groundwater at the Bangombé Site in the Oklo Area.* SKB Technical Report 96-01. Stockholm, Sweden: Svensk Karnbransleforsojning AB/Avdelning KBS. TIC 225494.

Penrose, W.R.; Polzer, W.L.; Essington, E.H.; Nelson, D.M.; and Orlandini, K.A. 1990. "Mobilitly of Plutonium and Americium through a Shallow Aquifer in a Semiarid Region." *Environmental Science and Technolgy, 24*, 228–234. Easton, Pennsylvania: American Chemical Society. TIC 224113.

Pentecost, A. 1992. "Travertine: Life Inside the Rock." *Biologist, 39,* 161-164. NNA.19940523.0009.

Perfect, D.L.; Faunt, C.C.; Steinkampf, W.C.; and Turner, A.K. 1995. *Hydrochemical Data Base for the Death Valley Region, California and Nevada.* USGS-OFR-94-305. Denver, Colorado: U.S. Geological Survey. TIC 213575.

Perry, Jr., E.A and Hower, J. 1970. "Burial Diagenesis in Gulf Coast Pelitic Sediments." *Clays and Clay Minerals 18*, 165–177. Long Island City, New York: Pergamon Press. TIC 217875.

Perry, Jr., E.A and Hower, J. 1972. "Late-stage Dehydration in Deeply Buried Pelitic Sediments." *American Association of Petroleum Geologists Bulletin 56,* 2013–2021. Tulsa, Oklahoma: American Association of Petroleum Geologists. TIC 235897.

Peterman, Z.E.; Spengler, R.; Futa, K.; Marshall, B.; and Mahan, S. 1991. "Assessing the Natural Performance of Felsic Tuffs Using the Rb-Sr and Sm-Nd Systems: A Study of the Altered Zone in the Topopah Spring Member, Paintbrush Tuff, Yucca Mountain, Nevada." *Scientific Basis for Nuclear Waste Management XIV.* Pittsburgh, Pennsylvania: Materials Research Society. GS960108319211.002; TIC 225943.

Peterman, Z.E.; Spengler, R.W.; Singer, F.R.; and Beason, S.C. 1996. "Localized Alteration of the Paintbrush Nonwelded Hydrologic Unit within the Exploratory Studies Facility." *High Level Radioactive Waste Management, Proceedings of the Seventh Annual International Conference, Las Vegas, Nevada, April 29-May 3, 1996,* 46-47. DTN: GS 960108319211.002 La Grange Park, Illinois: American Nuclear Society. TIC 235058.

Peterman, Z.E.; Spengler, R.W.; Singer, F.R.; and Dickerson, R.P. 1993. "Isotopic and Trace Element Variability in Altered and Unaltered Tuffs at Yucca Mountain, Nevada." *High Level Radioactive Waste Management, Proceedings of the Fourth Annual International Conference, Las Vegas, Nevada, April 26-30, 1993,* 1,940-1,947. La Grange Park, Illinois: American Nuclear Society. TIC 225931.

Peto, J.; Seidman, H.; and Selikoff, I.J. 1982. "Mesothelioma Mortality in Asbestos Workers: Implications for Models of Carcinogenesis and Risk Assessment." *British Journal of Cancer* 45: 124–135. London, England: Cancer Campaign for Research. TIC 236936.

Phillips, S.E. and Self, P.G. 1987. "Morphology, Crystallography, and Origin of Needle-Fibre Calcite in Quaternary Pedogenic Calcretes of South Australia." *Australian Journal of Soil Research, 25,* 429-444. Melbourne, Australia: Commonwealth Scientific and Industrial Research Organization. TIC 224414.

Plummer, M.A.; Phillips, F.M.; Fabryka-Martin, J.; Turin, H.J.; Wigand, P.E.; and Sharma, P. 1997. "Chlorine-36 in Fossil Rat Urine: An Archive of Cosmogenic Nuclide Deposition During the Past 40,000 Years." *Science, 277,* 538-541. Washington, D.C.: American Association for the Advancement of Science. TIC 237425.

Polzer, W.L. and Fuentes, H.R. 1988. "The Use of a Heterogeneity-Based Isotherm to Interpret the Transport of Reactive Radionuclides in Volcanic Tuff Media." *Radiochimica Acta, 44/45,* 361–365. München, Germany: Verlag. NNA.19900416.0103.

Polzer, W.L.; Essington, E.H.; and Fowler, E.B. 1983. *Influence of Soil Chemistry On the Mobility of PuEDTA.* LA-UR-83-3367. Los Alamos, New Mexico: Los Alamos National Laboratory. TBD

Post, J.E. and Bish, D.L. 1989. "Rietveld Refinement of Crystal Structures Using Powder X-Ray Diffraction Data." *Modern Powder Diffraction, 20,* 277–308. Bish, D.L. and Post, J.E., Eds. Washington, D.C.: Mineralogical Society of America. TIC 237912.

Post, J.E.; Von Dreele, R.B.; and Buseck, P.R. 1982. "Symmetry and Cation Displacements in Hollandites: Structure Refinements of Hollandite, Cryptomelane, and Priderite." *Acta Crystallographica B, 38,* 1056–1065. Chester, England: International Union of Crystallography. TIC 222522.

Pott, F. and Friedrichs, K.H. 1972. "Tumoren der Ratte Nach I. P.-Injektion Faserförmiger Stäube." *Naturwissenschaflen, 59,* 318. Berlin, Germany: Springer-Verlag. TIC 237808.

Pott, F.; Bellmann, B.; Muhle, H.; Rödelsperger, K.; Rippe, R.M.; Roller, M.; and Rosenbruch, M. 1990. "Intraperitoneal Injection Studies for the Evaluation of the Carcinogenicity of Fibrous Phyllosilicates." *Health Related Effects of Phyllosilicates,* 319-329. Bignon, J., Ed. Berlin, Germany: Springer-Verlag. TIC 235575.

Pott, F.; Huth, F.; and Friedrichs, K.H. 1974. "Tumorigenic Effect of Fibrous Dusts in Experimental Animals. *Environmental Health Perspectives, 9,* 313–315. Research Triangle Park, North Carolina: National Institute of Environmental Health Sciences. TIC 234184.

Potter, C.J.; Dickerson, R.P.; and Day, W.C 1995. *Nature and Continuity of the Sundance Fault, Yucca Mountain, Nevada.* USGS Administrative Report prepared in cooperation with the Nevada Operations Office, U.S. Department of Energy, under Interagency Agreement DE-AI08-92NV10874. Las Vegas, Nevada: U.S. Department of Energy, Nevada Operations Office. GS950808314221.004; MOL.19960403.0161.

Pourbaix, M. 1966. *Atlas of Electrochemical Equilibria in Aqueous Solutions.* Long Island City, New York: Pergamon Press. TIC 208955.

Price, E.H. and Ames, L.L. 1978. "Characteristics of Actinide-Bearing Sediments Underlying Liquid Waste Disposal Facilities at Hanford." *Transuranium Nuclides in the Environment* (IAEA publication SM-199/87), 191–211. Vienna, Austria: International Atomic Energy Agency. TIC 208955.

Quade, J. and Cerling, T.E. 1990. "Stable Isotopic Evidence for a Pedogenic Origin of Carbonates in Trench-14 Near Yucca Mountain, Nevada." *Science, 250,* 1549–1552. Washington, D.C.: American Association for the Advancement of Science. TIC 222617.

Quade, J.; Cerling, T.E.; and Bowman, J.R. 1989. *Systematic Variations in the Carbon and Oxygen Isotopic Composition of Pedogenic Carbonate along Elevation Transects in the Southern Great Basin.* Geological Society of America - Bulletin 101, 464-475. Boulder, Colorado: Geological Society of America. TIC 224417.

Rai, D. and Zachara, J.M. 1984. *Chemical Attenuation Rates, Coefficients, and Constants in Leachate Migration: Volume 1. A Critical Review.* Electric Power Research Institute Report EA-3356. Palo Alto, California: Electric Power Research Institute. TIC 237846.

Rai, D.; Felmy, A.R.; and Ryan. J.L. 1990. "Uranium(IV) Hydrolysis Constants and Solubility Product of $UO_2.xH_2O$(am)." *Inorganic Chemistry, 29,* 260–264. Washington, D.C.: American Chemical. TIC 237443.

Rai, D.; Serne, R.J.; and Moore, D.A. 1980. "Solubility of Plutonium Compounds and their Behavior in Soils." *Soil Science Society of America Journal 44,* 490–495. Madison, Wisconsin: Soil Science Society of America Special Publication Series. TIC 219108.

Raleigh, C.B.; Thompson, G.A.; Brace, W.F.; Brady, B,H.G.; Bredehoeft, J.D.; Burke, R.M.; Fournier, R.O.; Garg, S.K.; Hornberger, G.M.; McGuire, R.K.; Nur, A.M.; Ramey, H.J.; Roedder, E.W.; Rumble, D.; Spaulding, W.G.; Wernicke, B.P.; and Zoback, M.L. 1992. *Ground Water at Yucca Mountain: How High Can It Rise?* Washington, D.C.: National Academy Press. TIC 204931.

Rard, J.A. 1983. *Critical Review of the Chemistry and Thermodynamics of Technetium and Some of its Inorganic Compounds and Aqueous Species.* UCRL-53440. Livermore, California: Lawrence Livermore National Laboratories. TIC 212963.

Rautman, C.A. and Engstrom, D.A. 1996a. *Geology of the USW SD-7 Drill Hole Yucca Mountain, Nevada.* SDN E1.99:DE97000608; NTIS DE97000608. SAND96-1474. Albuquerque, New Mexico: Sandia National Laboratories. MOL.19971218.0442.

Rautman, C.A. and Engstrom, D.A. 1996b. *Geology of the USW SD-12 Drill Hole Yucca Mountain, Nevada.* SDN E 1.99:DE97001807; NTIS DE97001807. SAND96-1368. Albuquerque, New Mexico: Sandia National Laboratories. MOL.19970613.0101.

Rechard, R.P., Ed. 1995. *Performance Assessment of the Direct Disposal in Unsaturated Tuff of Spent Nuclear Fuel and High-Level Waste Owned by the U.S. Department of Energy.* SAND94-2563/1. Albuquerque, New Mexico: Sandia National Laboratories. TIC 237101.

Reheis, M.C.; Sowers, J.M.; Taylor, E.M.; McFadden, L.D.; and Harden, J.W. 1992. "Morphology and Genesis of Carbonate Soils on the Kyle Canyon Fan, Nevada, U.S.A." DTN: GS930108315141.001. *Geoderma, 52,* 303–342. Amsterdam, Netherlands: Elsevier Scientific Publishing Company. TIC 224418.

Relyea, J.F. 1982. "Theoretical and Experimental Considerations for the Use of the Column Method for Determining Retardation Factors." *Radioactive Waste Management and the Nuclear Fuel Cycle, 3(2),* 151–166. Williston, Vermont: Harwood Academic Publishers. TIC 235727.

Renders, P.J.N.; Gammons, C.H.; and Barnes, H.L. 1995. "Precipitation and Dissolution Rate Constants For Cristobalite From 150 to 300°C." *Geochimica et Cosmochimica Acta, 59,* 77–85. Oxford/New York: Pergamon Press. TIC 226987.

Reynolds, Jr., R.C. 1980. "Interstratified Clay Minerals." *Crystal Structures of Clay Minerals and their X-Ray Identification*, Chapter 4, 249–304. Brindley, G.W. and Brown, G., Eds. London, England: Mineralogical Society. NNA.19900508.0028.

Riehle, J. 1973. *Calculated Compaction Profiles of Rhyolitic Ash Flow Tuffs.* Geological Society of America - Bulletin 84, 2193-2216. Boulder, Colorado: Geological Society of America. TIC 224792.

Rimstidt, J.D. and Barnes, H.L. 1980. "The Kinetics of Silica-Water Reactions." *Geochimica et Cosmochimica Acta 44*, 1683–1699. Oxford/New York: Pergamon Press. TIC 219975.

Robbins, G.A. 1972. *Radiogenic Argon Diffusion in Muscovite under Hydrothermal Conditions.* Master's thesis. Providence, Rhode Island: Brown University. TIC 238552.

Roberson, H.E. and Lahann, R.W. 1981. "Smectite to Illite Conversion Rates: Effects of Solution Chemistry." *Clays and Clay Minerals 29,* 129–135. Long Island City, New York: Pergamon Press. TIC 217876.

Roberts, W.C.; Campbell, T.J.; and Rapp, Jr., G.R. 1989. *Encyclopedia of Minerals*, second edition. New York, New York: Van Nostrand Reinhold. TBD

Robie, R.A.; Hemingway, B.S.; and Fisher, J.R. 1979. *Thermodynamic Properties of Minerals and Related Substances at 298.15 K and 1 Bar (10^5 Pascals) Pressure and at Higher Temperature.* USGS Bulletin 1452. Denver, Colorado: U.S. Geological Survey. TIC 230505.

Robinson, B.A.; Wolfsberg, A.V.; Viswanathan, H.S.; Gable, C.W.; Zyvoloski, G.A.; and Turin, H.J. 1996. *Site-Scale Unsaturated-Zone Flow and Transport Model.* YMP Milestone Report 3672. Los Alamos, New Mexico: Los Alamos National Laboratory. MOL.19971111.0625.

Robinson, B.A.; Wolfsberg, A.V.; Viswanathan, H.S.; Bussod, G.Y.; Gable, C.W.; and Meijer, A. 1997. *The Site-Scale Unsaturated-Zone Transport Model of Yucca Mountain.* YMP Milestone Report SP25BM3. Los Alamos, New Mexico: Los Alamos National Laboratory. MOL.19980203.0570.

Robinson, B.A.; Wolfsberg, A.V.; Zyvoloski, G.A.; and Gable, C.W. 1995. *An Unsaturated Zone Flow and Transport Model of Yucca Mountain.* YMP Milestone Report 3468. Los Alamos, New Mexico: Los Alamos National Laboratory. MOL.19960415.0218.

Robinson, Jr., G.R. and Haas, Jr., J.L. 1983. "Heat Capacity, Relative Enthalpy, and Calorimetric Entropy of Silicate Minerals: An Empirical Method of Prediction." *American Mineralogist, 68*, 541–553. Washington, D.C.: Mineralogical Society of America. TIC 224442.

Robison, J.H. 1984. *Groundwater Level Data and Preliminary Potentiometric Surface Map of Yucca Mountain and Vicinity, Nye County, Nevada.* USGS Water Resources Investigation Report 84-4197. Denver, Colorado: U.S. Geological Survey. TIC 203217.

Roedder, E. 1984. "Fluid Inclusions." *Reviews in Mineralogy, 12.* Washington, D.C.: Mineralogical Society of America. TIC 236874.

Rogers, P.S.Z. and Chipera, S. 1994. *Sorption Characteristics of Yucca Mountain Tuffs as a Function of Sample Particle Size, Surface Area, and Water Composition.* LA-12805-MS. Los Alamos, New Mexico: Los Alamos National Laboratory. TBD

Rosch, F.; Milanov, M.; Hung, T.K.; Ludwig, R.; Buklanov, G.V.; and Khalkin, V.A. 1987. "Electromigration of Carrier-Free Radionuclides: 6. Ion Mobilities and Hydrolysis of Np(V) in Aqueous Perchlorate Solutions." *Radiochimica Acta 42*, 43. München, Germany: Verlag. MOL.19950202.0007.

Rosenbaum, J. 1986. "Paleomagnetic Directional Dispersion Produced by Plastic Deformation in a Thick Miocene Welded Tuff, Southern Nevada: Implications for Welding Temperatures." *Journal of Geophysical Research, 91*(B12), 12,817–12,834. Washington, D.C.: American Geophysical Union. TIC 233555.

Rosholt, J.N.; Prijana; and Noble, D.C. 1971. "Mobility of Uranium and Thorium in Glassy and Crystallized Silicic Volcanic Rocks." *Economic Geology, 66*, 1061–1069. El Paso, Texas: Economic Geology Publishing Company. TIC 219186.

Rosmanith, J.; Hilscher, W.; and Schyma, S.B. 1990. "The Effect of the Surface Quality on the Fibrogenicity of the Phyllosilicates Muscovite and Kaolinite." *Health Related Effects of Phyllosilicates*, 123-128. Bignon, J., Ed. Berlin, Germany: Springer-Verlag. TIC 235600.

Ross, C.S. and Smith, R.L. 1955. "Water and Other Volatiles in Volcanic Glasses." *American Mineralogist, 40,* 1071-1089. Washington, D.C.: Mineralogical Society of America. NNA.19910405.0048.

Ross, M.; Nolan, R.P.; Langer, A.M.; and Cooper, C.W. 1993. "Health Effects of Mineral Dusts Other than Asbestos." *Health Effects of Mineral Dusts,* 361–407. Guthrie, Jr., G.D. and Mossman, B.T., Eds. Washington, D.C.: Mineralogical Society of America. TIC 236770.

Rundberg, R.S. 1987. *Assessment Report on the Kinetics of Radionuclide Adsorption on Yucca Mountain Tuff.* LA-11026-MS. Los Alamos, New Mexico: Los Alamos National Laboratory. TIC 202372.

Rundberg, R.S.; Ogard, A.E.; and Vaniman, D.T. compilers 1985. *Research and Development Related to the Nevada Nuclear Waste Storage Investigations, April 1–June 30, 1984.* LA-10297-PR. Los Alamos, New Mexico: Los Alamos National Laboratory. TIC 202357.

Rundberg, R.S.; Partom, I.; Ott, M.A.; Mitchell, A.J.; Birdsell, K. 1987. *Diffusion of Nonsorbing Tracers in Yucca Mountain Tuff.* YMP Milestone Report R524. Los Alamos, New Mexico: Los Alamos National Laboratory. NNA.19930405.0074.

Runde, W. 1993. *Chemishes Verhalten von Drei- und Funfwertigem Americium in Salinen Losurgen.* Doctoral dissertation, Report RCM-01094. Munich, Germany: Technical University of Munich. TBD

Runde, W.; Meinrath, G.; and Kim, J.I. 1992. "A Study of Solid-Liquid Phase Equilibria of Trivalent Lanthanide and Actinide Ions in Carbonate Systems." *Radiochimica Acta 58/59,* 93-100. München, Germany: Verlag. TIC 237409.

Ryan, Jr., J.J. and Geschwend, P.M. 1990. "Colloid Mobilization in Two Atlantic Coastal Plain Aquifers." *Water Resources Research, 26*(2), 307–322. Washington, D.C.: American Geophysical Union. NNA.930920.0006.

Ryan, J.L. and Rai, D. 1983. "The Solubility of Uranium(IV) Hydrous Oxide in Sodium Hydroxide Solutions Under Reducing Conditions." *Polydedron, 2,* 947–952. Great Britain: Pergamon Press. TIC 236941.

Saffiotti, U. 1992. "Lung Cancer Induction by Crystalline Silica." *Relevance of Animal Studies to the Evaluation of Human Cancer Risk,* 51–69. New York, New York: Wiley-Liss, Inc. TIC 235700.

Saffiotti, U.; Daniel, L.N.; Mao, Y.; Williams, A.O.; Kaighn, M.E.; Ahmed, N.; and Knapton, A.D. 1993. "Biological Studies on the Carcinogenic Mechanisms of Quartz." *Health Effects of Mineral Dusts,* 523–544. Guthrie, Jr., G.D. and Mossman, B.T., Eds. Washington, D.C.: Mineralogical Society of America. TIC 236771.

Sakanoue, M. 1987. "Transuranium Nuclides in the Environment." *Radiochimica Acta, 42,* 103-112. München, Germany: Verlag. TIC 237412.

Sanchez, A.L.; Murray, J.W.; and Sibley, T.H. 1985. "The Adsorption of Plutonium IV and V on Goethite." *Geochimica et Cosmochimica Acta, 49*, 2297–2307. Oxford/New York: Pergamon Press. TIC 224091.

Sass, J.H. and Lachenbruch, A.H. 1982. *Preliminary Interpretation of Thermal Data from the Nevada Test Site.* USGS-OFR-82-973. Denver, Colorado: U.S. Geological Survey. NNA.19870406.0040.

Sass, J.H.; Lachenbruch, A.; Grubb, F.; and Moses, T. 1983. *Status of Thermal Observations at Yucca Mountain, Nevada.* USGS Letter Report. Denver, Colorado: U.S. Geological Survey. TIC 222539.

Savard, C.S. 1995. "Groundwater Recharge from Small to Large Stream Flow Events During El Nino Periods Under Fortymile Wash near Yucca Mountain, Nevada." Abstract in Fall Meeting Supplement of *EOS Transactions of the American Geophysical Union* 76(46), F241. Washington, D.C.: American Geophysical Union. TIC 237433.

Savard, C.S. 1996. *Selected Hydrologic Data from Fortymile Wash in the Yucca Mountain Area, Nevada, Water Years 1993–94.* USGS-OFR-95-709. Denver, Colorado: U.S. Geological Survey. TIC 225485.

Savard, C.S. 1997. *Estimated Groundwater Recharge from Stream Flow in Fortymile Wash near Yucca Mountain, Nevada.* USGS Water Resources Investigation Report. Denver, Colorado: U.S. Geological Survey. TIC 236848.

Sawyer, D.A.; Fleck, R.J.; Lanphere, M.A.; Warren, R.G.; Broxton, D.E.; and Hudson, M.R. 1994. *Episodic Caldera Volcanism in the Miocene Southwestern Nevada Volcanic Field: Revised Stratigraphic Framework, $^{40}Ar/^{39}Ar$ Geochronology, and Implications for Magmatism and Extension.* Geologic Society of America Bulletin 106, 1304–1318. Boulder, Colorado: Geologic Society of America. TIC 222523.

Scanlon, B.R. 1991. "Evaluation of Moisture Flux from Chloride Data in Desert Soils." *Journal of Hydrology, 128*, 137-156. Amsterdam, Netherlands: Elsevier. TIC 224126.

Schindler, P.W. 1985. "Grenzflächenchemie Oxidischer Mineralien." *Österreichische Chemie Zeitschrift* 86: 141–146. Germany. TBD

Schmid, R. 1981. "Descriptive Nomenclature and Classification of Pyroclastic Deposits and Fragments: Recommendations of the IUGS Subcommission on the Systematics of Igneous Rocks." *Geology, 9*, 41-43. Boulder, Colorado: Geological Society of America. TBD

Schuraytz, B.C.; Vogel, T.A.; and Younker, L.W. 1989. "Evidence for Dynamic Withdrawal from a Layered Magma Body: The Topopah Spring Tuff, Southwestern Nevada." *Journal of Geophysical Research, 94*, 5925–5942. Washington, D.C.: American Geophysical Union. TIC 225936.

Schwertmann, U. and Taylor, R.M. 1977. "Iron Oxides." Dixon, J.B. and Weed, S.B., Eds. *Minerals in Soil Environments,* 145-180. Madison, Wisconsin: Soil Science Society of America. TIC 239149.

Schyma, S.B. 1990. "The Physical Characterization of Muscovite and Kaolinite Dusts." *Health Related Effects of Phyllosilicates,* 97–105. Bignon, J., Ed. Berlin, Germany: Springer-Verlag. TIC 235601.

Scott, R.B. and Bonk, J. 1984. *Preliminary Geologic Map of Yucca Mountain, Nye County, Nevada with Geologic Sections.* USGS-OFR-84-494. Denver, Colorado: U.S. Geological Survey. HQS.19880517.1443.

Scott, R.B. and Castellanos, M. 1984. *Stratigraphic and Structural Relations of Volcanic Rocks in Drill Holes USW GU-3 and USW G-3, Yucca Mountain, Nye County, Nevada.* USGS-OFR-84-491. Denver, Colorado: U.S. Geological Survey. NNA.19890804.0017.

Scott, R.B.; Byers, F.M.; and Warren, R.G. 1984. "Evolution of Magma Below Clustered Calderas, Southwest Nevada Volcanic Field." *Transactions of the American Geophysical Union (EOS)* 65(45): 1126–1127. Washington, D.C.: American Geophysical Union. TIC 217934.

Scott, R.B.; Spengler, R.; Diehl, S.; Lappin, A.; and Chornack, M. 1983. "Geologic Character of Tuffs in the Unsaturated Zone at Yucca Mountain, Southern Nevada." *Role of the Unsaturated Zone in Radioactive and Hazardous Waste Disposal, Philadelphia, Pennsylvania, May 31- June 4,* 289–335. Ann Arbor, Michigan: Ann Arbor Science Publishers. GS930208314221.007; TIC 222160.

Seaman, J.; Bertch, P.; and Miller, W. 1995. "Chemical Controls on Colloid Generation and Transport in a Sandy Aquifer." *Environmental Science and Technology, 29*(7), 1808–1815. Easton, Pennsylvania: American Chemical Society. TIC 237337.

Sepulveda, M.H.; Vallyathan, V.; Attfield, M.D; Piacitelli, L.; and Tucker, J.H. 1983. "Pneumoconiosis and Lung Function in a Group of Kaolin Workers." *American Review of Respiratory Disease, 127,* 231–235. Baltimore, Maryland: National Tuberculosis Association. TIC 236816.

Sheppard, R.A. and Gude, III, A.J. 1968. *Distribution and Genesis of Authigenic Silicate Minerals in Tuffs of Pleistocene Lake Tecopa, Inyo County, California.* USGS Professional Paper 597. Denver, Colorado: U.S. Geological Survey. TIC 222488.

Sheppard, R.A. and Gude, III, A.J. 1969. *Diagenesis of Tuffs in the Barstow Formation, Mud Hills, San Bernardino County, California.* USGS Professional Paper 634. Denver, Colorado: U.S. Geological Survey. NNA.19910522.0036.

Sheppard, R.A. and Gude, III, A.J. 1973. *Zeolites and Associated Authigenic Silicate Minerals in Tuffaceous Rocks of the Big Sandy Formation, Mohave County, Arizona.* USGS Professional Paper 830. Denver, Colorado: U.S. Geological Survey. TIC 230775.

Sheppard, R.A.; Gude, III, A.J.; and Fitzpatric, J.J. 1988. *Distribution, Characterization, and Genesis of Mordenite in Miocene Silicic Tuffs at Yucca Mountain, Nye County, Nevada.* USGS Bulletin 1777. Denver, Colorado: U.S. Geological Survey. TIC 203084.

Sheppard, R.A.; Gude, III, A.J.; and Mumpton, F.A. 1983. "Sheaville Zeolite Deposit, Sheaville, Oregon." *Zeo-Trip '83*, 25–31. Mumpton, F.A., Ed. Brockport, New York: State University of New York. MOL.19941220.0123.

Sheridan, M.F. 1970. *Fumarolic Mounts and Ridges of the Bishop Tuff, California.* Geological Society of America Bulletin 81, 851–868. Boulder, Colorado: Geological Society of America. TIC 235739.

Short, S.A.; Lowson, R.T.; and Ellis, J. 1988. "$^{234}U/^{238}U$ and $^{230}Th/^{234}Th$ Activity Ratios in the Colloidal Phases of Aquifers in Lateritic Weathered Zones." *Geochimica et Cosmochimica Acta, 55*, 2555–2563. Oxford, New York: Pergamon. TBD

Siegel, M.D.; Hopkins, P.L.; Glass, R.J.; and Ward, D.B. 1992. "Design of an Intermediate-Scale Experiment to Validate Unsaturated-Zone Transport Models." *High Level Radioactive Waste Management: Proceedings of the Third International Conference, Las Vegas, Nevada, April 12-16, 1992.* La Grange Park, Illinois: American Nuclear Society. TIC 224542.

Siegel, M.D.; Ward, D.B.; Chang, W.C.; Bryant, C.; Chocas, C.S.; and Reynolds, C.G. 1993. "Preliminary Characterization of Materials for Reactive Transport Model Validation Experiment." *High Level Radioactive Waste Management: Proceeding of the Fourth Annual International Conference, Las Vegas, Nevada, April 26–30, 1993, 1*, 348–358. La Grange Park, Illinois: American Nuclear Society; and New York: American Society of Civil Engineers. TIC 224543.

Silva, R.J.; Bidoglio, G.; Rand, M.H.; Robouch, P.B.; Wanner, H.; and Puigdomenech, I. 1995. *Chemical Thermodynamics of Americium: Chemical Thermodynamics Series, 2.* Amsterdam, Netherlands: Elsevier Science Publications. TIC 237106.

Simkiss, K. and Wilbur, K.W. 1989. *Biomineralization.* 111-113. San Diego, California: Academic Press. TBD

Simonato, L., Baris, R.; Saracci, R.; Skidmore, J.; and Winkelmann, R. 1989. "Relation of Environmental Exposure to Erionite Fibres to Risk of Respiratory Cancer." *Non-Occupational Exposure to Mineral Fibres*, 398–405. Bignon, J.; Peto, J.; and Saracci, R. Eds. Lyons, France: International Agency for Research on Cancer. TIC 237365.

Smith, D.K.; Johnson, G.G.; Scheible, A.; Wims, A.M.; Johnson, J.L.; and Ullmann, G. 1987. "Quantitative X-Ray Powder Diffraction Method Using the Full Diffraction Pattern." *Powder Diffraction, 2*, 73–77. Woodbury, Long Island, New York: American Institute of Physics. TIC 237068.

Smith, D.K.; Nichols, M.C.; and Zolensky, M.E. 1982. *POWD10, A FORTRAN IV Program for Calculating X-Ray Powder Diffraction Patterns—Version 10.* Pennsylvania State University,

College of Earth and Mineral Sciences Report. College Station, Pennsylvania: Pennsylvania State University. NNA.19890602.0030.

Smyth, J.R. 1982. "Zeolite Stability Constraints on Radioactive Waste Isolation in Zeolite-Bearing Volcanic Rocks." *Journal of Geology, 90,* 195–201. Chicago, Illinois: University of Chicago Press. TIC 221104.

Snelling, A.A. 1980. "Uraninite and Its Alteration Products: Koongarra Uranium Deposit." *Uranium in the Pine Creek Geosyncline,* 487–498. Ferguson, J. and Goleby, A.B., Eds. Vienna, Austria: International Atomic Energy Agency. TIC 236806.

Snelling, A.A. and Dickson, B.L. 1979. "Uranium-Daughter Disequilibrium in the Koongarra Uranium Deposit, Australia." *Mineralium Deposita, 14,* 109–118. New York, New York: Springer-Verlag. TIC 237067.

Snodgrass, W.J. 1980. "Distribution and Behavior of Nickel in the Aquatic Environment." *Nickel in the Environment,* 203–274. Nriagu, J.O., Ed. New York, New York: John Wiley and Sons. TIC 237686.

Sonnenthal, E.L.; DePaolo, D.J.; and Bodvarsson, G.S. 1997. "Modeling the Strontium Geochemistry and Isotopic Ratio in the Unsaturated Zone." *The Site-Scale Unsaturated Zone Model of Yucca Mountain, Nevada, for the Viability Assessment,* 17-1 to 17-14. Bodvarsson, G.S., Bandurraga, T.M., and Wu, Y.S., Eds. LBNL-40376. Berkeley, California: Lawrence Berkeley National Laboratory. MOL.19971014.0232.

Sparks, D.L. 1995. "Kinetics of Metal Sorption Reactions." *Metal Speciation and Contamination of Soil,* 35–58. Hung, P., Bailey, G.W., and Boweres, A.R., Eds. Chelsea, Michigan: Lewis Publishers. TIC 236807.

Spaulding, W.G. 1983. *Vegetation and Climates of the Last 45,000 Years in the Vicinity of the Nevada Test Site, South-Central Nevada.* USGS-OFR-83-535. Denver, Colorado: U.S. Geological Survey. NNA.19890523.0110.

Spaulding, W.G. 1985. *Vegetation and Climates of the Last 45,000 Years in the Vicinity of the Nevada Test Site, South-Central Nevada.* USGS Professional Paper 1329. Denver, Colorado: U.S. Geological Survey. TIC 203210.

Spaulding, W.G.; Robison, S.W.; and Paillet, F.L. 1984. *Preliminary Assessment of Climatic Change During Late Wisconsin Time, Southern Great Basin and Vicinity, Arizona, California, and Nevada.* USGS Water Resources Investigations Report 84-4328. Denver, Colorado: U.S. Geological Survey. NNA.19910221.0114.

Spengler, R.W. and Chornack, M.P. 1984. *Stratigraphic and Structural Characteristics of Volcanic Rocks in Core Hole USW G-4, Yucca Mountain, Nye County, Nevada.* USGS-OFR-84-789. Denver, Colorado: U.S. Geological Survey. MOL.19980430.0203.

Spengler, R.W.; Byers, Jr., F.M.; and Warner J.B. 1981. *Stratigraphy and Structure of Volcanic Rocks in Drill Hole USW G1, Yucca Mountain, Nye County, Nevada.* USGS-OFR-81-1349. Denver, Colorado: U.S. Geological Survey. NNA.19870406.0222.

Spengler, R.W.; Muller, D.C.; and Livermore, R.B. 1979. *Preliminary Report on the Geology and Geophysics of Drill Hole UE-25 a-1, Yucca Mountain, Nye County, Nevada.* USGS-OFR-79-1244. Denver, Colorado: U.S. Geological Survey. NNA.19870406.0349.

Sposito, G. 1979. "Derivation of the Langmuir Equation For Ion Exchange Reactions in Soils." *Soil Science Society of America Journal 43*, 197–198. Madison, Wisconsin: Soil Science Society of America. TIC 236920.

Sposito, G. 1980. "Derivation of the Freundlich Equation for Ion Exchange Reactions in Soils." *Soil Science Society of America Journal 44*, 652–654. Madison, Wisconsin: Soil Science Society of America. TIC 223199.

Sposito, G. 1984. *The Surface Chemistry of Soils*, Chapter 4. New York, New York: Oxford University Press. TIC 217687.

Sposito, G. 1989. *The Chemistry of Soils*. New York, New York: Oxford University Press. TIC 237211.

Srodon, J. 1980. "Precise Identification of Illite/Smectite Interstratifications by X-Ray Powder Diffraction." *Clays and Clay Minerals 28*, 401–411. Long Island City, New York: Pergamon. TIC 236949.

Stakebake, J.L.; Larson, D.T.; and Haschke, J.M. 1993. *Journal of Alloys and Compounds, 202,* 251-263. Lausanne, Switzerland: Elsevier. TBD

Stalder, K. and Stöber, W. 1965. Haemolytic Activity of Suspensions of Different Silica Modifications and Inert Dusts. *Nature, 207,* 874–875. London, England: Macmillan Publishers, Ltd. TIC 235573.

Steiger, R.H. and Jager, E. 1977. "Subcommission on Geochronology: Convention on the Use of Decay Constants in Geo- and Cosmochronology." *Earth and Planetary Science Letters, 36,* 359-362. Amsterdam, Netherlands: Elsevier. TIC 236817.

Steiner, A. 1968. "Clay Minerals in Hydrothermally Altered Rocks at Wairakei, New Zealand." *Clays and Clay Minerals 16*, 193–213. Long Island City, New York: Pergamon. TIC 236968.

Stephens, D.B. and Rehfeldt, K.R. 1985. "Evaluation of Closed-Form Analytical Models to Calculate Conductivity in a Fine Sand." *Soil Science Society of America Journal, 49,* 12–19. Madison, Wisconsin: Soil Science Society of America. TIC 224082.

Stolper, E. 1982. "Water in Silicate Glasses: An Infrared Spectroscopic Study." *Contributions to Mineralogy and Petrology, 81,* 1-17. New York, New York: Springer-Verlag. TBD

Stumm, W. 1992. *Chemistry of the Solid-Water Interface.* New York, New York: John Wiley and Sons. TIC 237213.

Surdam, R.C. and Eugster, H.P. 1976. *Mineral Reactions in the Sedimentary Deposits of the Lake Magadi Region, Kenya.* Geological Society of America Bulletin, 87, 1739–1752. Boulder, Colorado: Geological Society of America. TIC 222525.

Surdam, R.C. and Sheppard, R.A. 1978. "Zeolites in Saline, Alkaline-Lake Deposits." *Natural Zeolites, Occurrence, Properties, Use*, 145–174. Sand, L.B. and Mumpton, F.A., Eds. New York, New York: Pergamon Press. NNA.19890501.0112.

Suzuki, Y. 1982. "Carcinogenic and Fibrogenic Effects of Zeolites: Preliminary Observations." *Environmental Research, 27,* 433–445. Tarrytown, New Jersey: Academic Press. NNA.19940104.0068; TIC 235567.

Suzuki, Y. and Kohyama, N. 1984. "Malignant Mesothelioma Induced by Asbestos and Zeolite in the Mouse Peritoneal Cavity." *Environmental Research, 35,* 277–292. Tarrytown, New Jersey: Academic Press. TIC 235560.

Suzuki, Y. and Kohyama, N. 1988. "Carcinogenic and Fibrogenic Effects of Erionite, Mordenite, and Synthetic Zeolite 4A." *Occurrence, Properties, and Utilization of Natural Zeolites*, 829–840. Kalló, D. and Sherry, H.S., Eds. Budapest, Hungary: Akadémiai Kiadó. TIC 235571.

Swadley, W. and Hoover, D. 1983. *Geology of Faults Exposed in Trenches in Crater Flat, Nye County, Nevada.* USGS-OFR-83-608. Denver, Colorado: U.S. Geological Survey. NNA.19870518.0074.

Swanberg, C.A. and Combs, J. 1986. "Geothermal Drilling in the Cascade Range: Preliminary Results from a 1387-m Core Hole, Newberry Volcano, Oregon." *American Geophysical Union Transactions, 67,* 578–580. Washington, D.C.: American Geophysical Union. TIC 237078.

Sweetkind, D.S.; Fabryka-Martin, J.; Flint, A.; Potter, C.; and Levy, S. 1997. *Evaluation of the Structural Significance of Bomb-Pulse ^{36}Cl at Sample Locations in the Exploratory Studies Facility, Yucca Mountain, Nevada.* Los Alamos, New Mexico: Los Alamos National Laboratory. TBD.

Szabo, B.; Carr, W.; and Gottschall, W. 1981. *Uranium-Thorium Dating of Quaternary Carbonate Accumulations in the Nevada Test Site Region, Southern Nevada.* USGS-OFR-81-119. Denver, Colorado: U.S. Geological Survey. NNA.19870518.0070.

Tait, C.D.; Clark, D.L.; Neu, M.P.; and Hobart, D.E. 1996. Los Alamos National Laboratory YMP Milestone Report 3411. Los Alamos, New Mexico: Los Alamos National Laboratory. TBD

Tait, C.D.; Palmer, P.D.; Ekberg, S.A.; and Clark, D.L. 1995. *Report on Neptunium Speciation by NMR and Optical Spectroscopies.* LA-13012-MS. YMP Milestone Report 3413. Los Alamos, New Mexico: Los Alamos National Laboratory. MOL.19971117.0011.

Taylor, E.M. 1986. *Impact of Time and Climate on Quaternary Soils in the Yucca Mountain Area of the Nevada Test Site.* Master's thesis. Boulder, Colorado: University of Colorado. TIC 218287.

Theis, T.L. and Richter, R.O. 1980. "Adsorption Reactions of Nickel Species at Oxide Surfaces." *Advances in Chemistry Series, 189*, 73–96. Washington, D.C.: American Chemical Society. TIC 236944.

Thomas, K.W. 1987. *Summary of Sorption Measurements Performed with Yucca Mountain, Nevada, Tuff Samples and Water from Well J-13.* LA-10960-MS. Los Alamos, New Mexico: Los Alamos National Laboratory. NNA.19890602.0026; NNA.19900604.0045.

Thomas, K.W., compiler 1988. *Research and Development Related to the Nevada Nuclear Waste Storage Investigations, October 1–December 31, 1984.* LA-11443-PR. Los Alamos, New Mexico: Los Alamos National Laboratory. NNA.19920131.0372.

Thordarson, W. 1965. *Perched Groundwater in Zeolitized Bedded Tuff, Rainier Mesa and Vicinity, Nevada Test Site.* USGS Technical Report TEI-862. Denver, Colorado: U.S. Geological Survey. NNA.19881021.0066.

Thordarson, W.; Rush, F.; Spengler, R.; and Waddell, S. 1984. *Geohydrologic and Drill-Hole Data for Test Well USW H-3, Yucca Mountain, Nye County, Nevada.* USGS-OFR-84-149. Denver, Colorado: U.S. Geological Survey. NNA.19870406.0056.

Thorstenson, D.C.; Weeks, E.P.; Haas, H.H.; and Woodward, J.C. 1989. "Physical and Chemical Characteristics of Topographically Affected Airflow in an Open Bore Hole at Yucca Mountain." *Proceedings of the Topical Meeting on the Unsaturated Zone, Focus ë89, September 17-21, 1989, Las Vegas, Nevada*, 256-270. La Grange Park, Illinois: American Nuclear Society. TIC 216833.

Tien, P.-L.; Siegel, M.D.; Updegraff, C.D.; Wahi, K.K.; and Guzowski, R.V. 1985. *Repository Site Data Report for Unsaturated Tuff, Yucca Mountain, Nevada.* NUREG CR 4110. (Also, SAND84-2668. Albuquerque, New Mexico: Sandia National Laboratories) Washington, D.C.: U.S. Nuclear Regulatory Commission. TIC 217172.

Torresan, M. 1987. *The Use of Sodium Polytungstate in Heavy Mineral Separations.* USGS-OFR-87-590. Denver, Colorado: U.S. Geological Survey. TIC 235391.

Torstenfelt, B.; Rundberg, R.S.; and Mitchell, A.J. 1988. "Actinide Sorption On Granites and Minerals As A Function of pH and Colloids/Pseudocolloids." *Radiochimica Acta 44/45*, 111-117. München, Germany: Verlag. TIC 237496.

Travis, B.J. and Birdsell, K.H. 1991. *TRACR3D: A Model of Flow and Transport in Porous Media.* LA-11798-M. Los Alamos, New Mexico: Los Alamos National Laboratory. NNA.19910515.0163.

Triay, I.R. and Rundberg, R.S. 1987. "Determination of Selectivity Coefficient Distributions By Deconvolution of Ion-Exchange Isotherms." *Journal of Physical Chemistry, 91*(20), 5269–5274. Washington, D.C.: American Chemical Society. TIC 233343.

Triay, I.R. and Rundberg, R.S. 1989a. "Application of Deconvolution to the Analysis of Univalent Ion-Exchange Isotherms in Zeolites X and Y." *Zeolites, 9,* 217–223. Guildford, Surrey, England: Elsevier. TIC 233342.

Triay, I.R. and Rundberg, R.S. 1989b. "Deconvolution of Multivalent Cation-Exchange Isotherms." *Journal of Physical Chemistry, 93*, 5617–5623. Washington, D.C.: American Chemical Society. TIC 203241.

Triay, I.R.; Birdsell, K.H.; Mitchell, A.J.; and Ott, M.A. 1993. "Diffusion of Sorbing and Nonsorbing Radionuclides in Tuff." *High Level Radioactive Waste Management: Proceedings of the Fourth Annual International Conference, Las Vegas, Nevada, April 26–30, 1993,* 2, 1527-1532. La Grange Park, Illinois: American Nuclear Society. TIC 222367.

Triay, I.R.; Cotter, C.R.; and Harrigan, P. 1995. *Interim Report: Sorption Isotherms.* Milestone 3339. Los Alamos, New Mexico: Los Alamos National Laboratory. MOL.19971111.0057.

Triay, I.R.; Cotter, C.R.; Huddleston, M.H.; Leonard, D.E.; Weaver, S.C.; Chipera, S.J.; Bish, D.L.; Meijer, A.; and Canepa, J.A. 1996. *Batch Sorption Results for Neptunium Transport through Yucca Mountain Tuffs.* Yucca Mountain Site Characterization Program Milestone 3349. LA-12961-MS. Los Alamos, New Mexico: Los Alamos National Laboratory. TIC 226359.

Triay, I.R.; Cotter, C.R.; Kraus, S.M.; Huddleston, M.H.; Chipera, S.J.; and Bish, D.L. 1996. *Radionuclide Sorption in Yucca Mountain Tuffs with J-13 Well Water: Neptunium, Uranium, and Plutonium.* Yucca Mountain Site Characterization Program Milestone 3338. LA-12956-MS. Los Alamos, New Mexico: Los Alamos National Laboratory. TIC 226117.

Triay, I.R.; Degueldre, C.; Wistrom, A.O.; Cotter, C.R.; and Lemons, W.W. 1996. *Progress Report on Colloid-Facilitated Transport at Yucca Mountain.* LA-12959-MS. Los Alamos, New Mexico: Los Alamos National Laboratory. TIC 225473.

Triay, I.R.; Furlano, A.; and Strietelmeier, B. 1996. *Comparison of Neptunium Sorption Results Using Batch and Column Techniques.* Yucca Mountain Site Characterization Program Milestone 3041. LA-12958-MS. Los Alamos, New Mexico: Los Alamos National Laboratory. TIC 226119.

Triay, I.R.; Hobart, D.E.; Mitchell, A.J.; Newton, T.W.; Ott, M.A.; Palmer, P.D.; Rundberg, R.S.; and Thompson, J.L. 1991. "Size Determinations of Plutonium Colloids Using Autocorrelation Photon Spectroscopy." *Radiochimica Acta 52/53*, 127–131. München, Germany: Verlag. TIC 222703.

Triay, I.R.; Meijer, A.; Cisneros, M.R.; Miller, G.G.; Mitchell, A.J.; Ott, M.A.; Hobart, D.E.; Palmer, P.D.; Perrin, R.E.; and Aguilar, R.D. 1991. "Sorption of Americium in Tuff and Pure Minerals Using Synthetic and Natural Groundwaters." *Radiochimica Acta 52/53*, 141–145. München, Germany: Verlag. TIC 222704.

Triay, I.R.; Meijer, A.; Conca, J.L.; Kung, K.S.; Rundberg, R.S.; Strietelmeier, B.A.; Tait, C.D.; Clark, D.L.; Neu, M.P.; and Hobart, D.E. 1997. *Summary and Synthesis Report on Radionuclide Retardation for the Yucca Mountain Site Characterization Project.* Yucca Mountain Site Characterization Program Milestone 3784M. LA-13262-MS. Los Alamos, New Mexico: Los Alamos National Laboratory. MOL.19971210.0177.

Triay, I.R.; Mitchell, A.J.; and Ott, M.A. 1991. "Radionuclide Migration as a Function of Mineralogy." *High Level Radioactive Waste Management, Proceedings of the Second Annual International Conference, Las Vegas, Nevada, April 28-May 3, 1991,* 494–498. La Grange Park, Illinois: American Nuclear Society. TIC 221953.

Triay, I.R.; Robinson, B.A.; Lopez, R.M.; Mitchell, A.J.; and Overly, C.M. 1993. "Neptunium Retardation with Tuffs and Groundwaters from Yucca Mountain." *High Level Radioactive Waste Management, Proceedings of the Fourth Annual International Conference, Las Vegas, Nevada, April 26-30, 1993,* 1504–1508. LaGrange Park, Illinois: American Nuclear Society. TIC 234719.

Triay, I.R.; Simmons, A.; Levy, S.; Nelson, S.; Nuttall, H.; Robinson, B.; Steinkampf, W.; and Viani, B. 1995. *Colloid-Facilitated Radionuclide Transport at Yucca Mountain.* LA-12779-MS. Los Alamos, New Mexico: Los Alamos National Laboratory. TIC 215159.

Tsuji, M. and Komarneni, S. 1993. "Selectivity Study of Alkaline-Earth and Divalent Transition Metal Ions on $[Al^{3+}+Na^{+}]$-Substituted Tobermorites." *Separation Science and Technology, 28,* 2061–2071. New York, New York: Marcel Dekker, Inc. TIC 236894.

Tsunashima, A.; Brindley, G.W.; and Bastovanov, M. 1981. "Adsorption of Uranium From Solutions by Montmorillonite: Compositions and Properties of Uranyl Montmorillonites." *Clays and Clay Minerals 29,* 10–16. Long Island, New York: Pergamon. TIC 236914.

van den Hul, H.J. and Lyklema, J.J. 1968. "Determination of Specific Surface Areas of Dispersed Materials: Comparison of the Negative Adsorption Method with Some Other Methods." *Journal of the American Chemical Society, 90*(12), 3,010–3,015. Washington, D.C.: American Chemical Society. TIC 236900.

Vaniman, D.T. 1994. *Calcite Deposits in Drill Cores USW G-2 and USW GU-3/G-3 at Yucca Mountain, Nevada: Preliminary Report.* LA-12720-MS. Los Alamos, New Mexico: Los Alamos National Laboratory. NNA.19931018.0075.

Vaniman, D.T. and Bish, D.L. 1995. "Importance of Zeolites in the Potential High-Level Radioactive Waste Repository at Yucca Mountain, Nevada." *Natural Zeolites '93, Occurrence, Properties, and Use,* 533-546. Ming, D.W. and Mumpton, F.A., Eds. Brockport, New York: International Committee on Natural Zeolites. TIC 217194.

Vaniman, D.T. and Chipera, S.J. 1996. "Paleotransport of Lanthanides and Strontium Recorded in Calcite Compositions from Tuffs at Yucca Mountain, Nevada, USA." *Geochimica et Cosmochimica Acta, 60,* 4417–4433. Oxford/New York: Pergamon Press. TIC 231351.

Vaniman, D.T. and Whelan, J.F. 1994. "Inferences of Paleoenvironment from Petrographic, Chemical and Stable-Isotope Studies of Calcretes and Fracture Calcites." *High Level Radioactive Waste Management: Proceedings of the Fifth Annual International Conference, Las Vegas, Nevada, May 22–26, 1994*, 2730–2737. La Grange Park, Illinois: American Nuclear Society. TIC 222137.

Vaniman, D.T.; Bish, D.; Broxton, D.; Byers, F.; Heiken, G.; Carlos, B.; Semarge, E.; Caporuscio, F.; and Gooley, R. 1984. *Variations in Authigenic Mineralogy and Sorptive Zeolite Abundance at Yucca Mountain, Nevada, Based on Studies of Drill Cores USW GU-3 and G-3.* LA-9707-MS. Los Alamos, New Mexico: Los Alamos National Laboratory. TIC 200553.

Vaniman, D.T.; Bish, D.L.; and Chipera, S. 1988. *Preliminary Comparison of Mineral Deposits in Faults Near Yucca Mountain, Nevada, with Possible Analogs.* LA-11289-MS. Los Alamos, New Mexico: Los Alamos National Laboratory. TIC 202377.

Vaniman, D.T.; Bish, D.; and Chipera, S. 1993. "Dehydration and Rehydration of a Tuff Vitrophyre." *Journal of Geophysical Research, 98*, 22,309-22,320. Washington, D.C.: American Geophysical Union. TIC 224612.

Vaniman, D.T.; Bish, D.L.; Chipera, S.J.; Carlos, B.A.; and Guthrie, Jr., G.D. 1996. "Chemistry and Mineralogy of the Transport Environment At Yucca Mountain," in *Summary and Synthesis Report on Mineralogy and Petrology Studies for the Yucca Mountain Site Characterization Project, Volume I.* YMP Milestone LA 3665. Los Alamos, New Mexico: Los Alamos National Laboratory. TIC 229849.

Vaniman, D.T.; Chipera, S.J.; and Bish, D.L. 1994. "Pedogenesis of Siliceous Calcretes at Yucca Mountain, Nevada." *Geoderma, 63*, 1–17. Amsterdam, Netherlands: Elsevier. TIC 212060.

Vaniman, D.T.; Chipera, S.J.; and Bish, D.L. 1995. *Petrography, Mineralogy, and Chemistry of Calcite-Silica Deposits at Exile Hill, Nevada, Compared with Local Spring Deposits.* LA-13096-MS. Los Alamos, New Mexico: Los Alamos National Laboratory. TIC 225488.

Vaniman, D.T.; Chipera, S.J.; and Bish, D.L. 1997. *Mineralogic and Chemical Analyses of Exploratory Studies Facility (ESF) and Core Calcites, Opals, Mn-Oxides, and Clays.* YMP Milestone Report SP321CM4. Los Alamos, New Mexico: Los Alamos National Laboratory. TBD

Vaniman, D.T.; Furlano, A.; Thompson, J.; and Triay, I. 1995. "Actinide Microautoradiography and the Characterization of Pu Retention by Clay Minerals." Abstract in *32nd Annual Meeting, Clay Minerals Society, Program and Abstracts, Baltimore, Maryland, June 3–8, 1995*, p. 122. Bloomington, Indiana: Clay Minerals Society. TIC 237724.

Vaughan, D.E.W. 1978. "Properties of Natural Zeolites." *Natural Zeolites: Occurrences, Properties, Use*, 353–371. Sand and, L.B.and Mumpton, F.A., Eds. Elmsford, New York: Pergamon Press. TIC 218699.

Veblen, D.R.; Guthrie, G.D., Jr.; and Livi, K.J.T. 1990. "High-Resolution Transmission Electron Microscopy and Electron Diffraction of Mixed-Layer Illite/Smectite: Experimental Results." *American Mineralogist 38*, 1–13. Washington, D.C.: Mineralogical Society of America. TIC 239136.

Venzl, G. and Ross, J. 1982. "Nucleation and Colloidal Growth in Concentration Gradients (Liesegang Rings)." *Journal of Chemical Physics, 77*, 1302–1307. New York, New York: American Institute of Physics. TIC 237064.

Viles, H.A. and Goudie, A.S. 1990. "Reconnaissance Studies of the Tufa Deposits of the Napier Range, N.W. Australia." *Earth Surface Processes and Landforms, 15*, 425-443. New York, New York: John Wiley and Sons. TIC 224428.

Vilks, P. and Degueldre, C. 1991. "Sorption Behavior of ^{85}Sr, ^{131}I, and ^{137}Cs on Grimsel Colloids and Suspended Particles from the Grimsel Test Site, Switzerland." *Applied Geochemistry, 6*, 553-563. New York, New York: Pergamon. TIC 236931.

Vilks, P.; Cramer, J.J.; Bachinski, D.B.; Doern, D.C.; and Miller, H.G. 1993. "Studies of Colloids and Suspended Particles, Cigar Lake Uranium Deposit, Saskatchewan, Canada." *Applied Geochemistry, 8*, 605–616. New York, New York: Pergamon. TIC 237449.

Vilks, P.; Miller, H.G.; and Doern, D.C. 1991. "Natural Colloids and Suspended Particles in the Whiteshell Research Area and their Potential Effect on Radiocolloid Formation." *Applied Geochemistry, 6*, 565–574. New York, New York: Pergamon Press. TIC 237339.

Volkov, Y.F.; Visyashcheva, G.I.; Tomilin, S.V.; Kapshukov, I.I.; and Rykov, A.G. 1981. "Carbonate Compounds of Pentavalent Actinides with Alkali-Metal Cations: X. Composition and Crystal Structure of Carbonates." *Radiokhimiya, 23,* 200 (English translation). New York, New York: Plenum Publishing Corporation. TIC 239010.

Volkov, Y.F.; Visyashcheva, G.I.; Tomilin, S.V.; Spiryakov, V.I.; Kapshukov, I.I.; and Rykov, A.G. 1979. "Carbonate Compounds of Pentavalent Actinides with Alkali-Metal Cations: VII. Synthesis and Crystal Structure of Hydrate Compounds with the Composition $Na_{0.6}NpO_2(CO_3)_{0.8}{\bullet}nH_2O$." *Radiokhimiya* 21: 583 (English translation). New York, New York: Plenum Publishing Corporation. TBD

von Ballmoos, R. 1984. *Collection of Simulated XRD Powder Patterns for Zeolites.* Great Britain: Butterworth & Co. TBD

Waddell, R.K.; Robison, J.H.; Blankennagel, R.K. 1984. *Hydrology of Yucca Mountain and Vicinity, Nevada-California: Investigative Results through Mid-1983.* USGS Water Resources Investigations Report 84-4267. Denver, Colorado: U.S. Geological Survey. TIC 203219.

Wagner, J.C. 1982. "Health Hazards of Substitutes." *Proceedings of the World Symposium on Asbestos, May 1982, Montreal*, 244–266. Montreal, Canada: Canadian Asbestos Information Centre. TIC 235616.

Wagner, J.C. 1990. "Review on Pulmonary Effects of Phyllosilicates after Inhalation." *Health Related Effects of Phyllosilicates*, 309–318. Bignon, J., Ed. Berlin, Germany: Springer-Verlag. TIC 236986.

Wagner, J.C.; Skidmore, J.W.; Hill, R.J.; and Griffiths, D.M. 1985. "Erionite Exposure and Mesotheliomas in Rats." *British Journal of Cancer, 51,* 727–730. London, England: Cancer Campaign for Research. TIC 218392.

Waite, T.O.; Davis, J.A.; Payne, T.E.; Waychunas, G.A.; and Xu, N. 1994. "Uranium(VI) Adsorption to Ferrihydrite: Application of a Surface-Complexation Model." *Geochimica et Cosmochimica Acta, 58*, 5465–5478. Oxford/New York: Pergamon Press. TIC 226322.

Walker, G.E. and Eakin, T.E. 1963. *Geology and Groundwater of Amargosa Desert, Nevada-California.* Nevada Department of Conservation and Natural Resources (Carson City, Nevada) Groundwater Resources-Reconnaissance Series Report 14. TIC 208665.

Walton, A. 1975. *Zeolitic Diagenesis in Oligocene Volcanic Sediments, Trans-Pecos, Texas.* Geological Society of America Bulletin, 86, 615–624. Boulder, Colorado: Geological Society of America. TIC 236815.

Warren, R.G. and Byers, Jr., F.M. 1985. "The Petrologic Unit: A Useful Tool in Deciphering a Complex Volcanic Terrane in SW Nevada." *Geological Society of America, Abstracts with Programs 1985 17*(4), 270. Boulder, Colorado: Geological Society of America. TIC 237062.

Warren, R.G.; Byers, Jr., F.M.; Broxton, D.E.; Freeman, S.H.; and Hagan, R.C. 1989. "Phenocryst Abundances and Glass and Phenocryst Compositions as Indicators of Magmatic Environments of Large-Volume Ash Flow Sheets in Southwestern Nevada." *Journal of Geophysical Research, 94*, 5987–6020. Washington, D.C.: American Geophysical Union. TIC 225939.

Warren, R.G.; Byers, Jr., F.M.; and Caporuscio, F.A. 1984. *Petrography and Mineral Chemistry of Units of the Topopah Spring, Calico Hills, and Crater Flat Tuffs, and Older Volcanic Units, with Emphasis on Samples from Drill Hole USW G-1, Yucca Mountain, Nevada Test Site.* LA-10003-MS. Los Alamos, New Mexico: Los Alamos National Laboratory. TIC 202351.

Wastiaux, A. and Daniel, H. 1990. "Pulmonary Toxicity of Kaolin in Rats Exposed by Inhalation." *Health Related Effects of Phyllosilicates*, 405–414. Bignon, J., Ed. Berlin, Germany: Springer-Verlag. TBD

Watts, N.L. 1980. "Quaternary Pedogenic Calcretes from the Kalahari (Southern Africa): Mineralogy, Genesis and Diagenesis." *Sedimentology, 27,* 661-686. Oxford, England: Blackwell Scientific Publishers. TIC 224430.

Waxweiler, R.; Zumwalde, R.D.; Ness, G.O.; and Brown, D.P. 1988. "A Retrospective Cohort Mortality Study of Males Mining and Milling Attapulgite Clay." *American Journal of Industrial Medicine, 13*, 305–315. NNA.940323.0299.

Weiss, S.I.; Noble, D.C.; and Larson, L.T. 1991. *Task 3: Evaluation of Mineral Resource Potential, Caldera Geology, and Volcano-Tectonic Framework at and near Yucca Mountain.* Report for October 1990 - September 1991. Reno, Nevada: Mackay School of Mines, University of Nevada, Reno. TIC 235554.

West, R.G. and Kelly, R.C. 1971. *A Selected, Annotated Bibliograhy of the Civil, Industrial, and Scientific Uses for Nuclear Explosions.* U.S. Atomic Energy Commission Report TID-3522 (9th rev.). TBD

Whelan, J.F.; Moscati, R.J.; Allerton, S.B.M.; and Marshall, B.D. 1996. *Applications of Isotope Geochemistry to the Reconstruction of Yucca Mountain Paleohydrology.* USGS Milestone Report 3GQH257M to DOE-YMPSCO. Denver, Colorado: U.S. Geological Survey. MOL.19961119.0006.

Whelan, J.F.; Vaniman, D.T.; Stuckless, J.S.; and Moscati, R.J. 1994. "Paleoclimatic and Paleohydrologic Records from Secondary Calcite: Yucca Mountain, Nevada." *High Level Radioactive Waste Management: Proceedings of the Fifth Annual International Conference, Las Vegas, Nevada, May 22–26, 1994*, 2738–2745. La Grange Park, Illinois: American Nuclear Society. TIC 222138.

White, A.F.; Benson, S.M.; Yee, A.W.; Wollenberg, H.A., Jr.; Flexser, S. 1991. "Groundwater Contamination at the Kesterson Reservoir, California 2: Geochemical Parameters Influencing Selenium Mobility." *Water Resources Research, 27*, 1085–1098. Washington, D.C.: American Geophysical Union. TIC 237455.

White, A.F.; Claassen, H.C.; and Benson, L.V. 1980. *The Effect of Dissolution of Volcanic Glass on the Water Chemistry in a Tuffaceous Aquifer, Rainier Mesa, Nevada.* USGS Water Supply Paper 1535-Q. Denver, Colorado: U.S. Geological Survey. TIC 221391.

White, D.E.; Brannock, W.W.; and Murata, K.J. 1956. "Silica in Hot-Spring Waters." *Geochimica et Cosmochimica Acta, 10,* 27-59. Oxford/New York: Pergamon Press. TIC 224431.

Whitfield, Jr., M.; Thordarson, W.; and Eshom, E. 1984. *Geohydrologic and Drill-Hole Data for Test Well USW H-4, Yucca Mountain, Nye County, Nevada.* USGS-OFR-84-449. Denver, Colorado: U.S. Geological Survey. NNA.19870407.0317.

Wieland, E. 1988. *Die Verwitterung schwerlöslicher Mineralien—ein Koordinationschemischer Ansatz zur Beschreibung der Auflösungskinetik.* Doctoral dissertation. ETH Zurich, Switzerland. TBD

Wilkin, R.T. and Barnes, H.L. 1995. "Solubilities of the Zeolites Analcime and Na-Clinoptilolite in Hydrothermal Solutions." *Program and Abstracts of the V. M. Goldschmidt Conference*, 97.. Barnes, H.L., Ed. Madison, Wisconsin: University of Wisconsin. TIC 235383.

Wilson, C.N. 1990. *Results from NNWSI Series-3 Spent Fuel Dissolution Tests.* Pacific Northwest Laboratory Report PNL-7170. Richland, Washington: Pacific Northwest Laboratory. TIC 200816.

Wilson, C.N. and Bruton, C.J. 1990. "Studies on Spent Fuel Dissolution Behavior Under Yucca Mountain Repository Conditions." *Nuclear Waste Management III. Ceramic Trans., 9,* 423–441. Richland, Washington: Pacific Northwest Laboratory. TIC 230177.

Wilson, M.L.; Gauthier, J.G.; Barnard, R.W.; Barr, G.E.; Dockery, H.A.; Dunn, E.; Eaton, R.R.; Guerin, D.C.; Lu, N; Martinez, M.J.; Nilson, R.; Rautman, C.A.; Robey, T.H.; Ross, B.; Ryder, E.E.; Schenker, A.R.; Shannon, S.A.; Skinner, L.H.; Halsey, W.G.; Gansemer, J.D.; Lewis, L.C.; Lamont, A.D.; Triay, I.R.; Meijer, A.; and Morris, D.E. 1994. *Total-System Performance Assessment for Yucca Mountain—SNL Second Iteration (TSPA-1993).* SAND93-2675. Albuquerque, New Mexico: Sandia National Laboratories. NNA.19940112.0123.

Winchester, J.W. and Duce, R.A. 1967. "The Global Distribution of Iodine, Bromine, and Chlorine in Marine Aerosols." *Naturwissenschaften, 54,* 110-113. Berlin, Germany: Springer-Verlag. TIC 226930.

Winograd, I.J. and Thordarson, W. 1975. *Hydrogeologic and Hydrochemical Framework, South-Central Great Basin, Nevada-California, with Special Reference to the Nevada Test Site.* USGS Professional Paper 712-C. Denver, Colorado: U.S. Geological Survey. TIC 206787.

WoldeGabriel, G. 1995a. *Ion Exchange and Dehydration Experimental Studies of Clinoptilolite: Implications to Zeolite Dating.* LA-12894-MS. Los Alamos, New Mexico: Los Alamos National Laboratory. TIC 217191.

WoldeGabriel, G. 1995b. "K/Ar Dating of Clinoptilolite, Mordenite, and Coexisting Illite/Smectite from Yucca Mountain, Nevada." *Natural Zeolites '93,* 141–156. Ming. D.S. and Mumpton, F.A., Eds. Brockport, New York: International Committee on Natural Zeolites. TIC 217192.

WoldeGabriel, G., and Goff, F. 1989. "Temporal Relations of Volcanism and Hydrothermal Systems in Two Areas of the Jemez Volcanic Field, New Mexico." *Geology, 17,* 986–989. Boulder, Colorado: Geological Society of America. TIC 236814.

Woldegabriel, G.; Broxton, D.E.; Bish, D.L.; and Chipera, S.J. 1992. "Preliminary Assessment of Clinoptilolite K/Ar Results from Yucca Mountain, Nevada: A Potential High-Level Radioactive Waste Repository Site." *Water-Rock Interaction, Proceedings of the 7th International Symposium.* Water-Rock Interaction, WRI-7, Park City Utah, July, 457-461. Capetown, South Africa: A.A. Balkema, Rotterdam and Brookfield. TIC 222009.

WoldeGabriel, G.; Broxton, D.E.; and Byers, Jr., F.M. 1996. "Mineralogy and Temporal Relations of Coexisting Authigenic Minerals in Altered Silicic Tuffs and their Utility as Potential Low-Temperature Dateable Minerals." *Journal of Volcanism and Geothermal Research, 71,* 155-165. Amsterdam, Netherlands: Elsevier. TIC 226682.

Wolery, T.J. 1983. *EQ3NR, A Computer Program For Geochemical Aqueous Speciation-Solubility Calculations: User's Guide and Documentation.* UCRL-53414. Livermore, California: Lawrence Livermore National Laboratory. TIC 1148.

Wright, V.P. 1986. "The Role of Fungal Biomineralization in the Formation of Early Carboniferous Soil Fabrics." *Sedimentology, 33,* 831-838. Oxford, England: Blackwell Scientific Publishers. TIC 224432.

Wright, V.P. 1989. "Terrestrial Stromatolites and Laminar Calcretes: A Review." *Sedimentary Geology, 65,* 1-13. Amsterdam/New York: International Association of Sedimentologists. TIC 224433.

Wronkiewicz, D.J.; Wang, L.M.; Bates, J.K.; and Tani, B.S. 1993. "Effects of Radiation Exposure on Glass Alteration in a Steam Environment," in "Scientific Basis for Nuclear Waste Management XVI." Interrante, C.G. and Pabalan, R.T., Eds. *Materials Research Society Symposium Proceedings, 294,* 183–190. Pittsburgh, Pennsylvania: Materials Research Society. TIC 206673.

Yajima, T.; Kawamura, Y.; and Ueta, S. 1995. "Uranium(IV) Solubility and Hydrolysis Constants Under Reduced Conditions." *Materials Research Society Symposium Proceedings, 353,* 1137–1142. Pittsburgh, Pennsylvania: Materials Research Society. TIC 237687.

Yamamoto, K.; Sugisaki, R.; and Arai, F. 1986. "Chemical Aspects of Alteration of Acidic Tuffs and their Application to Siliceous Deposits." *Chemical Geology, 55,* 61–76. Amsterdam/New York: Elsevier. TIC 237052.

Yang, I.C. 1992. "Flow and Transport Through Unsaturated Rock—Data from Two Test Holes, Yucca Mountain, Nevada." *High Level Radioactive Waste Management, Proceedings of the Third Annual International Conference, Las Vegas, Nevada, April 12-16, 1992,* 732–737. La Grange, Illinois: American Nuclear Society; and New York, New York: American Society of Civil Engineers. TIC 225238.

Yang, I.C.; Davis, G.S.; and Sayer, T.M. 1990. "Comparison of Pore-Water Extraction by Triaxial Compression and High-Speed Centrifugation Method." *Minimizing Risk to the Hydrologic Environment.* Zaporozec, A., Ed., 250-259. Dubuque, Iowa: Kendall/Hunt Publishing Company. NNA.19920117.0120.

Yang, I.C.; Peters, C.A.; and Thorstenson, D.C. 1993. "Carbon Isotopic Data from Test Hole USW UZ-1, Yucca Mountain, Nevada." *High Level Radioactive Waste Management, Proceedings of the Fourth Annual International Conference, Las Vegas, Nevada, April 26-30, 1993,* 401–406. La Grange Park, Illinois: American Nuclear Society; and New York, New York: American Society of Civil Engineers. TIC 235146.

Yang, I.C.; Rattray, G.W.; and Yu, P. 1996. *Interpretation of Chemical and Isotopic Data from Bore Holes in the Unsaturated Zone, Yucca Mountain, Nevada.* USGS Water Resources Investigation Report 96-4058. Denver, Colorado: U.S. Geological Survey. MOL.19970715.0408.

Yang, I.C.; Turner, A.K.; Sayre, A.M.; and Montazer, P. 1988. *Triaxial-Compression Extraction of Pore Water from Unsaturated Tuff, Yucca Mountain, Nevada.* USGS Water Resources Investigation Report 88-4189. Denver, Colorado: U.S. Geological Survey. TIC 206013.

Yang, I.C.; Yu, P.; Rattray, G.W.; and Thorstenson, D.C. 1998. *Hydrogeochemical Investigations and Geochemical Modeling in Characterizing the Unsaturated Zone at Yucca Mountain, Nevada.* USGS Water Resources Investigation Report 98-4132. Denver, Colorado: U.S. Geological Survey. TBD

Yariv, S. and Cross, H. 1979. *Geochemistry of Colloid Systems.* Berlin: Springer-Verlag. TBD

Yu, P. 1996. "The Isotopic Chemical Characterization of the Unsaturated Zone at Yucca Mountain." Doctoral dissertation, Department of Civil, Environmental, and Architectural Engineering. Boulder, Colorado: University of Colorado, Boulder. TIC 237275.

Zen, E.-A. 1961. "The Zeolite Facies: An Interpretation." *American Journal of Science, 259,* 401-409. New Haven, Connecticut: Kline Geology Laboratory, Yale University. TIC 236731.

Zielinski, R.A. 1980. "Uranium in Secondary Silica: A Possible Exploration Guide." *Economic Geology, 75,* 592–602. El Paso, Texas: Economic Geology Publishing Company. TIC 237418.

Zielinski, R.A. 1982. "Uraniferous Opal, Virgin Valley, Nevada: Conditions of Formation and Implications for Uranium Exploration." *Journal of Geochemical Exploration, 16,* 197–216 Amsterdam/New York: Elsevier. TIC 226039.

Zielinski, R.A. 1983. *Evaluation of Ash-Flow Tuffs as Hosts for Radioactive Waste: Criteria Based on Selective Leaching of Manganese Oxides.* USGS-OFR-83-480. Denver, Colorado: U.S. Geological Survey. TIC 218703.

Zielinski, R.A.; Bush, R.W.; Spengler, R.W.; and Szabo, B.J. 1986. "Rock-Water Interaction in Ash Flow Tuffs, Yucca Mountain, Nevada: the Record From Uranium Studies." *Uranium, 2,* 361–386. Amsterdam, Netherlands: Elsevier. TIC 222472.

6.5.2 Codes, Standards, Regulations

10 CFR Part 60. Energy: Disposal of High-Level Radioactive Wastes in Geologic Repositories; Licensing Procedures, 1996. TIC 232902.

10 CFR Part 960. Energy: Nuclear Waste Policy Act of 1982; General Guidelines for the Recommendation of Sites for the Nuclear Waste Repositories; Final Siting Guidelines, 1984. TIC 222719.

29 CFR 1910. Labor: Occupational Safety and Health Standards. TIC 238501.

INTENTIONALLY LEFT BLANK

TABLES

TABLES (Continued)

TABLES (Continued)

TABLES (Continued)

Table 6.1-1. Solubility and Oxidation State of Am(III) in Groundwaters (from Nitsche, Gatti et al. 1993; Nitsche, Roberts et al.1994)

Groundwater	pH	Solubility (M)	% Am(III)
J-13	7	1.2×10^{-9}	100
"	8.5	2.4×10^{-9}	100
UE-25p #1	7	3.2×10^{-7}	100
"	8.5	3.1×10^{-6}	100

Table 6.1-2. Solubility and Oxidation States of Pu in J-13 and UE-25p #1 Groundwater (from Nitsche, Gatti et al. 1993; Nitsche, Roberts et al. 1994)

Groundwater	pH	Solubility (M)	%Pu(III) + Polymer	% Pu(IV)	% Pu(V)	% Pu(VI)
J-13	7	2.3×10^{-7}	5 ± 1	6 ± 1	73 ± 7	18 ± 2
"	8.5	2.9×10^{-7}	3 ± 1	6 ± 1	63 ± 6	27 ± 3
UE-25p #1	7	5×10^{-7}	2 ± 1	12 ± 1	78 ± 7	9 ± 4
"	8.5	1×10^{-7}	3 ± 1	31 ± 1	64 ± 6	2 ± 1

Table 6.1-3. Chemical Variability in Drill-Core Data for High-Silica Rhyolite, Topopah Spring Tuff, Core UE-25UZ #16 (Normalized Anhydrous)

Sample	Range		Average (1 std. dev.)
	Minimum	Maximum	
Unaltered High-Silica Rhyolite (n = 17)			
SiO_2	76.37	77.40	76.92 31)
TiO_2	0.09	0.13	0.10 (1)
Al_2O_3	12.43	13.01	12.74 (17)
Fe_2O_3	0.97	1.07	1.00 (2)
MnO	0.058	0.074	0.068 (4)
MgO	0.00	0.24	0.12 (8)
CaO	0.43	0.50	0.46 (2)
K_2O	4.96	5.17	5.05 (6)
Na_2O	3.42	3.68	3.54 (6)
Trace Elements (ppm)			
Zn	44	62	50 (5)
Rb	177	195	185 (6)
Sr	13	44	29 (8)
Y	11	49	29 (9)
Zr	117	153	126 (11)
Nb	0	31	20 (8)
Altered High-Silica Rhyolite, Trace to 14% Stellerite (n = 21)			
Major Elements (%)			
SiO_2	75.91	77.60	77.07 (38)
TiO_2	0.09	0.10	0.10 (0)
Al_2O_3	12.41	13.23	12.68 (20)
Fe_2O_3	0.95	1.02	0.98 (2)
MnO	0.050	0.081	0.067 (6)
MgO	0.00	0.22	0.13 (8)
CaO	0.45	0.94	0.57 (13)
K_2O	4.74	5.35	4.96 (15)
Na_2O	3.02	3.65	3.44 (15)
Trace Elements (ppm)			
Zn	43	59	50 (4)
Rb	174	194	184 (6)
Sr	23	57	36 (9)
Y	16	39	28 (5)
Zr	117	133	123 (4)
Nb	0	25	20 (6)

Table 6.1-4. Chemical Variability in 105 Outcrop Samples of High-Silica Rhyolite, Topopah Spring Tuff (Normalized Anhydrous)

Sample	Range		Average (1 std. dev.)
	Minimum	Maximum	
SiO_2	74.14	76.73	75.64 (58)
TiO_2	0.09	0.16	0.10 (1)
Al_2O_3	11.99	13.08	12.37 (18)
Fe_2O_3	0.92	1.22	0.98 (4)
MnO	0.04	0.08	0.06 (1)
MgO	0.00	0.40	0.03 (7)
CaO	0.48	1.73	0.73 (28)
K_2O	4.60	5.10	4.86 (10)
Na_2O	3.04	4.06	3.44 (25)

Table 6.1-5. Electron Microprobe Analyses of Coarse (~50 mm) Calcites from Trench 14 Calcrete, of Dolomite and Calcite from the Site 199 Seep in Crater Flat, and of Calcites from Several Springs

Sample:	49,t1a	49,t1a	251,t1a1	251,t1a2	750,t1a	750,t2a	753,t1a	753,t1a
Locality:	Trench 14 Calcrete	Trench 14 Calcrete	Site 199 Seep	Site 199 Seep	GMC Spring Mound	GMC Spring Mound	IMV Spring	IMV Spring
CaO	54.3	56.4	29.8	50.0	56.0	55.7	55.4	54.0
MgO	0.88	0.20	22.5	5.59	0.42	0.33	0.91	1.06
FeO	0.0	0.0	0.0	0.0	0.0	0.0	0.0	0.0
MnO	0.0	0.0	0.0	0.04	0.0	0.0	0.0	0.0
SrO	0.0	0.0	0.0	0.22	0.0	0.0	0.0	0.0
BaO	0.0	0.0	0.0	0.0	0.0	0.0	0.0	0.0
*CO_2	44.8	43.4	47.7	44.1	43.5	43.9	43.7	44.9
Ca	0.960	1.011	0.489	0.881	1.002	0.995	0.989	0.954
Mg	0.022	0.005	0.515	0.137	0.010	0.008	0.023	0.026
Fe	0.000	0.000	0.000	0.000	0.000	0.000	0.000	0.000
Mn	0.000	0.000	0.000	0.001	0.000	0.000	0.000	0.000
Sr	0.000	0.000	0.000	0.002	0.000	0.000	0.000	0.000
Ba	0.000	0.000	0.000	0.000	0.000	0.000	0.000	0.000
*C	1.009	0.992	0.998	0.990	0.993	0.998	0.994	1.010
S	1.991	2.008	2.002	2.011	2.005	2.001	2.006	1.990
Sample:	**754,t1**	**754,t1**	**755,t1a**	**755,t1a**	**755,t1a**	**766,t1a**	**760,t1a**	**760,t1a**
Locality:	**Travertine-Point Vein**	**Travertine-Point Vein**	**Travertine-Point Vein**	**Travertine-Point Vein**	**Travertine-Point Vein**	**Grapevine-Spring Vein**	**Nevares Spring Mound**	**Nevares Ostracod Fossil**
CaO	54.1	54.8	52.5	52.3	53.4	53.3	54.2	54.3
MgO	1.64	0.26	2.47	2.63	1.53	1.90	2.06	0.33
FeO	0.0	0.0	0.0	0.0	0.0	0.0	0.0	0.0
MnO	0.0	0.0	0.0	0.0	0.0	0.0	0.0	0.0
SrO	0.0	0.0	0.14	0.26	0.0	0.11	0.0	0.46
BaO	0.0	0.0	0.0	0.0	0.0	0.0	0.0	0.0
*CO_2	44.2	44.9	44.9	44.7	45.0	44.7	43.7	44.9
Ca	0.960	0.970	0.924	0.922	0.941	0.940	0.964	0.961
Mg	0.040	0.006	0.060	0.064	0.037	0.047	0.051	0.008
Fe	0.000	0.000	0.000	0.000	0.000	0.000	0.000	0.000
Mn	0.000	0.000	0.000	0.000	0.000	0.000	0.000	0.000
Sr	0.000	0.000	0.001	0.002	0.000	0.001	0.000	0.004
Ba	0.000	0.000	0.000	0.000	0.000	0.000	0.000	0.000
*C	0.999	1.012	1.007	1.005	1.011	1.006	0.992	1.013
S	1.999	1.988	1.992	1.993	1.989	1.994	2.007	1.986

*CO_2 and C by difference.

Table 6.1-6. Stratigraphic Units Used in the 3-D Mineralogic Model

Buesch, Spengler et al. (1996)	Integrated Site 3-D Framework Model	CRWMS M&O (1996)	Units Used in This Study
			31 (Topography)
Tiva Canyon Tuff (Tpc)	Tpc		
Crystal-rich member (Tpcr)			
Vitric zone (Tpcrv)	Tpcrv1		
Nonlithophysal zone (Tpcrn)	Tpcrn		
Subvitrophyre transition subzone (Tpcrn4)			
Pumice-poor subzone (Tpcrn3)			
Mixed pumice subzone (Tpcrn2)			
Crystal transition subzone (Tpcrn1)			
Lithophysal zone (Tpcr1)			
Crystal-poor member (Tpcp)			
Upper lithophysal zone (Tpcpul)	Tpcpul		
Middle nonlithophysal zone (Tpcpmn)	Tpcpmn		
Lower lithophysal zone (Tpcpll)	Tpcpll		
Lower nonlithophysal zone (Tpcpln)	Tpcpln		
Hackly subzone (Tpcplnh)	Tpcplnh		
Columnar subzone (Tpcplnc)	Tpcplnc		
Argillic pumice interval (Tpcplnc)			
Vitric zone (Tpcpv)		44	30
Densely welded subzone (Tpcpv3v)	Tpcpv3		
Moderately welded subzone (Tpcpv2)	Tpcpv2		
Non- to part-welded subzone(Tpcpv1)	Tpcpv1	42	29
Pre-Tiva Canyon Tuff bedded tuff (Tpbt4)	Tpb4	41	28
Yucca Mountain Tuff (Tpy)	Tpy	40	27
Pre-Yucca Mountain Tuff bedded tuff (Tpbt3)	Tpbt3	39	26
Pah Canyon Tuff (Tpp)	Tpp	38	25
Pre-Pah Canyon Tuff bedded tuff (Tpbt2)	Tpbt2	37	24
Topopah Spring Tuff (Tpt)	Tpt	36	23
Crystal-rich member (Tptr)			
Vitric zone (Tptrv)			
Nonwelded subzone (Tptrv3)	Tptrv3		
Moderately welded subzone (Tptrv2)	Tptrv2		
Densely welded subzone (Tptrv1)	Tptrv1	34	22
Nonlithophysal zone (Tptrn)	Tptrn	33	21
Dense subzone (Tptrn3)			
Vapor-phase corroded subzone (Tptrn2)			
Lithophysal zone (Tptrl)	Tptrl		
Crystal-poor member (Tptp)			
Upper lithophysal zone (Tptpul)	Tptpul	32	20
Mid nonlithophysal zone (Tptpmn)	Tptpmn	31	19
Lower lithophysal zone (Tptpll)	Tptpll	30	18
Lower nonlithophysal zone (Tptpln)	Tptpln	29	17
Vitric zone (Tptpv)		28	16
Densely welded subzone (Tptpv3)	Tptpv3		
Moderately welded subzone (Tptpv2)	Tptpv2		
Nonwelded subzone (Tptpv1)	Tptpv1	26	15
Pre-Topopah Spring Tuff bedded tuff	Tpbt1	25	14

Table 6.1-6. Stratigraphic Units Used in the 3-D Mineralogic Model (Continued)

Buesch, Spengler et al. (1996)	Integrated Site 3-D Framework Model	CRWMS M&O (1996)	Units Used in This Study
Calico Hills Formation (Tac)		24	13
Unit 4 Pumiceous pyroclastic flow		Tac	
Unit 3 Lithic-rich pyroclastic flow			
Unit 2 Pumiceous pyroclastic flow			
Unit 1 Lithic-rich pyroclastic flow			
Bedded tuff (Tacbt)	Tabt1	23	12
Basal sandstone (Tacbs)			
Prow Pass Tuff (Tcp)	Tcp	22	11
Unit 4 Pyroxene rich			
Unit 3 Welded pyroclastic flow		21	10
Unit 2 Lithic-rich pyroclastic flow		18	9
Unit 1 Pumiceous pyroclastic flow			
Pre-Prow Pass bedded tuff (Tcpbt)	Tcbt3	17	8
Bullfrog Tuff (Tcb)	Tcb		
Upper nonwelded		16	7
Middle variably welded		15	6
Lower nonwelded/altered		12	5
Bedded tuff	Tcbt2	11	4
Tram Tuff (Tct)	Tct	10	3
Bedded tuff	Tcbt1		
Older tuff and lavas below Tcbt1		9	2
Paleozoic Basement		1	1

Table 6.1-7. Quantitative and Qualitative X-Ray Diffraction Results for Altered PTn Tuffs from Busted Butte (BB) and Harper Valley S (YM), SE Yucca Mountain (Weight %)

Sample	Smectite	Clino-ptilolite	Cristo-balite	Tridymite	Opal-CT	Quartz	Hematite	Feldspar	Glass/ Amorph.[1]	Opal-A	Calcite	Total
Tiva Canyon Tuff (Tpcpinc)												
YM-7-SSL[2]	1 ± 1[3]	—[4]	—	—	43 ± 13	56 ± 8	—	—	—	—	—	100 ± 16
Tiva Canyon Tuff (Tpcpv2,1)												
YM-2-SSL,p1	8 ± 2	29 ± 2	23 ± 2	—	—	1 ± 1	—	42 ± 7	—	—	—	103 ± 8
YM-2-SSL,p2	—	—	—	—	~100	—	—	—	—	—	—	~100
YM-11-SSL,p1	29 ± 9	—	18 ± 1	—	—	Trace[5]	—	32 ± 4	21 ± 9	—	—	100 ± 10
YM-11-SSL,p2	—	—	14 ± 1	—	—	—	—	22 ± 3	64 ± 3	—	—	100 ± 3
Pre-Tiva Canyon Tuff Bedded Tuff												
YM-4-SSL-1[6]	1 ± 1	—	Trace	—	—	trace	—	14 ± 5	—	85 ± 10	—	100 ± 10
Pre-Pah Canyon Tuff Bedded Tuff (Tpbt2), Ash Layer 2?												
BB-15-SSL	—	—	31 ± 7[7]	Note 7	19 ± 7[7]	3 ± 1	—	45 ± 6	—	—	1 ± 1	100 ± 7[8]
BB-16-SSL	35 ± 11	1 ± 1[9]	1 ± 1	—	—	2 ± 1	—	13 ± 2	47 ± 11	—	—	100 ± 11[8]
YM-5-SSL	—	1 ± 1[9]	33 ± 6[7]	Note 7	31 ± 6[7]	2 ± 1	—	32 ± 5	—	—	—	100 ± 6[8]
Upper Topopah Spring Tuff												
BB-14-SSL,p1	2 ± 1	—	73 ± 5[7]	Note 7	11 ± 5[7]	—	—	11 ± 2	—	—	1 ± 1	100 ± 5
BB-14-SSL,p2	—	—	—	—	47 ± 9	55 ± 3	—	—	—	—	Trace	102 ± 9
BB-14-SSL,p3	—	—	52 ± 5[7]	Note 7	40 ± 5[7]	4 ± 1	—	4 ± 1	—	—	—	100 ± 5
BB-23-SSL	Note 10	—	31 ± 2[7]	Note 7	24 ± 6[7]	1 ± 1	1 ± 1	35 ± 5	—	—	1 ± 1	100 ± 6

[1] Because glass is not distinguishable from opal-A or other amorphous materials by the x-ray diffraction techniques employed here, this column heading includes the possible presence of amorphous material other than glass, although microscopic examination of the samples supports the presence of glass.

[2] Fracture coating. Results for this sample are semiquantitative due to small sample size.

[3] Errors are conservative 2-sigma values.

[4] "—" = not detected.

[5] Trace = less than 0.5 weight percent.

[6] Opal cement of pumiceous tuff. Results for this sample are semiquantitative due to small sample size.

[7] Proportions of cristobalite, tridymite, and opal-CT are approximate. In particular, the presence of discrete cristobalite and tridymite in a sample containing abundant opal-CT may be difficult to document or quantify.

[8] Total includes 1 ± 1 wt % mica.

[9] Zeolite species uncertain.

[10] This includes 7 ± 2 weight % sepiolite.

Table 6.1-8. Quantitative and Qualitative X-Ray Diffraction Results for Tpcpv, Exploratory Studies Facility South Ramp (Weight%)

Sample	Smectite	Mica/ Illite	Opal-CT/ Cristobalite	Opal-A	Glass	Feldspar	Quartz	Zeolite	Hema-tite	Horn-blende	Other	Total
Tpcpv2												
LANL 2756,p1 Station 75+20 least altered	19 ± 6[1]	—[2]	13 ± 1[3]	—	41 ± 7	24 ± 3	—	3 ± 1[4]	—	trace[5]	—	100 ± 7
LANL 2756,p2 Station 75+20 most altered, within breccia	31 ± 9	—	14 ± 1[3]	—	—	32 ± 5	—	note 6	—	trace	—	95 ± 11
LANL 2756,p3 Station 75+20 white spherules on fracture surfaces	major	—	—	—	—	?[7]	major	note 8	—	—	note 9	—
LANL 2756,p4 Station 75+20 botryoidal silica on fracture surfaces	—	—	85 ± 31[10]	—	—	—	14 ± 3	1 ± 1[4]	—	—	—	100 ± 32
Tpcpv2/1												
LANL 2399,p1 Station 67+20 crystal-rich horizon	12 ± 4	—	7 ± 2	—	51 ± 6	29 ± 4	1 ± 1	—	trace	trace	—	100 ± 6
LANL 2466,p1 Station 67+22.5 crystal-rich horizon	7 ± 2	1 ± 1	6 ± 2	—	63 ± 4	24 ± 3	—	—	trace	trace	—	100 ± 4
LANL 2467,p1 Station 67+27 crystal-rich horizon	35 ± 11	5 ± 1	7 ± 2	—	29 ± 12	28 ± 4	1 ± 1	—	trace	—	—	100 ± 12
Tpcpv1												
LANL 2757,p1 Station 75+07 bedrock adjacent to fault/fracture	1 ± 1	—	—	—	97 ± 1	2 ± 1	—	—	—	—	—	100 ± 1
LANL 2757,p2 Station 75+07 fault/fracture coating	—	—	—	> 95	—	trace	trace	—	—	—	—	> 95
LANL 2757,p3 Station 75+07 fracture coating on p2	—	—	major	—	—	—	major	—	—	—	note 9	—

[1]Errors are conservative 2-sigma values.
[2]"—" = not detected or, for totals, not applicable.
[3]Cristobalite.
[4]Species uncertain.
[5]Trace = less than 0.5 weight percent.
[6]Clinoptilolite 4 ± 1; chabazite 13 ± 3; erionite 0.92.
[7]"?" = presence uncertain.
[8]Major kenyaite, minor clinoptilolite and chabazite.
[9]Major mogonite.
[10]Opal-CT.

Table 6.1-9. Quantitative X-Ray Diffraction Results for Station 75+20, Exploratory Studies Facility South Ramp (Weight %)

Sample	Smectite	Chabazite	Clino-ptilolite	Erionite[1]	Tridymite	Cristo-balite	Quartz	Feldspar	Hematite	Horn-blende	Calcite	Mica	Total
Tpcpinc													
75+20SSL05A,p1 bedrock	Trace[2]	—[3]	—	—	—	27 ± 5[4]	11 ± 2	61 ± 15	1 ± 1	—	—	—	100 ± 16
75+20SSL05B,p1 breccia	3 ± 1	—	1 ± 1	—	1±1[5]	25 ± 4	11 ± 2	58 ± 13	1 ± 1	trace	—	trace	100 ± 14
75+20SSL04A,p1 breccia	2 ± 1	—	—	—	trace[5]	31 ± 5	9 ± 2	57 ± 13	trace	trace	—	—	99 ± 14
Tpcpv2													
75+20SSL06,p1 fractured rock	41 ± 17	2 ± 1	3 ± 1	0.11	—	17 ± 3	—	37 ± 10	—	—	—	—	100 ± 20
75+20SSL02A,p1 bedrock	18 ± 7	23 ± 7	6 ± 2	0.13	—	15 ± 2	1 ± 1	37 ± 8	—	—	—	—	100 ± 13
75+20SSL02B,p1 bedrock + breccia	11 ± 4	2 ± 1	11 ± 2	0.01?[6]	—	22 ± 3	25 ± 4	25 ± 6	—	—	4 ± 1	—	100 ± 9
75+20SSL02C,p1 bedrock	45 ± 21	1 ± 1	1 ± 1	—	—	15 ± 3	—	38 ± 11	—	—	—	—	100 ± 24
75+20SSL02D, p1 bedrock	44 ± 19	1 ± 1	3 ± 1	—	—	15 ± 3	—	36 ± 10	—	1 ± 1	—	—	100 ± 22
75+20SSL03A,p1 bedrock	46 ± 21	4 ± 2	1 ± 1	0.90	—	13 ± 3	—	34 ± 10	—	—	—	—	99 ± 24
75+20SSL03B,p1 bedrock	47 ± 21	4 ± 2	2 ± 1	0.08	—	13 ± 3	—	34 ± 10	—	trace	—	—	100 ± 24
75+20SSL03C,p1 fracture wall	47 ± 21	1 ± 1	5 ± 2	—	—	14 ± 3	—	33 ± 10	—	trace	—	—	100 ± 24
75+20SSL03D,p1 bedrock	39 ± 17	trace	5 ± 2	—	—	16 ± 3	—	39 ± 11	—	1 ± 1	—	—	100 ± 21

NOTE: excluding glass and amorphous phases.

[1]Erionite determination by techniques described in Bish and Chipera (1991).
[2]Trace = less than 0.5 weight percent.
[3]"—" = not detected.
[4]Errors are conservative 2-sigma values.
[5]Tridymite may be component of opal-CT.
[6]Erionite believed to be present but below the absolute detection limit of 0.02 weight %.

Table 6.1-10. Quantitative and Qualitative X-Ray Diffraction Results for Altered Topopah Spring and Tiva Canyon Tuffs (Weight %)

Sample	Smectite	Clino-ptilolite	Cristo-balite	Tridymite	Opal-CT	Quartz	Hematite	Feldspar	Glass	Opal-A	Calcite	Total
Upper Topopah Spring Tuff												
BB-8-SSL	trace[1]	–[2]	major	major	present	Trace	minor	major		–	–	
BB-14-SSL,p1	2 ± 1[3]	–	73 ± 5[4]		11 ± 5[4]		–	11 ± 2		–	1 ± 1	100 ± 5
BB-14-SSL,p2	–	–	–		47 ± 9	55 ± 3	–	–		–	trace	102 ± 9
BB-14-SSL,p3	–	–	52 ± 5[4]		40 ± 5[4]	4 ± 1	–	4 ± 1		–	–	100 ± 5
Tiva Canyon Tuff												
YM-7-SSL[5]	1 ± 1	–	–	–	43 ± 13	56 ± 8	–	–		–	–	100 ± 16
YM-2-SSL,p1	8 ± 2	29 ± 2	23 ± 2	–	–	1 ± 1	–	42 ± 7		–	–	103 ± 8
YM-2-SSL,p2	–	–	–	–	~100	–	–	–		–	–	~100
YM-11-SSL,p1	29 ± 9	–	18 ± 1	–	–	Trace	–	32 ± 4	21 ± 9	–	–	100 ± 10
YM-11-SSL,p2	–	–	14 ± 1	–	–	–	–	22 ± 3	64 ± 3	–	–	100 ± 3
Pre-Tiva Canyon Bedded Tuff												
YM-4-SSL-1[5]	1 ± 1	–	trace	–	–	Trace	–	14 ± 5		85 ± 10	–	100 ± 10

[1]Trace = less than 0.5 weight percent.

[2]– = not detected.

[3]Errors are conservative 2-sigma values.

[4]Proportions of cristobalite, tridymite, and opal-CT are approximate.

[5]Results for this sample are semiquantitative due to small sample size.

Table 6.1-11. Electron Microprobe Analyses of Secondary Feldspars

BB-8-SSL.1, Western Busted Butte							
Sample	**X-1**	**X-2**	**X-3**	**X-4**	**X-5**	**X-6**	**X-7**
Weight Percent							
SiO_2	67.3	67.0	67.6	66.2	65.8	67.0	65.7
TiO_2	n.d.	0.00	0.00	0.00	n.d.	0.00	n.d.
Al_2O_3	18.4	19.5	18.2	18.9	18.9	18.8	18.9
FeO	n.d.	0.00	0.00	n.d.	n.d.	0.00	0.00
MgO	n.d.	n.d.	0.00	0.00	n.d.	0.00	0.00
BaO	0.00	0.00	0.00	n.d.	n.d.	0.00	0.00
CaO	0.17	0.51	0.04	0.06	0.06	0.00	0.00
Na_2O	5.10	6.72	4.48	4.86	3.96	4.98	4.81
K_2O	8.62	6.31	9.59	9.48	11.1	9.25	9.7
SrO	n.d.	0.00	n.d.	n.d.	n.d.	0.00	0.00
Total	99.6	100.0	99.9	99.5	99.8	100.0	99.1
Stoichiometry Based on 8-Oxygen Formula							
Si	3.026	2.985	3.041	2.997	2.987	3.010	2.992
Ti	0.000	0.000	0.000	0.000	0.000	0.000	0.000
Al	0.977	1.022	0.963	1.009	1.014	0.998	1.014
Fe	0.000	0.000	0.000	0.000	0.000	0.000	0.000
Mg	0.000	0.000	0.000	0.000	0.000	0.000	0.000
Ba	0.000	0.000	0.000	0.000	0.000	0.000	0.000
Ca	0.008	0.024	0.002	0.003	0.003	0.000	0.000
Na	0.445	0.581	0.391	0.426	0.348	0.434	0.424
K	0.494	0.359	0.550	0.548	0.645	0.531	0.561
Sr	0.000	0.000	0.000	0.000	0.000	0.000	0.000
End-Member Proportions							
Ab	46.9	60.2	41.4	43.6	35.0	45.0	43.1
An	0.9	2.5	0.2	0.3	0.3	0.0	0.0
Or	52.2	37.2	58.3	56.1	64.7	55.0	56.9
Cn	0.0	0.0	0.0	0.0	0.0	0.0	0.0

Table 6.1-11. Electron Microprobe Analyses of Secondary Feldspars (Continued)

BB-14-SSL.1, Eastern Busted Butte						
Sample	**A-1**	**A-2**	**A-3**	**A-5**	**A-6**	**A-7**
Weight Percent						
SiO_2	65.3	64.9	65.4	65.4	64.7	65.1
TiO_2	n.d.	n.d.	n.d.	n.d.	0.12	n.d.
Al_2O_3	18.4	18.3	18.2	18.1	18.4	18.4
FeO	0.10	n.d.	0.10	0.12	0.20	0.17
MgO	0.00	0.00	0.00	0.00	0.00	0.00
BaO	0.00	0.00	0.00	n.d.	0.00	0.00
CaO	0.00	0.00	0.00	0.00	0.00	0.00
Na_2O	2.27	2.10	2.55	2.11	2.11	2.29
K_2O	13.6	13.9	13.1	13.8	13.7	13.5
SrO	0.00	n.d.	n.d.	0.00	n.d.	n.d.
Total	99.7	99.2	99.4	99.5	99.2	99.5
Stoichiometry Based on 8-Oxygen Formula						
Si	3.002	3.000	3.008	3.009	2.988	2.998
Ti	0.000	0.000	0.000	0.000	0.004	0.000
Al	0.994	0.996	0.987	0.983	1.004	0.997
Fe	0.004	0.000	0.004	0.005	0.008	0.006
Mg	0.000	0.000	0.000	0.000	0.000	0.000
Ba	0.000	0.000	0.000	0.000	0.000	0.000
Ca	0.000	0.000	0.000	0.000	0.000	0.000
Na	0.203	0.189	0.228	0.189	0.189	0.205
K	0.795	0.819	0.768	0.809	0.810	0.795
Sr	0.000	0.000	0.000	0.000	0.000	0.000
End-Member Proportions						
Ab	20.3	18.7	22.9	18.9	18.9	20.5
An	0.0	0.0	0.0	0.0	0.0	0.0
Or	79.9	81.3	77.1	81.1	81.1	79.5
Cn	0.0	0.0	0.0	0.0	0.0	0.0

Table 6.1-11. Electron Microprobe Analyses of Secondary Feldspars (Continued)

BB-14.SSL.1, Eastern Busted Butte (Continued)					
Sample	**B-1**	**B-2**	**B-3**	**B-4**	**B-5**
Weight Percent					
SiO_2	65.3	65.6	65.3	64.8	65.1
TiO_2	0.00	0.00	0.00	0.00	0.00
Al_2O_3	18.3	18.1	18.0	18.4	18.4
FeO	n.d.	n.d.	0.00	n.d.	n.d.
MgO	n.d.	0.00	0.00	0.00	0.00
BaO	0.00	0.00	0.00	0.00	0.00
CaO	0.00	0.14	0.00	0.00	n.d.
Na_2O	1.77	1.45	1.72	1.66	1.84
K_2O	13.5	14.2	14.1	14.6	14.1
SrO	0.11	n.d.	0.00	n.d.	n.d.
Total	99.0	99.5	99.1	99.5	99.4
Stoichiometry Based on 8-Oxygen Formula					
Si	3.011	3.020	3.018	2.995	2.999
Ti	0.000	0.000	0.000	0.000	0.000
Al	0.997	0.980	0.981	1.001	1.000
Fe	0.000	0.000	0.000	0.000	0.000
Mg	0.000	0.000	0.000	0.000	0.000
Ba	0.000	0.000	0.000	0.000	0.000
Ca	0.000	0.007	0.000	0.000	0.000
Na	0.159	0.129	0.154	0.150	0.165
K	0.796	0.834	0.832	0.859	0.829
Sr	0.003	0.000	0.000	0.000	0.000
End-Member Proportions					
Ab	16.6	13.3	15.6	14.8	16.6
An	0.0	0.7	0.0	0.0	0.0
Or	83.4	85.9	84.4	85.2	83.4
Cn	0.0	0.0	0.0	0.0	0.0

Table 6.1-11. Electron Microprobe Analyses of Secondary Feldspars (Continued)

BB-14-SSL.1, Eastern Busted Butte (Continued)					
Sample	**X-2**	**X-3**	**X-4**	**X-5**	**X-6**
Weight Percent					
SiO_2	64.9	65.1	65.4	64.7	65.3
TiO_2	0.00	n.d.	n.d.	n.d.	n.d.
Al_2O_3	18.4	18.5	18.4	18.3	18.7
FeO	n.d.	0.13	0.08	0.09	n.d.
MgO	0.00	n.d.	0.00	0.00	0.00
BaO	n.d.	n.d.	n.d.	n.d.	0.20
CaO	0.00	0.00	0.00	0.00	0.00
Na_2O	1.53	1.49	1.31	1.50	1.49
K_2O	14.8	14.7	14.7	14.8	14.6
SrO	n.d.	n.d.	0.00	n.d.	0.00
Total	99.6	99.9	99.9	99.4	100.3
Stoichiometry Based on 8-Oxygen Formula					
Si	2.996	2.991	3.003	2.993	2.993
Ti	0.000	0.000	0.000	0.000	0.000
Al	1.000	1.004	0.997	0.999	1.009
Fe	0.000	0.005	0.003	0.003	0.000
Mg	0.000	0.000	0.000	0.000	0.000
Ba	0.000	0.000	0.000	0.000	0.004
Ca	0.000	0.000	0.000	0.000	0.000
Na	0.137	9.133	0.116	0.135	0.133
K	0.870	0.864	0.861	0.871	0.852
Sr	0.000	0.000	0.000	0.000	0.000
End-Member Proportions					
Ab	13.6	13.3	11.9	13.4	13.4
An	0.0	0.0	0.0	0.0	0.0
Or	86.4	86.7	88.1	86.6	86.2
Cn	0.0	0.0	0.0	0.0	0.4

Table 6.1-11. Electron Microprobe Analyses of Secondary Feldspars (Continued)

BB-14-SSL.2, Eastern Busted Butte							
Sample	**A-1**	**A-2**	**A-3**	**A1-1**	**A1-2**	**A1-3**	**A1-4**
Weight Percent							
SiO_2	66.1	65.7	66.5	66.9	66.2	65.6	66.0
TiO_2	n.d.	0.00	n.d.	n.d.	n.d.	n.d.	n.d.
Al_2O_3	18.5	18.5	18.4	18.7	18.8	18.9	18.9
FeO	n.d.	n.d.	0.00	n.d.	n.d.	0.00	n.d.
MgO	0.00	0.00	0.00	0.00	0.00	0.00	0.00
BaO	n.d.	n.d.	n.d.	0.19	n.d.	n.d.	n.d.
CaO	0.00	0.04	0.00	0.00	0.00	0.00	0.07
Na_2O	4.70	3.85	3.99	4.93	4.41	3.69	5.19
K_2O	10.0	11.5	11.2	9.80	9.91	11.6	9.28
SrO	n.d.	n.d.	n.d.	n.d.	n.d.	n.d.	n.d.
Total	99.3	99.6	100.1	100.5	99.3	99.8	99.4
Stoichiometry Based on 8-Oxygen Formula							
Si	3.004	2.996	3.010	3.004	3.003	2.988	2.990
Ti	0.000	0.000	0.000	0.000	0.000	0.000	0.000
Al	0.992	0.997	0.984	0.989	1.007	1.014	1.007
Fe	0.000	0.000	0.000	0.000	0.000	0.000	0.000
Mg	0.000	0.000	0.000	0.000	0.000	0.000	0.000
Ba	0.000	0.000	0.000	0.003	0.000	0.000	0.000
Ca	0.000	0.002	0.000	0.000	0.000	0.000	0.003
Na	0.414	0.341	0.350	0.430	0.388	0.326	0.456
K	0.581	0.671	0.648	0.562	0.574	0.672	0.537
Sr	0.000	0.000	0.000	0.000	0.000	0.000	0.000
End-Member Proportions							
Ab	41.6	33.6	35.1	43.1	40.3	32.7	45.8
An	0.0	0.2	0.0	0.0	0.0	0.0	0.3
Or	58.4	66.2	64.9	756.4	59.7	67.3	53.9
Cn	0.0	0.0	0.0	0.4	0.0	0.0	0.0

Table 6.1-11. Electron Microprobe Analyses of Secondary Feldspars (Continued)

YM-1-SSL, Northeast Flank of Harper Valley				
Sample	**A2-1**	**A2-2**	**A2-3**	**A2-4**
Weight Percent				
SiO_2	67.4	67.2	66.3	66.3
TiO_2	n.d.	n.d.	n.d.	n.d.
Al_2O_3	18.4	18.4	18.8	18.4
FeO	0.13	0.18	0.17	0.17
MgO	0.00	0.00	0.00	0.00
BaO	0.00	n.d.	n.d.	n.d.
CaO	0.31	0.38	0.43	0.46
Na_2O	3.78	3.93	4.38	3.59
K_2O	10.5	9.8	9.9	10.4
SrO	n.d.	n.d.	n.d.	n.d.
Total	100.5	99.9	100.0	99.3
Stoichiometry Based on 8-Oxygen Formula				
Si	3.027	3.024	2.996	3.013
Ti	0.000	0.000	0.000	0.000
Al	0.971	0.977	0.999	0.986
Fe	0.005	0.007	0.007	0.006
Mg	0.000	0.000	0.000	0.000
Ba	0.000	0.000	0.000	0.000
Ca	0.015	0.019	0.021	0.022
Na	0.329	0.343	0.384	0.317
K	0.601	0.564	0.569	0.601
Sr	0.000	0.000	0.000	0.000
End-Member Proportions				
Ab	34.9	37.0	39.4	33.7
An	1.6	2.0	2.1	2.4
Or	63.6	61.0	58.7	63.9
Cn	0.0	0.0	0.0	0.0

Table 6.1-12. Normative Alkali Feldspar Compositions

USW GU-3 1195, Cryptocrystalline-Devitrified Shards				
Analysis	**An**	**Ab**	**Or**	**Cn**
SL 55	1.6	46.9	51.3	0.2
SL 57	1.7	49.5	48.8	0.0
SL 63	1.5	50.3	48.2	0.0
SL-65	1.2	25.5	73.3	0.0
SL 67	0.9	44.0	55.1	0.0
SL 68	1.6	45.9	52.5	0.0
SL 69	1.4	57.0	41.6	0.0
SL 70	1.0	34.3	64.6	0.1
SL 71	1.6	30.4	68.0	0.0
SL 72	1.3	48.9	49.8	0.0
SL 73	1.3	30.9	67.8	0.0
SL 76	1.0	18.6	80.4	0.0

Table 6.1-13. Quantitative X-Ray Diffraction Results for Exploratory Studies Facility North Ramp (Weight %)

Sample	Smectite	Clino-ptilolite	Mord-enite	Cristo-balite	Opal-CT	Feldspar	Quartz	Hematite	Fluorite	Erionite	Total
NRST-7-SSL[1] SPC 501015	4 ± 2[2]	2 ± 1	57 ± 27	3 ± 2	n.d.[3]	26 ± 16	8 ± 3	n.d.	n.d.	b.d.l.[4]	100 ± 27
NR10+30SSL01,p1 SPC 509174	16 ± 5	7 ± 1	n.d.	n.d.	67 ± 18	14 ± 2	5 ± 1	n.d.	n.d.	n.a.	109 ± 19
NR10+30SSL01,p2 SPC 509174	3 ± 1	1 ± 1	n.d.	n.d.	109 ± 22	n.d.	5 ± 1	n.d.	n.d.	n.a.	118 ± 22
NR10+30SSL02,p1 SPC 509175	91 ± 27	5 ± 1	n.d.	n.d.	5 ± 1	8 ± 1	trace[5]	n.d.	n.d.	n.a.	109 ± 27
NR10+32SSL01,p1 SPC 510522	95 ± 29	4 ± 1	n.d.	n.d.	11 ± 2	2 ± 1	trace	1 ± 1	n.d.	n.a.	113 ± 29
NR10+32SSL01,p2 SPC 510522	99 ± 30	1 ± 1	n.d.	n.d.	1 ± 1	4 ± 1	trace	1 ± 1	n.d.	n.a.	106 ± 30
NR10+32SSL02,p1 SPC 509187	5 ± 2	73 ± 5	n.d.	n.d.	10 ± 3	12 ± 3	3 ± 1	n.d.	n.d.	n.a.	103 ± 7
NR10+32SSL02,p2 SPC 509187	6 ± 2	59 ± 5	n.d.	n.d.	25 ± 7	12 ± 2	4 ± 1	n.d.	n.d.	n.a.	106 ± 9
NR10+33SSL01,p1 SPC 509117	trace	n.d.	n.d.	n.d.	n.d.	n.d.	95 ± 5	n.d.	trace	n.a.	95 ± 5
NR10+33SSL01,p2 SPC 509117	n.d.	n.d.	n.d.	40 ± 5[6]	10 ± 5[6]	n.d.	49 ± 2	n.d.	1 ± 1	n.a.	100 ± 5
NR10+34SSL01,p1 SPC 510523	15 ± 5	70 ± 5	n.d.	n.d.	10 ± 2	5 ± 1	1 ± 1	n.d.	n.d.	n.a.	101 ± 7
NR10+34SSL01,p2 SPC 510523	74 ± 22	19 ± 1	n.d.	n.d.	1 ± 1	6 ± 1	trace	trace	n.d.	n.a.	100 ± 22

[1]Results for this sample are semiquantitative due to small sample size.
[2]Errors are conservative 2-sigma values.
[3]n.d. = not detected.
[4]For erionite only, b.d.l. means below the detection limit (~100 to 500 ppm) using specialized analytical techniques (Bish and Chipera 1991). For samples not analyzed using the special methods, undetected erionite is reported as n.a. = not analyzed.
[5]Trace = less than 0.5 weight percent.
[6]Proportions of cristobalite and opal-CT are approximate.

Table 6.1-14 X-Ray Diffraction Mineralogy of Altered Topopah Spring Vitrophyre (Weight%)

Sample	Depth (m)	Smectite	Heulandite	Quartz	Cristo-balite	Alkali feldspar	Opal-CT	Other
G-1[1]								
1286	392.0	33 ± 7	10 ± 1	3 ± 1	16 ± 1	38 ± 5	n.d.	
GU-3[1]								
1195.7	364.5	n.d.[2]	~1	8 ± 2	22 ± 3	70 ± 5	n.d.	trace[3]
G-4[1]								
1299	395.9	2 ± 1	5 ± 2	8 ± 2	23 ± 4	62 ± 10	n.d.	trace[3]
1314	400.5	45 ± 10	28 ± 5	2 ± 1	14 ± 4	11 ± 5	n.d.	
H-5								
1666	507.8	37 ± 16	20 ± 5	3 ± 1	n.d.	24 ± 7	15 ± 7	~0.6[4]

[1]adapted from Bish and Chipera (1989).
[2]n.d. = not detected.
[3]mica.
[4]erionite. Special techniques to detect erionite (Bish and Chipera 1991) were used for this sample only.

Table 6.1-15. Isotopic Compositions and Temperatures of Quartz Formation[1]

Sample	$\delta^{18}O$ (‰ vs. SMOW)	T_A (°C)[2]	T_B (°C)[3]
VH-2 3545-q	+13.0	65	95
VH-2 3565a	+11.9	70	100
YF-4-q	+17.8	40	70

[1]$\delta^{18}O$ value of -13.5‰ assumed for the water. Analyses reproducible to ±0.1‰.
[2]T_A calculated from Clayton et al.1972.
[3]T_B calculated from Bottinga and Javoy (1973).

Table 6.1-16. Chemical Compositions of Glasses and Secondary Minerals

Sample	1 GU-3 1195C Glass	2 GU-3 1394[1] Glass	3 H-5 1966 Glass	4 H-5 1666 Smectite	5 GU-3 1195 Heulandite	6 G-4 1392 Massive Clinopt.	7 G-4 1392 Prism. Clinopt.	8 G-3 2615 Massive Clinopt.	9 G-3 2615 Prism. Clinopt.
Weight Percent									
SiO_2	74.1	75.1	75.6	43.2	64.8	63.7	64.2	63.9	62.0
TiO_2	0.09	0.00	0.05	0.13	0.00	0.00	n.d.	0.00	0.00
Al_2O_3	12.4	12.0	12.1	21.4	12.0	11.5	11.2	11.6	12.5
FeO	0.82	0.86	0.82	1.57	n.d.	n.d.	n.d.	n.d.	0.13
MnO	0.00	n.a.	0.06	0.05	0.09	n.d.	n.d.	0.00	n.d.
MgO	0.02	0.02	0.00	0.89	0.88	n.d.	n.d.	0.08	0.09
CaO	0.19	0.44	0.39	2.48	3.84	1.91	1.59	1.70	1.46
BaO	0.06	0.00	0.00	0.00	0.00	0.00	0.00	0.00	0.00
Na_2O	3.55	3.55	2.95	0.14	0.59	1.91	2.01	2.75	3.19
K_2O	5.77	5.01	5.00	0.15	0.78	3.97	4.00	3.02	3.59
H_2O	3.0	3.0	3.0	30.0	17.0	17.0	17.0	17.0	17.0
Total	100.0	100.0	100.0	100.0	100.0	100.0	100.0	100.0	100.0
Density (g/cm^3)									
	2.36[2]	2.36[2]	2.36[2]	2.00[3]	2.20[3]	2.20[3]	2.20[3]	2.20[3]	2.20[3]
Mole/cm^3									
Si	0.02904	0.02950	0.02968	0.01437	0.02372	0.02334	0.02350	0.02339	0.02271
Al	0.00560	0.00555	0.00563	0.00840	0.00550	0.00495	0.00484	0.00499	0.00540
Ca	0.00008	0.00018	0.00017	0.00088	0.00160	0.00075	0.00062	0.00067	0.00057
Na	0.00270	0.00270	0.00224	0.00009	0.00045	0.00136	0.00143	0.00195	0.00227
K	0.00288	0.00251	0.00251	0.00006	0.00039	0.00185	0.00187	0.00141	0.00168

[1]Vaniman, Bish, Broxton et al. (1984). [2]Anderson (1984). [3]Deer et al. (1966).

Table 6.1-17. Modal Analysis of G-3 2615

Total Counts	1,140
Massive intergranular clinoptilolite cement	11.84%
Massive clinoptilolite pore filling	5.44%
Clinoptilolite replacement of glass clasts	54.91%
Secondary void space in former glass clasts	3.77%
Crystalline clasts (phenocrysts, lithic grains)	23.51%
Smectite	0.26%
Silica	0.26%
Inferred Original Textural Constituents	
Primary porosity (total massive clinoptilolite content)	17.2%
Original glass content (clinoptilolite replacement of glass + secondary void	58.7%
Crystaline clasts	23.5%
Other	0.6%
Total	100.0%

Table 6.1-18. Changes in Element Content During Zeolitization, G-3 2615

	Al	**Si**	**K**	**Na**	**Ca**
Total element addition (%)*	26	23	17	26	383
Total element losss	17	26	47	19	<<1
Total element transport	43	49	64	44	383
Net element transport	+9	-3	-31	+7	+383

*All values are expressed as % of element content in glass component of original tuff.

Table 6.1-19. Hypothetical Zeolitization of Ashflow Tuff

Textural Component	Proportion	Assumed Internal Porosity	Contribution to Total Porosity
Shard	30%	10%	3%
Pumice	40%	50%	20%
Ash	30%	30%	9%
Total original porosity			32%

Table 6.1-20. Abundance of Geopetal Fillings in Dissolved Shard Cavities, G-4 1392

Long Dimension of Dissolved Shard (mm)	Dissolved Shards with Fillings/ Dissolved Shards in Size Range	Percent
< 0.10	10/33	30
0.10–0.19	46/83	55
0.20–0.29	38/64	59
0.30–0.39	16/18	89
0.40–0.49	8/8	100
0.50–0.59	15/16	94
0.60–0.69	5/7	71
0.70–0.79	2/2	100
0.80–0.89	2/2	100
0.90–0.99	0/0	—
> 1.0	7/7	100
Cumulative ≥ 0.30	55/60	92
Total measurements: 240		

Table 6.1-21 Mineralogical and Potassium/Argon Analyses of Clinoptilolite, Mordenite, and I/S Separates from Yucca Mountain

Stratigraphic Unit, Sample Number	Size Fraction (μm)	Depth in Drill Hole/Depth to SWL[1] (m)	Authigenic Minerals[2]	K_2O (wt. %)	$^{40}Ar^3$ (10^{-11} mol/g)	$^{40}Ar^3$ (%)	Age (Ma)
Topopah Spring G-2 762	1–3	232.2/524.9	Cp, CT	1.99	0.06	0.5	~0
Topopah Spring G-2 1691	1–3	515.4/524.9	Cp, Mo, CT	4.13	2.3731	10	4.0 ± 0.7[4]
Topopah Spring G-4 1381	1–3	420.9/539.5	Cp, CT	4.79	2.8756	9	4.2 ± 0.9
Topopah Spring VH-2 3545	0.1–0.35	1080.5/163	Cp, Q, ?	1.63	1.5713	9	6.7 ± 1.6
Topopah Spring VH-2 3663	1–3	1116.5/163	Cp, ?	2.38	2.3412	19	6.8 ± 0.6
Calico Hills 3-15-82-8	1–3	outcrop/NA	Cp, Mo, CT	5.49	2.0271	8	2.6 ± 0.8
Calico Hills 3-15-82-8	1–3	outcrop/NA	Cp, Mo, CT	6.13	3.1094	15	3.5 ± 0.5
Calico Hills 3-15-82-8	1–3	outcrop/NA	Cp, Mo, CT	6.20	2.8931	11	3.2 ± 0.6
Calico Hills 3-15-82-8	3–20	outcrop/NA	Cp, Mo, CT	5.47	1.1439	8	1.5 ± 0.4
Calico Hills 3-15-82-8	3–20	outcrop/NA	Cp, Mo, CT	5.83	1.6997	10	2.0 ± 0.4
Calico Hills G-1 1561	1–3	475.8/571.7	Cp, Mo, CT	4.96	1.5677	8	2.2 ± 0.6
Calico Hills G-1 1561	1–3	475.8/571.7	Cp, Mo, CT	4.96	1.4006	10	2.0 ± 0.4
Calico Hills G-1 1561[5]	1–3	475.8/571.7	Cp, Mo, CT	4.99	2.2210	15	3.1 ± 0.5
Calico Hills G-1 1561[5]	1–3	475.8/571.7	Cp, Mo, CT	4.87	1.3491	7	1.9 ± 0.6
Calico Hills G-2 2430	1–3	740.7/524.9	Cp, Mo, CT, I/S	3.47	2.2875	17	4.6 ± 0.5
Calico Hills G-4 1734.3	1–3	528.5/539.5	Cp, Mo, CT	3.28	1.8338	5	3.8 ± 1.0
Calico Hills G-4 1734.3[5]	1–3	528.5/539.5	Cp, Mo, CT	3.29	2.2847	4	4.8 ± 2.0
Prow Pass G-1 2190.8	1–3	667.5/571.7	Cp, Mo, CT	4.86	4.7995	26	6.9 ± 0.4
Prow Pass G-1 2190.8[5]	1–3	667.5/571.7	Cp, Mo, CT	4.38	2.7158	7	4.3 ± 1.0
Prow Pass G-2 3191.5	1–3	972.9/524.9	Cp, Q, F, I/S	3.73	5.6058	27	10.4 ± 0.6
Prow Pass G-2 3191.5[5]	1–3	972.9/524.9	Cp, Q, F, I/S	2.30	2.3145	20	7.0 ± 0.7

[1]Depths in drill hole and to water table are from surface. Data on water tables from Robison (1984). NA = not applicable.
[2]Cp = clinoptilolite; Mo = mordenite; CT = opal-CT; Q = quartz; F = feldspar; I/S = illite/smectite; A = analcime; ? = incomplete XRD analysis.
[3]Radiogenic Ar.
[4]Total 2-σ percentage error.
[5]Heavy-liquid purified clinoptilolite.

Table 6.1-21 Mineralogical and Potassium/Argon Analyses of Clinoptilolite, Mordenite, and I/S Separates from Yucca Mountain (Continued)

Stratigraphic Unit, Sample Number	Size Fraction (μm)	Depth in Drill Hole/Depth to SWL[1] (m)	Authigenic Minerals[2]	K_2O (wt. %)	$^{40}Ar^3$ (10^{-11} mol/g)	$^{40}Ar^3$ (%)	Age (Ma)
Prow Pass G-2 3250	1–3	990.6/524.9	Cp,A,Q,F,I/S	1.64	3.1446	17	13.3 ± 1.4
Prow Pass G-2 3250	0.1–0.35	990.6/524.9	I/s	1.16	2.1283	10	12.7 ± 3.0
Prow Pass GU-3 1874	1–3	990.6/524.9	Cp,CT	3.99	1.4002	8	2.4 ± 0.6
Prow Pass G-4 1763.2	1–3	537.4/539.5	Cp, CT, Mo, F	3.09	1.9400	10	4.4 ± 0.8
Prow Pass G-4 1779.6	1–3	542.2/539.5	Cp, Mo, CT, F	7.13	7.6142	43	7.4 ± 0.2
Prow Pass G-4 1779.6[5]	1–3	542.2/539.5	Cp, Mo, CT, F	4.30	2.5421	18	4.1 ± 0.4
Prow Pass G-4 1779.6[5]	3–20	542.2/539.5	Cp, Mo, CT, F	4.34	2.7582	24	4.4 ± 0.3
Prow Pass G-4 1788.4	1–3	545.2/539.5	Cp, CT	6.85	7.1259	34	7.2 ± 0.3
Prow Pass Ue25P#1 1740-50	1–3	530.4/383.9	Cp, Mo, CT	4.72	5.6841	18	8.4 ± 0.8
Prow Pass Ue25P#1 1740-50[5]	1–3	530.4/383.9	Cp, Mo, CT	2.60	2.2415	11	6.0 ± 1.0
Prow Pass Ue25P#11790-1800	1–3	545.6/383.9	Cp, Mo, CT	3.24	3.9166	19	8.4 ± 0.8
Bullfrog GU-3 2013.15	1–3	613.6/750.3	Cp, CT	4.64	2.5681	19	3.8 ± 0.3
Tram G-1 3288.5	1–3	1002.2/571.7	Cp, Mo, A, Q, F, I/S	4.85	7.3396	35	10.5 ± 0.4
Tram G-1 3288.5[5]	1–3	1002.2/571.7	Cp, Mo, A, Q, F, I/S	4.64	6.7043	35	10.0 ± 0.4
Tram G-3 3589	1–3	1094.1/750.3	Cp, Q, F, I/S	6.12	8.2727	33	9.9 ± 0.5
Tram G-3 3589	1–3	1094.1/750.3	Cp, Q, F, I/S	5.66	8.0722	44	10.0 ± 0.3
Tram G-3 3589[5]	1–3	1094.1/750.3	Cp, Q, F, I/S	5.10	6.6200	29	9.0 ± 0.5
Tram G-3 3854.7	1–3	1174.9/750.3	Cp, Mo, Q, F, I/S	4.02	6.0061	45	10.4 ± 0.3
Older tuff B G-1 5458.4	1–3	1663.6/571.7	Cp, Q, F, I/S	3.58	6.1866	22	12.0 ± 0.9
Older tuff B G-1 5458.4	0.1–0.35	1663.6/571.7	I/S	3.09	3.9111	14	8.8 ± 1.0
Older tuff C G-1 5560	1–3	1694.7/571.7	Cp, Mo, Q, F, I/S	3.25	5.7686	23	12.3 ± 0.9

[1]Depths in drill hole and to water table are from surface. Data on water tables from Robison (1984). NA = not applicable.
[2]Cp = clinoptilolite; Mo = mordenite; CT = opal-CT; Q = quartz; F = feldspar; I/S = illite/smectite; A = analcime.
[3]Radiogenic Ar.
[4]Total 2-σ percentage error.
[5]Heavy-liquid purified clinoptilolite.

Table 6.1-22. Experimental Conditions and Results of Argon Retention

Experimental Conditions				Analytical Results	
Purification Method	Duration of Experiment	Temperature (°C)	Experimental Medium	K_2O (wt %)	$^{40}Ar^a$ (10^{-11} mol/g)
Water	n.a.[b]	n.a.	n.a.	5.28	0.8127 ± 23.78[c]
Heavy liquid	n.a.	n.a.	n.a.	5.34	0.6248 ± 22.83
Water	3 days	50	1 M KCl soln	9.22	1.0415 ± 16.30
Water	5 days	50	1 M KCl soln	8.45	1.2087 ± 12.54
Water	3 days	50	1 M $CaCl_2$ soln	3.09	0.9307 ± 18.71
Water	5 days	50	1 M $CaCl_2$ soln	2.67	1.0435 ± 15.93
Water	3 days	50	1 M NaCl soln	3.36	0.9141 ± 16.16
Water	5 days	50	1 M NaCl soln	2.93	0.4980 ± 29.43
Water	3 days	50	1 M CsCl soln	1.23	0.8580 ± 17.05
Water	5 days	50	1 M CsCl soln	1.04	1.8218 ± 6.24
Water	16 hours	50	Air	5.23	1.0777 ± 23.92
Water	16 hours	100	Air	5.45	1.2683 ± 20.37
Water	16 hours	150	Air	5.49	1.0280 ± 23.63
Water	16 hours	200	Air	5.55	0.4620 ± 76.42
Water	1 week	100	Water	5.48	0.7520 ± 21.83
Water	1 month	100	Water	5.67	1.5193 ± 11.68
Water	3 months	100	Water	5.17	1.0927 ± 16.69
Water	5.4 months	100	Water	5.15	1.1363 ± 15.01

[a]Radiogenic argon.
[b]n.a. = not applicable.
[c]Estimated total percent error (Cox and Dalrymple 1967).

Table 6.1-23. Potassium/Argon Dates (m.y.) for I/S Samples from Yucca Mountain, Nevada

I/S	Sample[1]	Date (my)
R=0	G-2 1246.6	10.9 ± 0.5
R=0	G-2 1508.5	10.0 ± 0.5
R=1	G-1 1511.2	9.9 ± 0.6
	duplicate	10.1 ± 0.4
R=1	G-2 1133.9	8.7 ± 0.4
	duplicate	9.7 ± 0.6
	duplicate	9.9 ± 0.6
R>3	G-1 1718.2	10.9 ± 0.6
R>3	G-2 1181.1	11.0 ± 0.6
R>3	G-2 1198.8	11.7 ± 0.7
	duplicate	11.3 ± 0.5
Illite	G-2 1576.1	11.0 ± 0.6
Average		**10.4**

[1]Drillhole and depth in meters.

Table 6.1-24. Quantitative Mineralogy of Eolian Dusts in Dust Traps Near Exile Hill

	< 425 µm				< 45 µm
Sample (LANL ID):	**1036**	**1037**	**1034**	**1033***	**1033****
Quartz	18(1)	22(2)	22(2)	22	24(2)
Tridymite	1(1)	1(1)	1(1)	tr	tr
Cristobalite	-	-	-	-	-
Feldspar	47(7)	45(6)	48(7)	46	38(5)
Amphibole	2(1)	2(1)	1(1)	tr	3(1)
Biotite†	3(1)	2(1)	2(1)	1	3(1)
Chlorite	1(1)	1(1)	1(1)	1	2(1)
Hematite	1(1)	1(1)	1(1)	1	1(1)
Amorphous (glass)‡	16(8)	15(7)	13(8)	16	16(7)
Illite	-	-	-	-	-
Smectite	8(2)	7(2)	8(2)	7	10(3)
Kaolinite	1(1)	1(1)	1(1)	1	2(1)
Calcite	Tr	tr	-	-	-
Zeolites	3(1)	4(1)	3(1)	4	4(1)
Gypsum	Tr	-	-	-	-

NOTE: Percentages with standard deviation in parentheses.

* = Composite of size-fraction data (425–180, 180–90, 90–45, 45–38, and < 38 mm).

** = Composite of size-fraction data (45–38 and < 38 mm).

† = Reported as "mica".

‡ = Including some opal-A (silica phytoliths).

Table 6.1-25. Summary of 25°C Dissolution Rate Constants for Minerals

Mineral	Logk_{diss}*	Logk_{diss} Normalized to 2 Structural Oxygens	Molar Volume (cm^3/mol)	Lifetime of 100-μm Crystal (Ma)
Wollastonite	-8	-8.18	39.93	0.00000794
Anorthite	-8.55	-9.15	100.79	0.000011
Nepheline	-8.55	-8.85	55.16	0.000020
Forsterite	-9.5	-9.80	43.79	0.00023
Diopside	-10.15	-10.63	66.09	0.00068
Enstatite	-10	-10.18	31.276	0.0010
Analcime[a]	-11	-11.48	97.1	0.0033
Gibbsite	-11.45	-11.63	31.956	0.028
Sanidine	-12	-12.60	109.008	0.029
Albite	-12.26	-12.86	100.07	0.058
Prehnite	-12.41	-13.19	140.33	0.058
Microcline	-12.50	-13.10	108.741	0.092
Epidote	-12.61	-13.42	139.2	0.093
Na-clinoptilolite[a]	-13.15	-14.23	420.87	0.106
Amorphous silica[b]	-12.2	-12.20	29	0.174
β-cristobalite[b]	-12.34	-12.34	27.38	0.253
Muscovite	-13.07	-13.85	140.71	0.265
Kaolinite	-13.28	-13.93	99.52	0.607
α-cristobalite[b]	-12.77	-12.77	25.74	0.725
Quartz	-13.39	-13.39	22.688	3.431
Na-clinoptilolite[c]	-15.623	-17.18	1262.6	10.542

*k_{diss} in moles/m^2s

All values from Lasaga, Soler et al. (1994) except as noted below:

[a]Murphy, W.M. et al. (1996)

[b]Rimstidt and Barnes (1980)

[c]MacInnis et al. (1995)

Table 6.1-26. Correlation of Stratigraphy and Sorption Samples

Unit Description*	Lithologic Notation	Number of Sorption Samples
Upper Tiva Canyon, undifferentiated	Tpc	1
Lower densely welded subunit of the Tiva Canyon Tuff	Tpcpv3	
Partially to nonwelded lower subzones of the Tiva Canyon Tuff	Tpcpv1-2	
Pre-Tiva Canyon Tuff bedded tuff	Tpbt4	
Yucca Mountain Tuff	Tpy	
Pre-Yucca Mountain Tuff bedded tuff	Tpbt3	
Pah Canyon Tuff	Tpp	V = 1
Pre-Pah Canyon Tuff bedded tuff	Tpbt2	
Topopah Spring Tuff: upper partially to nonwelded zones	Tptrv2-3	
Topopah Spring Tuff: upper densely welded vitrophyre	Tptrv1	2
Topopah Spring Tuff: crystal-rich nonlithophysal zone	Tptm	7
Topopah Spring Tuff: crystal-rich lithophysal zone	Tptrl	
Topopah Spring Tuff: lithic-rich zone	Tptf	
Topopah Spring Tuff: upper lithophysal zone	Tptpul	
Topopah Spring Tuff: middle nonlithophysal zone	***Tptpmn***	***5***
Topopah Spring Tuff: lower lithophysal zone	***Tptpll***	***1***
Topopah Spring Tuff: lower nonlithophysal zone	***Tptpln***	***3***
Topopah Spring Tuff: lower densely welded vitrophyre	***Tptpv3***	
Topopah Spring Tuff: lower partially welded zone	Tptpv2	
Topopah Spring Tuff: lower nonwelded zone	Tptpv1	4 (z = 1, v =3)
Pre-Topopah Spring Tuff bedded tuff	Tpbt1	4 (z = 2, v = 2)
Calico Hills Formation	Tac	19 (z = 18, v = 1)
Pre-Calico Hills Formation bedded tuff	Tacbt	
Prow Pass Tuff upper nonwelded zone	Tcpunw	2 (z = 1, v = 1)
Prow Pass Tuff upper welded zone	Tcpuw	2
Prow Pass Tuff lower nonwelded zone	Tcplnw	Z = 3
Bullfrog Tuff upper nonwelded zone	Tcbunw	
Bullfrog Tuff upper welded zone	Tcbuw	2
Bullfrog Tuff lower nonwelded zone	Tcblnw	
Tram Tuff upper nonwelded zone	Tctunw	
Tram Tuff upper nonwelded zone	Tctuw	1

*Quartz-latitic units shaded; units that could include potential waste emplacement horizons are in bold italics. Stratigraphy based on Figure 1 of Clayton et al. (CRWMS M&O 1997).

Table 6.1-27. Samples Used in Batch-Sorption Experiments

Representative Zeolitic Lithologies
Most-used sequence of zeolitic samples: G-4 1506, 1508,1510, 1515 (Tac Zeolitic) Additional zeolitic samples used specifically for Np batch-sorption studies: G-4 1505-1529, 1533 (Tac Zeolitic) G-4 1566 (Tac Zeolitic) G-4 1395 (Tptpv1 Zeolitic) G-4 1625 (Tac Zeolitic) G-4 1772 (Tcpunw Zeolitic) G-4 2077 (Tcplnw Zeolitic) G-1 1405 (Tpbt1 Zeolitic) G-1 1436 (Tac Zeolitic; p. 95) G-1 1936 (Tcplnw Zeolitic; p. 95) GU-3 1992 (Tcplnw Zeolitic - at Tcbt3 contact - p. 93) G-2 1813, 1951, 2000, 2222 (Tac Zeolitic) no XRD?
Representative Vitric Lithologies
GU-3 1394, 1405 (Tptpv1 Vitric) GU-3 1407 (Tpbt1 Vitric) GU-3 1414 (Tac Vitric) GU-3 1555 (Tcpunw Vitric) G-2 723 (Tpp Vitric; has 34% cc) G-2 767 (Tptrv1 QL Vitrophyre) G-2 770 (Tptrv1 QL Vitrophyre)
Representative Devitrified Lithologies
G-4 268, 270, 272 (Tptrn QL Devit) G-1 732 (Tptpmn Devit) G-1 1271 (Tptpln Devit; p. 95) G-1 1941 (Tcpuw Devit; p. 95) GU-3 747 (Tptpmn Devit) GU-3 2325 (Tcbuw Devit) Additional devitrified samples used specifically for Np batch-sorption studies: G-1 732 (Tptpmn Devit) G-4 747 (Tptpmn Devit) G-4 1067 (Tptpll Devit) G-4 2570 (Tcbuw Devit)
Pure-Mineral Samples Separated from Yucca Mountain Drill Cores
Calcite Samples (used for Ce, Eu, Am work) G-1 2901 (Tctuw Devit host) G-2 723 (Tpp Vitric host) Clay Sample G-1 3658 (Tll sub-Tram lava)
Other Pure-Mineral Samples from Sources Other than Yucca Mountain
Synthetic hematite Montmorillonite Clinoptilolite Calcite Gibbsite Hollandite Romanechite Albite Quartz

Table 6.1-28. Samples Used in Flow-Through Column Sorption Experiments

Representative Zeolitic Lithologies
G4-1508 (Tac Zeolitic) G4-1505 (Tac Zeolitic)
Representative Devitrified Lithologies
G4-268 (Tptrn Devit) G4-272 (Tptrn Devit)
Representative Vitric Nonwelded Lithologies
GU3-1405 (Tptpv1 Vitric GU3-1407 (Tpbt1 Vitric)

Table 6.1-29. Samples Used in Fracture-Flow Sorption Experiments

G-1 1941 (Tcpuw Devit; induced, fracture minerals = matrix feldspar + quartz) UZ-16 919 (Tptpln Devit; fracture minerals = stellerite + Fe oxides) G-4 2954, 2981 (Tctuw Devit, fracture minerals = hollandite + romanechite)

Table 6.1-30. Samples Used in Radionuclide Diffusion Experiments

Diffusion Tests Using Solid-Rock Beakers
G-4 737 (Tptpmn Devitrified) GU-3 304 (Tpcpln Devitrified) GU-3 433 (Tptrn QL Devitrified) GU-3 1119 (Tptpln Devitrified) Tpt outcrop sample
Diffusion Tests Using Diffusion Cells
G-4 287 (Tptrn QL Devitrified) UE-25 1362 (Tpbt1 Zeolitic) (if UE-25a #1)

Table 6.1-31. Drillholes Used to Construct the 3-D Mineralogic Model of Yucca Mountain

Drillhole	Source for Mineralogic Data
UE-25a #1	Bish and Chipera (1986, 1989)
UE-25b #1	Bish and Chipera (1989)
UE-25p #1	Chipera and Bish (1988); Bish and Chipera (1989)
UE-25UZ #16	Chipera, Vaniman, Carlos et al. (1995)
USW G-1	Bish and Chipera (1986,1989)
USW G-2	Bish and Chipera (1989)
USW G-3/GU-3	Bish and Chipera (1989)
USW G-4	Bish and Chipera (1989)
USW H-3	Levy (1984c); Bish and Chipera (1989)
USW H-4	Levy (1984c); Bish and Chipera (1989)
USW H-5	Levy (1984c); Bish and Chipera (1989)
USW H-6	Bish and Chipera (1989)
USW NRG-6	Chipera, Vaniman, Bish et al. (1997)
USW NRG-7/7a	Chipera, Vaniman, Bish et al. (1997)
USW SD-7	Chipera, Vaniman, Bish (1996); Chipera, Vaniman, Bish et al. (1997)
USW SD-9	Chipera, Vaniman, Bish (1996); Chipera, Vaniman, Bish et al. (1997)
USW SD-12	Chipera, Vaniman, Bish (1996); Chipera, Vaniman, Bish et al. (1997)
USW UZ#14	Chipera, Vaniman, Bish et al. (1997)
USW UZN-32	Levy and Chipera (1997)
USW WT-1	Bish and Chipera (1989)
USW WT-2	Bish and Chipera (1989)

Table 6.1-32. Linkage Between the Integrated Site 3-D Lithologic Model and the 3-D Mineralogic Model of Yucca Mountain

Buesch, Spengler et al. (1996)	Integrated Site 3-D Framework Model	Units Used in the 3-D Mineralogic Model
		31 (Topography)
Tiva Canyon Tuff (Tpc)	Tpc	
Crystal-rich member (Tpcr)		
Vitric zone (Tpcrv)	Tpcrv1	
Nonlithophysal zone (Tpcrn)	Tpcrn	
Subvitrophyre transition subzone (Tpcrn4)		
Pumice-poor subzone (Tpcrn3)		
Mixed pumice subzone (Tpcrn2)		
Crystal transition subzone (Tpcrn1)		
Lithophysal zone (Tpcr1)		
Crystal-poor member (Tpcp)		
Upper lithophysal zone (Tpcpul)	Tpcpul	
Middle nonlithophysal zone (Tpcpmn)	Tpcpmn	
Lower lithophysal zone (Tpcpll)	Tpcpll	
Lower nonlithophysal zone (Tpcpln)	Tpcpln	
Hackly subzone (Tpcplnh)	Tpcplnh	
Columnar subzone (Tpcplnc)	Tpcplnc	
Argillic pumice interval (Tpcplnc)		
Vitric zone (Tpcpv)		30
Densely welded subzone (Tpcpv3v)	Tpcpv3	
Moderately welded subzone (Tpcpv2)	Tpcpv2	
Non- to part-welded subzone (Tpcpv1)	Tpcpv1	29
Pre-Tiva Canyon Tuff bedded tuff (Tpbt4)	Tpb4	28
Yucca Mountain Tuff (Tpy)	Tpy	27
Pre-Yucca Mountain Tuff bedded tuff (Tpbt3)	Tpbt3	26
Pah Canyon Tuff (Tpp)	Tpp	25
Pre-Pah Canyon Tuff bedded tuff (Tpbt2)	Tpbt2	24
Topopah Spring Tuff (Tpt)	Tpt	23
Crystal-rich member (Tptr)		
Vitric zone (Tptrv)		
Nonwelded subzone (Tptrv3)	Tptrv3	
Moderately welded subzone (Tptrv2)	Tptrv2	
Densely welded subzone (Tptrv1)	Tptrv1	22
Nonlithophysal zone (Tptrn)	Tptrn	21
Dense subzone (Tptrn3)		
Vapor-phase corroded subzone (Tptrn2)		
Lithophysal zone (Tptrl)	Tptrl	

Table 6.1-32. Linkage Between the Integrated Site 3-D Lithologic Model and the 3-D Mineralogic Model of Yucca Mountain (Continued)

Buesch, Spengler et al. (1996)	Integrated Site 3-D Framework Model	Units Used in the 3-D Mineralogic Model
Crystal-poor member (Tptp)		
Upper lithophysal zone (Tptpul)	Tptpul	20
Mid nonlithophysal zone (Tptpmn)	Tptpmn	19
Lower lithophysal zone (Tptpll)	Tptpll	18
Lower nonlithophysal zone (Tptpln)	Tptpln	17
Vitric zone (Tptpv)		16
Densely welded subzone (Tptpv3)	Tptpv3	
Moderately welded subzone (Tptpv2)	Tptpv2	
Nonwelded subzone (Tptpv1)	Tptpv1	15
Pre-Topopah Spring Tuff bedded tuff	Tpbt1	14
Calico Hills Formation (Tac)	Tac	13
Unit 4 Pumiceous pyroclastic flow		
Unit 3 Lithic-rich pyroclastic flow		
Unit 2 Pumiceous pyroclastic flow		
Unit 1 Lithic-rich pyroclastic flow		
Bedded tuff (Tacbt)	Tabt1	12
Basal sandstone (Tacbs)		
Prow Pass Tuff (Tcp)	Tcp	11
Unit 4 Pyroxene rich		
Unit 3 Welded pyroclastic flow		10
Unit 2 Lithic-rich pyroclastic flow		9
Unit 1 Pumiceous pyroclastic flow		
Pre-Prow Pass bedded tuff (Tcpbt)	Tcbt3	8
Bullfrog Tuff (Tcb)	Tcb	
Upper nonwelded		7
Middle variably welded		6
Lower nonwelded/altered		5
Bedded tuff	Tcbt2	4
Tram Tuff (Tct)	Tct	3
Bedded tuff	Tcbt1	
Older tuff and lavas below Tcbt1		2
Paleozoic Basement		1

Table 6.1-33. Electron Microprobe Analyses of Gel Products

Component	U12t.02, Rainier Mesa				UE-25 a#1 1297			USW H-5 1917		USW G-4 1392	
	Silica-Rich Gel		Smectite		Smectite	Gel[1]	Opal	Opal (Layered)	Opal (Cement)	Opal	Gel[1]
	A1-1	A1-2	A1-3	A1-4						B7	B6
	Weight Percent										
SiO_2	20.8	85.8	55.4	57.5	53.6	58.7	64.6	91.0	88.6	94.9	85.2
TiO_2	0.00	0.08	0.14	0.22	0.18	0.00	0.00	0.00	0.00	0.00	0.00
Al_2O_3	3.18	2.27	23.8	24.2	26.9	10.1	12.3	1.1	1.3	1.63	6.5
Fe_2O_3	0.14	0.16	3.6	3.7	1.5	0.4	0.00	0.00	0.00	b.d.l.[2]	0.00
MnO	0.00	0.00	0.15	0.23	0.00	0.00	0.00	0.00	0.00	b.d.l.	0.00
MgO	0.00	0.00	1.19	1.15	0.74	0.35	0.58	0.00	0.00	0.00	0.00
CaO	0.36	0.18	0.55	0.63	3.18	3.45	4.60	0.23	0.25	0.39	0.99
Na_2O	0.42	0.47	0.58	0.54	0.34	0.44	0.37	0.26	0.13	0.21	1.09
K_2O	0.45	0.66	3.48	3.00	0.24	0.51	0.92	0.27	0.24	0.37	1.81
Total	25.3	89.6	88.9	91.2	86.7	74.0	83.4	93.0	90.6	97.5	95.6

[1]Probable mixture of heulandite-clinoptilolite with silica
[2]b.d.l. = below detection limit

Table 6.1-34. Quantitative XRD Results (Weight Percent) for Samples from USW SD-12 Used in Sorption and Microautoradiography Studies

Mineral	LANL Sample 1874 (Batch Sorption)	LANL Sample 1875 (Microautoradiography)
Smectite	Trace	1 (1)
Biotite	Trace	trace
Clinoptilolite	2 (1)	3 (1)
Opal-CT	5 (1)	5 (1)
Quartz	3 (1)	5 (1)
Feldspar	8 (1)	12 (2)
Glass	82 (2)	74 (2)

NOTE: 2 Sigma errors in parentheses.

Table 6.1-35. Quantitative XRD Results (Weight Percent) for Samples from USW SD-9 Used in Sorption and Microautoradiography Studies

Mineral	LANL Sample 1895
Smectite	2 (1)
Clinoptilolite	80 (6)
Opal-CT	9 (2)
Quartz	3 (1)
Feldspar	7 (2)

NOTE: 2 Sigma errors in parentheses.

Table 6.1-36. Quantitative XRD Results (Weight Percent) for Sample from UE-25UZ #16 Used in Both Sorption and Microautoradiography Studies

Mineral	LANL Sample 1286
Smectite	7 (2)
Biotite	1 (1)
Cristobalite	15 (1)
Quartz	20 (2)
Feldspar	55 (8)

NOTE: 2 Sigma errors in parentheses.

Table 6.1-37. Matrix of Microautoradiography and Batch-Sorption Experiments for Three Major Rock Types

Sample ID	Data from Batch Sorption				Data from Microautoradiography		
	Cpm/g of Original Tracer Solution	Cpm/g in Solution after Sorption	K_d Based on Batch Sorption	Cpm on Thin Section after Sorption	Thin Section ID	Rock Type	Optical Microautoradiography Notes
Uranium							
J13. SD-12 1388-JK1001-25	44989	40544	1.17E+00	19,545	1875, T1J	vitric, Tptpv1	Moderate (~2-3x, locally higher concentrations over matrix clay
J13. SD-12 1388-JK1002-25	44989	40925	1.13E+00				
SYNP1. SD-12 1388-JK1003-25	46784	41888	1.41E+00	19,835	1875, T1A	vitric, Tptpv1	Moderate (~2-3x) concentrations over matrix clays
SYNP1. SD-12 1388-JK1004-25	46784	41525	1.70E+00				Highest clay/track concentrations at margins of vesicle-poor pyroclasts
J13.UZ-16 1638-JK1005-25	44989	39365	2.09E+00	9693	1286, T1C2	devitrified, Tcpuw	Slight (~2x) concentration over matrix clays and over altered
J13.UZ-16 1638-JK1006-25	44989	39839	1.76E+00				Orthopyroxenes
SYNP1.UZ-16 1638-JK1007-25	46784	42108	1.45E+00	19,551	1286, T1F	devitrified, Tcpuw	Slight track concentrations over matrix clays and oxides
SYNP1.UZ-16 1638-JK1008-25	46784	42438	1.26E+00				
J13.SD-9 1465-JK1009-25	44989	25461	1.43E+01	23,499	1895,T1I	zeolitic, Tpbt1	Moderate (~2x) concentrations over matrix clays;
J13.SD-9 1465-JK1010-25	44989	25403	1.44E+01				No concentrations over Mn-oxides
SYNP1.SD-9 1465-JK1011-25	46784	42084	1.43E+00	24,848	1895,T1G	Zeolitic, Tpbt1	Moderate (~2x) concentrations over matrix clays;
SYNP1.SD-9 1465-JK1012-25	46784	42348	1.30E+00				Some concentration (~2-3x) over Mn-oxides
Plutonium							
J13. SD-12 1388-JK1013-25	6581	1379	7.42E+01	647	1875, T1A2	vitric, Tptpv1	No evident track concentrations over specific phases
J13. SD-12 1388-JK1014-25	6581	1215	8.64E+01				
SYNP1. SD-12 1388-JK1015-25	36091	10368	4.87E+01	7651	1875, T1H	vitric, Tptpv1	Moderate (~3x) track concentrations over oxide/clay associations
SYNP1. SD-12 1388-JK1016-25	36091	9529	5.48E+01				Apparent oxide<clay retention
J13.UZ-16 1638-JK1017-25	6581	1388	7.29E+01	1370	1286, T1B2	devitrified, Tcpuw	~2-3x concentration over groundmass clays and altered
J13.UZ-16 1638-JK1018-25	6581	1324	8.70E+01				Orthopyroxenes
SYNP1.UZ-16 1638-JK1019-25	36091	10343	4.88E+01	4747	1286, T1A2	devitrified, Tcpuw	~2-3x concentration over groundmass clays and altered
SYNP1.UZ-16 1638-JK1020-25	36091	10055	5.09E+01				Orthopyroxenes

Table 6.1-37. Matrix of Microautoradiography and Batch-Sorption Experiments for Three Major Rock Types (Continued)

Sample ID	Data from Batch Sorption				Data from Microautoradiography		
	Cpm/g of Original Tracer Solution	Cpm/g in Solution after Sorption	K_d Based on Batch Sorption	Cpm on Thin Section after Sorption	Thin-Section ID	Rock Type	Optical Microautoradiography Notes
J13.SD-9 1465-JK1021-25	6581	1922	4.74E+01	1568	1895, T1J	zeolitic, Tpbt1	Very strong (>10x) concentrations over Mn-oxides
J13.SD-9 1465-JK1022-25	6581	2001	4.45E+01				
SYNP1.SD-9 1465-JK1023-25	36091	527	1.35E+03	8347	1895, T1H	zeolitic, Tpbt1	Very strong (>10x) concentrations over Mn-oxides;
SYNP1.SD-9 1465-JK1024-25	36091	523	1.36E+03				Moderate ~2-3x concentration over matrix clay
Americium							
J13. SD-12 1388-JK1025-25	1191	12	1950	3500	1875, T1C	vitric, Tptpv1	Slight concentration over groundmass and over clays in
J13. SD-12 1388-JK1026-25	1191	15	1592				Pyroclast vesicles
SYNP1. SD-12 1388-JK1027-25	1798	3	11603	5286	1875, T1B	vitric, Tptpv1	Slight track concentrations over fine-grained groundmass
SYNP1. SD-12 1388-JK1028-25	1798	3	12936				
J13.UZ-16 1638-JK1029-25	1191	9	2517	2329	1286, T1C	devitrified, Tcpuw	No evident concentrations
J13.UZ-16 1638-JK1030-25	1191	9	2625				
SYNP1.UZ-16 1638-JK1031-25	1798	3	12274	2664	1286, T1B	devitrified, Tcpuw	Slight track concentrations over fine-grained groundmass
SYNP1.UZ-16 1638-JK1032-25	1798	3	12329				
J13.SD-9 1465-JK1033-25	1191	35	651	5301	1895, T1F	zeolitic, Tpbt1	Moderate (>3x) track concentrations over Mn-oxides
J13.SD-9 1465-JK1034-25	1191	36	645				Slight (~2x) concentrations over matrix clay
SYNP1.SD-9 1465-JK1035-25	1798	1	41614	7455	1895, T1E	zeolitic, Tpbt1	Moderate (~2-5x) track concentrations over Mn-oxides;
SYNP1.SD-9 1465-JK1036-25	1798	1	31850				Some track concentrations also over oxide grains in expanded biotites

Table 6.1-38. Signal/Background Silver Concentrations in Microautoradiography Emulsions Measured by EMP Using Local or Epoxy-Margin Background Correction

Tuff/Radionuclide/Water	Thin-Section#	Mineralogy	Signal/Background
Devitrified/Pu/SynP1	1286,T1A2	Smectite	5 x
"	"	Feldspar + Silica	1–2 x
Devitrified/Pu/J13	1286,T1B2	Smectite	6 x
"	"	Feldspar + Silica	1–2 x
Vitric/Pu/SynP1	1875,T1H	Smectite	30 x
"	"	Glass	1–2 x
Vitric/Pu/J13	1875,T1A2	Smectite	< 1.5 x
"	"	Glass	< 1.5 x
Zeolitic/Am/SynP1	1895,T1E	Smectite + Rancieite	5–7 x
"	"	Clinoptilolite	1–1.5 x
Zeolitic/Am/J13	1895,T1F	Smectite + Rancieite	1.3–1.9 x
"	"	Clinoptilolite	1–1.4 x
Zeolitic/U/SynP1	1895,T1G	Smectite + Rancieite	5–7 x
"	"	Clinoptilolite	1–2 x
Zeolitic/U/J13	1895,T1I	Smectite + Rancieite	1.8 x
"	"	Clinoptilolite	1–1.5 x
Zeolitic/Pu/SynP1	1895,T1H	Smectite + Rancieite	40 x
"	"	Clinoptilolite	1–2 x
Zeolitic/Pu/J13	1895,T1J	Smectite + Rancieite	27 x
"	"	Clinoptilolite	1–2 x

Table 6.1-39. Signal/Background Ag Concentrations in Microautoradiography Emulsions across Fracture Samples, Measured by EMP Using Local Background Correction

Sample/Radionuclide/Water	Thin-Section#	Mineralogy	Signal/Background
Calcite-lined/Pu/SynP1	996,T3E	Calcite core	8.5 x
"	"	Calcite rim	1.8 x
Mn-oxide/Pu/SynP1	1900,T1C	Cryptomelane?	8–10 x

INTENTIONALLY LEFT BLANK

Table 6.2-1. Surface-Based Boreholes for which Isotopic and Geochemical Data Are Available for Samples from the Unsaturated Zone, Yucca Mountain, Nevada

		Analyses of Pore Water or Leached Salts							
Borehole	Total Depth (m)	Chem	^{3}H	$^{13,14}C$ (pore)	D-^{18}O	^{36}Cl	Other	Gas Analyses	Perched Water Analyses
UE-25 ONC#1*	469	—	—	—	—	•	—	—	Chem, ^{36}Cl
UE-25 UZ#16	514	•	•	•	—	•	—	$^{13,14}C$	—
UE-25 UZ#4	112	•	•	•	—	—	—	—	—
UE-25 UZ#5	111	•	•	•	—	—	—	—	—
UE-25 UZ-7	63	—	•	—	—	—	—	—	—
UE-25 UZN#1	15	—	•	—	—	—	—	—	—
UE-25 UZN#2	15	—	—	—	—	—	—	—	Chem, ^{36}Cl
UE-25 UZN#8	14	—	•	—	—	—	—	—	—
UE-25 UZN#90	14	—	•	—	—	—	—	—	—
UE-25 UZ-N46	30	—	—	—	—	—	—	—	Chem
UE-29 UZN#91	29	—	—	—	—	—	—	—	^{36}Cl
USW G-2	1830	—	—	—	—	—	—	—	chem, D-^{18}O, ^{36}Cl
USW NRG-4	221	—	—	—	—	•	—	—	—
USW NRG-6	335	•	•	•	•	•	—	CO_2 $^{13,14}C$	—
USW NRG-7a	461	•	•	•	—	•	—	CO_2 $^{13,14}C$	chem, ^{3}H, $^{13,14}C$, D-^{18}O, ^{36}Cl
USW SD-12	660	•	•	•	—	•	—	$^{13,14}C$	
USW SD-7	815	•	•	•	—	—	^{87}Sr	$^{13,14}C$	chem, ^{3}H, $^{13,14}C$, D-^{18}O, ^{36}Cl
USW SD-9	678	•	•	•	—	—	—	$^{13,14}C$	chem, ^{3}H, $^{13,14}C$, D-^{18}O, ^{36}Cl
USW UZ-1*	387	—	—	—	—	—	—	gases $^{13,14}C$	^{36}Cl
USW UZ-14	678	•	•	•	•	•	—	$^{13,14}C$	chem, ^{3}H, $^{13,14}C$, D-^{18}O, ^{36}Cl, ^{87}Sr, U isotopes
USW UZ-6	575	•	•	•	—	•	—	—	—
USW UZ-6s	158	•	•	•	—	•	—	—	—
USW UZ-N11	26	—	—	—	—	•	—	—	—
USW UZ-N15	18	—	—	—	—	•	—	—	—
USW UZ-N16	18	—	—	—	—	•	—	—	—
USW UZ-N17	18	—	—	—	—	•	—	—	—
USW UZ-N27	62	—	—	—	—	•	—	—	—

Table 6.2-1. Surface-Based Boreholes for which Isotopic and Geochemical Data Are Available for Samples from the Unsaturated Zone, Yucca Mountain, Nevada (Continued)

Borehole	Total Depth (m)	Analyses of Pore Water or Leached Salts						Gas Analyses	Perched Water Analyses
		Chem	^{3}H	$^{13,14}C$ (pore)	D-^{18}O	^{36}Cl	Other		
USW UZ-N36	18	—	—	—	—	•	—	—	—
USW UZ-N37	83	—	—	—	—	•	—	—	—
USW UZ-N38	27	—	—	—	—	•	—	—	—
USW UZ-N39	18	—	—	—	—	•	—	—	—
USW UZ-N53	72	—	—	—	—	•	—	—	—
USW UZ-N54	75	—	—	—	—	•	—	—	—
USW UZ-N55	78	—	—	—	—	•	—	—	—
USW UZ-N61	36	—	—	—	—	•	—	—	—
USW UZ-N62	18	—	—	—	—	•	—	—	—
USW UZ-N64	18	—	—	—	—	•	—	—	—

• Data from these holes are non-Q.

Table 6.2-2. Precipitation Chemistry Data for 3 Springs Basin in the Kawich Range, Nevada, 1985 to 1992 (McKinley and Oliver 1994, 1995)

Date	Precipitation (cm)	Concentrations (mg/L)							
		Alkalinity as $CaCO_3$	Ca	Mg	Na	K	SO_4	Cl	SiO_2
3 Springs Creek near Warm Springs, NV (elevation: 7070 feet)									
850119	no data	—	0.74	0.1	0.17	0.08	0.47	0.2	< 1
850403	no data	—	1.5	0.16	2.4	0.1	1.8	0.68	< 1
850924	no data	—	1.3	0.2	0.1	—	1.2	0.34	0.4
860111	5.65	2	0.6	0.05	0.2	—	0.61	0.27	< 0.01
860401	4.62	< 3	0.24	0.03	0.19	0.03	0.45	0.13	0.1
860708	0.95	7	1.7	0.18	2.4	0.7	1.4	1.3	0.98
860930	2.71	2	0.86	0.11	0.47	0.15	1.2	0.52	—
861230	1.62	2	0.51	0.05	0.25	0.13	0.72	0.21	0.1
870331	5.33	3	0.64	0.04	0.68	0.23	0.82	0.59	—
870701	2.65	2	0.57	0.08	0.27	0.14	1	0.26	0.08
870927	0	6	1.7	0.24	0.59	0.48	2	0.67	0.63
871209	4.65	1	0.12	0.02	0.06	0.02	0.28	0.11	0.07
880109	1.33	2	0.59	0.04	0.17	0.07	0.27	0.16	0.06
880404	2.05	2	0.25	0.02	0.4	0.93	0.39	0.24	0.05
880625	6.38	3	0.94	0.08	0.64	0.1	1.1	0.43	0.18
880923	1.60	1	1.2	0.21	0.46	0.3	1.7	0.55	0.22
890223	4.21	4	1.3	0.09	1.3	0.24	1.3	0.62	0.07
890412	0.55	13	3	0.17	6.9	0.54	4.8	3.2	0.36
890524	2.40	2	0.47	0.33	< 0.36	0.06	0.51	0.17	0.07
890913	2.70	—	1.1	0.04	0.4	—	1.4	0.38	0.27
891108	0.20	8	2.2	0.3	1.5	—	3.1	1.2	0.13
900130	1.60	2	0.7	< 0.02	0.5	—	0.49	0.2	< 0.02
900404	3.10	2.8	1.1	0.08	1.4	—	2.1	0.48	< 0.01
900522	1.50	< 0.5	0.46	0.06	0.7	0.3	1.1	0.74	< 0.01
900710	2.25	0.7	0.52	0.06	0.3	0.2	0.5	0.19	< 0.1
900922	1.85	1.1	1.2	0.2	0.4	0.1	0.99	0.25	0.2
910130	2.32	0.6	0.71	0.07	1	0.2	0.98	1.4	< 0.1
910604	7.50	< 0.5	0.67	0.07	0.6	0.1	1.2	0.2	< 0.1
910925	4.15	< 0.5	0.84	0.09	0.2	0.3	1	0.35	0.2
920218	7.83	< 0.5	0.33	0.03	< 0.2	0.1	0.5	0.12	< 0.1
920408	2.85	< 0.5	0.18	0.02	< 0.2	< 0.1	0.51	0.08	< 0.1
920609	0.62	3.1	2.1	0.25	0.8	0.8	3.1	0.67	0.2
920728	1.50	1.5	0.73	0.07	0.2	0.2	1.2	0.28	0.1
920917	1.14	< 0.5	1.2	0.12	0.2	0.2	1.9	0.32	< 0.1

Table 6.2-2. Precipitation Chemistry Data for 3 Springs Basin in the Kawich Range, Nevada,1985 to 1992 (McKinley and Oliver 1994, 1995) (Continued)

Date	Precipitation (cm)	Concentrations (mg/L)							
		Alkalinity as $CaCO_3$	Ca	Mg	Na	K	SO_4	Cl	SiO_2
Kawich Peak near Warm Springs, NV (elevation: 9120 feet)									
890223	5.73	3	0.9	0.1	1	0.16	1.1	0.65	0.05
890412	0.95	8	1.6	0.05	4.4	0.38	3.2	1.7	0.17
890524	2.77	2	0.4	0.3	0.25	0.08	0.5	0.18	0.07
890912	3.74	—	1.3	0.18	0.6	—	1.6	0.71	0.56
891108	0.25	4	1.5	0.12	0.9	—	1.6	0.57	0.05
900130	2.24	2	0.72	0.04	0.4	—	0.56	0.2	0.04
900404	4.39	3.6	0.95	0.05	1.3	—	1.7	0.46	< 0.01
900522	1.65	< 0.5	0.6	0.05	0.3	< 0.1	0.86	0.17	< 0.1
900710	2.73	1.3	0.47	0.05	0.3	0.2	0.52	0.26	< 0.01
900922	1.82	< 0.5	0.88	0.09	0.2	0.1	0.79	0.18	0.1
910130	2.24	0.9	0.59	0.13	0.5	2	0.63	0.96	< 0.1
910604	10.05	< 0.5	0.61	0.06	0.6	< 0.1	0.92	0.22	< 0.1
920218	7.72	2.9	0.78	0.08	1.4	0.2	1	0.42	1.5
920408	3.90	< 0.5	0.17	0.02	< 0.2	< 0.1	0.55	0.12	< 0.1
920609	0.63	4	2.5	0.26	1	0.9	3.6	0.88	0.2
920728	1.23	0.5	0.66	0.08	0.3	0.2	1.4	0.52	< 0.1
920917	1.04	0.5	1.4	0.14	0.4	0.2	2.3	0.42	< 0.1

"—" Indicates that this parameter was not measured.

Table 6.2-3. Average Annual Weighted Concentrations for Precipitation, 3 Springs Basin, Nevada

Year	Start	End	Total Precip. (cm)	Annual Weighted Concentration (mg/L)								
				Alkalinity as $CaCO_3$	Equiv. HCO_3	Ca	Mg	Na	K	SO_4	Cl	SiO_2
3 Springs Creek												
1986	850924	860930	13.93	2.67	3.26	0.61	0.06	0.40	0.15	0.73	0.34	0.13
1987	860930	880109	15.58	2.04	2.49	0.46	0.04	0.34	0.13	0.63	0.31	0.08
1988	880109	890223	14.24	2.93	3.57	0.98	0.09	0.78	0.28	1.12	0.47	0.13
1989	890223	891108	5.85	4.30	5.25	1.06	0.18	1.03	0.15	1.41	0.59	0.19
1990	891108	910130	12.62	1.40	1.70	0.81	0.08	0.79	0.20	1.12	0.56	N/C
1991	910130	910925	11.65	N/C	N/C	0.73	0.08	0.46	0.17	1.13	0.25	N/C
1992	910925	920917	13.94	N/C	N/C	0.49	0.05	0.23	0.15	0.81	0.17	N/C
Kawich Peak												
1989	881001	891108	13.44	3.23	3.94	0.97	0.16	0.97	0.16	1.27	0.64	0.20
1990	891108	910130	15.07	1.83	2.23	0.73	0.07	0.62	0.64	0.96	0.39	N/C
1991	910130	920218	17.77	N/C	N/C	0.68	0.07	0.95	0.15	0.95	0.31	N/C
1992	920218	920917	6.8	N/C	N/C	0.66	0.07	0.32	0.21	1.25	0.31	N/C
Results of Linear Regression for Cl as the Independent Variable												
Y-intercept				0	0	0	0	0	0	0	N/A	0
Standard error of y-intercept				0.91	1.11	0.15	0.03	0.18	0.16	0.30	N/A	0.02
R squared				0.13	0.13	0.38	0.65	0.63	-0.22	-0.49	N/A	0.88
No. of observations				7	7	11	11	11	11	11	N/A	5
X coefficient				5.433	6.628	1.787	0.220	1.578	0.489	2.431	N/A	0.313
Standard error of X coefficient				0.707	0.863	0.111	0.019	0.127	0.116	0.213	N/A	0.016

"N/C" signifies not calculated.

Weighting procedure for calculating annual average concentrations:

1. Because samples were collected irregularly throughout each year, annual average concentrations cannot be calculated. Individual chemical analyses from Table 6.2-2 were assigned to the year for which the largest proportion of precipitation contributed to that sample.
2. The precipitation accumulated during each sampling period (McKinley and Oliver 1994, 1995) was used to weight that sample's contribution to the average annual concentration.
3. The weighted average concentration excludes samples for which no data are available in Table 6.2-2 for a given chemical species.
4. No weighted average was calculated for a given species during a given year if more than 50% of the total precipitation had concentrations that were below the detection limit for this species.
5. If a sample was below detection limit for a particular species, but the total quantity of precipitation below the detection limit was less than 50%, then the weighted average uses the detection limit in its calculation.

Table 6.2-4. Precipitation Chemistry Data for Red Rock Canyon, Nevada, 1985-1997(NADP/NTN 1997)

Summary Period	Year	Average Concentrations (mg/L)								Lab pH	Lab Cond.	Field pH	Field Cond.	Prec. (cm)
		Ca	Mg	K	Na	NH_4	NO_3	Cl	SO_4					
Spring	1985	1.38	0.193	0.076	0.306	0.61	3.35	0.48	2.21	5.61	18.8	-9	-9	1.34
Summer	1985	6.06	0.761	0.282	1.264	0.9	8.94	2.37	6.74	7.03	63.7	-9	-9	2.69
Fall	1985	0.44	0.06	0.023	0.064	0.09	0.61	0.12	0.41	5.99	6.1	-9	-9	7.12
Winter	1985	0.53	0.144	0.054	0.339	0.46	3.11	0.22	1.28	4.78	18	-9	-9	0.6
Annual	1985	0.85	0.12	0.046	0.182	0.25	1.67	0.29	1.07	5.57	11.9	-9	-9	11.79
Spring	1986	0.61	0.076	0.022	0.125	0.1	0.83	0.16	0.37	5.55	7.9	-9	-9	2.71
Summer	1986	0.64	0.128	0.038	0.188	0.4	2.22	0.31	1.41	5.08	15.2	-9	-9	2.33
Fall	1986	0.26	0.036	0.01	0.087	0.12	0.93	0.08	0.68	5.08	7.6	-9	-9	3.18
Winter	1986	0.23	0.036	0.009	0.058	0.14	0.7	0.12	0.49	5.61	4.5	-9	-9	4.23
Annual	1986	0.38	0.059	0.018	0.106	0.21	1.32	0.15	0.79	5.05	9.9	-9	-9	14.01
Spring	1987	0.52	0.083	0.022	0.079	0.42	2.06	0.15	1.1	5.4	10.3	5.1	16.2	6.83
Summer	1987	0.78	0.16	0.167	0.132	0.98	3.7	0.53	3	4.85	23.6	-9	-9	0.81
Fall	1987	0.16	0.029	0.008	0.077	0.19	0.84	0.13	0.46	5.46	5.5	-9	-9	5.28
Winter	1987	0.5	0.049	0.023	0.156	0.21	1.88	0.18	0.86	4.7	15.1	4.94	14.7	5.33
Annual	1987	0.39	0.053	0.019	0.102	0.23	1.42	0.16	0.72	5.17	9	5.01	15.5	19.02
Spring	1988	0.21	0.035	0.017	0.101	0.22	1.07	0.16	1.1	4.98	9.5	4.64	12.1	2.44
Summer	1988	1.49	0.222	0.102	0.269	0.35	2.95	0.34	1.71	6.4	18	6.12	13.7	2.08
Fall	1988	3.01	0.44	0.606	0.721	0.17	1.33	0.86	1.11	6.72	48.9	5.07	5.7	0.69
Winter	1988	0.18	0.023	0.011	0.106	0.06	1.24	0.15	0.51	5	8.3	4.67	13	5.98
Annual	1988	0.7	0.105	0.081	0.179	0.21	1.56	0.23	0.95	5.35	13	4.88	9.7	11.33
Spring	1989	0.8	0.128	0.021	0.217	0.84	1.72	0.17	1.1	6.74	14.6	5.12	17.7	1.59
Summer	1989	4.92	0.622	0.146	1.948	1.04	3.81	0.85	2.74	7.71	71.3	-9	-9	0.13
Fall	1989	-9	-9	-9	-9	-9	-9	-9	-9	-9	-9	-9	-9	0.05
Winter	1989	0.29	0.038	0.015	0.067	0.17	1.01	0.06	0.4	5.72	5.7	5.04	6.9	6.48
Annual	1989	0.53	0.075	0.022	0.133	0.4	1.21	0.1	0.67	5.89	9.4	5.07	9.9	5.73

Table 6.2-4. Precipitation Chemistry Data for Red Rock Canyon, Nevada, 1985 to 1997 (NADP/NTN 1997) (Continued)

Summary Period	Year	Average Concentrations (mg/L)								Lab pH	Lab Cond.	Field pH	Field Cond.	Prec. (cm)
		Ca	Mg	K	Na	NH_4	NO_3	Cl	SO_4					
Spring	1990	2.64	0.319	0.097	0.57	1.48	3.95	0.8	3.18	7.02	35.1	-9	-9	0.46
Summer	1990	0.77	0.109	0.021	0.054	0.57	1.29	0.15	0.59	6.58	10.1	6.34	13.8	9.55
Fall	1990	2.46	0.395	0.043	0.205	0.43	2.67	0.25	1.65	5.54	24.4	-9	-9	2.12
Winter	1990	0.23	0.032	0.003	0.057	0.2	0.88	0.09	0.41	5.2	7	4.88	7	6.8
Annual	1990	0.92	0.131	0.021	0.089	0.47	1.41	0.16	0.73	5.66	11.8	5.02	8.9	19.14
Spring	1991	1.09	0.14	0.02	0.182	0.09	1.48	0.22	0.64	5.72	12	-9	-9	11.51
Summer	1991	0.74	0.13	0.024	0.102	0.4	1.46	0.2	1.18	6.36	10.9	6.6	7.9	5.51
Fall	1991	0.83	0.087	0.024	0.057	0.29	1.71	0.1	0.81	5.95	10.1	5.33	9.8	2.21
Winter	1991	0.95	0.104	0.036	0.1	0.17	0.86	0.1	0.56	5.69	8.8	-9	-9	1.3
Annual	1991	0.86	0.119	0.022	0.127	0.22	1.44	0.18	0.82	5.8	10.8	5.64	8.8	21.33
Spring	1992	0.24	0.027	0.009	0.041	0.15	0.85	0.07	0.49	5.28	6.6	5.34	10	13.24
Summer	1992	2.38	0.27	0.111	0.764	0.79	3.84	0.8	2.84	6.79	29	6.43	25.1	0.84
Fall	1992	0.05	0.008	0.002	0.015	0.09	0.66	0.04	0.23	5.38	3.8	5.08	4.4	4.51
Winter	1992	0.09	0.012	0.004	0.043	0.15	0.75	0.08	0.63	5	7.9	-9	-9	12.68
Annual	1992	0.25	0.03	0.01	0.067	0.17	0.9	0.1	0.61	5.17	7.7	5.34	10.7	35.91
Spring	1993	2.86	0.49	0.181	0.674	1.18	7.53	0.93	4.22	6.72	38.8	-9	-9	1.25
Summer	1993	1.65	0.282	0.137	0.411	0.96	4.16	0.67	2.78	6.56	24	-9	-9	1.06
Fall	1993	0.82	0.105	0.033	0.262	0.53	3.76	0.3	0.93	5.36	16.3	-9	-9	1.05
Winter	1993	0.03	0.006	0.002	0.019	0.07	0.46	0.03	0.44	5.05	5.1	-9	-9	20.86
Annual	1993	0.52	0.073	0.032	0.134	0.29	1.74	0.19	0.88	5.24	10.4	7.3	8.1	19.55
Spring	1994	0.52	0.083	0.007	0.092	0.35	0.97	0.13	0.41	6.34	6.8	5.7	2.7	1.68
Summer	1994	5.94	0.699	0.1	0.261	0.92	3.48	0.35	2.55	7.25	46.5	6.65	40.6	1.4
Fall	1994	1.35	0.123	0.042	0.118	0.32	2.03	0.17	0.79	6.09	12.7	5.43	2.5	1.83
Winter	1994	0.42	0.05	0.015	0.097	0.18	1.32	0.11	0.42	5.58	6.7	7.3	8.1	3.52
Annual	1994	1.07	0.125	0.022	0.087	0.31	1.34	0.12	0.66	5.5	11.5	5.27	10.2	11.77

Table 6.2-4. Precipitation Chemistry Data for Red Rock Canyon, Nevada, 1985 to 1997 (NADP/NTN 1997) (Continued)

Summary Period	Year	Average Concentrations (mg/L)								Lab pH	Lab cond.	Field pH	Field Cond.	Prec. (cm)
		Ca	Mg	K	Na	NH_4	NO_3	Cl	SO_4					
Spring	1995	0.6	0.075	0.048	0.121	0.31	1.59	0.14	1	5.5	9.6	5.38	10.6	6.95
Summer	1995	0.94	0.143	0.021	0.209	0.56	2.37	0.29	1.28	5.19	14.4	5.21	10.2	2.46
Fall	1995	3.95	0.68	0.059	0.308	1.26	8.24	0.42	1.92	7.21	40.4	-9	-9	0.23
Winter	1995	0.07	0.008	0.003	0.034	0.11	0.71	0.05	0.31	5.03	6.3	4.9	6.1	22.65
Annual	1995	0.31	0.043	0.016	0.075	0.2	1.15	0.1	0.59	5.09	8.3	5	8	28.34
Spring	1996	1.93	0.21	0.042	0.219	0.25	1.9	0.24	0.84	5.63	16.6	-9	-9	2.05
Summer	1996	-9	-9	-9	-9	-9	-9	-9	-9	-9	-9	-9	-9	1
Fall	1996	11.3	0.436	0.289	0.609	0.26	4.19	0.58	3.08	7.23	62.8	-9	-9	4.38
Winter	1996	0.13	0.019	0.02	0.031	0.13	0.72	0.03	0.18	5.29	4.6	5.69	4.4	4.11
Annual	1996	1.11	0.093	0.036	0.113	0.16	1.2	0.12	0.5	5.4	10.4	5.57	4.1	13.09
Spring	1997	2.32	0.208	0.093	0.489	0.75	3.36	0.64	2.4	6.73	24.9	-9	-9	0.13
Winter	1997	0.26	0.037	0.014	0.057	0.11	0.97	0.09	0.26	5.47	5	5.31	4.5	4.36

NOTE: seasonal and annual precipitation-weighted means reported in mg/L; an entry of -9 means no data are available for this parameter.

Table 6.2-5a. Physical Characteristics and Major Ion Chemistry of Surface Runoff and Channel Flow Samples in the Yucca Mountain Area

Date (mm/dd/yy)	Water Temp. (°C)	Specific Cond. (µS/cm)	pH	Concentration (mg/L)								
				Ca	Mg	Na	K	Cl	SO_4	F	HCO_3	SiO_2
22 - Unnamed Tributary to Stockade Wash near Rattlesnake Ridge, Nevada Test Site, Nevada (Refs. 1 and 2)												
03/31/92	—	211	—	20	4.0	11	4.4	12	9.7	0.2	89	25
01/22/93	1.0	134	—	14	2.8	10	3.2	5.1	8.4	0.1	54	20
03/23/93	12.5	164	—	16	3.6	11	5.2	4.3	9.0	0.2	76	36
23 - Stockade Wash at Airport Road, Nevada Test Site, Nevada (Ref. 1)												
02/10/93	4.0	122	—	15	3.1	6.4	4.3	3.1	6.5	< 0.1	55	24
52 - Pah Canyon above Mouth (Refs. 3 and 4)												
02/23/93	—	140	8.0	14	2.6	9.3	—	4.3	10	0.3	54	34
01/26/95	—	145	7.9	16	2.9	8.2	4.3	4.0	7.6	0.3	55	30
53 - Overland Flow near Pah Canyon (Ref. 4)												
01/06/95	—	134	7.8	15	2.8	4.9	3.7	3.4	7.8	0.1	34	18
55 - Delirium Canyon at Mouth (Refs. 3 and 4)												
02/09/93	—	118	7.8	12	2.4	7.6	—	3.2	7.8	0.3	48	33
56 - Overland Flow in Fortymile Canyon (Ref. 4)												
01/24/95	—	164	8.1	20	2.9	8.4	4.5	2.6	8.5	0.2	72	23
26 - Yucca Wash near Mouth, Nevada Test Site, Nevada (Refs. 1 and 4)												
01/18/93	7.0	133	—	15	2.3	11	4.1	4.4	6.0	0.2	55	24
01/26/95	—	117	8.1	15	2.1	5.8	4.1	2.0	4.1	0.2	53	22
57 - Fortymile Wash above Drill Hole Wash (Ref. 5)												
08/14/84	—	70	8.4	8.1	0.9	4.1	5.6	1.3	6.2	< 0.1	44	8.7
29 - Pagany Wash #1 near Well UZ-4, Nevada Test Site, Nevada (Ref. 1)												
12/07/92	5.0	218	—	21	2.1	13	4.6	10	24	0.2	—	14
31 - Wren Wash at Yucca Mountain, Nevada Test Site, Nevada (Ref. 4)												
01/25/95	—	258	8.2	28	3.9	16	11	5.8	16	0.2	109	21
33 - Split Wash below Quac Canyon Wash, Nevada Test Site, Nevada (Ref. 4)												
01/25/95	—	199	8.2	24	3.4	9.3	8.8	3.7	8.7	0.2	88	19
58 - Drillhole Wash at Mouth (Ref. 5)												
08/14/84	—	100	8.3	9.5	1.3	8.6	7.4	2.2	12	0.3	51	20
59 - Fortymile Wash at H-Road (Ref. 5)												
08/15/84	21.3	170	8.0	21	2.9	8.2	9.1	1.4	10	0.2	91	24
60 - Busted Butte Wash (Ref. 5)												
08/14/84	—	120	8.3	12	1.8	7.0	8.1	1.7	7.9	0.3	57	23
61 - Fortymile Wash at J-12 (Ref. 5)												
08/14/84	—	59	8.2	6.7	0.7	2.4	6.3	2.0	6.3	< 0.1	32	4.5

NOTE: Sites listed by identifier on Fig. 6.2-7 and station name; references listed in footnote to Table 6.2-5b.

Table 6.2-5b. Trace Ion Chemistry and Isotopic Composition of Water Samples at Surface Water Sites in the Yucca Mountain Area

Date (mm/dd/yy)	Al (µg/L)	Fe (µg/L)	Br (mg/L)	Sr (µg/L)	^{3}H (pCi/L)*	δ D (‰)	$\delta\ ^{18}O$ (‰)	Total Dissolved Solids (mg/L)
22 - Unnamed Tributary to Stockade Wash near Rattlesnake Ridge, Nevada Test Site, Nevada (Ref 1 and 2)								
03/31/92	—	—	0.02	—	—	—	—	130
01/22/93	50	13	—	82	22	—	—	90
03/23/93	140	66	—	65	—	—	—	123
23 - Stockade Wash at Airport Road, Nevada Test Site, Nevada (Ref 1)								
02/10/93	100	34	—	80	19	—	—	90
52 - Pah Canyon above Mouth (Ref 3 and 4)								
02/23/93	—	19	—	21	32	-82.3	-11.28	—
01/26/95	—	24	<0.01	23	—	—	—	100
53 - Overland Flow near Pah Canyon (Ref 4)								
01/06/95	—	<3	<0.01	—	—	—	—	—
55 - Delirium Canyon at Mouth (Ref 3 and 4)								
02/09/93	—	27	—	18	33	-88.10	-12.37	—
56 - Overland Flow in Fortymile Canyon (Ref 4)								
01/24/95	—	9	<0.01	97	—	—	—	—
26 - Yucca Wash near Mouth, Nevada Test Site, Nevada (Ref 1 and 4)								
01/18/93	380	57	—	45	19	—	—	94
01/26/95	—	30	<0.01	44	—	—	—	—
57 - Fortymile Wash above Drill Hole Wash (Ref 5)								
08/14/84	70	18	<0.01	34	—	—	—	57
29 - Pagany Wash #1 near Well UZ-4, Nevada Test Site, Nevada (Ref 1)								
12/07/92	20	6	0.04	130	23	—	—	—
31 - Wren Wash at Yucca Mountain, Nevada Test Site, Nevada (Ref 4)								
01/25/95	—	32	<0.01	200	—	—	—	—
33 - Split Wash below Quac Canyon Wash, Nevada Test Site, Nevada (Ref 4)								
01/25/95	—	28	<0.01	160	—	—	—	—
58 - Drill Hole Wash at Mouth (Ref 5)								
08/14/84	280	100	<0.01	66	—	—	—	92
59 - Fortymile Wash at H-Road (Ref 5)								
08/15/84	170	77	<0.01	100	—	—	—	122
60 - Busted Butte Wash (Ref 5)								
08/14/84	810	200	<0.01	86	—	—	—	100
61 - Fortymile Wash at J-12 (Ref 5)								
08/14/84	90	28	<0.01	31	—	—	—	45

*Conversion factor: 1 PCi/L=305 tritium units.

NOTE: Sites listed by identifier on Fig. 6.2-7 and station name; references listed in footnote.

Data Sources:

1. Emett et al. 1994
2. U.S. Geological Survey NWIS file
3. Savard 1996
4. TDIF:305288 DTN:GS960308312133
5. Perfect et al. 1995

Table 6.2-6a. Physical Characteristics and Major Ion Chemistry of Water Samples Obtained at Surface Water Sites in the 3 Springs Basin of Central Nevada (McKinley and Oliver 1994, 1995)

Date (mm/dd /yy)	Water Temp. (°C)	Specific Cond. (µS/cm)	pH	Concentration (mg/L)								
				Ca	Mg	Na	K	Cl	SO_4	F	Alkalinity (as $CaCO_3$)	SiO_2
3 Springs Creek near 3 Spring #3, near Warm Springs, Nevada												
01/19/85	—	—	—	9.4	1.8	8.7	2.2	2.9	2.7	0.07	42	39
04/03/85	—	—	—	< 5	1.4	5.5	2.2	2.9	4.3	0.09	33	37
07/10/85	—	98	—	9.4	1.7	8.6	—	2.5	3.6	0.07	40	40
01/11/86	5.0	49	7.1	8.0	1.5	7.7	—	3.0	4.3	0.07	38	36
03/20/86	7.0	85	8.1	6.7	1.4	7.0	1.8	2.6	5.0	0.08	30	36
3 Springs Creek near Warm Springs, Nevada												
04/03/85	—	—	—	> 5	1.5	> 5	1.9	3.4	5.2	0.09	38	39
03/04/86	7.0	—	7.1	7.6	1.6	8.3	2.0	—	—	—	34	38
03/20/86	8.0	95	7.2	8.0	1.5	7.0	1.6	2.8	5.7	0.11	34	38
04/01/86	7.0	91	7.1	7.5	1.4	7.0	1.7	2.6	5.3	0.08	32	35
03/31/87	6.5	120	6.7	9.7	1.4	1.9	1.2	4.0	5.4	0.06	43	39
05/07/87	3.0	108	—	9.3	2.5	11	1.0	3.2	5.0	0.16	42	38
07/01/87	8.5	130	6.7	12	1.7	12	1.2	3.4	4.8	0.11	53	40
11/18/87	7.5	126	—	9.7	1.8	9.7	2.1	3.5	5.8	—	53	40
12/09/87	7.0	142	6.5	10	1.6	10	1.3	3.5	5.8	—	46	40
01/09/88	7.0	128	6.8	10	1.7	9.9	1.3	3.5	5.3	—	50	42
04/06/88	6.0	101	6.8	8.7	1.4	11	1.0	3.3	5.4	—	47	39
06/25/88	8.5	109	7.0	10	1.7	11	1.3	3.0	5.0	—	49	38
04/12/89	8.0	112	6.6	11	1.5	13	1.2	3.7	6.0	0.10	49	41
05/24/89	8.5	122	6.9	11	0.5	13	1.5	3.8	5.0	0.10	53	40
05/22/90	8.0	123	6.8	11	1.5	13	1.0	4.6	5.2	0.10	50	41
06/06/91	7.5	118	6.7	11	1.5	12	0.9	4.3	7.2	0.20	46	40
04/08/92	7.0	97	6.9	7.8	1.3	9.1	1.4	4.0	7.4	0.20	32	38

Table 6.2-6a. Physical Characteristics and Major Ion Chemistry of Water Samples Obtained at Surface Water Sites in the 3 Springs Basin of Central Nevada (McKinley and Oliver 1994, 1995) (Continued)

Date (mm/dd/yy)	Water Temp. (°C)	Specific Cond. (µS/cm)	pH	Concentration (mg/L)								
				Ca	Mg	Na	K	Cl	SO_4	F	Alkalinity (as $CaCO_3$)	SiO_2
3 Springs Creek near 3 Spring #2, near Warm Springs, Nevada												
07/10/85	—	95	—	9.2	1.7	8.2	—	2.4	3.7	—	37	39
09/25/85	9.5	99	7.5	8.8	1.7	7.7	—	2.6	3.5	0.07	41	36
07/08/86	9.0	96	6.6	8.0	1.9	6.9	2.0	2.8	4.0	0.06	39	36
09/30/86	6.5	105	7.4	7.9	1.9	8.0	2.1	3.8	3.4	—	43	—
12/30/86	6.0	99	6.8	7.0	1.7	7.8	1.9	2.7	3.5	0.05	39	38
03/31/87	6.5	100	6.5	8.3	1.6	8.0	0.57	3.3	3.8	0.03	39	36
07/01/87	8.5	88	6.6	8.2	1.5	8.6	1.9	2.8	3.7	0.10	39	36
09/30/87	9.0	103	7.1	5.9	1.8	8.2	2.4	3.2	3.2	—	43	38
01/09/88	7.0	101	6.8	8.0	1.6	8.6	1.8	2.9	4.4	—	38	39
04/06/88	7.0	85	6.7	6.6	1.5	8.4	1.7	2.6	4.2	—	39	37
06/25/88	8.0	85	7.0	6.5	1.5	8.2	1.8	2.6	4.1	—	36	36
09/23/88	9.0	95	6.8	9.5	1.9	8.9	2.1	2.0	3.9	—	40	38
02/23/89	7.0	86	7.1	7.9	1.5	7.8	2.0	3.1	3.3	0.13	37	35
04/12/89	8.5	93	6.5	8.7	1.6	9.1	1.2	3.4	3.6	0.11	39	36
05/24/89	8.0	97	7.0	8.4	1.6	9.4	2.1	3.4	3.9	0.11	41	37
01/30/90	4.0	86	7.2	8.3	1.5	8.5	—	4.3	3.3	0.13	38	37
04/04/90	8.0	90	7.1	8.2	1.6	8.8	—	3.1	5.1	0.11	38	38
05/22/90	9.0	98	7.2	9.0	1.7	8.6	1.9	4.1	4.2	0.20	41	25
01/30/91	2.0	—	—	9.1	1.5	9.7	1.9	3.7	5.1	< 0.10	—	36
06/05/91	8.0	97	6.8	9.1	1.7	8.8	1.8	3.8	5.8	0.12	40	38
02/18/92	5.0	90	7.4	7.7	1.4	8.9	1.8	3.0	4.1	0.16	35	36
04/08/92	7.0	90	6.7	7.3	1.4	7.9	1.6	3.7	7.3	0.08	34	38
06/09/92	8.0	88	6.3	7.4	1.4	7.8	1.9	4.1	5.0	0.15	34	42
07/28/92	11.5	95	6.7	8.2	1.5	8.1	1.9	3.6	4.8	0.17	38	39
09/17/92	12.0	102	6.8	9.2	1.6	9.7	2.6	3.6	4.4	0.10	44	49
3 Springs Creek near Ledge Spring, near Warm Springs, Nevada												
09/29/87	8.5	120	7.0	6.5	2.2	9.9	3.2	3.5	2.5	—	50	41
06/23/88	9.0	98	7.0	10	2.0	8.2	2.8	2.7	3.9	—	43	40
09/23/88	8.0	111	6.8	11	2.4	9.5	3.0	3.7	2.9	—	47	41
06/22/89	—	94	7.3	9.1	1.9	8.0	2.6	3.1	2.9	0.07	42	43
09/12/89	8.0	112	7.1	10	2.0	8.8	—	3.1	3.0	0.10	49	42
11/08/89	4.0	106	7.0	10	2.2	11	—	3.0	3.0	0.10	50	47
05/22/80	8.0	99	6.9	8.9	1.8	8.0	2.5	3.9	3.9	0.10	42	43
09/23/90	9.0	126	7.3	11	2.2	9.1	3.9	4.9	2.6	< 0.10	51	43
06/05/91	7.0	94	6.6	8.4	1.7	7.7	2.4	3.5	5.7	0.11	35	7.9
09/25/91	9.5	107	6.6	9.4	1.9	8.4	2.8	3.5	3.1	< 0.10	50	42
06/09/92	7.5	92	6.4	7.9	1.6	8.1	2.7	4.3	5.3	0.16	37	46

Table 6.2-6b. Physical Characteristics and Major Ion Chemistry of Water Samples Obtained at Surface Water Sites in the 3 Springs Basin of Central Nevada (McKinley and Oliver 1994, 1995)

Date (mm/dd/yy)	Al (µg/L)	Fe (µg/L)	Br (mg/L)	Sr (µg/L)	Tritium (pCi/L)	δ D (‰)	$\delta^{18}O$ (‰)*	Total Dissolved Solids (mg/L)
3 Springs Creek near 3 Spring #3, near Warm Springs, Nevada								
01/19/85	—	—	0.031	—	—	-101.0	-13.40	89
04/03/85	—	—	—	—	—	—	—	—
07/10/85	—	4.0	—	77	—	-97.0	-13.37	—
01/11/86	—	< 3.0	—	72	—	—	—	—
03/20/86	—	< 10	—	160	—	-101.0	-13.60	79
3 Springs Creek near Warm Springs, Nevada								
04/03/85	—	—	—	—	—	—	—	—
03/04/86	—	6.0	—	—	—	—	—	—
03/20/86	—	< 10	0.039	260	—	-100.0	-13.20	85
04/01/86	—	3.0	0.019	190	< 200	-100.0	-13.30	80
03/31/87	—	3.0	—	10	—	-101.5	-13.70	88
05/07/87	< 10	< 10	0.027	110	—	—	—	96
07/01/87	—	< 3.0	0.038	110	—	-103.5	-13.80	107
11/18/87	—	3.0	0.038	91	—	-102.0	-13.75	105
12/09/87	—	< 3.0	0.035	98	54	-105.0	-13.80	100
01/09/88	—	< 3.0	0.35	110	—	-103.0	-13.75	104
04/06/88	—	< 3.0	0.035	110	—	-102.0	-13.85	98
06/25/88	—	6.0	—	100	—	-101.5	-13.80	99
04/12/89	—	< 3.0	0.030	90	—	-102.5	-13.80	107
05/24/89	—	4.0	0.030	110	—	-102.5	-13.80	107
05/22/90	—	72	0.050	—	—	-102.0	-13.70	108
06/06/91	—	7.0	0.040	—	—	-104.0	-13.90	105
04/08/92	—	< 3.0	0.04	—	—	-103.0	-13.90	89

*Conversion factor: 1 pCi/L = 305 Tritium

Table 6.2-6b. Trace Ion Chemistry and Isotopic Composition of Water Samples Obtained at Surface Water Sites in the 3 Springs Basin of Central Nevada (McKinley and Oliver 1994, 1995) (Continued)

Date (mm/dd/yy)	Al (µg/L)	Fe (µg/L)	Br (mg/L)	Sr (µg/L)	Tritium (pCi/L)	δ D (‰)	$\delta^{18}O$ (‰)*	Total Dissolved Solids (mg/L)
3 Springs Creek near 3 Spring #2, near Warm Springs, Nevada								
07/10/85	—	4.0	—	75	—	-112.0	-13.89	—
09/25/85	—	20	0.040	77	—	-101.5	-13.85	—
07/08/86	—	9.0	0.025	71	—	-100.5	-13.75	85
09/30/86	—	< 10	—	170	—	-100.0	-10.25	53
12/30/86	—	7.0	—	73	—	-100.0	-13.80	86
03/31/87	—	36	—	8.0	—	-102.0	-13.85	85
07/01/87	—	< 3.0	0.027	72	53	-103.5	-13.95	86
09/30/87	—	5.0	—	77	—	-102.5	-13.95	88
01/09/88	< 10	< 3.0	0.032	81	51	-103.5	-14.05	89
04/06/88	—	< 3.0	0.025	77	—	-104.0	-13.95	85
06/25/88	—	< 3.0	—	67	—	-103.0	-14.05	82
09/23/88	< 10	5.0	0.030	79	54	-102.0	-14.00	90
02/23/89	—	5.0	< 0.010	50	47	-103.5	-13.95	83
04/12/89	—	< 3.0	< 0.010	60	—	-101.5	-14.00	87
05/24/89	—	< 3.0	0.030	78	—	-106.0	-14.00	91
01/30/90	—	< 3.0	< 0.010	—	44	-105.0	-13.90	—
04/04/90	—	120	0.040	—	—	-103.0	-14.05	—
05/22/90	—	34	0.030	—	—	-102.0	-13.95	79
01/30/91	—	76	0.050	—	—	-104.0	-14.00	—
06/05/91	—	8.0	0.040	—	41	-106.0	-14.30	93
02/18/92	—	6.0	0.040	—	—	-104.0	-14.25	84
04/08/92	—	< 3.0	0.040	—	—	-103.0	-13.85	89
06/09/92	—	< 3.0	0.020	—	—	-102.0	-14.00	91
07/28/92	—	4.0	0.040	—	—	-103.0	-14.05	90
09/17/92	—	8.0	0.030	—	—	-104.0	-14.05	108
3 Springs Creek near Ledge Spring, near Warm Springs, Nevada								
09/29/87	—	9.0	0.095	91	—	-103.5	-14.00	99
06/23/88	—	< 3.0	—	82	—	-104.5	-14.20	95
09/23/88	< 10	< 3.0	0.040	98	48	-103.5	-14.15	102
06/22/89	—	6.0	< 0.01	70	—	-105.0	-14.15	96
09/12/89	—	4.0	0.020	—	—	-106.0	-14.10	—
11/08/89	—	4.0	0.030	—	—	-104.5	-14.05	—
05/22/80	—	46	0.030	—	—	-103.0	-14.10	97
09/23/90	—	7.0	0.020	—	—	-102.0	-14.00	107
06/05/91	—	10	< 0.01	—	—	-106.0	-14.30	59
09/25/91	—	9.0	0.030	—	—	-104.0	-13.90	101
06/09/92	—	< 3.0	0.040	—	—	-103.0	-14.25	98

*Conversion factor: 1 pCi/L = 305 Tritium

Table 6.2-7a. Physical Characteristics and Major Ion Chemistry of Water Samples Obtained at Surface Water Sites in the Stewart Basin of Central Nevada (McKinley and Oliver 1994, 1995)

Date (mm/dd/yy)	Water Temp. (°C)	Specific Cond. (µS/cm)	pH	Concentration (mg/L)								
				Ca	Mg	Na	K	Cl	SO_4	F	Alkalinity (as $CaCO_3$)	SiO_2
Veg Spring Near Ione, Nevada												
09/19/84	4.5	38	7.1	2.6	0.30	3.1	—	0.76	1.2	0.04	13	16
07/09/85	—	—	5.8	2.4	0.30	3.2	—	0.61	1.2	0.03	—	16
09/27/85	4.0	23	6.1	2.5	0.40	2.8	—	0.56	1.2	0.04	12	16
07/10/86	4.0	31	7.1	2.2	0.24	3.3	0.46	0.63	1.2	0.03	13	17
09/30/86	5.0	34	6.7	2.1	0.24	3.4	0.50	0.59	1.1	—	12	—
12/30/86	—	32	6.7	2.3	0.29	3.4	0.51	0.62	1.1	0.01	12	17
05/06/87	4.0	40	—	3.0	0.38	3.7	0.63	1.2	1.7	0.04	—	16
06/30/87	4.5	33	6.7	2.3	0.33	3.0	0.50	0.72	1.4	0.05	11	16
09/25/87	4.5	33	7.0	2.4	0.31	3.1	0.50	0.64	1.3	—	12	17
06/28/88	4.5	29	7.0	2.6	0.33	3.2	0.45	0.65	1.3	—	12	16
09/27/88	4.5	28	6.3	2.6	0.40	3.3	0.58	0.65	1.2	—	12	16
05/25/89	8.5	30	7.0	2.5	0.07	3.1	0.51	0.60	1.0	< 0.10	13	16
09/14/89	5.0	29	6.9	2.6	0.20	3.3	—	0.65	1.3	0.05	11	16
11/07/89	4.0	28	6.9	2.3	0.29	3.5	—	0.68	1.2	0.05	12	17
01/31/90	3.0	23	6.9	2.2	0.33	3.4	—	0.60	1.2	0.05	12	17
04/03/90	4.0	27	6.9	2.4	0.27	3.1	—	0.73	1.4	0.04	12	15
05/24/90	4.0	31	7.0	2.7	0.35	3.4	0.50	0.97	1.9	0.06	12	17
09/25/90	4.5	33	7.0	2.4	0.31	3.4	0.50	0.66	1.2	0.05	13	16
07/24/91	4.5	26	6.6	2.0	0.35	2.6	0.50	0.59	1.3	0.06	12	15
09/24/91	4.5	28	6.3	2.3	0.29	3.2	0.50	0.62	1.2	0.05	12	16
06/11/92	5.0	30	6.3	2.3	0.31	3.1	0.50	0.55	1.2	0.03	12	18
07/29/92	4.5	28	6.6	2.2	0.27	3.2	0.40	0.56	1.1	0.07	12	17
09/16/92	4.5	30	6.6	2.3	0.28	3.3	0.50	0.59	1.2	0.05	12	19
East Stewart Creek Near Ione, Nevada												
09/19/84	7.5	25	7.6	3.2	0.50	3.0	—	0.99	1.6	0.05	12	14
01/19/85	—	—	—	2.9	0.43	3.5	0.56	0.76	1.5	0.05	12	10
04/03/85	—	—	—	2.8	0.42	3.8	0.60	0.83	1.7	0.04	—	16
07/09/85	—	32	—	2.3	0.24	1.0	—	0.60	1.3	0.04	13	0.30
09/27/85	5.0	52	6.5	2.9	0.40	3.0	—	0.75	1.4	0.04	14	16
01/11/86	2.0	34	7.1	2.8	< 0.40	3.1	—	0.75	1.5	0.05	13	16
03/20/86	2.5	34	8.2	3.0	0.39	3.4	0.60	0.73	1.5	0.04	15	15
04/01/86	3.0	30	7.1	3.0	0.38	3.3	0.70	0.76	1.5	0.04	14	16
05/29/86	5.5	—	7.3	2.3	0.28	3.0	0.60	0.67	1.2	0.04	12	13
07/10/86	5.5	36	7.5	2.5	0.30	2.9	0.46	0.74	1.3	0.04	13	—
09/30/86	5.0	38	6.8	2.4	0.31	3.3	0.60	0.93	1.3	0.04	12	—
10/09/86	—	33	—	2.5	0.31	3.3	0.60	0.78	1.3	0.02	14	—
12/30/86	1.0	35	6.6	2.7	0.41	3.3	0.56	0.85	1.4	0.03	13	16
03/31/87	2.0	23	6.7	2.7	0.39	1.5	0.59	0.83	1.4	0.03	12	15

Table 6.2-7b. Trace Element Chemistry and Isotropic Composition of Water Samples Obtained at Surface Water Sites in the Stewart Basin of Central Nevada (McKinley and Oliver 1994, 1995)

Date (mm/dd/yy)	Al (µg/L)	Fe (µg/L)	Br (mg/L)	Sr (µg/L)	Tritium (pCi/L)	δ D (‰)	$\delta^{18}O$ (‰)*	Total Dissolved Solids (mg/L)
Veg Spring near Ione, Nevada								
09/19/84	—	< 3.0	0.008	19	110	-122.0	-16.40	—
07/09/85	—	10	< 0.050	17	—	-118.5	-16.55	—
09/27/85	—	52	0.007	21	—	-122.0	-16.55	—
07/10/86	—	8.0	< 0.010	17	—	-121.0	-16.50	33
09/30/86	—	< 10	—	70	—	-121.0	-16.50	15
12/30/86	—	4.0	—	16	—	-121.5	-16.60	32
05/06/87	10	< 10	—	10	—	—	—	36
06/30/87	—	< 3.0	—	1.0	—	-120.5	-16.40	31
09/25/87	—	< 3.0	—	17	—	-122.0	-16.55	32
06/28/88	—	4.0	—	18	—	-120.5	-16.45	32
09/27/88	< 10	8.0	—	17	84	-122.5	-16.60	32
05/25/89	—	4.0	< 0.010	18	—	-122.0	-16.65	32
09/14/89	—	< 3.0	< 0.010	—	65	-124.5	-16.65	—
11/07/89	—	< 3.0	< 0.010	—	78	-123.0	-16.60	—
01/31/90	—	< 3.0	< 0.010	—	—	-121.0	-16.65	—
04/03/90	—	9.0	0.030	—	—	-121.0	-16.65	—
05/24/90	—	75	< 0.010	—	—	-119.0	-16.30	35
09/25/90	—	< 2.0	< 0.010	—	—	-120.0	-16.50	33
07/24/91	—	7.0	< 0.010	—	—	-121.0	-16.60	30
09/24/91	—	4.0	< 0.010	—	—	-122.0	-16.45	32
06/11/92	—	< 3.0	< 0.010	—	—	-121.0	-16.45	34
07/29/92	—	3.0	< 0.010	—	—	-122.0	-16.60	32
09/16/92	—	< 3.0	< 0.010	—	—	-121.0	-16.65	36
East Stewart Creek near Ione, Nevada								
09/19/84	—	7.0	—	26	140	-117.0	-15.70	—
01/19/85	—	—	0.007	—	—	-120.0	-16.30	27
04/03/85	—	—	0.008	—	—	-119.8	—	—
07/09/85	—	5.0	< 0.005	25	—	-118.2	-16.29	—
09/27/85	—	9.0	0.006	26	—	-120.0	-16.35	—
01/11/86	—	11	0.009	24	—	-119.0	-16.40	—
03/20/86	—	< 10	< 0.010	150	—	-122.0	-16.45	33
04/01/86	—	< 10	0.008	140	—	-120.0	-16.30	34
05/29/86	—	12	< 0.010	17	—	-120.0	-16.00	28
07/10/86	—	< 10	< 0.010	< 10	—	-119.0	-16.30	16
09/30/86	—	< 10	—	70	—	-120.5	-16.20	16
10/09/86	—	< 10	—	70	—	—	—	17
12/30/86	—	10	—	25	—	-119.0	-16.25	33
03/31/87	—	6.0	—	21	—	-119.0	-16.25	30
05/06/87	—	< 3.0	—	23	—	—	—	31
06/30/87	—	< 3.0	—	20	—	-119.0	-16.25	31
09/25/87	—	4.0	0.57	24	—	-120.5	-16.30	35

Table 6.2-7b. Trace Element Chemistry and Isotropic Composition of Water Samples Obtained at Surface Water Sites in the Stewart Basin of Central Nevada (McKinley and Oliver 1994, 1995) (Continued)

Date (mm/dd/yy)	Al (µg/L)	Fe (µg/L)	Br (mg/L)	Sr (µg/L)	Tritium (pCi/L)	δ D (‰)	δ ^{18}O (‰)*	Total Dissolved Solids (mg/L)
East Stewart Creek near Ione, Nevada, Continued								
01/09/88	—	3.0	—	< 0.50	—	-120.5	-16.45	33
04/05/88	—	< 3.0	—	26	—	-121.5	-16.35	33
06/27/88	—	< 3.0	—	19	—	-120.0	-16.40	29
09/28/88	< 10	< 3.0	—	25	110	-119.5	-16.30	33
02/22/89	—	10	< 0.010	< 10	—	-121.0	-16.35	32
04/11/89	—	5.0	< 0.010	20	—	-120.0	-16.60	33
05/25/89	—	6.0	< 0.010	22	—	-117.5	-16.55	32
09/14/89	—	3.0	< 0.010	—	110	-122.0	-16.25	—
11/07/89	—	< 3.0	< 0.010	—	98	-120.5	-16.35	—
01/31/90	—	< 3.0	< 0.010	—	100	-122.5	-16.35	—
04/03/90	—	10	< 0.010	—	—	-123.0	-16.55	—
05/24/90	—	5.0	< 0.010	—	—	-119.0	-16.25	32
09/25/90	—	4.0	< 0.010	—	—	-119.0	-16.20	34
01/29/91	—	< 3.0	< 0.010	—	—	-122.0	-16.35	34
06/01/91	—	5.0	0.020	—	—	-118.0	-16.20	31
07/24/91	—	< 3.0	< 0.010	—	89	-121.0	-16.35	30
09/24/91	—	6.0	< 0.010	—	—	-120.0	-16.30	33
02/19/92	—	7.0	< 0.010	—	—	-119.0	-16.35	33
04/09/92	—	4.0	< 0.010	—	—	-120.0	-16.30	33
06/11/92	—	< 3.0	< 0.010	—	—	-119.0	-16.25	32
07/29/92	—	4.0	< 0.010	—	—	-122.0	-16.35	33
09/16/92	—	4.0	< 0.010	—	—	-118.0	-16.30	36
Hellebore Spring near Ione, Nevada								
05/29/86	—	6.0	0.023	33	—	-120.0	-16.00	44
07/31/86	—	54	< 0.010	37	—	-121.0	-16.20	44
09/30/86	—	< 10	—	140	—	-121.0	-16.20	44
12/30/86	—	< 3.0	—	35	—	-118.0	-16.20	42
05/06/87	—	< 3.0	—	33	—	—	—	42
06/30/87	—	3.0	—	36	—	-120.5	-16.20	43
09/25/87	—	< 3.0	—	36	—	-120.5	-16.25	43
05/10/88	—	< 3.0	< 0.010	38	—	-120.0	-16.20	44
06/28/88	—	< 3.0	—	34	—	-120.5	-16.15	41
09/29/88	< 10	< 3.0	0.010	37	110	-119.5	-16.20	43
04/11/89	—	—	—	—	—	-121.0	-16.25	—
05/25/89	—	5.0	< 0.010	35	—	-124.5	-16.30	43
11/07/89	—	< 3.0	< 0.010	—	—	-120.0	-16.25	—
04/03/90	—	5.2	0.030	—	—	-120.0	-16.25	—
05/24/90	—	3.0	< 0.010	—	—	-118.0	-16.10	43
07/24/91	—	4.0	< 0.010	—	—	-121.0	-16.25	43
06/11/92	—	< 3.0	< 0.010	—	—	-119.0	-16.25	45

*Conversion factor: 1 pCi/L = 305 Tritium Units

Table 6.2-8. Chemical Composition of Pore Water Samples from the Unsaturated Zone in Boreholes USW UZ-14, NRG-6, NRG-7a, SD-7, SD-9, SD-12, and UZ-16, Yucca Mountain, Nevada (Yang, Rattray et al. 1996; Yang, Yu et al. 1998)

Borehole	Depth Interval (ft)	Hydro-geologic Unit[2]	Litho-stratigraphic Unit[2]	Average Depth (m)	pH	Specific Cond. (µS/cm)	Concentration (mg/L)										Charge Balance[1]
							Ca	Mg	Na	SiO_2	Al	HCO_3	CO_3	Cl	NO_3	SO_4	
UZ-14	45.0–45.4	PTn	Tpy	13.78	8.6	1320	19.6	6.1	249	59.5	1	245	18	245	35	33	-1.8
UZ-14	85.2–85.6	PTn	Tpbt3	26.03	6.9	630	49.9	13.2	43.5	89.8	0.3	131	0	60	22	66	-0.9
UZ-14	91.0–91.3	PTn	Tpbt3	27.80	7.6	530	40.7	10.1	37.1	80.6	0.0	87	0	47	26	81	-4.1
UZ-14	95.5–95.9	PTn	Tpbt3	29.17	7.2	600	53.3	13.2	38.1	81.5	0	73	0	79	29	83	-1.9
UZ-14	96.2–96.6	PTn	Tpbt3	29.38	6.9	550	46.9	12.7	33.6	79.6	0	79	0	59	26	75	-0.9
UZ-14	100.4–100.8	PTn	Tpbt3	30.66	7.0	600	51.1	13.8	41.3	91.8	0.0	128	0	44	23	83	0.5
UZ-14	114.8–115.0	PTn	Tpp	35.02	6.6	540	49.0	10.5	35.9	93.9	0	67	0	61	25	90	-2.1
UZ-14	135.5–135.8	PTn	Tpp	41.36	6.9	690	68.5	14.3	56.2	92.0	0	105	0	83	23	96	4.6
UZ-14	144.8–145.2	PTn	Tpp	44.20	7.7	650	65.5	12.0	48.2	81.5	0	118	0	77	22	102	-1.7
UZ-14	147.7–148.1	PTn	Tpp	45.08	6.9	640	54.8	11.5	51.6	77.3	0	79	0	83	22	102	-1.5
UZ-14	177.6–177.9	PTn	Tpp	54.19	6.5	730	67.8	11.3	48.7	77.5	0	49	0	100	23	130	-2.0
UZ-14	178.1–178.4	PTn	Tpp	54.35	6.8	740	64.0	10.6	49.1	93.1	0	62	0	97	21	120	-3.0
UZ-14	215.7–216.1	PTn	Tpp	65.81	6.9	710	65.5	10.7	39.4	97.8	0	55	0	85	14	130	-3.0
UZ-14	225.9–226.2	PTn	Tpp	68.92	7.9	640	58.6	10.4	48.4	91.2	0	55	0	93	16	116	-2.6
UZ-14	235.1–235.4	PTn	Tpp	71.72	7.1	630	67	10.5	29	63	0.0	96	N/S	84	15	94	-5.7
UZ-14	240.8–241.1	PTn	Tpbt2	73.46	7.6	810	32	1	103	61	3	162	N/S	99	17	100	-11.7
UZ-14	245.5–245.8	PTn	Tpbt2	74.89	6.8	580	65	12	9	46	0	66	N/S	77	12	79	-4.7
UZ-14	1258.5–1258.8	TSw	Tptpln	383.65	—	—	43	3.7	67	35	0.0	170	N/S	88	16	19	-4.9
UZ-14	1277.4–1277.7	TSw	Tptpln	389.41	—	—	62	4.5	49	44	0.0	170	N/S	87	17	45	-7.1
UZ-14	1277.7–1278.0	TSw	Tptpln	389.50	—	—	74	5.1	45	38	0.0	170	N/S	130	15	38	-10.3
UZ-14	1409.4–1409.8	CHn	Tpbt1	429.65	7.8	720	30.0	0.7	88.0	57.0	0.1	160	0	75	5	106	-13.2
UZ-14	1419.5–1419.8	CHn	Tpbt1	432.72	8.3	410	20.0	0.6	68.0	60.0	1.4	166	0	24	6	21	1.0
UZ-14	1461.9–1462.1	CHn	Tac3	445.62	7.6	570	9.2	0.1	128	68.7	1.2	265	0	24.2	6.2	37.3	1.1
UZ-14	1495.8–1496.0	CHn	Tac2	455.95	8.4	500	2.1	0.0	122	56.7	0.3	228	0	28.0	10.8	14.3	3.9
UZ-14	1524.55–1524.75	CHn	Tac2	464.73	7.7	560	1.1	0.1	137	54.8	1.1	232	0	26.2	12.5	22.3	7.2
UZ-14	1542.3–1542.8	CHn	Tac2	470.18	8.6	760	3.6	0.5	207	143.0	13.8	384	46	20	4	28	1.0
UZ-14	1563.6–1563.8	CHn	Tac2	476.62	8.7	660	1.2	0.2	155.0	72.0	13.9	160	97	16	4	14	1.2

Table 6.2-8. Chemical Composition of Pore Water Samples from the Unsaturated Zone in Boreholes USW UZ-14, NRG-6, N4G-7a, SD-7, SD-9, and SD-12, Yucca Mountain, Nevada (Yang, Rattray et al. 1996; Yang, Yu et al. 1998) (Continued)

Borehole	Depth Interval (ft)	Hydro-geologic Unit[2]	Litho-stratigraphic Unit[2]	Average Depth (m)	pH	Specific Cond. (µS/cm)	Concentration (mg/L)										Charge Balance
							Ca	Mg	Na	SiO_2	Al	HCO_3	CO_3	Cl	NO_3	SO_4	
UZ-14	1564.6–1564.8	CHn	Tac2	476.92	9.0	590	1.3	0.2	129	140.4	9.4	61	113	16	4	17	0.4
UZ-14	1564.9–1565.0	CHn	Tac2	477.01	8.3	690	1.7	0.5	169.0	54.0	15.5	376	0	23	1	30	0.1
UZ-14	1585.0–1585.2	CHn	Tac2	483.14	8.9	460	0.9	0.3	106.8	74.5	5	98	67	14	7	10	1.6
UZ-14	1585.3–1585.6	CHn	Tac2	483.23	9.3	400	1.2	0.5	85.0	75.0	16.3	148	18	11	6	9	2.4
UZ-14	1605.9–1606.1	CHn	Tac2	489.51	8.9	470	1.0	0.3	87.8	67.2	6	178	0	18	6	9	2.4
UZ-14	1644.3–1644.5	CHn	Tac2	501.21	8.8	420	2.2	0.7	110.0	74	30.9	74.0	79	14	0	9	5.5
UZ-14	1674.8–1675.1	CHn	Tac1	510.54	7.2	N/S	1.8	0.6	58.0	64.6	18	104	0	10	4	9	8.6
UZ-14	1695.4–1695.6	CHn	Tabt1	516.79	7.9	N/A	1.4	1.1	115.8	55.9	10	203	18	21	5	26	0.6
UZ-14	1715.0–1715.3	CHn	Tabt1	522.79	7.3	390	0.2	0.0	88	52.9	0.6	168	0	11.9	3.1	16.0	5.1
UZ-14	1734.5–1734.7	CHn	Tabt1	528.71	8.7	750	2.0	0.3	184	50.7	0.1	211	79	39.4	5.6	17.5	2.9
UZ-14	1735.3–1735.53	CHn	Tabt1	528.95	9.0	700	1.7	0.0	158	46.9	0.0	288	18	37	3.4	15	1.5
UZ-14	1804.5–1804.7	CHn	Tcp4	550.04	8.7	480	0.5	0.2	111	43.0	1.0	181	12	25	15.3	15	2.5
UZ-14	1825.8–1826.0	CHn	Tcp3	556.53	9.4	590	0.6	0.1	138	47.9	0.9	42	112	24	11.8	13	4.3
UZ-14	1854.9–1855.1	CHn	Tcp3	565.40	9.2	460	0.5	0.2	107	34.5	1.6	181	23	19	13.7	16	-1.4
UZ-14	1865.7–1865.9	CHn	Tcp3	568.70	9.1	480	0.3	0.0	115	30.4	0.8	204	18	17	11.7	13	1.4
UZ-14	2014.7–2014.9	CHn	Tcp1	614.11	9.3	1520	3.2	0.2	392	37.7	0.2	409	219	32	1.8	22	5.6
UZ-14	2015.2–2025.7	CHn	Tcp1	615.85	9.2	1450	0.9	0.0	313	68.6	—	339	176	23	0.5	22	4.2
UZ-14	2025.1–2025.3	CHn	Tcp1	617.28	9.3	1550	4.0	0.2	414	54.8	0.2	493	189	36	6.9	26	6.3
UZ-14	2095.6–2095.8	Cfu	Tcb	638.71	9.0	530	0.0	0.0	113	63.0	—	143	29	30	0.3	29	1.3
UZ-14	2104.05–bottom	Cfu	Tcb	641.33	9.4	—	2.1	0.7	143	352	38	229	19	10	4	23	10.
NRG-6	158.2–158.6	PTn	Tpbt4	48.28	6.8	1070	122	23.3	35.6	97.4	0	34	0	185	32	159	-0.2
NRG-6	160.8–161.2	PTn	Tpbt4	49.07	8.0	860	104	18	35.0	84.0	1.6	55	0	148	35	139	-2.0
NRG-6	171.0–171.3	PTn	Tpbt3	52.18	7.4	620	70.5	11.5	29.2	79.4	0	48	13	58	43	94	2.0
NRG-6	175.6–176.0	PTn	Tpp	53.58	7.3	520	49.2	8.6	29.4	78.1	0	60	0	47	42	64	1.5
NRG-6	219.9–220.2	PTn	Tpp	67.09	7.4	660	24.3	4.2	99.3	61.4	1	92	0	77	47	77	-1.3
NRG-6	244.6–245.0	PTn	Tpbt2	74.62	7.2	630	33	4.9	72.0	51.0	0.6	61	0	49	40	115	-2.3
NRG-6	255.9–256.1	PTn	Tptrv3	78.03	6.7	1920	176	19	215.0	68.0	0.9	61	0	115	35	840	-6.2
NRG7A	165.8–166.0	PTn	Tpbt3	50.57	7.3	500	55.3	5.6	31.7	68.3	0	89.0	0	38.9	45.5	63.4	0
NRG7A	258.0–258.4	PTn	Tpp	78.70	8.3	595	43	3.7	82	68.9	1.0	128	0	53.6	43.7	65.5	2.9
NRG7A	1483.6	CHn	Tptpv1	452.22	8.0	580	61	0.6	94	48.6	0.3	323	0	33.1	16.7	24.4	1.3

Table 6.2-8. Chemical Composition of Pore Water Samples from the Unsaturated Zone in Boreholes USW UZ-14, NRG-6, N4G-7a, SD-7, SD-9, and SD-12, Yucca Mountain, Nevada (Yang, Rattray et al. 1996; Yang, Yu et al. 1998) (Continued)

Borehole	Depth Interval (ft)	Hydro-geologic Unit[2]	Litho-stratigraphic Unit[2]	Average Depth (m)	pH	Spec. Cond. (µS/cm)	Concentration (mg/L)										Charge Balance[1]
							Ca	Mg	Na	SiO_2	Al	HCO_3	CO_3	Cl	NO_3	SO_4	
NRG7A	1492.9	CHn	Tptpv1	455.04	8.6	510	30.6	0.3	74.7	71.5	0.0	104	34	39	18	23	0.9
NRG7A	1498.8	CHn	Tac	456.83	8.3	500	28.7	0.5	73.2	83.0	1	156	0	50	17	18	0.4
SD-7	339.7–340.2	PTn	Tpbt3	103.63	7.2	720	110	15	20	82.8	—	220	0	77.2	1.5	76.7	1.3
SD-7	370.3–370.6	PTn	Tpbt2	112.93	6.7	1420	289	0.2	39	25.9	—	73	0	133	0.6	650	-6.7
SD-7	1498.4–1498.6	CHn	Tac2	456.74	7.4	405	31	0.6	67	63.5	—	171	0	28.9	13.6	14.1	4.4
SD-7*	1524.6–1525.7	CHn	Tac1	464.85	7.7	490	38.7	0.9	57.6	68.6	—	203	0	30.1	12.4	15.9	-0.2
SD-7	1558.4–1558.6	CHn	Tac1	475.03	7.4	370	39	0.9	43	69.3	—	171	0	25.1	9.0	14.9	-1.0
SD-7	1617.0–1617.2	CHn	Tacbs	492.87	7.2	570	40.2	0.4	79	62.2	—	194	0	65	11.0	14	0.0
SD-7	1890.9	CHn	Tcp1	576.35	8.7	850	0	0.2	206	67	—	334	78	18	4.8	10	0.6
SD-7	1952.6	CHn	Tcp1	595.15	8.8	980	0	0.3	251	67.4	—	353	120	22	6.7	11	0.9
SD-7	2596.1–2596.3	CHn	Tcbts	791.28	9.1	670	0.6	0.2	158	64.3	—	79	65	83	3.2	12	6.4
SD-7	2598.3–2598.5	CHn	Tct	791.95	8.8	630	0.9	0.0	152	94.8	—	231	59	22	4.0	18	-1.2
SD-9	94.2–94.4	PTn	Tpbt4	28.74	6.2	1050	125	24	43	74	—	37	0	170	11	260	-4.3
SD-9	154.0–154.2	PTn	Tpbt3	46.97	6.9	650	72	13	36	55	—	90	0	93	4.7	106	-1.1
SD-9	1452.6–1452.8	CHn	Tptpv1	442.78	7.5	520	6.9	0	112	62.5	—	256	0	15.7	10.6	62.5	1.4
SD-9*	1535.2–1535.4	CHn	Tac3	467.96	7.4	530	0.8	0.1	112	54.9	—	226	0	15.6	10.6	15.5	4.7
SD-9*	1619.9–1661.4	CHn	Tac2	500.09	8.9	610	0.4	0	136.6	55.6	—	232	12	50.2	9	18.3	-0.7
SD-9	1661.1–1661.3	CHn	Tac2	506.33	9.1	670	0.7	0.0	164	48.8	—	317	0	42.0	8.2	18.9	1.9
SD-9	1741.0–1741.2	CHn	Tac1	530.69	9.1	520	0.2	0	125	52	—	185	41	19	4.4	10	2.2
SD-9	1741.7–1741.9	CHn	Tac1	530.90	8.8	310	0.2	0	74	53	—	113	12	15	3.8	8.7	5.0
SD-9*	1800.8	CHn	Tacbt1	548.88	9.3	790	0.8	0	180.7	59.6	—	137	106	32.3	4.6	20.9	5.6
SD-12*	265.8–266.1	PTn	Tpbt4	81.08	7.2	470	48.9	7.6	28.6	62.7	—	107	0	49.6	15.9	47.5	-0.1
SD-12	278.6–278.8	PTn	Tpp	84.95	7.3	580	74	12.7	27	71.2	—	159	0	46	16.0	75	1.7
SD-12	296.1–296.6	PTn	Tpbt2	90.34	7.1	490	75	8.0	21	72.2	—	163	0	60	18.0	21	2.2
SD-12	1460.7–1461.0	CHn	Tac4	445.28	8.5	490	31	0	89	65.5	—	98	30	55.9	7.3	30.1	4.7
SD-12	1495.5–1495.8	CHn	Tac3	455.89	8.5	550	16	0.2	108	87.3	—	49	57	57	8.1	55	-0.7
SD-12	1517.0–1517.4	CHn	Tac3	462.44	8.3	660	14	0	150	56.9	—	323	0	35.6	6.4	22.5	2.5
SD-12	1600.6–1603.0	CHn	Tac1	488.23	9.1	540	2.6	0	129	65.7	—	79	90	27.8	2.6	12.6	3.2
SD-12	1636.9	CHn	Tacbt	498.93	9.0	535	3.8	0	129	64.6	—	67	102	15.2	1.7	11.2	5.6
SD-12	1901.5	CHn	Tcp2	579.55	9.1	470	1.3	0	122	90.7	—	151	59	22	5.7	9.3	0.2

Table 6.2-8. Chemical Composition of Pore Water Samples from the Unsaturated Zone in Boreholes USW UZ-14, NRG-6, N4G-7a, SD-7, SD-9, and SD-12, Yucca Mountain, Nevada (Yang, Rattray et al. 1996; Yang, Yu et al. 1998) (Continued)

Borehole	Depth Interval (ft)	Hydro-geologic Unit[2]	Litho-stratigraphic Unit[2]	Average Depth (m)	pH	Spec. Cond. (µS/cm)	Concentration (mg/L)										Charge Balance[1]
							Ca	Mg	Na	SiO_2	Al	HCO_3	CO_3	Cl	NO_3	SO_4	
SD-12	1938.8	CHn	Tcp2	590.93	8.8	625	1.4	0	165	55.0	—	171	66	34.0	1.0	26.1	5.2
SD-12	1942.4	CHn	Tcp2	592.04	9.1	520	1.3	0	140	60.1	—	134	66	24.0	3.5	24.4	4.3
UZ-16	163.5–163.9	PTn	Tpbt4	49.90	7.6	425	42.5	13.4	21.5	77.5	0.5	114.7	45.0	32.4	23.1	72.3	-19.4
UZ-16	180.9–181.3	PTn	Tpbt3	55.20	7.5	430	55	11	20	83	0.1	120	0.0	38	33	38	1.8
UZ-16	1166.19–1166.47	CHn	Tptpv1	367.74	8.7	710	28.9	13.7	83.6	57.1	0	196	0	82	17	28	-1.4
UZ-16	1227.4–1227.7	CHn	Tac4	374.17	8.1	430	26.5	6.2	47.9	62.2	0.3	137.0	0	24	23	26	1.2
UZ-16	1235.1–1235.41	CHn	Tac4	376.52	8.2	480	33.5	7.9	51.3	52.9	0	154	0	52	26	29	-4.7
UZ-16	1269.6–1269.9	CHn	Tac3	387.04	8.5	430	14.1	2.4	67.5	57.1	0	139	13	27	18	14	-2.7
UZ-16	1280.4–1280.8	CHn	Tac3	390.33	8.3	530	20.5	3.7	92.0	71.8	1.5	192.0	0	28	19	19	6.9
UZ-16	1296.8–1297.06	CHn	Tac3	395.33	7.4	930	32.4	19.7	98.2	46.7	0	324	12	50	19	18	-1.9
UZ-16	1317.9–1318.2	CHn	Tac3	401.76	7.3	420	20.6	5.1	60.1	131.6	1.1	171	0	32	20	18	-4.0
UZ-16	1343.7–1344.0	CHn	Tac2	409.62	8.4	530	17	2.4	99	62.1	1.7	47.6	58.8	56	18	23	2.5
UZ-16	1358.0–1358.4	CHn	Tac2	413.98	7.5	550	3.4	0.3	76.7	47.9	1.1	140.3	0	22.8	16.1	18.7	-0.08
UZ-16	1379.6–1379.9	CHn	Tac2	420.56	8.6	490	4.4	0.6	95	66.3	2.6	72	46.8	21	18	25	3.0
UZ-16	1389.3–1389.6	CHn	Tac2	423.52	7.0	530	3.6	0.9	114.6	62.5	2.0	122	36.0	23.5	18.5	23.8	5.9
UZ-16	1395.5–1395.9	CHn	Tac2	425.41	7.8	710	5.4	0.3	155	88.0	3.9	216.0	24.0	17	16	22	11.9
UZ-16	1397.7–1398.0	CHn	Tac2	426.08	8.7	550	5	0.5	124	79.2	4.7	131.8	35.4	45	25	45	-2.3
UZ-16	1398.5–1398.7	CHn	Tac2	426.29	8.0	710	5	0.4	145	123	7.8	237.0	31.0	14	16	20	4.8
UZ-16	1408.2–1408.6	CHn	Tac2	429.28	9.2	580	3.3	0.3	104	68.5	3.4	72	70.8	20	14	16	0.5
UZ-16	1412.9–1413.2	CHn	Tac2	430.71	8.7	450	1.2	0.1	101	75.9	1.0	165.0	0	26	24	30	0.1
UZ-16	1428.1–1428.4	CHn	Tac2	435.35	8.8	570	1.9	0.1	134	80.5	3.4	160.0	43.0	23	19	23	3.9
UZ-16	1434.2–1434.6	CHn	Tac2	437.21	8.5	550	3.2	0.6	113	109.1	6.1	72	70.8	23	16	19	2.8
UZ-16	1442.8–1443.2	CHn	Tac2	439.83	7.6	550	1.7	0.8	79.9	68.9	1.2	18.3	87.6	18.9	11.3	13.7	-7.7
UZ-16	1486.9–1487.3	CHn	Tcp4	453.27	9.2	360	6.3	0.8	79.5	233.3	26.2	137.0	0	38	6	11	2.7
UZ-16	1601.1–1601.5	CHn	Tcp3	488.08	8.9	570	10	0.3	100	36	0.7	181.0	0	53	13	27	-3.6
UZ-16	1607.7–1608.1	CHn	Tcp3	490.09	9.0	660	25	0.3	108	34	1.0	170.0	0	71	10	33	2.8
UZ-16	1643.4–1647.2	CHn	Tcp3	501.49	9.0	490	91	12	34	70	3	162.0	0	70	8	28	13.6
UZ-16	1651.6–1651.7	CHn	Tcp3	503.44	8.4	420	17.3	0.3	66	47.4	0.7	87.0	19.0	27	6	20	6.1

"—" data not available. "0" values below detection limit. [1]Charge balance calculated from data shown using the formula: (meq cation-meq anion)/(meq cation + meq anion)*100

[2]Hydrogeologic unit and lithostratigraphic unit nomenclature from Tables 3.6-1 and 3.6-2 (Geology Chapter). Stratigraphic depths for these boreholes are from Moyer and Geslin 1995; Moyer et al. 1996, GS940408314211.020 (NRG-7A); Engstrom and Rautman 1996; Rautman and Engstrom 1996a, 1996b.

*K concentrations measured for pore waters extracted from core from the following boreholes and depth intervals (in feet): SD-7 1524.6-1525.7, 7 mg/L; SD-9 1619.9-1661.4, 4 mg/L; SD-9 1800.8, 6 mg/L; and SD-12 265.8-266.1, 3 mg/L.

Table 6.2-9. Chloride, Bromide, and Sulfate Concentrations Measured for Exploratory Studies Facility Pore Water Samples (Fabryka-Martin, Turin et al. 1998)

Borehole ID	ESF Station[1]	Hydro-geologic Unit[2]	Lithologic Unit[3]	Concentration (mg/L)			Weight Ratios	
				Cl	Br	SO_4	Cl/Br	SO_4/Cl
North Ramp Holes								
NR#1a	727	TCw	Tpcplnc	29	0.38	37	75	1.3
NR#2	750	TCw	Tpcplnc/mw	20	0.23	32	88	1.6
NR#3	770	TCw	Tpcplnc/mw	35	0.26	47	134	1.3
NR#4	772	PTn	Tpcpv2	46	0.36	60	130	1.3
NR#5	783	PTn	Tpcpv2	27	0.20	31	133	1.1
NR#6	821	PTn	Tpcpv1	69	0.70	92	99	1.3
NR#7	867	PTn	Tpbt4	16	0.17	28	98	1.7
NR#8	870	PTn	Tpy	18	0.22	27	81	1.5
NR#10	880	PTn	Tpbt3	16	0.17	34	97	2.0
NR#13	1008	PTn	Tpbt2	10	0.14	21	74	2.1
LCPA #2	Alc #4	PTn	Tpbt2	18	0.25	36	71	2.0
LCPA #3	Alc #4	PTn	Tpbt2	17	0.24	41	72	2.4
NR#15	1054	PTn	Tptrv3/rv2	21	0.17	37	122	1.8
NR#16	1069	PTn	Tptrv2	13	0.12	22	106	1.8
South Ramp Holes								
SR#5	6300	TSw	Tptpul	27	0.02	18	1129	0.6
SR#6	6388	TSw	Tptpul	87	0.35	106	250	1.2
SR#7	6480	TSw	Tptpul	63	0.27	64	231	1.0
SR#9	6641	TSw	Tptrn	86	0.43	100	198	1.2
SR#10	6648	TSw	Tptrv2	20	0.16	47	125	2.3
SR#11	6658	TSw	Tptrv3	26	0.16	42	165	1.6
SR#12	6668	PTn	Tpbt2	29	0.17	32	174	1.1
SR#13	6679	PTn	Tpbt2	37	0.21	26	178	0.7
SR#14	6696	PTn	Tpbt4	33	0.16	39	205	1.2
SR#15	6704	PTn	Tpcpv1	26	0.18	33	149	1.2
SR#16	6721	PTn	Tpcpv1	46	0.22	43	209	0.9
SR#18r	6748	TCw	Tpcplnc	45	0.12	50	382	1.1
SR#19	6826	TSw	Tptpul	17	0.11	13	158	0.8
SR#20	6936	TSw	Tptrn	129	1.16	74	111	0.6
SR#21	7054	PTn	Tpbt2	89	0.46	104	193	1.2
SR#22	7056	PTn	Tpbt2	108	0.57	127	190	1.2
SR#22r	7056	PTn	Tpbt2	100	0.57	132	175	1.3
SR#25	7435	TSw	Tptrn	34	0.17	27	209	0.8
SR#27	7444	PTn	Tptrv1	36	0.18	37	199	1.0
SR#28	7446	TSw	Tptrv2	42	0.21	51	200	1.2
SR#29	7453	TSw	Tptrv3	56	0.30	49	187	0.9
SR#30	7460	PTn	Tpbt2	101	0.51	101	200	1.0
SR#31	7465	PTn	Tpbt2	86	0.64	103	135	1.2

[1]Stationing indicates the distance in m from the North Portal entrance of the ESF Boreholes LCPA#2 and #3 were drilled in Alcove #4, which intersects the Main Drift at Station 1028.

[2]TCw: Tiva Canyon welded; TSw: Topopah Spring welded; PTn: Paintbrush nonwelded.

[3]Lithostratigraphic units follow the nomenclature of Buesch, Spengler et al. (1996).

Table 6.2-10. Chemical Composition of Transient Shallow Perched Water Samples from Boreholes UE-25 UZ-N2 and UZ-N46, Yucca Mountain, Nevada (Yang, Rattray et al. 1996)

Borehole[1]	Date	Concentration (mg/L)										Charge Balance[2]
		Ca	Mg	Na	SiO_2	Al	HCO_3	CO_3	Cl	NO_3	SO_4	
[3]Rain	03-31-92	0.7	0.5	0.8	0.9	0	23.3	0	2.4	2	4.1	-0.5
[4]UZN#2	08-18-89	14	2.3	51	18	—	112	0	10	—	29	6.6
UZN#2	02-14-92	1.4	0.5	1.7	0	0	11.7	0	12	8.2	7.8	-63.4
UZN#2	03-16-92	14	3.9	25	5.8	0	58.2	0	10	27.3	21	-0.1
UZN#2	03-31-92	25	4.7	16	11.8	0	128	0	5.8	19.7	15.6	-10.9
UZ-N46	02-14-92	0.8	0.5	1.6	0.2	0	23.3	0	3.3	1.6	4.7	-59.8

"—" data not available.
"0" Values below detection limit.

[1]Sampling depths for perched water: UE-25 UZN#2, 15.8 m; UE-25 UZ-N46, 30.1 m. Shallow perched water from UZN #2 may be at least partially attributed to surface runoff that flowed down the borehole casing.

[2]Charge balance calculated from data shown using the formula (meq cation - meq anion)/(meq cation + meq anion)*100.

[3]Rain sample collected at USW UZ-N2.

[4]pH 7.7, specific conductivity 308 µS/cm.

Table 6.2-11. Chemical Composition of Perched Water at Yucca Mountain, Nevada (Yang, Rattray et al. 1996)

Sample ID	Average Depth (m)	Date	Temp. (°C)	pH	Spec. Cond. (µS/cm)	Concentration (mg/L)											Charge Balance*
						Al	Ca	Mg	K	Na	SiO_2	HCO_3	CO_3	Cl	NO_3	SO_4	
NRG-7A	460.25	03-07-94	—	8.7	224	0.0	3	0	6.8	42	9	114	—	7	1	4	-0.4
SD-9/TS	453.85	07-17-94	27.0	8.6	445	2.1	2.9	0.2	9.8	98	64.2	197	10	5.6	3.3	27.6	7.6
UZ-14 A	384.60	08-02-93	27.1	7.6	312	0.7	23	1.8	5.6	39	34.2	150	0	7.9	8.6	14.3	0.3
UZ-14 A2	384.60	08-02-93	27.1	7.8	308	1.0	24	1.8	3.9	38	36.4	148.8	0	9.1	12.5	13.8	-1.4
UZ-14 B	387.68	08-03-93	23.8	8.1	335	6.1	31	2.7	4.4	40	51.4	147.6	0	8.3	16.9	16.3	5.2
UZ-14 C	390.75	08-05-93	24.2	8.3	518	0.0	45	4.1	5.8	88	7.7	106.1	0	15.5	0	223	-1.9
UZ-14 PT-1	390.75	08-17-93	—	—	—	0.0	37	3.1	6.3	40	21.4	144	0	7.2	12.7	57.3	0.5
UZ-14 PT-2	390.75	08-19-93	—	—	—	0.0	30	2.4	3.3	35	25.7	144	0	7.0	15.4	22.9	0.3
UZ-14 PT-4	390.75	08-27-93	—	—	—	0.0	27	2.1	1.8	34	32.1	141.5	0	6.7	14.5	14.1	0.2
UZ-14 D	390.75	08-31-93	—	7.8	—	0.0	31	2.5	4.1	35	40.7	146.4	0.	7.0	17.1	24.2	0.1
ONC#1	432.97	12-15-94	—	8.7	302	11	13.3	1.1	3.6	50.6	26.5	115	8.8	7.1	5.2	23.6	4.1
USW G-2	649.22	02-08-95	—	7.7	259	—	7.9	0.5	5.2	46	51	116	—	6.5	—	13	4.3
SD-7(3/8)	479.76	03-08-95	—	—	—	0.28	14.2	0.13	5.3	45.5	62.3	112	0	4.4	33.8	9.1	2.5
SD-7(3/16)	488.29	03-16-95	21.8	8.1	239	0.44	13.3	0.13	5.3	45.3	57.4	128	0	4.1	33.8	9.1	-2.9
SD-7(3/17)	488.29	03-17-95	22.6	8.2	285	0	12.8	0.08	5.5	45.8	50.9	130	0	4.1	22.8	8.6	-0.3
SD-7(3/20)	488.29	03-20-95	23.3	8.0	265	0	12.9	0.07	5.4	45.5	55	127	0	4.1	13.4	8.5	3.3
SD-7(3/21)	488.29	03-21-95	23.2	8.2	259	0	13.5	0.08	5.5	44.6	55.9	128	0	4.1	13.2	10.3	2.2

"—" data not available.
"0" values below detection limit.
*Charge balance calculated from data shown using the following formula (meq cation - meq anion)/(meq cation + meq anion)*100.

Table 6.2-12. Isotopic Composition of Perched Water at Yucca Mountain, Nevada

Sample ID	Depth (m)	Date	$\delta^{13}C$ (‰)	^{14}C (pmc)*	H^3 (TU)	δD (‰)	$\delta^{18}O$ (‰)	$\delta^{87}Sr$ (‰)	$^{36}Cl/Cl$ (x 10^{-15})
SD-7(3/8)	479.76	03-08-95	-10.4	34.4	6.2	-99.8	-13.4	—	511
SD-7(3/16)	488.29	03-16-95	-9.4	28.6	—	-99.7	-13.3	—	—
SD-7(3/17)	488.29	03-17-95	-9.5	28.4	—	-99.6	-13.4	—	657
SD-7(3/20)	488.29	03-20-95	-9.5	27.9	—	-99.6	-13.4	—	—
SD-7(3/21)	488.29	03-21-95	-9.5	28.4	—	-99.6	-13.3	—	609
SD-9/TS	453.85	07-17-94	-14.4	41.8	0	-97.8	-13.3	5.92[1]	449
UZ-14 A	384.60	08-02-93	-10.2	41.7	0.3	-98.6	-13.8	4.51	559
UZ-14 A2	384.60	08-02-93	-10.1	40.6	3.1	-97.5	-13.5	4.47	538
UZ-14 B	387.68	08-03-93	-9.5	36.6	0	-97.1	-13.4	4.34	566
UZ-14 C	390.75	08-05-93	-9.2	66.8	0.4	-87.4	-12.1	4.37	389
UZ-14 PT-1	390.75	08-17-93	-9.8	32.3	1.8	-97.8	-13.3	3.91–4.30	644
UZ-14 PT-2	390.75	08-19-93	—	28.9	3.1	-97.9	-13.4	3.51–4.19	656
UZ-14 PT-4	390.75	08-27-93	-9.6	27.2	0	-97.3	-13.4	4.45–4.49	675
UZ-14 D	390.75	08-31-93	-11.3	29.2	0	-97.6	-13.1	—	690
NRG-7a	460.25	03-07-94	-16.6	66.9	10.4	-93.9	-12.80	2.54–11.7	474
UZN#91	28.7	03-05-92	—	—	—	—	—	—	880
UZN#2	15.2	04-09-91 02-22-95	— —	— —	— —	— —	— —	— —	2012† 3150†

Data sources:

Yang, Rattray et al. 1996 (Table 7); Rousseau et al. 1996 (Table 4.2.4-2); Fabryka-Martin, Turin et al. 1998 (Table 7-1).

[1] = Sampling date: 9/12/94

* = percent modern carbon

"—" = not available

† = non-Q data

Table 6.2-13. Data for Carbon Isotopes in Pore Water of the Unsaturated Zone in Drillholes NRG-6, NRG-7a, SD-12, SD-7, SD-9, UZ#4, UZ#5, UZ-14, and UZ-161

Drillhole	Hydrogeologic Unit[2]	Lithostratigraphic Unit[2]	Approx. Depth (m)	^{14}C (pmc)	$\delta^{13}C$ (‰)
NRG-6	PTn	Tpbt2	71.6	92.1	-14.9
NRG-7a	CHn	Tpbt1	456.0	58.4	-18.6
SD-12	PTn	Tpcbt4	82.8	80.3	-14.0
SD-12	CHn	Tac3	462.5	69.9	-17.4
SD-12	CHn	Tacbt	499.5	66.5	-16.9
SD-12	CHn	Tcp2	591.7	59.2	-16.3
SD-7	PTn	Tpbt3	103.5	74.1	-18.1
SD-7	CHn	Tac2	456.8	73.5	-15.1
SD-7	CHn	Tac1	464.8	62.8	-17.5
SD-7	CHn	Tac1	475.0	60.6	-27.4
SD-9	CHn	Tptpv1	442.8	85.9	-14.1
SD-9	CHn	Tac3	468.0	88.9	-15.3
SD-9	CHn	Tac2	500.0	95.3	-14.5
SD-9	CHn	Tacbt	549.1	82.3	-16.4
UZ#4	PTn	Tpbt2	98.0	88.6	-20.0
UZ#5	PTn	Tpbt2	104.0	55.1	-26.7
UZ-14	PTn	Tpbt3	26.1	83.2	-17.1
UZ-14	PTn	Tpbt3	29.3	83.3	-15.0
UZ-14	PTn	Tpp	35.1	86.9	Not measured
UZ-14	PTn	Tpp	44.3	84.9	-13.0
UZ-14	PTn	Tpp	67.4	96.2	-25.0
UZ-14	PTn	Tpbt2	73.4	89.6	-10.5
UZ-14	PTn	Tpbt2	81.1	70.8	-21.2
UZ-14	CHn	Tpbt1	431.3	81.8	-12.4
UZ-14	CHn	Tac3	435.8	69.9	-11.1
UZ-14	CHn	Tac3	445.4	96.3	-13.4
UZ-14	CHn	Tac2	464.9	93.4	-11.8
UZ-14	CHn	Tac2	476.7	76.8	-15.8
UZ-14	CHn	Tac2	476.8	80	-15.2
UZ-14	CHn	Tac2	483.2	93.7	-11.3
UZ-14	CHn	Tac2	489.5	81.1	-14.6
UZ-14	CHn	Tac2	501.4	86.3	-16.0
UZ-14	CHn	Tac1	510.5	91.3	-13.7
UZ-14	CHn	Tacbt	516.8	92.3	-10.3
UZ-14	CHn	Tacbt	522.7	96.3	-11.6
UZ-14	CHn	Tcp1	615.7	94	-14.7
UZ-14	CHn	Tcb	638.7	84.6	-15.7
UZ#16	PTn	Tpcpv1	48.2	87	-9.3
UZ#16	PTn	Tpbt3	55.2	89.8	-9.0
UZ#16	PTn	Tpbt2	66.9	87.3	-9.4
UZ#16	CHn	Tac2	409.7	87	-23.3
UZ#16	CHn	Tac2	415.0	58.2	-17.5
UZ#16	CHn	Tac2	420.7	71.8	-23.3
UZ#16	CHn	Tac2	425.8	97.7	-12.6
UZ#16	CHn	Tac2	426.2	88.3	-23.3
UZ#16	CHn	Tac2	433.2	53.1	-16.6
UZ#16	CHn	Tac2	439.8	61.5	-10.3

[1]Carbon isotope data from Yang, Rattray (1996); Yang, Turner et al. (1988); Yang et al. 1997.

[2]Hydrogeologic unit and lithostratigraphic unit nomenclature from Tables 3.6-1 and 3.6-2 (Geology Chapter). Stratigraphic depths for these boreholes are from Moyer and Geslin 1994; Moyer et al. 1995, GS940408314211.020 (NRG-7A); Engstrom and Rautman 1996, Rautman and Engstrom 1996a, 1996b.

Table 6.2-14. USW UZ-1 Dry-Gas Composition (Volume %) at Yucca Mountain, Nevada (Yang, Rattray et al. 1996)

Probe No.	Depth (m)	April 1984				September 1984				July 1994		
		N_2	O_2	Ar	CO_2	N_2	O_2	Ar	CO_2	N_2	O_2	CO_2
1	12.8	79.6	18.5	0.99	0.83	78.4	19.4	0.97	1.30	78.2	20.8	0.79
2	18.9	79.7	19.3	1.01	0.02	79.0	19.7	0.98	0.39	77.8	20.6	0.53
3	28.3	79.2	19.8	1.01	0.03	79.1	19.9	0.99	0.05	77.1	20.4	0.22
4	39.9	79.1	20.1	0.90	0.03	—	—	—	—	77.1	20.4	0.41
5	61.3	78.5	20.3	0.92	0.24	—	—	—	—	77.7	20.4	0.23
6	81.1	78.4	20.5	0.98	0.08	—	—	—	—	78.5	20.8	0.20
7	106.1	78.4	20.6	0.95	0.07	78.4	20.6	0.97	0.10	78.1	20.8	0.11
8	128.3	78.4	20.5	1.01	0.09	—	—	—	—	77.9	20.8	0.10
9	152.7	78.4	20.6	0.96	0.05	—	—	—	—	78.0	20.8	0.08
10	189.3	78.6	20.4	0.96	0.04	—	—	—	—	77.7	20.6	0.08
11	227.7	78.7	20.3	0.96	0.03	—	—	—	—	77.4	20.4	0.11
12	265.5	78.5	20.6	0.98	0.00	—	—	—	—	76.7	20.5	0.11
13	304.2	78.5	20.5	1.02	0.01	78.5	20.6	0.96	0.02	76.9	20.5	0.05
14	335.3	—	—	—	—	78.6	20.4	0.97	0.07	78.1	20.9	0.13
15	367.9	—	—	—	—	80.3	18.5	0.99	0.26	78.1	20.6	0.36

"—" data not available

Table 6.2-15. Carbon Dioxide, Carbon-14, and Carbon-13 (Gas) Data from Boreholes NRG-6, NRG-7a, UZ-16, and SD-12, Yucca Mountain, Nevada

Borehole	Depth (m)	Hydrogeologic Unit[1]	Lithostratigraphic Unit[1]	CO_2* (vol. %)	^{14}C* (pmc)	$\delta\ ^{13}C$* (‰)
NRG-6	6.1	TCw	Tpcpll	0.07	—	-12.83
NRG-6	6.1	TCw	Tpcpll	—	—	-15.18
NRG-6	6.1	TCw	Tpcpll	—	—	-15.15
NRG-6	24.4	TCw	Tpcpln	0.11	—	-14.25
NRG-6	24.4	TCw	Tpcpln	—	92.1	-15.2
NRG-6	26.8-38.1	TCw	Tpcpln	0.07	—	-14.60
NRG-6	26.8-38.1	TCw	Tpcpln	—	61.0	-13.9
NRG-6	26.8-38.1	TCw	Tpcpln	—	—	-14.62
NRG-6	26.8-38.1	TCw	Tpcpln	—	—	-14.61
NRG-6	26.8-38.1	TCw	Tpcpln	—	—	-14.63
NRG-6	26.8-38.1	TCw	Tpcpln	—	—	-14.99
NRG-6	26.8-38.1	TCw	Tpcpln	—	—	-15.02
NRG-6	61.0	PTn	Tpp	0.10	—	-14.14
NRG-6	61.0	PTn	Tpp	—	—	-14.24
NRG-6	61.0	PTn	Tpp	—	91.0	-14.9
NRG-6	83.8	TSw	Tptrn	0.05	—	-15.05
NRG-6	83.8	TSw	Tptrn	—	—	-15.05
NRG-6	107	TSw	Tptrn	—	—	-17.24
NRG-6	183	TSw	Tptpul	0.10	83.2	-15.5
NRG-6	183	TSw	Tptpul	—	—	-14.06
NRG-6	183	TSw	Tptpul	—	—	-15.18
NRG-6	221	TSw	Tptpmn	0.07	—	-14.69
NRG-6	221	TSw	Tptpmn	—	—	-14.69
NRG-6	233-238	TSw	Tptpmn	—	—	-10.14
NRG-6	233-238	TSw	Tptpmn	—	—	-10.31
NRG-6	282	TSw	Tptpll	0.11	94.2	-16.1
NRG-6	282	TSw	Tptpll	—	—	-14.14
NRG-6	305	TSw	Tptpll	0.07	—	-14.43
NRG-6	305	TSw	Tptpll	—	—	-14.34
NRG-7a	42.7	PTn	Tpy	0.12	108.0	-16.8
NRG-7a	42.7	PTn	Tpy	—	—	-17.24
NRG-7a	149	TSw	Tptrl	0.19	—	-17.69
NRG-7a	149	TSw	Tptrl	—	—	-17.68
NRG-7a	149	TSw	Tptrl	—	111.7	-18.2
NRG-7a	271	TSw	Tptpll	0.15	111.0	-19.0
NRG-7a	271	TSw	Tptpll	—	—	-17.75
NRG-7a	271	TSw	Tptpll	—	—	-17.73
NRG-7a	370	TSw	Tptpll	0.19	—	-17.61
UZ-16	45.7	TCw	Tpcplnc	—	73.2	-15.5
UZ-16	45.7	TCw	Tpcplnc	—	—	-13.82
UZ-16	45.7	TCw	Tpcplnc	—	—	-13.72
UZ-16	14.3-74.1	TCw-TSw	Tpcpll-Tptrn	—	72.7	-14.0
UZ-16	14.3-74.1	TCw-TSw	Tpcpll-Tptrn	—	—	-12.32

Table 6.2-16. Comparison of Stable Carbon Isotopes in Pore Water and Gas Samples Collected from Similar Intervals of Drillholes SD-12, NRG-6, and NRG-7a

Borehole and Depth (m)	$\delta^{13}C$ in Pore Water (‰)	$\delta^{13}C$ in Borehole Gas (‰)
SD-12 (82)*	-14	-22.4 and -16.4
SD-12 (211)	-13.7	-24.7
SD-12 (384)	-17	-22.9
SD-12 (462)	-17.4	-17.3
NRG-6 (235)	-14.9	-10.2
NRG-7a (50)	-12.9	-17.2
NRG-7a (50)	-13.5	-17.0
NRG-7a (50)	-11.6	-17.5

*This pore water sample is bracketed by gas samples at 65.2 and 91.7 m.

Table 6.2-17. Locations and Other Physical Characteristics of Wells Sampled for Chemical and Isotopic Analyses of Groundwater in the Vicinity of Yucca Mountain

Site Name	UTM-x (m)	UTM-y (m)	Latitude Degrees N	Longitude Degrees E	Site Elevation (m)	Well Depth (m)	WT Depth (m)	Aquifer
15S/49E-13dda	553312.5	4055302	36.644	116.404	796	174	90	Qal
15S/49E-22a1	550086.3	4054974	36.641	116.440	796	174	90	Qal
15S/49E-22dcc	549672.5	4053523	36.628	116.444	784	148	78	Qtal
15S/49E-27acc	549552.9	4052722	36.621	116.446	777	467	73	Qal
15S/50E-18ccc	553710.0	4055273	36.643	116.399	812	120	105	Qal
15S/50E-18cdc	553934.3	4055151	36.642	116.397	812	120	105	Qal
15S/50E-19b1	553862.5	4054720	36.638	116.398		110	103	Qal
16S/49E-05acc	546664.5	4049439	36.591	116.478	746	87	21	Qal
Airport Well	553289.0	4055086	36.642	116.404	804	229	76	Qal
BGMW-11	534410.9	4062631	36.711	116.615	786		72	Qal
Cind-R-Lite Well	544027.0	4059809	36.685	116.507	831	140	101	Tv
Cowboy Joe's	554132.4	4055245	36.643	116.394				Qal
Gexa Well 4	534068.9	4086110	36.922	116.618	1198	488	188	Tv
JF-3	554498.3	4067974	36.758	116.389	944	347	216	Tv
NDOT well	554132.4	4055245	36.643	116.394	810	151	105	Qal
TW-5	562605.0	4054686	36.638	116.300	931	244	207	Qal
UE-25 b#1 (0-1220 m)	549954.5	4078422	36.852	116.440	1201	1220	470	Th/Tct
UE-25 b#1 (853-914 m)	549954.5	4078422	36.852	116.440	1201	1220	470	Tcb
UE-25 c#1	550957.7	4075943	36.830	116.429	1131	914	401	Tcb/Tct
UE-25 c#2	550944.0	4075867	36.829	116.429	1132	914	401	Tcb
UE-25 c#3	550919.8	4075886	36.829	116.429	1132	914	402	Tcb/Tct
UE-25 J-11	563816.0	4071049	36.785	116.285	1050	405	317	Tb
UE-25 J-12	554435.8	4068767	36.765	116.390	953	347	226	Tv
UE-25 J-13	554004.4	4073550	36.808	116.395	1011	1063	283	Tpt
UE-25 ONC-1	550479.9	4076608	36.836	116.434	1163	469	433	Th/Tcp
UE-25 p#1 (0-1200 m)	551508.7	4075663	36.827	116.423	1114	1805	382	Tcp
UE-25 p#1 (1300-1800 m)	551508.7	4075663	36.827	116.423	1114	1805	382	DSlm
UE-25 WT#12	550162.9	4070647	36.782	116.438	1075	399	345	Tpt/Th
UE-25 WT#14	552638.0	4077337	36.842	116.410	1076	399	346	Th
UE-25 WT#15	554033.7	4078702	36.854	116.394	1083	415	354	Tpt
UE-25 WT#4	550445.9	4079420	36.861	116.434	1169	482	438	Th
UE-25 WT-7	546148.2	4075461	36.826	116.483	1197	491	421	Tv
UE-29 a#2 (250-355 m)	555753.3	4088351	36.941	116.374	1215	422	29	Th
UE-29 a#2 (87-213 m)	555753.3	4088351	36.941	116.374	1215	422	28	Th
USW G-2	548138.6	4082554	36.889	116.460	1554	1831	534	Th/Tct
USW G-4	548938.0	4078590	36.854	116.451	1270	915	541	Tct
USW H-1 (572-687 m)	548721.8	4079944	36.866	116.453	1303	1829	572	Tcp
USW H-1 (687-1829 m)	548721.8	4079944	36.866	116.453	1303	1829	572	Tcb
USW H-3	547537.0	4075762	36.828	116.467	1483	1219	751	Tct
USW H-4	549195.0	4077322	36.842	116.448	1249	1219	519	Tcb/Tct
USW H-5	547665.5	4078838	36.856	116.465	1477	1219	704	Tcb/Tct
USW H-6 (525-1220 m)	546196.1	4077816	36.847	116.482	1302	1220	526	Tcb/Tct
USW H-6 (600-650 m)	546196.1	4077816	36.847	116.482	1302	1220	526	Tcb/Tct
USW H-6 (753-835 m)	546196.1	4077816	36.847	116.482	1302	1220	526	Tcb/Tct
USW VH-1	539986.2	4071718	36.792	116.552	963	762	184	Tcb
USW VH-2	537737.6	4073222	36.806	116.577	974	1219	164	Tv
USW WT-10	545976.0	4073389	36.807	116.485	1123	431	347	Tpt

"0" designates analyzed for but not detected.
Information compiled by Oliver and Root 1997.

Table 6.2-18. Chemical Composition of Groundwater in the Vicinity of Yucca Mountain, Nevada

Site Name	Temp. (°C)	pH	Charge Balance	Concentration (mg/L)														
				Ca	Mg	Na	K	Cl	SO_4	HCO_3	CO_3	NO_3	F	SiO_2	B	Mn	Li	TDS Calc.
15S/49E-13dda	—	8.2	0.1	14	1.5	106	4.4	20	103	160	0	6.3	2.0	48	—	0	—	384
15S/49E-22a1	27.8	8.0	-0.9	25	2.4	41	5.2	8.0	33	145	0	3.5	1.4	52	—	0	—	243
15S/49E-22dcc	29.5	7.8	0.8	28	2.1	41	4.8	7.6	33	148	0	1.5	1.0	49	—	0.0200	0.040	240
15S/49E-27acc	44.1	7.9	-1.3	22	1.3	49	2.6	7.5	38	149	0	0.08	0.85	21	—	0.0200	0.045	215
15S/50E-18ccc	—	7.5	-1.0	17	0.60	93	4.1	13	100	157	0	0.86	2.1	34	—	0	0.090	342
15S/50E-18cdc	28.5	8.0	3.3	17	0.83	110	4.0	15	110	160	0	—	1.9	46	—	0	—	384
15S/50E-19b1	23.9	8.1	0.6	20	3.9	108	6.0	18	128	168	0	6.5	1.4	44	—	0	—	417
16S/49E-05acc	—	7.8	4.5	29	2	35	5.2	6.0	26	135	0	2	1.0	62	0	0	0.050	235
Airport Well	27.5	9.0	0.2	5.6	0.23	70	1.5	10	46	110	7.0	—	1.8	40	—	—	—	236
Cind-R-Lite Well	—	7.8	-2.2	12	6.2	72	4.0	9.2	46	194	—	1.1	2.5	54	—	0.0020	0.068	302
Gexa Well 4	31.8	7.9	-2.3	12	0.37	71	3.3	14	46	150	—	—	3.2	48	—	0.0090	—	270
JF-3	26.6	7.7	1.4	18	3.1	39	8.5	9.9	31	120	—	—	1.6	56	—	0.0020	0.037	226
NDOT well	—	8.0	-0.4	16	0.81	101	3.8	15	110	160	—	—	1.9	44	—	—	—	371
TW-5	30.0	7.9	-1.6	33	17	130	12	21	99	395	—	—	3.4	19	0.58	0.1900	0.190	529
UE-25 b#1 (0-1220 m)	36.0	7.5	-0.9	17	0.59	46	3.5	8.5	22	134	—	4.0	1.6	52	—	—	—	221
UE-25 b#1 (853-914 m)	37.2	7.1	-0.5	18	0.72	46	2.8	7.5	21	138	—	4.0	1.6	51	—	—	0.621	221
UE-25 c#1	41.5	7.6	-0.9	12	0.36	56	2.1	7.5	22	141	—	5.0	2.2	56	—	—	0.138	230
UE-25 c#2	40.5	7.9	-3.0	12	0.35	54	2.1	7.1	22	143	—	5.3	2.1	54	—	—	0.093	226
UE-25 c#3	41.0	7.7	-2.8	11	0.33	57	1.9	6.6	20	150	—	5.8	2.2	57	—	0.0108	0.095	230
UE-25 J-11	35.0	7.9	0.6	81	14	155	16	23	465	103	—	7.1	1.1	56	1.5	—	—	857
UE-25 J-12	26.2	7.6	-0.9	14	2.4	42	5.0	12	21	118	—	5.1	2.3	48	0.32	0.0400	0.041	206
UE-25 J-13	30.5	7.3	-0.3	13	2.1	44	5.0	7.2	20	124	—	6.3	2.4	55	0.10	0.0748	0.048	215
UE-25 ONC-1	—	8.7	1.6	13	1.1	51	3.6	7.1	24	115	8.8	5.2	—	27	0.12	0.6900	0.084	196
UE-25 p#1 (0-1200 m)	57.0	6.7	-3.0	94	31	150	12	26	78	753	—	—	4.9	44	—	—	0.310	811
UE-25 p#1 (1300-1800 m)	56.0	6.6	-2.3	100	39	150	12	28	160	694	—	—	4.7	41	—	—	0.590	877
UE-25 WT#12	—	7.6	2.1	14	0.30	64	2.2	7.4	26	152	—	1.1	3.1	47	—	0.0550	0.063	202

Data compiled by Oliver and Root 1997

Table 6.2-18. Chemical Composition of Groundwater in the Vicinity of Yucca Mountain, Nevada (Contined)

Site Name	Temp. (°C)	pH	Charge Balance	Concentration (mg/L)														
				Ca	Mg	Na	K	Cl	SO_4	HCO_3	CO_3	NO_3	F	SiO_2	B	Mn	Li	TDS Calc.
UE-25 WT#14	—		-1.6	10	0.80	45	5.0	8.2	22	119	—	—	1.8	57	—	—	0.050	208
UE-25 WT#15	—	7.5	2.3	12	1.7	62	4.6	12	16	166	—	—	—	53	—	—	0.380	243
UE-25 WT-7	—	8.7	-2.5	2.6	0.18	97	2.1	13	7.2	252	—	—	—	20	—	—	0.150	266
UE-29 a#2 (250-355 m)	25.1	7.2	-2.3	10	0.20	44	1.1	11	22	107	—	—	1.0	44	—	—	0.100	186
UE-29 a#2 (87-213 m)	22.7	7.0	-3.4	10	0.30	44	1.3	8.8	21	107	—	9.7	0.90	44	—	—	0.110	193
USW G-2	33.8	7.5	0.8	8.2	0.51	47	5.5	6.3	15	125	—	0.68	1.0	51	—	0.0743	0.046	191
USW G-4	35.6	7.7	3.7	13	0.20	57	2.1	5.9	19	139	—	—	2.5	45	—	—	0.067	213
USW H-1 (572-687 m)	33.0	7.7	-1.8	4.5	0	51	2.4	5.7	18	122	—	—	1.2	47	—	—	0.040	190
USW H-1 (687-1829 m)	34.7	7.5	1.4	6.2	0	51	1.6	5.8	19	115	—	—	1.0	40	—	—	0.040	181
USW H-3	26.5	9.0	-2.7	0.80	0.02	120	1.1	5.5	31	274	—	0.10	5.5	43	—	—	0.220	342
USW H-4	34.8	7.4	3.8	17	0.29	73	2.6	6.9	26	173	—	—	4.6	46	—	—	0.130	262
USW H-5	35.9	7.9	2.7	2.0	0.01	60	2.1	6.4	16	124	—	—	1.4	48	—	—	0.067	197
USW H-6 (525-1220 m)	—	8.1	-2.0	4.1	0.09	86	1.3	7.6	29	188	—	—	4.7	48	—	—	0.082	273
USW H-6 (600-650 m)	37.2	8.3	-0.4	4.7	0.07	88	1.4	7.4	32	184	—	—	4.7	49	—	—	0.063	278
USW H-6 (753-835 m)	41.6	8.3	0.1	1.4	0.02	88	1.4	7.2	25	183	—	—	3.9	47	—	—	0.071	264
USW VH-1	35.4	7.6	0.8	10	1.5	76	1.9	10	43	160	—	—	2.8	50	—	0.0500	0.090	274
USW VH-2	32.8	7.1	-1.3	79	30	71	8.1	16	143	392	—	—	1.1	26	—	0.0090	0.090	566
USW WT-10	38.5	8.4	-3.0	2.6	0.05	95	1.0	7.8	34	186	10	2.7	3.7	47	—	0.0400	0.086	287

Data Compiled by Oliver and Root 1997.
Sr and U concentrations are reported on Table 6.2-19.
"0" designates analyzed for but not detected.

Table 6.2-19. Isotopic Composition of Groundwater in the Vicinity of Yucca Mountain*

Site Name	^{3}H (TU)	δD (‰)	$\delta^{18}O$ (‰)	$\delta^{13}C$ (‰)	^{14}C (pmc)	$^{36}Cl/Cl$ (x 10^{-15})	U (µg/L)	$^{234}U/^{238}U$ AR	Sr (mg/L)	$^{87}Sr/^{86}Sr$	$\delta^{87}Sr$ (‰)
15S/49E-22dcc	—	-102.0	-12.80	-10.20	15.6	—	—	—	—	—	—
16S/49E-05acc	—	-103.0	-13.20	-7.10	19.3	—	—	—	—	—	—
BGMW-11	—	—	—	—	—	—	—	—	2.16	0.71702	11.0
Cind-R-Lite Well	—	-102.0	-13.65	—	—	—	1.5	2.4	0.10	0.71217	4.2
Cowboy Joe's	—	—	—	—	—	—	—	—	—	0.71178	3.6
Gexa Well 4	—	—	—	—	—	—	—	—	—	0.70975	0.8
JF-3	—	-97.4	-13.18	-8.60	30.7	511	0.81	4.1	—	0.71133	3.0
NDOT well	—	—	—	—	—	—	2.5	2.5	—	0.71081	2.3
TW-5	—	-113.2	-15.40	—	—	—	—	—	1.51	0.71505	8.2
UE-25 b#1 (0–1220 m)	—	-101.0	-13.40	-10.40	16.7	—	—	—	—	—	—
UE-25 b#1 (853–914 m)	0.62	-99.5	-13.50	-8.60	18.9	—	—	—	—	—	—
UE-25 c#1	—	-102.0	-13.50	-7.10	15.0	—	—	—	—	—	—
UE-25 c#2	—	-101.0	-13.40	-7.00	15.3	—	—	—	—	—	—
UE-25 c#3	2.0	-100.5	-13.43	-7.50	15.7	475	1.1	8.1	0.05	0.70980	0.9
UE-25 J-11	—	—	—	—	—	—	—	—	0.26	0.70935	0.2
UE-25 J-12	8.2	-96.8	-12.88	-7.90	32.2	—	0.30	5.5	—	0.71151	3.3
UE-25 J-13	14	-96.8	-13.00	-7.30	29.2	506	0.56	6.7	0.04	0.71145	3.2
UE-25 ONC-1	—	—	—	—	—	—	0.57	5.7	1.72	0.71040	1.7
UE-25 p#1 (0–1200 m)	11	-107.0	-13.80	—	—	—	—	—	—	—	—
UE-25 p#1 (1300–1800 m)	3.1	-106.0	-13.80	-2.30	2.3	—	13.34	2.3	—	0.71176	3.6
UE-25 WT#12	—	-102.5	-13.69	-7.07	11.4	563	2.6	7.2	0.02	0.70992	1.0
UE-25 WT#14	—	-97.5	-12.75	-12.70	24.1	—	—	—	—	—	—
UE-25 WT#15	0.40	-97.5	-13.20	-11.80	21.6	—	—	—	—	—	—
UE-25 WT#4	—	—	—	—	—	—	—	—	—	0.71001	1.1
UE-25 WT-7	2.3	—	-13.95	-9.01	—	—	—	—	—	0.71027	1.5
UE-29 a#2 (250–355 m)	37	-93.5	-12.80	-13.00	62.3	—	—	—	—	—	—
UE-29 a#2 (87–213 m)	37	-93.0	-12.80	-13.10	60.0	—	—	—	—	—	—
USW G-2	1.0	-98.9	-13.30	-11.25	20.5	457	1.1	7.8	0.01	0.71070	2.1
USW G-4		-103.0	-13.80	-9.10	22.0	—	—	—	—	—	—
USW H-1 (572–687 m)	—	-103.0	-13.40	—	19.8	—	—	—	—	—	—
USW H-1 (687–1829 m)	—	-101.0	-13.50	-11.40	22.4	—	—	—	—	—	—
USW H-3	2.0	-101.0	-13.90	-4.90	10.5	—	—	—	—	—	—
USW H-4	10	-104.0	-14.00	-7.40	11.8	—	—	—	—	—	—
USW H-5	—	-101.5	-13.60	-10.30	19.8	—	—	—	—	—	—
USW H-6 (525–1220 m)	—	-106.0	-13.80	-7.50	16.3	—	—	—	—	—	—
USW H-6 (600–650 m)	1.00	-107.0	-14.00	-7.10	12.4	—	—	—	—	—	—
USW H-6 (753–835 m)	4.0	-105.0	-14.00	-7.30	10.0	—	—	—	—	—	—
USW VH-1	—	-106.5	-14.10	-7.75	10.8	540	3.4	5.5	—	0.71079	2.5
USW VH-2	—	—	—	—	—	—	3.0	3.1	—	0.71300	5.4
USW WT-10	11	-103.0	-13.82	-6.10	7.3	526	2.8	4.8	0.004	0.71007	1.2

"0" designates analyzed for but not detected.

*The $^{36}Cl/Cl$ analyses are reported in DTN LA000000000064.001, LAJF831222AN95.004, and LAJF831222AQ97.011. All other data were compiled by Oliver and Root (1997).

INTENTIONALLY LEFT BLANK

Table 6.3-1. Summary of Results for Solubility Experiments on Neptunium in J-13 Groundwater

	Steady-State Concentration (M)		
	25°C	**60°C**	**90°C**
pH 6.0	$(6.45 \pm 1.11) \times 10^{-4}$	$(9.40 \pm 1.22) \times 10^{-4}$	$(9.11 \pm 1.81) \times 10^{-4}$
pH 7.0	$(3.06 \pm 0.20) \times 10^{-5}$	$(1.58 \pm 0.57) \times 10^{-5}$	$(8.61 \pm 2.26) \times 10^{-6}$
pH 8.5	$(1.47 \pm 0.59) \times 10^{-5}$	$(1.66 \pm 0.92) \times 10^{-5}$	$(5.50 \pm 1.97) \times 10^{-6}$

Table 6.3-2. Summary of Results for Solubility Experiments on Plutonium in J-13 Groundwater

	Steady-State Concentration (M)		
	25°C	**60°C**	**90°C**
pH 6.0	$(4.70 \pm 1.13) \times 10^{-8}$	$(9.01 \pm 2.01) \times 10^{-9}$	$(4.23 \pm 1.06) \times 10^{-9}$
pH 7.0	$(2.36 \pm 1.23) \times 10^{-8}$	$(8.25 \pm 0.74) \times 10^{-9}$	$(4.29 \pm 2.05) \times 10^{-9}$
pH 8.5	$(9.35 \pm 1.60) \times 10^{-9}$	$(6.22 \pm 1.75) \times 10^{-9}$	$(3.62 \pm 1.14) \times 10^{-9}$

Table 6.3-3. Summary of Results for Solubility Experiments on Americium in J-13 Groundwater (Am Tracer in Nd)

	Steady-State Concentration (M)		
	25°C	**60°C**	**90°C**
pH 6.0	$(1.8 \pm 0.06) \times 10^{-9}$	$(2.5 \pm 0.7) \times 10^{-6}$	$(1.7 \pm 1.9) \times 10^{-9}$
pH 7.0	$(1.2 \pm 0.3) \times 10^{-9}$	$(9.9 \pm 0.74) \times 10^{-9}$	$(3.1 \pm 2.05) \times 10^{-10}$
pH 8.5	$(2.4 \pm 1.9) \times 10^{-9}$	$(1.2 \pm 1.3) \times 10^{-8}$	$(3.4 \pm 2.1) \times 10^{-10}$

Table 6.3-4. Extractions of Solubility Values for TSPA

Element	Minimum Value (M)	Maximum Value (M)	Expected Value (M)	Coefficient of Variation	Distribution
Americium	10^{-10}	10^{-6}	5×10^{-7}		uniform
Plutonium	3×10^{-9}*	10^{-6}	5.1×10^{-7}		uniform
Uranium	10^{-8}	10^{-2}	3.2×10^{-5}	0.20	log beta
Thorium	10^{-10}	10^{-7}			log uniform
Radium	10^{-9}	10^{-5}	10^{-7}	0.10	log beta
Lead	10^{-8}	10^{-5}	$10^{-6.5}$	0.08	log beta
Neptunium	5×10^{-6}	10^{-3}*	1.4×10^{-4}	0.20	log beta
Protactinium	10^{-10}	10^{-5}			log uniform
Actinium	10^{-10}	10^{-6}			uniform
Tin	10^{-11}	10^{-7}			uniform
Nickel	10^{-6}	10^{-1}	$10^{-2.7}$	0.25	log beta
Strontium	10^{-6}	10^{-3}	10^{-4}	0.12	log beta
Samarium	10^{-10}	10^{-6}			uniform
Zirconium	10^{-12}	10^{-7}			log uniform
Niobium	10^{-9}	10^{-7}			log uniform

*New data from Efurd et al. (1996).

Table 6.3-5. Plutonium Sorption Distribution Coefficients

Solid Phase	K_d Range in J-13 Water (mL/g)	K_d Range in Synthetic UE-25 p#1 Water (mL/g)
Vitric tuff	600–2,000	100–400
Zeolitic tuff	300–500	100–400
Devitrified tuff	40–100	20–70
Synthetic hematite	> 10,000	> 10,000
Montmorillonite	> 10,000	> 10,000
Clinoptilolite	600–3,000	2,000–5,000
Calcite	200–1,000	100–800
Gibbsite	0–10	10–90
Albite	3–10	< 10
Quartz	< 10	< 10

NOTE: Under Atmospheric Conditions

Table 6.3-6. Solubility and Speciation of Neptunium in Groundwaters at 25°C

Water	pH	Solubility (M)	NpO_2^+	$NpO_2CO_3^-$
J-13	6	5×10^{-3}	90%	10%
	7	1×10^{-4}	45%	55%
	8.5	4×10^{-5}	40%	60%
UE-25 p#1	6	3×10^{-3}	100%	0%
	7	5×10^{-4}	60%	40%
	8.5	7×10^{-6}	0%	100%

Table 6.3-7. Neptunium Sorption in J-13 Water under Oxidizing Conditions

Solid Phase	pH	K_d (mL/g)*
G4-268, devitrified tuff	7	7×10^{-3}
	8.5	-4×10^{-2}
GU3-1405, vitric tuff	7	2×10^{-1}
	8.5	3×10^{-1}
Quartz	7	-1×10^{-1}
	8.5	-2×10^{-1}
Albite	7	-8×10^{-2}
	8.5	-1×10^{-1}

*The uncertainties in the data are ± 0.5.

Table 6.3-8. Prediction of Neptunium Sorption on Clinoptilolite-Rich G4-1510 Tuff in J-13 Water

Initial Concentration (M)	pH	Measured K_a (m)	Predicted K_a (m)*
1×10^{-7} to 3×10^{-5}	7	1×10^{-7}	9×10^{-8}
	8.5	6×10^{-8}	5×10^{-8}

*Assuming clinoptilolite is the only sorbing mineral in the tuff.

Table 6.3-9. Neptunium Sorption onto Clinoptilolite-Rich Tuffs in J-13 Water*

Tuff sample	Measured K_a (m)	Predicted K_a (m)	Clinoptilolite %
G1-1405	1×10^{-7}	1×10^{-7}	68 ± 7
G4-1505	9×10^{-8}	1×10^{-7}	74 ± 7
G4-1506	1×10^{-7}	1×10^{-7}	62 ± 7
G4-1510	8×10^{-8}	1×10^{-7}	59 ± 7
G4-1529	7×10^{-8}	1×10^{-7}	59 ± 8
G4-1625	9×10^{-8}	1×10^{-7}	61 ± 7
G4-1772	1×10^{-7}	1×10^{-7}	63 ± 5
G4-2077	5×10^{-8}	8×10^{-8}	51 ± 8

*Atmospheric conditions; initial neptunium concentrations ranged from 6 to 8×10^{-7} M; tuffs were wet-sieved to particle sizes ranging from 75 to 500 µm; the pretreatment period was 2 to 14 days; and the sorption period was 3 to 23 days.

Table 6.3-10. Uranium Sorption in J-13 Water under Oxidizing Conditions

Solid Phase	pH	K_d (mL/g)*
G4-268, devitrified tuff	7	2×10^{-1}
	8.5	7×10^{-1}
GU3-1405, vitric tuff	7	-5×10^{-1}
	8.5	6×10^{-1}
Quartz	7	1×10^{-1}
	8.5	7×10^{-2}
Albite	7	-5×10^{-2}
	8.5	-1×10^{-1}

*The uncertainties in the data are ± 3.

Table 6.3-11. Prediction of Uranium Sorption on Clinoptilolite-Rich G4-1510 Tuff in J-13 Water

Initial Concentration (M)	pH	Measured K_a (m)	Predicted K_a (m)*
2×10^{-7} to 4×10^{-7}	7	8×10^{-7}	8×10^{-7}
	8.5	8×10^{-7}	4×10^{-7}

*Assuming clinoptilolite is the only sorbing mineral in the tuff.

Table 6.3-12. Minerals in Yucca Mountain Tuff with High Cation Exchange Capacities

Mineral	Maximum Abundance	Capacity (meq/g)
Clinoptilolite	90%	2.3
Mordenite	60%	2.3
Montmorillonite	40%	0.8–1.5
Illite	20%	0.13–0.42

Table 6.3-13. Intrinsic Constants for Metal Oxides

Metal Oxide	log K_{a1}	log K_{a2}	Point of Zero Charge
SiO_2	–0.5	–8.2	4.3
Al_2O_3	–7.8	–11.3	9.3
FeOOH	–7.6	–11.4	8.5

Table 6.3-14. Equations and Parameters Used to Model Neptunium Adsorption Onto Zeolitic Tuff

Type of Reaction	Equilibrium Reactions	log K
Aqueous Reactions:	$NpO_2^+ + H_2O \leftrightarrow NpO_2OH(aq) + H^+$	–10.8
	$NpO_2^+ + 2\ H_2O \leftrightarrow NpO_2(OH)_{2-} + 2\ H^+$	–23.5
	$NpO_2^+ + CO_3^{2-} \leftrightarrow NpO_2CO_{3-}$	4.13
	$HCO_{3-} \leftrightarrow CO_3^{2-} + H^+$	–10.25
	$CO_2(g) + H_2O \leftrightarrow H_2CO_3 \leftrightarrow HCO_{3-} + H^+$	–7.8
Metal-Oxide Surface Protolysis:	$MOH + H^+ \leftrightarrow MOH_2^+$	7.6
	$MOH_2^+ + ClO_{4-} \leftrightarrow MOH_2^+ClO_{4-}$	2.0
	$MOH \leftrightarrow MO^- + H^+$	–11.4
	$MO^- + Na^+ \leftrightarrow MO\text{–}Na^+$	1.2
Neptunyl Adsorption Reactions:	$t\text{-Al–}Na^+ + NpO_2^+ \leftrightarrow t\text{-Al–}NpO_2^+ + Na^+$	2.1
	$MOH + NpO_2^+ \leftrightarrow MONpO_2 + H^+$	–2.2
Extension to Groundwater:	$2\ t\text{-Al–}Na^+ + Ca^{2+} \leftrightarrow t\text{-}Al_2^{2-}Ca^{2+} + 2\ Na^+$	5.0
	$MOH + Ca^{2+} \leftrightarrow MOCa^+ + H^+$	–5.85
	$MOCa^+ + Cl\text{–} \leftrightarrow MOCa^+Cl\text{–}$	2.0

Parameters

Type of Site	Site Density (eq/kg)	Layer	Capacitance (F/m^2)
Tetrahedral(*t*) aluminum	2×10^{-4}	Inner Helmholtz	1.1
Octahedral aluminum (edge)	3×10^{-6}	Outer Helmholtz	0.2

Table 6.3-15. Groundwater Compositions Used for Neptunium Sorption Modeling

Constituent	Concentration (mg/L)		
	J-13 Water	UZ Water	UE-25p #1 Water
Sodium	45	26–70	171
Potassium	5.3	5–16	13.4
Magnesium	1.8	5–21	31.9
Calcium	11.5	27–127	87.8
Silicon	30	72–100	30
Fluoride	2.1	—	3.5
Chloride	6.4	34–106	37
Sulfate	18.1	39–174	129
Bicarbonate	143	—	698
pH	6.9	6.5–7.5	6.7

Table 6.3-16. Additional Equations and Parameters Used to Model Uranium Adsorption Onto Devitrified Tuff

Type of Reaction	Equilibrium Reaction	log *K*
Aqueous Reactions:	$UO_2^{2+} + H_2O \leftrightarrow UO_2OH^+ + H^+$	–5.8
	$UO_2^{2+} + 2\ H_2O \leftrightarrow UO_2(OH)_2 + 2\ H^+$	–12.5
	$2\ UO_2^{2+} + 2\ H2O \leftrightarrow (UO_2)_2(OH)_2^{2+} + 2\ H^+$	–5.62
	$3\ UO_2^{2+} + 5\ H_2O \leftrightarrow (UO_2)_3(OH)_5^+ + 5\ H^+$	–15.63
Uranyl Adsorption Reactions:	$2\ t\text{-}AlNa^+ + UO_2^{2+} \leftrightarrow (t\text{-}Al)_2UO_2^{2+} + 2\ Na^+$	1.8
	$t\text{-}AlNa^+ + UO_2^{2+} + H_2O \leftrightarrow t\text{-}AlUO_2OH^+ + Na^+ + H^+$	–1.5
	$MOH + UO_2^{2+} \leftrightarrow MOUO_2^+ + H^+$	0.60
	$MOH + UO_2^{2+} + Cl^- \leftrightarrow MOUO_2^+Cl^- + H^+$	2.8
	$2\ MOH + UO_2^{2+} \leftrightarrow (MO)_2UO_2 + 2\ H^+$	–2.8
Parameters:	**Type of Site**	**Site Density (eq/kg)**
	Tetrahedral(*t*) aluminum	2×10^{-2}
	Octahedral aluminum (edge)	2×10^{-3}

Table 6.3-17. Sorption-Coefficient Distributions for Unsaturated-Zone Units

Element	Rock Type	Min K_d (mL/g)	Max K_d (mL/g)	E[x]	COV*	Distribution Type
Americium	Devitrified	100	2000			Uniform
	Vitric	100	1000	400	0.20	Beta
	Zeolitic	100	1000			Uniform
	Iron oxide	1000	5000			Uniform
Plutonium	Devitrified	20	200	100	0.25	Beta
	Vitric	50	200	100	0.25	Beta
	Zeolitic	30	200	100	0.25	Beta
	Iron oxide	1000	5000			Uniform
Uranium	Devitrified	0	4.0	2.0	0.3	Beta
	Vitric	0	3.0	1.0	0.3	Beta
	Zeolitic	0	30.0	7.0	1.0	Beta(exp)
	Iron oxide	100	1000			Uniform
Neptunium	Devitrified	0	6.0	1.0	0.3	Beta
	Vitric	0	15.0	1.0	1.0	Beta(exp)
	Zeolitic	0	3.0	0.5	0.25	Beta
	Iron oxide	500	1000			Uniform
Radium	Devitrified	100	500			Uniform
	Vitric	50	100			Uniform
	Zeolitic	1000	5000			Uniform
	Iron oxide	0	500	30	1.0	Beta(exp)
Cesium	Devitrified	20	1000			Uniform
	Vitric	10	100			Uniform
	Zeolitic	500	5000			Uniform
	Iron oxide	0	500	30	1.0	Beta(exp)
Strontium	Devitrified	10	50			Uniform
	Vitric	0	20			Uniform
	Zeolitic	500	2000			Uniform
	Iron oxide	0	30	10	0.25	Beta
Nickel	Devitrified	0	500	100	0.33	Beta
	Vitric	0	100	50	0.33	Beta
	Zeolitic	0	500	100	0.33	Beta
	Iron oxide	0	1000			Uniform
Lead	Devitrified	100	500			Uniform
	Vitric	100	500			Uniform
	Zeolitic	100	500			Uniform
	Iron oxide	100	1000			Uniform
Tin	Devitrified	20	200			Uniform
	Vitric	20	200			Uniform
	Zeolitic	100	300			Uniform
	Iron oxide	0	5000			Uniform
Protactinium	Devitrified	0	100			Uniform
	Vitric	0	100			Uniform
	Zeolitic	0	100			Uniform
	Iron oxide	500	1000			Uniform
Selenium	Devitrified	0	30	3	1.0	Beta(exp)
	Vitric	0	20	3	1.0	Beta(exp)
	Zeolitic	0	15	2	1.0	Beta(exp)
	Iron oxide	0	500	30	1.0	Beta(exp)
Carbon	Iron oxide	10	100			Uniform
Actinium, Niobium, Samarium, Thorium, Zirconium: see Americium						
Chlorine, Technetium, Iodine		0	0			

*Coefficient of variation: COV = s[x]/E[x].

Table 6.3-18. Sorption-Coefficient Distributions for Saturated-Zone Units

Element	Rock Type	Min K_d (mL/g)	Max K_d (mL/g)	E[x]	COV*	Distribution Type
Americium	Devitrified	100	2000			Uniform
	Vitric	100	1000	400	0.20	Beta
	Zeolitic	100	1000			Uniform
	Iron oxide	1000	5000			Uniform
Plutonium	Devitrified	50	300	100	0.15	Beta
	Vitric	50	300	100	0.15	Beta
	Zeolitic	30	300	100	0.15	Beta
	Iron oxide	1000	5000			Uniform
Uranium	Devitrified	0	5.0	2.0	0.3	Uniform
	Vitric	0	4.0	1.0	0.3	Uniform
	Zeolitic	5	20.0	7.0	0.3	Beta
	Iron oxide	100	1000			Uniform
Neptunium	Devitrified	0	10.0	3.0	0.3	Beta
	Vitric	0	15.0	1.5	1.0	Beta(exp)
	Zeolitic	0	12.0	4.0	0.25	Beta
	Iron oxide	500	1000			Uniform
Radium	Devitrified	100	500			Uniform
	Vitric	100	500			Uniform
	Zeolitic	1000	5000			Uniform
	Iron oxide	0	1500	30	1.0	Beta(exp)
Cesium	Devitrified	20	1000			Uniform
	Vitric	10	100			Uniform
	Zeolitic	500	5000			Uniform
	Iron oxide	0	500	30	1.0	Beta(exp)
Strontium	Devitrified	10	200			Uniform
	Vitric	20	50			Uniform
	Zeolitic	2000	5000			Log uniform
	Iron oxide	0	30	10	0.25	Beta
Nickel	Devitrified	0	500	100	0.33	Beta
	Vitric	0	200	100	0.33	Beta
	Zeolitic	0	500	100	0.33	Beta
	Iron oxide	0	1000			Uniform
Lead	Devitrified	100	500			Uniform
	Vitric	100	500			Uniform
	Zeolitic	100	500			Uniform
	Iron oxide	100	1000			Uniform
Tin	Devitrified	20	200			Uniform
	Vitric	20	200			Uniform
	Zeolitic	100	300			Uniform
	Iron oxide	0	5000			Uniform
Protactinium	Devitrified	0	100			Uniform
	Vitric	0	100			Uniform
	Zeolitic	0	100			Uniform
	Iron oxide	500	1000			Uniform
Selenium	Devitrified	0	30	3	1.0	Beta(exp)
	Vitric	0	20	3	1.0	Beta(exp)
	Zeolitic	0	15	2	1.0	Beta(exp)
	Iron oxide	0	500	30	1.0	Beta(exp)
Carbon	Iron oxide	10	100			Uniform
Actinium, Niobium, Samarium, Thorium, Zirconium: see Americium						
Chlorine, Technetium, Iodine		0	0			

*Coefficient of variation: COV = s[x]/E[x].

Table 6.3-19. Comparison of Neptunium K_d Values from Batch and Column Measurements

Column Number	Tuff Sample	Water Type	Batch K_d (mL/g)	Column K_d(mL/g)
1	G4-1508, zeolitic	J-13	1.7 ± 0.4 (G4-1510)	1.7
2	G4-1508, zeolitic	J-13	1.7 ± 0.4 (G4-1510)	1.2
3	G4-1505, zeolitic	J-13	2.1 ± 0.4	2.8
4	G4-1505, zeolitic	Syn. UE-25 p#1	0.2 ± 0.3 (G4-1506)	0.4
5	G4-1505, zeolitic	Syn. UE-25 p#1	0.2 ± 0.3 (G4-1506)	0.2
6	G4-1505, zeolitic	Syn. UE-25 p#1	0.2 ± 0.3 (G4-1506)	0.2
7	G4-268, devitrified	J-13	–0.04 ± 0.2	0.07
8	G4-268, devitrified	J-13	–0.04 ± 0.2	0.01
9	G4-268, devitrified	J-13	–0.04 ± 0.2	0.02
10	G4-268, devitrified	J-13	–0.04 ± 0.2	0.01
11	G4-272, devitrified	Syn. UE-25 p#1	0.2 ± 0.3 (G4-270)	0.06
12	G4-268, devitrified	Syn. UE-25 p#1	0.2 ± 0.3 (G4-270)	0.03
13	G4-268, devitrified	Syn. UE-25 p#1	0.2 ± 0.3 (G4-270)	0.03
14	GU3-1407, vitric	J-13	0.1 ± 0.5	0.2
15	GU3-1407, vitric	J-13	0.1 ± 0.5	0.1
16	GU3-1405, vitric	J-13	0.03 ± 0.2	0.1
17	GU3-1405, vitric	Syn. UE-25 p#1	0.2 ± 0.4 (GU3-1407)	0.1
18	GU3-1405, vitric	Syn. UE-25 p#1	0.2 ± 0.4 (GU3-1407)	0.1
19	GU3-1405, vitric	Syn. UE-25 p#1	0.2 ± 0.4 (GU3-1407)	0.1

Table 6.3-20. Selenium Batch Adsorption on Nonwelded Zeolitic Tuff*

Pretreatment Period (days)	Sorption period (days)	K_d (mL/g)
6.9	0.04	–0.2
6.9	0.04	0.3
6.8	13.9	0.0
6.8	13.9	0.2

*Experimental conditions: J-13 water; 20°C; 75-500 μm tuff particle sizes; 1.1 ppm initial selenium concentration; solution pH after sorption of 8.4; and samples from the same location in G-Tunnel, Bed-5, as the tuff used in the column experiments.

Table 6.3-21. Minerals Coating Fracture Walls in Yucca Mountain Tuffs

Zeolites		
Heulandite ↔ Clinoptilolite	$Ca_4Al_8Si_{28}O_{72}\cdot 24H_2O \leftrightarrow (Na, K)_6Al_6Si_{30}O_{72}\cdot 24H_2O$	
(range of compositions with arbitrary division of Si/Al < 4.4 for heulandite and Si/Al > 4.4 for clinoptilolite)		
Mordenite	$(Ca,Na_2,K_2)_4Al_8Si_{40}O_{96}\cdot 28H_2O$	
Analcime	$NaAlSi_2O_6\cdot H_2O$	
Chabazite	$CaAl_2Si_4O_{12}\cdot 6H_2O$	
Phillipsite	$(K_2,Na_2,Ca)Al_2Si_4O_{12}\cdot 4–5H_2O$	
Erionite	$(Ca,Na_2,K_2)_4Al_8Si_{28}O_{72}\cdot 27H_2O$	
Stellerite	$CaAl_2Si_7O_{18}\cdot 7H_2O$	
Silica		
Quartz	SiO_2—low-temperature polymorph of silica	
Tridymite	SiO_2—high-temperature polymorph of silica	
Cristobalite	SiO_2—highest-temperature polymorph of silica	
Opal	$SiO_2\cdot nH_2O$	
Feldspars		
Plagioclase (albite)	Solid solutions of albite ($NaAlSi_3O_8$) and anorthite ($CaAl_2Si_2O_8$)	
K-feldspar (sanidine)	Solid solutions of orthoclase ($KAlSi_3O_8$) and albite ($NaAlSi_3O_8$)	
Clays		
Smectite family:		
Dioctahedral (montmorillonite)	$(Na,K,Mg_{0.5},Ca_{0.5},\text{possibly others})_{0.33}Al_{1.67}Mg_{0.33}Si_4O_{10}(OH)_2\cdot nH_2O$	
Trioctahedral (saponite)	$(Ca_{0.5},Na)_{0.33}(Mg,Fe)_3(Si_{3.67}Al_{0.33})O_{10}(OH)_2\cdot 4H_2O$	
Sepiolite	$Mg_4(Si_2O_5)_3(OH)_2\cdot 6H_2O$	
Palygorskite	$(Mg,Al)_2Si_4O_{10}(OH)\cdot 4H_2O$	
Illite	$(H_3O,K)_y(Al_4Fe_4Mg_4Mg_6)(Si_{8-y}Al_y)O_{20}(OH)_4$	
Manganese Oxides/Hydroxides		
Pyrolusite	MnO_2	(1x1 tunnel structure)
Cryptomelane family:	$A_{0-2}(Mn^{4+},Mn^{3+})_8(O,OH)_{16}$	(2x2 tunnel structure)
Cryptomelane	A = K	
Hollandite	A = Ba	
Coronadite	A = Pb	
Romanechite	$(Ba,H_2O)_2Mn_5O_{10}$	(2x3 tunnel structure)
Todorokite	$(Na,Ca,Ba,Sr)_{0.3–0.7}(Mn,Mg,Al)_6O_{12}\cdot 3.2–4.5H_2O$	(3x3 tunnel structure)
Aurorite	(Mn2+,Ag,Ca)Mn3O7·3H2O	
Lithiophorite	$m\{Al_{0.5}Li_{0.5}MnO_2(OH)_2\}\cdot n\{Al_{0.667}(Mn^{4+},Co,Ni,Mn^{2+})O_2(OH)_2\}\cdot pH_2O$	
Rancieite	$(Ca,Mn^{2+})(Mn^{4+})_4O_9\cdot 3H_2O$	
Iron Oxides/Hydroxides		
Hematite	Fe_2O_3	
Magnetite	$(Fe,Mg)Fe_2O_4$	
Carbonates		
Calcite	$CaCO_3$	
Halides		
Fluorite	CaF_2	

Table 6.3-22. Characteristics of Fractured Devitrified-Tuff Columns

Column #1	Column #2	Column #3	Column #4
Tuff Type			
G1-1941	UE-25 UZ-16 919	G4-2981	G4-2954
SMF Number			
N/A	0029365	0029366	0029368
Major Minerals in Tuff Matrix			
Alkali Feldspar and Quartz	Alkali Feldspar and Quartz	Alkali Feldspar and Opal CT	Alkali Feldspar and Opal CT
Minerals Coating the Fracture			
None (apparent induced fracture)	Stellerite Magnetite	Hollandite Romanechite	Hollandite Romanechite
Water Type			
Synthetic J-13	Synthetic UE-25p #1	Synthetic J-13	Synthetic J-13
pH			
8.6	8.8	8.6	8.6
Concentration of ^{237}Np (M)			
1.4×10^{-5}	4.8×10^{-6}	1.4×10^{-5}	1.4×10^{-5}
Length (cm)			
12.6	6.1	6.0	To be determined
Diameter (cm)			
6.1	5.2	5.2	To be determined
Fracture Aperture			
To be determined	To be determined	To be determined	To be determined
Porosity			
To be determined	To be determined	To be determined	To be determined
Volumetric Flow Rate (mL/hr)			
0.5	0.5	0.5	0.5

Table 6.3-23. Batch-Sorption Results for ^{237}Np in J-13 Well Water

Major Mineral in Solid Phase	K_d (mL/g)	Solid-Phase Composition*
Stellerite	~ 0	N/A
Hollandite	700	100% Hollandite
Romanechite	600	N/A
Magnetite	7	85% Magnetite 12% Hematite 3% Goethite

*Determined by x-ray-diffraction analysis.

Table 6.3-24. Rock-Beaker Diffusion Results for Nonsorbing Radioisotopes and Devitrified Tuffs

Tuff Sample	Major Minerals	Diffusion Coefficient, d (cm^2/s)		
		Porosity	HTO	TcO_4^-
G4-737	Alkali feldspar 68% Cristobalite 28%	0.07	2.2×10^{-6}	3.9×10^{-7}
GU3-304 #1 GU3-304 #2	Alkali feldspar 75% Cristobalite 25%	0.06	1.5×10^{-6} 1.6 x 10–6	3.0×10^{-7} 3.0 x 10–7
GU3-433	Alkali feldspar 76% Cristobalite 15%	0.10	3.5×10^{-6}	
GU3-1119	Alkali feldspar 70% Quartz 19%	0.10	2.0×10^{-6}	4.9×10^{-7}
Topopah outcrop	Alkali feldspar 59% Cristobalite 23% Quartz 12%	0.07	1.0×10^{-6}	1.0×10^{-7}

Table 6.3-25. Batch Sorption Coefficients for Devitrified Tuffs

Tuff Sample	Major Minerals	Sorption Coefficient, K_d (mL/g)				
		Np	Am	Cs	Sr	Ba
G4-737	Alkali feldspar 68% Cristobalite 28%	8	134	532	52	28
GU3-304	Alkali feldspar 75% Cristobalite 25%	8		342	18	19
GU3-433	Alkali feldspar 76% Cristobalite 15%	9	154	1264	20	61
GU3-1119	Alkali feldspar 70% Quartz 19%	8	136	494	42	27
Topopah outcrop	Alkali feldspar 59% Cristobalite 23% Quartz 12%	9		465	20	25

Table 6.3-26. Dimensions of Diffusion Cells

Diameter of Tuff slab	6 cm
Length of tuff slab	1 cm
Volume of traced chamber	750 cm^3
Volume of untraced chamber	80 cm^3

Table 6.3-27. Rock Composition in Water-Conducting Features.

Site	Rock	Quartz	Feldspar	Biotite	Clay	Calcite	Zeolite	Organic
Transitgas Tunnel	S.-Aare Granite	X	X	X	(X)	—	—	—
Grimsel Test Site	Mylonite Granite	X	X	X	(X)	—	—	—
Leuggren	Conderite Granite	X	X	X	(X)	—	—	—
Äspö	Granite	X	X	X	(X)	—	—	—
Yucca Mountain	Tuff	X	X	—	—	—	X	—
Morro de Ferro	Phonolite	X	X	—	(X)	—	—	—
Gorleben	Marl Sand	X	—	—	X	X	—	X
Wellenberg	Marl	X	—	—	X	X	—	(X)
Bagombé	Pelite Sandstone	X	—	—	X	X	—	(X)
Markham	Marl Sandstone	X	—	—	X	(X)	—	—

NOTE: X represents more than 10% of the weight; (X) more than 2% but less than 10%.

Table 6.3-28. Hydrochemical Properties of Studied Groundwaters

Sources	Transitgas-Tunnel			Menzen-schwand	Bad Säckingen	Grimsel Test Site	Zurach	Leuggern
	Zone 3	Zone 1	Zone 2					
Water type	$Ca\text{-}HCO_3$	$Na\text{-}Ca\text{-}SO_4\text{-}HCO_3$	$Na\text{-}SO_4$	$Ca\text{-}Na\text{-}HCO_3$	Na-Cl	$Na\text{-}Ca\text{-}HCO_3\text{-}F$	$Na\text{-}SO_4\text{-}HCO_3\text{-}Cl$	$Na\text{-}SO_4\text{-}HCO_3\text{-}Cl$
pH	9.2	8-9	9.2	6.5	6.5	9.6	8	7.8
pe	+6	+6	0	+6	+6	-3	-3	-3
pNa	4.5	4.5-4.1	2.6-2.3	3.9	1.3	3.2	1.9	1.9
pCa	3.4	3.9-3.5	4.2-3.8	3.4	2.4	3.9	3.4	3.6
T&Tgeo/°C	4&2	6&5	22&90	12&13	29&50	12&13	39&45	66&66

NOTE: pX signifies the negative log of the concentration of X, and pe ~ Eh.

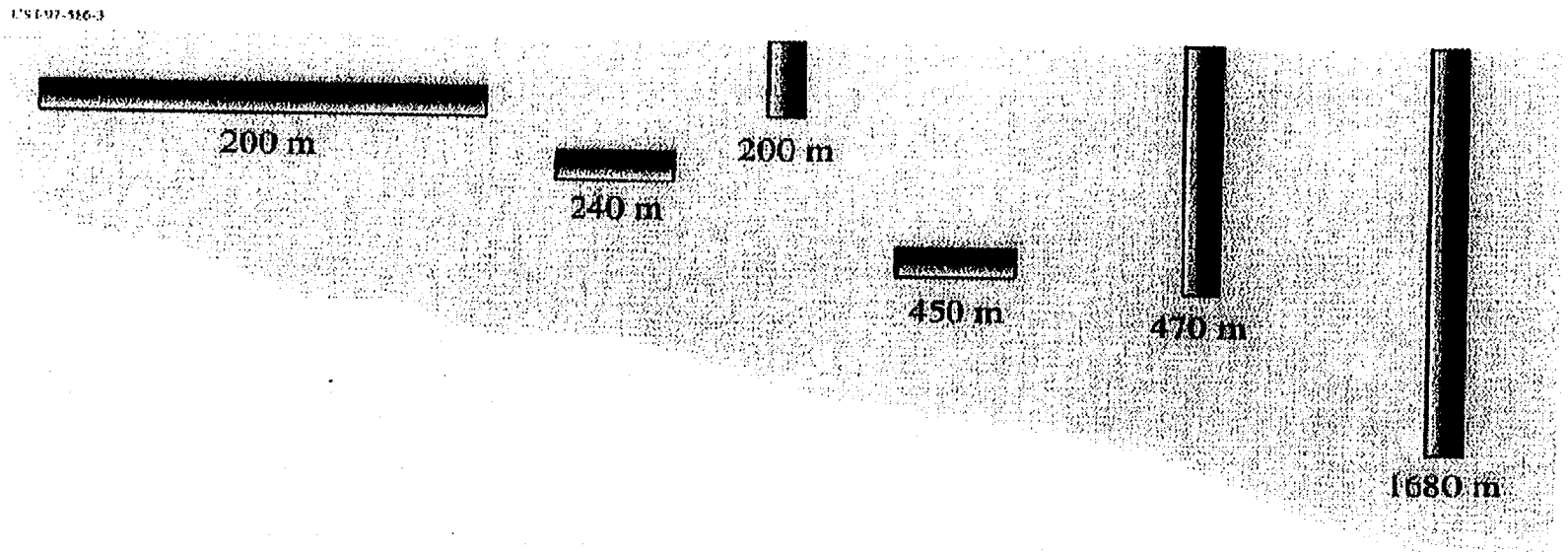

Table 6.3-28. Hydrochemical Properties of Studied Groundwaters (Continued)

Site	Äspö S	Whiteshell CD	Morro BZ	Yucca USA	Wellenberg CH	Gorleben D	Cigar Lake CD	Bagombé GA	Markham UK
Water	Na-Ca-HCO_3	Na-Ca-Cl	K-So_4-F	Na-HCO_3-$Si0_2$	Na-HCO_3	Na-HCO_3-OC	Na-HCO_3	Na-Ca-Mg-HCO_3	Mg-HCO_3
pH	7.5	8.9	6.1	6.9	8.5	8.8 8.3	6.5	5.9 6.2	7.8
pe	-4	--	+1	+6	-5.2	0 -1	--	0 +2	+7
pAlk	1.5	0.4	3.5	2.7	1.7	2.1 2.5	3.0	3.5 4.3	3.6
pEAlk	2.0	0.7	4.3	3.4	4.1	4.1 3.6	3.3	4.1 3.7	2.8
pOC	3.7	--	4.4	--	4.2	2.7 2.5	3.0	-- --	--

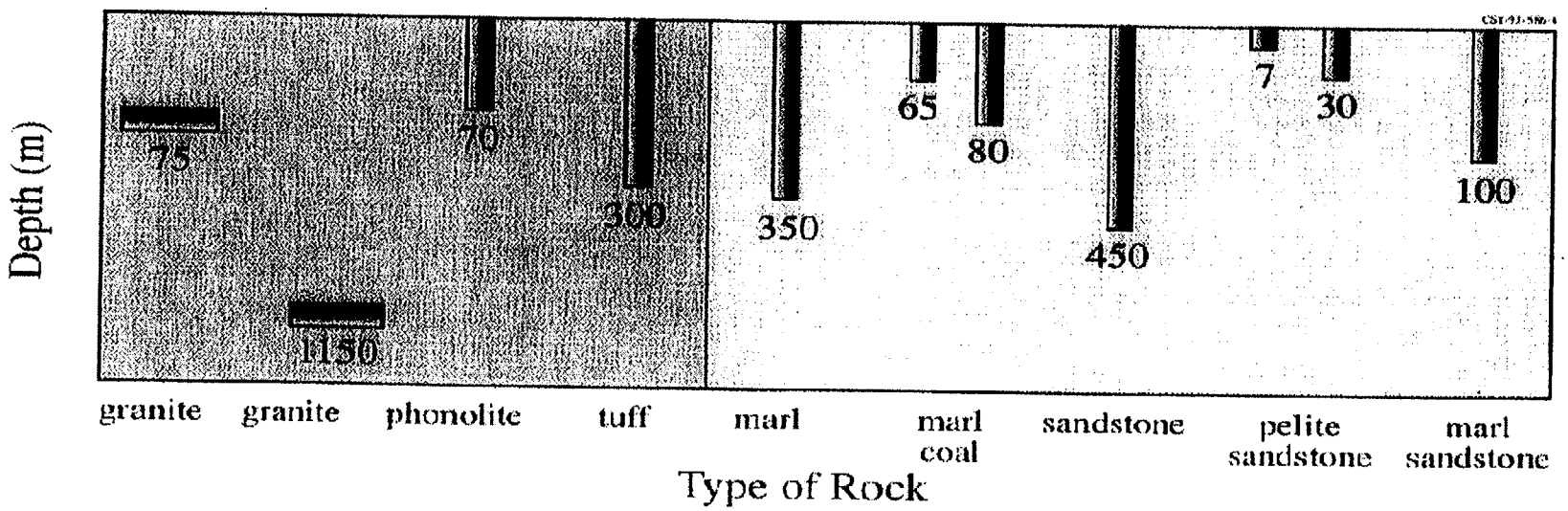

Table 6.3-29. Percentage of ^{239}Pu Adsorbed onto Hematite Colloids in Natural Groundwater and Synthetic Groundwater

Time (min)	Fe_2O_3 J-13 Pu(V) %	Fe_2O_3 J-13 Pu(IV) %	Fe_2O_3 Syn. J-13 Pu(V) %	Fe_2O_3 Syn. J-13 Pu(IV) %
10	43.5	56.9	81.8	65.9
30	45.2	58.8	84.2	66.0
60	48.1	59.7	83.3	65.6
240	54.7	59.7	87.2	65.5
360	59.0	59.7	86.9	65.8
1440	70.4	59.7	86.7	65.5
2880	73.5	59.8	87.1	65.8
5760	76.4	60.3	86.9	65.8

Table 6.3-30. Percentage of ^{239}Pu Adsorbed onto Geothite Colloids in Natural Groundwater and Synthetic Groundwater

Time (min)	FeOOH J-13 Pu(V) %	FeOOH J-13 Pu(IV) %	FeOOH Syn. J-13 Pu(V) %	FeOOH Syn. J-13 Pu(IV) %
10	19.2	28.5	63.3	34.2
30	20.5	31.0	63.0	36.9
60	23.5	45.1	63.8	48.0
240	35.6	40.3	68.4	48.0
360	40.5	38.9	70.0	52.6
1440	53.2	37.2	74.2	52.2
2880	58.6	39.2	74.8	49.4
5760	61.8	34.4	74.1	52.8

INTENTIONALLY LEFT BLANK

Table 6.4-1. Unique Zeolite Sequences in Fractures in Drillhole UE-25a #1 and USW GU-3, Yucca Mountain, Nevada

Sample*	Depth (m)	Smectite	Clinoptilolite	Mordenite	Erionite	Phillipsite
UE-25a #1						
1252.3	381.6	Trace	Minor	Major	X	X
1274.5	388.4	Major	Major	Trace	X	X
1276.0/1276.2	388.9	Major	Minor	Minor	X	X
1282.6	390.9	Major	Major	Trace	X	X
1296.2	395.1	Minor	Major	X	Major	X
1301.5/1302.0	396.6	Minor	Major	X	X	Major
1309.0/1309.2	399.0	Minor	Major	X	X	X
1318.4/1319.5	402.0	Trace	Major	Minor	X	X
1322.9/1323.2	403.2	Minor	Major	Minor	X	X
1339.5/1339.7	408.3	Minor	Major	Major	X	X
1361.8/1362.0	415.1	Minor	Major	Minor	X	X
USW GU-3						
1162.7/1163.0	354.5	Major	X	Minor	X	X
1189.3/1189.6	362.4	Minor	Major	X	Minor	X
1200.1/1200.6	365.7	Minor	Minor	X	X	Major
1210.2/1210.6	368.8	Major	X	Trace	X	X
1232.0/1232.1	375.5	Major	X	X	X	X

*Sample label is equivalent to the sample depth in feet.

Major = Major phases compose greater than ~70% of the sample.
Minor = minor phases compose less than ~30% of the sample.
Trace = trace phases compose less than ~5% of the sample.
X = not detected.

Table 6.4-2. Summary of the Potential Risk Posed by Minerals at Yucca Mountain

Mineral	Data for Carcinogenicity[b]		Ranking by IARC[a]	Concern at Yucca Mountain
	Humans	Animals		
quartz	S	S	Group 1	Yes
cristobalite	S	S	Group 1	Yes
tridymite	L	S	Group 2A	Yes
opal-CT	(L)	(S)	NL (Group 3)	Yes
glass[c]				No
amorphous silica	I	I	Group 3	
glasswool	I	S	Group 2B	
erionite	S	S	Group 1	Yes
mordenite	(ND)	(I)	Group 3	Yes
clinoptilolite/heulandite	(ND)	(I)	Group 3	No
chabazite	(ND)	(ND)	NL (Group 3)	No
stellerite	(ND)	(ND)	NL (Group 3)	No
phillipsite	(ND)	(ND[f])	Group 3	No
palygorskite[d]	I	L	Group 2B	Yes
sepiolite	I	I	Group 3	Yes
smectite	(I)	(I)	NL (Group 3)	No
mica	(I)	(I)	NL (Group 3)	No
kaolinite	L	L	NL (Group 3)	No
feldspar	(I)	(I)	NL (Group 3)	No
hematite	I	I/ESL[e]	Group 3[e]	No
fluorite	(ND)	(ND)	NL (Group 3)	No
calcite	(I)	(I)	NL (Group 3)	No
Mn-oxides	(I)	(I)	NL (Group 3)	No

a. Described in the text. Data taken from IARC monographs 1 (1971), 42 (1987b), 43 (1988), 68 (1997), and IARC *Supplement 7* (1987a). "NL" indicates that the mineral was not listed by an IARC monograph through Vol. 54 (1992). Data in parentheses represent our evaluations using the criteria outlined in IARC *Supplement 7* (1987a).

b. "ND" indicates no data; "ESL" indicates evidence suggesting lack of carcinogenicity; "I" indicates inadequate; "L" indicates limited; "S" indicates sufficient. Data taken from IARC monographs 1 (1971), 42 (1987b), and 43 (1988), and IARC *Supplement 7* (1987a). Data in parentheses represent our evaluations using the criteria outlined in IARC *Supplement 7* (1987a).

c. "Glass" can be bracketed by amorphous silica and glass wool.

d. Long-fiber (> 5 ?m) palygorskite is listed as group 2B, whereas short-fiber (< 5 ?m) palygorskite is listed as group 3 by the IARC monographs.

e. *Supplement 7* (IARC 1987a) lists hematite at "I" for animal data and lists ferric oxide as "ESL." There is no discussion regarding the difference between ferric oxide and hematite, although hematite is ferric oxide. Although hematite is listed as Group 3 in *Supplement 7* (IARC 1987a), a combined hematite + radon exposure during underground mining is listed as Group 1.

f. No study has been published in the western literature on phillipsite carcinogenicity. See text.

Table 6.4-3. Estimated Rates of Mesothelioma in Three Turkish Villages Based on Measured Zeolite Fiber Levels and an Asbestos Exposure Model

Village:	Karain	Tuzköy	Sarihidir
Fibers/mL:	0.0016–0.0080	0.004–0.021	0.0006–0.0174
Rate, age 50:	0.02–0.10	0.05–0.26%	0.01–0.22%
Rate, age 60:	0.04–0.21%	0.10–0.54%	0.02–0.45%
Rate, age 70:	0.08–0.38%	0.19–1.00%	0.03–0.84%
Observed rate:	1.1%	0.4%	0.1%

Table 6.4-4. Quantitative XRD Results for Samples from Drill Core USW UZ-14

Sample	LANL #	Depth (m)	Smectite	Erionite	Clino-ptilolite	Mor-denite	Opal-CT	Quartz	Feld-spar	Glass	Mica	Total	Comments
Topopah Spring Tuff			78.8–428.0 m										
1277.4/1277.7	#1619p1	389.4	15 ± 5	—	58 ± 5	—	20 ± 5	1 ± 1	6 ± 1	—	Tr.	100 ± 9	Al Yang Sample
Vitrophyre Subzone			389.9–409.7 m										
1298.6/1299.1	#1876p1	396.0	50 ± 15	—	32 ± 2	—	9 ± 2	2 ± 1	7 ± 1	—	Tr.	100 ± 15	
Moderately Welded Subzone			409.7–421.5 m										
1358.6/1358.8	#1714p1	414.2	4 ± 1	—	3 ± 1	—	1 ± 1	1 ± 1	3 ± 1	88 ± 2	Tr.	100 ± 2	
1361.8/1361.9	#1877p1	415.1	8 ± 2	2 ± 1	4 ± 1	—	—	5 ± 1	13 ± 2	64 ± 3	Tr.	100 ± 3	Cristobalite 4 ± 1
1362.6/1363.0	#1878p1	415.4	22 ± 7	17 ± 3	10 ± 1	—	—	1 ± 1	6 ± 1	44 ± 8	—	100 ± 8	
1364.4/1364.6	#1715p1	415.9	9 ± 3	34 ± 7	23 ± 2	—	—	1 ± 1	12 ± 2	21 ± 8	Tr.	100 ± 8	
1365.8/1366.0	#1716p1	416.4	5 ± 2	17 ± 3	37 ± 3	—	17 ± 4	4 ± 1	8 ± 1	12 ± 6	Tr.	100 ± 6	
1370.1/1370.3	#1717p1	417.7	11 ± 3	5 ± 1	23 ± 2	—	10 ± 2	1 ± 1	8 ± 1	42 ± 4	—	100 ± 4	
1370.3/1370.7	#1657p1	417.8	17 ± 5	7 ± 1	14 ± 1	—	3 ± 1	1 ± 1	4 ± 1	54 ± 5	Tr.	100 ± 5	
1371.8/1372.0	#1718p1	418.2	14 ± 4	2 ± 1	7 ± 1	—	4 ± 1	1 ± 1	3 ± 1	69 ± 5	—	100 ± 5	
1372.7/1372.9	#1879p1	418.5	8 ± 2	Tr.	19 ± 1	—	6 ± 1	1 ± 1	4 ± 1	62 ± 3	Tr.	100 ± 3	
1375.2/1375.4	#1720p1	419.2	5 ± 2	—	8 ± 1	—	3 ± 1	1 ± 1	4 ± 1	79 ± 3	Tr.	100 ± 3	
Non- to Partially Welded Subzone			421.5–428.0 m										
1387.0/1387.2	#1726p1	422.8	3 ± 1	—	14 ± 1	—	3 ± 1	Tr.	4 ± 1	76 ± 2	Tr.	100 ± 2	
1398.5/1398.7	#1732p1	426.3	1 ± 1	—	77 ± 6	1 ± 1	12 ± 3	3 ± 1	9 ± 2	—	Tr.	103 ± 7	
Calico Hills Formation			428.0 m–bottom										
1414.9/1415.1	#1739p1	431.3	2 ± 1	—	66 ± 5	1 ± 1	14 ± 4	5 ± 1	11 ± 2	—	Tr.	99 ± 7	
1417.6/1417.8	#1746p1	432.1	2 ± 1	—	65 ± 5	1 ± 1	13 ± 3	6 ± 1	12 ± 3	—	Tr.	99 ± 7	
Bottom of Drillhole			437.3 m										

Table 6.4-5. Alkali and Alkaline-Earth Elements in Samples from USW UZ-14

	Na_2O (%)	K_2O (%)	CaO (%)	Rb (µg/g)	Sr (µg/g)	Ca (µg/g)	Ba (µg/g)
vitrophyre	2.81	4.60	0.80	177	136	11	45
smectite	0.13	0.26	2.70	22	488	19	14
erionite/ heulandite	0.70	2.13	4.20	143	625	29	43

INTENTIONALLY LEFT BLANK